

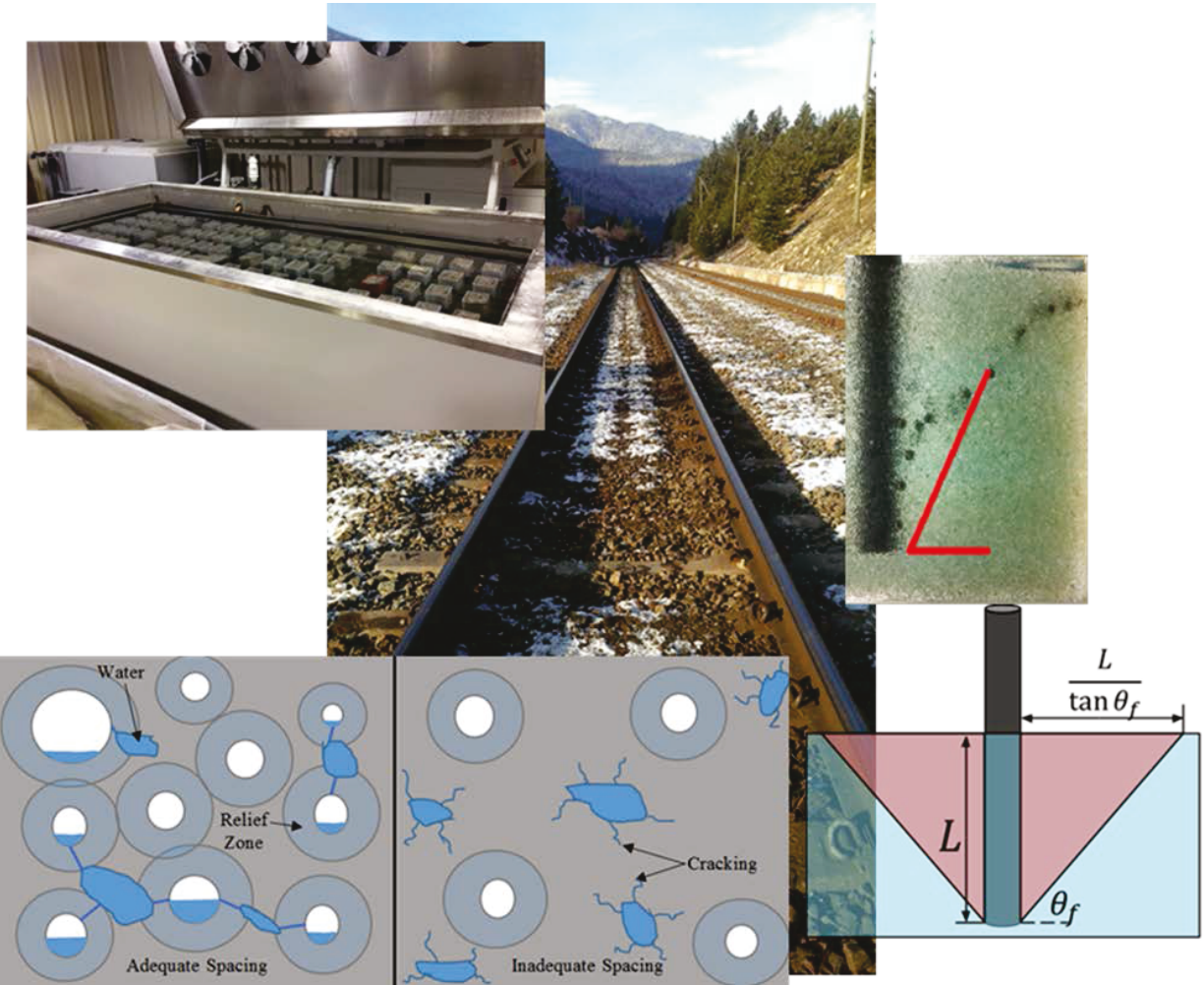


U.S. Department of
Transportation

Federal Railroad
Administration

Material and Manufacturing Requirements for Freeze-Thaw Durable Concrete Railroad Ties: Volume II

Office of Research,
Development
and Technology
Washington, DC 20590



NOTICE

This document is disseminated under the sponsorship of the Department of Transportation in the interest of information exchange. The United States Government assumes no liability for its contents or use thereof. Any opinions, findings and conclusions, or recommendations expressed in this material do not necessarily reflect the views or policies of the United States Government, nor does mention of trade names, commercial products, or organizations imply endorsement by the United States Government. The United States Government assumes no liability for the content or use of the material contained in this document.

NOTICE

The United States Government does not endorse products or manufacturers. Trade or manufacturers' names appear herein solely because they are considered essential to the objective of this report.

REPORT DOCUMENTATION PAGE*Form Approved*
OMB No. 0704-0188

Public reporting burden for this collection of information is estimated to average 1 hour per response, including the time for reviewing instructions, searching existing data sources, gathering and maintaining the data needed, and completing and reviewing the collection of information. Send comments regarding this burden estimate or any other aspect of this collection of information, including suggestions for reducing this burden, to Washington Headquarters Services, Directorate for Information Operations and Reports, 1215 Jefferson Davis Highway, Suite 1204, Arlington, VA 22202-4302, and to the Office of Management and Budget, Paperwork Reduction Project (0704-0188), Washington, DC 20503.

1. AGENCY USE ONLY (Leave blank)		2. REPORT DATE August 2018	3. REPORT TYPE AND DATES COVERED Technical Report	
4. TITLE AND SUBTITLE Material and Manufacturing Requirements for Freeze-Thaw Durable Concrete Railroad Ties: Volume II			5. FUNDING NUMBERS DTFR53-12-C-00026	
6. AUTHOR(S) Kyle A. Riding, David A. Lange, Daniel Castaneda, Jeremy Koch, Mohammed Albahtiti, Ahmad Ghadban, Yu Song, and Ruofei Zou, Naga Bodapati, Robert Peterman, B. Terry Beck				
7. PERFORMING ORGANIZATION NAME(S) AND ADDRESS(ES) Kansas State University 2118 Fiedler Hall Manhattan, KS 66506			8. PERFORMING ORGANIZATION REPORT NUMBER	
9. SPONSORING/MONITORING AGENCY NAME(S) AND ADDRESS(ES) U.S. Department of Transportation Federal Railroad Administration Office of Railroad Policy and Development Office of Research, Development and Technology Washington, DC 20590			10. SPONSORING/MONITORING AGENCY REPORT NUMBER DOT/FRA/ORD-18/31	
11. SUPPLEMENTARY NOTES COR: Cameron D. Stuart				
12a. DISTRIBUTION/AVAILABILITY STATEMENT This document is available to the public through the FRA Web site at http://www.fra.dot.gov .			12b. DISTRIBUTION CODE	
13. ABSTRACT (Maximum 200 words) This study was performed to determine the effects of vibration on concrete air voids and freeze-thaw durability, and applicable freeze-thaw quality control tests. Volume I of the research provided a summary of project findings and recommendations, while Volume II contains a detailed description of project methods, results, and findings. During this study, a fundamental understanding of vibration transmission for immersion vibrators was developed, leading to improvements of models of concrete rheology and vibration transmission. Vibration intensity was shown to have a positive correlation with air loss and increased spacing factor. Total air content before and after vibration was not found to correlate with freeze-thaw durability of vibrated concrete. Spacing factor after vibration was found to be a good quality control parameter for concrete acceptance for freeze-thaw durability, but not rejection. It was found that excising samples from pre-stressed concrete by saw-cutting may induce micro-cracking, and therefore should be avoided in quality control protocols. It was also found that the concrete tie surface could become critically saturated in the field and cause progressive damage and mass loss, especially on the tie sides and bottom.				
14. SUBJECT TERMS Concrete consolidation, air void system, freeze-thaw durability, concrete crossties, vibration			15. NUMBER OF PAGES 322	
			16. PRICE CODE	
17. SECURITY CLASSIFICATION OF REPORT Unclassified	18. SECURITY CLASSIFICATION OF THIS PAGE Unclassified	19. SECURITY CLASSIFICATION OF ABSTRACT Unclassified	20. LIMITATION OF ABSTRACT	

NSN 7540-01-280-5500

Standard Form 298 (Rev. 2-89)
Prescribed by
ANSI Std. Z39-18
298-102

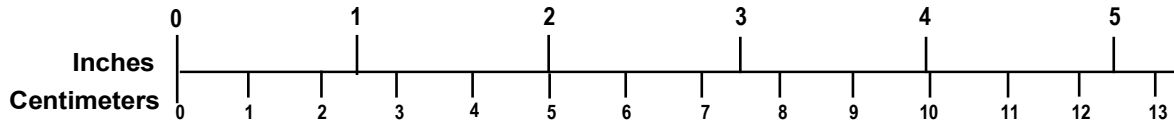
METRIC/ENGLISH CONVERSION FACTORS

ENGLISH TO METRIC

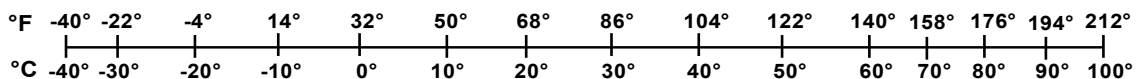
METRIC TO ENGLISH

<p>LENGTH (APPROXIMATE)</p> <p>1 inch (in) = 2.5 centimeters (cm) 1 foot (ft) = 30 centimeters (cm) 1 yard (yd) = 0.9 meter (m) 1 mile (mi) = 1.6 kilometers (km)</p>	<p>LENGTH (APPROXIMATE)</p> <p>1 millimeter (mm) = 0.04 inch (in) 1 centimeter (cm) = 0.4 inch (in) 1 meter (m) = 3.3 feet (ft) 1 meter (m) = 1.1 yards (yd) 1 kilometer (km) = 0.6 mile (mi)</p>
<p>AREA (APPROXIMATE)</p> <p>1 square inch (sq in, in²) = 6.5 square centimeters (cm²) 1 square foot (sq ft, ft²) = 0.09 square meter (m²) 1 square yard (sq yd, yd²) = 0.8 square meter (m²) 1 square mile (sq mi, mi²) = 2.6 square kilometers (km²) 1 acre = 0.4 hectare (he) = 4,000 square meters (m²)</p>	<p>AREA (APPROXIMATE)</p> <p>1 square centimeter (cm²) = 0.16 square inch (sq in, in²) 1 square meter (m²) = 1.2 square yards (sq yd, yd²) 1 square kilometer (km²) = 0.4 square mile (sq mi, mi²) 10,000 square meters (m²) = 1 hectare (ha) = 2.5 acres</p>
<p>MASS - WEIGHT (APPROXIMATE)</p> <p>1 ounce (oz) = 28 grams (gm) 1 pound (lb) = 0.45 kilogram (kg) 1 short ton = 2,000 pounds (lb) = 0.9 tonne (t)</p>	<p>MASS - WEIGHT (APPROXIMATE)</p> <p>1 gram (gm) = 0.036 ounce (oz) 1 kilogram (kg) = 2.2 pounds (lb) 1 tonne (t) = 1,000 kilograms (kg) = 1.1 short tons</p>
<p>VOLUME (APPROXIMATE)</p> <p>1 teaspoon (tsp) = 5 milliliters (ml) 1 tablespoon (tbsp) = 15 milliliters (ml) 1 fluid ounce (fl oz) = 30 milliliters (ml) 1 cup (c) = 0.24 liter (l) 1 pint (pt) = 0.47 liter (l) 1 quart (qt) = 0.96 liter (l) 1 gallon (gal) = 3.8 liters (l) 1 cubic foot (cu ft, ft³) = 0.03 cubic meter (m³) 1 cubic yard (cu yd, yd³) = 0.76 cubic meter (m³)</p>	<p>VOLUME (APPROXIMATE)</p> <p>1 milliliter (ml) = 0.03 fluid ounce (fl oz) 1 liter (l) = 2.1 pints (pt) 1 liter (l) = 1.06 quarts (qt) 1 liter (l) = 0.26 gallon (gal) 1 cubic meter (m³) = 36 cubic feet (cu ft, ft³) 1 cubic meter (m³) = 1.3 cubic yards (cu yd, yd³)</p>
<p>TEMPERATURE (EXACT)</p> <p>$[(x-32)(5/9)] \text{ } ^\circ\text{F} = y \text{ } ^\circ\text{C}$</p>	<p>TEMPERATURE (EXACT)</p> <p>$[(9/5) y + 32] \text{ } ^\circ\text{C} = x \text{ } ^\circ\text{F}$</p>

QUICK INCH - CENTIMETER LENGTH CONVERSION



QUICK FAHRENHEIT - CELSIUS TEMPERATURE CONVERSION



For more exact and or other conversion factors, see NIST Miscellaneous Publication 286, Units of Weights and Measures. Price \$2.50 SD Catalog No. C13 10286

Updated 6/17/98

Acknowledgements

This project was performed with the cooperation of industry partners CXT Concrete Ties Inc., voestalpine Nortrak, and Canadian National Railway. The assistance of Jim Parsley, Steve Mattson, Tara Ross, and Nigel Peters is gratefully acknowledged. We also acknowledge assistance from researchers at the University of British Columbia who helped with data retrieval from sensors installed in track at Lytton, BC. Professors Gord Lovegrove and Ahmad Rteil, and students Trevor Billows and Kyle Stratton assisted in that effort. We appreciate the assistance of Tim Crouch, a volunteer at the Monticello Railway Museum, who helped us install sensors in track at their facility in Monticello, IL.

Contents

Chapter 1 – Organization of Volume II	1
Chapter 2 – Rheology and Fluid Mechanics.....	2
2.1 The Importance of Rheology.....	2
2.2 Air Bubble Rise in Newtonian and Non-Newtonian Fluids.....	4
2.3 Granular Solids, Liquids, and Gases	5
2.4 Conclusions	8
Chapter 3 – Experimental Evidence for a Concrete Rheological Model.....	9
3.1 Introduction and Background.....	9
3.2 Description of Concrete, Mortar, and Surrogate Materials	10
3.3 Rheological Behavior of Surrogate Systems – Results	13
3.4 Conclusions from Experimental Work.....	16
3.5 Practical Implication of Concrete as a Granular Material: “Cone of Action”.....	17
3.6 Development of the Bubble Rise Model	19
3.7 Conclusions	28
Chapter 4 – Influence of Vibration in Portland Cementitious Materials and Model Materials....	30
4.1 The Practice of Concrete Vibration.....	30
4.2 Significance of Research	33
4.3 Experimental Methods	33
4.4 Experimental Results and Discussion	36
4.5 Conclusions	49
Chapter 5 – Experimental Measurement of Effects of Concrete Materials and Rheology on Air Void Systems and Freeze-Thaw Durability	51
5.1 Freeze-Thaw Damage.....	51
5.2 Materials Characterization	66
5.3 Equipment and Common Tests Description.....	72
5.4 Stability of Air Void System.....	91
5.5 Conclusions	134
Chapter 6 – Measurement of Plant Conditions	135
6.1 Introduction	135
6.1.1 Concrete Railroad Tie Manufacturing Process	135
6.2 Plant A – Immersion Vibrator on Placing Machine	139
6.3 Plant B – Form Vibrator	141
6.4 Plant C – Handheld Immersion Vibrator.....	144
6.5 Hardened Air Analysis	144
6.6 Results and Discussion.....	147
6.7 Conclusions	174
Chapter 7 – Temperature and Relative Humidity Profiles in Concrete Crossties	175
7.1 Deterioration of Railroad Concrete Crossties	175
7.2 Significance of Research	180
7.3 Sensor Type and Preparation of Installation Method.....	180

7.4	Experimental Results.....	188
7.5	Internal Relative Humidity Distribution.....	193
7.6	Conclusions	205
Chapter 8 – Relationship Between Relative Humidity and Concrete Degree of Saturation		207
8.1	Critical Degree of Saturation for Freeze-Thaw Damage.....	207
8.2	Significance of Research	213
8.3	Sensor Types	214
8.4	Experimental Results, Discussion, and Empirical Modeling.....	222
8.5	Conclusions	230
Chapter 9 – Freeze-thaw Damage Potential Based on Climatic Data		231
9.1	Introduction and Background.....	231
9.2	Modeling Framework	234
9.3	Modeling Results.....	238
9.4	Discussion of Modeling Results and Framework.....	242
9.5	Conclusions	251
Chapter 10 – Effects of Prestressing and Saw-Cutting on Freeze-Thaw Durability		253
10.1	Introduction	253
10.2	Test Methods	254
10.3	Results	263
10.4	Bursting Strains During Sawcutting.....	275
10.5	Conclusions	286
References		287
Abbreviations and Acronyms		296

Illustrations

Figure 2.1. A comparison of the stress vs. strain rate constitutive laws for Bingham and Newtonian fluids (left), and plot of demonstrating that viscosity is constant in a Newtonian fluid, while the viscosity is shear-thinning in a Bingham fluid (right).....	3
Figure 2.2. Roscoe’s equation predicts the factor by which viscosity is increased due to the presence of spherical particles in the suspending fluid.....	5
Figure 2.3. Form vibration (left) oscillates the whole fresh concrete domain, while probe vibration (right) agitates the concrete locally	6
Figure 2.4. Theoretical predictions from the constitutive law for unvibrated and vibrated granular materials.....	7
Figure 3.1. Concrete (left) and mortar (right) can be fit with reasonable accuracy using the simple Bingham model	9
Figure 3.2. Vibration from a probe does not propagate more than a few millimeters into simple Bingham fluids, suggesting additional material properties are necessary to describe the mechanism of air void removal in concrete	10
Figure 3.3. Depth-dependent rheology was measured by changing the amount the measurement geometry was submerged in the fluid (left), with the location defined as the center of the vane (right).....	12
Figure 3.4. Shaker table for concrete vibration (left) and ultrasonic bath for the vibration of the surrogate yield-stress fluid, granular material, and mortar (right).....	12
Figure 3.5. The rheology of simple yield stress fluids (left) is unaffected by variation in depth, while there is a marked increase in the flow stresses for granular materials (right) as the depth is increased.....	13
Figure 3.6. Response of simple yield-stress fluid (left) and granular material (right) to vibration, at different measurement depths, with data taken during vibration labeled with bright symbols and unvibrated data faded.....	14
Figure 3.7. Rheological measurements of mortar at various depths (with Bingham fits), demonstrating that the flow stresses increase with increasing depth.....	15
Figure 3.8. Vibration causes a substantial reduction/elimination of the unvibrated yield stress in both concrete (left) and mortar (right), a result predicted by granular theory	15
Figure 3.9. Though mortar displays depth-dependent rheology when not vibrated, when vibrated the depth-dependence disappears at low shear rates.....	16
Figure 3.10. Mohr’s circle for fresh concrete being acted on by a vibrating probe (left) and the resulting partial fluidization of the domain of concrete, with predicted failure angle θ_f (right)	18
Figure 3.11. Probe vibration activates a cone-shaped region with volume dependent on the depth of the probe and the failure angle (left), a result confirmed experimentally in the translucent granular surrogate fluid (right) with predicted failure angle of 59 degrees in red.....	19

Figure 3.12. A saw cut, polished, and treated 50 mm x 50 mm sample of concrete, with aggregates appearing black, cement paste appearing gray, and air bubbles appearing white	21
Figure 3.13. Histogram of air bubble diameter for two polished concrete samples, one without vibration applied (red) and the other with two minutes of vibration (blue), and theoretical log-normal distribution (black)	22
Figure 3.14. Normalized total air volume vs. time, demonstrating an air loss of an order of magnitude within the first minute of vibration	23
Figure 3.15. Images of the fluid domain with bubble population (with diameters magnified 100x) as time evolves.....	24
Figure 3.16. Contour plot of vibrated viscosity as a function of plastic viscosity and yield stress	25
Figure 3.17. Variation in the time history of the normalized air volume for various viscosity values, with the experimentally-derived model viscosity in black	26
Figure 3.18. The normalized air content as a function of vibration time, using the experimentally-determined bubble distribution (black) and a hypothetical distribution with mean and mode larger by one order of magnitude (red).....	27
Figure 4.1. Circularly emanating compression waves from internal (left) and external (right) source of vibration (from ACI 309)	30
Figure 4.2. Maximization of radius of action of a 2.5 in. diameter immersion probe with varying frequency and amplitude settings (from ACI 309)	31
Figure 4.3. A polished cross-section of concrete is stained with phenolphthalein and its air voids are impregnated with fine, orange powder in order to enhance the contrast in a scanned image (Song et al., 2015)	33
Figure 4.4. Illustration of immersion pencil (probe) vibrator in 15.24 x 15.24 x 122 cm Plexiglas mold where stars represent the nominal location of an immersed accelerometer during vibratory testing	35
Figure 4.5. Illustration of saw-cut cylinders (left) and beams (right); samples extracted for hardened air analysis	35
Figure 4.6. Average fresh air content of fresh, Portland cement-based concrete, mortar, and paste as measured by ASTM C231 after various durations of vibration atop a 60 Hz horizontal table.....	37
Figure 4.7. Mean peak resultant acceleration value at varying distances in a 122-cm long Plexiglas beam mold of Portland cement-based paste and mortar. The fresh material is vibrated using an 18 volt DeWalt vibrator at 7.62 cm. Each data point represents the average of at least four 1-second duration pulses of vibration	39
Figure 4.8. Mean peak resultant acceleration value at varying distances in a 122-cm long Plexiglas beam mold of Portland cement-based concrete. The fresh material is vibrated using an 18 volt DeWalt vibrator at 7.62 cm. Each data point represents the average of at least four 1-second duration pulses of vibration	40

Figure 4.9. Mean peak resultant acceleration value at varying distances in a 122-cm long Plexiglas beam mold of Carbopol-based gel and “mortar.” The fresh material is vibrated using an 18 volt DeWalt vibrator at 7.62 cm. Each data point represents the average of at least four 1-second duration pulses of vibration	42
Figure 4.10. Mean peak resultant acceleration value at varying distances in a 122-cm long Plexiglas beam mold of Carbopol-based “concrete.” The fresh material is vibrated using an 18 volt DeWalt vibrator at 7.62 cm. Each data point represents the average of at least four 1-second duration pulses of vibration	43
Figure 4.11. Log distribution of air voids in cross-section of cylindrical mold with hardened paste vibrated for 0, 1, and 2 minutes atop a 60 Hz vibration table.....	45
Figure 4.12. Log distribution of air voids in cross-section of cylindrical mold with hardened mortar vibrated for 0, 1, and 2 minutes atop a 60 Hz vibration table	46
Figure 4.13. Log distribution of air voids in cross-section of cylindrical mold with hardened concrete vibrated for 0, 1, and 2 minutes atop a 60 Hz vibration table	46
Figure 4.14. Cumulative hardened air content in excised samples of prismatic beams of hardened paste vibrated for 0 sec and 45 seconds at one end using a 220 Hz immersion probe	47
Figure 4.15. Cumulative hardened air content in excised samples of prismatic beams of hardened mortar vibrated for 0 sec and 45 seconds at one end using a 220 Hz immersion probe	48
Figure 4.16. Cumulative hardened air content in excised samples of prismatic beams of hardened concrete vibrated for 0 seconds and 60 seconds at one end using a 220 Hz immersion probe	49
Figure 5.1. Type I popout a) schematic, and b) occurrence in concrete	53
Figure 5.2. Type II popout a) schematic, and b) occurrence in concrete	54
Figure 5.3. Relief zones in air-entrained concrete (Meininger, R., and Tanesi, J., 2006).....	56
Figure 5.4. Effect of air void size on relief zones showing the same air content in figure a) and b) (Meininger, R., and Tanesi, J., 2006)	56
Figure 5.5. Spacing factor effect.....	57
Figure 5.6. Air meter for ASTM C 173 volumetric test (W.W Grainger, Inc., n.d.).....	60
Figure 5.7. Type B air meter to measure air content using the pressure method.....	61
Figure 5.8. Linear traverse method on a concrete sample	63
Figure 5.9. Modified point count method on a concrete sample	64
Figure 5.10. Pixel line analysis performed on scanned concrete sample.....	66
Figure 5.11. Particle size distribution of coarse aggregate	68
Figure 5.12. Particle size distribution of fine aggregate	68
Figure 5.13. Concrete after mixing.....	73

Figure 5.14. Rheometer concrete container	74
Figure 5.15. ICAR rheometer a) electronic equipment with vane and b) in concrete sample.....	74
Figure 5.16. Large vibrating table.....	75
Figure 5.17. Immersion vibrator	76
Figure 5.18. Control unit for the large vibrating table.....	76
Figure 5.19. Vibrating motor attached to the bottom of the table top	77
Figure 5.20. Vibrating motor weights inside the motor for the small vibrating table	77
Figure 5.21. Concrete block at the bottom of the large vibrating table	78
Figure 5.22. Freeze-thaw molds placed at the top of the large vibrating table.....	78
Figure 5.23. ASTM C231 concrete air content container bolted to the top of the large vibrating table.....	79
Figure 5.24. The large vibrating table with two freeze-thaw specimen molds and ASTM C231 specimen container bolted to the table top.....	80
Figure 5.25. The small vibrating table	80
Figure 5.26. Freeze-thaw machine.....	81
Figure 5.27. Electric saw	83
Figure 5.28. Saw-cut sample.....	84
Figure 5.29. Polishing machine	85
Figure 5.30. A concrete sample fixed to the plastic cylinder.....	86
Figure 5.31. Polishing machine during operation.....	86
Figure 5.32. Polishing discs (left to right: 80-grit, 1200-grit, 2200-grit).....	87
Figure 5.33. Polished sample.....	87
Figure 5.34. Scanned image with orange powder.....	88
Figure 5.35. Black and white image	88
Figure 5.36. Immersion vibrator placement.....	90
Figure 5.37. Long beam after hardening.....	90
Figure 5.38. Saw-cutting long beams	91
Figure 5.39. Rheological properties of HRWR + LRWR + synthetic AEA mixtures that experienced 3 g of vibration	92
Figure 5.40. Air loss vs time for HRWR + LRWR + synthetic AEA mixtures that experienced 3 g of vibration.....	93
Figure 5.41. Rheological properties of HRWR + wood rosin AEA mixtures that experienced 3 g of vibration.....	94

Figure 5.42. Air loss vs time for HRWR + wood rosin AEA mixtures that experienced 3 g of vibration	94
Figure 5.43. Rheological properties of HRWR + synthetic AEA mixtures that experienced 3 g of vibration	95
Figure 5.44. Air Loss vs Time for HRWR + Synthetic AEA mixtures that experienced 3 g of vibration	96
Figure 5.45. Rheological properties of HRWR + tall oil AEA mixtures that experienced 3 g of vibration	96
Figure 5.46. Air loss vs time for HRWR + tall oil AEA mixtures that experienced 3 g of vibration	97
Figure 5.47. Rheological properties of selected mixtures that experienced 3 g of vibration	98
Figure 5.48. Air loss vs time for selected mixtures that experienced 3 g of vibration	98
Figure 5.49. Rheological properties of selected mixtures that experienced 10 g of vibration	99
Figure 5.50. Air loss vs time for selected mixtures that experienced 10 g of vibration	99
Figure 5.51. Rheological properties of tall oil AEA + HRWR mixtures (10 g vs 3 g vibrations)	100
Figure 5.52. Air loss vs time for tall oil AEA + HRWR mixtures (10 g vs 3 g vibrations)	101
Figure 5.53. Durability factor vs. fresh air content before vibration (effect of admixtures on the air system).....	102
Figure 5.54. Durability factor vs. fresh air content after vibration (effect of admixtures on the air system)	102
Figure 5.55. Effect of vibration duration on the durability factor with vibration acceleration of 8 g at 75 Hz	103
Figure 5.56. Effect of vibration duration on final spacing factor with vibration acceleration of 8 g at 75 Hz	104
Figure 5.57. Effect of vibration duration on decrease in air content with vibration acceleration of 8 g at 75 Hz	104
Figure 5.58. Effect of vibration duration on final fresh air content (different frequencies and peak accelerations).....	105
Figure 5.59. Effect of vibration duration on final hardened air content (different frequencies and peak accelerations).....	105
Figure 5.60. Effect of vibration duration on final spacing factor (different frequencies and peak accelerations)	106
Figure 5.61. Rheological properties for the study of the effect of vibration acceleration	107
Figure 5.62. Effect of vibration acceleration on the F-T performance of rheological combination 4.....	107

Figure 5.63. Effect of vibration acceleration on the increase in the spacing factor of rheological combination 4.....	108
Figure 5.64. Effect of vibration acceleration on the decrease in the air content of rheological combination 4.....	108
Figure 5.65. Effect of vibration acceleration on the hardened spacing factor of rheological combination 4.....	109
Figure 5.66. Effect of vibration acceleration on the hardened air content of rheological combination 4.....	109
Figure 5.67. Effect of vibration acceleration on the F-T performance of rheological combination 1.....	110
Figure 5.68. Effect of vibration acceleration on the final spacing factor of rheological combination 1.....	111
Figure 5.69. Effect of vibration acceleration on the final air content of rheological combination 1	111
Figure 5.70. Rheological properties for the study of the effect of vibration frequency	112
Figure 5.71. Effect of vibration frequency on the F-T performance of rheological combination 4	113
Figure 5.72. Effect of vibration frequency on the final spacing factor of rheological combination 4.....	113
Figure 5.73. Effect of vibration frequency on the final air content of rheological combination 4	114
Figure 5.74. Effect of vibration frequency on the F-T performance of rheological combination 1	115
Figure 5.75. Effect of vibration frequency on the final spacing factor of rheological combination 1.....	115
Figure 5.76. Effect of vibration frequency on the final air content of rheological combination 1	116
Figure 5.77. Rheological properties for the study of the effect of vibration velocity.....	117
Figure 5.78. Effect of peak vibration velocity on the F-T performance of rheological combination 4.....	117
Figure 5.79. Effect of vibration velocity on the final spacing factor of rheological combination 4	118
Figure 5.80. Effect of vibration velocity on the final air content of rheological combination 4	118
Figure 5.81. Effect of peak vibration velocity on the F-T performance of rheological combination 1.....	119
Figure 5.82 Effect of vibration velocity on the final spacing factor of rheological combination 1	120
Figure 5.83. Effect of vibration velocity on the final air content of rheological combination 1	120

Figure 5.84. Rheological properties of rheological combination 4 of chemical admixture combination A for the study of the effect of air content before vibration	121
Figure 5.85. Effect of air content before vibration on the F-T performance of rheological combination 4 of chemical admixture combination A.....	122
Figure 5.86. Rheological properties of rheological combination 1 and 4 of chemical admixture combination C for the study of the effect of air content before vibration	123
Figure 5.87. Effect of air content before vibration on the F-T performance of rheological combination 1 and 4 of chemical admixture combination C	123
Figure 5.88. Effect of dynamic yield stress on the freeze-thaw durability	124
Figure 5.89. Effect of plastic viscosity on the freeze-thaw durability	125
Figure 5.90. Durability factor vs. spacing factor before vibration.....	126
Figure 5.91. Durability factor vs. spacing factor after vibration	126
Figure 5.92. Durability factor vs. fresh air content before vibration	127
Figure 5.93. Durability factor vs. hardened air content before vibration	128
Figure 5.94. Durability factor vs. hardened air content after vibration	128
Figure 5.95. Final length change vs. spacing factor after vibration.....	129
Figure 5.96. Durability factor vs. final length change	130
Figure 5.97. Final weight change vs. spacing factor after vibration.....	131
Figure 5.98. Durability factor vs. final weight change	132
Figure 5.99. Rheological properties for the immersion vibrator experiment	133
Figure 5.100. Freeze-thaw performance of rheological combination 4 (immersion vibrator experiment)	133
Figure 5.101. Freeze-thaw performance of rheological combination 3 (immersion vibrator experiment)	134
Figure 6.1. a) Forms cleaning and oiling, and b) shoulder installation in Plant A	135
Figure 6.2. Casting beds in Plant A	136
Figure 6.3. Casting beds in Plant B.....	136
Figure 6.4. a) Reinforcing steel wires during installation, and b) enforcing the wire spacing pattern in Plant A	137
Figure 6.5. a) Dispensing concrete in the delivery bucket, and b) dropping concrete in the casting machine hopper in Plant A	137
Figure 6.6. Plant A vibration rods attached to the casting machine	138
Figure 6.7. a) Plant B vibrator schematics with labeled cavities, and b) actual vibrator in position	138
Figure 6.8. Summary of the entire manufacturing process of the three plants	139

Figure 6.9. Accelerometer attached to the casting machine between two embedded vibrators	141
Figure 6.10. Two accelerometers in position for recording.....	142
Figure 6.11. Vibration measurement depth location.....	143
Figure 6.12. Half-tie representation for vibration measurement locations for 1-ft intervals (measurements were taken on the other end of the tie)	143
Figure 6.13. Vibration measurement locations for width of tie.....	143
Figure 6.14. Scans of a) polished sample untreated, b) polished sample treated (with phenolphthalein), and c) polished sample powdered with orange chalk	145
Figure 6.15. a) Aggregate image, and b) Air void image	146
Figure 6.16. Three-color simplified image (black: aggregate; gray: paste; white: air)	146
Figure 6.17. Air content of fresh concrete at Plant A	150
Figure 6.18. Air content of fresh concrete at Plant B	150
Figure 6.19. Air content of fresh concrete at Plant C	151
Figure 6.20. Concrete-hardened air content versus fresh air content at various stages of manufacturing process at Plant A	152
Figure 6.21. Air spacing factor at various stages of manufacturing process at Plant A	152
Figure 6.22. Concrete-hardened air content versus fresh air content at various stages of the manufacturing process at Plant B	153
Figure 6.23. Air spacing factor at various stages of the manufacturing process at Plant B	153
Figure 6.24. Average air void size distribution after vibration (AV), before vibration (BV), and mixer (M) samples for Plants A and B	154
Figure 6.25. Concrete-hardened air content at various stages of the manufacturing process at Plant C.....	155
Figure 6.26. Air spacing factor at various stages of the manufacturing process at Plant C	155
Figure 6.27. Concrete unit weight at Plant A.....	156
Figure 6.28. Temperature of fresh concrete at Plant A.....	156
Figure 6.29. Slump of fresh concrete at Plant A.....	157
Figure. 6.30 Concrete unit weight at Plant B.....	158
Figure 6.31. Temperature of fresh concrete at Plant B.....	158
Figure 6.32. Slump of fresh concrete at Plant B	159
Figure 6.33. Yield stress of fresh concrete at the mixer level in Plant A	160
Figure 6.34. Plastic viscosity of fresh concrete at the mixer level in Plant A	160
Figure 6.35. Yield stress of fresh concrete at Plant B.....	161
Figure 6.36. Plastic viscosity of fresh concrete at Plant B.....	162

Figure 6.37. Rheological parameters versus time for a single batch at Plant B	162
Figure 6.38. Frequency variation of vibration of Bed 4 at Plant A for 1 hour and 40 minutes. .	163
Figure 6.39. Average frequency in an 80-second interval at the end of Bed 2 of Plant A	164
Figure 6.40. Acceleration with maximum acceleration envelope recorded over 1 second at the end of Bed 2 with an accelerometer attached to the casting machine of Plant A.....	164
Figure 6.41. Acceleration with the envelope recorded over 12 seconds at the end of Bed 2 with the accelerometer attached to the forms of Plant A	165
Figure 6.42. Average frequency in a 123-second interval at the end of Bed 2 in Cavity 1 of Plant B with the immersed accelerometer at a depth of 3.5 inches.....	166
Figure 6.43. Vertical acceleration envelope along the length of Cavity 1 at a depth of 4.25 in. with 2-ft intervals for Plant B	167
Figure 6.44. Average peak acceleration versus location along the length of Cavity 1 at a depth of 4.25 in. with 2-ft intervals without off periods for Plant B.....	167
Figure 6.45. Average peak acceleration versus location along the length of Cavity 2 at a depth of 4.25 in. with 1-ft intervals for Plant B	168
Figure 6.46. Average peak acceleration versus location across the depth of Cavity 2 at the middle of the crosstie cavity for Plant B.....	169
Figure 6.47. Average peak acceleration versus location across the depth of Cavity 2 1 in. from the edge of the crosstie cavity for Plant B	169
Figure 6.48. Average peak acceleration versus location across the depth of Cavity 2 under the rail seat for Plant B	170
Figure 6.49. Average peak acceleration versus location across the width of Cavity 2 1 in. from the edge of the cavity for Plant B.....	171
Figure 6.50. Average peak concrete acceleration versus location across 30 ft. of length of the bed in Cavity 1 1 in. from the start of the bed for Plant B.....	172
Figure 6.51. Average peak concrete and form acceleration versus location across the length of the entire bed in Cavity 1 1 in. from the start of the bed for Plant B.....	172
Figure 6.52. Acceleration recorded over 37 seconds at the start of bed with the accelerometer at 4.5 in depth for Plant C	173
Figure 6.53. Frequency recorded over 37 seconds at the start of bed with the accelerometer at 4.5 in depth for Plant C	173
Figure 7.1. Depiction of a concrete crosstie at the rail seat area (left) where the steel rail line, polyurethane pad, concrete crosstie, and aggregate ballast are depicted as layered, infinite halfspaces (right).....	176
Figure 7.2. Depiction of a concrete crosstie at the rail seat area where the steel rail line, polyurethane pad, concrete crosstie, and aggregate ballast are depicted as layered, infinite halfspaces	180

Figure 7.3. Construction of iButton sensors (left), fitted with rubber bands (center), and covered in gore-tex fabric (right).....	181
Figure 7.4. Depiction of nine in. tall brackets (left) with half-in. clearance at top and bottom. Sensors (orange) were affixed in regular two-in. increments (right).....	182
Figure 7.5. De-molded concrete crossties with square cap added to PVC access plug where multi-conductor shielded cables are encased.....	183
Figure 7.6. Three-compartment model ballast box housing three of the crossties atop yard ballast	184
Figure 7.7. Construction of ballast box (left) and final configuration (right).....	185
Figure 7.8. Google satellite image showing approximate location of four ties installed in track near Cisco Bridges, Lytton, BC (annotated and re-printed in accordance to Google Maps license of printed report and presentation media).....	186
Figure 7.9. Diagram of instrumented modulus of rupture beam complementarily installed in model ballast in Rantoul, IL.....	187
Figure 7.10. Diagram of instrument model crosstie complementarily installed in model ballast in Rantoul, IL	188
Figure 7.11. Measured relative humidity at depths of 0.5 in. (12.7 mm), 2.5 in.s (63.5 mm), 5.5 in. (139.7 mm), and 8.5 in. (215.9 mm) from the surface of a model concrete crosstie (labeled YeRail) installed in ballast in Rantoul, IL, between November 29, 2014, through December 21, 2014. An 8 mm thick polyurethane pad and 12 in. (30.48 cm) length 136 lb/yd (67.5 kg/m) section of steel rail are additionally installed atop the model concrete crosstie	189
Figure 7.12. Measured relative humidity at depths of 0.5 in. (12.7 mm), 1.5 in. (38.1 mm), 4.5 in. (114.3 mm), and 5.5 in. (139.7 mm) from the surface of a modulus of rupture beam (labeled A) installed in ballast in Rantoul, IL, between October 19, 2014, through November 30, 2014.....	190
Figure 7.13. Measured relative humidity at depths of 0.5 in. (12.7 mm), 1.5 in. (38.1 mm), 4.5 in. (114.3 mm), and 5.5 in. (139.7 mm) from the surface of a modulus of rupture beam (labeled A) located inside an environmentally controlled room (50% RH, 23 °C) between July 29, 2014, through September 9, 2014	191
Figure 7.14. Measured air temperature and measured temperature values at depths of 0.5 in. (12.7 mm), 2.5 in. (63.5 mm), 4.5 in. (114.3 mm), 6.5 in. (139.7 mm), and 8.5 in. (215.9 mm) from the surface of a concrete crosstie (labeled CXT447IDS) installed in track near Lytton, BC, between November 22, 2013, through February 14, 2014. An 8 mm thick polyurethane pad and steel rail are additionally installed atop the concrete crosstie	192
Figure 7.15. Measured air temperature and measured temperature values at depths of 2.5 in. (63.5 mm), 4.5 in. (114.3 mm), and 8.5 in. (215.9 mm) from the surface of a concrete crosstie (labeled CXT449IDS) without a polyurethane pad nor rail installed in ballast in Rantoul, IL, between April 17, 2014, through May 21, 2014.....	192
Figure 7.16. Measured (markers) and modeled (continuous line) relative humidity profile distribution as a function of depth inside a model concrete crosstie (labeled YeRail)	

installed in ballast in Rantoul, IL, between November 29, 2014, through December 21, 2014. An 8 mm thick polyurethane pad and 12 in. (30.48 cm) length 136 lb/yd (67.5 kg/m) section of steel rail are additionally installed atop the model concrete crosstie. The model does not incorporate a polyurethane pad nor steel rail line. Triangular markers denote relative humidity value from KTIP weather station, square markers denote measured relative humidity values from ballast, and circular markers denote measured relative humidity values inside concrete..... 193

Figure 7.17. Correlation between measured and predicted relative humidity values 0.5 in. (12.7 mm), 2.5 in. (63.5 mm), 5.5 in. (139.7 mm), and 8.5 in. (215.9 mm) from the surface of a model concrete crosstie (labeled YeRail) installed in ballast in Rantoul, IL, between November 29, 2014, through December 21, 2014. An 8 mm thick polyurethane pad and 12 in. (30.48 cm) length 136 lb/yd (67.5 kg/m) section of steel rail are additionally installed atop the model concrete crosstie. The model does not incorporate a polyurethane pad nor steel rail line..... 194

Figure 7.18. Measured (markers) and modeled (continuous line) relative humidity profile distribution as a function of depth inside modulus of rupture beam (labeled A) installed in ballast in Rantoul, IL, between October 19, 2014, through November 30, 2014. Triangular markers denote relative humidity value from KTIP weather station, square markers denote measured relative humidity values from ballast, and circular markers denote measured relative humidity values inside concrete..... 195

Figure 7.19. Correlation between measured and predicted relative humidity values 0.5 in. (12.7 mm), 1.5 in. (38.1 mm), 4.5 in. (114.3 mm), and 5.5 in.s (139.7 mm) from the surface of a modulus of rupture beam (labeled A) installed in ballast in Rantoul, IL, between October 19, 2014, through November 30, 2014 195

Figure 7.20. Measured (markers) and modeled (continuous line) relative humidity profile distribution as a function of depth inside modulus of rupture beam (labeled A) located inside an environmentally controlled room (50% RH, 23 °C) between July 29, 2014, through September 9, 2014. Triangular markers denote relative humidity value from control panel, square markers denote measured relative humidity values from ambient sensors, and circular markers denote measured relative humidity values inside concrete . 196

Figure 7.21. Correlation between measured and predicted relative humidity values 0.5 in. (12.7 mm), 1.5 in. (38.1 mm), 4.5 in. (114.3 mm), and 5.5 in. (139.7 mm) from the surface of a modulus of rupture beam (labeled A) located inside an environmentally controlled room (50% RH, 23 °C) between July 29, 2014, through September 9, 2014 197

Figure 7.22. Temperature and relative humidity collected from weather station KTIP in Rantoul, IL, from November 12, 2013, through December 18, 2013. Solar radiation is estimated over this same timeframe 198

Figure 7.23. Temperature and relative humidity collected from weather station CWLY in Lytton, BC, from February 18, 2014, through May 14, 2014. Solar radiation is estimated over this same timeframe 198

Figure 7.24. Measured (markers) and modeled (continuous line) temperature profile distribution as a function of depth inside a concrete crosstie (labeled CXT447IDS) installed in track near Lytton, BC, between November 22, 2013, through February 14, 2014. An 8-mm thick

polyurethane pad and steel rail are additionally installed atop the concrete crosstie. The model does not incorporate a polyurethane pad nor steel rail line. Triangular markers denote temperature value from CWLY weather station, square markers denote assumed temperature values in ballast, and circular markers denote measured temperature values inside concrete	200
Figure 7.25. Correlation between measured and predicted temperature values 0.5 in. (12.7 mm), 2.5 in. (63.5 mm), 4.5 in. (114.3 mm), 6.5 in. (139.7 mm), and 8.5 in. (215.9 mm) from the surface of a concrete crosstie (labeled CXT447IDS) installed in track near Lytton, BC, between November 22, 2013, through February 14, 2014. An 8 mm thick polyurethane pad and steel rail are additionally installed atop the concrete crosstie. The model does not incorporate a polyurethane pad nor steel rail line	201
Figure 7.26. Measured (markers) and modeled (continuous line) temperature profile distribution as a function of depth inside a concrete crosstie (labeled CXT449IDS) without a polyurethane pad nor rail installed in ballast in Rantoul, IL, between April 17, 2014, through May 21, 2014. Triangular markers denote temperature value from KTIP weather station, square markers denote measured temperature values from ballast, and circular markers denote measured temperature values inside concrete	202
Figure 7.27. Correlation between measured and predicted temperature values 2.5 in. (63.5 mm), 4.5 in. (114.3 mm), and 8.5 in. (215.9 mm) from the surface of a concrete crosstie (labeled CXT449IDS) without a polyurethane pad nor rail installed in ballast in Rantoul, IL, between April 17, 2014, through May 21, 2014	203
Figure 7.28. Measured relative humidity of model ballast at top and bottom of concrete crosstie in Rantoul, IL, between August 1, 2015, through September 13, 2015. Ambient relative humidity measured from a nearby weather station KTIP is also shown.....	204
Figure 7.29. Measured temperature of model ballast at top and bottom of concrete crosstie in Rantoul, IL, between August 1, 2015, through September 13, 2015. Ambient air temperature measured from a nearby weather station KTIP is also shown.....	205
Figure 8.1. Simplification of concrete microstructure with a) cylinders (left) and b) ink-bottles (right)	210
Figure 8.2. a) Wetting of the interior of a cylindrical pore with an adsorbate layer (left) and b) drying of the interior of a cylindrical pore with an adsorbate layer (right)	210
Figure 8.3. Idealized adsorption isotherm of cylindrical pores undergoing wetting and drying	211
Figure 8.4. Adsorption isotherms for concrete with different water-to-cement ratios (Hansen, 1986)	213
Figure 8.5. Simple illustration of one moisture sensor connected to two 1500 Ω resistors, two diodes (1N4148), and an Arduino Uno R3 microcontroller at Pins 6, 7, A0, A1, and GND	215
Figure 8.6. Simplified depiction of circuitry when a) Pin 6 voltage is HIGH (left) and b) when Pin 7 voltage is HIGH (right).....	216
Figure 8.7. Complete circuitry scheme where six moisture sensor blocks (G0-G5) are measured for their change in impedance when Pin 7 on an Arduino Uno R3 microcontroller board is	

set to HIGH. In order to prevent electrochemical deterioration processes, Pin 6 is also set to HIGH in an alternative manner in order to mimic an alternating current.....	218
Figure 8.8. Image of hardware where an SD shield is connected above an Arduino Uno R3 microcontroller board. The Arduino and shield are securely fastened with a rubber band onto a circuit board that is wired in accordance in Figure Figure 8.7. A 10000 mAh external battery back provides an approximate 7-day charge for the hardware to operate independently. The entire setup is encased in a metal junction box.....	219
Figure 8.9. Construction of hygrochron sensors seated inside an iButton retainer installed in a plastic dip coated eye bolt and sealed with a single layer of GORE-TEX fabric. A rubber band securely holds the fabric in place. Moisture sensor blocks are additionally installed along the orthogonal face of the angled steel bracket.....	220
Figure 8.10. Depiction of 9 in. tall bracket (left) with 0.5-in. clearance at top and bottom. Hygrochron sensors (orange) and moisture sensors (white) are affixed at depths as depicted (right)	220
Figure 8.11. Diagram of instrumented model crosstie with both hygrothermal sensors and moisture sensors installed at various depths (left)	221
Figure 8.12. De-molded model concrete crossties with PVC access plug where multi-conductor shielded cables are encased.....	222
Figure 8.13. Model crossties installed in model ballast in Rantoul, IL	222
Figure 8.14. Measured relative humidity at depths of 0.5 in. (12.7 mm), 2.5 in. (63.5 mm), 5.5 in. (139.7 mm), and 8.5 in. (215.9 mm) from the surface of a model concrete crosstie (labeled NoRail) without a polyurethane pad nor rail installed in ballast in Rantoul, IL, between November 29, 2014, through December 21, 2014	223
Figure 8.15. Change of mass and impedance of two moisture sensors undergoing drying and soaking	224
Figure 8.16. Measured degree of saturation at depths of 0.5 in. (12.7 mm), 2.5 in. (63.5 mm), and 8.5 in. (215.9 mm) from the surface of a model concrete crosstie (labeled NoRail) without a polyurethane pad nor rail installed in model ballast in Rantoul, IL, between December 1, 2014, through December 21, 2014	225
Figure 8.17. Measured degree of saturation at depths of 0.5 in. (12.7 mm), 2.5 in. (63.5 mm), and 8.5 in. (215.9 mm) from the surface of a model concrete crosstie (labeled NoRail) without a polyurethane pad nor rail installed in model ballast in Rantoul, IL, between May 14, 2015, through June 20, 2015.....	226
Figure 8.18. Measured degree of saturation at depths of 0.5 in. (12.7 mm), 2.5 in. (63.5 mm), and 8.5 in. (215.9 mm) from the surface of a model concrete crosstie (labeled NoRail) without a polyurethane pad nor rail installed in model ballast in Rantoul, IL, between June 20, 2015, through August 1, 2015.....	227
Figure 8.19. Correlation between measured relative humidity and degree of saturation at depth of 8.5 in. (215.9 mm) from the top surface of a model concrete crosstie (labeled NoRail) without a polyurethane pad nor rail installed in model ballast in Rantoul, IL. The data	

represents two periods from December 1, 2014, though December 21, 2014, and June 20, 2015, through September 11, 2015	228
Figure 8.20. Correlation between measured relative humidity and degree of saturation at depth of 8.5 in. (215.9 mm) from the top surface of a model concrete crosstie (labeled NoRail) without a polyurethane pad nor rail installed in model ballast in Rantoul, IL.....	229
Figure 9.1. Correlation between measured relative humidity and measured degree of saturation of instrumented high performance concrete prism	235
Figure 9.2. Modeled instances of drying when the concrete is initially wetted to S=100, 95, 90, 85, 80, 60, 40, or 20% of its degree of saturation	236
Figure 9.3. Modeled instances of wetting when the concrete is initially wetted to S=100%, then dried to S = 0, 20, 40, 60, 80, 85, 90, and 95% of its degree of saturation before being re-wetted to S=100%.....	237
Figure 9.4. Measured air temperature and predicted temperature inside model concrete in Rantoul, IL, from September 3, 2013, through September 8, 2015.....	239
Figure 9.5. Predicted degree of saturation inside a one-layered concrete system in Rantoul, IL, from September 3, 2013, through September 8, 2015	240
Figure 9.6. Measured air temperatures and predicted temperature inside model concrete in Lytton, BC, from October 8, 2013, through March 17, 2015	241
Figure 9.7. Predicted degree of saturation inside a one-layered concrete system in Lytton, BC, from October 8, 2013, through March 17, 2015	242
Figure 9.8. Cumulative number of freeze-thaw cycles in Rantoul, IL, from September 3, 2013, through September 8, 2015	243
Figure 9.9. Predicted (left) and measured (right) cumulative number of freeze-thaw cycles in Lytton, BC, from October 8, 2013, through March 17, 2015	244
Figure 9.10. Cumulative number of freeze-thaw cycles in Lytton, BC, from October 8, 2013, through March 17, 2015, at a depth of 5 mm when both freezing air temperatures and minimum degree of saturation is achieved at time of freezing. Predicted degree of saturation is defined by a diffusivity (at S=100%) value of $0.86 \times 10^{-6} \text{ m}^2/\text{hr}$, a regression coefficient, n, of 15, α value of 0.05, and an empirical correlation between relative humidity and degree of saturation. The simulation is initialized with an even distribution of 85 percent RH throughout the depth of the concrete	245
Figure 9.11. Cumulative number of freeze-thaw cycles in Lytton, BC, from October 8, 2013, through March 17, 2015, at a depth of 5 mm when both freezing temperatures and minimum degree of saturation is achieved at time of freezing	246
Figure 9.12. Cumulative number of freeze-thaw cycles in Lytton, BC, from October 8, 2013, through March 17, 2015, when both freezing air temperatures and minimum rate of freezing is achieved at time of freezing	247
Figure 9.13. Cumulative number of freeze-thaw cycles in Rantoul, IL, from September 3, 2013, through September 8, 2015, when both freezing temperatures at a depth of 5 mm and minimum rate of freezing is achieved at time of freezing	248

Figure 9.14. Predicted degree of saturation inside a one-layered concrete system in Lytton, BC, from October 8, 2013, through March 17, 2015. The concrete is defined by a diffusivity (at S=100%) value of $1.29 \times 10^{-6} \text{ m}^2/\text{hr}$, a regression coefficient, n, of 15, α value of 0.05, and an empirical correlation between relative humidity and degree of saturation.....	250
Figure 9.15. Cumulative number of freeze-thaw cycles in Lytton, BC, from October 8, 2013, through March 17, 2015, at a depth of 5 mm when both freezing temperatures and minimum degree of saturation is achieved at time of freezing. Predicted degree of saturation is defined by a diffusivity (at S=100%) value of $1.29 \times 10^{-6} \text{ m}^2/\text{hr}$	251
Figure 10.1. Soaked half ties covered with burlap.....	255
Figure 10.2. Measurement locations on half ties (R represents the receiver and T represents the transmitter).....	256
Figure 10.3. Typical freeze-thaw cycle temperatures measured 4.5 in. (114 mm) from the concrete tie surface	257
Figure 10.4. Saw-cutting samples from the tie end	258
Figure 10.5. Three saw-cut samples from the tie end.....	259
Figure 10.6. Typical 4 x 3 x 11 in. saw-cut freeze-thaw sample	259
Figure 10.7. Average RDME results of the six sets of excised samples	264
Figure 10.8. Cracking pattern in saw-cut samples in freeze-thaw testing (SHT3).....	264
Figure 10.9. Change in mass for the six sets of excised samples	265
Figure 10.10. Mass loss for saw-cut samples in freeze-thaw testing (SHT4).....	265
Figure 10.11. Change in length for the six sets of excised samples	265
Figure 10.12. Change in mass for the saw-cut non-prestressed, saw-cut plain, and cast prisms samples with and without air entrainment	266
Figure 10.13. Change in length for the saw-cut non-prestressed, saw-cut plain, and cast prisms samples with and without air entrainment	266
Figure 10.14. Average RDME results for the saw-cut non-prestressed, saw-cut plain, and cast prisms samples with and without air entrainment.....	267
Figure 10.15. Half ties that developed cracking from the saw-cut (epoxied) end.....	268
Figure 10.16. Average RDME results for half ties as compared to excised samples from the same ties.....	268
Figure 10.17. Half ties with excessive deterioration (HT6 made with 0.9% fresh air content and no air-entraining agent).....	269
Figure 10.18. Freeze-thaw performance of Plain vs Reinforced vs Reinforced Saw-Cut concrete	272
Figure 10.19 Cracked saw-cut sample (angle 1).....	273
Figure 10.20. Cracked saw-cut sample (angle 2).....	273
Figure 10.21. Cracked saw-cut sample (angle 3).....	274

Figure 10.22. Cracked saw-cut sample (angle 4).....	274
Figure 10.23. Cracked saw-cut sample (angle 5).....	275
Figure 10.24. Vibration wire gauges inside the ties.....	276
Figure 10.25. Vibrating wire gages in the tie next to the two stirrups.....	276
Figure 10.26. Unreinforced tie covered in plastic.....	277
Figure 10.27. Saw-cutting locations on ties (red) and saw-cutting locations on the gauge (VWG) (green).....	280
Figure 10.28. Longitudinal strain development in non-air-entrained concrete samples versus air-entrained concrete	282
Figure 10.29. Longitudinal strain development in non-air-entrained concrete samples.....	283
Figure 10.30. Transverse strain development in non-air-entrained concrete samples.....	283
Figure 10.31. Longitudinal strain development in air-entrained concrete samples.....	284
Figure 10.32. Vertical strain development in air-entrained concrete samples.....	285
Figure 10.33. Cracking due to stress release from saw-cutting.....	285

Tables

Table 3.1: Concrete mix design	11
Table 3.2: Parameter Choices for the Bubble Rise Model.....	21
Table 4.1. Nominal Paste Mix Design	34
Table 4.2. Gradation of Sand (percent passing).....	34
Table 4.3. Gradation of Gravel (percent passing).....	34
Table 4.4. Average Bingham Parameters of Fresh Concrete, Mortar, and Paste	36
Table 4.5. Bingham Parameters of Fresh Concrete, Mortar, and Paste with Varying Aggregate Volume Content Values	38
Table 4.6. Bingham Parameters of Carbopol Gel with Varying Volume Content of Graded Silica Sand (FA) and 1 in. (2.5 cm) Diameter Glass Marbles (CA)	41
Table 4.7. Bingham Parameters of Fresh Concrete, Mortar, and Paste Vibrated in Cylindrical Molds	43
Table 4.8. Cumulative Percent Area of Hardened Air and Paste in Vibrated Paste Cylindrical Molds Cross-Sections	44
Table 4.9. Cumulative Percent Area of Hardened Air and Mortar in Vibrated Mortar Cylindrical Molds Cross-Sections	44
Table 4.10. Cumulative Percent Area of Hardened Air, Mortar, and Coarse Aggregate in Vibrated Concrete Cylindrical Molds Cross-Sections	44
Table 4.11. Bingham Parameters of Fresh Concrete, Mortar, and Paste Vibrated in Beam Molds	47
Table 5.1. Cement Chemical and Physical Properties	67
Table 5.2. Basic Concrete Mixture Proportions.....	69
Table 5.3. Concrete Mixture Properties	70
Table 5.4. Mixture Proportions of Externally-Vibrated Mixtures Used for Target Air Content of 3.5% to 4.5%.....	71
Table 5.5. AEA Dosages of the Mixtures Used for Studying the Effect of the Initial Air Content	72
Table 5.6. Mixture Proportions of Internally-Vibrated Mixtures	72
Table 6.1. Experimental Results at Plant A, Plant B and Plant C.....	148
Table 6.2. Measured Air Void Systems for Plant A, Plant B and Plant C.....	149
Table 7.1. Moisture Diffusivity at Saturation Estimated from w/c Ratio (from ¹ (Kang, S. -T., Kim, J. -K., Kim, J. -S., Lee, Y., and Park, Y. -D., 2012), and ² (Hiller, J. E., and Qin, Y., 2014)).....	176

Table 7.2. Modified Boundary Condition at the Top of Concrete Crossties and Beams as Subject to Reported Weather Conditions (Adapted from (Hiller, J. E., and Qin, Y., 2014)).....	177
Table 7.3. Approximate Concrete Mix Design of Railroad Crossties	183
Table 7.4. Nominal Concrete Mix Design of Modulus of Rupture Beams and Model Crossties	187
Table 7.5. Thermal Conductivity and Thermal Diffusivity of Material Types used in the Temperature Predictive Modeling. Values are Adapted from Either Reference Values, ¹ (Hiller, J. E., and Qin, Y., 2014) or ² (Pielichowski, J., Prociak, A., and Sterzynski, T., 2000).	199
Table 8.1. Change in Saturation Vapor Pressure with Respect to Temperature (Rotronic, 2005)	209
Table 8.2. Nominal Concrete Mix Design of Model Crossties.....	221
Table 8.3. Fit Parameters used for 3-Parameter S-Shaped Curves for Wetting and Drying Curves	230
Table 9.1. Moisture Diffusivity at Saturation Estimated from w/c ratio (from ¹ (Kang, S. -T., Kim, J. -K., Kim, J. -S., Lee, Y., and Park, Y. -D., 2012) and ² (Hiller, J. E., and Qin, Y., 2014)).....	232
Table 9.2. Modified Boundary Condition at the Top of Concrete as Subject to Reported Weather Conditions (Adapted from (Hiller, J. E., and Qin, Y., 2014))	233
Table 9.3. Fit Parameters Used for 3-Parameter S-Shaped Curves in Equation 4-6 for Wetting and Drying Curves	233
Table 9.4. Mean, Median, and Mode of Freezing Rates in Lytton, BC, from October 8, 2013, Through March 17, 2015. Instances of Freeze Rate are as Large as 8 °C/hr Because of Observed 2 °C Change in the Span of a 15-Minute Time Interval.....	249
Table 9.5. Mean, Median, and Mode of Freezing Rates in Lytton, BC, from October 8, 2013, Through March 17, 2015. Instances of Freeze Rate are as Large as 3 °C/hr Because of Observed 3 °C Change in the Span of a 60-Minute Time Interval.....	249
Table 10.1. Freeze-Thaw and Non-Destructive Testing Performed on Large Concrete Tie Samples	261
Table 10.2. Fresh and Hardened Air Content of all Tested Samples.....	263
Table 10.3. Summary of all Sample Results at Failure Compared to Initial Values	269
Table 10.4. Summary of Ties Made and Vibrating Wire Gauges Used	278
Table 10.5. Properties of Concrete Used	279
Table 10.6. Vibrating Wire Gauges that Remained Operational After Concrete Hardening	281

Chapter 1 – Organization of Volume II

This is a companion report to “Concrete Material and Manufacturing Requirements for Freeze-Thaw Durable Concrete Railroad Ties: Volume I,” available via FRA’s eLibrary at: https://www.fra.dot.gov/eLib/details/L19610#p1_z5_gD. This report documents the detailed research activities and results from the project.

The organization of this report is as follows:

Chapter 2 – Rheology and Fluid Mechanics

Chapter 3 – Experimental Evidence for a Concrete Rheological Model

Chapter 4 – Influence of Vibration in Portland Cementitious Materials and Model Materials

Chapter 5 – Experimental Measurement of Effects of Concrete Materials and Rheology on Air Void Systems and Freeze-Thaw Durability

Chapter 6 – Measurement of Plant Conditions

Chapter 7 – Temperature and Relative Humidity Profiles in Concrete Crossties

Chapter 8 – Relationship Between Relative Humidity and Concrete Degree of Saturation

Chapter 9 – Freeze-thaw Damage Potential Based on Climatic Data

Chapter 10 – Effects of Prestressing and Saw-Cutting on Freeze-Thaw Durability

Chapter 2 – Rheology and Fluid Mechanics

2.1 The Importance of Rheology

The key to understanding air bubble motion in concrete is to understand the rheology of concrete. Rheology is the study of how fluids and soft solids respond to applied stresses and strains/strain rates. The two fluids encountered most often—air and water—are characterized as Newtonian fluids. Newtonian fluids obey the following constitutive law:

$$\sigma = \mu\dot{\gamma} \qquad \text{Equation 2-1}$$

Where σ is the stress, $\dot{\gamma}$ is the strain rate, and μ is the viscosity. Here viscosity is a constant parameter that is a measure of internal friction or resistance to flow. Fluids are called “Newtonian” when Equation 2-1 is obeyed over all relevant conditions in a particular environment. What makes the concrete bubble rise problem very challenging is that concrete is a non-Newtonian fluid, meaning that the viscosity is not constant. In general, non-Newtonian fluids can have viscosity that can change with time, stress, strain, strain rate, and even the time history of these variables.

Typically, rheology is measured in terms of torque (in Newton-meters) and speed (revolutions per minute). Stress (measured in Newtons per square meter) and strain rate (inverse seconds) are essentially transformations of torque/speed into more fundamental, geometry-independent variables.

2.1.1 Concrete Rheology: Is it a Bingham Plastic?

Concrete is known to have a yield stress and is typically characterized as a Bingham fluid (Banfill, P. F., and Tattersall, G. H., 1983). Bingham fluids are a special class of non-Newtonian fluids that possess the property of being solid-like below a stress threshold known as the yield stress (σ_y), while being liquid-like above the yield stress. The following constitutive law is used to characterize such fluids:

$$\sigma = \sigma_y + \mu_p\dot{\gamma} \qquad \text{Equation 2-2}$$

Where material parameter, μ_p , is plastic viscosity. A comparison of the constitutive laws of Newtonian and Bingham fluids can be seen in Figure 2.1:

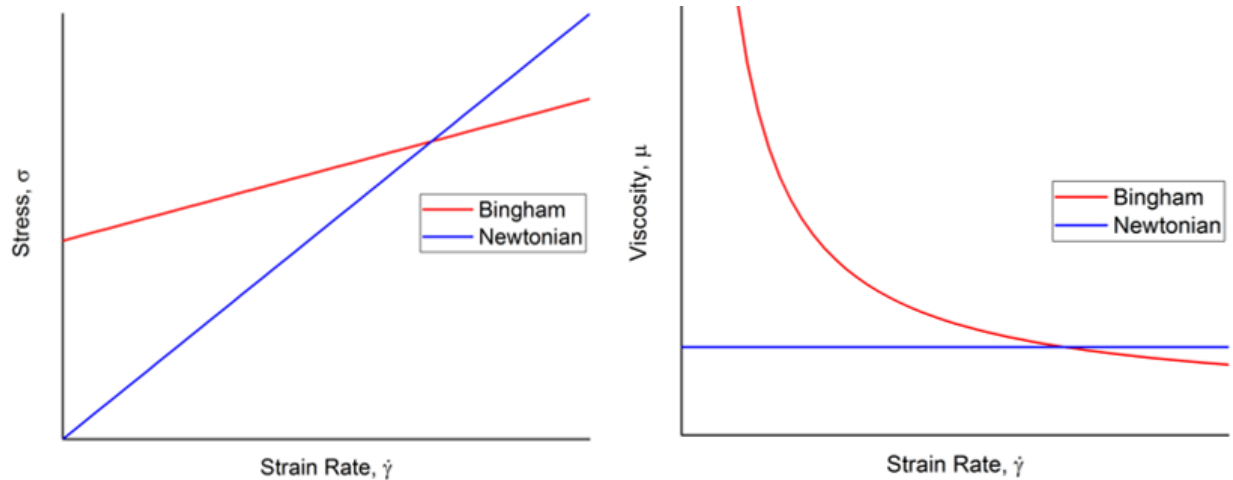


Figure 2.1. A comparison of the stress vs. strain rate constitutive laws for Bingham and Newtonian fluids (left), and plot of demonstrating that viscosity is constant in a Newtonian fluid, while the viscosity is shear-thinning in a Bingham fluid (right)

An interesting phenomenon associated with Bingham materials is the fluid's ability to entrap small particles (that impose stresses less than the yield stress) and hold them in place indefinitely. Adapted from the criterion for a particle becoming entrapped is (Beris, A. N., and Tsamopoulos, J. A., 1985):

$$\frac{\sigma_y}{\Delta\rho gD} > \frac{1}{21} \quad \text{Equation 2-3}$$

As an example: for a material with $\sigma_y = 10 \text{ Pa}$ and $\Delta\rho = 1000 \text{ kg/m}^3$, one can calculate that bubbles with diameter less than 2 cm will be entrapped and motionless in the fluid.

2.1.2 Flow Viscosity vs. Plastic Viscosity

It is important to understand the difference between the actual viscosity μ , which governs the fluid dynamics of a given problem, and the plastic viscosity μ_p . The true definition of viscosity is $\mu = \sigma / \dot{\gamma}$. For a Newtonian fluid (Equation 2-1), the viscosity μ is constant for all strain rates:

$$\mu = \frac{\sigma}{\dot{\gamma}} = \frac{\bar{\mu}\dot{\gamma}}{\dot{\gamma}} = \bar{\mu} \quad \text{Equation 2-4}$$

The coefficient of proportionality the between stress and strain rate is denoted as $\bar{\mu}$ for notational purposes, even though it is, by definition, the viscosity. The viscosity in a Newtonian fluid is constant.

However, for non-Newtonian fluids, the viscosity is in general not constant, and can increase or decrease as a function of the strain rate (among other factors). For example, in a Bingham fluid (Equation 2-2):

$$\mu = \frac{\sigma}{\dot{\gamma}} = \frac{\sigma_y + \mu_p \dot{\gamma}}{\dot{\gamma}} = \frac{\sigma_y}{\dot{\gamma}} + \mu_p \quad \text{Equation 2-5}$$

That is, for low strain rates ($\dot{\gamma} \rightarrow 0$) the viscosity approaches infinity, and at high strain rates ($\dot{\gamma} \rightarrow \infty$) the viscosity asymptotes to the plastic viscosity μ_p . Thus, a Bingham material is an example of a shear-thinning fluid, since its viscosity decreases with increasing strain rate. This phenomenon is observed in Figure 2.1.

2.2 Air Bubble Rise in Newtonian and Non-Newtonian Fluids

The influence of viscosity on air bubble rise in a fluid can be understood through the example of a small buoyant sphere in a simple Newtonian fluid. By balancing the Stokes drag force ($F_d = 3\pi U\mu D$) against the buoyant force ($F_B = \pi\Delta\rho g D^3/6$), the following is the relationship for the terminal rise velocity of the particle:

$$U_p = \frac{1}{18} \frac{\Delta\rho g D^2}{\mu} \quad \text{Equation 2-6}$$

For fluid viscosity μ , particle diameter D , density difference $\Delta\rho$, and gravitational acceleration g . From this, it is noted that the rise speed is very sensitive to particle size (scales with the diameter squared), and that the rise speed is inversely proportional to the viscosity.

Equation 2-6 is derived assuming the particle is solid. For a fluid particle (i.e. an air bubble), there are two additional complications. Firstly, the particle shape is not necessarily spherical. This effect can be quantified using the dimensionless capillary number:

$$Ca = \frac{\mu\dot{\gamma}}{2\Gamma/D} = \frac{\sigma}{2\Gamma/D} \quad \text{Equation 2-7}$$

Were Γ is the surface tension in dimensions of force per unit length. This number essentially compares the relative strength of viscous stresses, which deform the bubble's shape, to the surface tension, which in a sense tries to reshape the bubble into a sphere, minimizing surface area. For $Ca < 1$, it can be safely assumed that the bubbles maintain a spherical shape (Chateau, X., Ducicou, L., Goyon, J., Kogan, M., and Pitois, O., 2013). Estimating the stress a buoyant bubble imposes on the fluid as:

$$\sigma = \frac{F}{A} \approx \frac{\frac{4}{3}\pi R^3 \Delta\rho g}{2\pi R^2} = \frac{1}{3} \Delta\rho g D \quad \text{Equation 2-8}$$

Which is approximately 6 Pa for a $D=1$ mm bubble, and taking $\Gamma=0.07$ N/m (close to water), $Ca \approx 0.04$ was found well-below the threshold for bubble shape variation to be a concern.

Secondly, there are different boundary conditions at a fluid-fluid interface than there are at a fluid-solid interface. However, when the viscosity inside the bubble is much smaller than the viscosity outside the bubble, Equation 2-6 is simply modified with a coefficient of 3/2 (Bond, 1927). So, the rise speed of an air bubble in a liquid is:

$$U = \frac{1}{12} \frac{\Delta\rho g D^2}{\mu} \quad \text{Equation 2-9}$$

While the trends described by this equation provide a starting point for understanding more complex systems, the motion of air in fresh concrete is not as easily analyzed or understood. There are three main reasons for this:

1. Concrete is a yield-stress fluid, not a Newtonian fluid.
2. The presence of hard aggregates at a large volume fraction makes concrete a granular material.
3. Concrete is typically vibrated to encourage large air void removal, a process which influences the rheology.

2.3 Granular Solids, Liquids, and Gases

Concrete can potentially be analyzed as a granular material, since in it the volumetric packing fraction of hard particles is typically higher than 60 percent. In general, granular materials possess unique physical properties. At rest, the grains interlock, providing a solid-like structure that remains stable to sufficiently small applied stresses. If a shearing force is imposed, the grains will overcome this interlocking and flow past each other, behaving like a liquid with a measurable (though non-Newtonian) viscosity. During particularly vigorous motion, like shaking, the grains will separate from each other and will adopt similar collision characteristics as an ideal gas (Behringer, R. P., Jaeger, H. M., and Nagel, S. R., 1996).

2.3.1 Roscoe's Equation and the Viscosity of a Suspension

Roscoe's equation predicts the factor by which the viscosity of a suspending fluid increases due to the addition of particles. As first presented by Roscoe (Roscoe, 1952), for diverse-sized spherical particles:

$$\mu = \mu_o(1 - c)^{-2.5} \quad \text{Equation 2-10}$$

Where μ_o is the viscosity of the suspending fluid and c is the total volume fraction of particles. This equation reduces to the famous Einstein relationship for dilute suspensions (Einstein, 1905), but also captures the dramatically non-linear viscosity increase as the concentration increases, as seen in Figure 2.2.

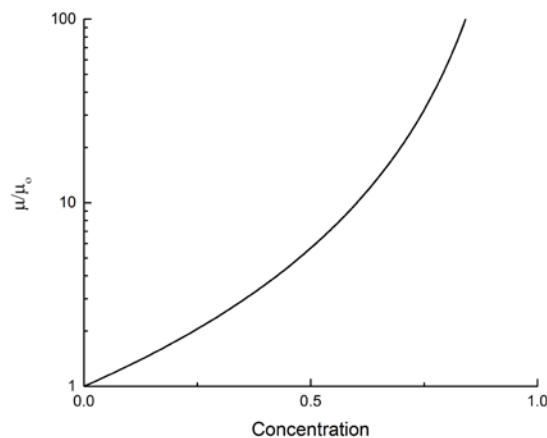


Figure 2.2. Roscoe's equation predicts the factor by which viscosity is increased due to the presence of spherical particles in the suspending fluid

Roscoe’s equation was adapted for use in concrete (Vazques, 2004), with the calculation of viscosity increase from the suspending paste to concrete occurring over two steps:

$$\mu_{mortar} = \mu_{paste} \left(1 - \frac{1}{r} V_{sand}\right)^{0.89m-9.31} \quad \text{Equation 2-11}$$

$$\mu_{concrete} = \mu_{mortar} \left(1 - \frac{1}{\tilde{r}} V_{coarse}\right)^{0.57\tilde{m}-3.40} \quad \text{Equation 2-12}$$

Where r is the ratio of the volume of solute to solvent (e.g., sand to paste), V_{sand} and V_{coarse} are the volume concentrations of sand and coarse aggregate, and m and \tilde{m} are the fineness coefficients for sand and coarse aggregate.

2.3.2 Mechanism by Which Vibration Influences the Rheology of Granular Materials

Concrete is often vibrated to encourage the removal of large air voids, leading to a more durable structure. Vibration typically occurs by either of two means: form vibration, which involves oscillation of the entire concrete domain, and probe vibration, which utilizes a probe inserted into the freshly poured concrete to agitate the concrete locally.

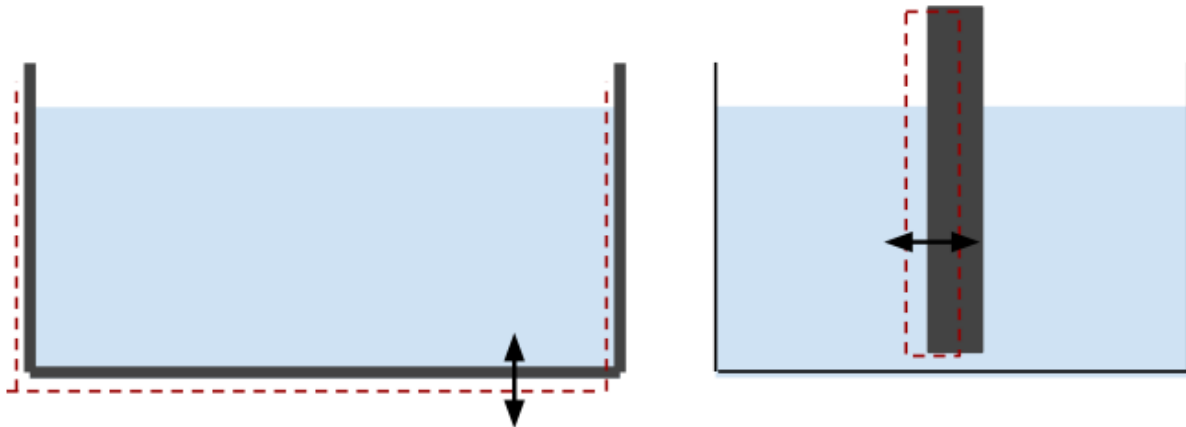


Figure 2.3. Form vibration (left) oscillates the whole fresh concrete domain, while probe vibration (right) agitates the concrete locally

It is important to understand the physical mechanism by which vibration influences concrete. Hypothesizing that the granular nature of concrete is important to the vibration propagation, the technical literature describes a constitutive law based on fundamental processes which could prove useful to understanding air bubble behavior in concrete (Hanotin, C., Michot, L. J., and de Richter, S. K., 2015).

Granular materials derive their strength from the formation of “force chains,” which are alignments of grains in a single direction, providing compressive strength. The paper hypothesizes that vibration disrupts these chains by separating the grains, in a process akin to adding thermal energy to a Brownian system. This interpretation is well-received in the granular literature (Barrat, A., D’anna, G., Loreto, V., Mayor, P., and Nori, F., 2003). This leads to the development of the following constitutive law:

$$\dot{\sigma}(t) + \left[\frac{\dot{\gamma}(t)}{\gamma_c} + f_b \right] \sigma(t) = [G + \eta_H f_b] \dot{\gamma}(t) + \eta_H \frac{[\dot{\gamma}(t)]^2}{\gamma_c} + \eta_H \ddot{\gamma}(t) \quad \text{Equation 2-13}$$

Which has three material fitting parameters: G , γ_c , and η_H ; and one vibration fitting parameter f_b . Note that this is a differential equation, with time derivatives (dot accents) of both stress and strain rate. With proper assumptions, the equation adopts much simpler forms. For steady, constant shear rate without vibration the equation reduces to:

$$\sigma = G\gamma_c + \eta_H \dot{\gamma} \quad \text{Equation 2-14}$$

Equation 2-14 is similar to the Bingham Equation 2-2 with $\sigma_y = G\gamma_c$, i.e. unvibrated granular materials possess yield-stress behavior. For steady, constant shear rate with vibration, the equation reduces to:

$$\sigma = \frac{G\gamma_c + \eta_H f_b \gamma_c}{\dot{\gamma} + f_b \gamma_c} \dot{\gamma} + \frac{\eta_H}{\dot{\gamma} + f_b \gamma_c} \dot{\gamma}^2 \quad \text{Equation 2-15}$$

Equations 2-14 and 2-15 are plotted in Figure 2.4.

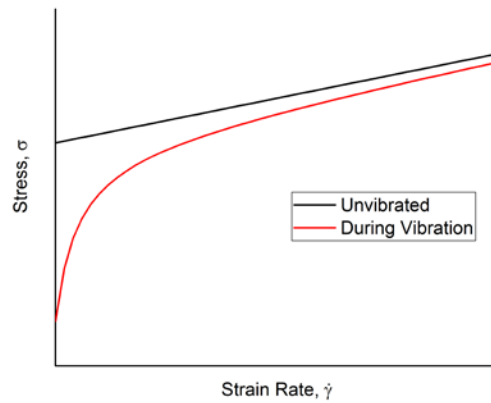


Figure 2.4. Theoretical predictions from the constitutive law for unvibrated and vibrated granular materials

In the limit of infinite strain rate, $\sigma \sim \eta_H \dot{\gamma}$, this is the same limit that is seen in Equation 2-14 for an unvibrated medium. This suggests that vibration has no influence on rheology at large strain rates. In the limit of near-zero strain rate, the regime that is important to air bubble rise, Equation 2-15 becomes:

$$\sigma = \left[\frac{G}{f_b} + \eta_H \right] \dot{\gamma} \quad \text{Equation 2-16}$$

Which means that, at small strain rates, vibration causes the material to become essentially Newtonian with viscosity:

$$\mu = \frac{G}{f_b} + \eta_H \quad \text{Equation 2-17}$$

It is postulated that vibration eliminates the yield-stress behavior of granular materials. These results will be compared to experimental results for concrete and mortar in Chapter 3.

2.4 Conclusions

Concrete rheologic properties significantly influence the behavior of air bubbles in freshly-placed concrete. Concrete is a complex yield-stress fluid with a high-volume fraction of hard aggregates. This study has explored rheological models that are useful for describing the behavior of concrete, and one of the most important findings has been that concrete can be described as a granular fluid whereby its yield stress arises from the presence of aggregate in the paste fluid. This study has shown that Roscoe's equation for granular fluid is a useful model of concrete rheology. Roscoe's equation allows for the calculation of the factor by which viscosity is increased due to the presence of aggregates in a suspending fluid. A constitutive model for vibrated granular materials predicts Newtonian (constant viscosity) behavior during vibration, and yield-stress behavior without vibration.

One of the strong contributions of this study is the development of a sound theoretical basis for modeling behavior of fresh concrete as a granular fluid that will be vibrated during handling and placement. The modeling demonstrates that vibration defeats yield stress, allowing the vibrated concrete to flow and air bubbles within the concrete to move under buoyant forces. The modeling confirms the observation that bubbles rise when concrete is vibrated, but bubbles immediately stop rising when vibration is stopped. The rise speed of small bubbles can be calculated for a Newtonian fluid (i.e., a vibrated concrete with zero yield stress).

The findings of this study underpin our understanding of the behavior of vibrated concrete. This study helps us ascertain the movement of air in the fresh material—both large entrapped air voids and small entrained air bubbles. The study equips us to assess the best duration of vibration to remove large air voids without depleting small entrained air bubbles that are necessary for freeze-thaw protection.

Chapter 3 – Experimental Evidence for a Concrete Rheological Model

3.1 Introduction and Background

The rheology of fresh concrete determines its flow behavior. Two practical examples of flow are placing concrete to fill a form, and air voids rising through the concrete due to buoyancy. Concrete flow into forms and the removal of entrapped air are often augmented with the use of vibration. The effectiveness of these actions is also dependent on the rheology. While there have been many studies empirically examining the rheology of fresh concrete (Banfill, P. F., and Tattersall, G. H., 1983), and a few studies on the effect of vibration on fresh concrete (Baker, 1988) (Banfill, P. F., Craik, R. J., and Teixeira, M. A., 2011), there is still an incomplete understanding of how the rheology should be fundamentally analyzed, and of the mechanism by which vibration alters this rheology.

Figure 3.1 shows rheological data for concrete and mortar. It is the current practice of concrete engineers to classify both of these as simple yield-stress fluids and fit the data to a Bingham model:

$$\sigma = \sigma_y + \mu_p \dot{\gamma} \quad \text{Equation 3-1}$$

σ is the shear stress, $\dot{\gamma}$ is the strain rate, and the material fit parameters are the yield stress σ_y and the plastic viscosity μ_p . These models are used to experimentally characterize concrete, and are used as inputs into concrete flow simulations (Kuhne, H. C., Meng, B., Roussel, N., and Vasilic, K., 2011).

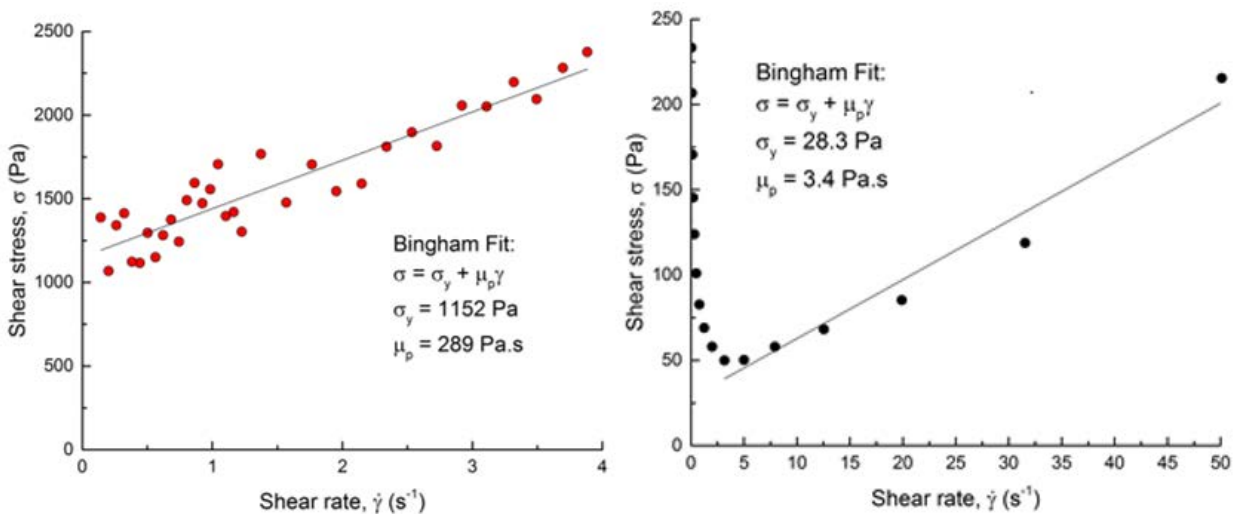


Figure 3.1. Concrete (left) and mortar (right) can be fit with reasonable accuracy using the simple Bingham model

The Bingham model is not sufficient to explain why concrete responds to probe and form vibration. Figure 3.2 shows a transparent Bingham fluid being acted on by a vibrating probe. The heavy spheres suspended in the fluid are only disturbed if they are within a few millimeters of the vibrating probe. That is, a simple Bingham fluid does not propagate vibration in a way that leads to compaction or air removal. This indicates that there are additional physical properties necessary to explain the mechanism of vibration in fresh concrete.

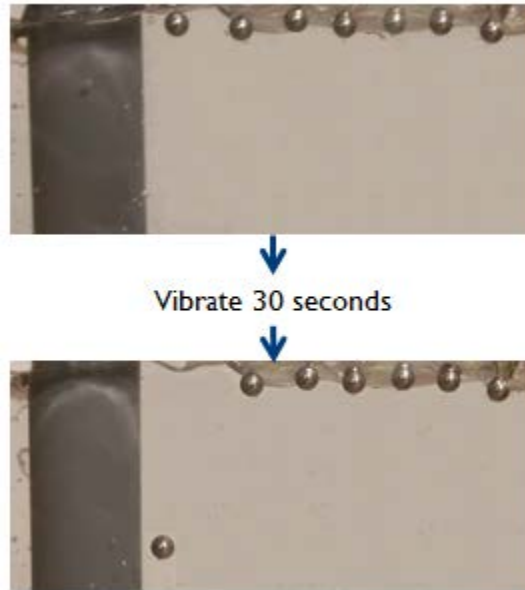


Figure 3.2. Vibration from a probe does not propagate more than a few millimeters into simple Bingham fluids, suggesting additional material properties are necessary to describe the mechanism of air void removal in concrete

3.2 Description of Concrete, Mortar, and Surrogate Materials

The concrete mixture used was a conventional mixture that included Type I Portland cement, potable city water, crushed limestone aggregate, and river sand. The coarse aggregate was crushed and blended to a CA07 Specification pursuant to the Illinois Department of Transportation (IDOT) while the sand was blended pursuant to FA02 Specification of IDOT. The water-to-cementitious (w/cm) ratio (by mass) of the conventional mixtures was 0.40, and in order to achieve adequate workability, a nominal 4.2 fl. oz. of high-range water reducing (superplasticizing) chemical admixture was added with every 100 lb. of cement. Lastly, a small dosage of air-admixture was added in order to increase the number of 10-micron sized air bubbles. This concrete mixture had a slump of 4-6 in. pursuant to ASTM C143, and the rheological properties were measured using the International Center for Aggregate Research (ICAR) rheometer (Section 3.3.1).

Table 3.1: Concrete mix design

Type III Portland Cement	674 lb per cubic yard
#7 Aggregate	1956 lb per cubic yard
#2 Sand	1180 lb per cubic yard
Water	270 lb per cubic yard
Sika Air Entraining Admixture 14	1.5 fl. oz/ 100 lb cementitious
Sika Viscocrete 2100 High Range Water Reducer	4.2 fl. oz/ 100 lb cementitious

In the case of Portland cement-based mortar, the material was prepared in accordance to ASTM C109 and the w/cm ratio was set to 0.30, with silica sand used in lieu of river sand.

A solution of Carbopol 980 neutralized in water at 0.30wt% (hereafter referred to as “carbopol”) was chosen as a surrogate for simple yield-stress materials. Carbopol is considered a quintessential simple yield-stress fluid, owing to its agreement with the Bingham model (with yield stress increasing with concentration) and fast material restructuring times. Additionally, it has the benefit of being transparent at low concentrations.

A surrogate granular material was created by mixing 100 cSt silicone oil ($\mu = 0.096$ Pa.s, $\rho=960$ kg/m³) with monodisperse spherical glass beads of $D=1$ mm. Because the beads are denser than the silicone oil they sink to form a random close pack, with a packing fraction of approximately 0.61.

3.2.1 Rheological Measurements and Vibration Environment

Rheological measurements on concrete were made using an ICAR concrete rheometer (Amzjane, S., Ferraris, C. F., Fowler, D. W., and Koehler, E. P., 2006). The probe geometry was a vane measuring 12.7 cm long with a 12.7 cm diameter. The containing vessel was a scalloped bucket with 28.6 cm diameter.

Rheological measurements on all other materials were made using the TA Instruments AR-G2 rotational rheometer. The probe geometry was a vane, with length 42 mm and diameter 28 mm. The containing vessel was a glass beaker with height 123 mm and diameter 68 mm.

Depth-dependent measurements were made on the rheometer by changing the depth the measurement vane was submerged into the fluid. The depth was measured from the top surface of the fluid volume to the center of the vane geometry, as seen in Figure 3.3. Since the measurement vane has a fixed height, the measurements represent the average rheological properties of the mortar at the vane location. Variation in depth was limited, with the minimum depth being chosen as 25 mm, which leaves a 4-mm layer of fluid between the top of the geometry and the fluid surface, and the maximum depth chosen to be 59 mm, beyond which the rheometer support would enter the fluid domain.

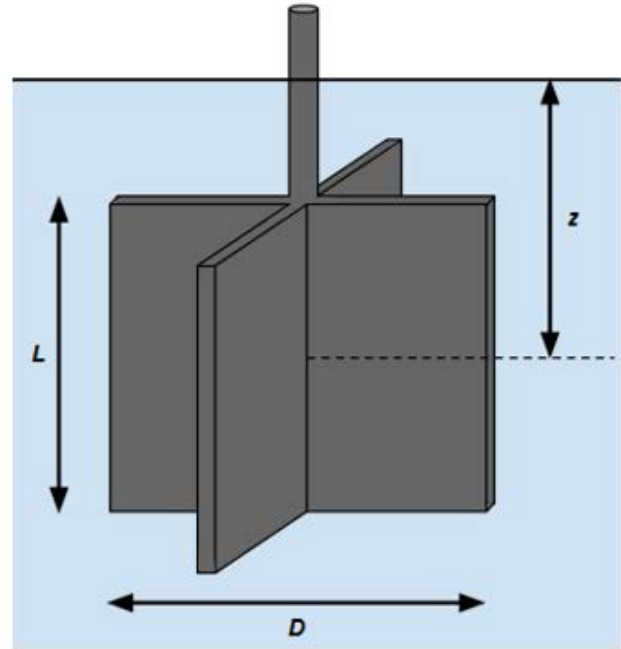


Figure 3.3. Depth-dependent rheology was measured by changing the amount the measurement geometry was submerged in the fluid (left), with the location defined as the center of the vane (right)

The vibrating environment for concrete was created using a concrete vibrating table, commonly used to compact fresh concrete. The rheometer bucket was placed on the table, and the measurement geometry and motor were isolated slightly above the bucket to eliminate direct propagation of vibration into the measurement geometry. For all other materials, vibration was achieved by placing the beaker in an ultrasonic bath. These setups can be seen in Figure 3.4.



Figure 3.4. Shaker table for concrete vibration (left) and ultrasonic bath for the vibration of the surrogate yield-stress fluid, granular material, and mortar (right)

3.3 Rheological Behavior of Surrogate Systems – Results

Both simple yield-stress materials and granular materials can be modeled as Bingham materials (Equation 3-1) during steady flow. However, their rheologies are expected to respond differently when the depth is varied, and when uniform vibration is applied. First, the behavior of simple yield-stress materials from granular materials using surrogate fluids was experimentally differentiate.

Figure 3.5 shows the effect of depth on the material properties of simple yield-stress fluids and granular materials. For simple yield-stress fluids, depth is not expected to influence the rheological properties, and indeed the only changes in the rheological measurements for carbopol can be attributed to the slightly increasing contact area of the geometry's support. For granular materials, the expectation is that the stresses will increase with depth, as deeper grains support additional weight and are therefore harder to displace and rearrange. The experimental results show that flow stresses increase by 120 Pa, a factor of 2.5, over a depth increase of just 34 mm.

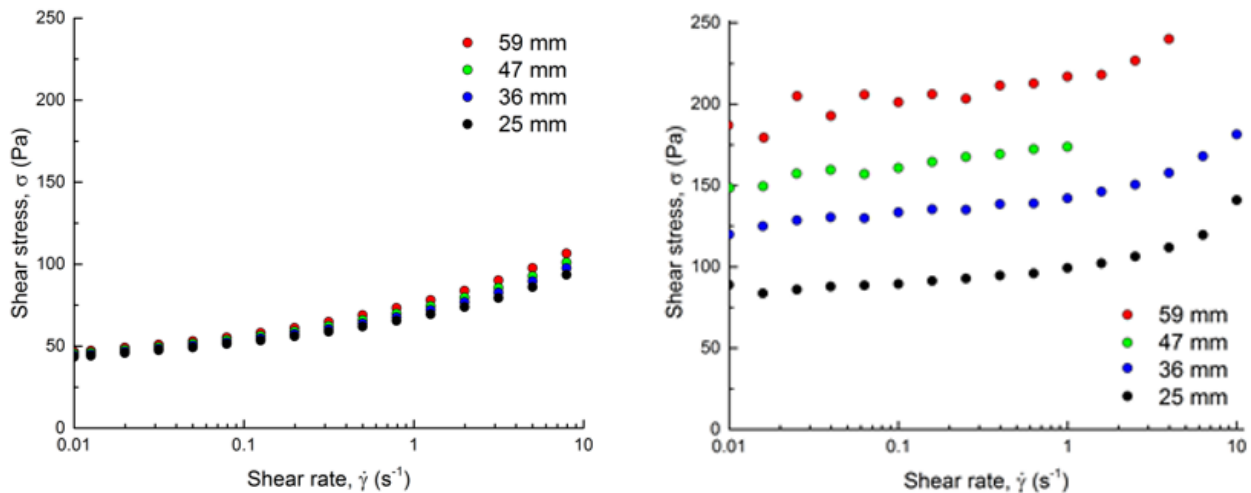


Figure 3.5. The rheology of simple yield stress fluids (left) is unaffected by variation in depth, while there is a marked increase in the flow stresses for granular materials (right) as the depth is increased

Figure 3.6 shows the effect of vibration on simple yield-stress fluids and on granular materials. No known studies demonstrate that uniform vibration will have any effect on the material properties of simple yield-stress fluids. There is a minor difference in the flow sweeps of the surrogate material, with the difference being attributable to measurement error due to vibration propagating into the measurement geometry. Most notably, the simple yield-stress fluid maintains a yield stress of approximately 40 Pa regardless of whether the sample is being vibrated, or not.

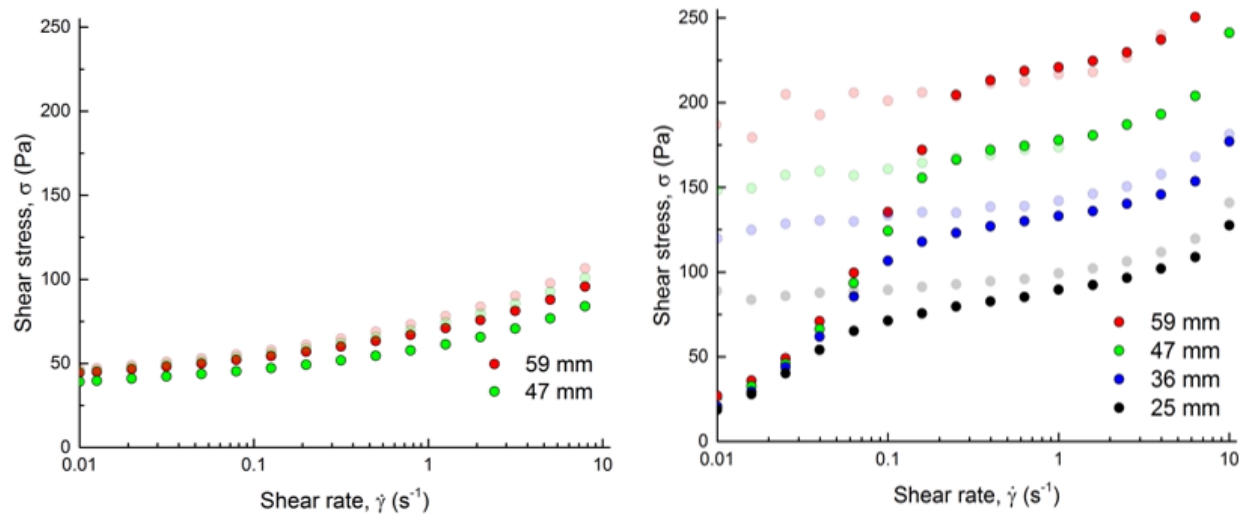


Figure 3.6. Response of simple yield-stress fluid (left) and granular material (right) to vibration, at different measurement depths, with data taken during vibration labeled with bright symbols and unvibrated data faded

The vibrated granular constitutive model predicts that vibration will eliminate the yield stress and make the material effectively Newtonian at small strain rates (Hanotin, C., Michot, L. J., and de Richter, S. K., 2015). It also predicts that vibration will not affect the rheology at high strain rates. These characteristics are seen in the experimental data for the surrogate granular system. Notably, the shear stress of the system decreased appreciably as the shear rate decreased. The rheometer was not capable of measuring lower shear rates. It is unknown if the material would converge to a yield stress at zero shear rate or if the yield stress would be eliminated if the shear rate went to zero. In addition, though granular materials have depth-dependent rheology when they are not being vibrated, this depth-dependence disappears for low strain rates ($\dot{\gamma} < 0.05 \text{ s}^{-1}$) during vibration. Assuming small flow perturbations, i.e., from a bubble rising, this means that the whole fluid domain adopts the same Newtonian viscosity during vibration.

3.3.1 Rheological Behavior of Concrete and Mortar

As mentioned previously, a single flow sweep measurement of concrete/mortar can be reasonably modeled with a Bingham constitutive model (Figure 3.1). A comparison was sought of the rheological responses of the concrete and mortar to those of the surrogate simple yield-stress system and surrogate granular system.

Figure 3.7 shows the results of varying the depth of measurement for mortar. Similar to the granular surrogate fluid, the flow stresses increase by a factor of four over a change in depth of only 34 mm. This is a strong indication that the sand grains within the mortar are experiencing larger normal forces as depths increase, which increases the torque necessary to induce a shearing motion. It should be noted that the plastic viscosity in the mortar is higher, and the yield stress is lower, than in the surrogate granular fluid. Nevertheless, both materials fit within the Bingham curves, and the dramatic increases in the measured stresses indicate that mortar should be considered a granular material.

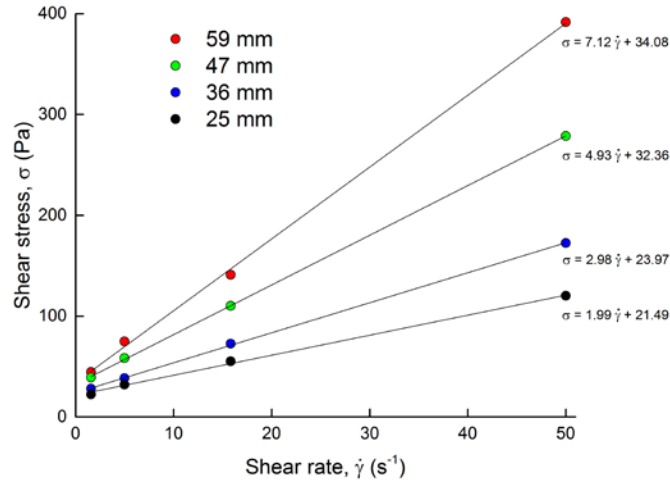


Figure 3.7. Rheological measurements of mortar at various depths (with Bingham fits), demonstrating that the flow stresses increase with increasing depth

Figure 3.8 compares the rheology of concrete and mortar during vibration and without vibration. Note the dramatic departure of the vibrated stresses from the unvibrated stresses at low shear rates in both cases, with an apparent elimination of the yield stress and development of approximately Newtonian behavior. This signature was also seen in the surrogate granular system, and is predicted in the vibrated granular constitutive model.

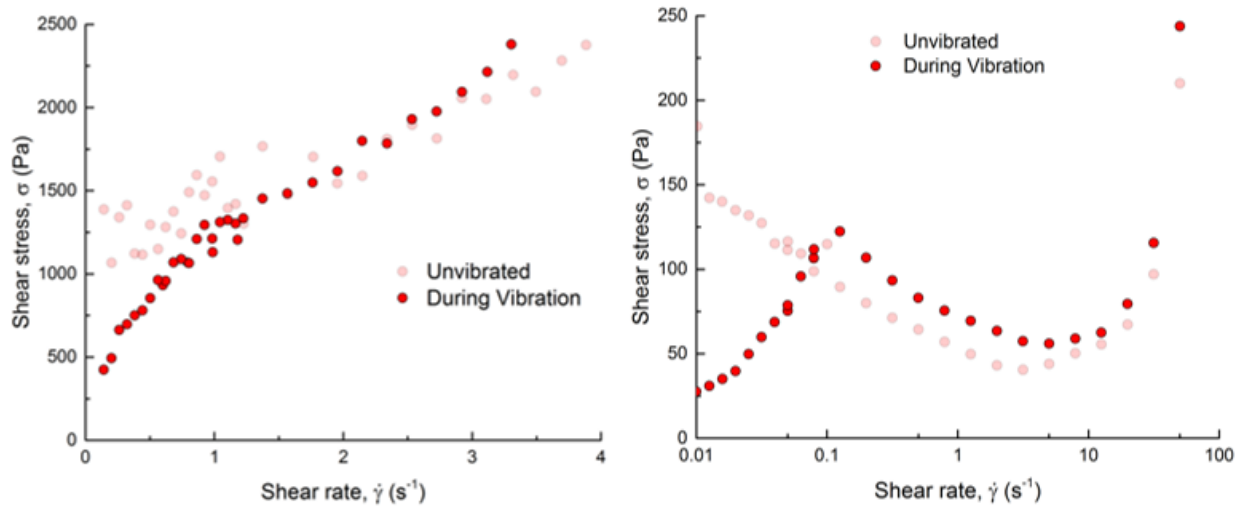


Figure 3.8. Vibration causes a substantial reduction/elimination of the unvibrated yield stress in both concrete (left) and mortar (right), a result predicted by granular theory

Mortar also loses its depth-dependent rheology during vibration at low strain rates, as seen in Figure 3.9. After a small factor representing the stiffening of the mix with time is subtracted from the four data sets, they all collapse onto nearly the same curve for strain rates $\dot{\gamma} < 0.05 \text{ s}^{-1}$, giving a fit viscosity of approximately 1380 Pa.s regardless of the depth. This trend again agrees with the surrogate granular fluid (Figure 3.6).

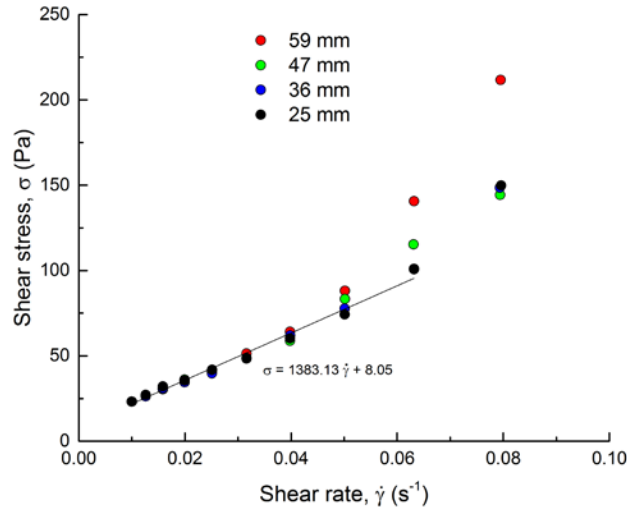


Figure 3.9. Though mortar displays depth-dependent rheology when not vibrated, when vibrated the depth-dependence disappears at low shear rates

3.4 Conclusions from Experimental Work

Inadequacies in the understanding of vibration propagation through fresh concrete inspired the development of a new approach to the constitutive modeling of concrete and mortar.

Experiments demonstrated that these materials should not be interpreted as simple yield-stress fluids, though such models prevail in the literature. It was experimentally justified that these materials are better understood through granular constitutive models.

Two signatures were sought that differentiate the behavior of simple yield-stress fluids and granular materials. The first is depth-dependent rheology. Experiments demonstrated that the depth of measurement does not influence the rheological properties of simple yield-stress fluids. However, the flow stresses in granular materials were seen to increase with depth, an effect that is attributable to the additional weight that is supported by grains that are at greater depths in the material. Similar measurements made on mortar demonstrated the same signature as the surrogate granular system, with flow stresses increasing by a factor of four over a change in depth of 34 mm.

The second signature is the effect of uniform vibration on rheology. It was shown that vibration had a negligible effect on the properties of simple yield-stress fluids. In granular fluids, vibration eliminated the yield stress, making the material quasi-Newtonian at low shear rates. This result was predicted by a constitutive model for vibration granular materials, and is a strong indication that the mechanism of fluidization results from vibration imposing a physical separation of grains. Rheological measurements made during uniform vibration of both concrete and mortar show that, at low shear rates, the yield stresses of these materials are largely eliminated, while at high shear rates the rheology of both was unaffected by vibration—trends predicted by the vibrated granular constitutive model.

The behavior of concrete and mortar in these two situations strongly suggest that these materials should be analyzed as granular in relevant applications, which has important implications for understanding air bubble rise in concrete. This interpretation may explain why vibrating

concrete and mortar causes the removal of air—the vibration induces a separation of aggregate—and has additional implications for the practice of vibrating freshly-placed concrete.

3.5 Practical Implication of Concrete as a Granular Material: “Cone of Action”

The vibration experiments in Section 3.3 were performed in a homogenous environment, where the whole fluid domain was put in motion by a vibration source. Vibration environments can also be inhomogeneous, notably via the use of a vibrating probe as seen in Figure 2.3. It is known that the probe vibration has a finite radius of effect—called the “radius of action” in concrete literature (Banfill, P. F., Craik, R. J., and Teixeira, M. A., 2011). Current practice is to insert the vibration probe in various locations around newly-placed concrete such that the observed radii of action overlap. However, it will be shown that this practice is potentially insufficient to ensure vibration of the entire concrete domain. The derivation is adapted from (Winter, 2011).

3.5.1 Assumptions

There are three key postulates in the understanding of this mechanism:

1. The stress-state of concrete can be described with a positive coefficient or lateral earth pressure, which implies that its horizontal effective stress is a fraction of its vertical effective stress.
2. A vertically-positioned vibrating probe will reduce the horizontal normal stresses but will not affect the vertical normal stresses.
3. There exists a Mohr-Coulomb failure criterion for concrete based on a friction angle. Failure occurs when vibration causes the Mohr’s circle to intersect the Mohr-Coulomb failure envelope, leading to fluidization of the concrete.

The concept of a Mohr-Coulomb failure envelope is frequently seen in soil sciences, and can be represented by:

$$\tau_{fail} = \sigma \tan \alpha \quad \text{Equation 3-2}$$

Which is to say the shear stress necessary to fail the material, τ_{fail} , depends on the normal stress σ , with the proportionality being the tangent of the friction angle α . This means that granular materials require more shear stress to fail when the normal stress is larger—precisely the result seen in Figure 3.5 and Figure 3.7, wherein the flow stress of the granular surrogate and of mortar increases with increasing depth, which causes larger normal stress due to the weight of the grains. Note this law is reminiscent of Coulomb’s law of friction, where the friction force scales with the normal force, with the proportionality called the coefficient of friction. Equation 3-2 can be modified to include cohesiveness which can be interpreted as a zero-depth yield stress. However, the cohesiveness does not factor into the following derivation, so it is assumed to be zero.

3.5.2 Derivation of Failure Angle

It is postulated that vibration will reduce the horizontal stress of the concrete, expanding the Mohr’s circle until it intersects the failure envelope, a scenario explained in Figure 3.10. The horizontal stresses cannot be reduced beyond this point, so a line can be drawn perpendicular to

the failure envelope through the center of the circle (c^*). Recall that traversing an angle ϕ in physical space corresponds to traversing an angle of 2ϕ on the Mohr's circle. So from simple trigonometry, a failure angle θ_f can be determined as:

$$\theta_f = \frac{\pi}{4} + \frac{\alpha}{2} \quad \text{Equation 3-3}$$

In two dimensions, this angle sets the line that separates the fluidized region from the region that remains rigid.

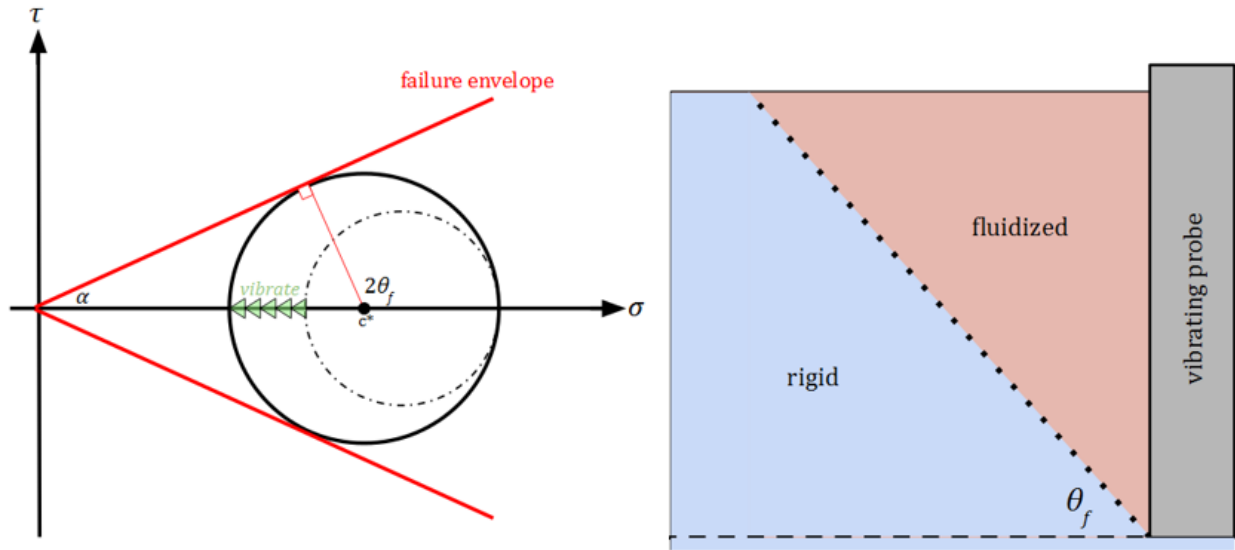


Figure 3.10. Mohr's circle for fresh concrete being acted on by a vibrating probe (left) and the resulting partial fluidization of the domain of concrete, with predicted failure angle θ_f (right)

This means that, for a probe of length L , the observed radius of action at the surface will be as seen in Figure 3.11.

$$R = \frac{L}{\tan \theta_f} \quad \text{Equation 3-4}$$

As a practical example, using the friction angle of sand ($\alpha=32^\circ$), one can predict a failure angle of concrete to be $\theta_f=61^\circ$ and an observed radius of $R=5.5$ cm.

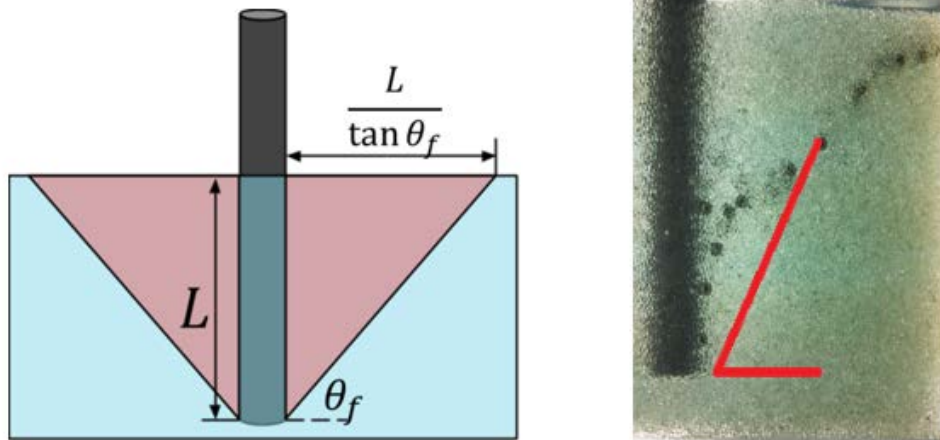


Figure 3.11. Probe vibration activates a cone-shaped region with volume dependent on the depth of the probe and the failure angle (left), a result confirmed experimentally in the translucent granular surrogate fluid (right) with predicted failure angle of 59 degrees in red

3.5.3 Experimental Confirmation in Granular Surrogate Fluid

The failure angle phenomenon was observed experimentally in the translucent granular surrogate fluid. A small-scale vibration probe (0.75" diameter) was constructed, along with a rectangular acrylic domain with dimensions 2" by 6" by 6". By seeding the top surface with heavy ball bearings, it was observed that the bearings were mobilized by vibration, sinking to a depth that decreased approximately linearly with the distance from the probe. The angle formed between the horizontal and the line along which the bearings stopped (extrapolated the probe end) agreed very well with the predicted $\theta_f=59^\circ$ calculated based on the friction angle of the glass beads, which is plotted in red in Figure 3.11.

3.5.4 Implications for Concrete Practice

These results suggest that the region mobilized at the surface around a vibrating probe is not indicative of a cylindrical region of activation within the concrete, as is implied by "radius of action." Instead, granular theory predicts the region of activation is shaped like an inverted cone, a result that is substantiated experimentally with lab-scale probe in a surrogate granular material. The cone-shaped region of activation makes creating a homogenous distribution of small air bubbles in vibrated fresh concrete a practical impossibility.

While vibration probes remain useful for encouraging the compaction of fresh concrete, especially around obstacles such as rebar, the effect on the entrained air bubble population varies as a function of location and depth within the fresh concrete.

3.6 Development of the Bubble Rise Model

The experimental evidence presented in the previous sections informs the development of a model for air bubble rise in concrete. The key observation is that concrete is a granular material, with a response to vibration that is predicted by theory (Hanotin, C., Michot, L. J., and de Richter, S. K., 2015) to be Newtonian at low strain rates—the regime that is important to small bubbles. The bubble rise model is built from the associated vibrated granular constitutive model.

The model is based on experimentally-obtained rheological data for concrete. However, it must be realized that the rheology seen at the scale of the concrete rheometer, which involves the movement and entanglement of aggregates, is not the rheology seen at the bubbles' scale, since the bubbles move through the paste phase, and have very little effect on aggregate motion. To address this, the experimentally-measured concrete viscosity is processed through Roscoe's equation for concrete (Vazques, 2004) to arrive at a paste-phase viscosity relevant to the bubble motion.

3.6.1 Model Construction

The model for an individual bubble's rise speed is built using Equations 2-9 (speed) and 2-11 and 2-12 (Roscoe's equation for concrete), with theoretical extrapolations to be made using Equation 2-17 (vibration-dependent viscosity), as shown in Chapter 2. These equations are repeated here for convenience:

$$U = \frac{1}{12} \frac{\Delta\rho g D^2}{\mu} \quad \text{Equation 2-9}$$

$$\mu_{conc} = \frac{G}{f_b} + \eta_H \quad \text{Equation 2-17}$$

$$\mu_{mortar} = \mu_{paste} \left(1 - \frac{1}{r} V_{sand}\right)^{0.89m-9.31} \quad \text{Equation 2-11}$$

$$\mu_{conc} = \mu_{mortar} \left(1 - \frac{1}{\tilde{r}} V_{coarse}\right)^{0.57\tilde{m}-3.40} \quad \text{Equation 2-12}$$

Combining these equations gives Equation 3-5 and 3-6:

$$U = \frac{1}{12} \frac{\Delta\rho g D^2}{B \mu_{conc}} \quad \text{Equation 3-5}$$

$$B = \frac{\mu_{mortar}}{\mu_{conc}} \cdot \frac{\mu_{paste}}{\mu_{mortar}} \quad \text{Equation 3-6}$$

With the experimentally-measured concrete viscosity μ_{conc} , density difference $\Delta\rho$, gravitational acceleration g , and bubble diameter D . B represents the factor by which the concrete viscosity exceeds the paste viscosity owing to the presence of aggregate in suspension. Equation 2-17 further allows us to see how modification of the model fit parameters G , μ_p , and f_b will influence bubble rise behavior.

Importantly, even though granular materials have a yield stress that increases with depth, vibration causes a separation of grains that eliminates this effect, meaning that, during uniform vibration (as in form vibration), the concrete adopts a uniform viscosity throughout its domain. This result is seen in Figure 3.6 (for the surrogate granular system) and Figure 3.8 (for mortar), and greatly simplifies the model construction.

3.6.2 Parameter Selection

Choices for the parameters are based on experimental fits and typical values, as summarized in Table 3.2.

Table 3.2: Parameter Choices for the Bubble Rise Model

Parameter	Value	Notes
σ_y	1134 Pa	Fit from Figure 3.6 (unvibrated)
μ_p	298 Pa.s	Fit from Figure 3.6 (unvibrated)
μ_{conc}	1415 Pa.s	Fit from Figure 3.6 (vibrated)
γ_c	0.05	Fit from additional experimental data
G	22680 Pa	$G = \sigma_y / \gamma_c$
f_b	20.3 Hz	$f_b = G(\mu_{conc} - \mu_p)^{-1}$
$\Delta\rho$	1700 kg/m ³	w/cm=0.40 by mass
B	0.0102	Assumed $(r, m, \tilde{r}, \tilde{m}) = (1, 3, 0.67, 6)$

3.6.3 Initial Bubble Distribution

One key parameter in the model is the starting distribution of bubble sizes. The air bubble distribution was derived experimentally from polished concrete specimens in a process detailed extensively in Section 6.5. A saw-cut sample of concrete is polished, treated with phenolphthalien to stain the cement paste, and then dusted with a fine orange powder to fill air voids, and imaged via a high-resolution flatbed scanner. A spectral analysis is used to segment the image into three phases—aggregate, paste, and air bubbles. Such an image, shown as a gray-scale image with three phases (i.e., black, gray, white) can be seen in Figure 3.12.

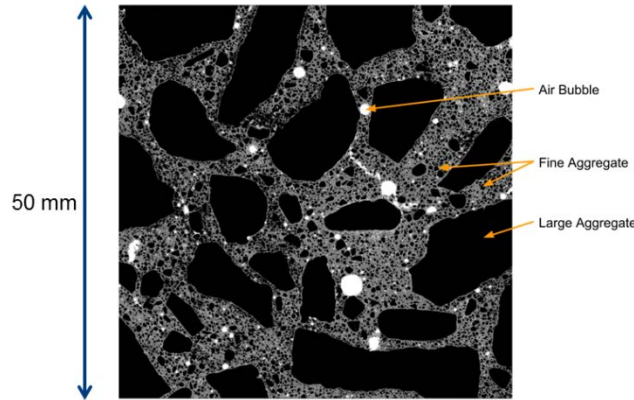


Figure 3.12. A saw cut, polished, and treated 50 mm x 50 mm sample of concrete, with aggregates appearing black, cement paste appearing gray, and air bubbles appearing white

The results of the analysis are plotted in Figure 3.13 as a histogram, along with a log-normal distribution with mean $n=-8.5$ and standard deviation $s=1.2$.

$$f(x) = \frac{1}{xs\sqrt{2\pi}} e^{-\frac{(\ln x - n)^2}{2s^2}} \quad \text{Equation 3-7}$$

This log-normal distribution is used as the initial distribution of bubble sizes in the simulation, with 1000 bubbles generated, while the bubble positions are assumed to be distributed uniformly

across the domain. Additionally, the figure plots the bubble size distribution of a concrete sample that has undergone 2 minutes of vibration, which can be used to verify the accuracy of the model.

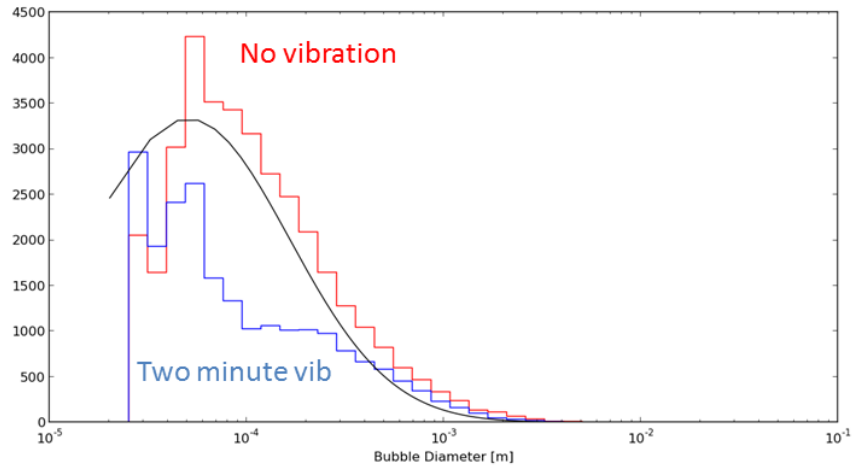


Figure 3.13. Histogram of air bubble diameter for two polished concrete samples, one without vibration applied (red) and the other with two minutes of vibration (blue), and theoretical log-normal distribution (black)

3.6.4 Model Results

A two-dimensional domain of width 2.5 m and height 0.25 m was chosen, and total air volume V is calculated via Equation 3-8:

$$V = \frac{1}{6} \pi \sum_{y_i < H - D_i/2} D_i^3 \quad \text{Equation 3-8}$$

Where the summation is performed for all bubbles that have not left the domain of height H . The simulation was run for a time of 600 seconds, with the results plotted in Figure 3.14, normalized by the initial volume of air.

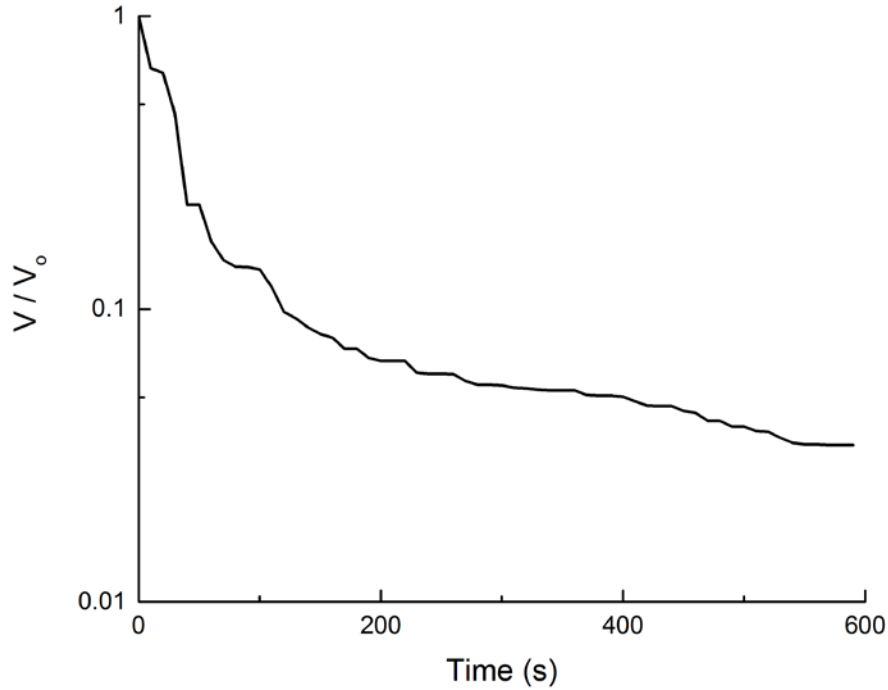


Figure 3.14. Normalized total air volume vs. time, demonstrating an air loss of an order of magnitude within the first minute of vibration

It can be seen that there is a significant reduction in air content within the first minute of vibration, with the normalized volume dropping by an order of magnitude. This is a manifestation of the fact that larger bubbles have the largest volume (which scales with D^3) and the fastest rise speed (scaling with D^2). For the remaining 5 minutes of vibration, the air content drops by only an additional half-order of magnitude, suggesting that, once the large bubbles vacate in the first minute, there exists a population of small bubbles that endures due to their very slow rise speeds.

A qualitative picture providing intuition of this process can be seen in Figure 3.15, which shows images of the bubble population within the fluid domain, with bubble diameter increased by a factor of 100 for visualization purposes, at times of 0, 300, and 600 seconds. The populations appear vastly different between the initial image and the image at 300 seconds, but the difference between the images at 300 and 600 seconds is miniscule.

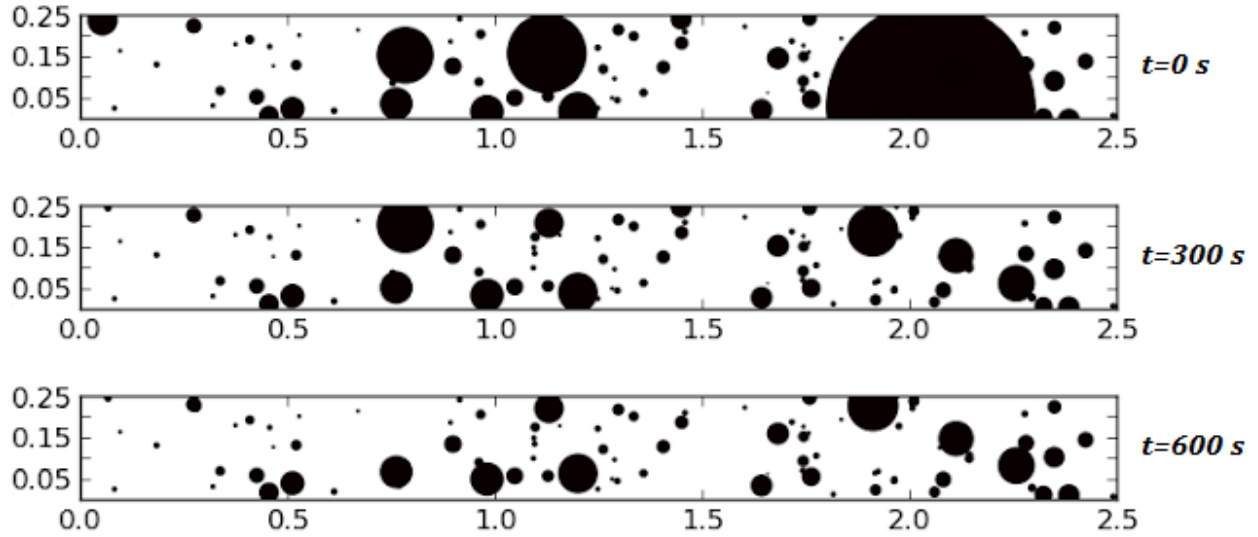


Figure 3.15. Images of the fluid domain with bubble population (with diameters magnified 100x) as time evolves

3.6.5 Variation of the Parameters that Influence the Vibration Viscosity

Equation 2-17 for the low-strain rate viscosity of a vibrated granular material can be rewritten in the form shown in Equation 3-9:

$$\mu = \frac{1}{\gamma_c} \frac{\sigma_y}{f_b} + \mu_p \quad \text{Equation 3-9}$$

Assuming the critical strain γ_c and vibration parameter f_b are constant, this reveals that the viscosity during vibration is linearly dependent on both the plastic viscosity μ_p and the measured yield stress σ_y . A consequence of this is that, if it is desirable to maintain the same vibrational behavior, a decrease in yield stress can be compensated by an increase in the plastic viscosity and vice versa, as seen in Figure 3.16.

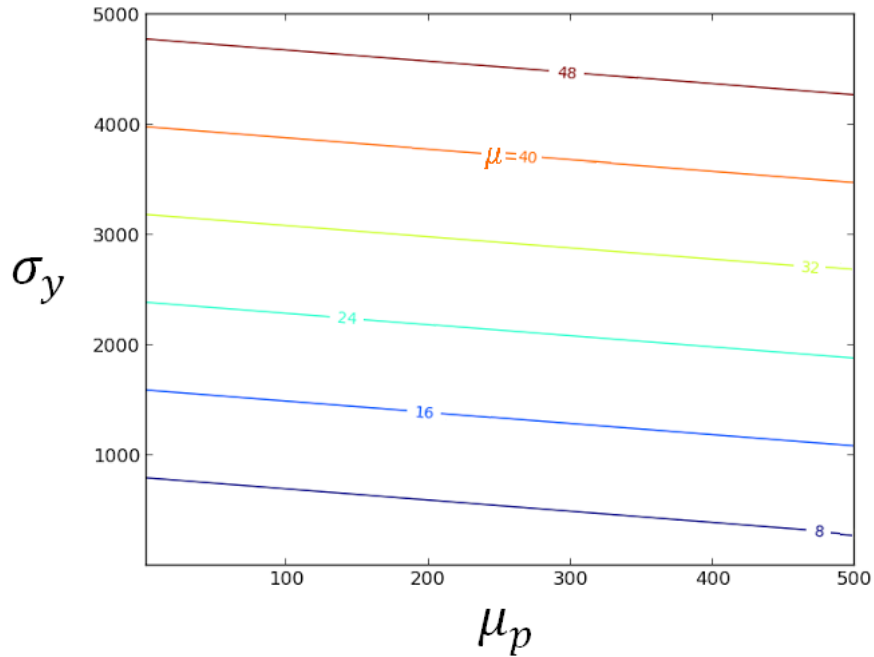


Figure 3.16. Contour plot of vibrated viscosity as a function of plastic viscosity and yield stress

3.6.6 Dependence of Air Volume on Model Viscosity

As described in Equation 3-9, the model predicts that there are several ways to modify the viscosity, including changing the plastic viscosity, yield stress, and vibration intensity. Changing the viscosity will change the rise speed and thus will affect the air content. Figure 3.17 plots the air content as predicted by the simulations for model viscosities ranging from 1 to 60 Pa.s, with the experimentally-derived viscosity of 14.4 Pa.s plotted in black.

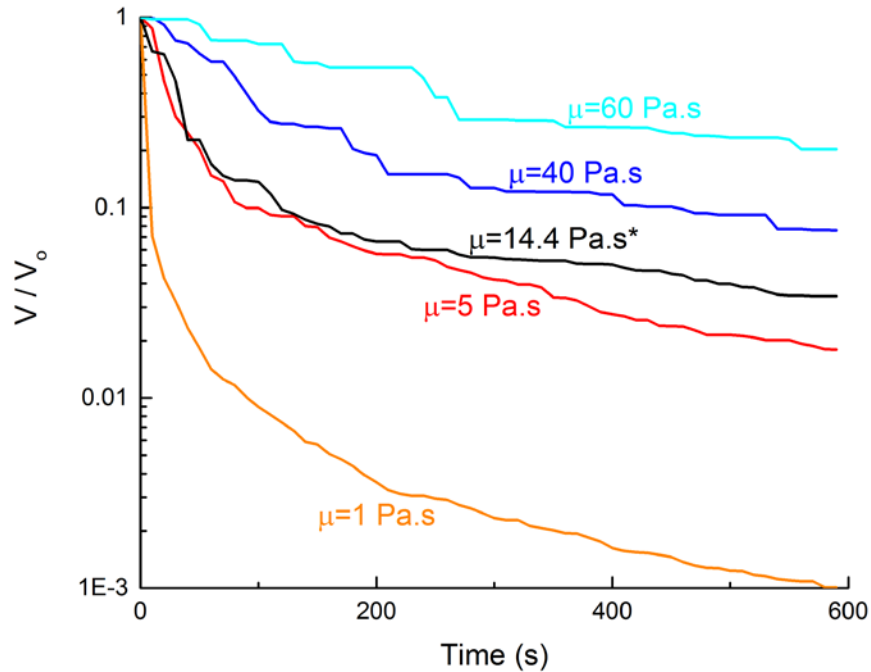


Figure 3.17. Variation in the time history of the normalized air volume for various viscosity values, with the experimentally-derived model viscosity in black

The large spread of the predictions suggests that there may indeed be an optimal viscosity for maintaining a distribution of entrained air in a concrete after vibration. A viscosity near 1 Pa.s causes air content to decrease by more than an order of magnitude within 10 seconds, and the air content continues to rapidly decrease through the entire duration of vibration. At a viscosity of 60 Pa.s there was very slow air removal, with the normalized air volume remaining above 0.2 even after 10 minutes of vibration. Perhaps not coincidentally, the viscosity derived from the experimental measurements of a conventional concrete vibrated on a standard concrete shake table leads to an apparently good balance of ease in placement and air loss, with air content decreasing by an order of magnitude after a minute of vibration, and slowly decreasing after that. Again, it should be emphasized that the viscosity referenced here is a product of the model, and can be modified via changes to the plastic viscosity, yield stress, and/or vibration parameters.

3.6.7 Fundamental Dependence of the Vibration Parameter on Physical Variables

The vibration parameter f_b is presented as a fit parameter, with no discussion of its dependence on vibration frequency and amplitude, material parameters such as aggregate size, or any other factor. Though it has units of Hz, it is not simply the vibration frequency.

In granular literature, the criterion for judging vertical vibration intensity is typically chosen as the dimensionless acceleration shown in Equation 3-10:

$$\Gamma = \frac{A\omega^2}{g} \quad \text{Equation 3-10}$$

For vibration amplitude A , radial frequency ω , and gravitational acceleration g . For $\Gamma > 1$, the intensity of vibration is enough to cause the grains to “lift off” for at least a portion of the oscillation period, inducing a separation in the grains that causes fluidization (Behringer, R. P., Jaeger, H. M., and Nagel, S. R., 1996). However, there is evidence in the literature that the dependence depends instead on the vibration velocity ($A\omega$) (Banfill, P. F., Craik, R. J., and Teixeira, M. A., 2011), (Banfill, P. F., and Tattersall, G. H., 1983).

Note from Equation 3-9 that the minimum vibration viscosity $\mu = \mu_p$ is seen when $f_b \rightarrow \infty$. The parameters derived from the experimental results suggest a value of $f_b=20.3$ Hz, making the contribution to the viscosity from the yield-stress/vibration term larger than the contribution from the plastic viscosity term by nearly a factor of four. It is unclear if the yield-stress contribution can be completely eliminated with vigorous-enough vibration, or if f_b has an upper limit. This item deserves further consideration in future work.

3.6.8 Variation in the Initial Bubble Distribution

The experimentally-determined initial distribution of air (Figure 3.13) was taken from a concrete with a high amount of air entrainment, leading to a large population of bubbles with $D < 10^{-4}$ m. The simulation was repeated using the same functional dependence of the bubble distribution (Equation 3-7), but with $n=-6.2$ and $s=1.2$, which increases the median and mode bubble sizes by one order of magnitude. The results of initializing the simulation with this distribution are plotted in Figure 3.18 (along with the original result with data from the polished sample).

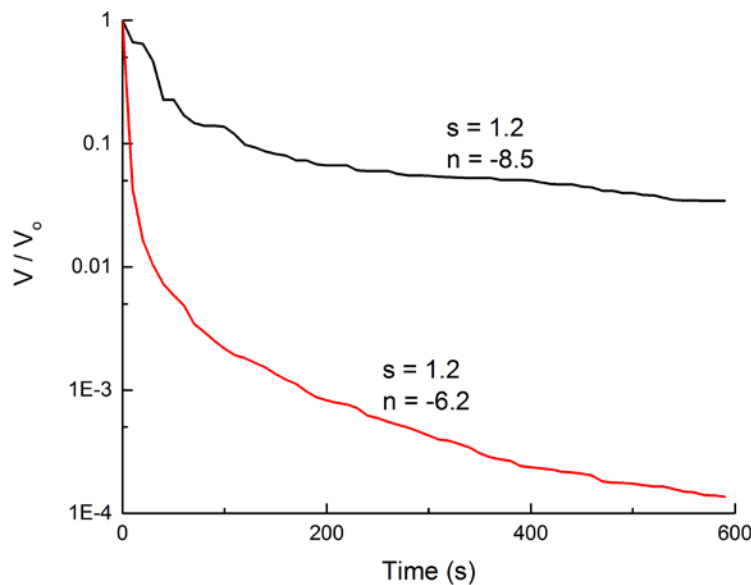


Figure 3.18. The normalized air content as a function of vibration time, using the experimentally-determined bubble distribution (black) and a hypothetical distribution with mean and mode larger by one order of magnitude (red)

The simulations suggest the initial bubble distribution has a dramatic effect on the air content with time. Increasing the mode bubble size from 0.05 mm to 0.5 mm and the median bubble size from 0.2 mm to 2.0 mm causes the air content to drop by nearly three orders of magnitude in 120 seconds of vibration, and it continues dropping nearly another order of magnitude by 600

seconds. Compare this to the distribution obtained from the polished sample, which drops by only about 1.5 orders of magnitude in 600 seconds. This means that fresh concrete with an initial bubble distribution having relatively small mode bubble size will exhibit superior ability to retain entrained air when vibrated.

However, it should be noted that the definition of air content used here, normalized over the initial volume of air, weighs heavily towards larger air bubbles. This means that a large percentage air loss in time is not indicative of the disappearance of all bubbles in the system. Rather, there still exists a population of small bubbles that endure through the vibration process, with these bubbles carrying a small fraction of the total volume.

3.6.9 Implications for Concrete Practice

The model predicts that uniform vibration can be used to eliminate large air voids in freshly-placed concrete, while allowing a population of small air bubbles to endure. Physically, this result is a manifestation of the sensitivity of rise speed to bubble size—since the speed scales with diameter squared, a bubble that is, say, 5 mm in diameter, will rise and leave the system 100x faster than a bubble that is 0.5 mm in diameter.

While every geometry and concrete is different, the model predicts that the vibration time necessary to remove large air voids from a system is on the order of one minute. Vibration times of several minutes are, therefore, potentially unnecessary, though the rise speeds of the smallest bubbles are slow enough that such a practice is unlikely to be harmful unless taken to an extreme.

Small bubbles were shown in the model to remain in the concrete during vibration. A wide distribution of bubbles helps ensure that all areas of the concrete are protected from freeze thaw. The common practice of measuring total air content is unable to inform the question of air bubble size, and indeed total air content is most highly sensitive to the larger air bubbles in the distribution. Selection of air entraining admixture, mixing action, mixing time in consort with mixture proportioning will govern the achievement of an air bubble distribution with a satisfactory population of small air bubbles.

The parameter dependency of the model viscosity implies that changes in the yield stress can be compensated by changes to the plastic viscosity to keep the same vibration behavior, and there is potential that vibration conditions can be modified to achieve the same compensation, though the dependency of the model's vibration parameter on physical variables warrants further study. Clearly, every concrete producer will encounter unique form geometry, vibrator characteristics, and concrete material properties. It is a practical imperative that producers study these issues under their local conditions.

3.7 Conclusions

Experiments demonstrated that the flow stresses of mortar increase with increasing depth of measurement, a result attributable to the increasing overburden of aggregate and therefore increasing difficulty of aggregate rearrangement. Further, it was demonstrated that mortar and concrete see a reduction (almost eliminated) of the yield stress during uniform vibration, with the rheological behavior at high strain rates being uninfluenced by vibration. These two results were compared to responses for a simple yield-stress material and a spherical bead granular system, with both concrete and mortar finding greater similarity in the surrogate granular system. This is

a strong indication that the Bingham model (Equation 3-1), which sees widespread use in concrete literature and is applicable to simple yield-stress fluids, is an insufficient model for understanding the behavior of concrete under vibration.

These experimental results have important implications. First, in the scenario of probe vibration, the granular nature of concrete will lead to a region of fluidization shaped like an inverted cone. This is a departure from the understanding currently present in concrete literature, which discusses the “radius of action”—a term which implies that the action of the vibration is uniform with depth. Significantly, this implies that the observed region of fluidization at the surface does not extend vertically downward, meaning that probe vibration is not uniform and could potentially lead to inhomogeneous material properties.

Second, confirmation of the numerical model by the experimental results for concrete under vibration allows for the prediction of the viscosity experienced by an air bubble population during uniform vibration. The experimental evidence informs the construction of a bubble rise model, based on the analytically-derived expression for the rise speed of a bubble in a Newtonian fluid and Roscoe’s equation, which predicts the factor by which viscosity is increased by the inclusion of aggregates in a suspending fluid. Using an experimentally-derived initial bubble population, the model results predict the diameter-squared scaling of the bubble rise speed is sufficiently sensitive to cause an elimination of larger bubbles within a minute of vibration, while allowing a population of smaller bubbles to be maintained.

The results are extended based on the predictions of a vibrated granular constitutive model. Decreasing the model viscosity by an order of magnitude was shown to cause rapid, continuous removal of air bubbles, potentially eliminating even small bubbles from the fluid domain. Increasing the model viscosity by half an order of magnitude caused very slow air motion, maintaining a population of both large and small air bubbles even through 10 minutes of vibration. The vibrated viscosity can be modified via changing the yield stress, plastic viscosity, or vibration properties, though the precise effect of physical vibration variables such as frequency and amplitude require further study.

The results of the model suggest that it is possible to predict and control the final distribution of air in a concrete system by optimizing the initial distribution of air, concrete properties, and vibration parameters.

Chapter 4 – Influence of Vibration in Portland Cementitious Materials and Model Materials

4.1 The Practice of Concrete Vibration

Concrete is vibrated in order to drive out entrapped air and to minimize defects (honeycombing, bug-holes, pockets, etc.) around the reinforcements and form walls. ACI Committee 309 (reports 309.1. and 309.8) provide guidance about consolidation methods for concrete practitioners (American Concrete Institute, 2008). Figure 4.1 shows the principle of internal vibration and surface vibration where rapidly recurring compression waves emanate from the source of vibration. Each pulse is generated by an eccentrically positioned mass rotating about an axis encased in a housing. The eccentricity of the vibrator imparts energy onto the fresh material through the housing directly (as is the case in an immersion pencil probe vibrator) or imparts energy onto the formwork directly. Thereafter, the formwork imparts the vibrational energy onto the fresh material.

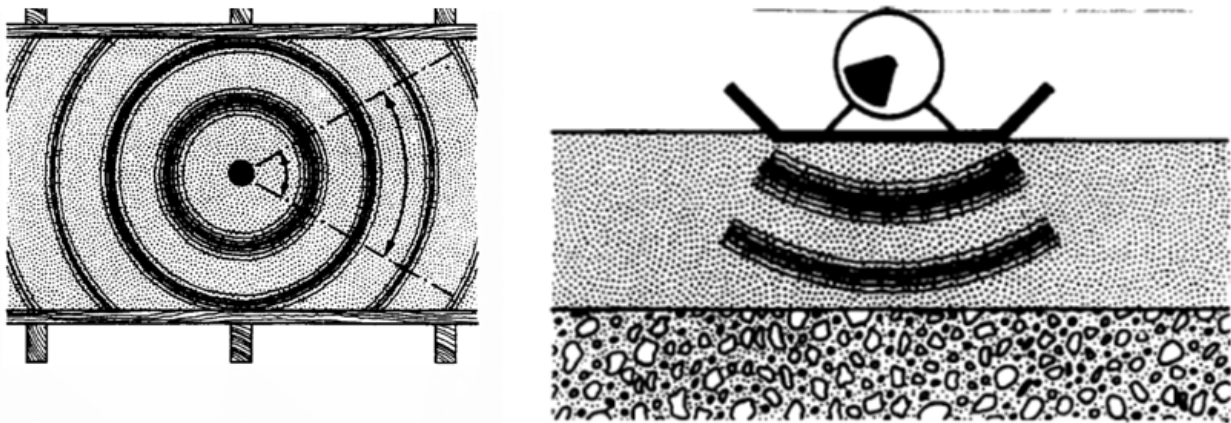


Figure 4.1. Circularly emanating compression waves from internal (left) and external (right) source of vibration (from ACI 309)

The effectiveness of the vibration source to impart energy onto the fresh material is dependent upon several factors, including the frequency of the impulse and the amplitude of the impulse. The efficiency of consolidating vibration is often considered with regards to final material density and ultimate compressive strength. Figure 4.2 shows optimized curves of frequency and amplitude in order to achieve a radius of action in which a favorable density is achieved across a large volume of fresh material. Peaks in the curve suggest that a frequency or amplitude that is set too large can lead to a reduction in the compacted volume of material. This set of curves informs the industry to design consolidating vibration equipment to target approximately 200–240 Hz and a large amplitude (as allowable by the frequency) in order to maximize consolidation of the fresh concrete material. However, relatively little information is relayed about the effects of duration of vibration, mold geometries, material proportioning, and entrained air bubble size distribution on fresh concrete. Control of entrained air can be challenging for concrete products that undergo vibration during final placement.

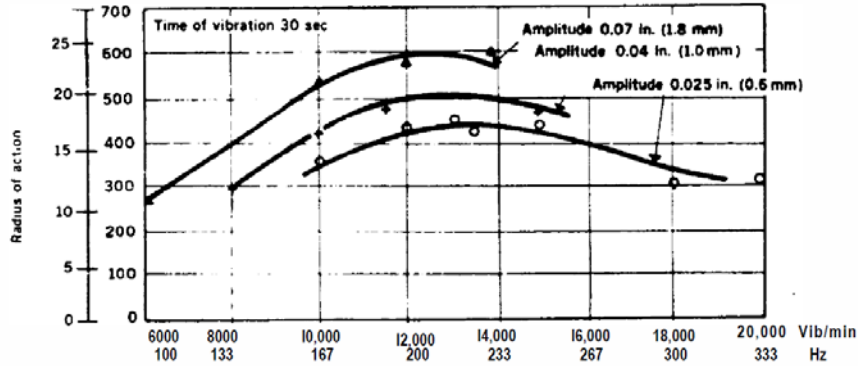


Figure 4.2. Maximization of radius of action of a 2.5 in. diameter immersion probe with varying frequency and amplitude settings (from ACI 309)

4.1.1 Rheology of Concrete as Affected by Aggregate Volume Fraction and Consolidating Vibration

Fresh concrete flows and is deformable, like a fluid. Fluids can be characterized in a number of different ways. A Newtonian fluid, for example, will readily flow at a rate that is directly proportional to the rate at which an external force shears it. This flowability is termed viscosity, η , and is a constant value that is independent of the magnitude of external shearing. Some materials do not readily flow at very low shearing rates, however. These fluids require an external shear rate of some appreciable magnitude before the fluid flows. This minimum shearing force is called the yield stress, σ_y , and is typical in Bingham fluids (or Bingham plastics). After a sufficient yield stress is applied, then the material flows at a non-constant rate that is a ratio of the applied shearing stress with respect to the shearing strain rate, $\dot{\gamma}$. At low shearing strain rates, this flow or apparent viscosity, η_{app} , is very high while at large shearing strain rates, this apparent viscosity asymptotes to the plastic viscosity, μ_p . The plastic viscosity is the apparent viscosity observed at appreciably high shearing strain rates. The description of a Bingham fluid, with a yield stress and plastic viscosity, is typified by:

$$\sigma = \sigma_y + \mu_p \dot{\gamma} \quad \text{Equation 4.1}$$

The flow of concrete is altered by its granular nature as it is a Bingham fluid (cement paste) with sand and gravel particles. The interaction between the particles increases the shearing force required to sustain steady flow. As such, the yield stress and plastic viscosity of concrete is modified as the volume of aggregates (and their shape and size distribution) are modified. The Modified Krieger-Dougherty equation predicts the viscosity of the fluid based on the volume fraction, Φ , of the suspension fluid, the maximum concentration of particles, Φ_M , and the underlying viscosity of the suspension fluid, $\eta_{suspension}$ (Struble, L. J., and Sun, G. -K., 1993). The Modified Krieger-Dougherty relationship is expressed as:

$$\frac{\eta}{\eta_{suspension}} = \left(1 - \frac{\Phi}{\Phi_M}\right)^{-k\Phi_M} \quad \text{Equation 4.2}$$

Where k is a factor that depends on particle shape and applied shear stress. For spherical aggregates, the k value is assumed to be 2.5. The maximum concentration of particles is dependent on both particle size distribution and applied shear stress. For spherical aggregates, the value is assumed to be between 0.6 and 0.7. The yield stress is similarly affected by the

interaction of particles. The Chateau-Ovarlez-Trung model empirically predicts the yield stress as:

$$\frac{\sigma_y(\Phi)}{\sigma_y(\Phi=0)} = \sqrt{(1 - \Phi) \left(1 - \frac{\Phi}{\Phi_M}\right)^{-2.5\Phi_M}} \quad \text{Equation 4.3}$$

Where Φ_M is 0.56 for monodisperse spherical particles (Chateau, X., Mahaut, F., Mokeddem, S., Ovarlez, G., and Roussel, N., 2008).

In addition to aggregates, the use of chemical admixtures (superplasticizers, viscosity modifying agents, etc.) affects the rheology of concrete (Jolicœur, C., and Mikanovic, N., 2008) (Papo, A., and Piani, L., 2004). Consolidating vibration also affects the rheology of concrete. When vibrated strongly, the shearing contact between aggregates is temporarily removed. This loss of aggregate-to-aggregate contact leads to a reduction in the yield stress and a reduction in the overall measured plastic viscosity. The reduction of the yield stress can be so much that the Bingham fluid can transform to a Power-law fluid, that is to say the magnitude of the yield stress approaches zero and the fresh concrete readily flows (Baker, 1988). It is this vibration effect that allows for aggregates to settle downward and entrapped air to float upward. This achieves an increase in concrete density.

4.1.2 Hardened Air Analysis: ASTM C457 and Flatbed Scanner

Air content can be measured in fresh concrete using ASTM C231 *Standard Test Method for Air Content of Freshly Mixed Concrete by the Pressure Method*. However, this test methods assesses the air system when it is contained within fresh concrete material, which may not reflect the actual entrained air system in concrete if the concrete is over-consolidated or over-finished during its final placement.

Another test, ASTM C457 *Standard Test Method for Microscopical Determination of Parameters of the Air-Void System in Hardened Concrete*, is a method which determines the air content, specific surface, void frequency, spacing factor, and cement paste-to-air void content in hardened concrete. In this test method, a polished cross-section of hardened concrete is observed under a microscope and a linear traverse is made while the number of air, paste, or aggregates phases across the linear traverse. The total air content, spacing factor, and void frequency are critical factors. Low air contents, spacing factors greater than 0.20 mm, and void frequencies less than 300/m can result in freeze-thaw damage susceptible concrete in aggressive wet, wintry environments.

A new technique has been created to measure the total air content in polished, two-dimensional sections (Peterson, K., Sutter, L., and Van Dam, T., 2002). The optical microscope was replaced with a high-resolution flatbed scanner. Peterson *et al* blackened the surface of the polished cross-section of concrete with black ink and impregnated the air voids with a fine, white powder in order to enhance the contrast. In such a manner, total air void content can be measured. However, due to the blackened surface, paste content information cannot be inferred.

In a new method that extends Peterson *et al*'s concept, a polished cross-section of concrete is stained with 5 percent phenolphthalein solution to create a pink hued surface of the hydrated cement paste (Castaneda, D. I., Lange, D. A., Riding, K. A., Song, Y., and Zou, R., 2017). A fluorescent orange powder is impregnated into the air voids. After the image is scanned, each of three phases can be identified: paste, air, and aggregates. Air voids contained within porous

aggregate can be filtered through a corrective algorithm in order to reconstruct a three-phase scanned image (see Figure 4.3) that is quantifiable and statistically significant for its air-void parameters.

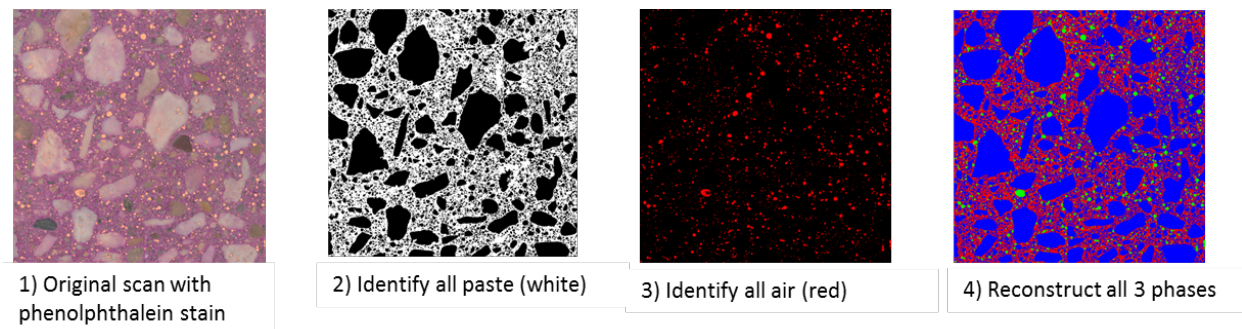


Figure 4.3. A polished cross-section of concrete is stained with phenolphthalein and its air voids are impregnated with fine, orange powder in order to enhance the contrast in a scanned image (Song et al., 2015)

4.2 Significance of Research

Extended consolidation of fresh concrete flows and can result in aggregate segregation and loss of entrained air. To better understand the effects of the loss of entrained air in concrete that is installed in wet, wintry environments, it is necessary to understand the rheology of concrete, the effect of consolidating vibration on rheology, and the extent of air loss in differentially vibrated concrete. In this study, cementitious and model materials were used to investigate the extent of vibrational influence (radius of action) on the movement and loss of air bubbles. In doing so, the effect of amplitude and frequency can be better understood as it relates to retaining entrained air and retaining the freeze-thaw damage resiliency of concrete.

4.3 Experimental Methods

A significant drawback of measuring the rheology of Portland cementitious materials is that they undergo hydration that results in gelling, increasing yield stress and plastic viscosity with respect to time. Carbopol 980 Polymer is an unreactive Bingham fluid that can serve as a surrogate fluid of Portland cement paste. As such, effects of hydration and thixotropy can be ignored in these surrogate fluids.

4.3.1 Materials

The first material system considered was Portland-cement based paste, mortars, and concrete. The paste is a water-to-cement ratio of 0.30 (by mass) that is dosed with a set-retarding and air-entraining chemical admixtures (see Table 4.1). In order to make mortar, varying volume fractions of river sand is added. The size distribution of sand particles is given in Table 4.2. Specifically, the sand used in the Portland cement-based mortars and concrete conforms to IDOT FA02 blend. In order to make concrete, sand and gravel is used. The gravel used in the Portland cement-based concrete is crushed limestone, and its size distribution conforms to IDOT CA07 blend (see Table 4.3). Similarly, the volume fraction of the crushed limestone varies.

Table 4.1. Nominal Paste Mix Design

Material Type	Pounds Per Cubic Yard	Kilograms Per Cubic Meter
Type I Portland Cement	2696	1599
Water	809	480
Set-Retarding Agent	6 fl. oz. per 100 lb. of cementitious	
Air-Entraining Agent	6 fl. oz. per 100 lb. of cementitious	

Table 4.2. Gradation of Sand (percent passing)

3/8" (9.5 mm)	No. 4 (4.75 mm)	No. 16 (1.18 mm)	No. 50 (300 μm)	No. 100 (150 μm)
100	97 ± 3	65 ± 20	20 ± 10	5 ± 5

Table 4.3. Gradation of Gravel (percent passing)

1.5" (37.5 mm)	1" (25.4 mm)	½" (12.5 mm)	No. 4 (4.75 mm)
100	95 ± 5	45 ± 15	5 ± 5

Carbopol 980 Polymer is a crosslinked polyacrylate polymer that is mixed with water to form a clear gel which is stable at neutral pH. The gel features design-controllable yield stress and viscosities that can suspend particles and air while maintaining a high amount of clarity through the material. The gel has been utilized in other rheological studies as a surrogate material for fiber reinforced concrete (Amziane, S., Boulkebach, B., Chemrouk, M., and Hamrat, M., 2010). In order to make Carbopol-based mortar, ASTM C778 graded sand was used and the particle size distribution is shown in Table 4.2. In order to make Carbopol-based concrete, ASTM C778 graded sand and one in. (25 mm) diameter opaque white checker marbles. These glass marbles are unreactive and do not alter the pH of the Carbopol 980 polymer gel ensuring rheological stability throughout testing. Similarly, the volume fraction of the graded sand and marbles was varied in order to draw insight into the effect of aggregates on rheology.

4.3.2 Equipment and Sensor Types

Both the cementitious and model materials were treated as Bingham plastics, which were characterized by a dynamic yield stress (tangent intercept) and plastic viscosity (slope at large shear strain rate). The static yield stress was also measured, but is not considered in the determination of the Bingham fit parameters. The rheological properties were measured using an ICAR rheometer or an AR-G2 Rheometer both of which measure the rheology using a rotating vane propeller. The ICAR rheometer was developed at the University of Texas at Austin in order to better characterize the rheological properties of concrete (Amziane, S., Ferraris, C. F., Fowler, D. W., and Koehler, E. P., 2006).

The fresh air content of paste, mortar, and concrete was measured using a Type B air meter conforming to ASTM C231. When not subjected to vibration, the air meter was appropriately

filled and compacted in two lifts. The fresh material was struck even and finished such that that the unit weight and fresh air content could be measured. When the fresh material was subjected to vibration, the air meter was similarly struck and finished, then placed atop a 60 Hz vibration table. The vibration table was powered on and vibrated for the desired duration. At the end of vibration, new (un-vibrated) material was added to the air meter and struck to an even finish.

A 15.24 cm by 15.24 cm by 122 cm Plexiglas mold was constructed to hold fresh Portland cement-based materials and Carbopol 980 polymer-based materials. A 220 Hz 2.67 cm diameter DeWalt pencil vibrator was positioned at one end of the prismatic mold approximately 7.6 cm away from the three form walls to a depth of 14 cm. A tri-axial accelerometer was positioned using an adjustable lever arm at increasing distances from the immersion probe at a constant depth of 7.62 cm. Figure 4.4 shows the relative location of the immersion rod and the multiple locations where the accelerometer was positioned.



Figure 4.4. Illustration of immersion pencil (probe) vibrator in 15.24 x 15.24 x 122 cm Plexiglas mold where stars represent the nominal location of an immersed accelerometer during vibratory testing

A sub-set of paste, mortar, and concrete samples were similarly vibrated in 10.16 x 20.32 cm (4 x 8 in) plastic cylinder molds atop the 60 Hz table and also in 15.24 x 15.24 x 53.34 cm (6 x 6 x 21 in) steel beam molds. Once hardened, the samples were extracted and saw-cut in order to perform image analysis. The cylindrical samples were saw-cut horizontally 5 cm (2 in) away from the top and bottom surface (see Figure 4.5). The circular cross-section face near the top was labeled TH (top-half) while the circular cross-section face near the bottom was labeled BH (bottom-half). The beams were saw-cut in order to extract several 15.24 x 15.24 cm (6 x 6 in) faces that were orthogonal to the long-axis of the beam. Each face was labeled by its distance from the edge of the beam nearest the source of vibration, where an excised sample at the point of vibration was nominally 7.62 cm (3 in) from the edge.

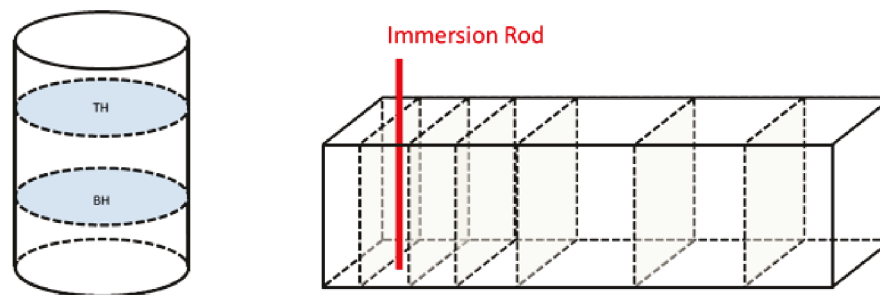


Figure 4.5. Illustration of saw-cut cylinders (left) and beams (right); samples extracted for hardened air analysis

Each excised hardened concrete sample was polished using a 45.72 cm (18 in.) diameter horizontal grinding wheel. Each sample was successively ground using #60, #180, and #600 grit polishing discs in order to create a highly polished surface. The polished surface was then sprayed with an even film of 5 percent phenolphthalein solution such that the hydrated cement paste took on a pink hue due to its naturally high pH. After this polished surface dried, fluorescent orange powder was carefully poured onto the surface and impregnated into the voids using both a silicone stopper and razor blade. After a visual inspection confirmed the air voids were sufficiently impregnated, the polished surface was struck of excess powder with the razor blade, and the polished sample was carefully inverted onto the glass surface of a CanoScan 9000F high resolution scanner. 5 x 5 cm (2 x 2 in) square sections of hardened samples originating from a cylindrical specimen were scanned at a resolution of 4,800 dpi. Larger hardened samples originating from a beam specimen were scanned in their entirety of 15.24 x 15.24 cm (6 x 6 in) area at a reduced resolution of 1,600 dpi.

4.4 Experimental Results and Discussion

The following sections detail the experimental results obtained from this research effort.

4.4.1 Fresh Air Loss Due to Vibration and Aggregates

Fresh Portland cement-based concrete, mortar, and paste were filled inside an ASTM C231 Type B air meter and vibrated atop a 60 Hz horizontal vibration table. The rheological properties of the three mix types at rest are shown in Table 4.4. The nominal mix design of the concrete was similar to Table 5.1 with 27 percent sand and 43 percent gravel by volume. The nominal mix design of the mortar was similar to that shown Table 4.1 with 62 percent sand by volume. The average fresh air content of each nominal mix design is shown in Figure 4.6. In the concrete mixture, unvibrated materials had a fresh air content of approximately 8 percent. After vibration atop the 60 Hz table for 1, 2, 3, 4, and 8 minutes, the average fresh air content was measured to be 8, 6.5, 6, 4.5, and 4.5 percent, respectively. In the mortar mixture, the average fresh air content before any vibration was 18 percent. The average fresh air content after similar vibration times was 16, 15, 12, 8, and 9 percent, respectively. In the paste, the average fresh air content before vibration was 10 percent and after a similar regiment of vibration that the concrete and mortar mixtures undergo, the average fresh air content was 10, 10, 10.5, 9.5, and 10 percent, respectively.

Table 4.4. Average Bingham Parameters of Fresh Concrete, Mortar, and Paste

Sample Name	Yield Stress (Pa)	Plastic Viscosity (Pa.s)
Concrete	476.6	30.9
Mortar	314.6	192.9
Paste	609.1	34.6

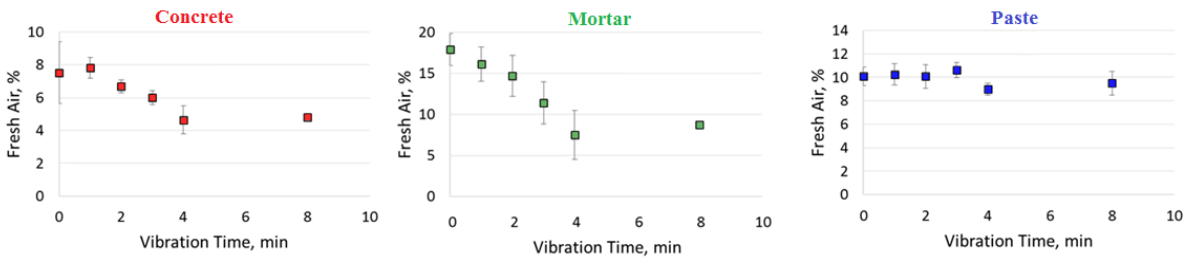


Figure 4.6. Average fresh air content of fresh, Portland cement-based concrete, mortar, and paste as measured by ASTM C231 after various durations of vibration atop a 60 Hz horizontal table

The average plastic viscosity of the concrete and paste presented in Table 4.4 were similar in magnitude at approximately 30 Pa.s. Yield stress values were also relatively comparable for the two mixture types. However, Figure 4.6 shows that the extent of air loss in concrete was appreciably higher than it was in plain Portland cement paste. Moreover, the presence of sand in the mortar also allowed for a high loss of fresh air content. This loss of fresh air is significant despite the mortar having a high plastic viscosity of about 190 Pa.s. This plastic viscosity was nearly six times higher than either plain Portland cement paste or concrete. As a consequence, the movement of air bubbles in a fluid with high viscosity should have been significantly slowed as the drag force was larger. However, this behavior was not seen in the data. The rheological properties measured and shown in Table 4.4 of each mixture type at rest is not indicative of the movement and loss of air content after vibration.

Vibration fluidizes the material. The fluidization of each mixture type due to external vibration leads to a reduction in the resistance to flow of each air bubble. A decrease in the resistance to flow denotes a decrease in the viscosity. However, this viscosity decrease does not occur equally in all mixture types—concrete and mortar are more strongly affected than paste. Thus, the presence of fine and coarse aggregates has an effect on the efficiency of the vibrational energy to act through the bulk of material. Secondly, it is known that the presence of aggregates and their aggregate-to-aggregate interactions increases the yield stress and plastic viscosity of an underlying fluid. When this composite fluid (concrete or mortar) is fluidized by external vibration, the paste viscosity is also reduced from its viscosity under static conditions. The defeating of yield stress and the reduction of viscosity leads to a loss of fresh air content. In the case of cement paste, the loss of air is significantly lower than the other mixes, suggesting a strong coupling effect between aggregates, external vibration, and the efficiency of vibration.

4.4.2 Efficiency of Vibration in Cement Paste, Mortar, and Concrete Beams

The efficiency of vibration was observed for Portland cement-based mixtures types by filling a beam with fresh material of known rheological properties and batched aggregate volume fractions, and subjecting the fresh material to vibration at one end. A 2.5 in. (6.35 cm) diameter immersion pencil (probe) vibrator was vibrated and the mean resultant peak acceleration was measured at various distances using a triaxial accelerometer. Table 4.5 shows the rheological properties of the paste (labeled Mortar – 0% FA; 100% CP), the mortar with increasing volume fractions of fine aggregate (20, 40, and 60% FA), and the concrete with increasing volume fractions of coarse aggregate (0, 22, 33, and 45% CA). The concrete mixture type was initially designed as a mortar with 40% FA content and was later made to approximately 49% FA with

increasing coarse aggregate volume fraction. It was observed that the measured plastic viscosity increased with increasing aggregate volume as suggested by Equation 4.2. The measured yield stress varied upon increasing aggregate volume fraction, but at very high volume fraction of fine or coarse aggregate, the measured yield stress was appreciably larger when compared against the same mixture type with no aggregates, as suggested by Equation 4.3.

Table 4.5. Bingham Parameters of Fresh Concrete, Mortar, and Paste with Varying Aggregate Volume Content Values

Sample Name	Yield Stress (Pa)	Plastic Viscosity (Pa.s)
Mortar – 0% FA; 100% CP	164.2	31.8
Mortar – 20% FA; 80% CP	114.2	49.1
Mortar – 40% FA; 60% CP	90.1	68.3
Mortar – 60% FA; 40% CP	276.6	423.7
Concrete – 00% CA; 40% FA; 60 % CP	207.3	10.5
Concrete – 22% CA; 40% FA; 38 % CP	130.1	22.8
Concrete – 33% CA; 34% FA; 33 % CP	208.5	33.5
Concrete – 45% CA; 28% FA; 27 % CP	467.3	101.1

These fresh materials were dosed with a set-retarding admixture (6 fl. oz per 100 lb of cementitious material) in order to slow the rate of hydration during the vibratory testing. Each mixture type was placed in a 122 cm long Plexiglas beam after measuring the rheological properties. A triaxial accelerometer (measuring accelerations in the X, Y, and Z directions) was immersed 3 in. (7.62 cm) from the top surface of the fresh mixture. Figure 4.7 and Figure 4.8 shows the average of four impulse vibrations where the resultant of the three axes are shown. In Figure 4.7 and Figure 4.8 there is an attenuation of the peak acceleration with respect to distance from the immersion probe. In ACI 309, a peak acceleration above 2 to 3 g is described to be fluidized. As such, there is a significant volume that is being fluidized in each of these beam tests at approximate distances between 30 to 60 cm from the vibration source. However, the fluidized radius from the immersion probe varies with the aggregate content (which is also strongly inter-related to the plastic viscosity). As the sand volume content in Figure 4.7 increases, the peak acceleration both increases in magnitude and the radius of action shifts rightward suggesting that more material was fluidized. In Figure 4.8, the attenuation of the peak acceleration near the immersion probe was minimal, as the peak acceleration immediately adjacent from the probe measured approximately 35 g. In Figure 4.8, a similar trend was observed where the peak acceleration shifted upward and rightward at 22 percent and 33 percent coarse aggregate volume. At 45 percent, the attenuation was far greater and the peak acceleration significantly depreciated to small values. This observation occurred despite a large yield stress and large plastic viscosity as seen in Table 4.5.

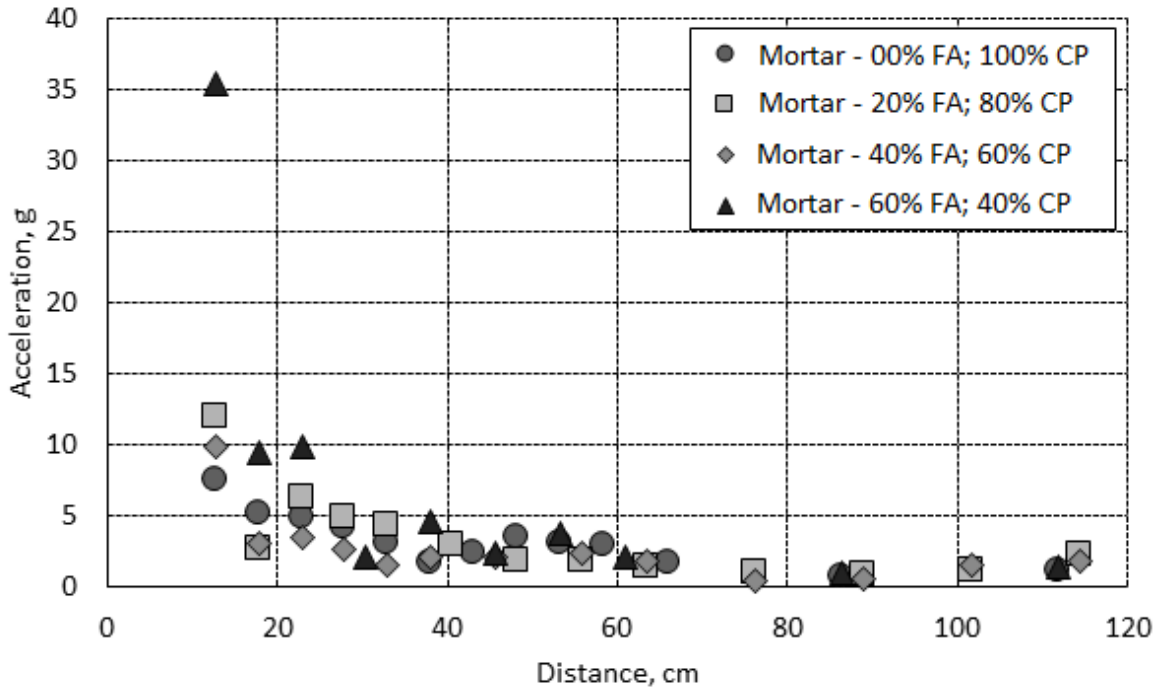


Figure 4.7. Mean peak resultant acceleration value at varying distances in a 122-cm long Plexiglas beam mold of Portland cement-based paste and mortar. The fresh material is vibrated using an 18 volt DeWalt vibrator at 7.62 cm. Each data point represents the average of at least four 1-second duration pulses of vibration

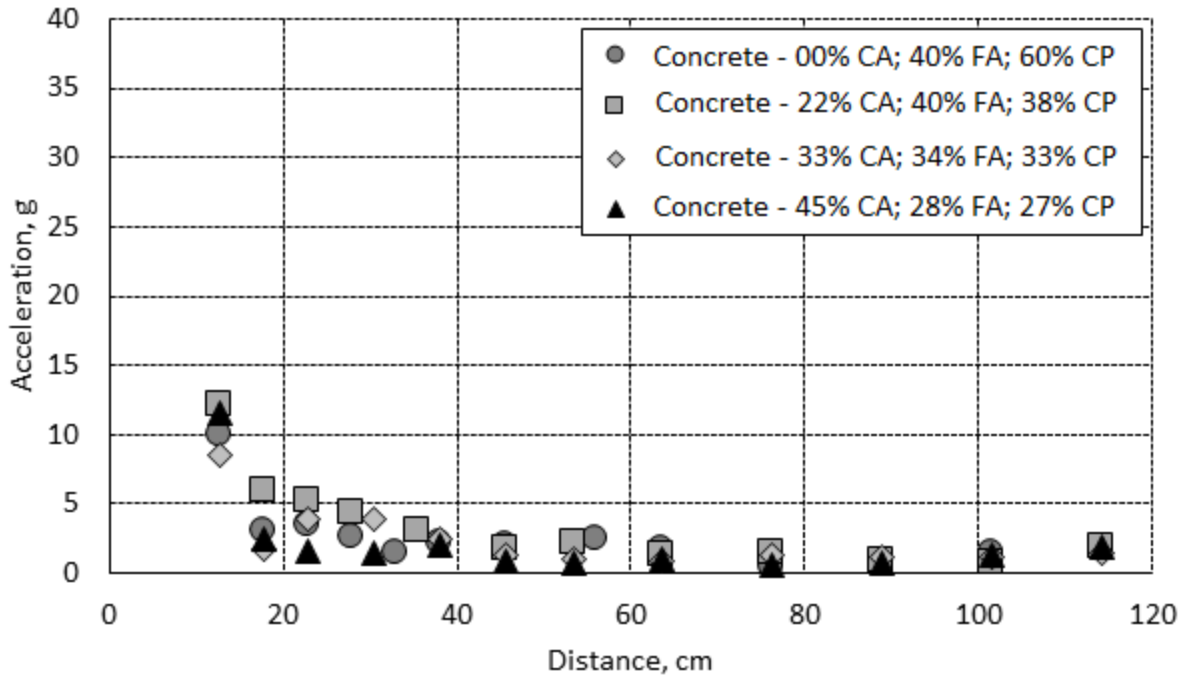


Figure 4.8. Mean peak resultant acceleration value at varying distances in a 122-cm long Plexiglas beam mold of Portland cement-based concrete. The fresh material is vibrated using an 18 volt DeWalt vibrator at 7.62 cm. Each data point represents the average of at least four 1-second duration pulses of vibration

This discrepancy in the results in Figure 4.8 at a coarse aggregate volume fraction of 45 percent can be attributable to several factors. First, the nominal dosage of the water-reducing, superplasticizing chemical admixture was slightly increased in order to enhance the workability of the mixture in order to attain a slump greater than 4 in. (10.16 cm). This was done to allow the ICAR rheometer top operate properly. The increased fluidity of the mixture was still accounted for in the measured rheological properties shown in Table 4.5 suggesting that the irregularity of the dosage of superplasticizer did not severely alter the rheology. A second consideration is that this mixture was made up of 73 percent total aggregate by volume content. At such a high value, it is possible that the fluidization of a mixture with such high aggregate content was less effective. However, the distribution of sand and gravel was partly optimal (where sand particles fill interstitial gaps made by the gravel). As such, 45 percent coarse aggregate content by volume did not nearly approach a jammed particle state, which is closer to 56 percent volume fraction of a mono-sized distribution of spheres (Chateau, X., Mahaut, F., Mokeddem, S., Ovarlez, G., and Roussel, N., 2008). Lastly, it is known that a set-retarding agent can slow, but not halt, hydration kinetics. This effect, in addition to variability in sand and gravel distributions between each successive mixture type, was a strong factor in the observation.

4.4.3 Efficiency of Vibration in Model Materials Beams

Similar to the rheological results of the Portland cement-based mixture types, the model material consisting of Carbopol gel and increasing volume fractions of graded silica sand and glass marbles led to an increase of the plastic viscosity as shown in Table 4.6. Additionally, the plastic viscosity when the fine aggregate volume content increases to 60 percent was significantly

higher in both Table 4.5 and Table 4.6. There was a comparable trend of the yield stress where the value generally increased for increasing volume fraction of material.

Table 4.6. Bingham Parameters of Carbopol Gel with Varying Volume Content of Graded Silica Sand (FA) and 1 in. (2.5 cm) Diameter Glass Marbles (CA)

Sample Name	Yield Stress (Pa)	Plastic Viscosity (Pa.s)
Carbo24 – 0% CA; 00% FA; 100% CP	12.1	0.7
Carbo24 – 00% CA; 20% FA; 80% CP	23.2	1.4
Carbo24 – 00% CA; 40% FA; 60% CP	56.0	2.7
Carbo24 – 00% CA; 49% FA; 51% CP	34.6	8.0
Carbo24 – 00% CA; 60% FA; 40% CP	1370.3	77.2
Carbo24 – 20% CA; 39% FA; 41% CP	66.4	9.5
Carbo24 – 33% CA; 33% FA; 34% CP	181.6	18.5
Carbo24 – 45% CA; 27% FA; 28% CP	241.0	50.6

The mean resultant acceleration of the Carbopol-based gel and surrogate mortar and concrete are shown in Figure 4.9 and Figure 4.10. In Figure 4.9, a similar trend to Figure 4.7 was observed where increasing sand volume fractions led to a shift upward and rightward of the mean peak resultant acceleration. In the case of sand volume content of 60 percent, the peak acceleration was higher than other values. In terms of magnitude, the peak acceleration was approximately 16 g versus 35 g of the Portland cement-based mortar. Although the sand volume content was comparable, the rheological properties between Table 4.5 and Table 4.6 were not. In Table 4.6, the plastic viscosity was much lower. This observation suggests that aggregate volume fraction has the capacity to extend the volume of material being fluidized, but the aggregate volume fraction alone does not predict the peak mean resultant acceleration.

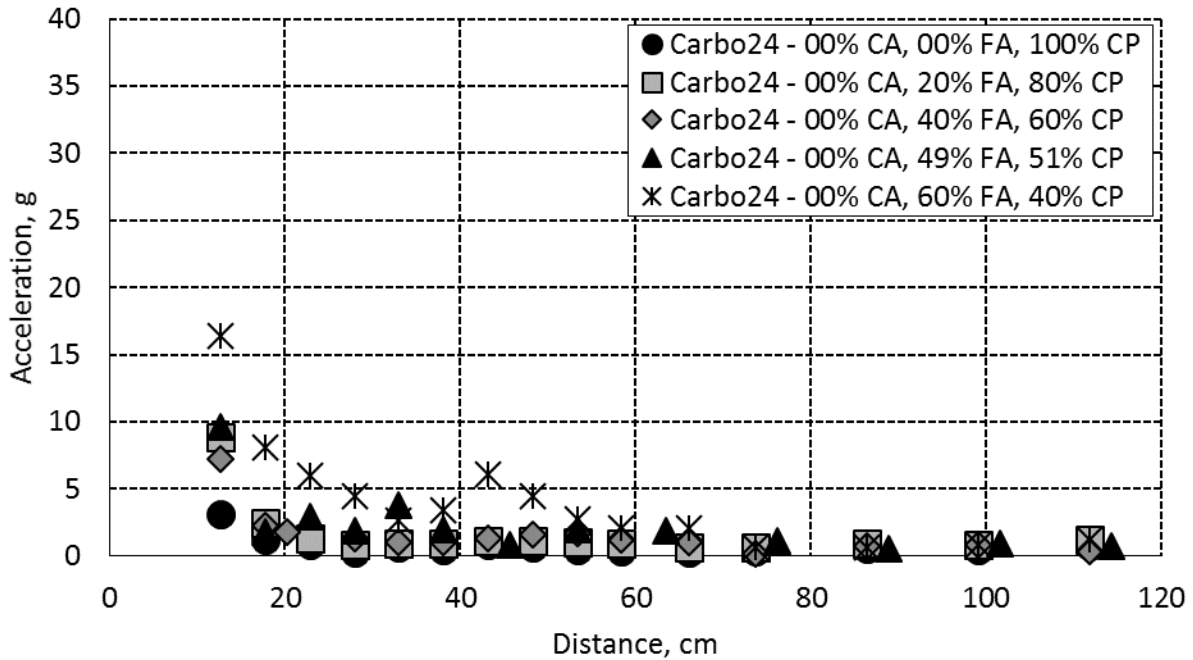


Figure 4.9. Mean peak resultant acceleration value at varying distances in a 122-cm long Plexiglas beam mold of Carbopol-based gel and “mortar.” The fresh material is vibrated using an 18 volt DeWalt vibrator at 7.62 cm. Each data point represents the average of at least four 1-second duration pulses of vibration

The Carbopol used was an inert gel fluid with rheological properties that did not change with time, unlike the concrete where ongoing hydration changes the rheological properties. The Carbopol used also had a well-known aggregate distribution and shape. In this ideal Carbopol-based model material system, it was observed that the increasing volume fraction of glass marbles had little effect on the change in the mean peak resultant acceleration. This observation was in stark difference with Figure 4.7 and Figure 4.9 where sand particles had a stronger effect on the peak acceleration.

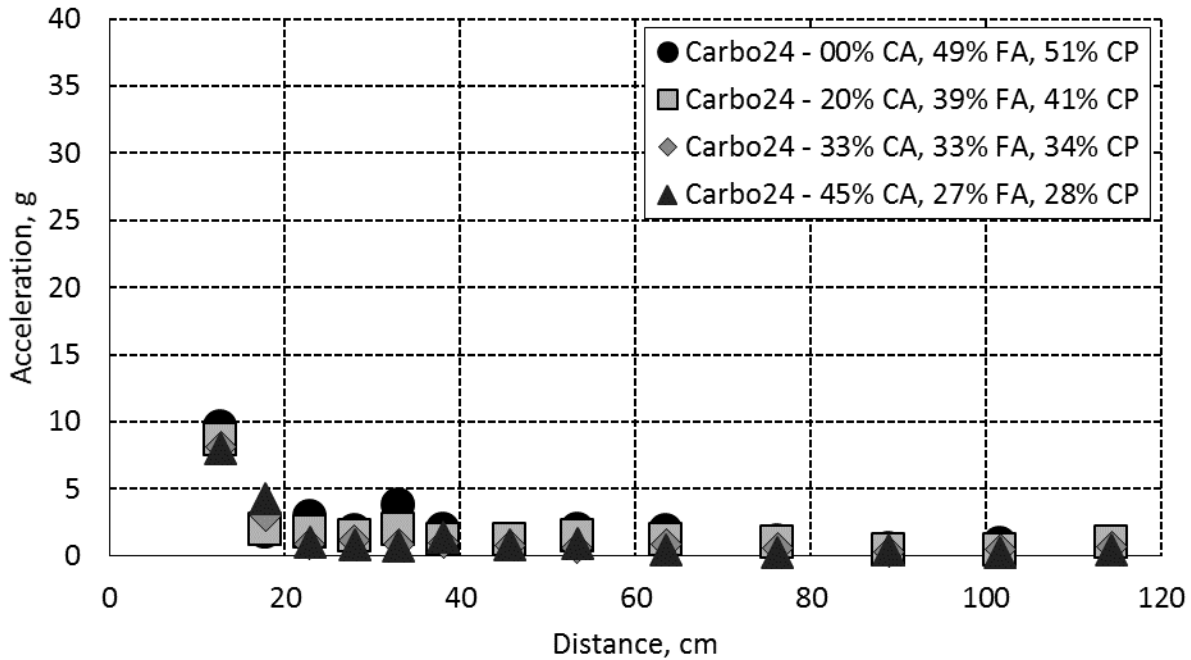


Figure 4.10. Mean peak resultant acceleration value at varying distances in a 122-cm long Plexiglas beam mold of Carbopol-based “concrete.” The fresh material is vibrated using an 18 volt DeWalt vibrator at 7.62 cm. Each data point represents the average of at least four 1-second duration pulses of vibration

4.4.4 Measured Hardened Air Content in Vibrated and Non-Vibrated Cement Paste, Mortar, and Concrete Cylinders

Hardened paste, mortar, and concrete cylinders were placed into 10.16 cm by 20.32 cm (4 in by 8 in) cylindrical molds and were either not vibrated, vibrated for 1 minute, or vibrated for two minutes. The Bingham fit parameters for each mixture type is shown in Table 4.7. After each mixture type had hardened, a conventional concrete saw cutter was used to extract a cross-section of the cylinder. The extracted cross-section was polished, stained, impregnated with fluorescent powder, and image-scanned across a 5 cm by 5 cm (2 in by 2 in) area at the interior of the 10.16 cm diameter cross-section. The scanned image was segmented for its pink-hued paste phase, fluorescent-powered air void phase, and remaining coarse aggregate phase. The cumulative (total) phase percentage of each mixture type across various vibration times atop the 60 Hz vibration table is shown across Table 4.8, Table 4.9, and Table 4.10.

Table 4.7. Bingham Parameters of Fresh Concrete, Mortar, and Paste Vibrated in Cylindrical Molds

Sample Name	Yield Stress (Pa)	Plastic Viscosity (Pa.s)
P30-1012-TH	875.8	33.6
M30-1012-TH	983.7	159.0
C30-1012-TH	117.6	235.5

Table 4.8. Cumulative Percent Area of Hardened Air and Paste in Vibrated Paste Cylindrical Molds Cross-Sections

Sample Name	Vibration Time	Hardened Air Content (%)	Paste Content (%)
P30-1012-TH	0	4.136	95.864
	1	4.742	95.258
	2	3.660	96.340

Table 4.9. Cumulative Percent Area of Hardened Air and Mortar in Vibrated Mortar Cylindrical Molds Cross-Sections

Sample Name	Vibration Time	Hardened Air Content (%)	Mortar Content (%)
M30-1012-TH	0	28.718	71.860
	1	24.360	75.640
	2	27.860	72.140

Table 4.10. Cumulative Percent Area of Hardened Air, Mortar, and Coarse Aggregate in Vibrated Concrete Cylindrical Molds Cross-Sections

Sample Name	Vibration Time	Hardened Air Content (%)	Mortar Content (%)	Coarse Aggregate Content (%)	Norm. Hard. Air (%) [A/(M+A)]
C30-1012-TH	0	5.905	51.328	42.767	10.317
	1	4.897	52.346	42.757	8.555
	2	3.203	40.199	56.598	7.380

The yield stress in the paste mixture in Table 4.7 was somewhat larger than shown in Table 4.4 or Table 4.5. However, the plastic viscosity of the paste mixture was comparable. At the onset of significant particle (air or aggregate) movement, drag speed would be governed by similar flow rates. The rheological properties of mortar and concrete shown in Table 4.7 were comparable to those shown in Table 4.5. After increasing times of vibration, the cumulative hardened air content shown in Table 4.8 was relatively stable at about 4 percent of air. This was comparable to Figure 4.6 where the fresh air content was relatively stable for increasing vibration times. The cumulative hardened air content in the mortar cylindrical cross-sections was relatively high and also showed relative stability and retention of air after increasing vibration times. This observation was unlike Figure 4.11 where the fresh air content was observed to drop with respect to increasing vibration times.

A significant consideration is the timing of the measurement of entrained air and the subjected vibration type. In the fresh material, the fresh air content was measured soon after mixing and within a Type B air meter pot whose geometry differed from a plastic cylindrical mold. It is possible that the mold geometry and propagation of energy through the mold type could affect

the results. A second consideration is that the hardened air content is a “post-mortem” measurement where early loss of entrapped air (more buoyant and susceptible to becoming lost) is not captured in the unvibrated sample. However, this second consideration is not strongly supported per the results shown in Table 4.10 where the cumulative hardened air content measured in concrete appreciably fell from 5.9 percent to 4.9 percent and 3.2 percent after 1 and 2 minutes of vibration, respectively. In order to account for the presence of coarse aggregates in a scanned image (whose percent phase can drastically alter the representative analysis area), a normalization of cumulative hardened air with respect to mortar and air phases is additionally shown. In such a case, increasing vibration times leads to a change of cumulative hardened air content of 10.3, 8.6, and 7.4 percent.

The cumulative air content values in Table 4.8, Table 4.9, and Table 4.10 represent entrapped and entrained air within the hardened mixture type. In order to better understand the preferential loss of entrapped air (whose buoyancy is greater than that of a small entrained air bubble), it is beneficial to observe the change in the distribution of air voids as measured in a scanned sample. Figure 4.11, Figure 4.12, and Figure 4.13 shows the distribution of air voids (as a density to the paste or mortar phase), with respect to the equivalent diameter of a circumscribed circle around each air void. In Figure 4.11, the distribution of air inside hardened paste vibrated for 0, 1, and 2 minutes is shown. It is evident that there is a single peak centered on 20 μm which did not significantly deviate upon increased vibration. Similarly, the distribution of air density in mortar (see Figure 4.12) was relatively unchanged. Both of these observations correlate well to the cumulative hardened air in Table 4.9 and Table 4.10. In Figure 4.13, the distribution of air in concrete cross-sections is shown. It is evident that there is a bi-modal distribution of air centered at 40 and 200 μm . However, there is a significant drop in the 40 μm peak and very little drop in the 200 μm peak. It is likely that the peak centered at 200 μm is that of air contained within porous coarse aggregate that will not escape the mortar system. However, the 40 μm peak is more likely that of entrained air buoyantly moving upward and escaping the system.

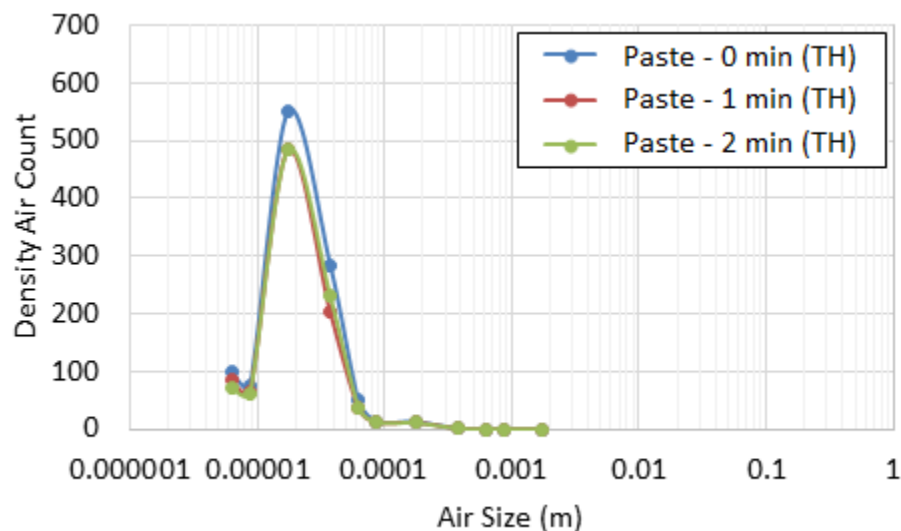


Figure 4.11. Log distribution of air voids in cross-section of cylindrical mold with hardened paste vibrated for 0, 1, and 2 minutes atop a 60 Hz vibration table

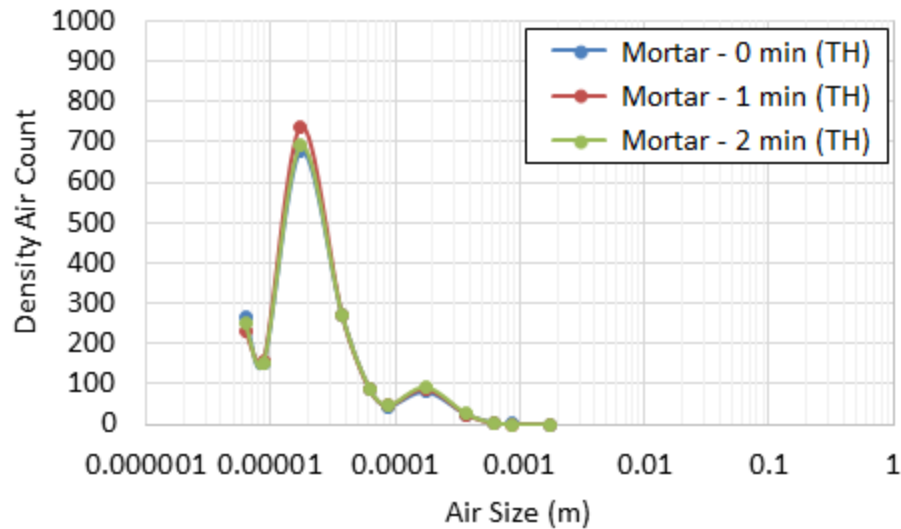


Figure 4.12. Log distribution of air voids in cross-section of cylindrical mold with hardened mortar vibrated for 0, 1, and 2 minutes atop a 60 Hz vibration table

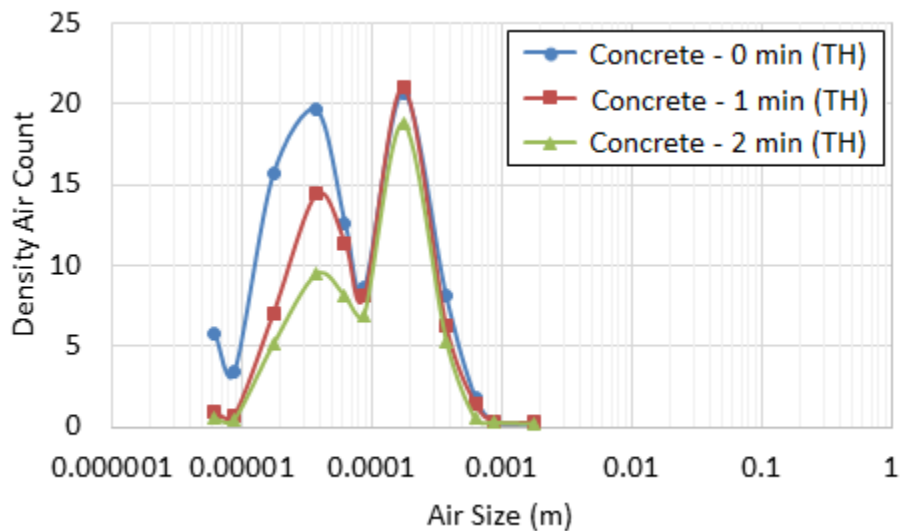


Figure 4.13. Log distribution of air voids in cross-section of cylindrical mold with hardened concrete vibrated for 0, 1, and 2 minutes atop a 60 Hz vibration table

4.4.5 Measured Hardened Air Content in Vibrated and Non-Vibrated Cement Paste, Mortar, and Concrete Beams

Sets of hardened Portland cement-based paste, mortar, and concrete modulus of rupture beams were cast. Both beams in each set were cast simultaneously while one beam in each set was additionally vibrated at 3 in. (7.62 cm) from one end using an immersion probe vibrator. The companion beam within a set was not vibrated. The rheology of the fresh paste, mortar, and concrete is shown in Table 4.11. The mixture of paste and mortar were from the same mixture as done for the cylindrical molds meaning that their rheology was the same. However, the concrete

was from a different mixture which led to slightly different values. When compared to Table 4.7, the yield stress of the concrete was slightly higher, but the plastic viscosity was fairly similar.

Table 4.11. Bingham Parameters of Fresh Concrete, Mortar, and Paste Vibrated in Beam Molds

Sample Name	Yield Stress (Pa)	Plastic Viscosity (Pa.s)
Paste	875.8	33.6
Mortar	983.7	159.0
Concrete	205.7	230.4

Figure 4.14, Figure 4.15, and Figure 4.16 shows the cumulative hardened air content of each excised sample with respect to the position of the excised sample within the beam. The beam was restrained at 0 and 53.34 cm while the immersion probe was positioned at approximately 7.62 cm. In Figure 4.14, the cumulative hardened air of the non-vibrated beam at five locations was shown to fluctuate across the length of the beam, but was on average a value of 5.88 percent. This cumulative hardened air content was slightly larger than the value reported in Table 4.8 for a sample excised from a cylindrical mold. For a paste beam vibrated for 45 seconds at one end, the cumulative hardened air content shown in Figure 4.14 did not seem to significantly deviate from the un-vibrated beam sample.

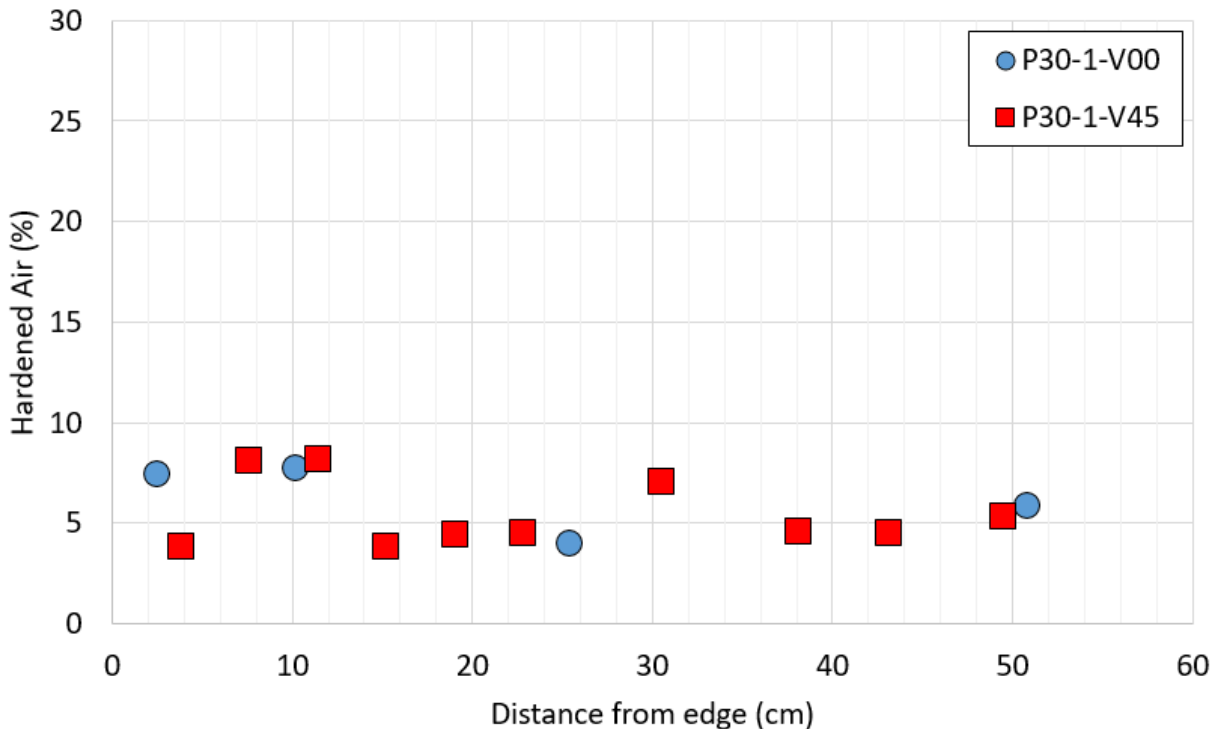


Figure 4.14. Cumulative hardened air content in excised samples of prismatic beams of hardened paste vibrated for 0 sec and 45 seconds at one end using a 220 Hz immersion probe

Similar to the hardened paste beam, the hardened mortar beam also showed very little effect from external vibration. In Figure 4.15, the average cumulative hardened air content was 20.54 percent for the non-vibrated beam. This value was appreciably lower than the values reported in Table 4.9. However, the range of cumulative hardened air values was upwards of 28 percent and as low as 18.6 percent. There was significant variation of cumulative hardened air within a vibrated beam meaning that a larger sample of samples must be tested in order to assess the statistical significance of the results in Figure 4.14 and Figure 4.15.

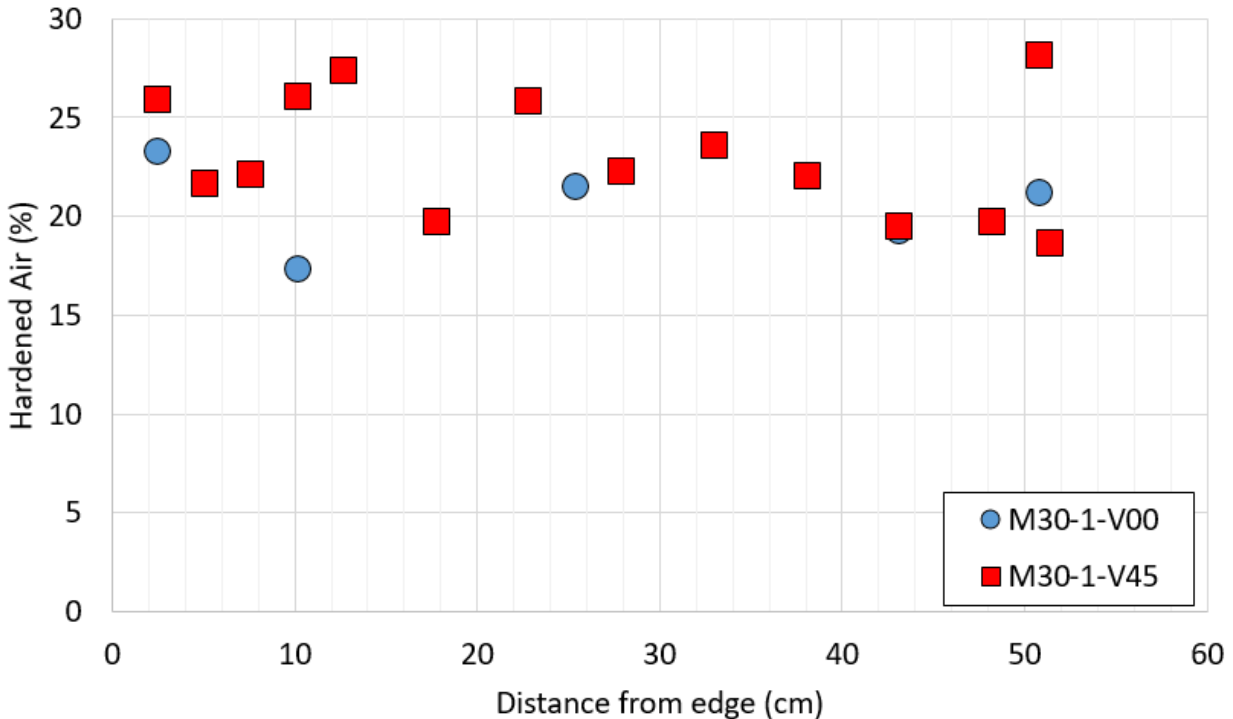


Figure 4.15. Cumulative hardened air content in excised samples of prismatic beams of hardened mortar vibrated for 0 sec and 45 seconds at one end using a 220 Hz immersion probe

In hardened concrete, however, the effect of external vibration on the cumulative hardened air content was pronounced (see Figure 4.16). The non-vibrated beam was seen to have approximately 10 percent hardened air, while the cumulative hardened air content in the 60 second vibrated beam seemingly varied as a function of distance from the source of the vibration. Between the near end of the beam and the immersion probe (between 0 and 7.62 cm), the cumulative hardened air content was 4.8 percent and 3.4 percent. The hardened air value dropped in magnitude going toward the immersion probe. Between the far end of the beam and the immersion probe (between 7.62 and 53.34 cm), the cumulative hardened air increased from a value of 3.2 percent near the probe to 6.6 percent at 38.1 cm. Past 38.1 cm, the measured cumulative hardened air content fell to 5.1 percent at the far end of the beam. This loss of air agrees with the results observed in Figure 4.6 and Table 4.10.

The yield stress varied from as low as 118 Pa to as high as 477 Pa in the concrete used to make the cylindrical cross-section specimens and prismatic beams. The plastic viscosity ranged from as low as 30 Pa.s to as high as 235 Pa.s. In all of these rheological configurations, appreciable air loss was observed. This was unlike mortar where the only fresh air loss was observed in

vibratory testing at 60 Hz atop a vibration table. The mortar yield stress ranged as low as 314 Pa to as high as 984 Pa. The plastic viscosity of mortar ranged from 159 Pa.s to 192 Pa.s. As such, a low yield stress of 314 Pa allowed for an appreciable amount of air loss in fresh mortar after 1 minute (as shown in Figure 4.6) whereas at higher yield stress values, appreciable air loss after 45 seconds (at a higher frequency) was less effective at reducing hardened air content. In the Portland cement-based paste, no significant air loss was observed at any rheological combination in this study.

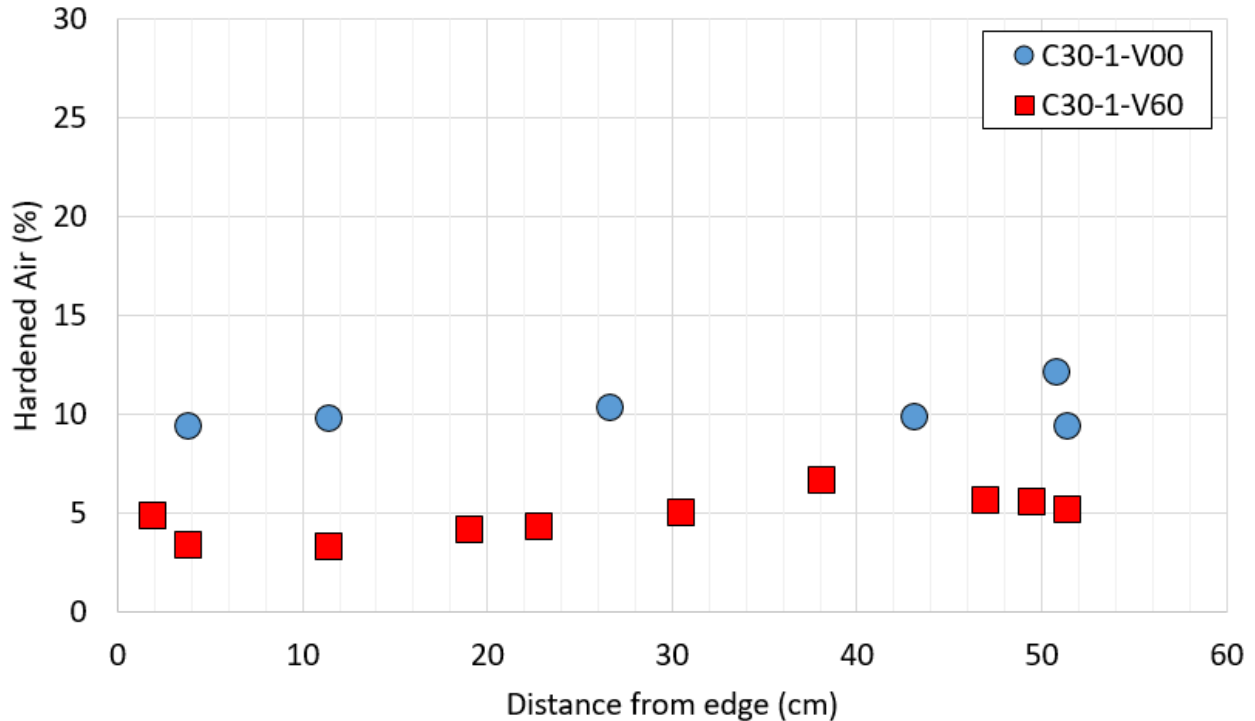


Figure 4.16. Cumulative hardened air content in excised samples of prismatic beams of hardened concrete vibrated for 0 seconds and 60 seconds at one end using a 220 Hz immersion probe

4.5 Conclusions

Air entraining chemical admixtures in fresh concrete creates microscopically-sized air bubbles that can relieve the stresses arising from freezing events. However, early-age vibratory consolidation of a fresh concrete can overcome the yield stress of the fresh material allowing for aggregates to settle downward and for entrapped and entrained air to float upwards. The upward flow velocity of the air bubbles is driven by buoyancy and is slowed by drag forces. Drag forces are functionally dependent upon the viscosity of the suspending liquid and the diameter of the air bubble. In this study, it was observed that:

- Loss of entrapped and entrained air as measured by an ASTM C231 Type B air meter vibrated atop a 60 Hz vibration table was more significant in mixture types with the presence of coarse and fine aggregates.
- The peak acceleration and attenuation of peak acceleration of a 220 Hz immersion probe vibrator was dependent upon the presence of aggregates. A high-volume fraction of sand

(past its theoretically predicted jammed state) resulted in a large radius of vibratory influence. The presence of coarse aggregates in typical concrete mixtures did not significantly extend the radius of vibratory influence of the vibration probe despite the increase in yield stress due to a higher volume fraction of aggregates. This observation is expected considering that the maximum coarse aggregate volume fraction in this study did not exceed 45 percent, and did not exceed the theoretical maximum packing fraction.

- The influence of vibration time on different Portland cement-based mixture types varied based on the rheological properties of the fresh material and the aggregate volume fraction. When no aggregates were present (hydrated Portland cement-based paste), there was no measured air loss. When fine aggregates were present, air loss was observed when the yield stress was relatively low, indicating that the external peak vibration must exceed the yield stress in order to enable the onset of air bubble movement. When fine and coarse aggregates were present, there was measured air loss indicating that high-flow concrete with appreciably low yield stress will have a high amount of measured air loss due to external vibration.

The movement of air bubbles and subsequent loss from the fresh Portland cement-based mixture was found to be highly dependent on the rheology of the fresh material. However, the extent of material yielded due to external vibration was not wholly dependent on the rheology alone. Instead, the extent of vibratory influence was found to be dependent, in part, on the aggregate volume fraction. The volume fraction of the fine aggregate seemed to play a larger role since the incorporation of coarse aggregate at low water-to-cementitious ratios often requires the use of water-reducing superplasticizing chemical admixtures which enhances the workability of the fresh material. As such, the incorporation of different superplasticizing chemical admixtures is expected to result in different rheological behaviors and different percent loss of entrapped and entrained air due to external vibration.

Chapter 5 – Experimental Measurement of Effects of Concrete Materials and Rheology on Air Void Systems and Freeze-Thaw Durability

Precast concrete railroad ties are often made with low water-cementitious material ratio (w/cm) concrete mixtures that are vibrated to consolidate the concrete and reduce the occurrence of bug holes on the concrete surface. Large dosages of high range water reducers (HRWR) are typically used to enable the use of low w/c concrete to achieve high early strengths in order to increase plant productivity. There is a concern that vibration of low w/c concrete with high dosages of chemical admixtures could cause air entrainment loss and reduced freeze-thaw durability. To quantify the effects of vibration on the entrained air system and freeze-thaw durability of concrete containing low w/c, an experimental program was conducted. This program examined: 1) the effects of time from mixing until vibration on air entrainment loss, 2) the effects of chemical admixture combinations on the air entrainment system and freeze-thaw durability, 3) the effects of vibration properties and concrete rheology on air entrainment loss and freeze-thaw durability, and 4) the air entrainment requirements to achieve freeze-thaw durability.

5.1 Freeze-Thaw Damage

Repeated cycles of freezing and thawing may lead to concrete damage that varies from spalling to complete degradation of concrete. Observations and testing of construction material durability in freezing conditions have been conducted since the 1800s (Nmai, 2006). Freeze-thaw deterioration typically manifests itself in one of two manifestations; surface scaling and internal or bulk damage (Auberg, R., Heine, P., Kasparek, S., Palecki, S., and Setzer, M. J., 2001). Surface scaling typically occurs as a result of exposure to salts such as de-icing salt or sea water during freeze-thaw cycles. Concrete surface scaling is defined as the progressive loss of cement or mortar particles only a few millimeters in thickness (Pigeon, M., and Pleau, R., 1995).

Bulk concrete freeze-thaw damage occurs because of internal pressures that develop from water during a freezing event. The pressure has been theorized to come from hydraulic pressure, ice accretion, or osmotic pressure. The hydraulic pressure theory states that freeze-thaw damage is caused by buildup of hydraulic pressure caused by unfrozen water's resistance to flow in cement paste capillaries (Powers, T. C., and Willis, T. F., 1949). Because cement paste does not expand to accommodate water expansion in the capillaries, unfrozen water is forced to flow through the capillaries during a freezing event. Hydraulic pressure, the force that causes unfrozen water to move, is affected by permeability, flow rate, and fluid viscosity. Although permeability depends on cement paste microstructure, flow rate correlates to freezing rate. The faster the freezing rate is, the faster the flow of water will be and the higher the hydraulic pressure. For fluid viscosity, change in viscosity remains minimal for freezing water. The maximum length that water can flow is calculated based on equating the change in pressure to cement tensile strength and using fixed values for permeability, flow rate, and fluid viscosity (Meininger, R., and Tanesi, J., 2006). Powers estimated this length to be 0.008 in. (0.2 mm) based on concrete made with Vinsol resin air entraining admixture (Meininger, R., and Tanesi, J., 2006).

Flow resistance of unfrozen water through capillaries in concrete structures could result in accumulation of hydraulic pressure, thereby damaging the concrete. Ice accretion and osmotic pressure theory explain results unaccounted for by the previous two theories. During freezing, water in the gel pores travels to capillaries according to thermodynamics laws (Abu-Lebdeh, T.,

Hamoush, S., Mohamed, A., and Picornell-Darder, M., 2011). However, water in the gel pores cannot freeze at temperatures above $-78\text{ }^{\circ}\text{C}$ due to the small size of these pores (Meininger, R., and Tanesi, J., 2006). When the water temperature is less than $0\text{ }^{\circ}\text{C}$, the water energy becomes higher than that of ice, causing water to flow from the gel pores to the capillaries. The energy gradient causes this water to freeze once it reaches the capillaries. Water continues to flow from the gel pores to the capillaries until the water energy equalizes with the ice energy. Because ice forms as pure water, not all the liquid freezes to fill pores completely with ice. Ions accumulate in the capillaries, causing continuation of water flow even when the capillaries are full. This continuation of water flow is a result of the system's attempt to equalize the solution concentration, consequently causing pressure buildup and internal damage (Cao, 2014).

Pop-outs are small holes in the concrete surface that occur when a near-surface aggregate expands and fractures mortar between the aggregate and surface. They can occur when saturated porous or weak aggregate splits as a result of frost action. This frost action exerts internal pressure inside the aggregate or when water is ejected from the aggregate due to the same pressure, thereby causing mortar or paste cover pop-out. These two types of pop-outs are referred to as Classical or Type I popouts and Type II (Pigeon, M., and Pleau, R., 1995). Type I popouts occur when the fracture passes through the aggregate, as shown in Figure 5.1, whereas Type II popouts occur when the fracture occurs immediately above the aggregate as shown in Figure 5.2.

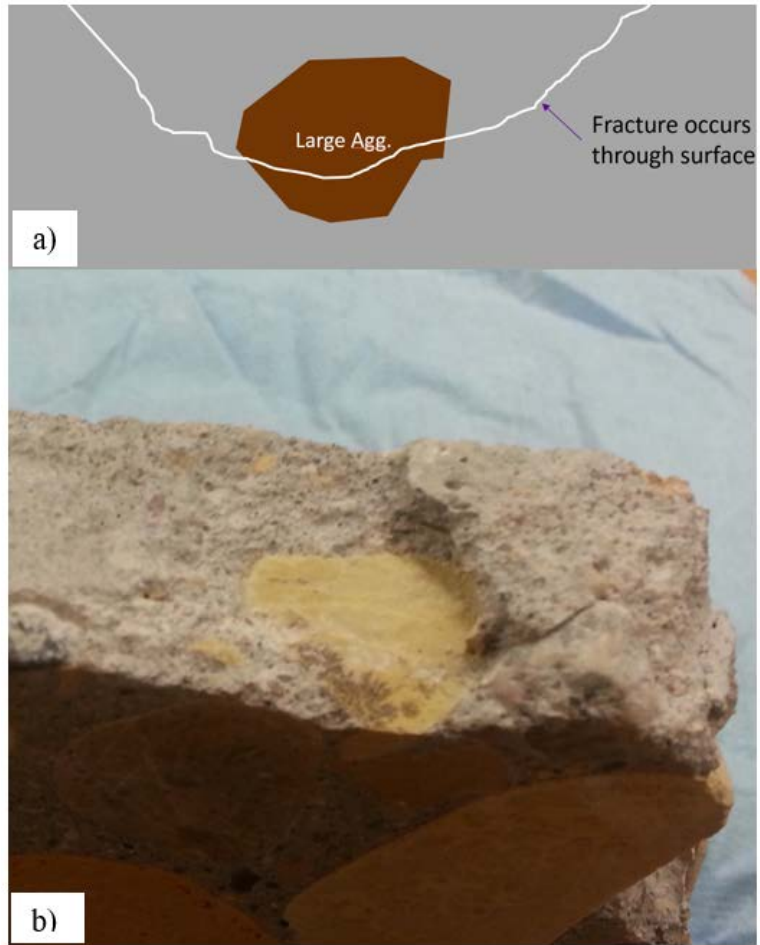


Figure 5.1. Type I popout a) schematic, and b) occurrence in concrete

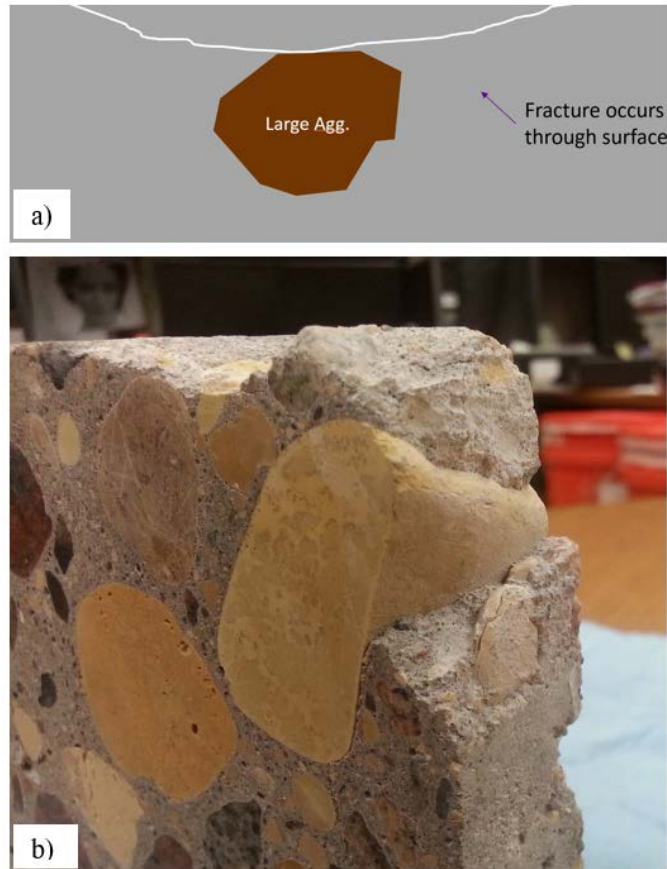


Figure 5.2. Type II popout a) schematic, and b) occurrence in concrete

5.1.1 Preventing Freeze-Thaw Damage

Three main concrete material properties control freeze-thaw deterioration in concrete. These are aggregate characteristics, concrete permeability, and the air void system (Page, C. L., and Page, M. M. (Eds.), 2007). Sixty to 80 percent of the volume of a typical concrete is comprised of aggregates. Similar to cement paste, freeze-thaw durability of aggregate depends primarily on its pore structure and level of saturation during freezing. Aggregate subjected to freezing, while fully saturated, must accommodate increased volume resulting from ice formation or be able to expel water from the aggregate to an air void in the cement paste before it freezes in the aggregate (Chen, F., McLean, D. I., and Qiao, P., 2012).

Aggregate freeze-thaw durability depends on aggregate type, size, absorption capacity, degree of saturation, pore size, and distribution (ACI Committee 621, 1961). Aggregate type can affect the strength of interfacial transition zones (ITZ) and development of micro-cracking (Mehta, 1990). When the weak transition zones suffer micro-cracking, permeability of the cement paste increases and the concrete becomes more susceptible to freeze-thaw damage (Chen, F., McLean, D. I., and Qiao, P., 2012). In addition to aggregate type, aggregate size is an important factor for freeze-thaw durability. Small aggregate subjected to freeze-thaw cycles without the cement matrix were able to withstand freeze-thaw for longer periods than large aggregates following the internal hydraulic pressures mechanism (Landgren, R., and Verbeck, G., 1960). For absorption, aggregates with high absorption capacities and very fine pore structures cause more freeze-thaw

damage (Helmuth, 1961). Water can be expelled from aggregates during the freezing cycle, resulting in increased hydraulic pressure and damage to the ITZ. The increased pressure and the freezing of the water cause aggregates to expand, thereby causing damage to the surrounding paste (Sawan, 1987). Aggregates with pores smaller than 5 μm tend to remain saturated in concrete for longer periods of time than aggregates with larger pores, and they tend to have low permeability that causes increased hydraulic pressure in the cement paste during freezing (Pigeon, M., and Pleau, R., 1995).

High-performance concrete with low permeability is typically made with a very low water to cement ratio and with the aid of water reducers. Low-permeability concrete has two main benefits: reduction of the amount of water that can enter the concrete and reduction of the amount of excess water in the hydrated cement. Reduction in the amount of water absorbed lowers the concrete degree of saturation, consequently decreasing damage during freezing (Chen, F., McLean, D. I., and Qiao, P., 2012).

Air System

Agitation and folding action during mixing naturally includes air into concrete. Without air-entraining chemical admixtures, air bubbles are unstable and quickly leave the concrete. Air-entraining agents stabilize air mixed into the concrete. Powers described two main processes to generate air in concrete (Powers, T.C., 1968) (Du, L., and Folliard, K. J., 2005). The first process is the entrainment of air through folding during the vortex action of the mixing. The second process involves the flowing and falling mass of the fine aggregate onto itself during mixing, trapping air bubbles under the aggregates. Mielenz et al. stated that air is already in the system of materials and can be entrapped as a result of the mixing process (Backstrom, J. E., Flack, H. L., Mielenz, R. C., and Wolkodoff, V. E., 1958) (Du, L., and Folliard, K. J., 2005). Air bubbles are naturally unstable in the concrete and will normally escape, combine, or collapse. Air-entraining agents are used to stabilize the air bubbles in the concrete. These surfactants typically consist of various surfactants that are composed of hydrophilic heads and hydrophobic tails (Du, L., and Folliard, K. J., 2005). Although surfactants orient themselves randomly in bulk solutions, they tend to demonstrate a preferred orientation to form spheres with hydrophilic heads on the outside surrounded by water, and hydrophobic tails on the inside, surrounded by air (Du, L., and Folliard, K. J., 2005).

Air bubbles are locations to which water in concrete capillaries can travel in order to form ice crystals, thereby relieving stress resulting from freezing action (Scherer, G. W., and Sun, Z., 2008). A good distribution of air voids results in increased accessibility of air bubble sites and less freeze-thaw damage. The distance that water in concrete capillaries can travel without causing damage depends on factors such as rate of freezing, degree of saturation, porosity, permeability, water viscosity, degree of hydration, and tensile strength of the concrete (Powers T. C., 1945) (Hover K. C., 2006). Critical thickness is the average maximum distance that water in the capillaries can travel without causing any damage. According to Powers' calculation, theoretical critical thickness in concrete is 0.008 in. (0.2 mm) (Pigeon, M., and Pleau, R., 1995) (Hover K. C., 2006). Based on this calculation, each air void would contain a spherical zone that is 0.008 in. (0.2 mm) beyond the radius of the bubble. These spheres are typically referred to as relief (protection) zones, as shown in Figure 5.3 (Meininger, R., and Tanesi, J., 2006).

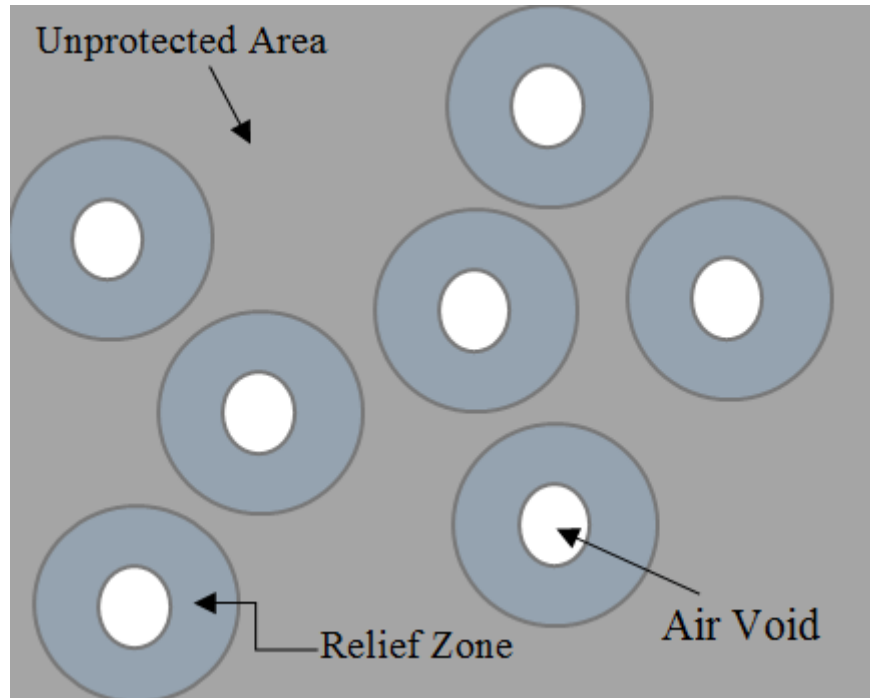


Figure 5.3. Relief zones in air-entrained concrete (Meininger, R., and Tanesi, J., 2006)

Air volume required to accommodate water expansion is fairly small. A fully saturated concrete sample containing 30 percent paste requires approximately 1.3 percent air content in order to accommodate expansion (Meininger, R., and Tanesi, J., 2006). Therefore, the number and distribution of air voids is more important than the total volume of air content. As shown in Figure 5.4, small air voids can produce large relief zone coverage, whereas the same amount of air content with larger air voids leaves more paste vulnerable to freeze-thaw deterioration (Pigeon, M., and Pleau, R., 1995).

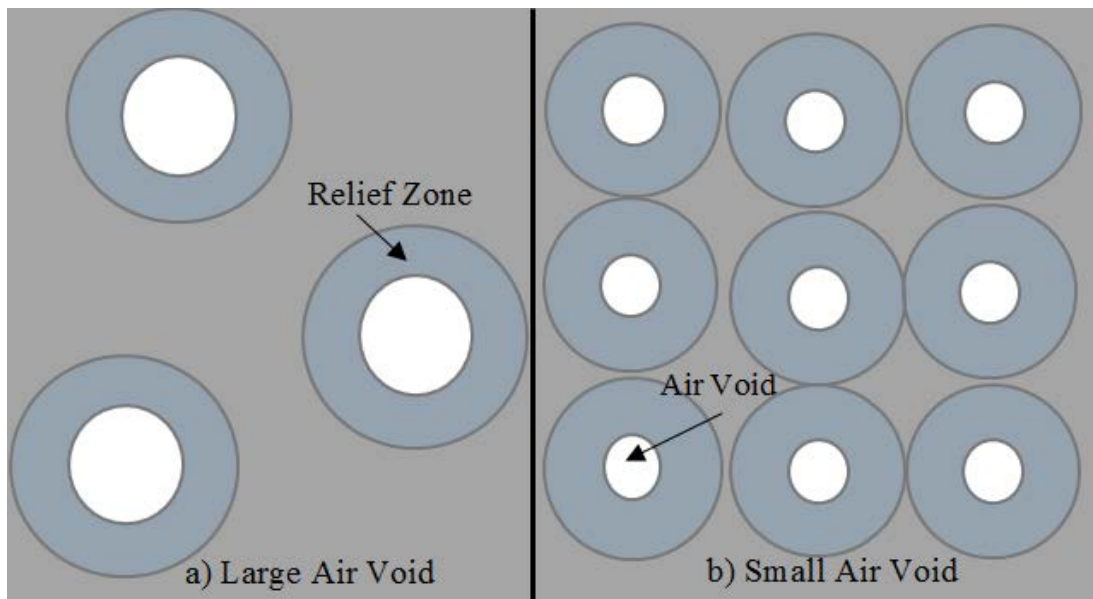


Figure 5.4. Effect of air void size on relief zones showing the same air content in figure a) and b) (Meininger, R., and Tanesi, J., 2006)

Spacing factor refers to the average maximum distance that water must travel in order to reach the closest air void. Regardless of air void size, it can provide freeze-thaw protection to concrete within its relief zone (Hover K. C., 2006). According to Powers' calculations, an increase in flow rate and/or fluid viscosity causes the size of the relief zone to shrink (Meininger, R., and Tanesi, J., 2006). Figure 5.3 illustrates the effect of proper spacing on freeze-thaw durability. Water in concrete capillaries moves to the nearest air void without causing damage or cracking because these water capillaries are situated within a relief zone. However, when air voids are inadequately spaced, water freezes in the capillaries causing cracking and deterioration in the cement matrix, as shown in Figure 5.5 (Meininger, R., and Tanesi, J., 2006).

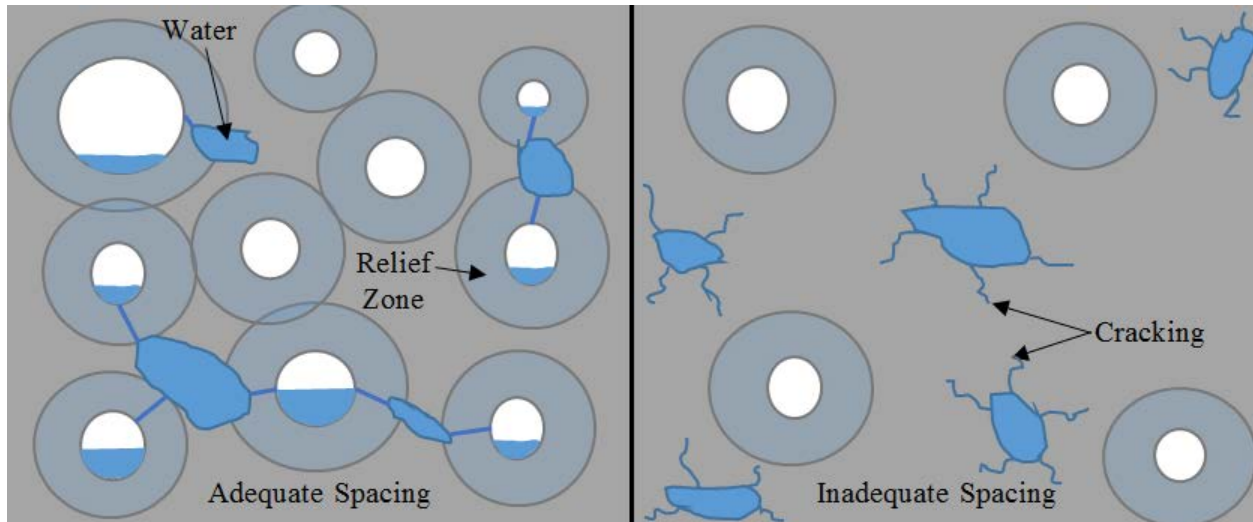


Figure 5.5. Spacing factor effect

Factors Affecting Air Void System

Air void systems in concrete are influenced by factors such as cement, admixtures, rheology, mixing procedures, temperature, handling, and vibration. Research has shown that high cement alkali levels lead to a rise in air content, while an increase in the fineness of cement leads to a drop in air content (Pomeroy, 1987) (Stark, D., and Whiting, D., 1983) (Kerkhoff, B., Kosmatka, S. H., and Panarese, W. C., 2002). As cement fineness increases, the surface area also increases, requiring additional air-entraining agents to give the mix the desired air content (Nagi, 2007). Cementitious materials can affect air entrainment by adsorbing or otherwise interfering with the air-entraining admixture. Carbon in fly ash works as an absorbent for surfactants used in the air-entraining admixture (Klieger, P., and Perenchio, W. F., 1976). If the carbon adsorbs the air-entraining agent, it will not be available to stabilize air bubbles in the concrete. However, silica fume and slag cement can reduce air content as a result of its high fineness and the presence of unburned carbon (Kerkhoff, B., Kosmatka, S. H., and Panarese, W. C., 2002). Metakaolin does not have any apparent effect on air content (Kerkhoff, B., Kosmatka, S. H., and Panarese, W. C., 2002).

The effect of admixtures on the air system vary depending on the rheological properties of the concrete. For conventional, vibrated concrete, admixtures containing lignin-based materials tend to increase the air content and the spacing factor (Kerkhoff, B., Kosmatka, S. H., and Panarese, W. C., 2002). Retarders demonstrate similar effects as lignin-based materials; however, accelerators have a negligible effect on air content (Kerkhoff, B., Kosmatka, S. H., and Panarese,

W. C., 2002). Self-consolidating concrete (SCC) can require increased dosages of air-entraining agent in order to compensate for air loss (Łazniewska-Piekarczyk, 2012) (Kamal, H., Khayat, K. H., and Assaad, J., 2002) (Foy, C., Pigeon, M., and Plante, P., 1989). In highly fluid SCC, air bubbles experience more movement, causing ruptures and merging in the bubbles (Łazniewska-Piekarczyk, 2012) (Łazniewska-Piekarczyk, 2013). In SCC with low fluidity, however, the air bubbles can remain stable (Du, L., and Folliard, K. J., 2005). When VMAs are used, increased dosages of superplasticizers are needed in order to maintain concrete workability. Cement particles absorb the superplasticizer as a result of this increase, thereby causing interference that prevents air bubbles from attaching to the cement (Kamal, H., Khayat, K. H., and Assaad, J., 2002).

Correlation of the effects of rheological properties on air content is very difficult because the addition of air alters the concrete's rheological properties (Jiang, Q., and Struble, L. J., 2004). Increased air content causes a decrease in plastic viscosity and an increase in yield stress (Jiang, Q., and Struble, L. J., 2004). Increased mixing speed also results in increased air content (Dolch, 1996). Studies have shown that air content gradually increases with speeds up to 20 rpm and decreases at higher speeds (Kerkhoff, B., Kosmatka, S. H., and Panarese, W. C., 2002). The relationship between mixing time and air content was found to increase up to a certain mixing time, after which time the air content begins to destabilize (Litwinowicz, F. J., and Scripture, E. W. J., 1949). Concrete with higher temperatures tends to have lower air content even when maintaining constant slump by adjusting the water (Dolch, 1996).

Effects of Vibration on the Concrete Air System

During vibration, buoyancy causes air bubbles to be lost when they rise to the top of the fluid concrete or consolidate into large bubbles that readily rise to the concrete surface. Air bubble rise depends on concrete fluid properties and bubble size. In order for a bubble to begin rising in concrete, the applied shear stress provided by the upward buoyancy force and vibrational energy must be greater than the yield stress of the concrete. Concrete yield stress is defined as the applied shearing stress needed to initiate the flow of concrete (i.e., make the concrete behave like a fluid). Bubble rise speed is affected by the viscosity of concrete, which is consequently affected by the applied shearing stress. Buoyancy force is proportional to bubble volume, whereas resistance to bubble motion by the concrete is proportional to the surface area. The larger the bubble, the larger the buoyancy relative to forces resisting motion and the higher its tendency to rise in concrete. Vibration increases forces acting on the bubble, causing them to rise. Vibration primarily eliminates large voids in the concrete and improves smoothness of the concrete finish on formed surfaces (Hover K. C., 2001).

Similar to other congested concrete members, prestressed concrete ties are typically vibrated in order to consolidate the concrete and avoid honeycombing and bug holes on the ties during placement. Vibration of concrete, however, can affect the entrained air content, bubble size, bubble spacing, and frost-resistance of hardened concrete. Excessive vibration results in loss of entrained air, thereby causing frost resistance in the concrete (Hover, K., 2003). Researchers have found that concrete loses the most air within the first few seconds of vibration. As vibration time increases, air loss decreases (Higginson, 1952), indicating a proportionality between air loss and vibration time. A correlation also exists between air loss and vibration of higher slump concrete (Higginson, 1952).

5.1.2 Methods to Measure Air Voids in Fresh Concrete

Three main methods are typically used to measure air voids in fresh concrete: the Gravimetric method, the Volumetric method, and the Pressure method. The Gravimetric method compares the theoretical unit weight of concrete and the measured unit weight. Per ASTM C138, air content can be computed using the Gravimetric method, Equation 5.1 and Equation 5.2 (ASTM Standard C 138, 2013).

$$A = \frac{U_t - U}{U_t} \times 100 \quad \text{Equation 5.1}$$

$$A = \frac{V - V_i}{V} \times 100 \quad \text{Equation 5.2}$$

Where:

A =Air content (%)

V =Volume of concrete produced per batch, m^3 [yd^3]

V_i =Total volume of batch ingredients, m^3 [ft^3]

U =Unit weight of concrete, kg/m^3 [lb/ft^3]

U_t = Theoretical unit weight of concrete excluding the air, kg/m^3 [lb/ft^3]

Unfortunately, a minor error in measurements can lead to a significant error in calculated air content. This method is typically used as a comparison baseline for air content of a concrete batch, but it lacks precision provided by other methods (Pigeon, M., and Pleau, R., 1995).

The Volumetric method compares concrete volume to the volume of the same concrete after expelling air by agitating the concrete under water. Figure 5.6 shows an illustration of the volumetric air meter used in ASTM C173 (ASTM Standard C 173, 2014). The volumetric air meter has two sections. The top section of the meter must be larger than the bottom section by at least 20 percent, and the bottom section must have a minimum volume of 0.002 m^3 (0.075 ft^3). In addition, both sections must be watertight when assembled with the concrete sample inside. After the bottom section is filled with concrete, the two sections are assembled using clamps. Then, using a funnel inserted onto the top section, water is poured slowly into the top section until the water level reaches the calibration mark. The vessel is sealed from the top using the screw cap. Finally, the concrete is agitated in order to release the entrained air from the concrete and allow it to rise to the water surface. When the air is stabilized and remains constant at the top of the vessel, the difference in water level and air content are calculated using Equation 5.3.

$$A = \frac{(h_i - h_f)A_{top}}{V_{bottom}} \times 100 \quad \text{Equation 5.3}$$

Where:

h_i =Initial water height before agitation, mm [in]

h_f =Final water height when air became constant and stable, mm [in]

A_{top} =Cross-sectional area of the top section of the vessel, mm^2 [in^2]

V_{bottom} =Volume of the bottom section, mm^3 [in^3]

Although, this method is not affected by aggregate type and properties such as moisture content and absorption, measurements are difficult to make in the field and require significant physical effort, leading to results with decreased accuracy and reduced use in practice (Pigeon, M., and Pleau, R., 1995).

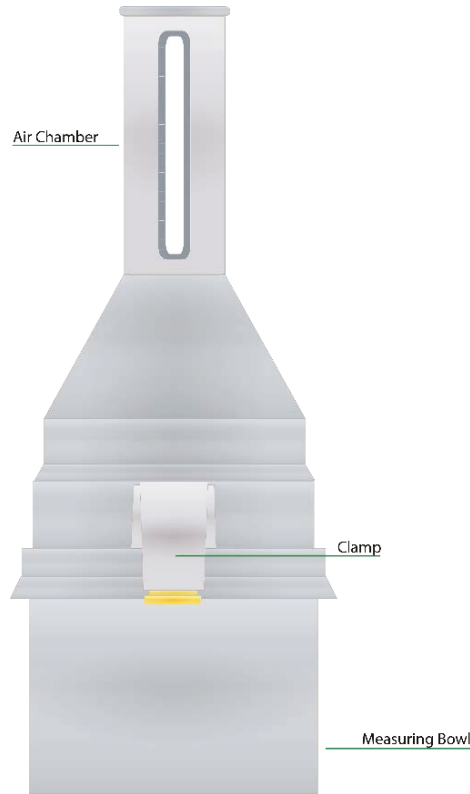


Figure 5.6. Air meter for ASTM C 173 volumetric test (W.W Grainger, Inc., n.d.)

The pressure method measures the air volume by measuring the concrete response to an applied pressure. Air in the paste or aggregate is compressed by the applied pressure causing a volume reduction in the concrete. According to ASTM C231, two types of air meters measure air content (ASTM Standard C 231, 2010). A Type A air meter employs differences in volume measurement. Similar to the volumetric vessel, the Type A air meter utilizes a watertight seal in addition to water filled to a fixed level in order to measure air content. Implementation of Boyle’s law, which states that multiplication of the pressure and volume of an ideal gas at a given temperature is constant, allows calculation of concrete sample air content (Pigeon, M., and Pleau, R., 1995). Because water is an incompressible substance, air is identified as the only material that changes volume, as shown in Equation 5.4:

$$A = \frac{(h_i - h_f)A_{top}}{V_{bottom}} \times \left(\frac{P}{P - P_{atm}} \right) \times 100 \quad \text{Equation 5.4}$$

Where:

P_{atm} =Atmospheric pressure

P =Pressure of the air meter that can be checked using Equation 5.5

$$P = \frac{V_{bottom} P_{atm}}{V_{bottom} - A_{top}(h_i - h_f)} \quad \text{Equation 5.5}$$

Type B air meters measure the pressure difference in order to calculate the air content of a concrete sample. Although predominantly similar to the previous two vessels, this apparatus also contains two parts joined by clamps to form a watertight seal. Water is introduced through one of two petcocks in order to fill the remaining void between the concrete sample and top section of the apparatus, as shown in Figure 5.7. The top section is pressurized. After that, the two petcocks are closed, and the sample is pressurized by releasing air pressure from the top section of the vessel to the concrete sample using the main air valve. The decrease in air pressure in the top section is related to the change in volume of the concrete in the bottom section. Boyle's law is applied as shown in Equation 5.6 to calculate air content (ASTM Standard C 231, 2010).

$$A = \frac{V_i}{V_{bottom}} \times \left(\frac{P_i - P_f}{P_f - P_{atm}} \right) \times 100 - G \quad \text{Equation 5.6}$$

Where:

V_i = The initial volume of air in the top section

P_i = The initial pressure of the air meter

P_f = The final pressure of the air meter

G = The aggregate correction factor measured using the ASTM C231 method

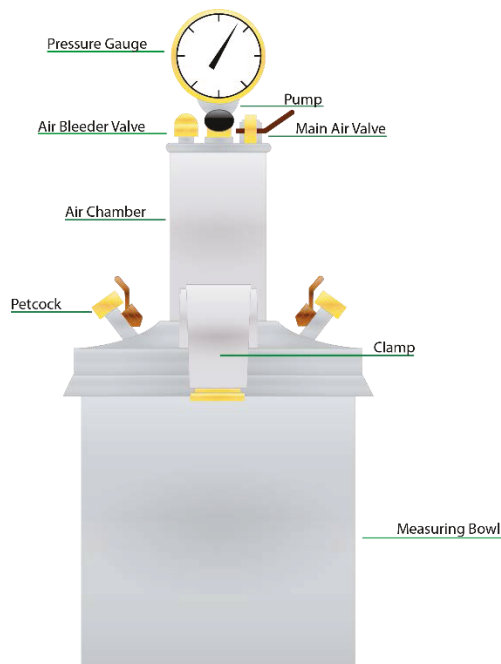


Figure 5.7. Type B air meter to measure air content using the pressure method

5.1.3 Hardened Air Void Measurements

Concrete air content changes immediately after mixing through delivery, placement, and vibration. Therefore, actual air content and spacing in the actual elements after hardening must

be known. Several methods are available for quantifying the air void system in hardened concrete. Three-dimensional scanning of a concrete sample is now possible using X-ray microtomography, but this method cannot be used on large concrete samples to measure air voids, is slow, and expensive. Quantitative stereology has been used to determine air void characteristics in three-dimensional volumes from two-dimensional concrete cross sections (Choo, J., Kang, D. H., Kim, K. Y., Shin, H. S., and Yun, T. S., 2012). Quantitative analysis is usually done by taking a plane section from the analyzed three-dimensional volume (Hover, K., Natesaiyer, K., and Snyder, K., 2001). When a saw-cut plane intersects air void spheres, it creates two-dimensional voids. These voids may not accurately represent the void maximum cross sectional area. This misrepresentation can yield useful information regarding variation in the spheres' radii distribution (Hover, K., Natesaiyer, K., and Snyder, K., 2001). Two assumptions are typically made for air void systems: a) air void microstructural sphere systems do not overlap, and b) air voids are distinct spheres (Hover, K., Natesaiyer, K., and Snyder, K., 2001). A concrete petrographer can choose between several probes when performing stereological analysis. These probes include points, lines, surfaces, or volumes. A concrete petrographer must choose a probe based on the amount of data required for the test. For example, point probes are used to determine volume fractions, while line probes characterize the size and spacing of air voids (Hover, K., Natesaiyer, K., and Snyder, K., 2001). Although the number of air voids can be calculated from surface probe data, it can only be approximated in line probe data. Two methods for quantifying air void system quality are described in ASTM C457 (ASTM Standard C 457, 2012): the linear traverse and modified point count methods (Lane, D., Stutzman, P. E., and Walker, H. N., 2006).

Linear Traverse

The linear traverse method records individual and cumulative chord length of the paste, aggregate, and air voids across predefined parallel lines across the specimen surface (ASTM Standard C 457, 2012). Air content is calculated by dividing the cumulative chord length crossing air voids by the total length of chords multiplied by 100. Figure 5.8 shows parallel lines on a concrete sample used to measure air content in the linear traverse method.

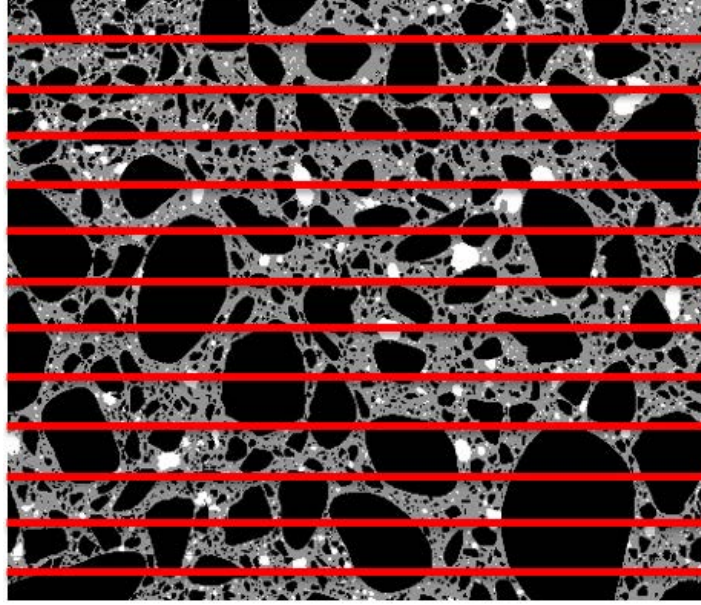


Figure 5.8. Linear traverse method on a concrete sample

Two main concrete properties, air content and paste content, can be calculated using Equation 5.7 and Equation 5.8 (ASTM Standard C 457, 2012). The spacing factor can be calculated using Equation 5.9 (ASTM Standard C 457, 2012).

$$A = 100 \left(\frac{T_a}{T_t} \right) \quad \text{Equation 5.7}$$

$$p = 100 \left(\frac{T_p}{T_t} \right) \quad \text{Equation 5.8}$$

$$\bar{L} = \begin{cases} \frac{T_p}{4N} & \text{for } \frac{p}{A} \leq 4.342 \\ \frac{3T_a}{4N} \left[1.4 \left(1 + \frac{p}{A} \right)^{\frac{1}{3}} - 1 \right] & \text{for } \frac{p}{A} > 4.342 \end{cases} \quad \text{Equation 5.9}$$

Where:

P =Paste content (%)

\bar{L} =Spacing factor

N =Total number of air voids intersected

T_t =Total length of traverse

T_a =Traverse length through air

T_p =Traverse length through paste

The linear transverse method has been found to give air content 10 to 20 percent less than what is measured for fresh concrete using the pressure method and volumetric method, especially when air content exceeds 4 percent (Khayat, K. H., and Nasser, K. W., 1991). However, Celik Ozyildirim reported no significant difference between air content measured by the pressure

method and air content measured by the linear transverse method using untampered concrete from the same batch (Ozyildirim, 1991). He also attributed that difference to the admixture used to entrain air in the concrete (Ozyildirim, 1991).

Modified Point Count

In the modified point count method, a grid of points is used as a testing reference for which the constituent under each point on the grid is identified. Figure 5.9 shows a grid drawn on a concrete sample. Concrete characteristics can be identified by recording the total number of air voids intersected, total number of points on the grid, total number of paste points, and total number of air points. Equation 5.10 and Equation 5.11 are used to calculate the paste and air content of the sample, respectively (ASTM Standard C 457, 2012). Equation 5.12 is used to calculate the spacing factor of air in the concrete sample (ASTM Standard C 457, 2012).

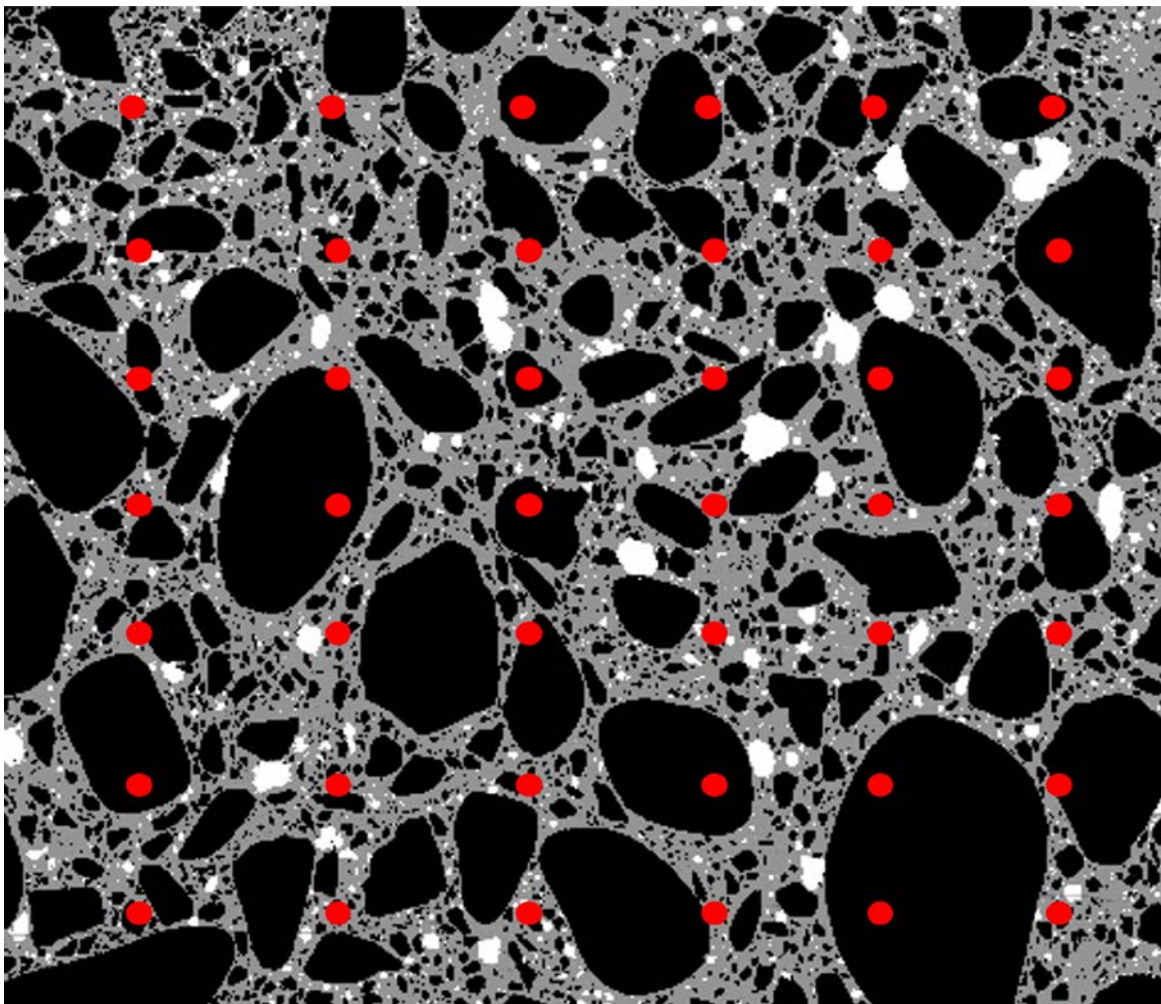


Figure 5.9. Modified point count method on a concrete sample

$$p = 100 \left(\frac{N_p}{N_t} \right) \quad \text{Equation 5.10}$$

$$A = 100 \left(\frac{N_a}{N_t} \right) \quad \text{Equation 5.11}$$

$$\bar{L} = \begin{cases} \frac{p N_t}{400 N} & \text{if } p/A \leq 4.342 \\ \frac{3 N_t A}{400 N} \left[1.4 \left(1 + \frac{p}{A} \right)^{\frac{1}{3}} - 1 \right] & \text{if } p/A > 4.342 \end{cases} \quad \text{Equation 5.12}$$

Where:

N_t =Total number of points on the grid

N_p =Total number of paste points

N_a =Total number of air points

Image Analysis

Image analysis is a process in which an algorithm is used to separate out air voids from the paste and aggregate in a cross-section of the concrete using an image of the concrete surface instead of manual examination of the surface. Image analysis follows the same sample preparation as ASTM C457 methods (ASTM Standard C 457, 2012). Samples are polished before scanning. Image analysis performed on scanned images utilizes either of the two methods in ASTM C457 (ASTM Standard C 457, 2012) (Schlorholtz, 1998). Image analysis involve separating scanned images based on color or other features into cross-sectional images of the cement paste, air content and aggregate. Several methods are available to perform image analysis in order to obtain various air parameters. One of the main methods involves analyzing black and white enhanced samples using a microscope, a camera, and a computer (Hanson, 2012). A commercial system known as the RapidAir 457 utilizes that method with the help of computer image processing software. Results obtained from the RapidAir 457 have shown excellent correlation with air void parameters obtained using ASTM C457 (Hanson, 2012).

The image analysis method can also be used in conjunction with a flatbed scanner and image processing software. In 2001, Karl Peterson developed a novel procedure to study hardened concrete samples using a flatbed scanner (Peterson, K., 2001). This method consisted of three stages: non-stained scanned sample, phenolphthalein-stained scanned sample, and black and white-treated scanned sample. A computer program that uses an automated modified point count method to determine air content properties is utilized. In his study, Peterson conducted four analyses on each image while changing sampling point locations for each analysis in order to optimize results throughout the entire sample. His tests of 570 microscopic images yielded 90.2 percent accuracy using an automated modified point count compared to a modified point count method manually performed on the same samples. In addition, air void frequencies and specific surfaces were lower than those calculated and measured according to the manual modified point count method. Spacing factors were also slightly higher than spacing factors measured using the manual modified point count method.

Although the automated modified point count method successfully measured air content parameters, small variations occurred when changing sampling points (Peterson, K., 2001). Similar to the linear traverse method in which every pixel line can be analyzed, as shown in Figure 5.10, utilization of computational capabilities of current computers can achieve better results by sampling every pixel as a point in the image. Peterson et. al. (2002) concluded that standard deviations calculated for samples analyzed by the modified point count method were

consistently larger than that of identical standard deviations calculated for samples analyzed by the linear traverse method (Peterson, K. W., Sutter, L. L., and Van Dam, T. J., 2002).

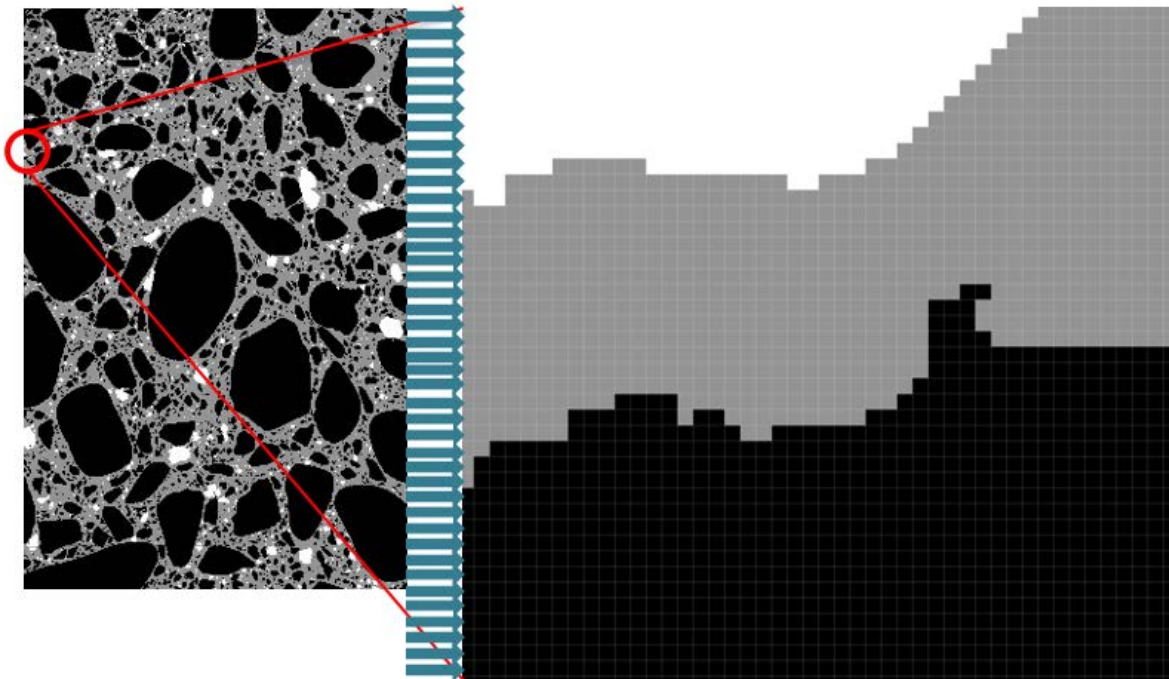


Figure 5.10. Pixel line analysis performed on scanned concrete sample

Ramezaniapour and Hooton (2010) compared two image analysis methods of measuring air content in hardened concrete and concluded that lack of knowledge of concrete paste content leads to less accurate air content reading with a flatbed scanner and RapidAir 547 (Hooton, R. D., and Ramezaniapour, A. M., 2010). They also stated that results obtained using the flatbed scanner were in better agreement with the manual method from ASTM C457 as compared to RapidAir 457. They reported that the RapidAir 457 detected very small air voids (30 μm) compared to ASTM C457 methods. Radlinski et. al. compared air analysis performed on hardened concrete samples using the modified point count method and the flatbed scanner method (Olek, J., Peterson, K., Radlinski, M., and Zhang, Q., 2010). They concluded that air content measurements were higher for the modified point count method compared to flatbed scanner results, but the estimated specific surface of the air was higher for the flatbed scanner compared to results of the modified point count method (Olek, J., Peterson, K., Radlinski, M., and Zhang, Q., 2010). They also stated that air contents measured by the flatbed scanner method were closer to the air content in fresh concrete measured by the pressure method than that from the modified point count method (Olek, J., Peterson, K., Radlinski, M., and Zhang, Q., 2010).

5.2 Materials Characterization

All concrete mixtures were prepared in the laboratory using ASTM C150 Type III cement, a natural siliceous sand, and a limestone coarse aggregate. Table 5.1 shows the cement physical and chemical properties. The coarse aggregate had a specific gravity of 2.69 and absorption of 0.39 percent while the fine aggregate had a specific gravity of 2.66, absorption of 0.74 percent and fineness modulus of 3.02. Figure 5.11 and Figure 5.12 show the particle size distribution of coarse and fine aggregates, respectively. The size of the mixture ranged from 1 to 2.7 ft^3

depending on the purpose of the test. The mixture proportions varied depending on the targeted rheological properties. The following admixtures were used: a lignosulfonate-based low-range water reducer (LRWR), two different polycarboxylate-based HRWR, and synthetic, wood rosin, tall oil and vinsol resin air entraining agents (AEA).

Table 5.1. Cement Chemical and Physical Properties

Property	Value
Silicon dioxide (%)	22.03
Ferric oxide (%)	3.41
Aluminum oxide (%)	4.18
Calcium oxide (%)	63.45
Magnesium oxide (%)	1.96
Sulphur trioxide (%)	3.21
Loss on ignition (%)	1.45
Insoluble residue (%)	0.25
Free lime (%)	0.96
Sodium oxide (%)	0.16
Potassium oxide (%)	0.49
Equivalent alkalies (%)	0.48
C ₃ S (%)	48.8
C ₂ S (%)	26.4
C ₃ A (%)	5.3
C ₄ AF (%)	10.4
Blaine Fineness (cm ² /g)	5920

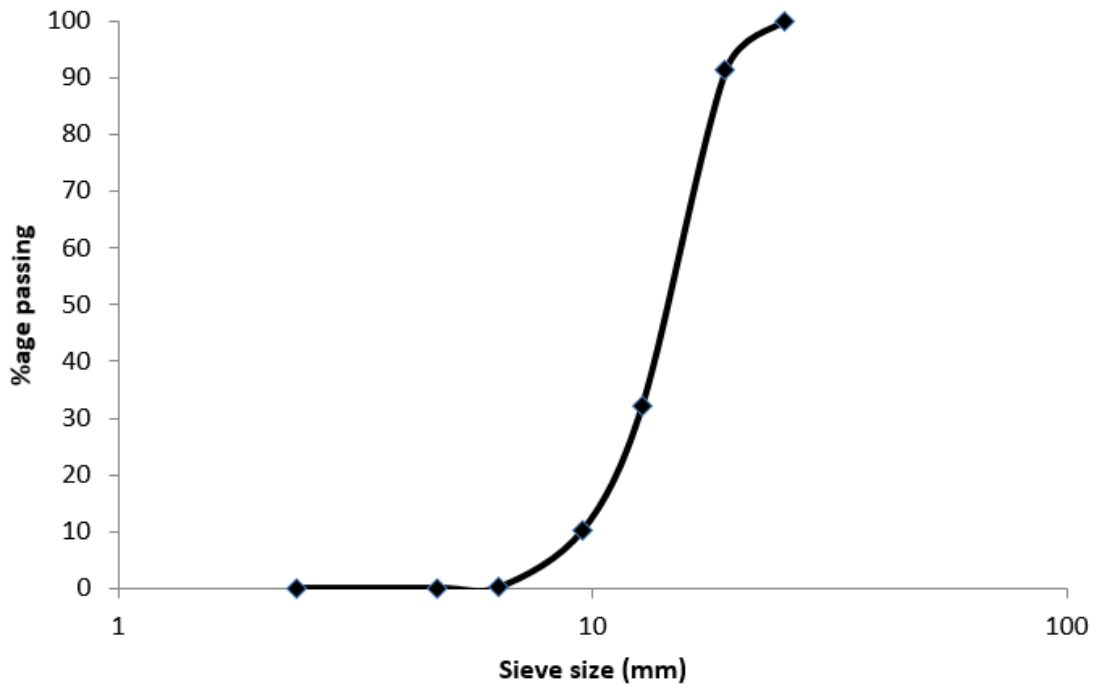


Figure 5.11. Particle size distribution of coarse aggregate

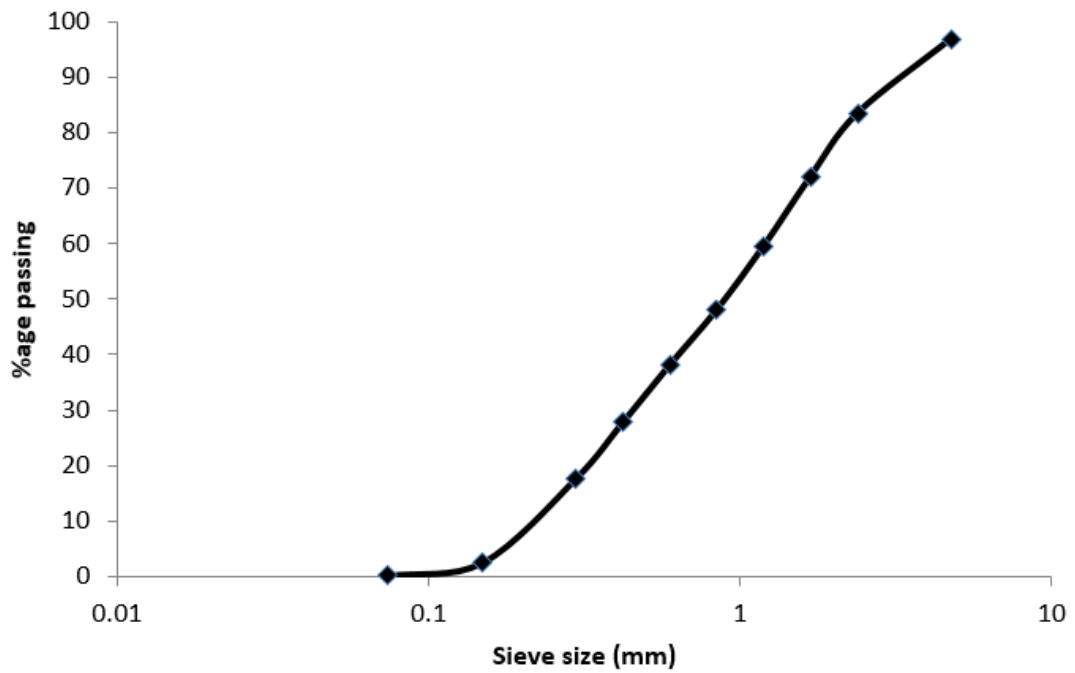


Figure 5.12. Particle size distribution of fine aggregate

5.2.1 Mixture Proportions

Stability of Air Void System

In this part of the study, the size of mixtures ranged from 2.1 to 2.7 ft³ depending on the number of times the air content was measured. The mixture proportions for all these mixtures were the same except for the mixture without any water reducers (WR), as shown in Table 5.2. The admixture dosages were also different for each mixture.

Table 5.2. Basic Concrete Mixture Proportions

Material	Weight (lb/yd ³)	
	No WR	Mixtures Containing WR
Cement	834.90	887.04
Water	358.45	270.07
Rock (SSD)	1677.63	1,778.25
Sand (SSD)	852.66	896.67

The rheological properties of the mixtures were varied by using different LRWR, HRWR and AEA dosages. The LRWR used was a lignosulfonate-based admixture. A polycarboxylate-based HRWR admixture was used. For the AEA, synthetic, wood rosin, and tall oil admixtures were used. Details for concrete mixtures used in this study can be found in Table 5.3. The air content values shown in Table 5.3 were taken after mixing but before vibration.

Table 5.3. Concrete Mixture Properties

Peak Vibration Acceleration	AEA	Dosage (Oz/100 lb of Cement)	Water Reducer	Dosage (Oz/100 lb of Cement)	Temp. (°F)	Unit Weight (lb/ft ³)	Air Before Vibration (%)	Slump (in)
3g	Synthetic	1.8	None	N/A	76	137.24	7.8	8
	Synthetic	1.3	HRWR	7	75.4	140.56	9	6.5
	Synthetic	0.6	HRWR	7.5	73.3	142.72	7.5	6.25
	Synthetic	0.6	LRWR + HRWR	4.5+3.5	68.4	143.12	7.8	2.875
	Synthetic	0.6	LRWR + HRWR	4.5+4.5	75.9	141.56	8	4.5
	Synthetic	0.6	LRWR + HRWR	5+5	75	141.64	8.5	8
	Synthetic	0.5	LRWR + HRWR	5+4.5	66.1	-	7.4	4.5
	Synthetic	0.5	LRWR + HRWR	5+5	74.6	-	8.5	6.75
	Wood Rosin	0.6	HRWR	7.5	72.2	-	7.4	9.25
	Wood Rosin	0.8	HRWR	7	74.2	-	6.2	6
	Tall Oil	1	HRWR	7	77.3	-	9.5	4.5
	Wood Rosin	0.9	HRWR	7	74	144.84	5.6	6
	Tall Oil	0.6	HRWR	7.25	74.9	143.36	7	5.5
	Tall Oil	0.65	HRWR	7.25	75.5	144.32	6.2	4
10g	Synthetic	0.6	HRWR	7.5	75.4	139.12	9.5	6.5
	Synthetic	0.5	LRWR + HRWR	5+5	77.1	-	6.9	4.5
	Tall Oil	0.65	HRWR	7.5	76.4	-	7	4
	Wood Rosin	1.1	HRWR	7.5	76.1	-	6.2	5.5

Freeze-Thaw Durability of Externally-Vibrated Concrete

The size of each mixture used to study the freeze-thaw durability of externally-vibrated concrete was 1.1 ft³. Concrete mixtures of different rheological properties were used in this study. They ranged from low yield stress and plastic viscosity mixtures to high yield stress and plastic viscosity mixtures that had a target 4 in. slump. The rheological properties were varied by changing the water to cement ratio and volume fraction of coarse and fine aggregates. The HRWR dosage for a particular HRWR admixture was kept constant in these mixtures in order to study the effect of admixtures type rather than dosages. Two types of polycarboxylate HRWRs

were used. Synthetic and vinsol resin air entraining admixtures were used. Mixtures with HRWR1 and vinsol resin AEA were labelled as combination A. Mixtures with HRWR1 and synthetic AEA were labelled as combination B. Mixtures with HRWR2 and synthetic AEA were labelled as combination C. Table 5.4 shows the quantities of the constituent materials in each mixture used in this part of the study. Each of the four mixtures were designed to have considerable differences in terms of rheological properties. The HRWR dosages of combination C were significantly higher than those of combination A and B in order to obtain similar rheological properties among the different combinations that could not be achieved using the same dosage. It can also be observed that the AEA dosages were also different among the various combinations and mixtures. This was done to obtain the desired initial fresh air content since mixtures with different AEA type, HRWR type and rheological properties require different AEA dosages. Mixtures which had the same rheological combination number were designed to have the same rheological properties. Generally, rheological combination 1 would always have the highest yield stress and plastic viscosity while rheological combination 4 would have the lowest yield stress and plastic viscosity. Also, rheological combination 2 tended to have higher yield stress compared to rheological combination 3 which tells us that, for approximately the same w/c ratio, increasing the sand volume fraction increases the yield stress while increasing the rock volume fraction reduces it.

Table 5.4. Mixture Proportions of Externally-Vibrated Mixtures Used for Target Air Content of 3.5% to 4.5%

Admixture Combination	Rheological Combination	AEA Dosage (oz/cwt)	HRWR Dosage (oz/cwt)	W/C Ratio	Paste (% Vol.)	Rock (% Vol.)	Sand (% Vol.)
A	1	1.44	7.67	0.29	28.8	32.4	32.8
	2	0.48	7.67	0.30	29.3	21.7	44.0
	3	0.72	7.67	0.31	29.6	36.7	27.8
	4	0.48	7.67	0.33	30.5	31.6	31.9
B	1	0.07	7.67	0.29	28.8	32.4	32.8
	2	0.07	7.67	0.30	29.3	21.7	44.0
	3	0.07	7.67	0.31	29.6	36.7	27.8
	4	0.07	7.67	0.33	30.5	31.6	31.9
C	1	0.38	13.43	0.29	28.8	32.4	32.8
	2	0.01	13.43	0.32	29.8	21.6	43.6
	3	0.48	13.43	0.32	29.9	36.5	27.7
	4	0.19	13.43	0.33	30.7	31.5	31.9

The AEA dosages shown in Table 5.4 are for the most frequently used mixtures where the initial air content was intended to be constant. These dosages were changed for some mixtures in order to study the effect of initial air content and are shown in Table 5.5.

Table 5.5. AEA Dosages of the Mixtures Used for Studying the Effect of the Initial Air Content

Admixture Combination	Rheological Combination	Target Air Content (%)	AEA Dosage
B	4	3	0.02
		5	0.1
C	1	4	0.77
		5.5	1.53
	4	4	0.48
		5.5	1.06
		7	1.44

Freeze-Thaw Durability of Internally-Vibrated Concrete

In this study, rheological combinations 3 and 4 of chemical admixture combination B (Table 5.4) were used. Two mixtures of each rheological combination category were tested. The AEA dosages were changed to have one high and one low air content for rheological combinations 3 and 4. Table 5.6 shows the mixture proportions used for these mixtures.

Table 5.6. Mixture Proportions of Internally-Vibrated Mixtures

Admixture Combination	Rheological Combination	AEA Dosage (oz/cwt)	HRWR Dosage (oz/cwt)	W/C Ratio	Paste (% vol.)	Rock (% vol.)	Sand (% vol.)
B	3	0.07	7.67	0.31	29.6	36.7	27.8
		0.14	7.67	0.31	29.6	36.7	27.8
	4	0.07	7.67	0.33	30.5	31.6	31.9
		0.14	7.67	0.33	30.5	31.6	31.9

5.3 Equipment and Common Tests Description

Concrete Mixing

Concrete mixing was carried out according to ASTM C192 in a horizontal pan-style mixer. All constituent materials were preconditioned to laboratory temperature. The WR was added to 1/3 of the water while the AEA was separately added to the remaining 2/3 of the water. This was done in order to prevent interactions between chemicals prior to mixing. The mixing started by adding the coarse and fine aggregates along with 2/3 of the water and the AEA to the mixer. The constituents were then mixed for 3 minutes after which the cement and the remaining 1/3 of water and WR were added gradually while mixing. The mixing continued for another 3 minutes followed by 3 minutes of resting. The mixer was run for another 2 minutes before using the

obtained mixture (Figure 5.13) to measure the concrete's temperature, slump, unit weight, fresh air content and rheological properties.



Figure 5.13. Concrete after mixing

Rheology

The rheological properties were measured for each mixture using an ICAR rheometer. For this test method, the sample container shown in Figure 5.14 was filled with concrete up to the top of the plastic strips attached to the inside wall of the bucket. These strips help in eliminating slippage of the concrete at the wall of the bucket during the test. A vane (Figure 5.15 (a)) was then inserted into the concrete as shown in Figure 5.15 (b). The concrete was then sheared via the rotating vane. The torque developed by the resistance of concrete to the rotational motion of the vane was measured by the rheometer. This rheometer is capable of performing two tests, the stress growth test and the flow curve test. Assuming Bingham plastic behavior of fresh concrete, the stress growth test was used to measure static yield stress (i.e., yield stress without prior shearing history) while the flow curve test was used to measure the concrete dynamic yield stress (i.e. yield stress after breaking the thixotropic effect) and plastic viscosity. During the stress growth test, the vane was rotated using a slow constant speed while recording the increase in torque with time. Once the value of the torque started decreasing, the maximum torque was considered to have been reached. The yield stress was obtained from the maximum torque measured and is called the concrete static yield stress. For the flow curve test, a pre-shear period was performed before taking measurements. During this period, the vane was rotated at its maximum speed in order to minimize the effects of thixotropy and to provide a consistent shearing history. After completing the pre-shear period, the rheometer applied a series of vane rotations at different rotational speeds while measuring the corresponding developed torque at each speed. A line was fit to the measured torque vs rotational speed resulting in an equation

that can be used to obtain the dynamic yield stress and the plastic viscosity of the Bingham model (Amziane, S., Ferraris, C. F., and Koehler, E. P., 2005).



Figure 5.14. Rheometer concrete container



(a)



(b)

Figure 5.15. ICAR rheometer a) electronic equipment with vane and b) in concrete sample

Vibration

Depending on the measurement, table vibrators (Figure 5.16) or an immersion vibrator (Figure 5.17) were used to vibrate the concrete. Both were rotary vibrators that produced sinusoidal shear and compression waves. The immersion vibrator had a fixed frequency of 230 Hz, whereas the table vibrators had the option of changing frequency and amplitude. The small table vibrator was used for low frequencies of 30 to 110 Hz. The large table vibrator was used for high frequencies of 120 to 180 Hz. The table vibrators were custom-made at the Kansas State University lab. Each vibrating table had a control unit attached to digitally control the frequency (Figure 5.18). The vibrating motor was attached to the bottom of the table top as shown in Figure 5.19. The vibration acceleration was adjusted by changing the offset of the weights on the vibrating motor (Figure 5.20). A large concrete block was placed in the bottom of the vibrating table (Figure 5.21) to ensure the stability of the table during vibration. The freeze-thaw molds were rigidly attached to the top of the table using bolts at each of the four corners of the mold (Figure 5.22). The freeze-thaw molds used had dimensions of 16 X 4 X 3 in. The bottom pot for the fresh air test was fixed to the vibrating table by bolting a steel arch (Figure 5.23) on the steel rods coming from the top of the table (Figure 5.16) which held the handles of the air pot securely. The large vibrating table is shown in Figure 5.24. The small vibrating table could only fit either two freeze-thaw molds or one freeze-thaw mold and one air pot as shown in Figure 5.25. The acceleration of vibration was measured using a three-axis submersible accelerometer. In the case of the immersion vibrator, the accelerometer was placed at several distances away from the vibrator. In the case of the table vibrators, the vibration acceleration was taken at the middle of the mold. The duration of vibration was either 30 seconds, 2 minutes or 4 minutes.



Figure 5.16. Large vibrating table



Figure 5.17. Immersion vibrator



Figure 5.18. Control unit for the large vibrating table



Figure 5.19. Vibrating motor attached to the bottom of the table top

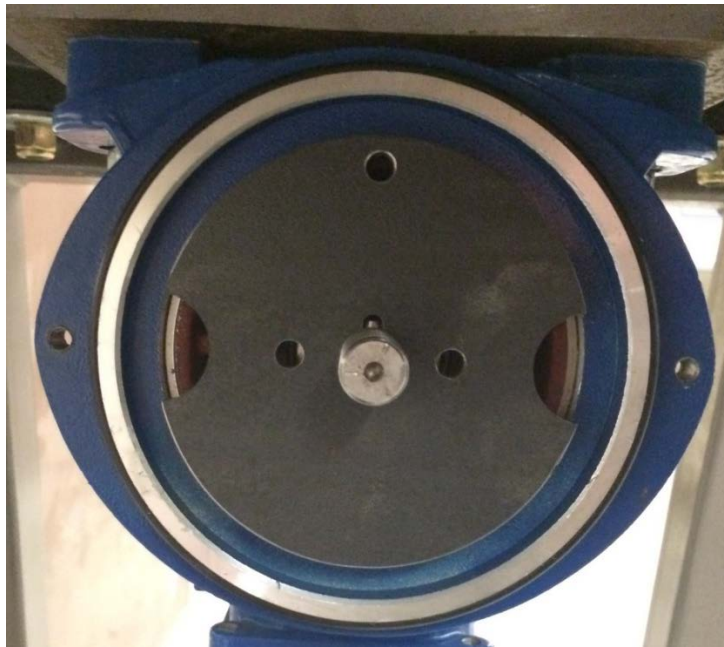


Figure 5.20. Vibrating motor weights inside the motor for the small vibrating table



Figure 5.21. Concrete block at the bottom of the large vibrating table

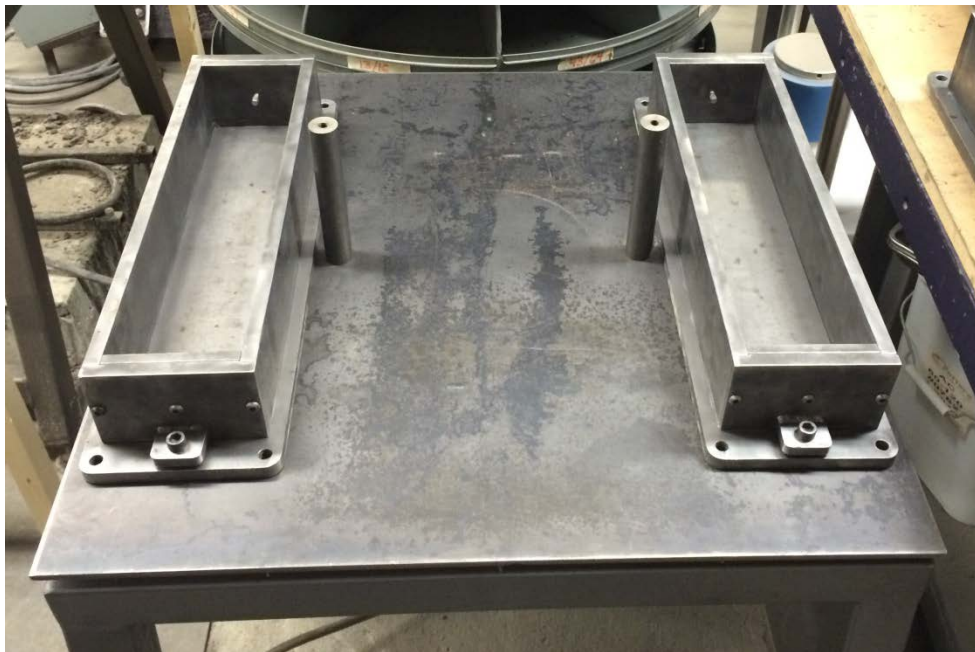


Figure 5.22. Freeze-thaw molds placed at the top of the large vibrating table



Figure 5.23. ASTM C231 concrete air content container bolted to the top of the large vibrating table



Figure 5.24. The large vibrating table with two freeze-thaw specimen molds and ASTM C231 specimen container bolted to the table top



Figure 5.25. The small vibrating table

Freeze-Thaw Testing

Freeze-thaw testing was performed using an automated freeze-thaw machine (Figure 5.26) that can fit up to 80 prisms. All prisms went through 300 cycles of freezing and thawing or until the durability factor (DF) dropped below 60 percent according to ASTM C666 method A. Initial concrete prisms' dimensions were measured prior to initiation of the test. Weight, length change and resonant frequency of each prism were taken before the initiation of testing and after each 30 to 36 freeze-thaw cycles. The sample was considered to have failed once the durability factor reached 60 percent or lower.



Figure 5.26. Freeze-thaw machine

Prior to freeze-thaw testing, concrete prisms were cured in limewater for 14 days then brought down to 40 ± 3 °F before taking initial measurements. Freeze-thaw cycles used in this study started with 225 minutes of freezing from 40 ± 3 °F to 0 ± 3 °F followed by 75 minutes of thawing from 0 ± 3 °F to 40 ± 3 °F. The samples were protected from loss of moisture at all times. The following calculations were made each 30 to 36 cycles in order to assess the performance of the specimens. Equation 5.13 was used to calculate the relative dynamic modulus of elasticity. Equation 5.14 was used to calculate the durability factor DF. Equation 5.15 was used to calculate the length change.

$$P_c = \frac{n_1^2}{n^2} \times 100 \quad \text{Equation 5.13}$$

Where:

P_c =Relative dynamic modulus of elasticity after c cycles of freeze-thaw (%)

n =Relative dynamic modulus of elasticity after c cycles of free-thaw (%)

n_f =Fundamental transverse frequency after c cycles of freeze-thaw (Hz)

$$DF = \frac{PN}{300} \quad \text{Equation 5.14}$$

Where:

P =Relative dynamic modulus of elasticity after N cycles of freeze-thaw (%)

N =Number of cycleas at which the test is terminated

$$L_c = \frac{(l_2 - l_1)}{L_g} \times 100 \quad \text{Equation 5.15}$$

Where:

L_c =Length change after c cycles of freeze-thaw (%)

l_1 =Length comparator reading after 0 cycles of freeze-thaw (in.)

l_2 =Length comparator reading after c cycles of freeze-thaw (in.)

L_g =Length of the specimen (in.)

Hardened Air Void Analysis

The hardened samples from before and after vibration and the freeze-thaw prisms were saw-cut using the electric saw shown in Figure 5.27. One in. thick samples were obtained from each specimen for hardened air void analysis. These samples were then polished prior to scanning and image processing. Scanning of polished samples was performed at a resolution of 4800 dpi. A modification of the Peterson method was adopted for scanning and image processing (Peterson, K., 2001). The goal of image processing was to obtain a black and white image where the white was the air voids and the black was everything else. This image was then used along with the paste content value obtained from the mixture design to calculate air content and spacing factor. Analysis was done using a software that utilizes the principles of the linear traverse method described in ASTM C457.



Figure 5.27. Electric saw

Figure 5.28 shows a saw-cut sample prior to polishing. Polishing was performed using the polishing machine shown in Figure 5.29. The two motors on the left and right of the machine were used to rotate the samples while the polishing wheel was rotated in the opposite direction. The different magnetic polishing discs were placed on top of the metal polishing wheel shown in Figure 5.29. The bucket shown at the top of Figure 5.29 was used to ensure a continuous stream of water for lubrication was applied on the polishing disc during the polishing operation. The polishing procedures began by applying a solution made of 80 percent acetone and 20 percent lacquer to the surface of the concrete that was to be polished in order to strengthen the paste and preserve the air voids during polishing. After the solution dried, the sample was bonded to a plastic cylinder, (Figure 5.30), using hot glue. This assembly was then placed on the polishing disc and connected to the two motors using rubber bands as shown in Figure 5.31. As shown in Figure 5.31, this procedure allowed four samples to be polished at the same time.

Polishing was performed using progressively finer-grit discs: 80-grit, 1200-grit and 2200-grit discs respectively (Figure 5.32). The purpose of these discs was to level the specimen, remove the macro-scratches and remove the micro-scratches, respectively. An example of a polished specimen is shown in Figure 5.33. Prior to scanning, an orange powder was applied to the polished surface in order to fill all the voids with a machine-distinguishable color. The sample was then scanned. An example of a scanned sample after the colored powder was applied is shown in Figure 5.34. The scanned image after application of the colored powder was then processed in Adobe® Photoshop® in order to convert the orange color into white and the rest of the sample into black, resulting in the final black and white image (Figure 5.35). This image was

then analyzed using a software to obtain the air content and the spacing factor using Equation 5.7 and Equation 5.9.



Figure 5.28. Saw-cut sample



Figure 5.29. Polishing machine



Figure 5.30. A concrete sample fixed to the plastic cylinder



Figure 5.31. Polishing machine during operation



Figure 5.32. Polishing discs (left to right: 80-grit, 1200-grit, 2200-grit)

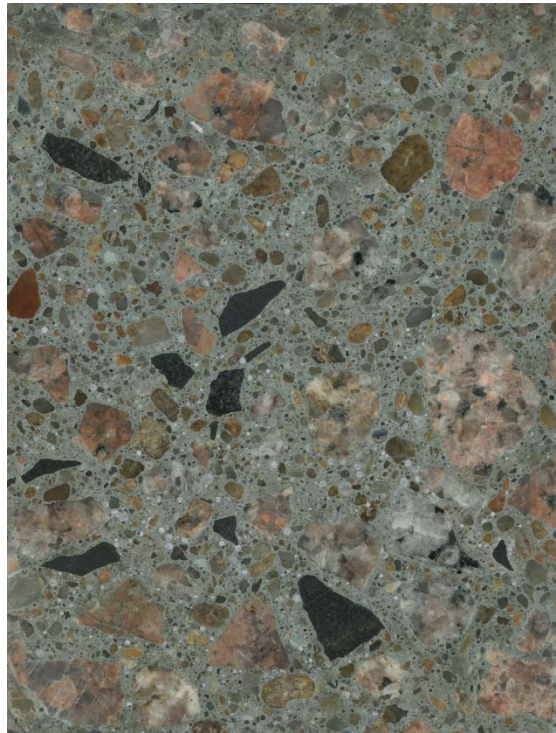


Figure 5.33. Polished sample

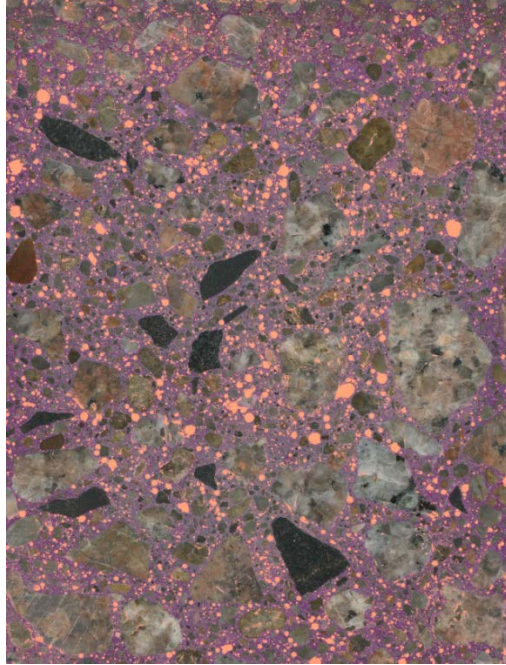


Figure 5.34. Scanned image with orange powder

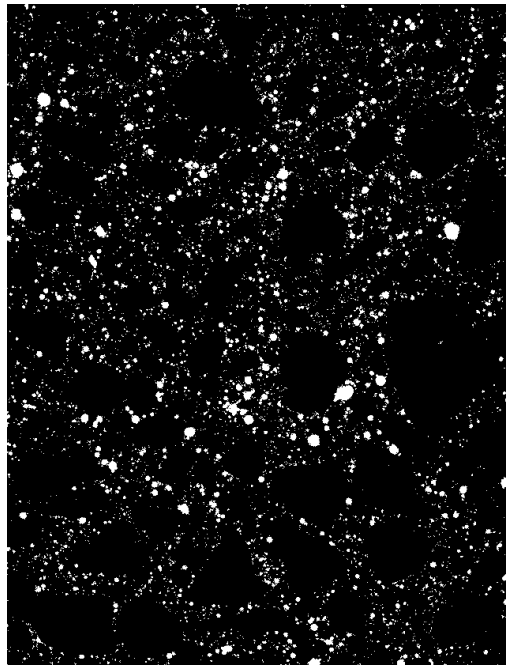


Figure 5.35. Black and white image

5.3.1 Specific Methods

Stability of Air Void System

The procedures for each test started with mixing the concrete after which the rheological properties were immediately measured. Temperature, slump, unit weight and air content before vibration were measured after finishing the rheology test. The fresh air content was measured using ASTM procedures of rodding and tamping according to ASTM C231. The small table vibrator was then used to vibrate the air pressure test container and freeze-thaw prism molds filled with concrete. The vibration was done at several times after the start of mixing, each time for new concrete molds and air pressure tests. Fresh air content was taken after each vibration. The concrete samples obtained from the molds were used for freeze thaw testing. Each vibration period was carried out at a frequency of 75 Hz for 2 minutes. Two different peak vibration accelerations were used. Tests were done at a peak acceleration of either 3g or 10g. All measurements reported for the durability factor and hardened air parameters presented in Section 5.4 are the average of two specimens.

Freeze-Thaw Durability of Externally-Vibrated Concrete

After mixing, rheological properties were immediately measured using the ICAR rheometer. Temperature, unit weight and fresh air content before vibration were measured after finishing the rheology test. The fresh air content was measured using ASTM procedures of rodding and tamping according to ASTM C231. A hardened concrete sample was also obtained before vibration in order to measure hardened concrete air void parameters before vibration. A table vibrator was then used to vibrate molds filled with concrete. Molds were vibrated for either 30 seconds or for 4 minutes. Some of the concrete prisms obtained from the molds were later used for hardened air void analysis while others were used for freeze-thaw testing followed by hardened air void analysis. The frequency of vibration ranged from 33 Hz to 160 Hz and the peak acceleration ranged from 4 g to 25 g. After freeze-thaw testing, the prisms were saw-cut, polished then scanned. The scans were then used for hardened air void analysis. All measurements for the durability factor and hardened air parameters presented in Section 5.4.1 are the average of two specimens.

Freeze-Thaw Durability of Internally-Vibrated Concrete

Experiments to determine the freeze-thaw durability of internally-vibrated concrete were performed using 85 in. long concrete beams that were 3 in. x 4 in. in cross section. After mixing, rheological properties, temperature, unit weight and fresh air content before vibration were measured. The fresh air content was measured using ASTM procedures of rodding and tamping according to ASTM C231. Concrete in these experiments was consolidated using an immersion vibrator at one end as shown in Figure 5.34. The vibration was then executed for 30 seconds. The first sample was expected to experience the highest acceleration whereas the last one was expected to experience almost no vibration. After hardening as shown in Figure 5.37, the long beams were saw-cut into 5 specimens using a hand-held gas-powered saw as shown in Figure 5.38. These specimens were then subjected to freeze-thaw testing according to ASTM C666 method A.

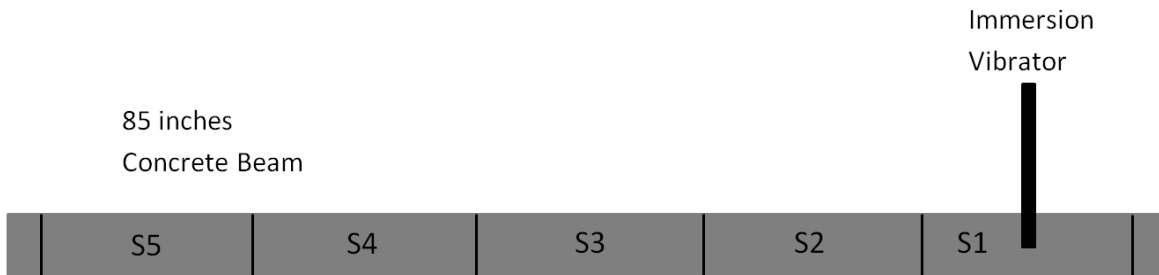


Figure 5.36. Immersion vibrator placement



Figure 5.37. Long beam after hardening



Figure 5.38. Saw-cutting long beams

5.4 Stability of Air Void System

Looking at the mixtures that contained the HRWR, the LRWR and the synthetic AEA, one can observe from Figure 5.39 the different rheological properties of these mixtures. All these mixtures had similar plastic viscosities. The mixtures in Figure 5.39 and Figure 5.40 are labeled with their admixtures' dosages (i.e., HRWR Dosage / LRWR Dosage / AEA Dosage in oz/cwt).

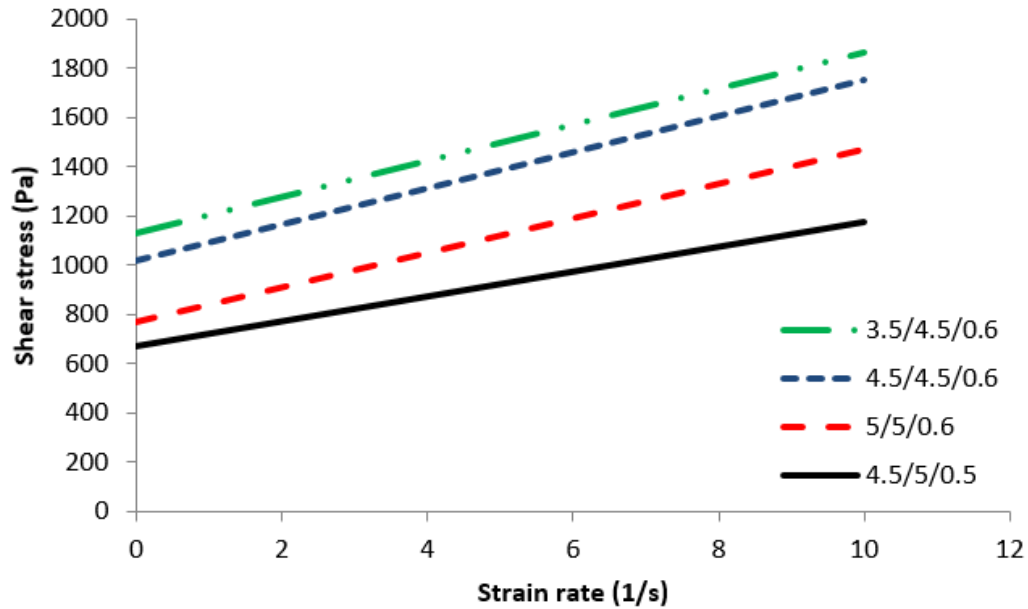


Figure 5.39. Rheological properties of HRWR + LRWR + synthetic AEA mixtures that experienced 3 g of vibration

Figure 5.40 shows the percentage air loss due to the 3g vibration at different times from the start of mixing. The air content in concrete becomes more unstable with time causing higher air loss due to vibration. The maximum percentage air loss was found to be around 55 percent for mixtures 3.5/4.5/0.6 and 4.5/4.5/0.6 at 100 minutes from the start of the mixing. The relationship between the percentage air loss and time seems to be somewhat linear which makes it possible to predict air loss with time. Also, per Figure 5.40 the rate at which air loss increases with time is similar for all mixtures. This gives an indication that mixtures with the same set of admixtures tend to have the same air system stability, once air loss begins. Figure 5.39 and Figure 5.40 show that mixtures with higher yield stress (i.e., stiffer mixtures) tend to lose more air with time than mixtures with lower rheological properties (i.e., more fluid mixtures). The air loss was also higher in mixtures with lower HRWR, contradicting the notion that polycarboxylate admixtures bear primary responsibility for the loss of air void stability. This may be because the mixtures with the higher yield stress should also stiffen faster and increase the pressure acting on the bubbles during vibration, possibly causing them to go into solution and form larger bubbles after reemerging from solution, or fracturing the shell formed around the air bubble by the air entraining agent and hydration products (Assaad, J., and Khayat, K. H., 2002; Chancey, R., Folliard, K. J., Juenger, M. C., and Ley, M. T., 2009).

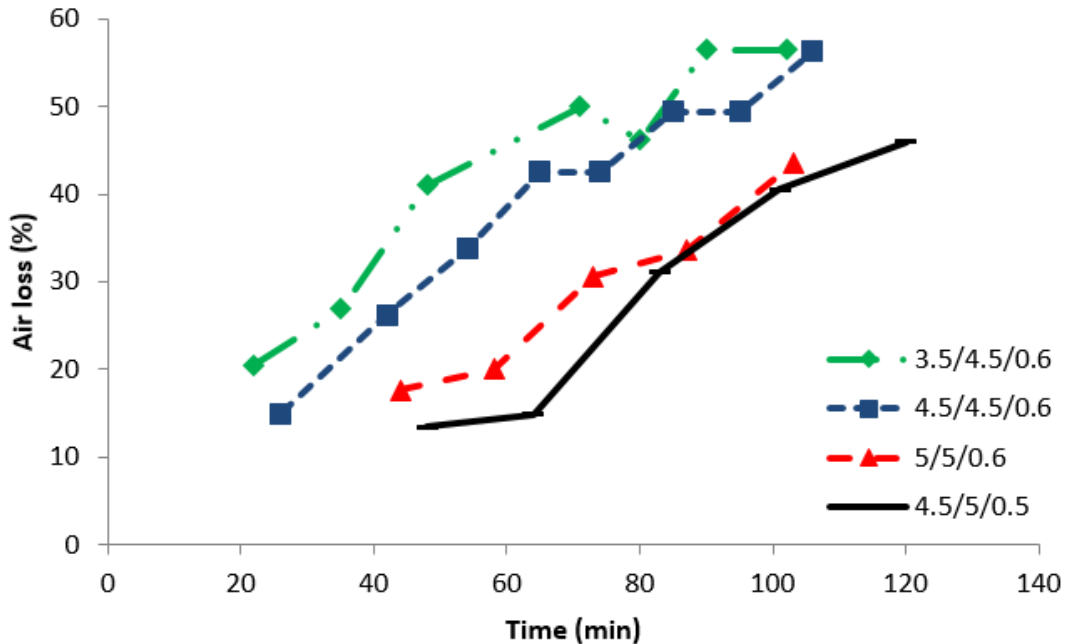


Figure 5.40. Air loss vs time for HRWR + LRWR + synthetic AEA mixtures that experienced 3 g of vibration

Figure 5.41 and Figure 5.42 show the results obtained for the set of mixtures that contained the HRWR and the wood rosin AEA. The mixtures in Figure 5.41 and Figure 5.42 are labeled with their admixtures' dosages (i.e., HRWR Dosage / AEA Dosage in oz/cwt). Just like the previously described experiments, this set of experiments also shows increased instability of the air system with time (Figure 5.42). Maximum air loss was observed to be around 45 percent at about 100 minutes from the start of mixing. This set also shows the linear relation between percentage air loss and time. Moreover, the rate at which air loss increases with time was similar for all mixtures which further confirms the observation that mixtures with the same set of admixtures tended to have the same rate of air loss once air loss began. Figure 5.41 and Figure 5.42 show that mixtures with higher viscosity lose similar amounts of air with time, probably because the similar dosages of HRWR give similar slump retention with time. Changes in the plastic viscosity or air entraining agent dosage did not appear to have a significant effect on the air loss rate.

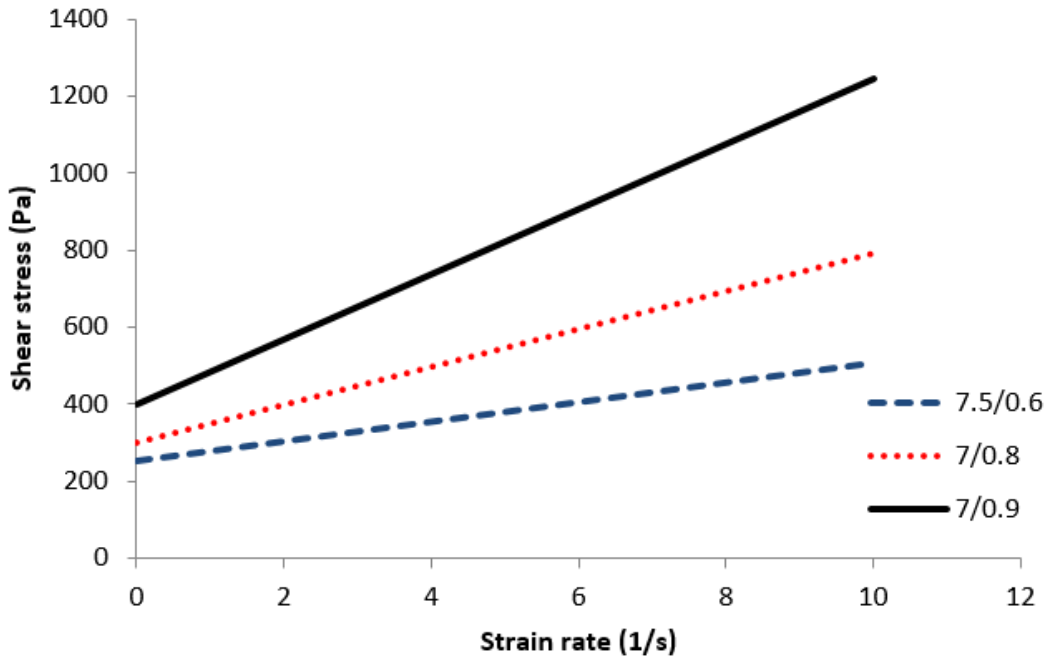


Figure 5.41. Rheological properties of HRWR + wood rosin AEA mixtures that experienced 3 g of vibration

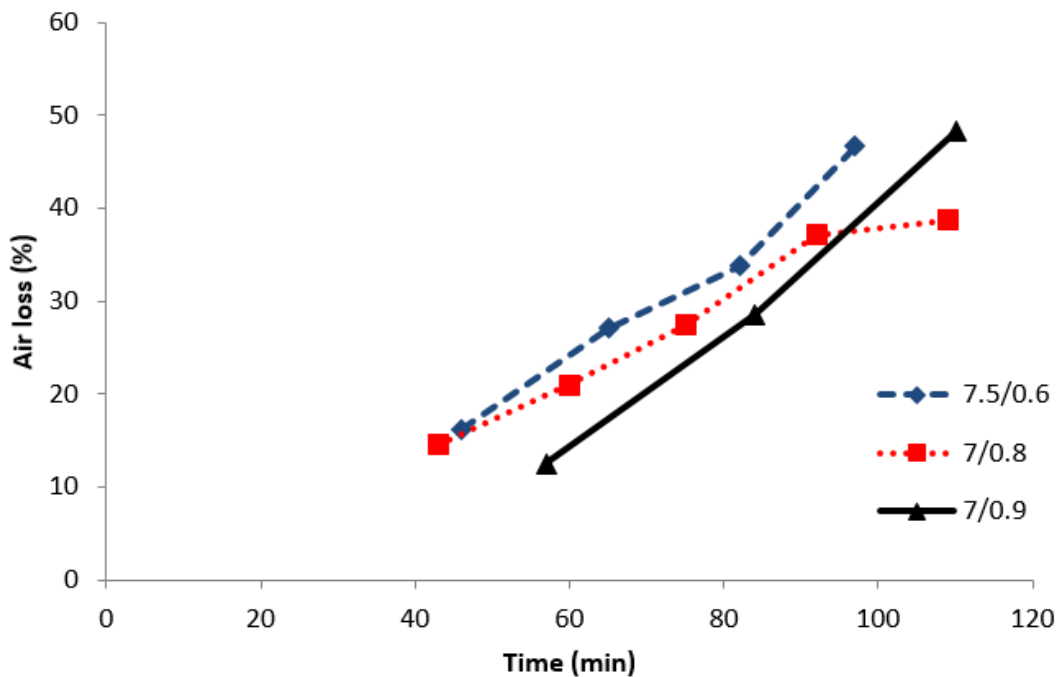


Figure 5.42. Air loss vs time for HRWR + wood rosin AEA mixtures that experienced 3 g of vibration

Figure 5.43 through Figure 5.46 show two other sets of mixtures made to examine the effects of air entraining agent type. The first set (Figure 5.43 and Figure 5.44) consists of mixtures that

contained the HRWR and the synthetic AEA, while the second set (Figure 5.45 and Figure 5.46) consists of mixtures that contained the HRWR and the tall oil AEA. The mixtures in Figure 5.43 through Figure 5.46 are labeled with their admixtures' dosages (i.e., HRWR Dosage / AEA Dosage in oz/cwt). Similar to the previous sets, these sets also show the trend of increased air loss with time. In the case of the synthetic AEA, the mixture with the lower yield stress lost more air. This is probably because the mixture that used more AEA either stabilized more bubbles with shells containing AEA, or the shells produced were of higher quality when more AEA was used. Clearly the mechanisms that contribute to air void instability are complex and dependent on many variables. The synthetic and tall oil-based AEA experienced similar rates of air loss with time.

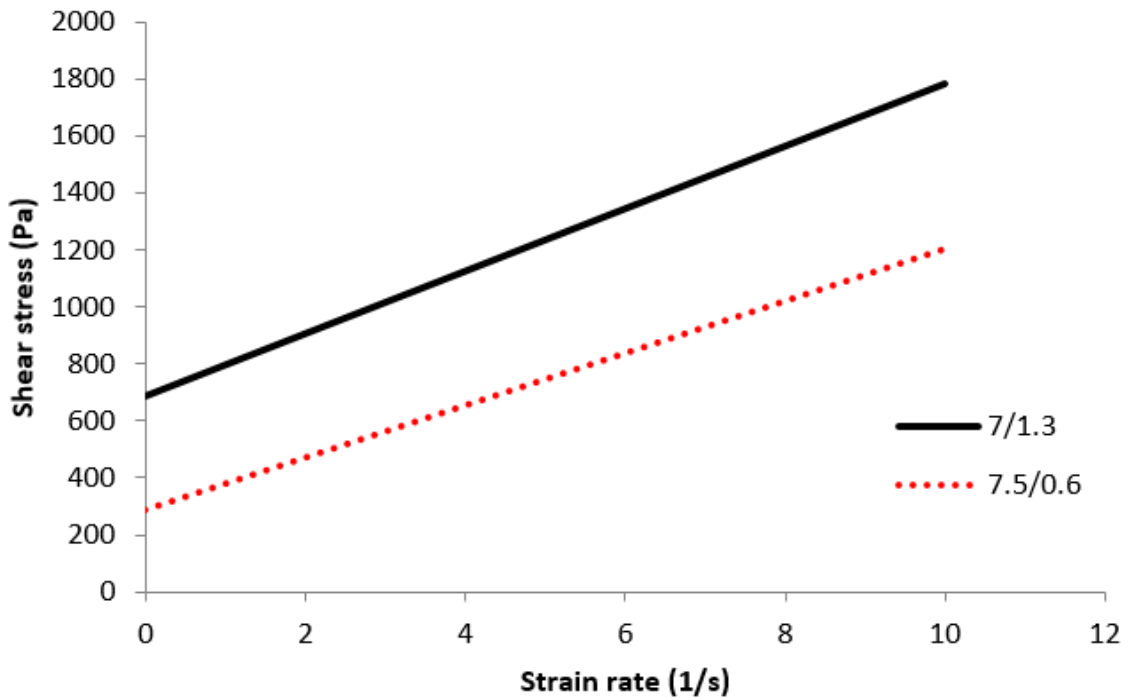


Figure 5.43. Rheological properties of HRWR + synthetic AEA mixtures that experienced 3 g of vibration

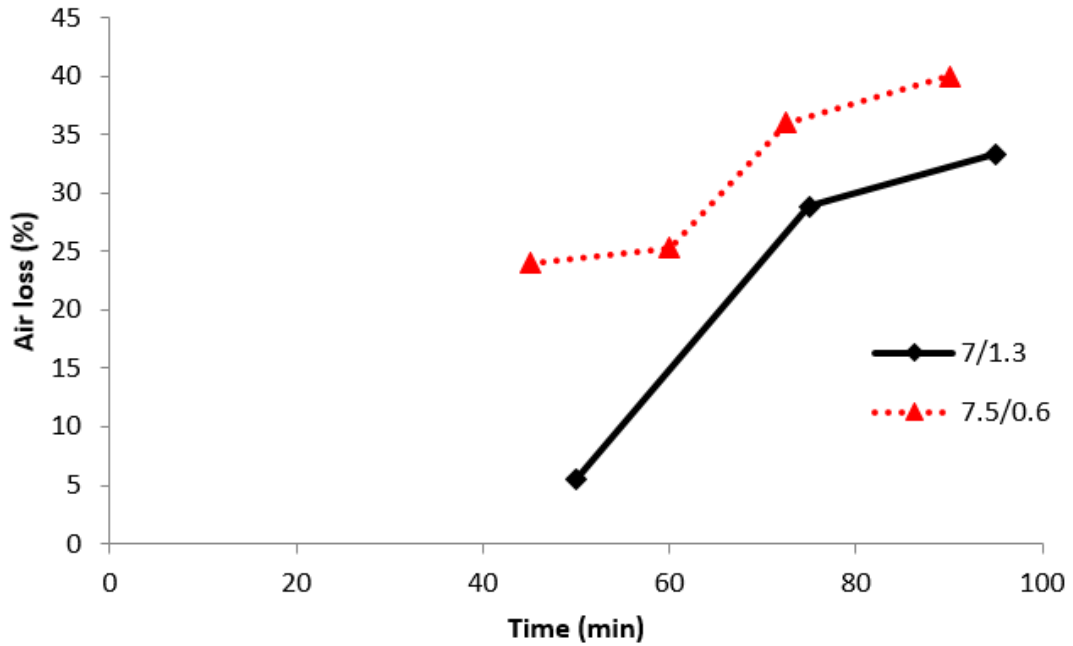


Figure 5.44. Air Loss vs Time for HRWR + Synthetic AEA mixtures that experienced 3 g of vibration

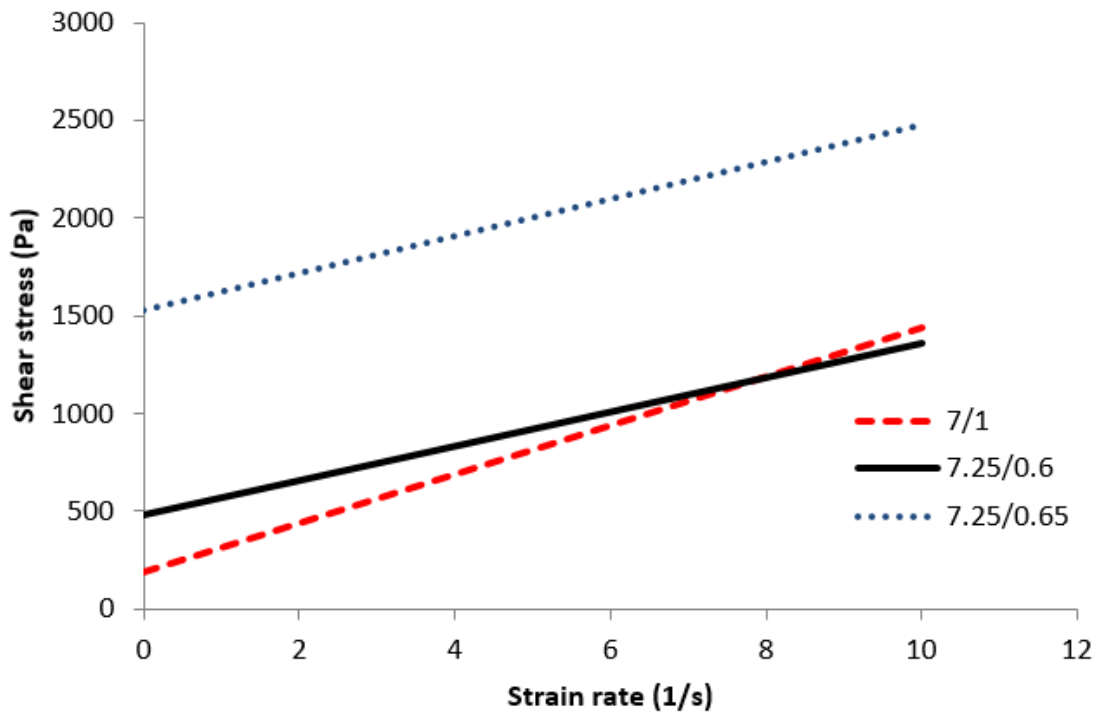


Figure 5.45. Rheological properties of HRWR + tall oil AEA mixtures that experienced 3 g of vibration

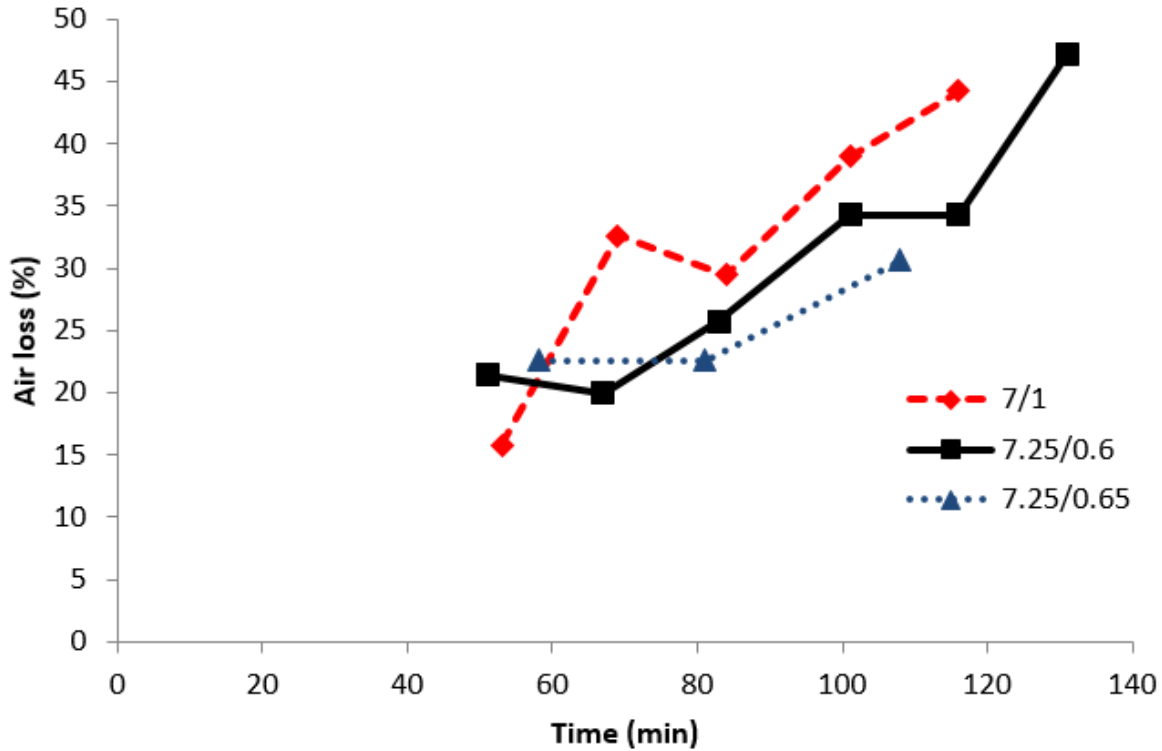


Figure 5.46. Air loss vs time for HRWR + tall oil AEA mixtures that experienced 3 g of vibration

In an attempt to compare the effect of different admixtures combinations on the stability of the air system of concrete, while isolating the effect of rheological properties, mixtures with similar rheological properties were grouped together for comparison. Figure 5.47 and Figure 5.48 display the results for this group. It can be observed from Figure 5.47 that the rheological properties were not identical since it is very difficult to create mixtures with similar rheological properties, especially if different materials are used in each mixture. However, the shown properties are considered to be fairly close to each other. The first observation from Figure 5.48 is the fact that the mixture with no HRWR took longer to begin to show air void instability. This could be because of the higher w/cm required to achieve similar yield stress as the mixtures with HRWR, and should have better slump retention with time. The synthetic AEA + HRWR mixture experienced slightly higher air loss by percentage. However, the difference was small. Looking at the slope of percentage air loss versus time (Figure 5.48), it can be observed that the tall oil AEA + HRWR mixture and the synthetic AEA + HRWR mixture had slightly smaller slopes compared to the other two. However, the difference was not enough to say that it is significant.

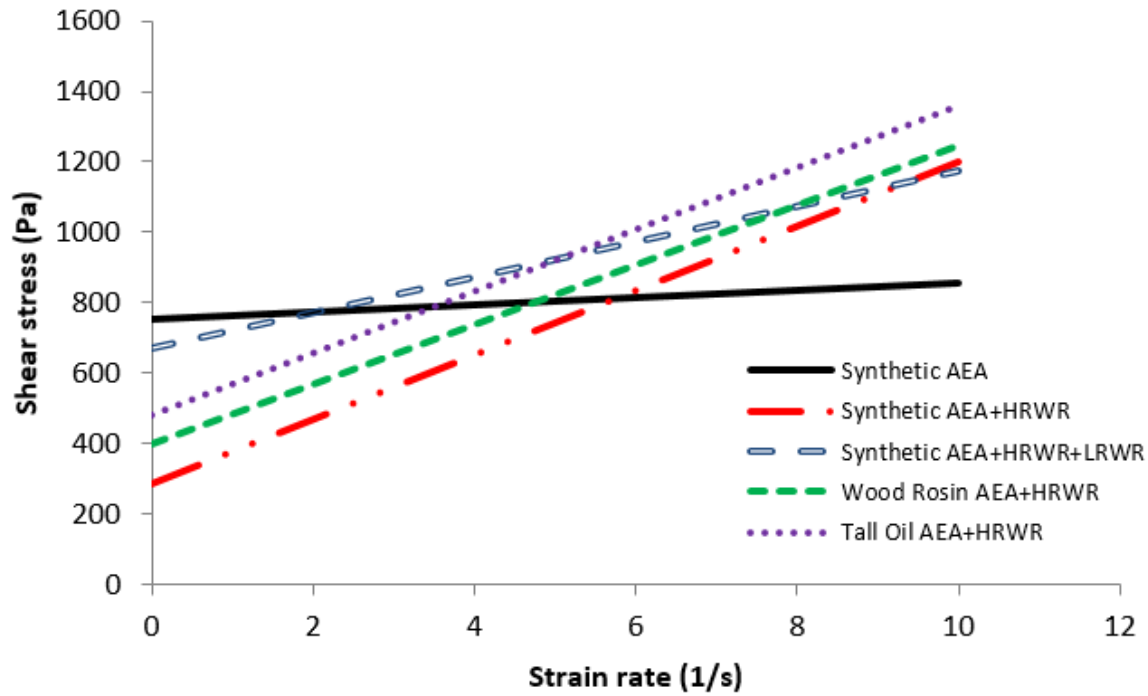


Figure 5.47. Rheological properties of selected mixtures that experienced 3 g of vibration

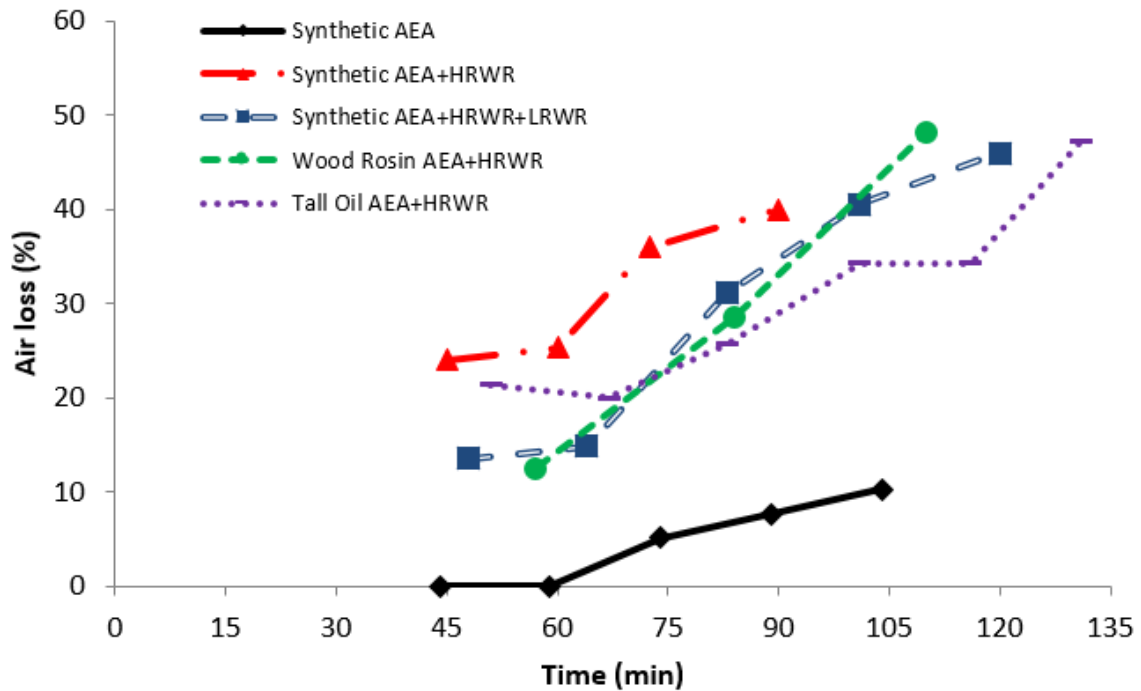


Figure 5.48. Air loss vs time for selected mixtures that experienced 3 g of vibration

A similar group was constructed for the case of concrete mixtures vibrated using 10 g of vibration acceleration (Figure 5.49 and Figure 5.50). This group yielded similar results to the

previous group. The air entraining agent type appeared to have little effect on the rate of air loss with waiting time.

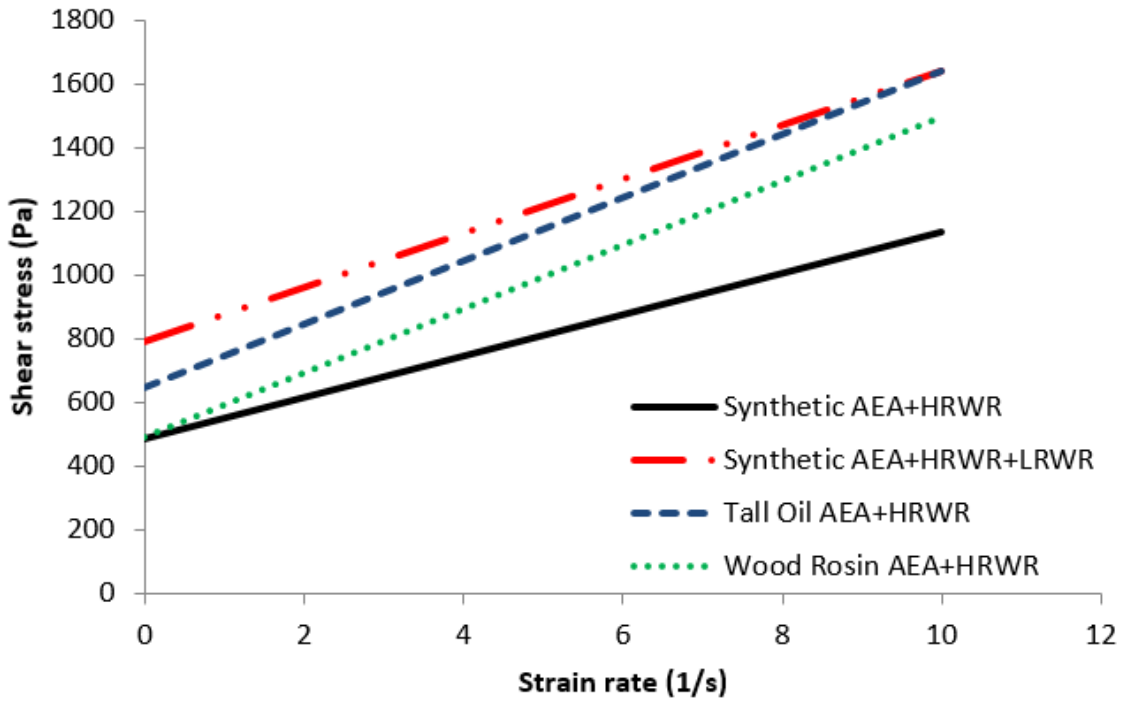


Figure 5.49. Rheological properties of selected mixtures that experienced 10 g of vibration

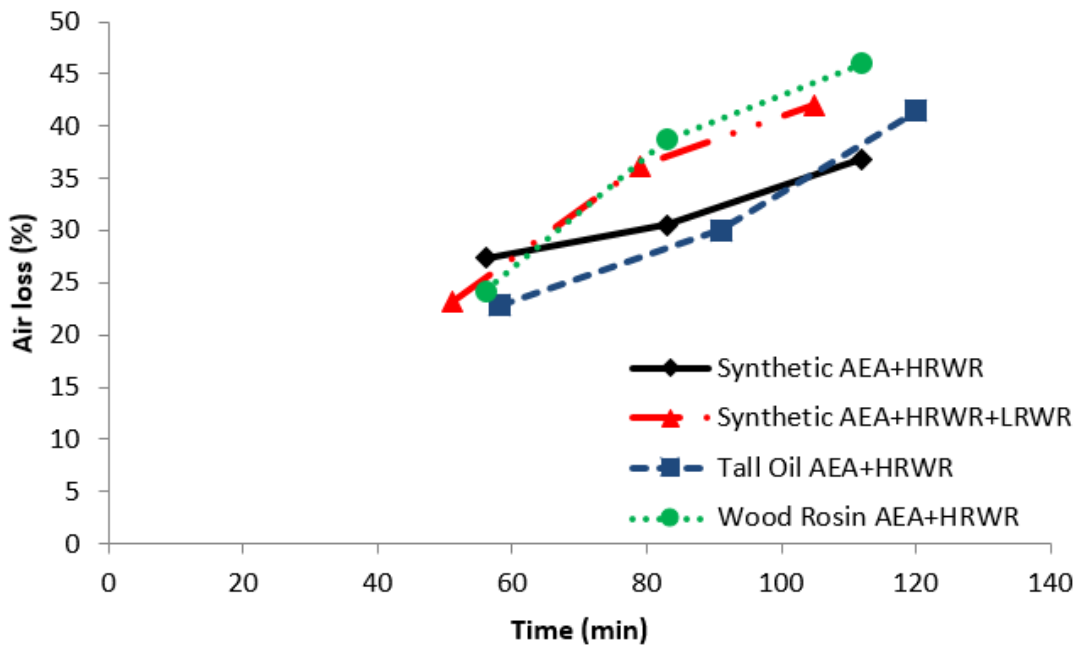


Figure 5.50. Air loss vs time for selected mixtures that experienced 10 g of vibration

Figure 5.51 and Figure 5.52 show the results for two tall oil AEA + HRWR mixtures vibrated at two different vibration accelerations. These results show the effect of the vibration acceleration on the percentage air loss. The increase from 3 g to 10 g of acceleration did not cause added air loss with time after mixing.

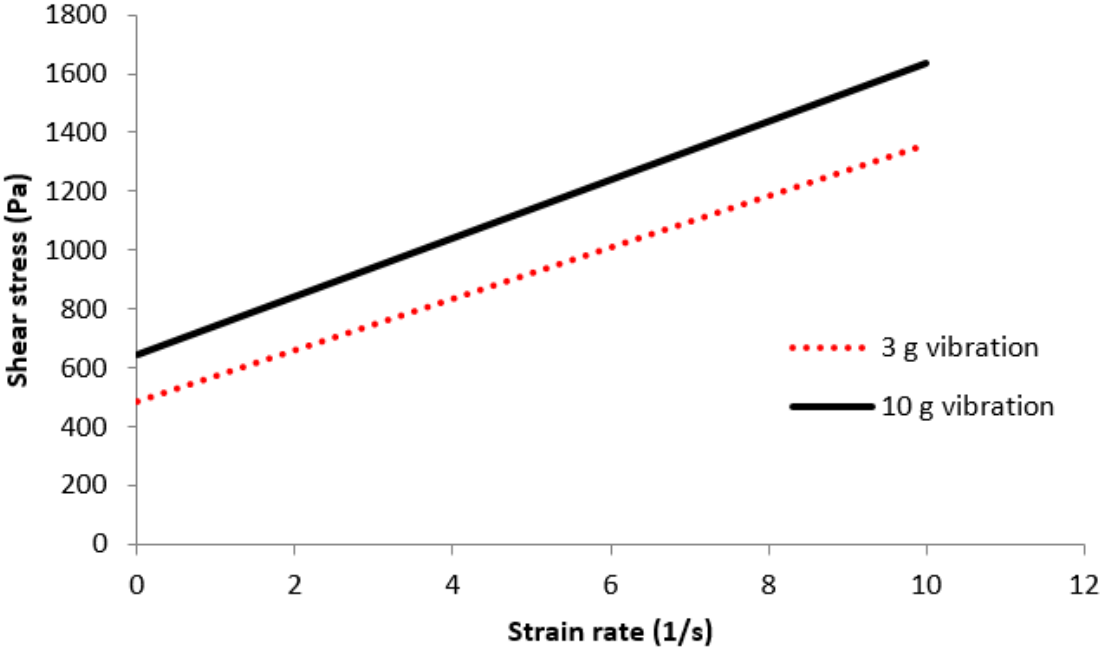


Figure 5.51. Rheological properties of tall oil AEA + HRWR mixtures (10 g vs 3 g vibrations)

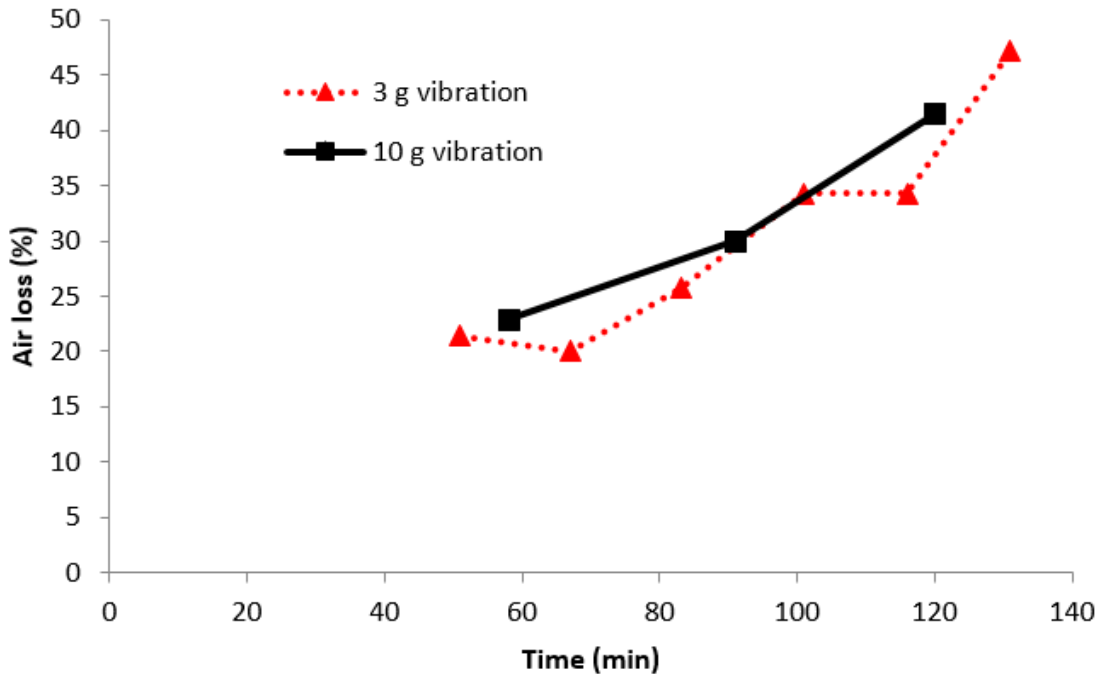


Figure 5.52. Air loss vs time for tall oil AEA + HRWR mixtures (10 g vs 3 g vibrations)

As shown in Figure 5.53, all the specimens in this study passed freeze-thaw testing even after losing 55 percent of the initial air content. This is most probably due to the fact that the initial air content was fairly high in all mixtures. Even after vibration, almost all specimens retained final air contents above 3 percent (Figure 5.54). There are, however, some specimens that experienced some decrease in the relative dynamic modulus of elasticity, although they still passed. These specimens had the lowest initial air content (5.45 percent) among all specimens. Their durability factors were found to be 82 percent, 62 percent and 76 percent corresponding to spacing factors of 0.0087, 0.0089 and 0.0099 in., respectively. These spacing factors are higher than the recommended maximum limit by ACI. The freeze-thaw testing showed that even though the tested mixtures experienced large air losses as a percentage of the air content before mixing, this did not necessarily translate into performance issues.

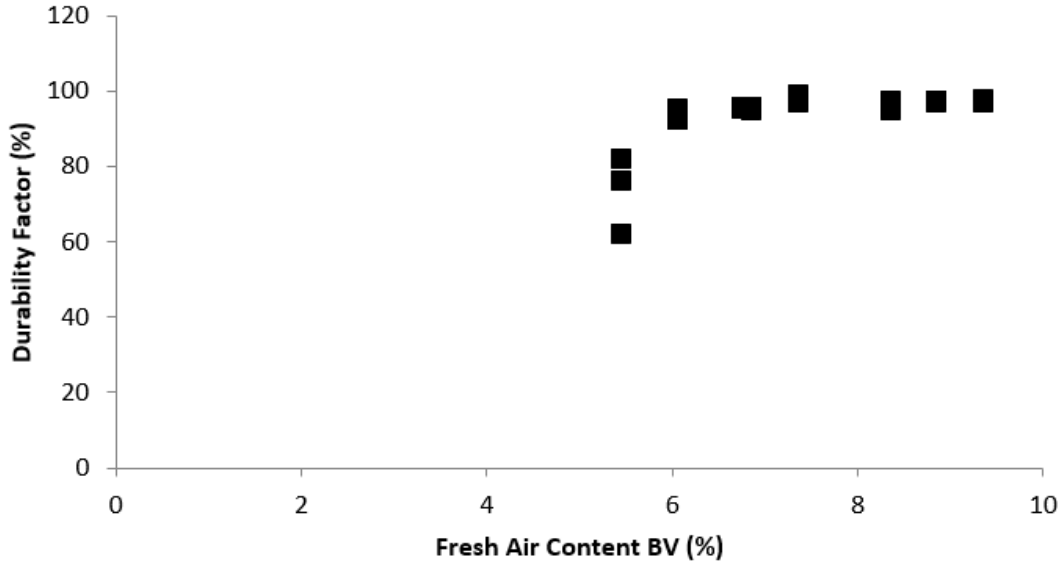


Figure 5.53. Durability factor vs. fresh air content before vibration (effect of admixtures on the air system)

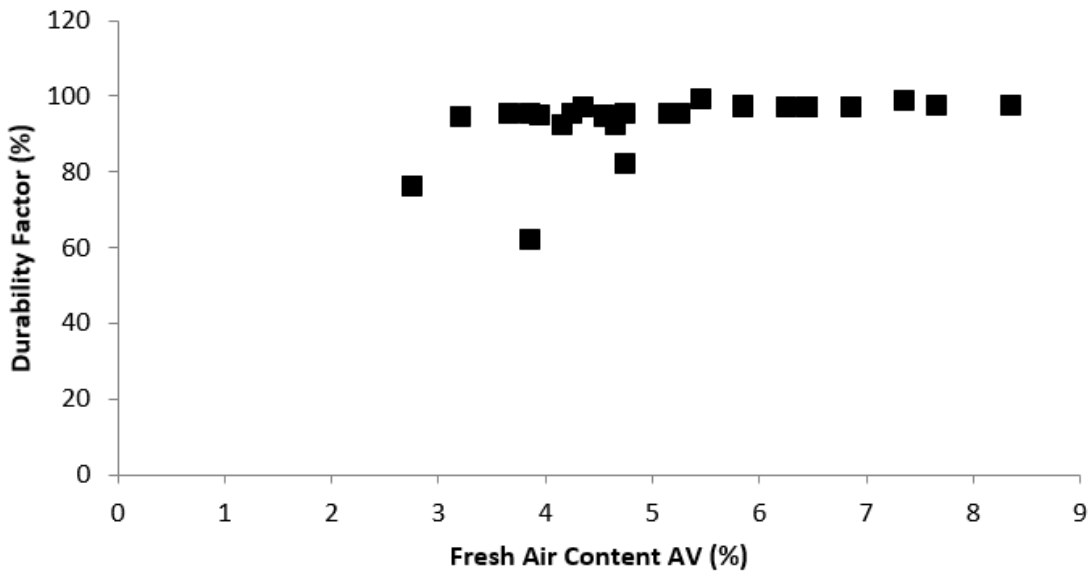


Figure 5.54. Durability factor vs. fresh air content after vibration (effect of admixtures on the air system)

5.4.1 Freeze-Thaw Durability of Externally-Vibrated Concrete

Effect of Vibration Duration

To isolate the effect of the vibration duration and the admixture combination, some of the concrete mixtures were vibrated at the same frequency (75 Hz) and peak acceleration (8 g) for different amounts of time. The average of the fresh air content before vibration for this set of experiments was 4.23 percent which is normally considered to be sufficient for freeze-thaw

durability. The average for the hardened air content before vibration, however, was lower at 3.53 percent. It is usually observed that the hardened air content is slightly lower than the fresh air content for each test. This could be due to the loss of large air bubbles during the hardening period.

Figure 5.55 illustrates the effect of vibration duration on the freeze-thaw performance. All but two tests performed almost the same way whether vibrated for 30 seconds or 4 minutes. Even though Figure 5.56 indicates that the final spacing factor value was slightly higher in the case of 4 minutes' vibration, the average difference was only 0.001 in. On the other hand, there was a notable difference in terms of the amount of total air loss (Figure 5.57). The air loss due to 4 minutes' vibration was 0.5 percent to 1.5 percent more than the air loss due to 30 seconds' vibration.

This big difference in air loss compared to the small difference in durability performance indicates that extended vibration will impact the larger bubbles more than the small bubbles, confirming the conclusions from the model results described in Section 3.6.4. Small bubbles are essential for freeze-thaw resistance. Therefore, spacing factor was only marginally affected which explains the similarity in durability factor values. Another observation from Figure 5.55 is the fact that admixture combination C performed very poorly compared to combinations A and B. This was true despite the fact that corresponding mixtures had comparable rheological properties and initial air content. This indicates that admixture combinations can play a critical role in the freeze-thaw performance of the vibrated system. The durability factor results were supported by the high final spacing factor values shown in Figure 5.56. This particular admixtures' combination could be producing larger than desired air bubbles resulting in a poor air structure. Alternatively, the chemicals could be producing a very unstable shell around the air bubbles that could be easily destroyed under vibration.

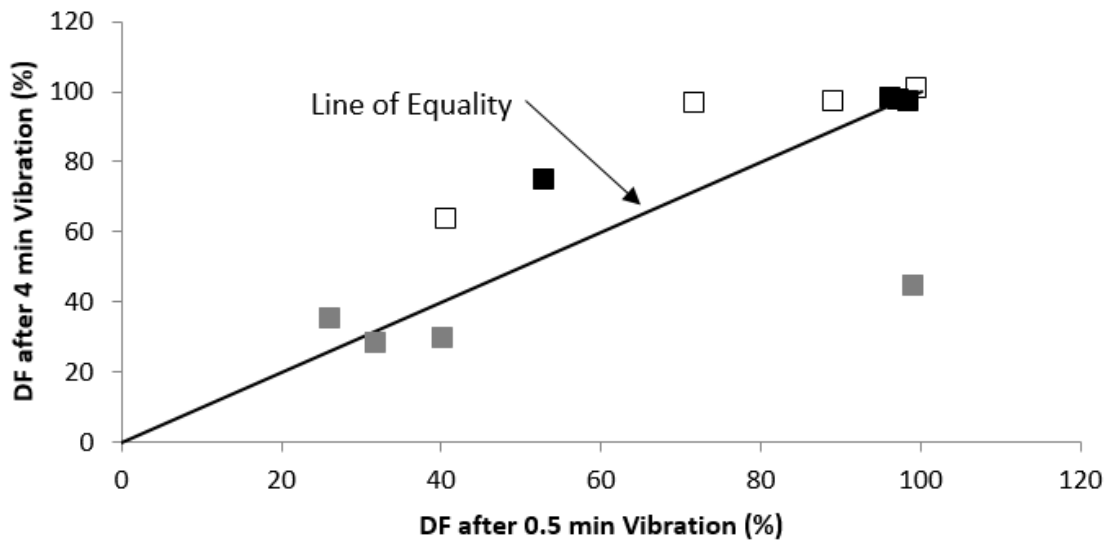


Figure 5.55. Effect of vibration duration on the durability factor with vibration acceleration of 8 g at 75 Hz

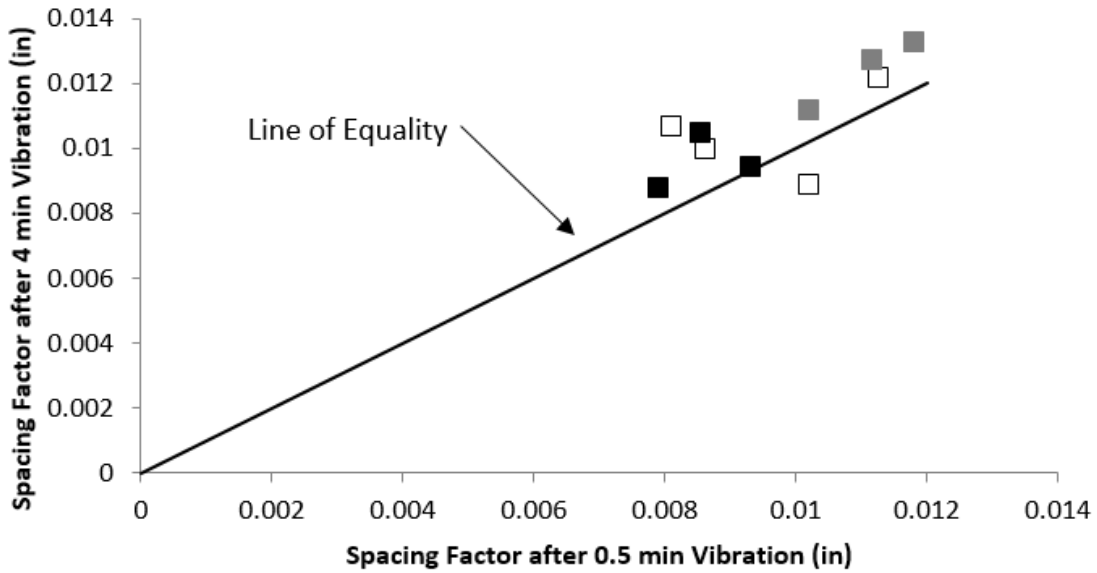


Figure 5.56. Effect of vibration duration on final spacing factor with vibration acceleration of 8 g at 75 Hz

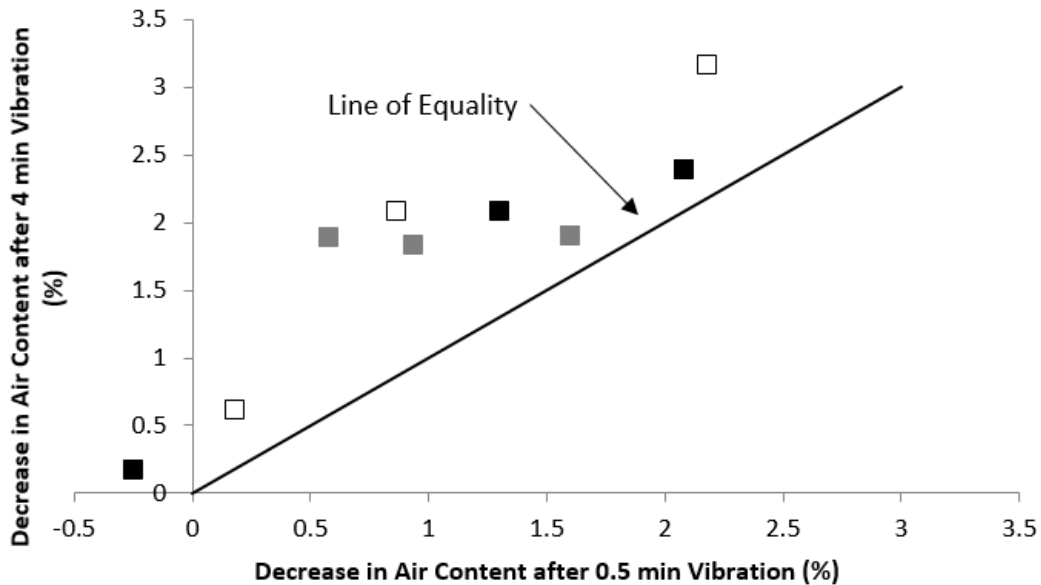


Figure 5.57. Effect of vibration duration on decrease in air content with vibration acceleration of 8 g at 75 Hz

A comparison was made of air void systems vibrated for 30 seconds and 4 minutes to determine the effect of vibration time on air void systems. Concrete samples vibrated at 75, 110, or 160 Hz at 8, 15, or 20 g of acceleration were used in the comparison. From Figure 5.58 and Figure 5.59, both the final fresh and hardened air content values supported the previous results that 4 minutes' vibration resulted in a significantly higher air loss. The difference in air loss was as high as 3 percent in some cases. However, Figure 5.60 suggests that the difference in the final spacing

factor is, in most cases, very marginal. These results support the previous conclusions that longer vibration periods will result in loss of large air bubbles rather than small ones.

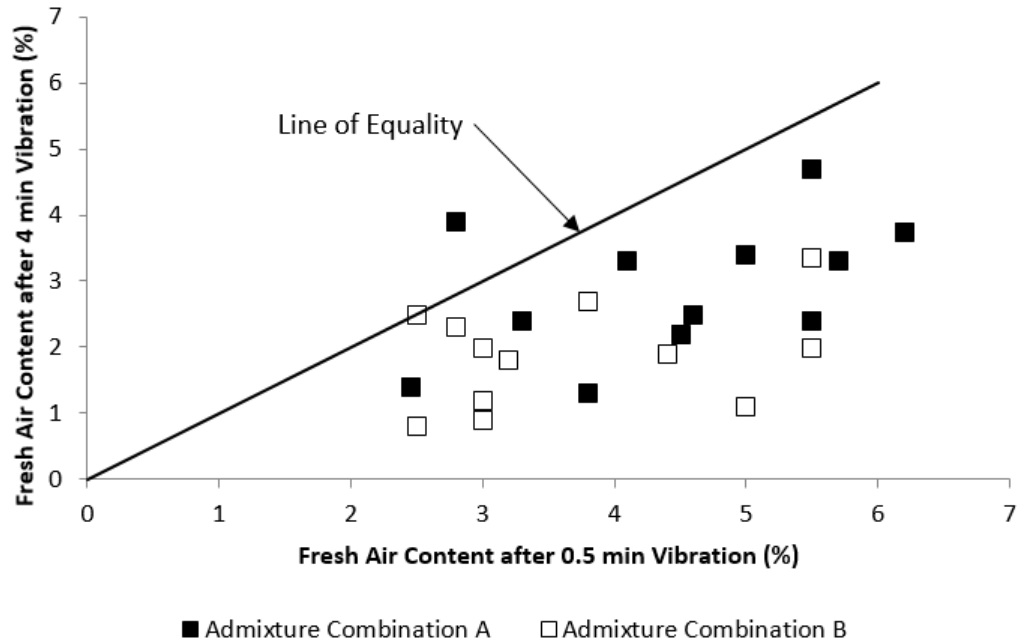


Figure 5.58. Effect of vibration duration on final fresh air content (different frequencies and peak accelerations)

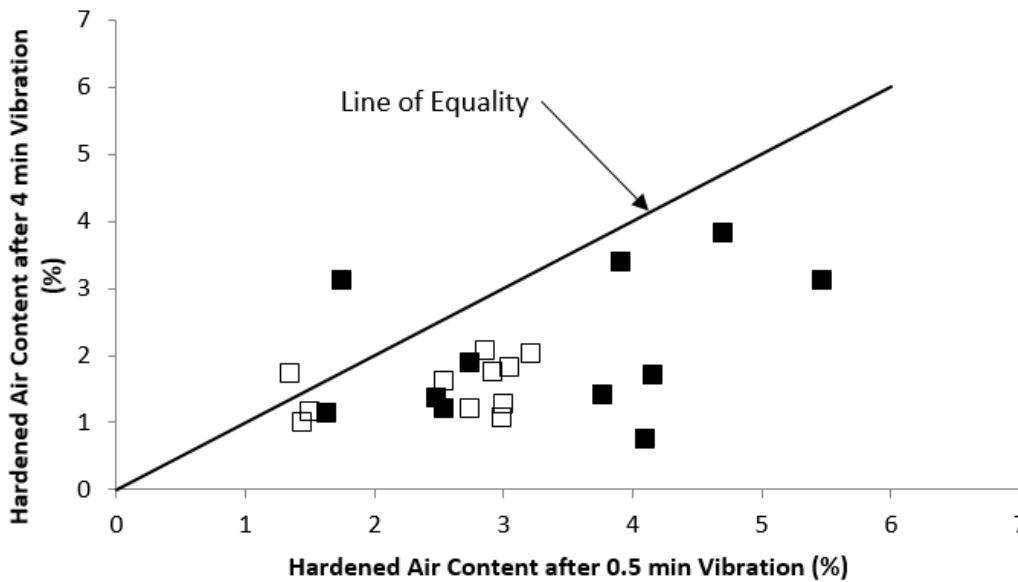


Figure 5.59. Effect of vibration duration on final hardened air content (different frequencies and peak accelerations)

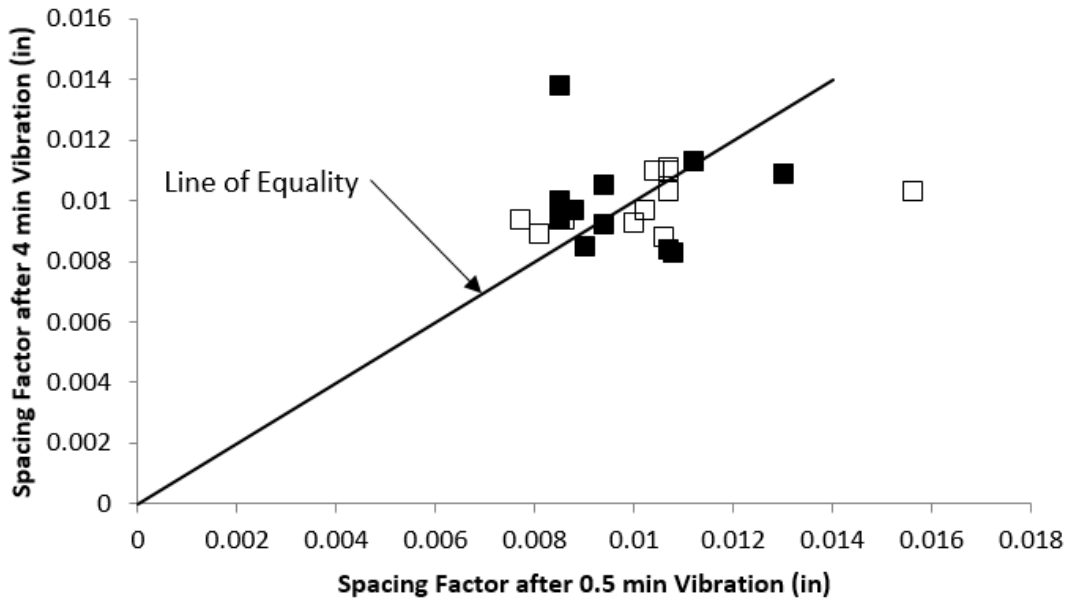


Figure 5.60. Effect of vibration duration on final spacing factor (different frequencies and peak accelerations)

Effect of Vibration Acceleration

In order to examine the effects of rheological properties on air void system response to vibration, the peak vibration acceleration was varied for rheological combinations 1 (the stiffest mixture) and 4 (the most fluid mixture), for admixture combination B. The concrete air void systems were measured after vibration and freeze-thaw durability testing. The concrete mixtures were subjected to 4 minutes of vibration with a vibration frequency of 75 Hz with varied peak accelerations. Figure 5.61 demonstrates the rheological properties for both rheological combinations 1 and 4. The size of the markers in this figure corresponds to the amount of peak acceleration applied to the mixture. It can be observed that the rheological properties were significantly different between rheological combination 4 and rheological combination 1, with some variability observed between batches. Figure 5.62 shows the freeze-thaw results for rheological combination 4 under different peak vibration accelerations. The size of and the number on the bubbles in this figure corresponds to the value of the initial air content. It can be observed that the batches, which underwent peak accelerations of 15 g and higher, experienced deterioration which led to failure in the case of 15 and 20 g peak accelerations. The interesting thing to be observed from Figure 5.62 is that 25 g peak acceleration caused less deterioration (i.e., no failure) compared to lower peak accelerations. This occurred even though the batch vibrated at 25 g had lower air content (Figure 5.62), yield stress and plastic viscosity (Figure 5.61) compared to the batch vibrated at 20 g. This could be just a natural experimental variation. Nevertheless, considering the deterioration of the specimens regardless of failure, one can conclude that for very fluid mixtures vibration acceleration above a threshold amount can contribute to freeze-thaw damage. Looking at the air void parameters, Figure 5.63 and Figure 5.64 show the effect of peak acceleration on the increase in spacing factor and the decrease in air content, respectively. Looking at the final spacing factor (Figure 5.65) and final air content (Figure 5.66), some conclusions can be made. Figure 5.65 indicates that the final spacing factor increases with the increase in peak acceleration. However, this increase is very small (around

0.001 in between the 8 g and the 25 g specimens). Figure 5.66 shows that the final air content decreases with increase in peak acceleration. The total air content after vibration was similar for concrete vibrated at 8 g or higher. This is most likely because vibration at 8 g or higher for 4 minutes removed most of the air from the concrete.

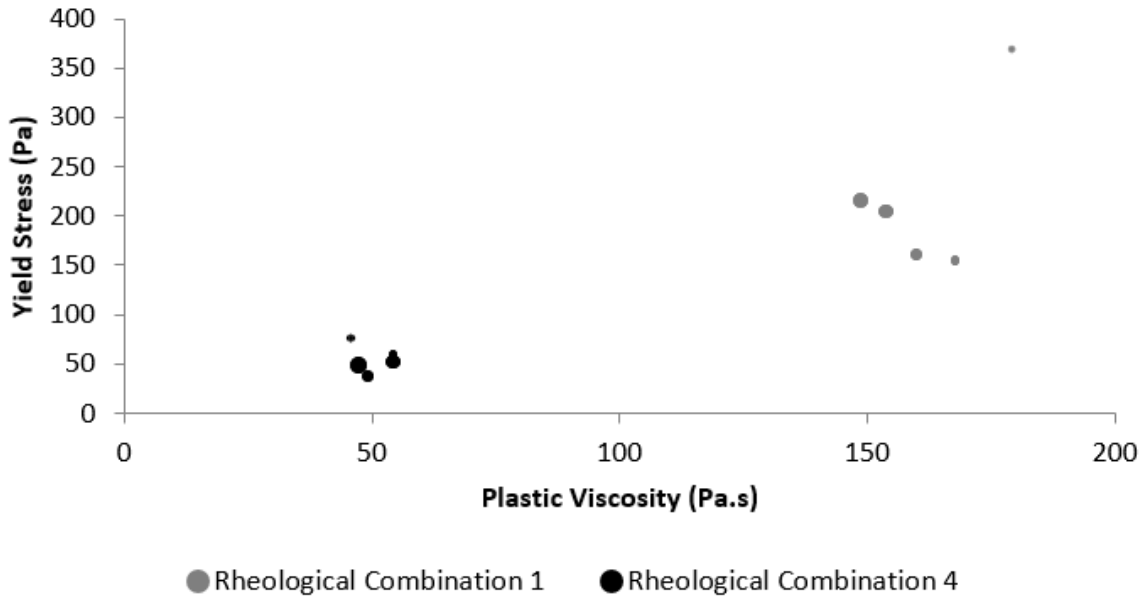


Figure 5.61. Rheological properties for the study of the effect of vibration acceleration

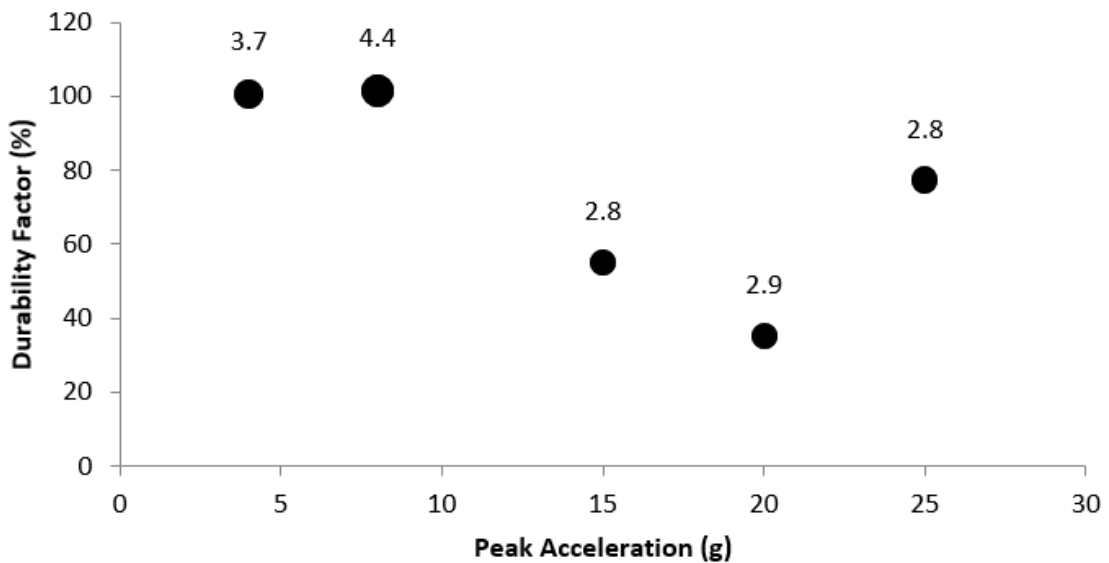


Figure 5.62. Effect of vibration acceleration on the F-T performance of rheological combination 4

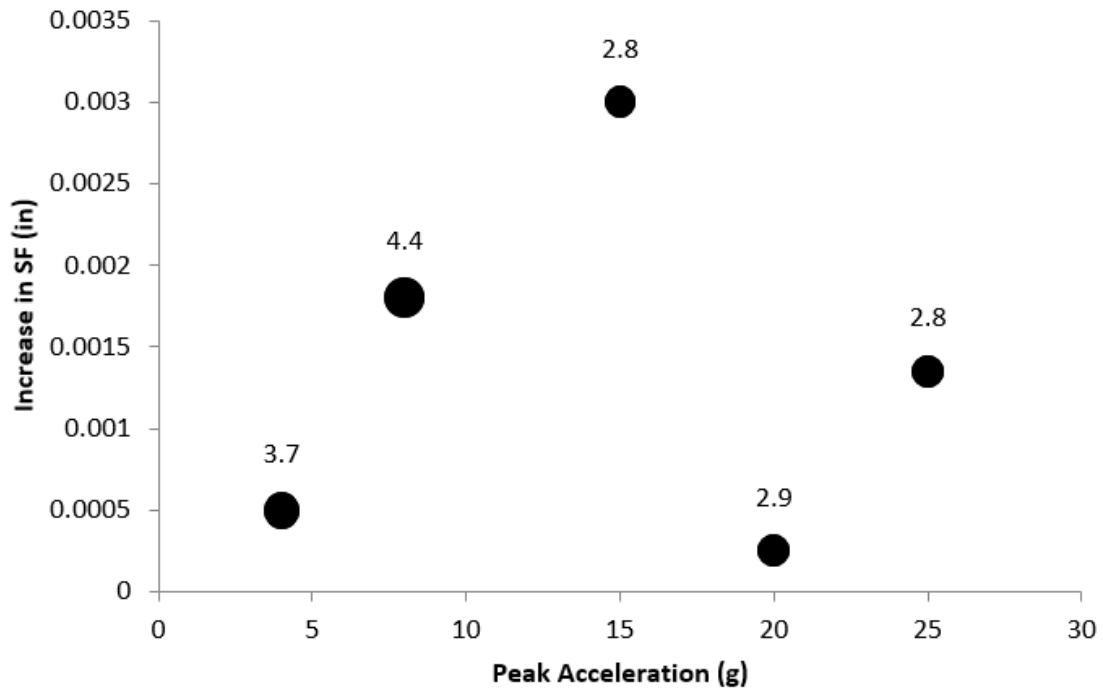


Figure 5.63. Effect of vibration acceleration on the increase in the spacing factor of rheological combination 4

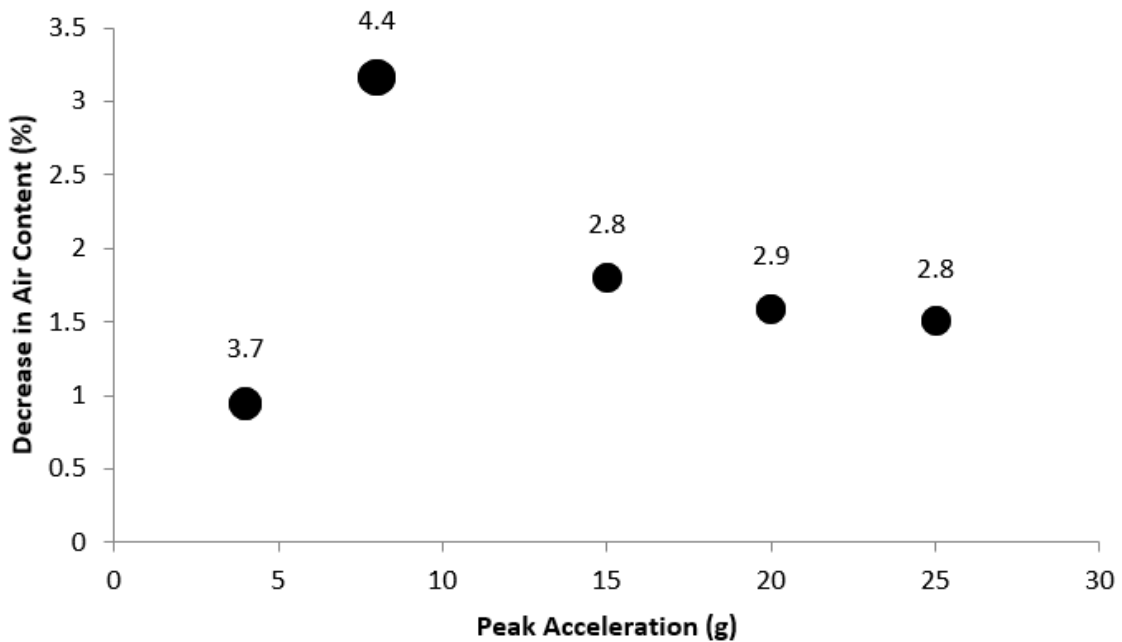


Figure 5.64. Effect of vibration acceleration on the decrease in the air content of rheological combination 4

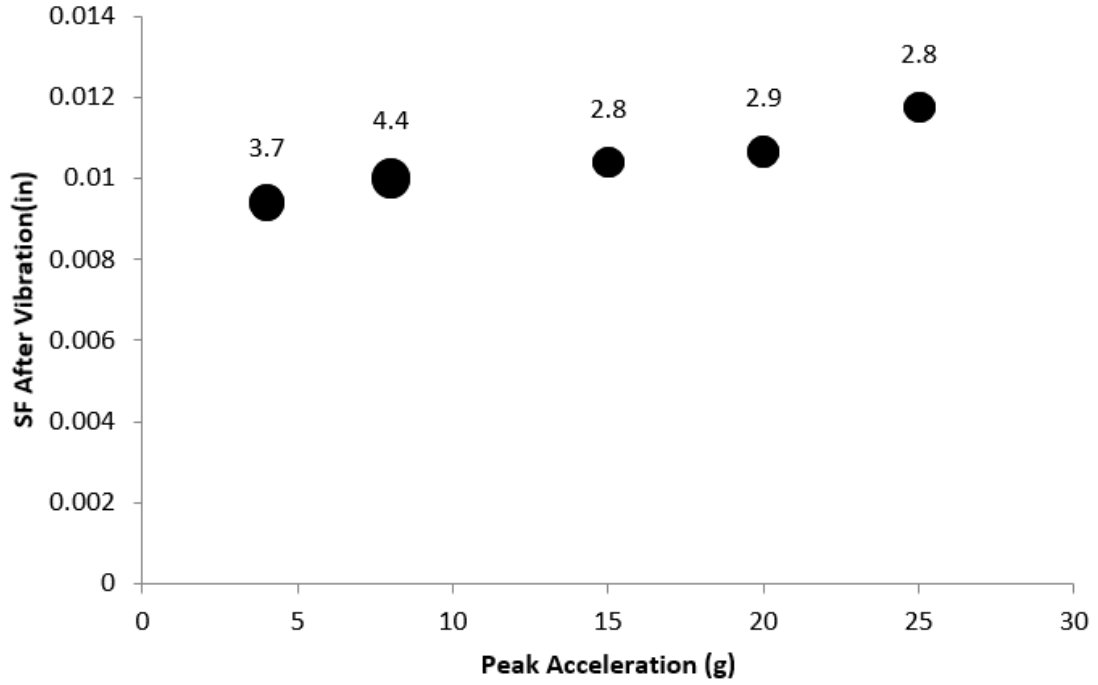


Figure 5.65. Effect of vibration acceleration on the hardened spacing factor of rheological combination 4

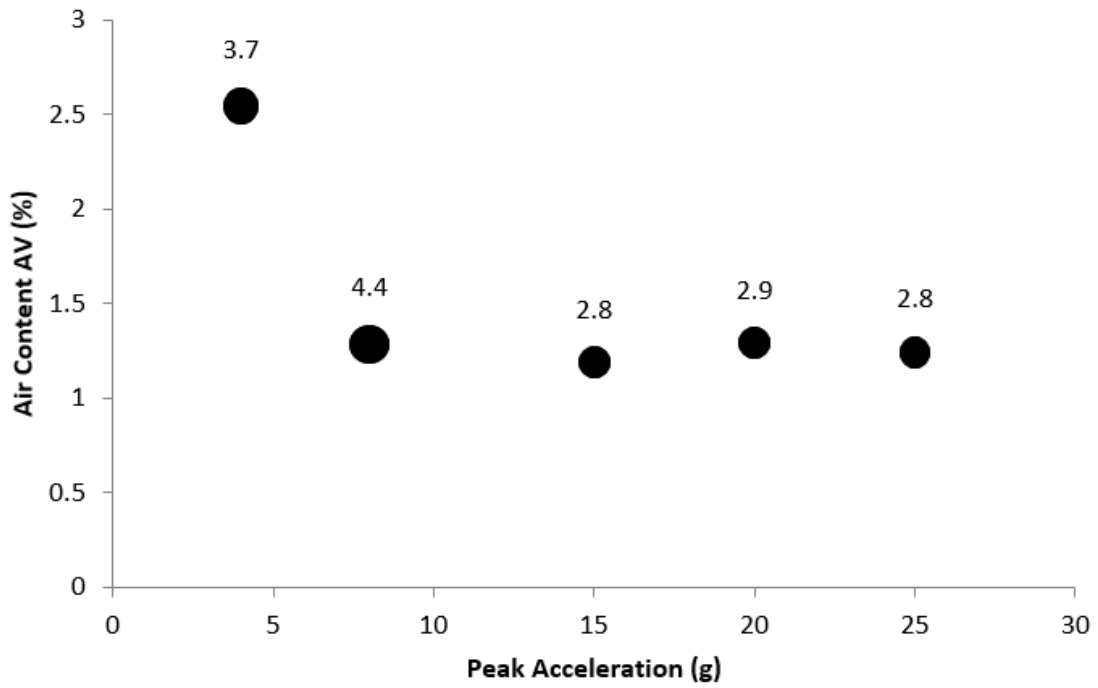


Figure 5.66. Effect of vibration acceleration on the hardened air content of rheological combination 4

All stiff concrete mixture specimens made using rheological combination 1 (Figure 5.65) passed the freeze-thaw testing, regardless of vibration acceleration. This indicates that mixtures with high yield stress and plastic viscosity have a higher chance of resisting the negative effect of excessive vibration for a given chemical admixture combination. Figure 5.68 and Figure 5.69 show the effect of different vibration acceleration on final spacing factor and air content. While it seems that higher acceleration resulted in more total air loss, the final spacing factor increased slightly with peak vibration acceleration. The total air content did decrease with acceleration; however, the total air content after vibration was still higher than seen with rheological combination 4. The higher yield stress and plastic viscosity made the vibrated concrete flow at high viscosities which provided higher resistance to air bubble rising. This in turn preserved more of the air system necessary for freeze-thaw resistance. Although the spacing factors seen after vibration with both rheological combinations were similar, very little freeze-thaw deterioration was seen with rheological combination 1.

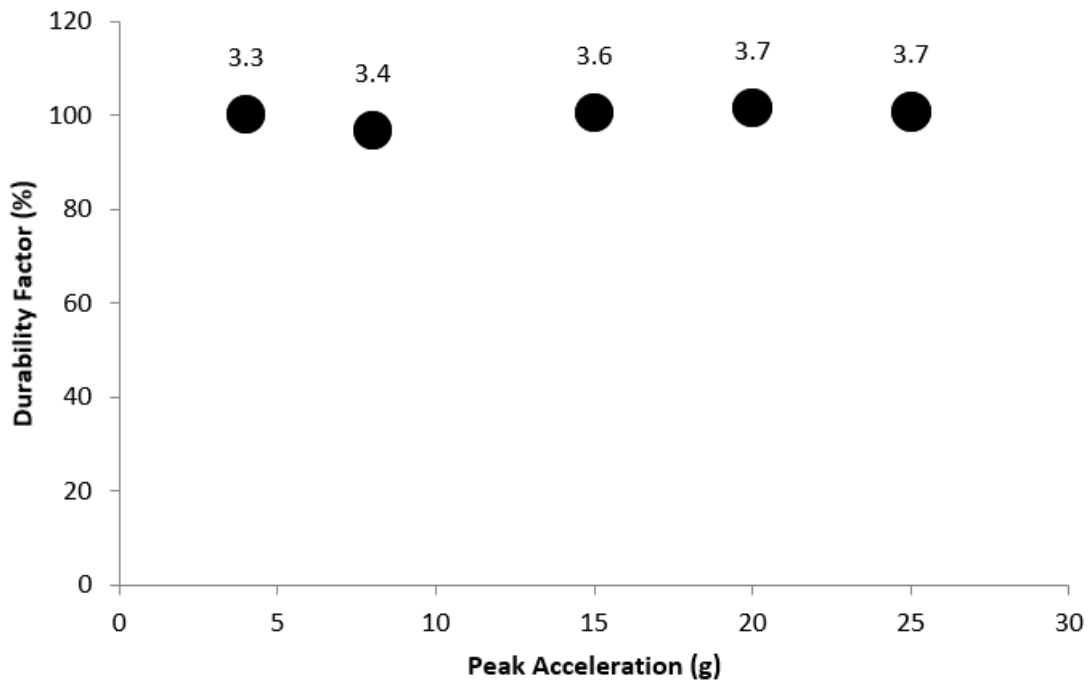


Figure 5.67. Effect of vibration acceleration on the F-T performance of rheological combination 1

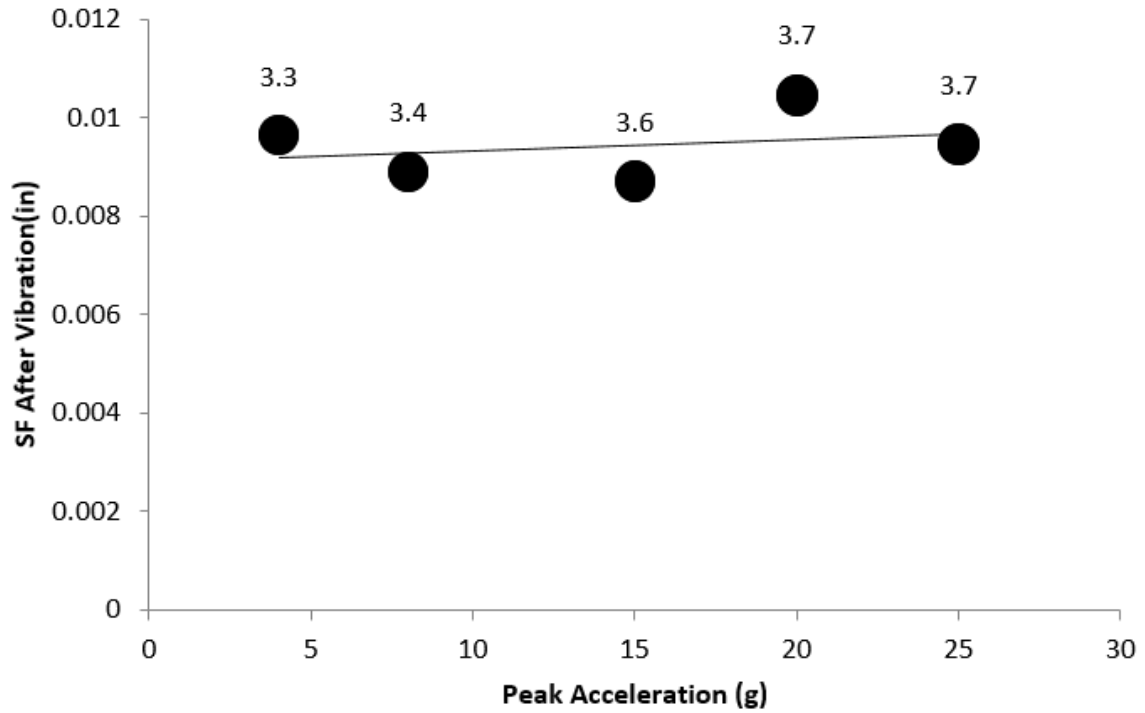


Figure 5.68. Effect of vibration acceleration on the final spacing factor of rheological combination 1

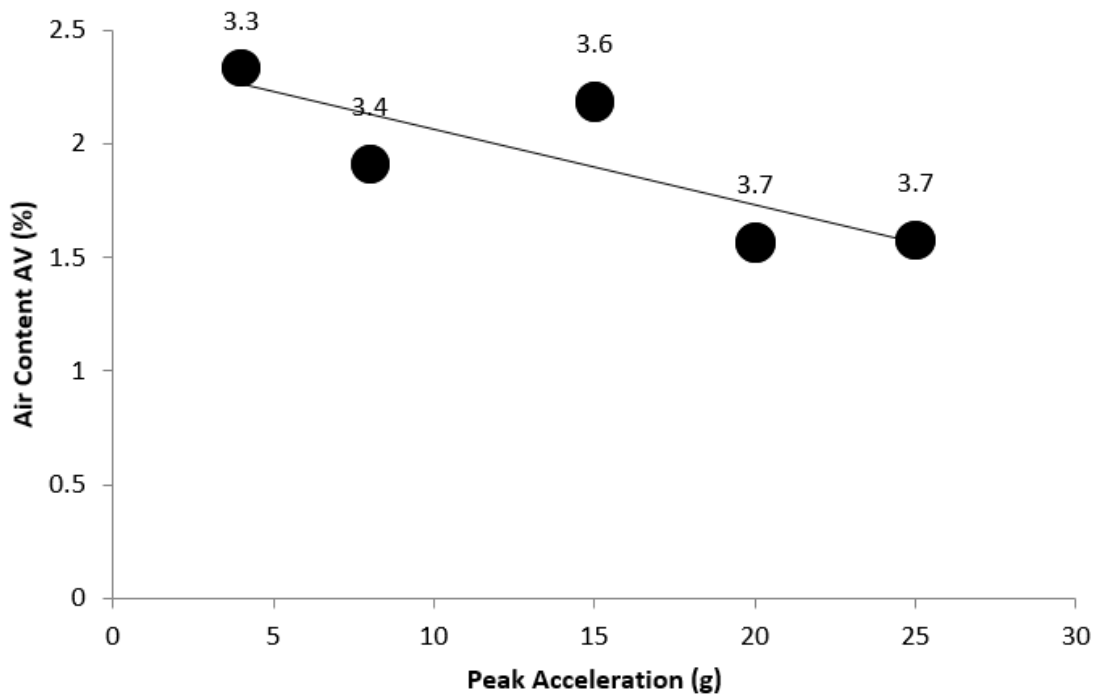


Figure 5.69. Effect of vibration acceleration on the final air content of rheological combination 1

Effect of Vibration Frequency

The effect of vibration frequency during vibration on freeze-thaw durability was studied using rheological combinations 1 and 4 with chemical admixture combination B. The mixtures in this section were subjected to 4 minutes of vibration with a peak vibration acceleration of 8 g. Figure 5.70 shows the rheological properties for both rheological combinations 1 and 4 batches. The size of the markers in this figure corresponds to the amount of vibration frequency applied to the particular mixture. Figure 5.71 illustrates the freeze-thaw results for rheological combination 4 under different vibration frequencies. The size of and the number on the markers in this figure corresponds to the value of the initial air content. Even though no failure occurred, samples vibrated at 33, 110 and 160 Hz showed more deterioration. Since the air content before vibration for the specimens vibrated at 55 and 75 Hz was higher than the others, it is likely that the improved performance was because of the higher air content. The experiments showed that vibration frequency ranges between 33 and 160 Hz has a minor effect for concrete vibrated at 8 g. Supporting the conclusion that vibration frequency has limited effect, Figure 5.72 and Figure 5.73 show that the vibration frequency has minimal to no effect on the final air parameters. It seems from Figure 5.72 that the final spacing factor values for the deteriorated samples were higher than those of the others—enough to cause the concrete to not be frost resistant.

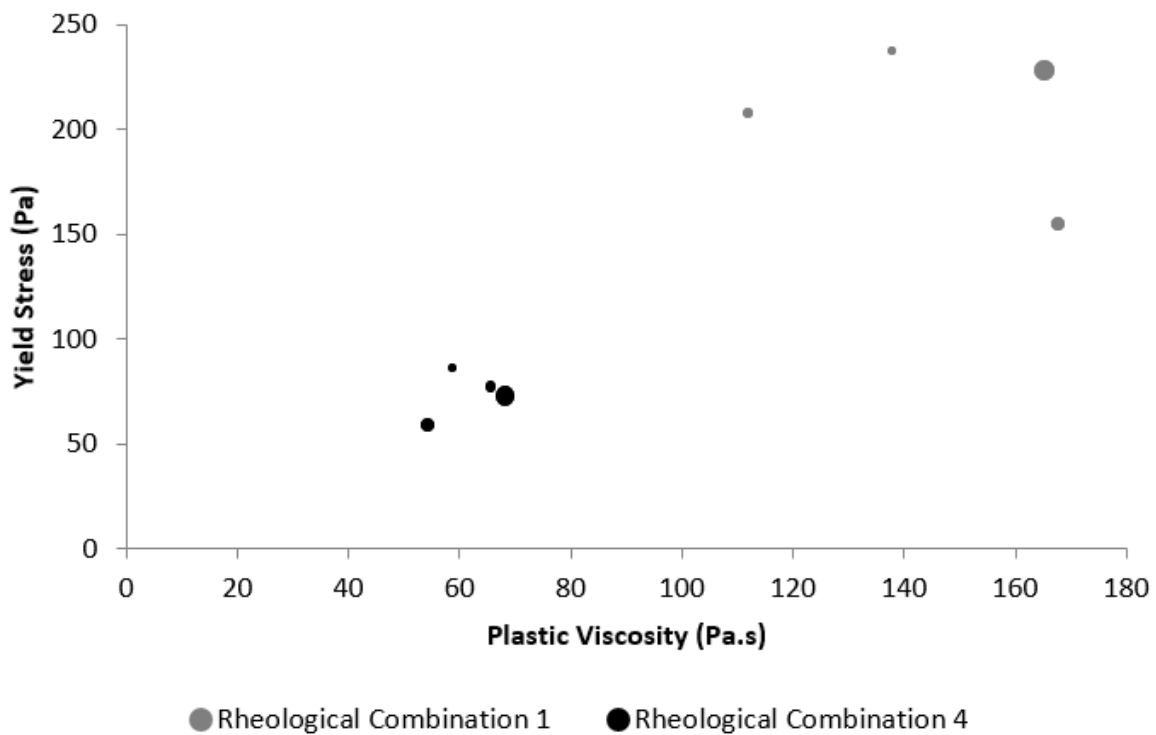


Figure 5.70. Rheological properties for the study of the effect of vibration frequency

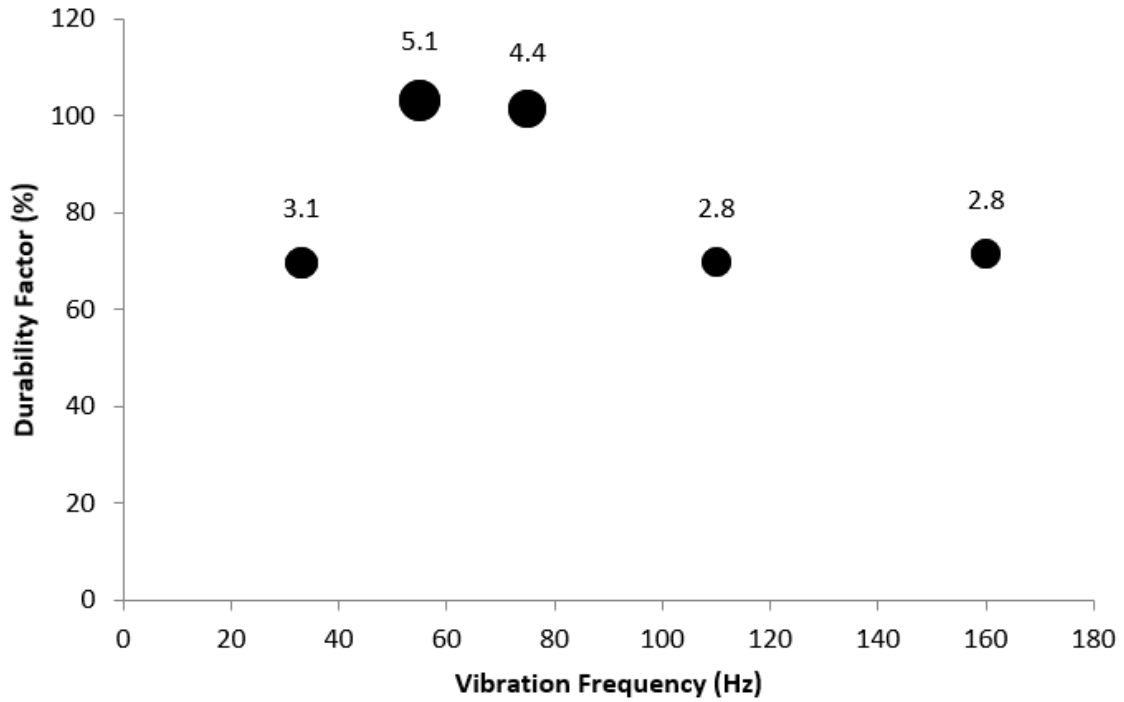


Figure 5.71. Effect of vibration frequency on the F-T performance of rheological combination 4

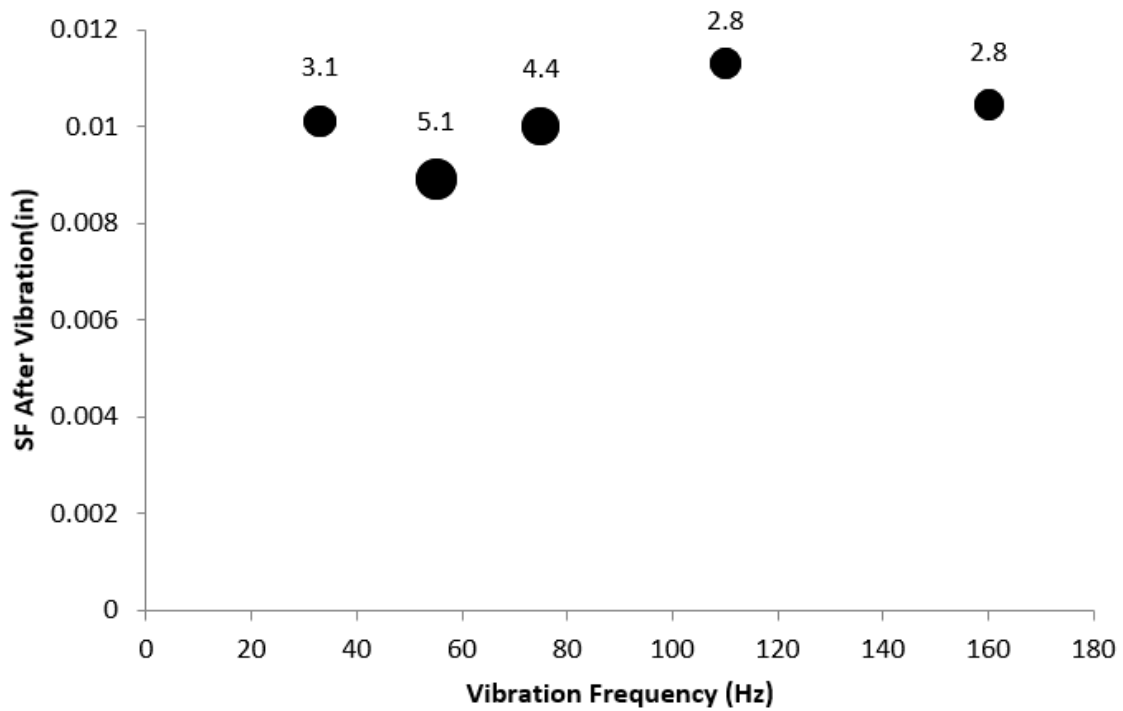


Figure 5.72. Effect of vibration frequency on the final spacing factor of rheological combination 4

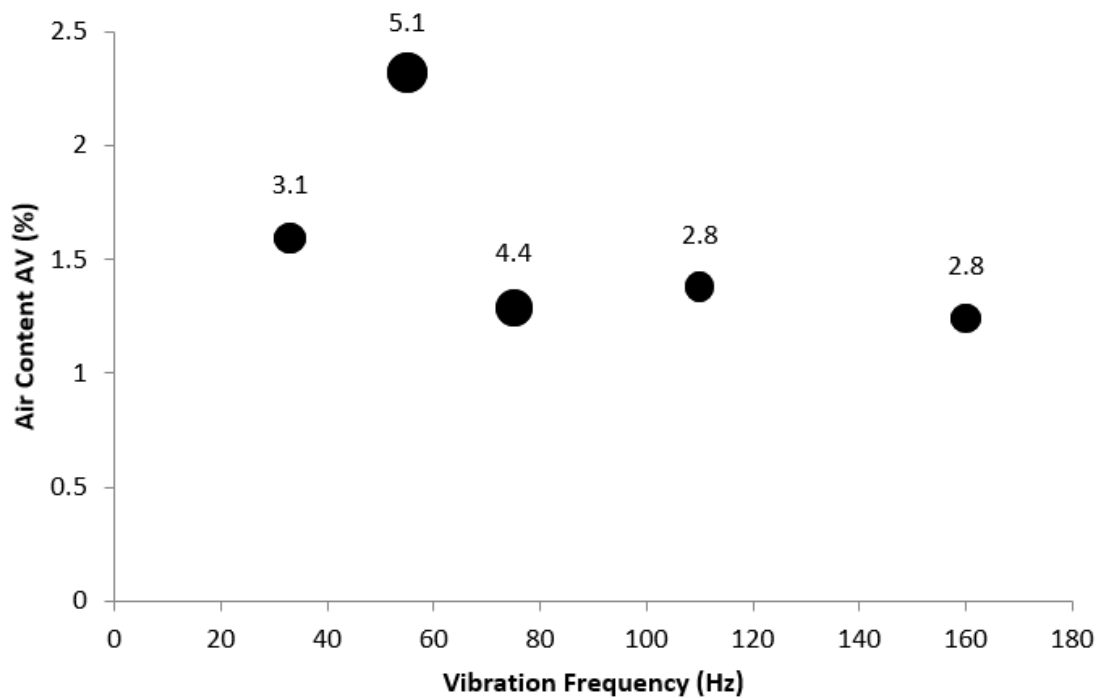


Figure 5.73. Effect of vibration frequency on the final air content of rheological combination 4

For concrete made at rheological combination 1, Figure 5.74 illustrates the freeze-thaw results of chemical admixture combination B. Once again, it was observed that unlike rheological combination 4, rheological combination 1 did not experience any deterioration regardless of the vibration frequency. This could be attributed to the high yield stress and plastic viscosity that provided more resistance to air loss than seen with rheological combination 4. As shown in Figure 5.75 and Figure 5.76, like rheological combination 4, there did not appear to be any significant effect of vibration frequency on the final air parameters.

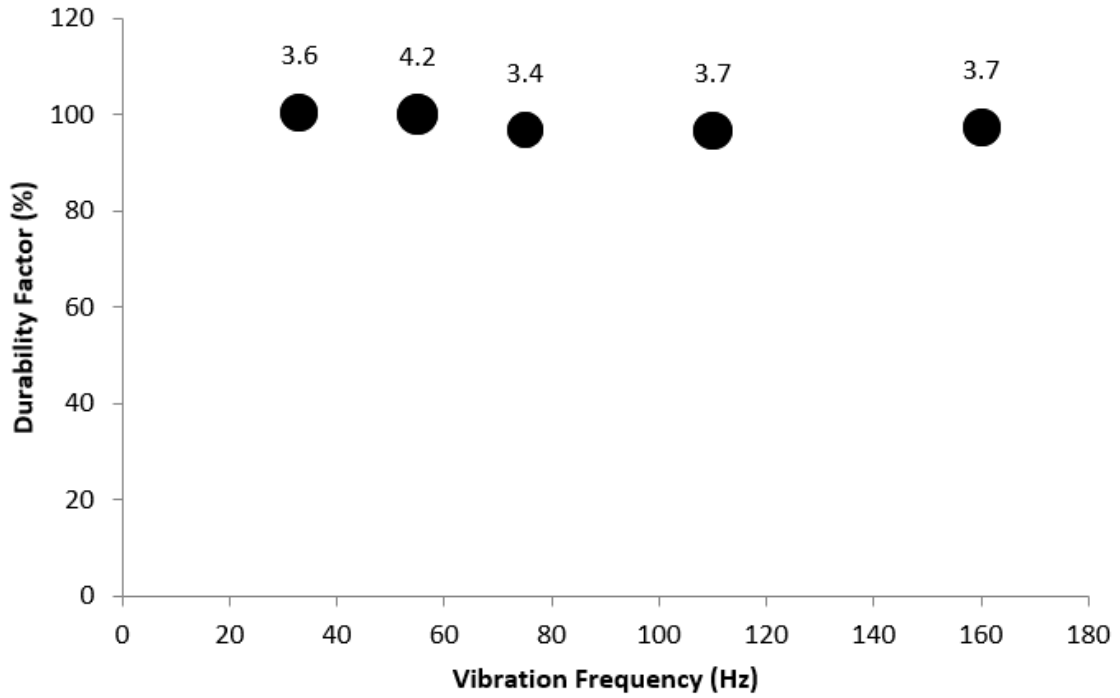


Figure 5.74. Effect of vibration frequency on the F-T performance of rheological combination 1

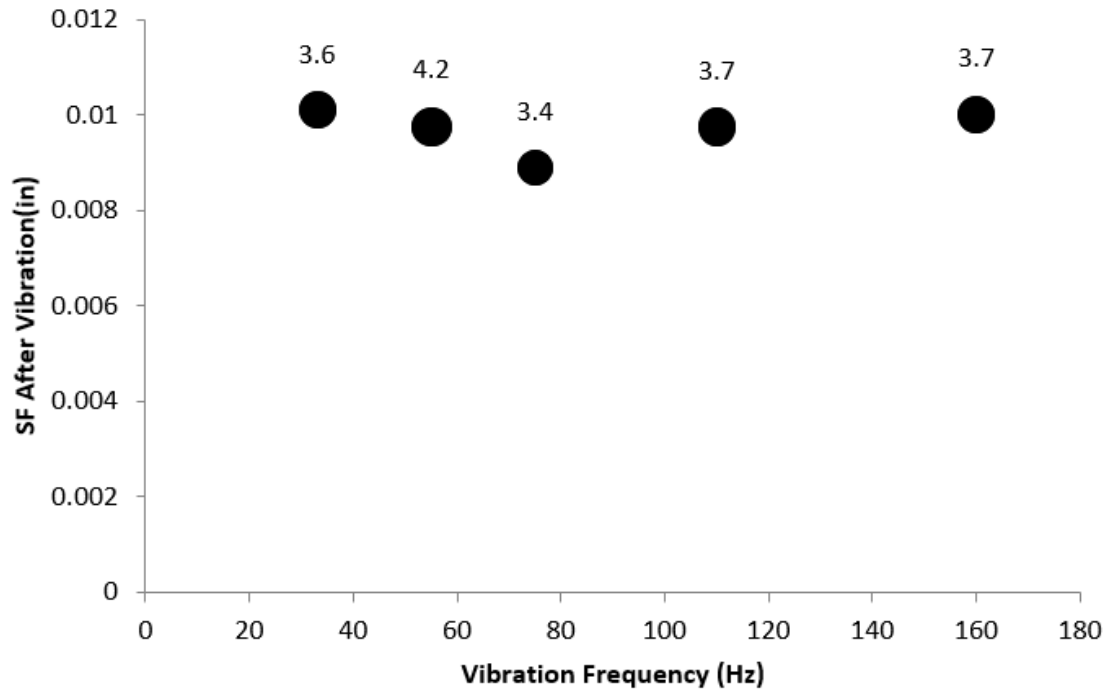


Figure 5.75. Effect of vibration frequency on the final spacing factor of rheological combination 1

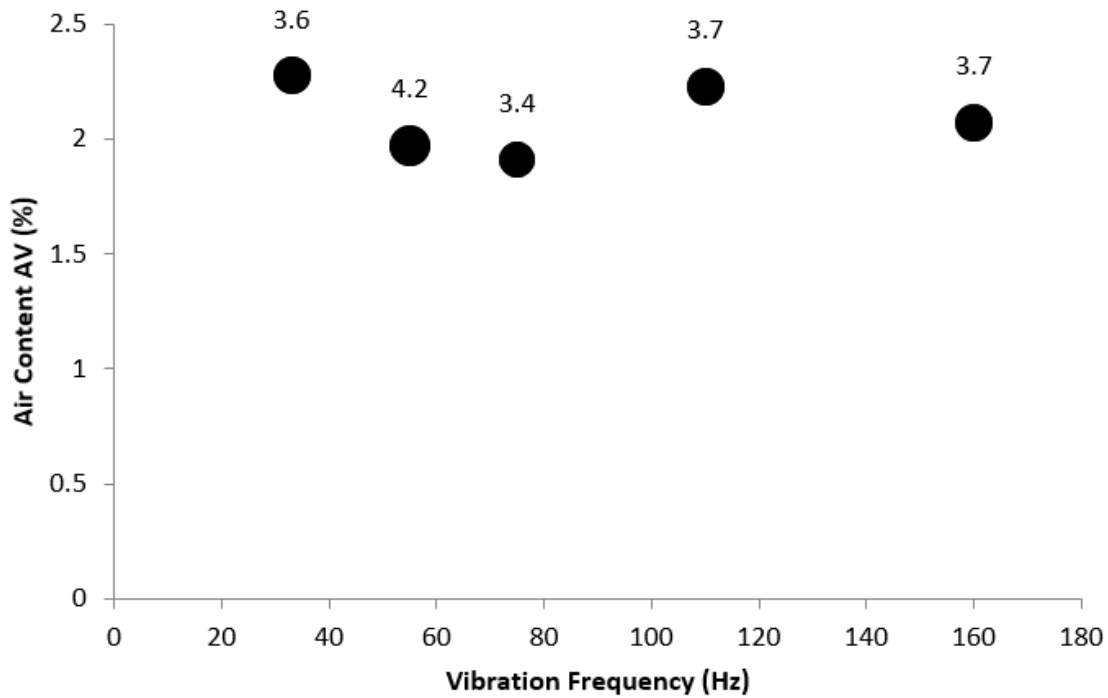


Figure 5.76. Effect of vibration frequency on the final air content of rheological combination 1

Effect of Vibration Velocity

In order to examine the combined effect of variation in vibration frequency and acceleration, the effect of peak vibration velocity on the freeze-thaw performance of rheological combination 1 and 4 of chemical admixture combination B was studied. The peak velocity can be obtained by dividing the peak vibration acceleration by the angular frequency of vibration. The mixtures in this section were subjected to 4 minutes of vibration. Figure 5.77 shows the rheological properties for both rheological combination 1 and 4 batches. The size of the bubbles in this figure corresponds to the amount of peak vibration velocity applied to the particular mixture. Starting with rheological combination 4, one can observe from Figure 5.78 that deterioration occurred at almost all values of peak velocities. The very weak effect of vibration velocity on the final air parameters (Figure 5.79 and Figure 5.80) supports the conclusion that the variation in the vibration velocity does not have a significant effect on the freeze-thaw performance.

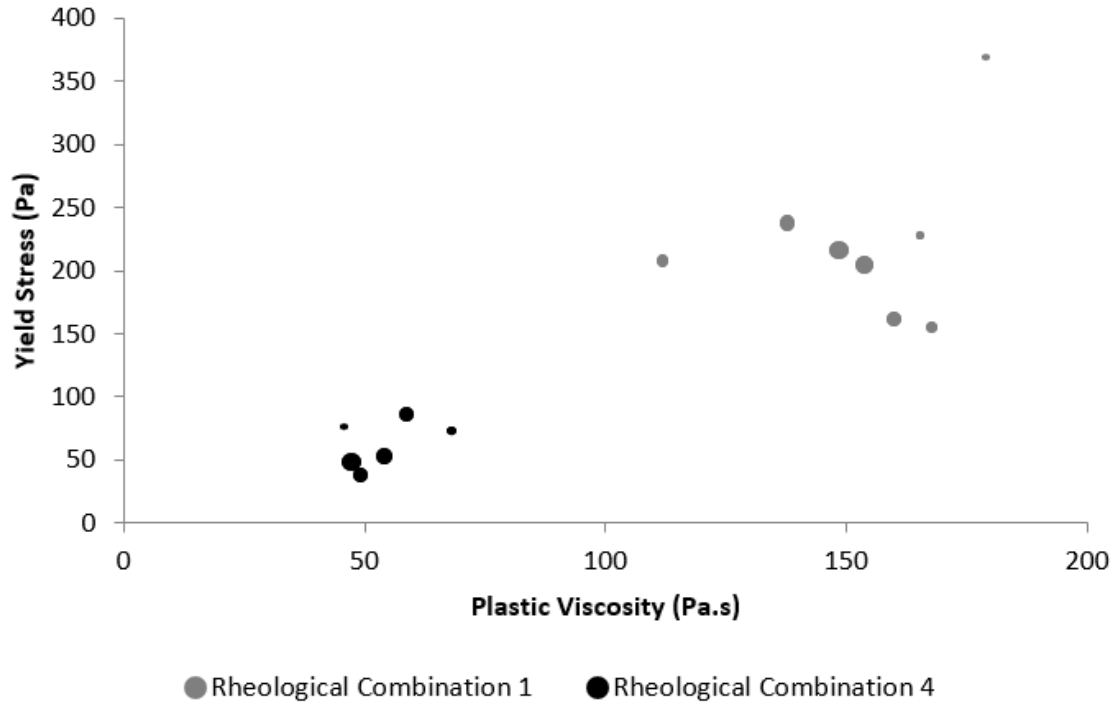


Figure 5.77. Rheological properties for the study of the effect of vibration velocity

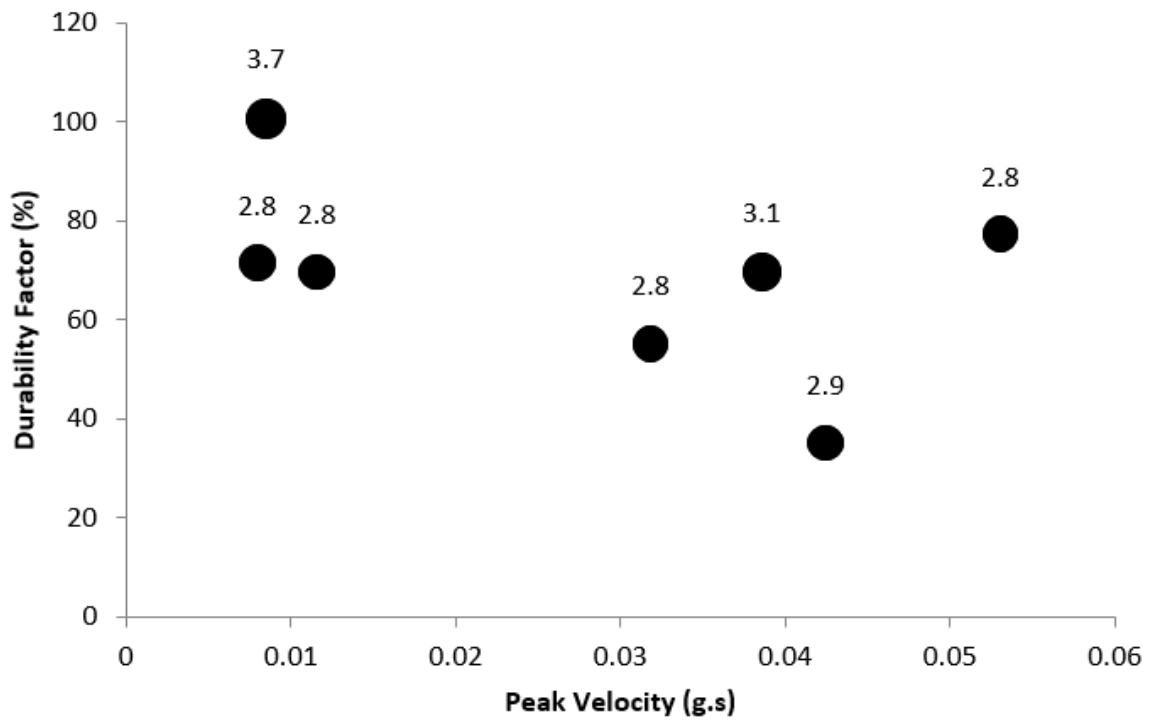


Figure 5.78. Effect of peak vibration velocity on the F-T performance of rheological combination 4

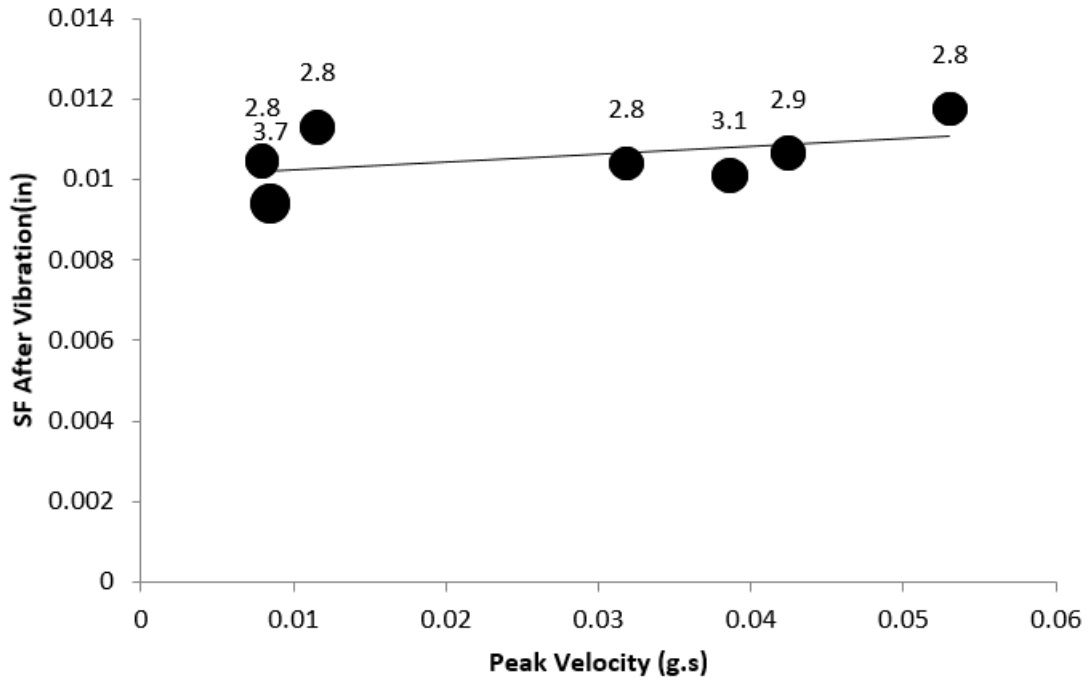


Figure 5.79. Effect of vibration velocity on the final spacing factor of rheological combination 4

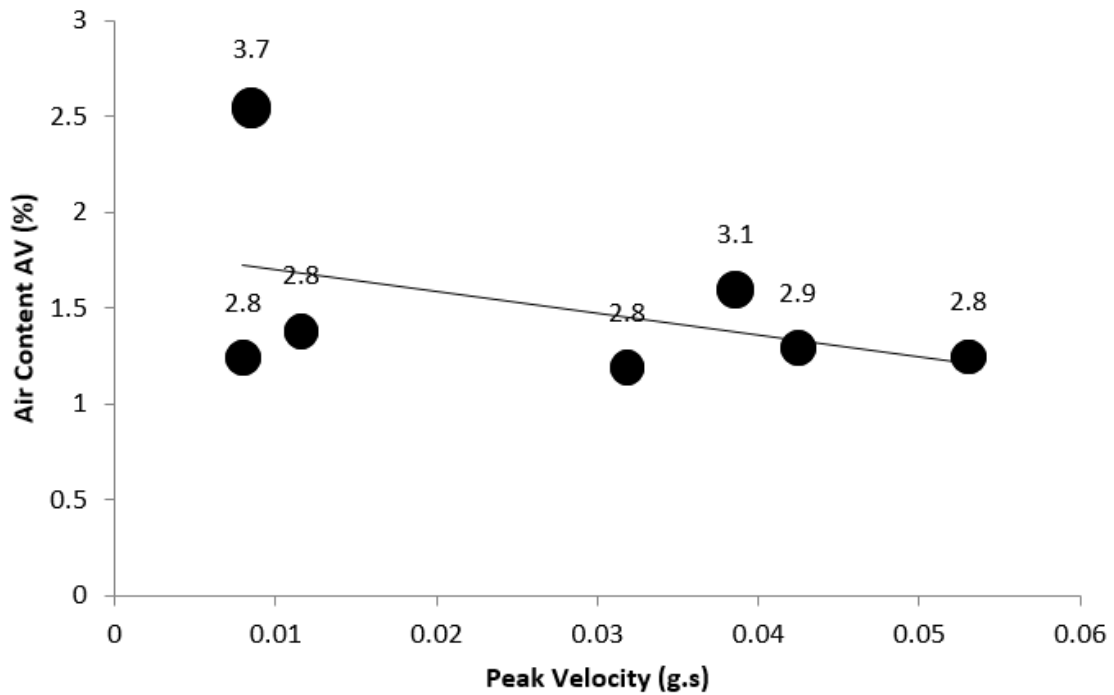


Figure 5.80. Effect of vibration velocity on the final air content of rheological combination 4

Rheological combination 1 results, shown in Figure 5.81, suggest that the stiff mixture performed well in freeze-thaw regardless of the peak vibration velocity due to its high rheological properties. Similarly, there was no apparent relation between the peak vibration velocity and the final air parameters (Figure 5.82 and Figure 5.83). The peak vibration acceleration might be the main vibration factor dictating the freeze-thaw performance of the vibrated concrete.

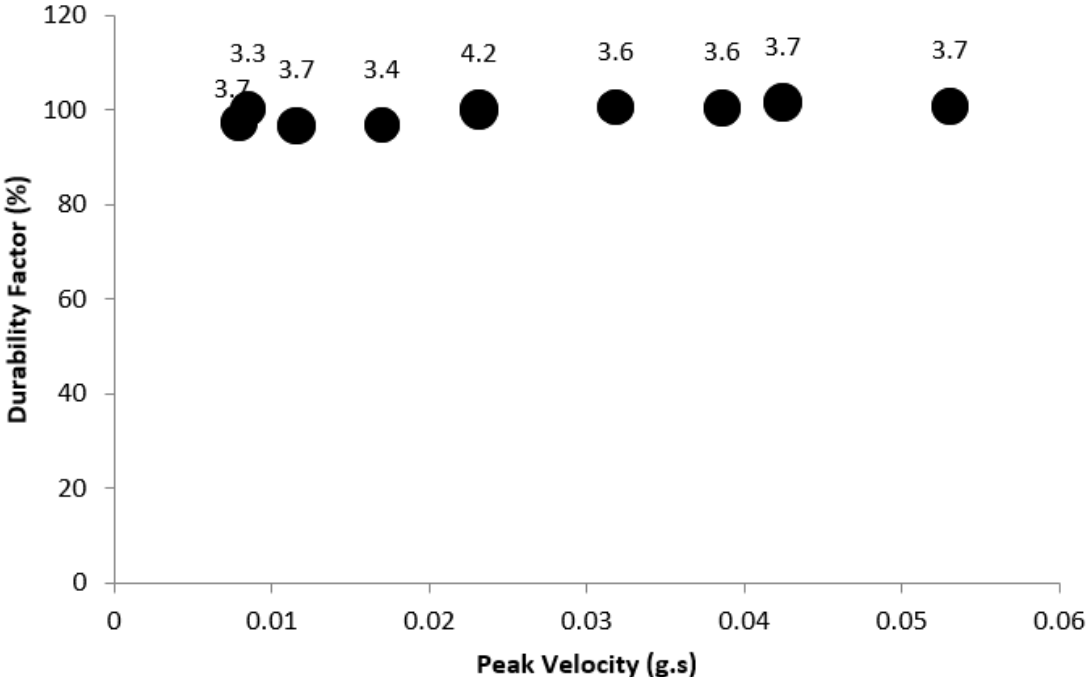


Figure 5.81. Effect of peak vibration velocity on the F-T performance of rheological combination 1

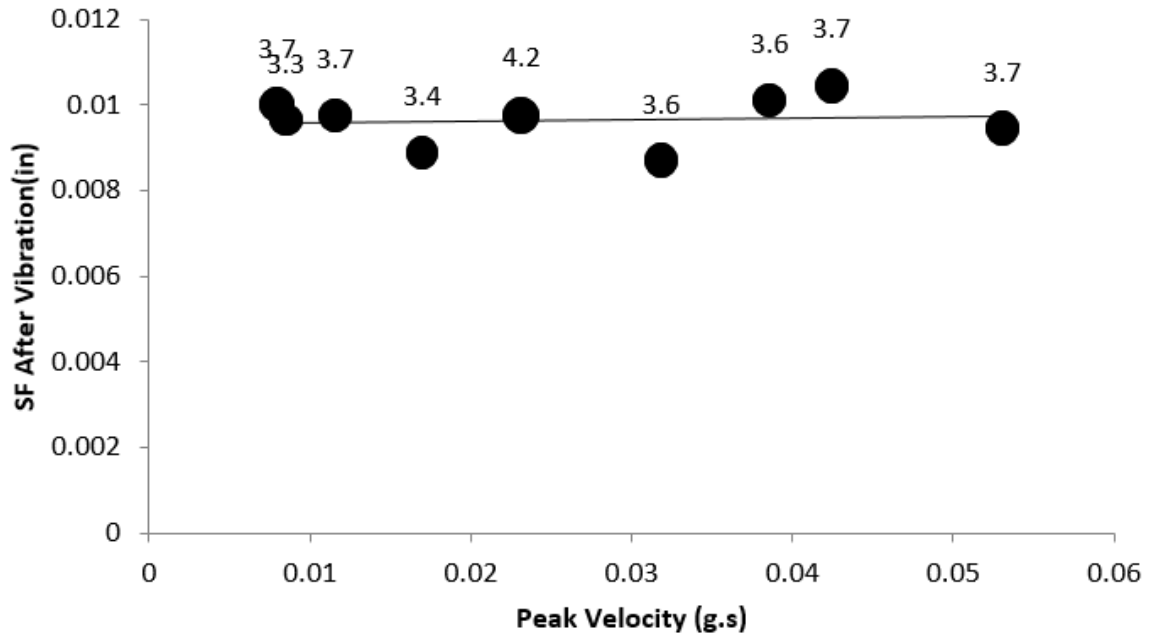


Figure 5.82 Effect of vibration velocity on the final spacing factor of rheological combination 1

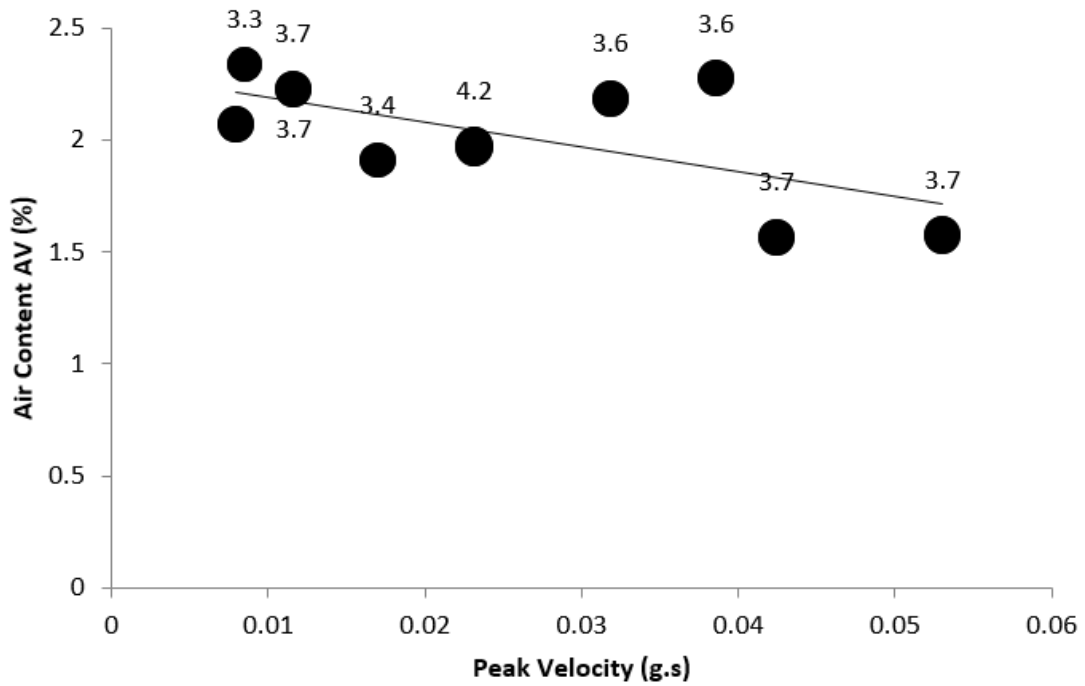


Figure 5.83. Effect of vibration velocity on the final air content of rheological combination 1

Effect of Air Content Before Vibration

The relationship between concrete fresh air content before vibration for different chemical admixture combinations and freeze-thaw durability was examined. Fresh air content is the most used quality control test for concrete freeze-thaw durability. Determination of the concrete fresh air content required to maintain a good air system after vibration is needed to ensure that concrete tie manufacturers can continue to use this quality control test. Both chemical admixture combination B and C were used in order to determine the difference between the minimum initial air required to achieve good freeze-thaw resistance for different chemical admixtures combinations. Only rheological combination 4 of chemical admixture combination B was examined in this section since previous sections showed that the stiffest mixture (rheological combination 1) did not experience any deterioration under any vibration condition. Moreover, results also showed that initial air contents as low as 3.5 percent can safely pass ASTM C666 at a DF of 60 or higher even with the most fluid mixture (rheological combination 4). However, both rheological combinations 1 and 4 of chemical admixture combination C were examined since it was shown that chemical admixture combination C experienced freeze-thaw failure. Starting with chemical admixture combination B, Figure 5.84 shows the rheological properties of batches made with rheological combination 4 vibrated at different frequencies. All these mixtures were vibrated for 4 minutes at a peak vibration acceleration of 8 g. The size of the markers in this figure corresponds to the initial air content of the particular mixture. The rheological properties of the 110 Hz mixtures do not appear on the figure because they exactly match with the 160 Hz mixtures. Figure 5.85 shows that the critical value of initial air content is somewhere between 3.1 percent and 4.2 percent under which vibrated concrete starts to experience some freeze-thaw deterioration for chemical admixture combination B. This conclusion seems to be the same regardless of the vibration frequency.

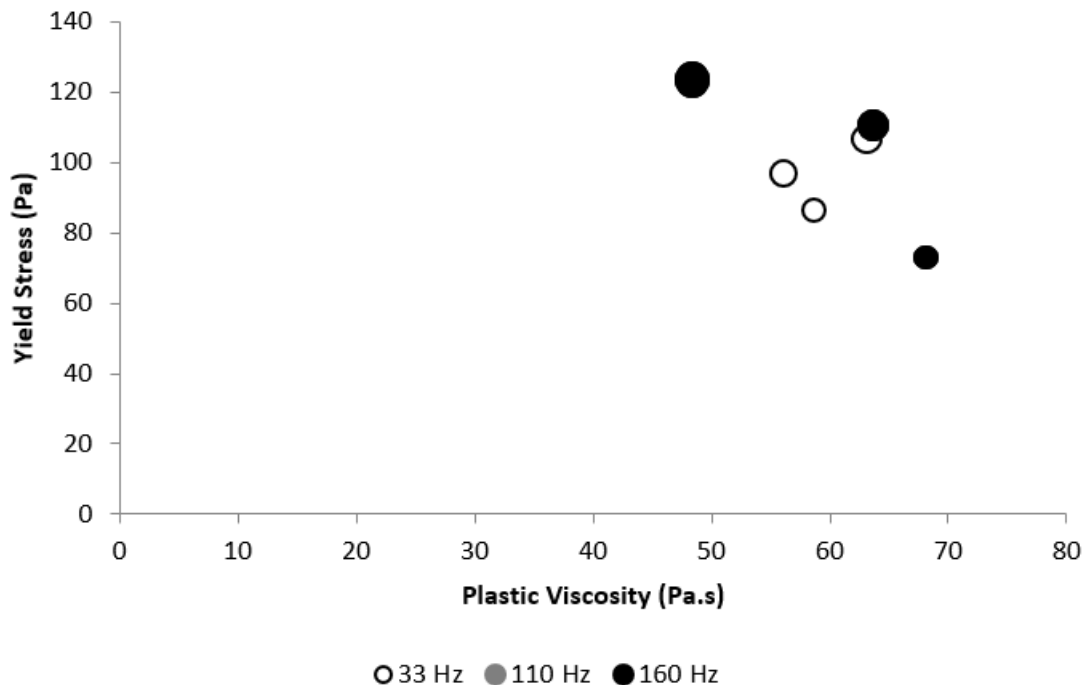


Figure 5.84. Rheological properties of rheological combination 4 of chemical admixture combination A for the study of the effect of air content before vibration

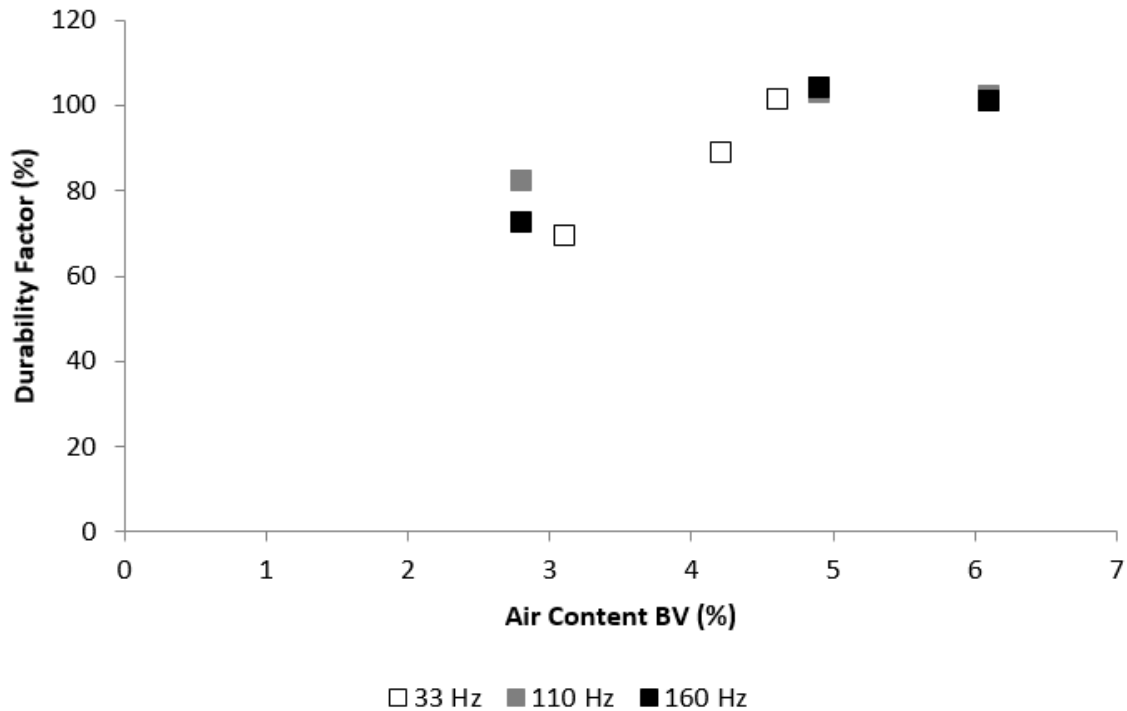


Figure 5.85. Effect of air content before vibration on the F-T performance of rheological combination 4 of chemical admixture combination A

The results for rheological combination 1 and 4 of chemical admixture combination C are shown in Figure 5.86 and Figure 5.87. The size of the markers in Figure 5.86 corresponds to the amount of initial air content of the mixture. All these mixtures were subjected to 4 minutes of 75 Hz vibration at 8 g peak acceleration. While the rheological properties for one of the rheological combination 1 batches were significantly different (Figure 5.86), Figure 5.87 shows that failure occurred for the 3.6 percent air batch even though it is the one that had a high yield stress and plastic viscosity. Figure 5.87, also demonstrates that, even with rheological combination 1, an initial air content of 4.1 percent is not sufficient to provide good freeze-thaw resistance for this chemical admixture combination. The freeze-thaw results also showed that for this admixture combination, it required more air before vibration to provide durability after the air loss associated with vibration. It can be observed that all specimens of rheological combination 4 experienced some deterioration, even those with 6.9 percent initial air content. This work suggests that concrete railroad ties producers should always test the performance of their admixture combination and rheological properties in the vibration system planned for their manufacturing process in order to determine the required initial air content sufficient for freeze-thaw resistance.

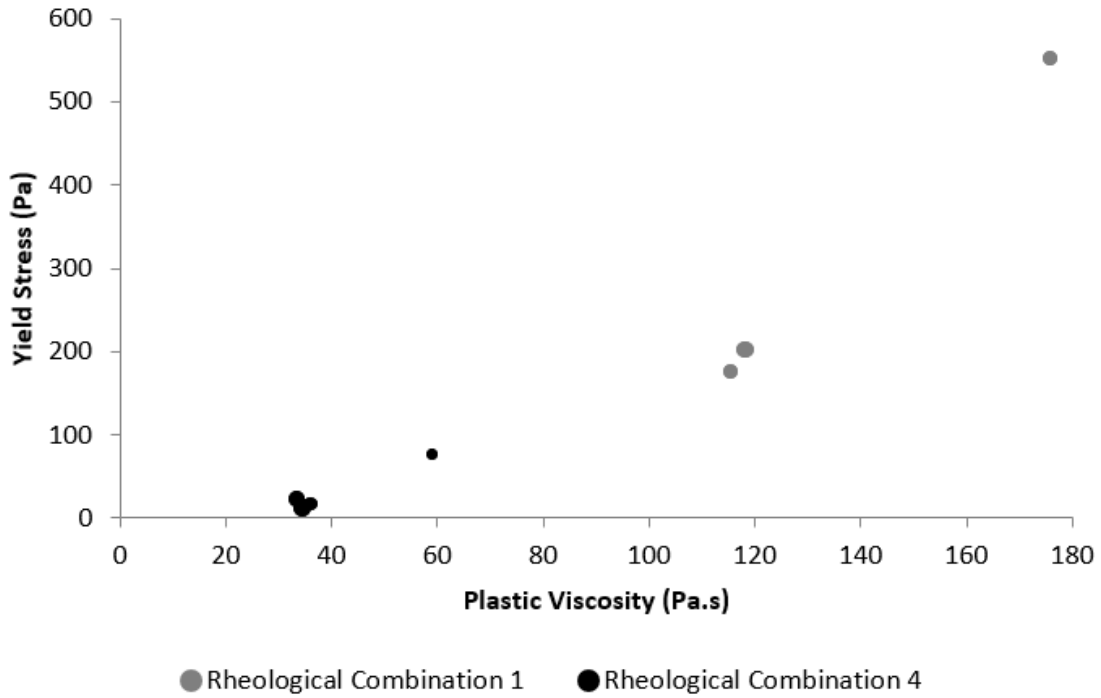


Figure 5.86. Rheological properties of rheological combination 1 and 4 of chemical admixture combination C for the study of the effect of air content before vibration

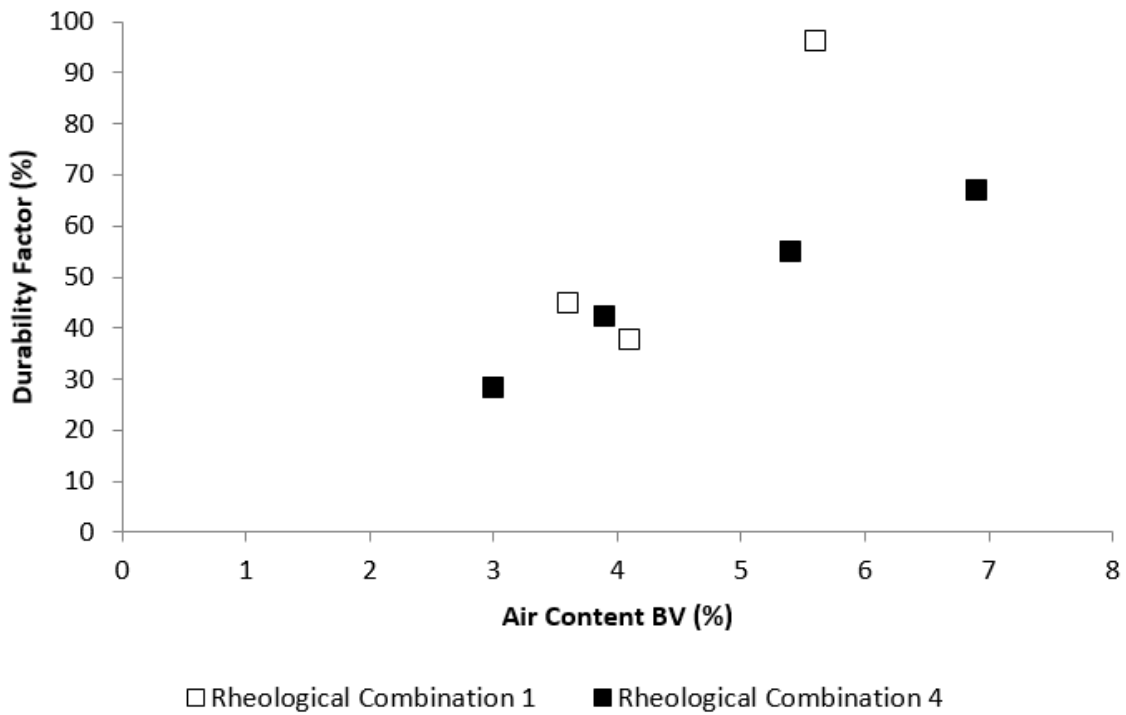


Figure 5.87. Effect of air content before vibration on the F-T performance of rheological combination 1 and 4 of chemical admixture combination C

Effect of Rheological Properties

The effect of the rheological properties on the concrete freeze-thaw performance of all mixtures was examined. The chosen batches for this section all had initial air contents in the range of 3 percent to 4 percent. Figure 5.88 and Figure 5.89 illustrate the effect of rheological properties on the freeze-thaw performance. The size of the markers in both these figures corresponds to the amount of initial air content of the particular mixture. Figure 5.88 shows that the failed specimens for chemical admixture combination B were concentrated in the low yield stress range, specifically less than 200 Pa. Concrete with a marginal air void system such as made with chemical admixture combination C was even more sensitive to vibration when made with low yield stress and plastic viscosity as shown in Figure 5.87. Figure 5.88 shows the relationship between yield stress and freeze-thaw durability, while Figure 5.89 shows the relationship between plastic viscosity and freeze-thaw durability for all chemical admixture combinations. Figure 5.88 and Figure 5.89 show that uniform rheology parameter limits for all concrete mixtures can be given to ensure that vibration will not cause durability problems.

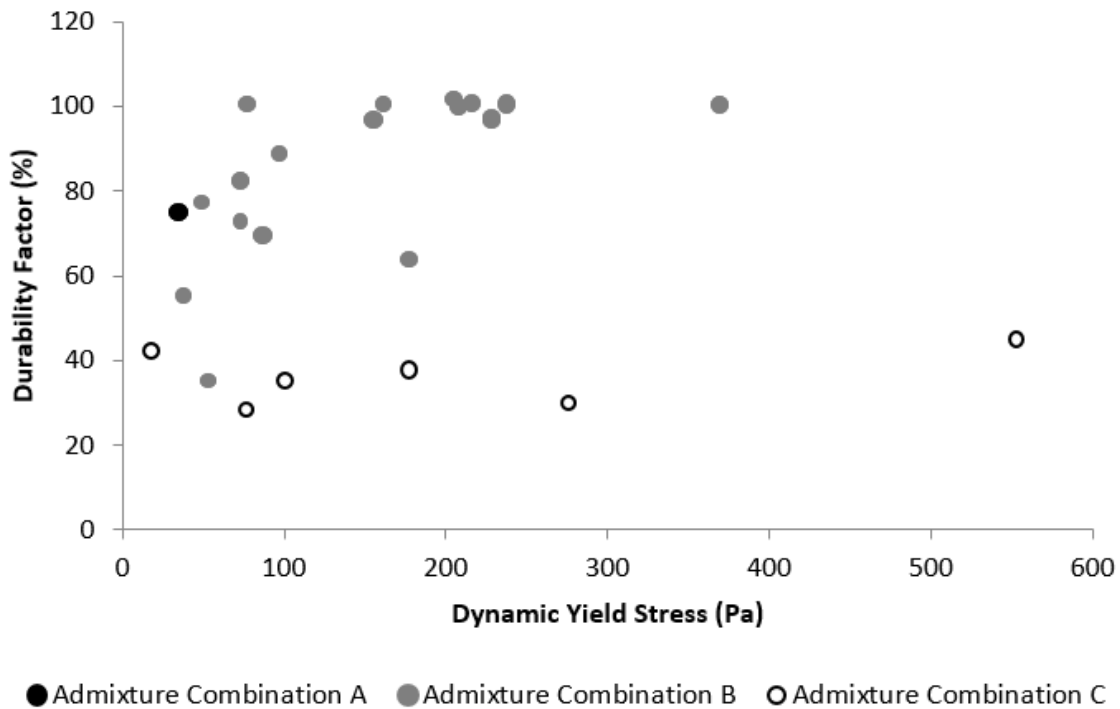


Figure 5.88. Effect of dynamic yield stress on the freeze-thaw durability

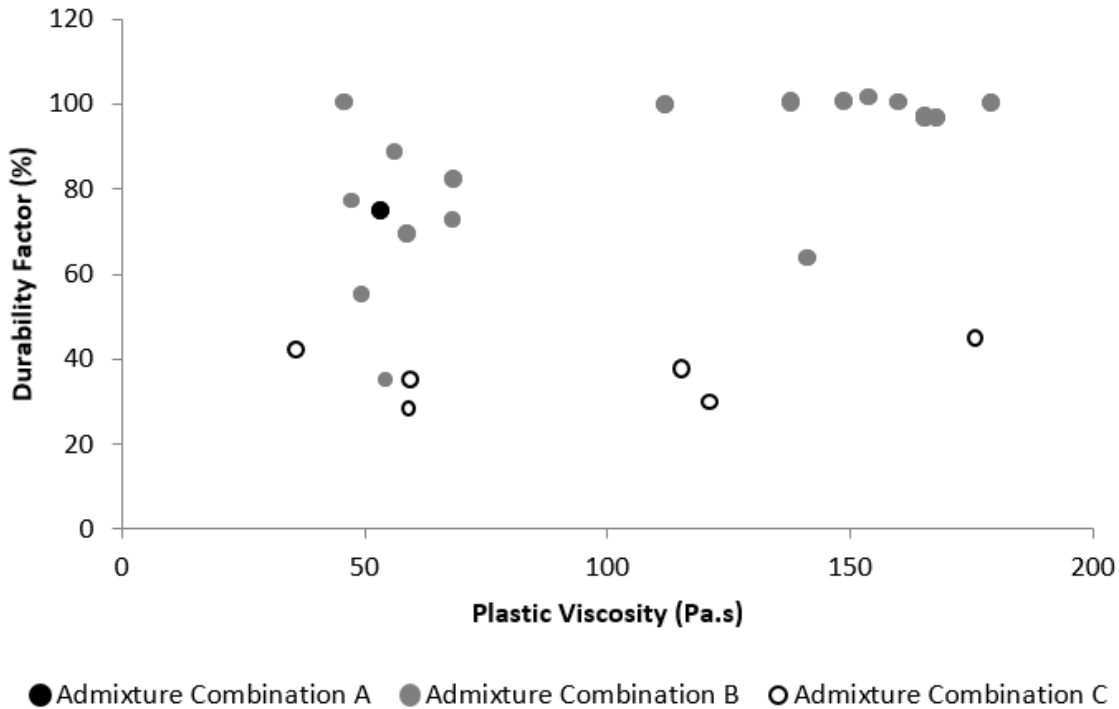


Figure 5.89. Effect of plastic viscosity on the freeze-thaw durability

Air Entrainment Requirements to Achieve Freeze-Thaw Durability

Figure 5.90 shows the relationship between the durability factor and the initial spacing factor. It can be observed that deterioration occurs even at spacing factor values as low as 0.007 in. Therefore, the spacing factor before vibration is not a reliable parameter to determine the susceptibility to freeze-thaw damage. Figure 5.91 illustrates the correlation between the durability factor and the spacing factor after vibration which showed a better relationship between the spacing factor and freeze-thaw durability. It is evidently apparent from the figure that as the spacing factor increases the samples are more susceptible to freeze-thaw failure. It can be observed that chemical admixture combination C had the highest average spacing factors. The most interesting thing to be observed from Figure 5.91 is the fact that specimens were able to pass the freeze-thaw test as long as they had a spacing factor less than 0.01 in. This maximum limit is, however, 0.002 in larger than the one specified in ACI recommendations. The commonly used 0.008 in spacing factor criteria is known to be a conservative limit and is confirmed by this testing to be very conservative for vibrated concrete. According to the Canadian standards A23.1, the upper limit for the spacing factor is 0.23 mm (0.009 in) for normal concrete and 0.26 mm (0.01 in) for high strength concrete. Being high strength concrete, the results presented here seem to match nicely with the 0.01 in limit. Not all concrete railroad ties are made with high strength concrete. Therefore, it is concluded that 0.0087 in. is the conservative limit that should be adopted for these results. It is also possible to conclude from Figure 5.91 that good freeze-thaw performance can always be achieved regardless of vibration parameters, rheology or chemical admixture combination if the required final spacing factor value is achieved.

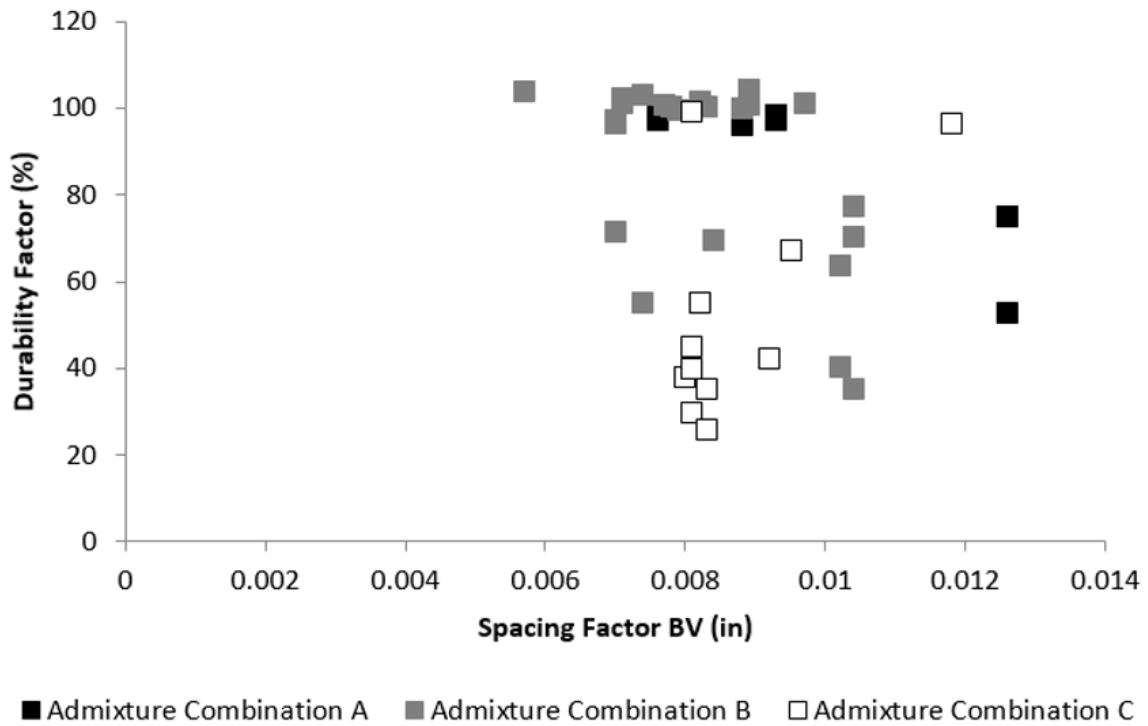


Figure 5.90. Durability factor vs. spacing factor before vibration

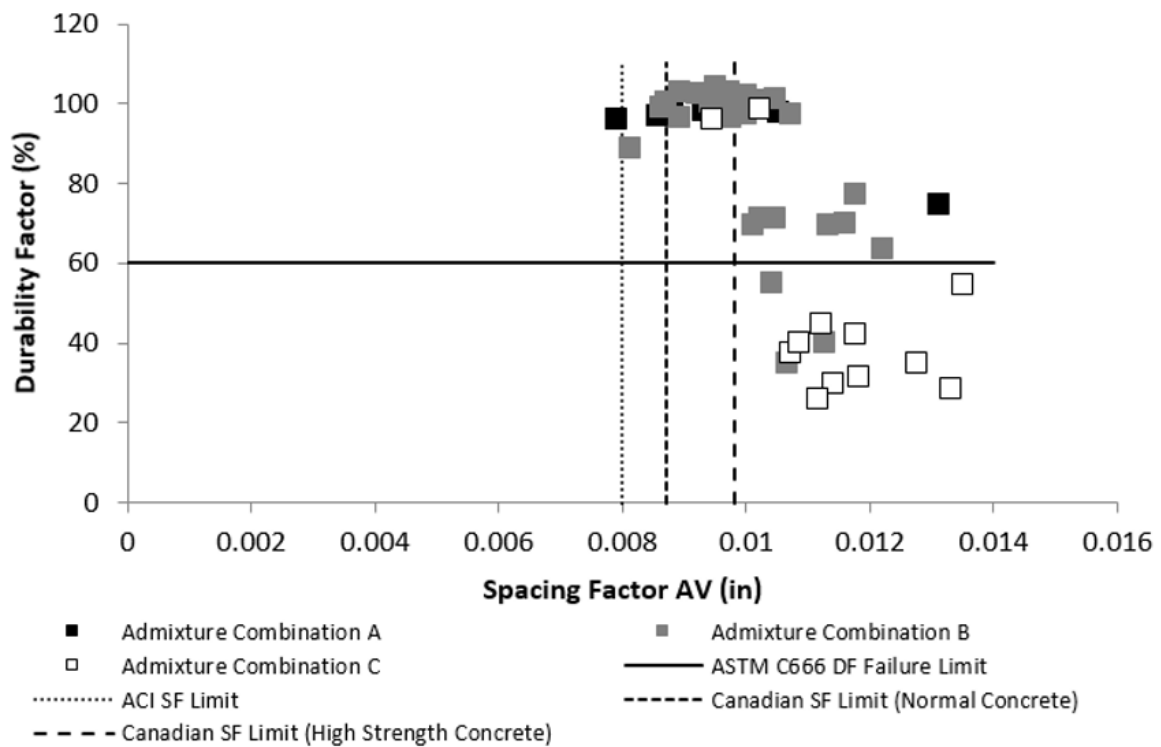


Figure 5.91. Durability factor vs. spacing factor after vibration

Figure 5.92 and Figure 5.93 show the relation between the durability factor and fresh and hardened air content before vibration. For the case of chemical admixture combination C, like the spacing factor before vibration, the total air content before vibration was meaningless since even air contents as high as 6 percent were not sufficient in some cases. The concrete fresh air content before vibration could be helpful for a given vibration condition if it were correlated to durability after vibration for a given mixture and rheological properties. Figure 5.94 presents the relation between the durability factor and the hardened air content after vibration. The total air content after vibration was not a reliable predictor of durability after vibration.

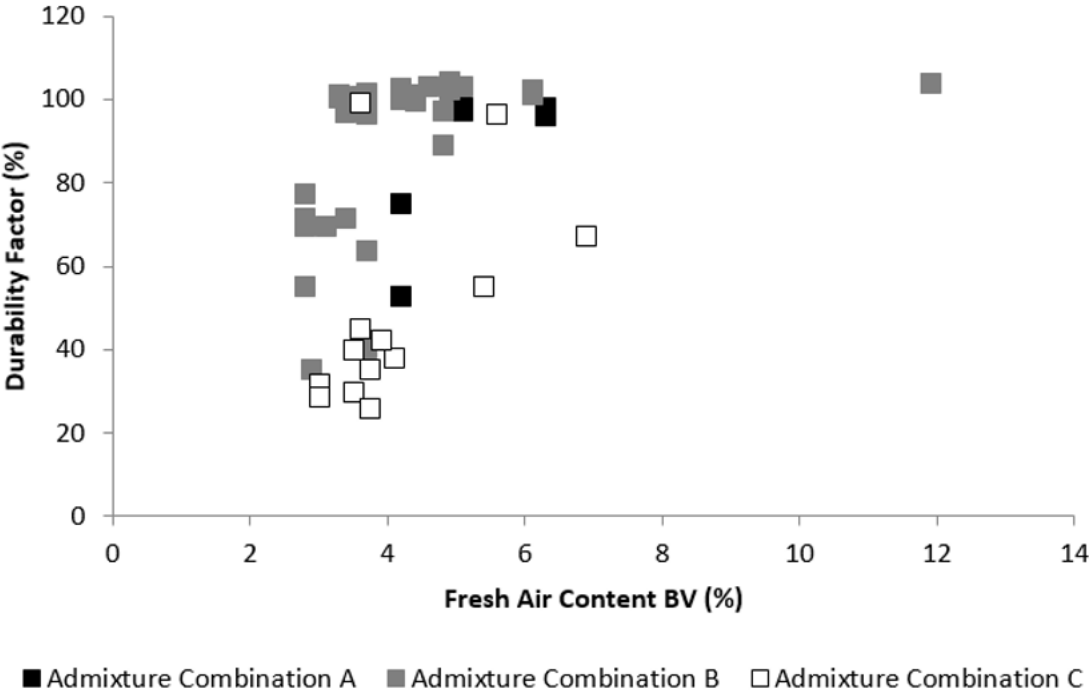


Figure 5.92. Durability factor vs. fresh air content before vibration

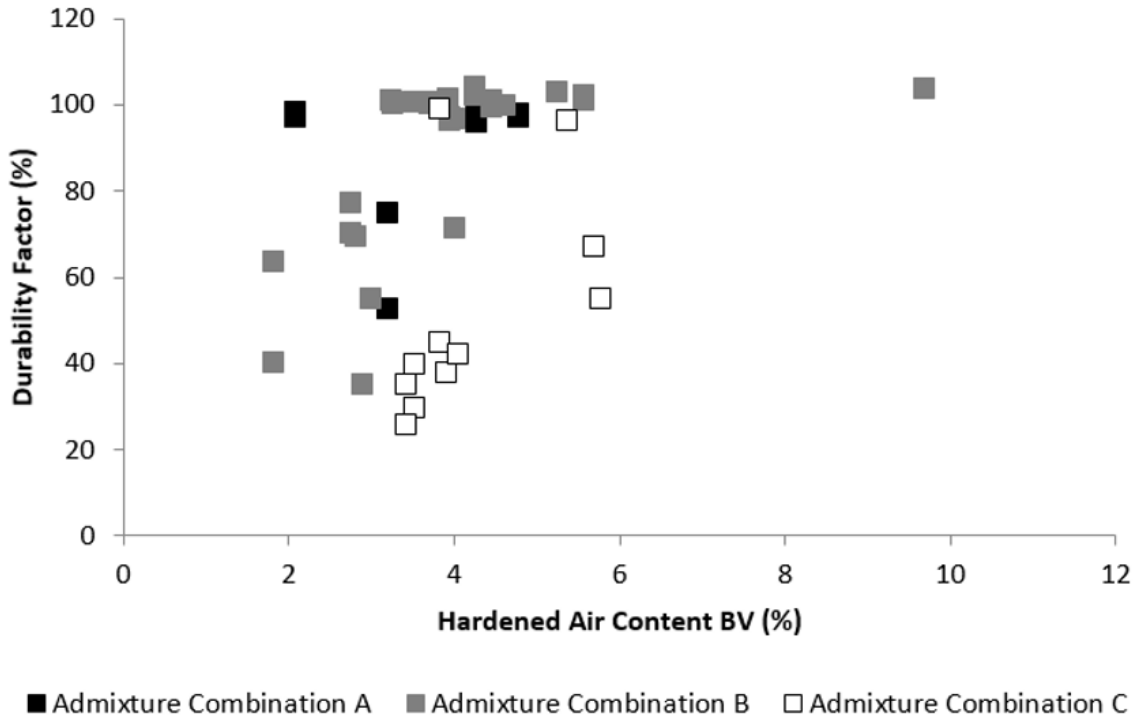


Figure 5.93. Durability factor vs. hardened air content before vibration

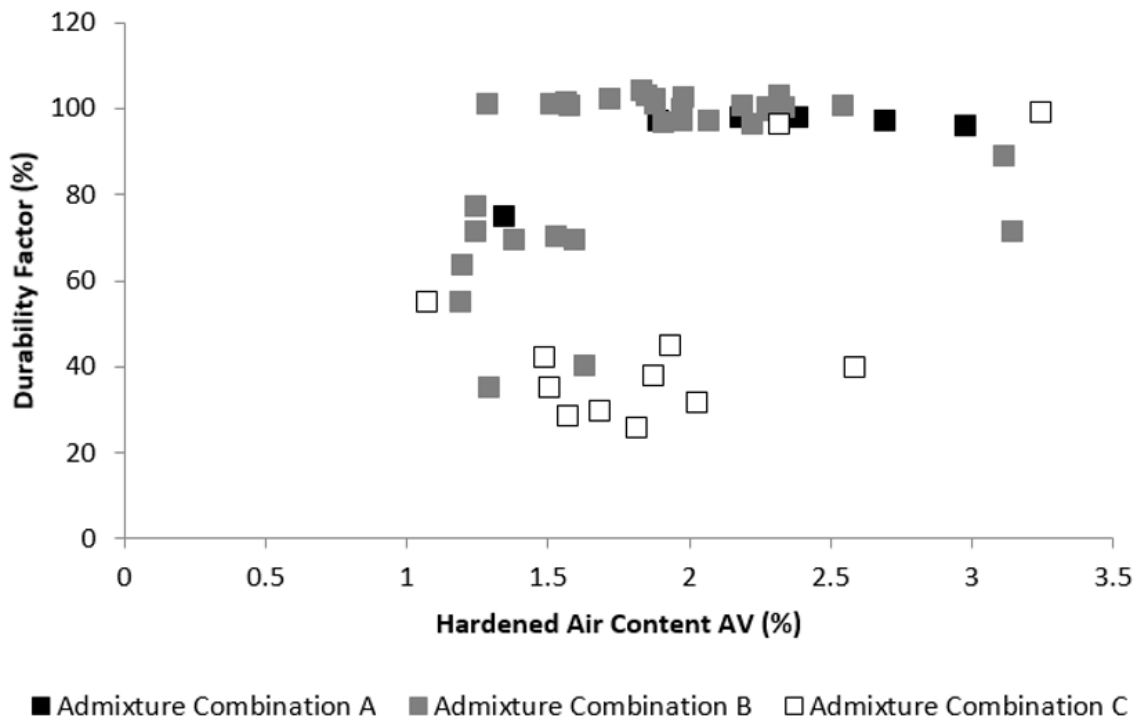


Figure 5.94. Durability factor vs. hardened air content after vibration

Figure 5.95 illustrates the correlation between final length change and final spacing factor. The samples are considered to be failed if the length change exceeds 0.1 percent. It seems from

Figure 5.95 that the 0.01 in Canadian limit for the spacing factor also works when considering the length change as a failure criterion. However, it is still not very conservative. The 0.008 spacing factor limit on the other hand, proves to be very conservative even when considering the length change failure criterion. All failed samples had positive or expansive length change values indicating internal cracking. Figure 5.96 shows the relation between the two failure criteria, durability factor and final length change. There is an obvious correlation between the two criteria where the length change increases as the durability factor decreases.

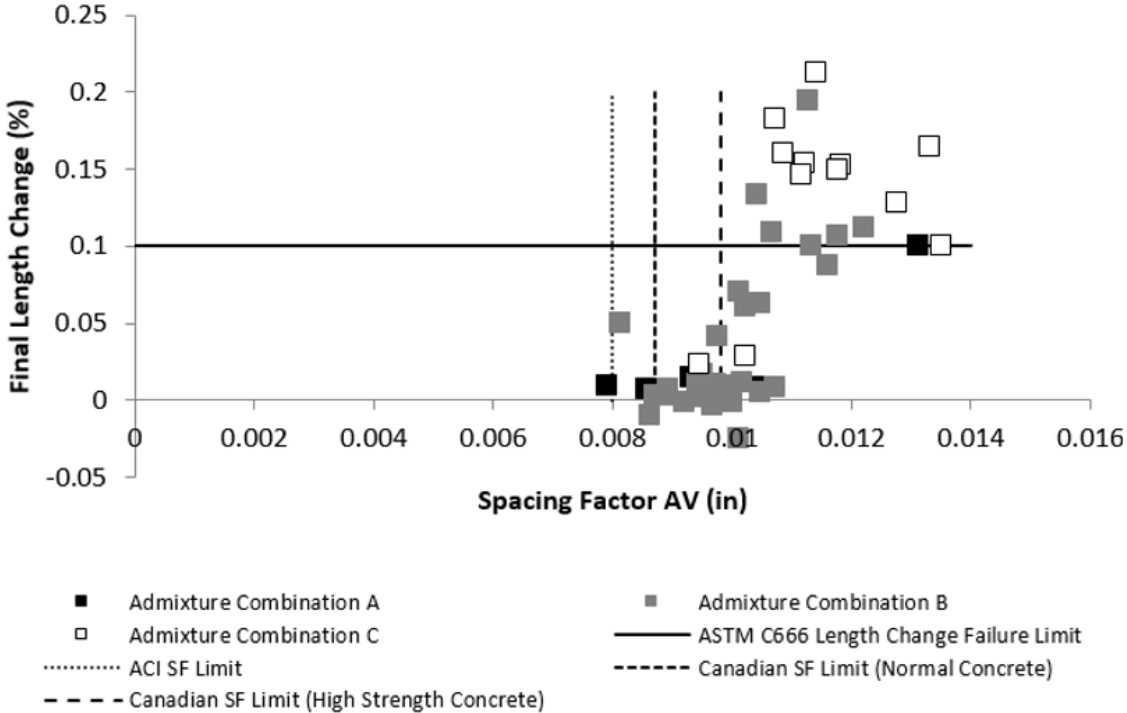


Figure 5.95. Final length change vs. spacing factor after vibration

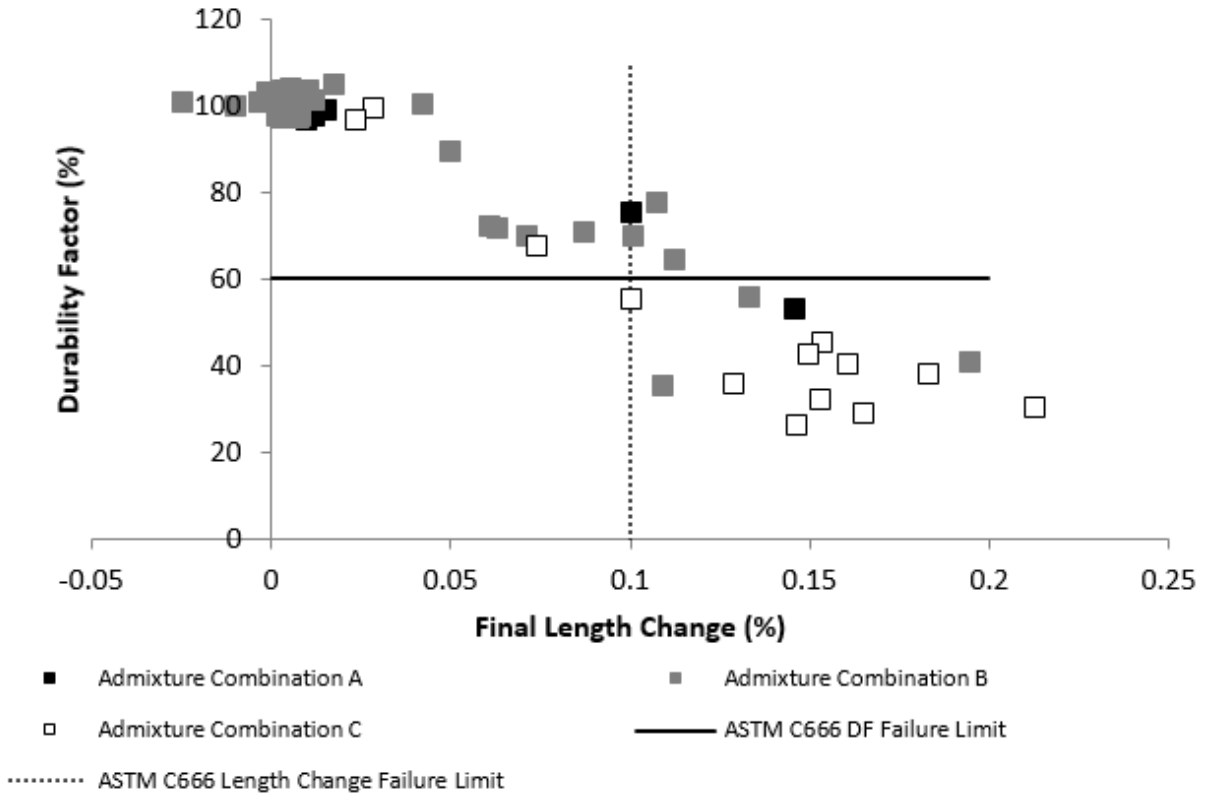


Figure 5.96. Durability factor vs. final length change

Figure 5.97 presents the relationship between final weight change and final spacing factor. It shows that samples with high spacing factors tend to have higher weight change. This indicates that there might be a correlation between failure and weight change. Figure 5.98 illustrates the relation between the durability factor and the weight change. While all failed samples had an increase in weight, there are some unaffected samples that also had an increase in weight. The increase in weight in failed samples might be due to some water absorption, but not enough to critically saturate the concrete.

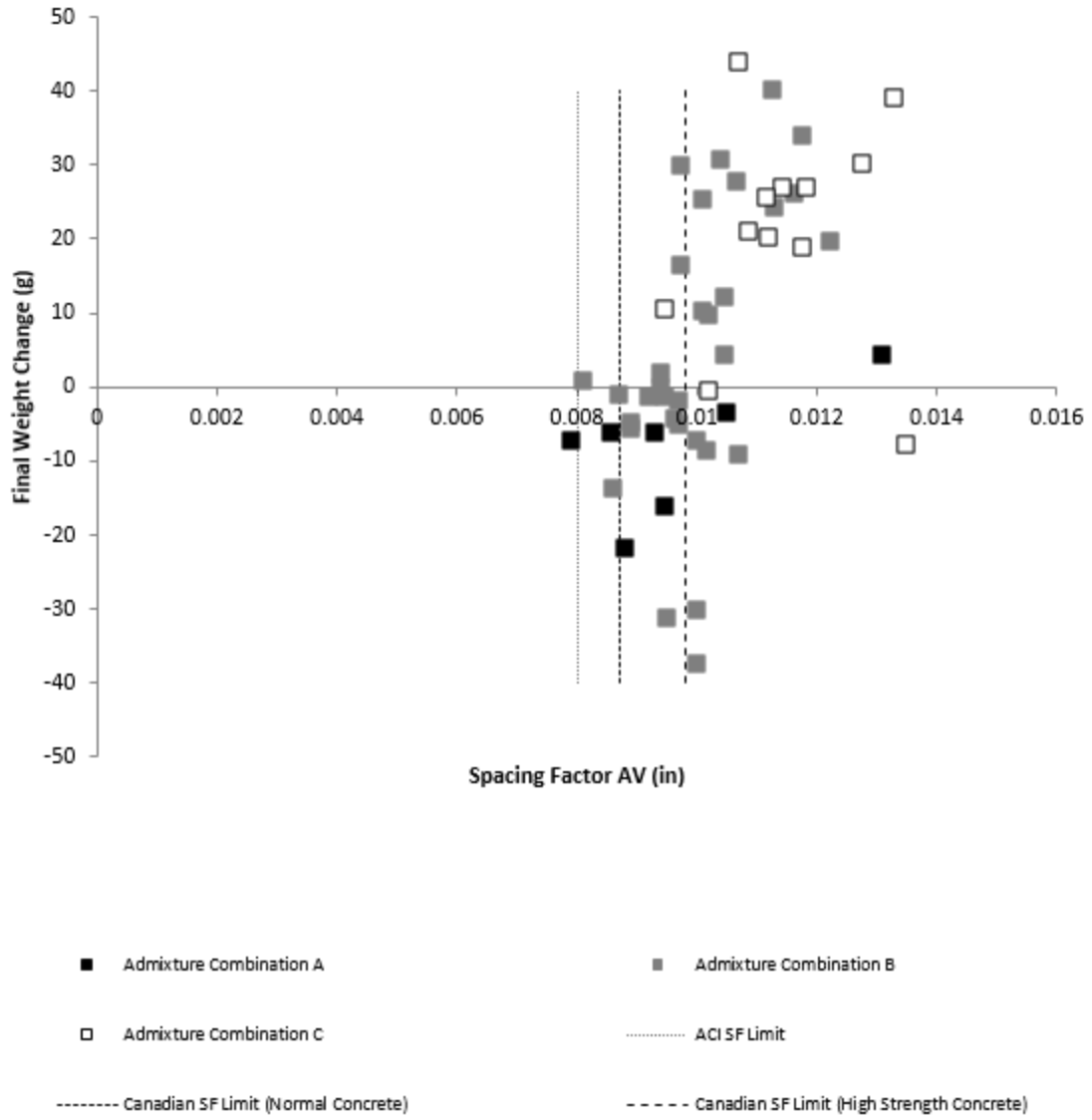


Figure 5.97. Final weight change vs. spacing factor after vibration

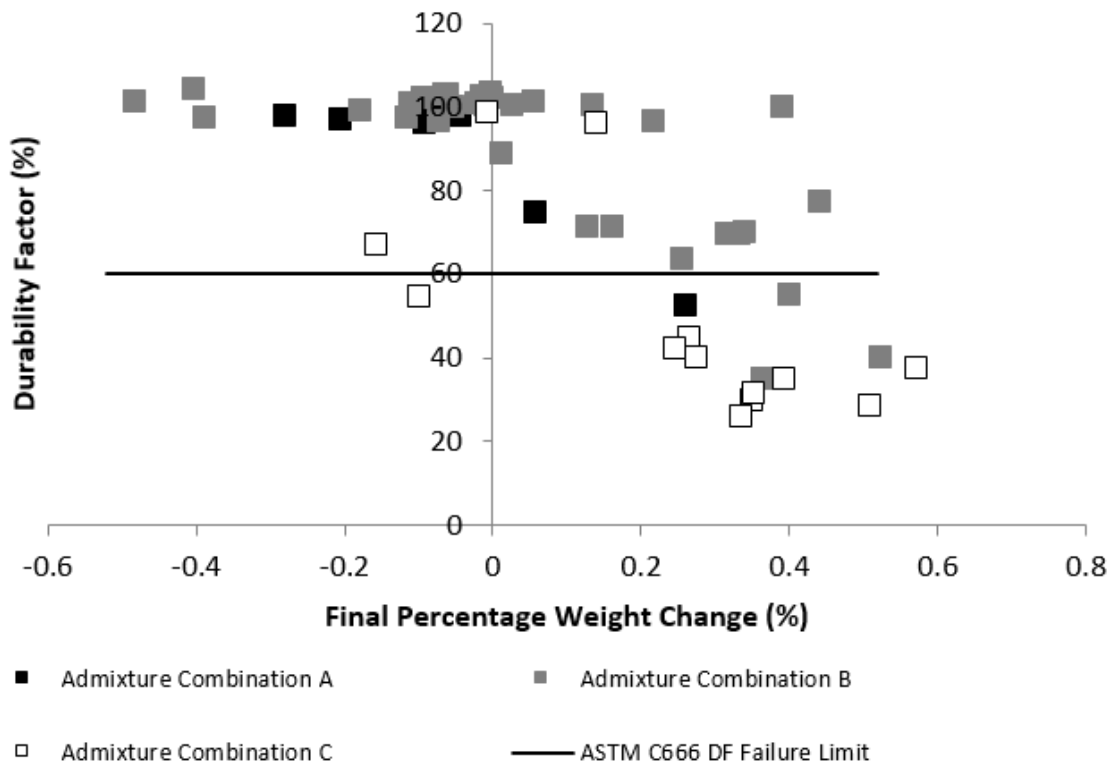


Figure 5.98. Durability factor vs. final weight change

5.4.2 Freeze-Thaw Durability of Internally-Vibrated Concrete

Figure 5.99 shows the rheological properties for all four concrete batches used in internally-vibrated concrete. The size of the markers in the figure corresponds to the initial air content of the particular mixture. Concrete rheological combination 4 batches were clearly more fluid than rheological combination 3 batches. Figure 5.100 and Figure 5.101 show the freeze-thaw performance of all mixtures versus the distance from the center of vibration. It seems that as the distance increases the probability of deterioration decreases. Figure 5.100 indicates that if sufficient air content was used, even the point of vibration could escape freeze-thaw damage. However, similar to what was found in the table vibration experiments, the more fluid concrete mixture (rheological combination 4) with the lower initial air content mixture at the point of vibration became susceptible to freeze-thaw failure. Figure 5.101, on the other hand, shows that the higher yield stress mixture had good durability even at the low initial air content. All concrete mixtures tested indicate that the influence of immersion vibrators is very local.

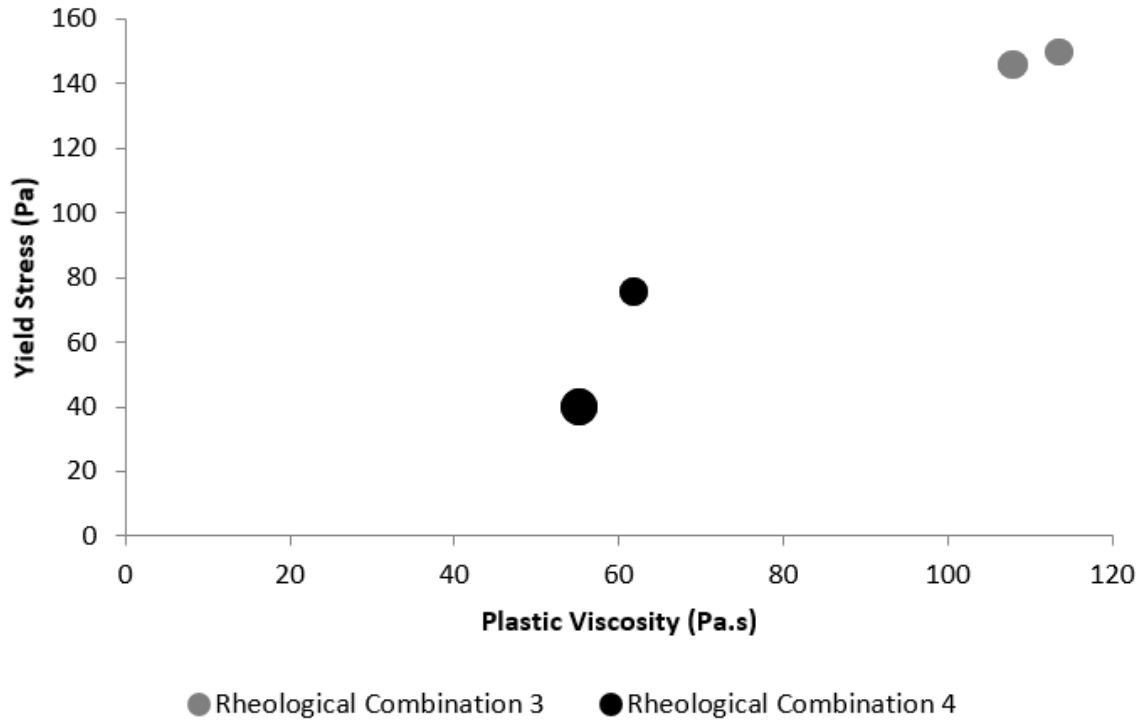


Figure 5.99. Rheological properties for the immersion vibrator experiment

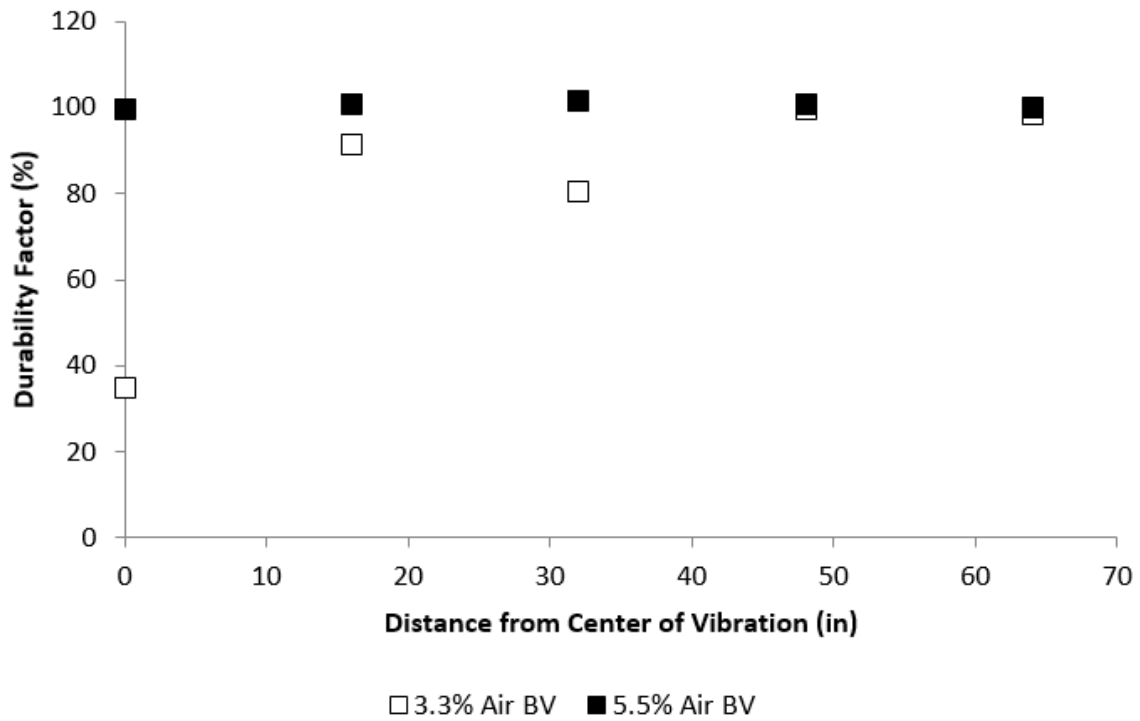


Figure 5.100. Freeze-thaw performance of rheological combination 4 (immersion vibrator experiment)

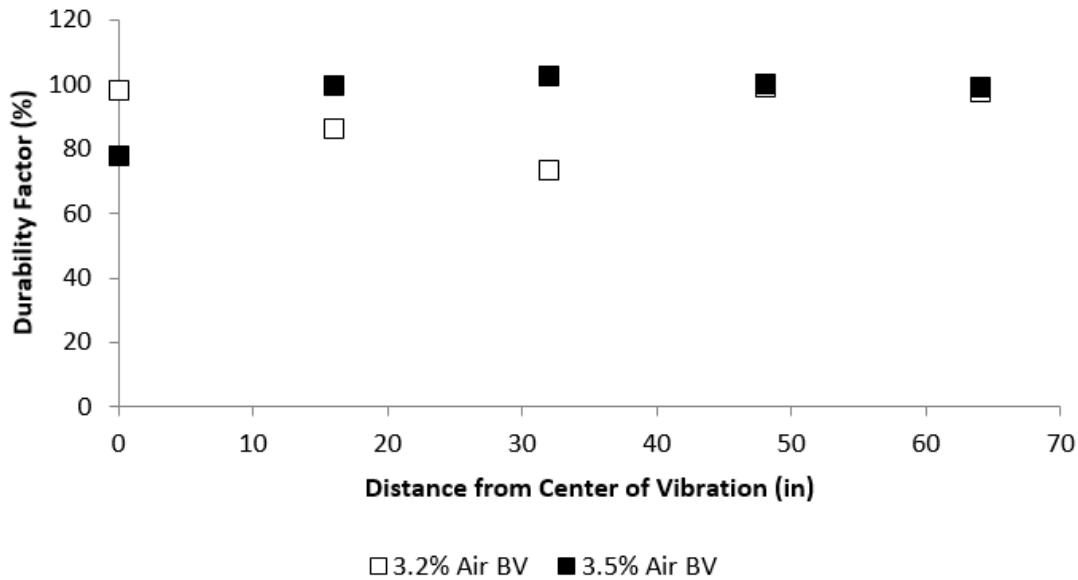


Figure 5.101. Freeze-thaw performance of rheological combination 3 (immersion vibrator experiment)

5.5 Conclusions

Based on the experimental results obtained, the following conclusions about the effects of concrete constituent materials and rheological properties on the air void system of vibrated concrete can be made:

- Delayed vibration increases air loss. This loss was found to be linear with time. Sometimes there is a delay between concrete mixing and placement because of equipment malfunction or other reasons. Independent of the concrete constituent materials used, delays should be limited to less than 30 minutes to avoid an increase the risk of freeze-thaw durability problems.
- Most of the air loss affecting freeze-thaw durability appears to occur during the initial few seconds of vibration. Longer periods of vibration cause large percentages of air loss, but only minimally affect the spacing factor. Vibration, even if only for a short period of time, can cause detrimental air loss.
- Increased vibration acceleration correlated with higher air void spacing factors and higher susceptibility to freeze-thaw damage. Vibration frequency and velocity showed minimal effect on the air system and the freeze-thaw durability.
- Concrete tie producers should closely monitor concrete fluidity. A concrete mixture with a normally stable air void system during vibration can experience a significant reduction in freeze-thaw durability from vibration when the fluidity is increased.
- The spacing factor limit for concrete measured after vibration can be increased to match that used by the Canadian Standards Association of 0.23 mm (0.009 in.) for normal strength concrete or 0.26 mm (0.0098 in.) for concrete with a specified 28-day strength greater than 70 MPa (10,000 psi) without increasing the risk of freeze-thaw durability.

Chapter 6 – Measurement of Plant Conditions

6.1 Introduction

The manufacturing process can significantly affect the air content of prestressed concrete railroad ties. To understand and quantify these effects, measurements of material properties and vibration exposure during concrete placement were made at three concrete tie manufacturing plants. Plants with unique placement and vibration mechanisms were observed in order to determine how differences in materials and fabrication techniques affect entrained air. Measurements at the three plants included fresh concrete air content, slump, unit weight, temperature, vibration measurements, rheology, and hardened air void sampling.

6.1.1 Concrete Railroad Tie Manufacturing Process

The manufacturing process in the three concrete railroad tie plants began with cleaning and oiling the formwork. Identification tags and rail shoulders were then placed in the form cavities for each tie as shown in Figure 6.1. Precast concrete factories usually have several lines of production in order to increase productivity. Each form that spans the entire bed length is called a cavity. A collection of adjacent cavities is called a casting bed, as shown in Figure 6.2 for Plant A and Figure 6.3 for Plant B. The final step in the manufacturing process before placing the concrete was to install reinforcing steel wires in the cavities of the casting bed, as shown in Figure 6.4. This installation process included running the wires through each cavity, applying initial stress in order to enforce the design pattern of the wires, and applying full design stress to the wires. Prestressed wires for one bed were tensioned together using the same hydraulic jack. After bed and wire preparation, the concrete was mixed and placed in the crosstie cavities. Concrete mixed at the three plants included the addition of chemical admixtures such as high range water reducer and air-entraining admixtures. After mixing, the batch operator sampled concrete to perform slump, fresh concrete air content, unit weight, and temperature tests to ensure that the concrete met specification. Upon completion of these tests, the operator dispensed the concrete into the delivery bucket, as shown in Figure 6.5. At Plant A and C, the delivery bucket brought the concrete to the casting machine and dispensed the concrete into the casting machine hopper (Figure 6.5). At Plant B, the delivery bucket traveled the length of the plant and delivered the concrete to a secondary bucket used to transport the concrete the width of the plant to the casting machine.



Figure 6.1. a) Forms cleaning and oiling, and b) shoulder installation in Plant A

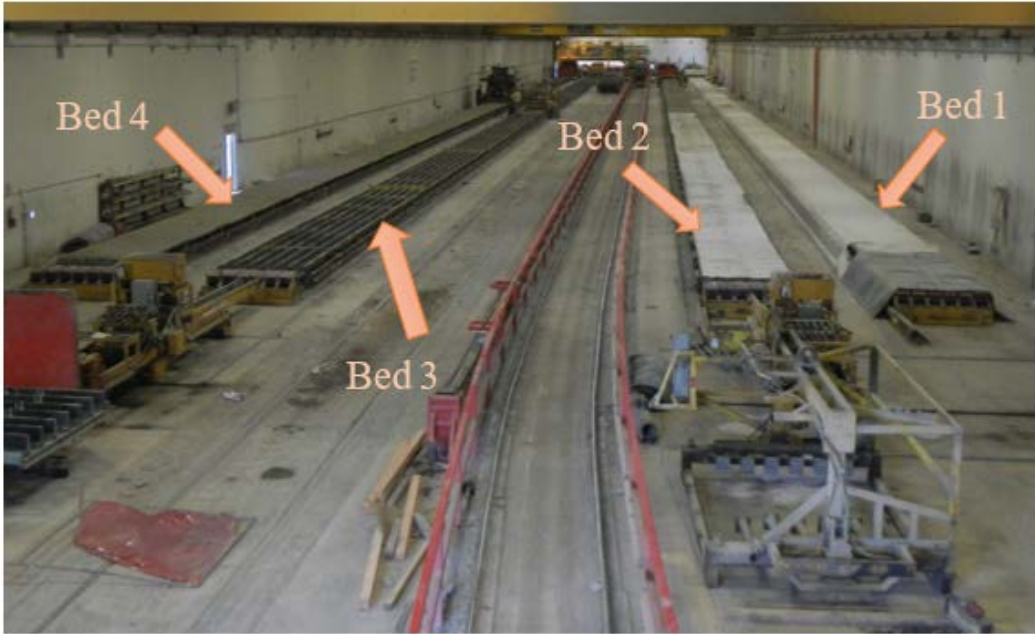


Figure 6.2. Casting beds in Plant A



Figure 6.3. Casting beds in Plant B



Figure 6.4. a) Reinforcing steel wires during installation, and b) enforcing the wire spacing pattern in Plant A

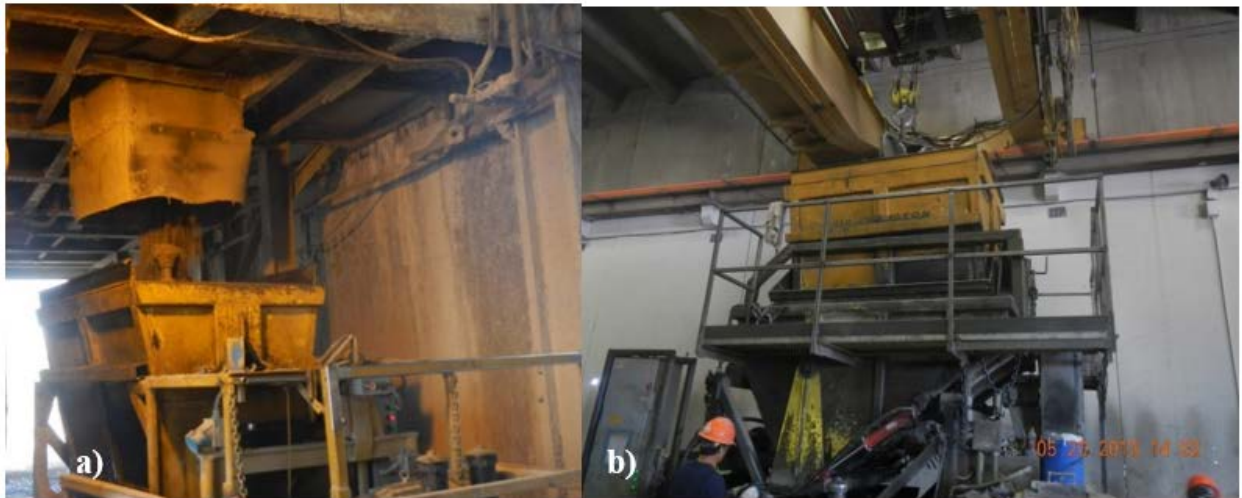


Figure 6.5. a) Dispensing concrete in the delivery bucket, and b) dropping concrete in the casting machine hopper in Plant A

In Plant A, the concrete was vibrated as it was placed into the six cavities of the bed using six tilted rod vibrators built into the casting machine, as shown in Figure 6.6. At Plant B, four tie cavities adjacent to one another were vibrated by a form vibrator attached to the bottom of the middle section of the cavities, located in the middle of the ties lengthwise, as shown in Figure 6.7. At Plant C, the vibration was performed using a handheld rod vibrator. The vibration duration and location varied depending on the operator of the vibrator at plant C.



Figure 6.6. Plant A vibration rods attached to the casting machine

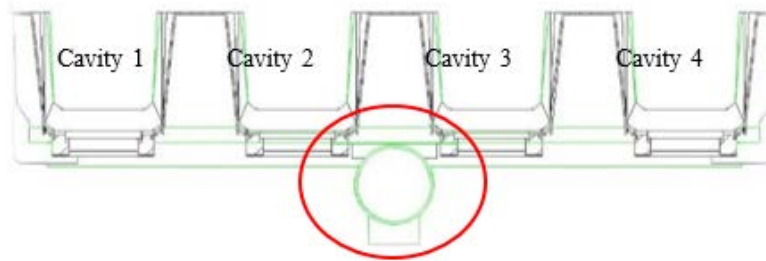


Figure 6.7. a) Plant B vibrator schematics with labeled cavities, and b) actual vibrator in position

Quality control samples for strength testing, slump, air content, unit weight, and temperature were taken once at the end of each bed. During the concrete placement and vibration, the placing crew followed the casting machine and finished the concrete surface. Because the concrete ties were placed upside down, the finished side became the bottom side of the tie. In Plant A, workers applied texturing to the surface for roughness. After finishing, the concrete was left to cure under nylon sheets until the concrete compressive strength met the required strength for detensioning the steel wires. Once the samples for compressive strength reached the required strength, the bed was detensioned slowly. The concrete ties were cast continuously in the longitudinal direction and saw-cut after detensioning into individual crossties. Figure 6.8 summarizes the crosstie manufacturing process in the three plants with the differences highlighted.

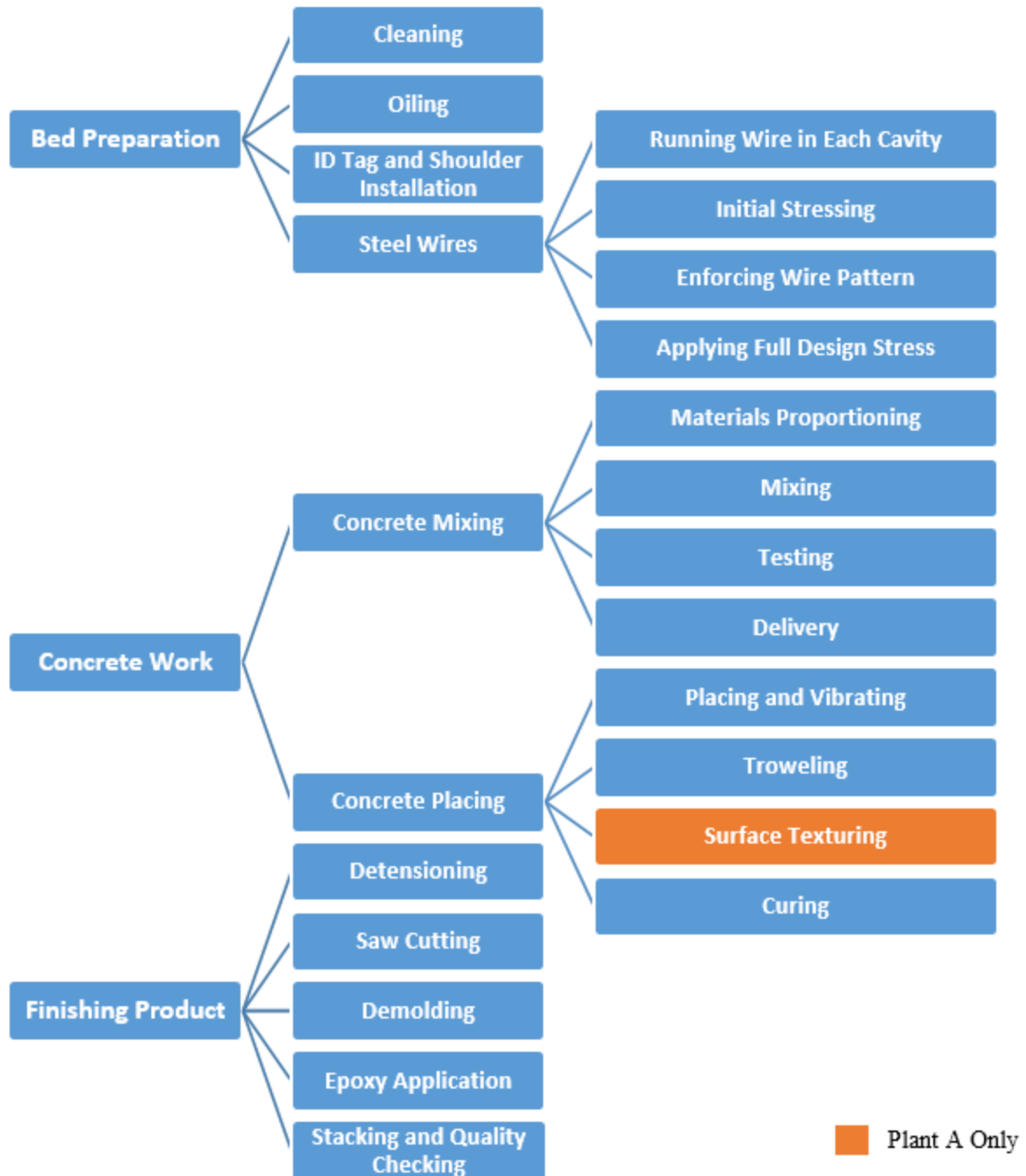


Figure 6.8. Summary of the entire manufacturing process of the three plants

6.2 Plant A – Immersion Vibrator on Placing Machine

Concrete was sampled for slump, air content, unit weight, and temperature tests twice per casting bed. The first sample was collected from the second concrete batch directly from the mixer. The second sample was collected from the 14th, 15th, or 17th concrete batch made per bed after concrete delivery to the casting machine. The exact batch number sampled depended on the total number of batches made per bed. In addition to these tests, hardened air void samples were

collected nine times per casting bed: three from the mixer (one from the 2nd batch, one from the 9th batch, and one from the 14th, 15th, or 17th batch), three from the casting machine before vibration (one from the 2nd batch, one from the 9th batch, and one from the 14th, 15th, or 17th batch), and three from the casting machine after vibration (one from the 2nd batch, one from the 9th batch, and one from the 14th, 15th, or 17th batch). All samples were collected between April 22, 2013, and May 17, 2013.

6.2.1 Fresh Concrete Properties

Slump, fresh air content, unit weight, and temperature were measured for concrete sampled from the mixer after transporting to the casting machine. The slump test was performed according to ASTM C 143 (2012) (ASTM Standard C 143/C 143M-12, 2012). This test gives an indirect indication of concrete yield stress since the concrete height stabilizes the moment its stress from gravity becomes less than the yield stress necessary for flow. A large drop in concrete height results in a high slump value and indicates a low yield stress. Concrete temperature and unit weight were measured according to ASTM C 1064 (ASTM Standard C 1064/C 1064M-12, 2012) and ASTM C 138 (ASTM Standard C 138, 2013), respectively. Air content was measured using the pressure method according to Method B in ASTM C 231 (ASTM Standard C 231, 2010). An ICAR Rheometer was used to measure the concrete rheological properties as described in Section 5.3.

In Plant A, rheology tests were performed on concrete sampled from the mixer because the concrete mixture was designed to have a high yield stress that increased during the handling process due to mixing water being absorbed by the aggregates. Once the concrete reached the casting machine, the concrete was too stiff to measure using the ICAR rheometer.

6.2.2 Vibration

Plant A used moving immersion vibrators in the casting process to consolidate low slump concrete. Because the submersible accelerometer could become entangled with the placing equipment, only surface-mounted accelerometers were used to measure concrete vibration. An accelerometer was fixed to the form and casting machine surface using a magnetic base in order to measure the frequency and amplitude of vibrators attached to the casting machine. Measurements taken on the casting machine gave a composite acceleration of the six immersion vibrators used in each tie cavity. Figure 6.9 shows the accelerometer attached to the casting machine in one of the locations before the test began.

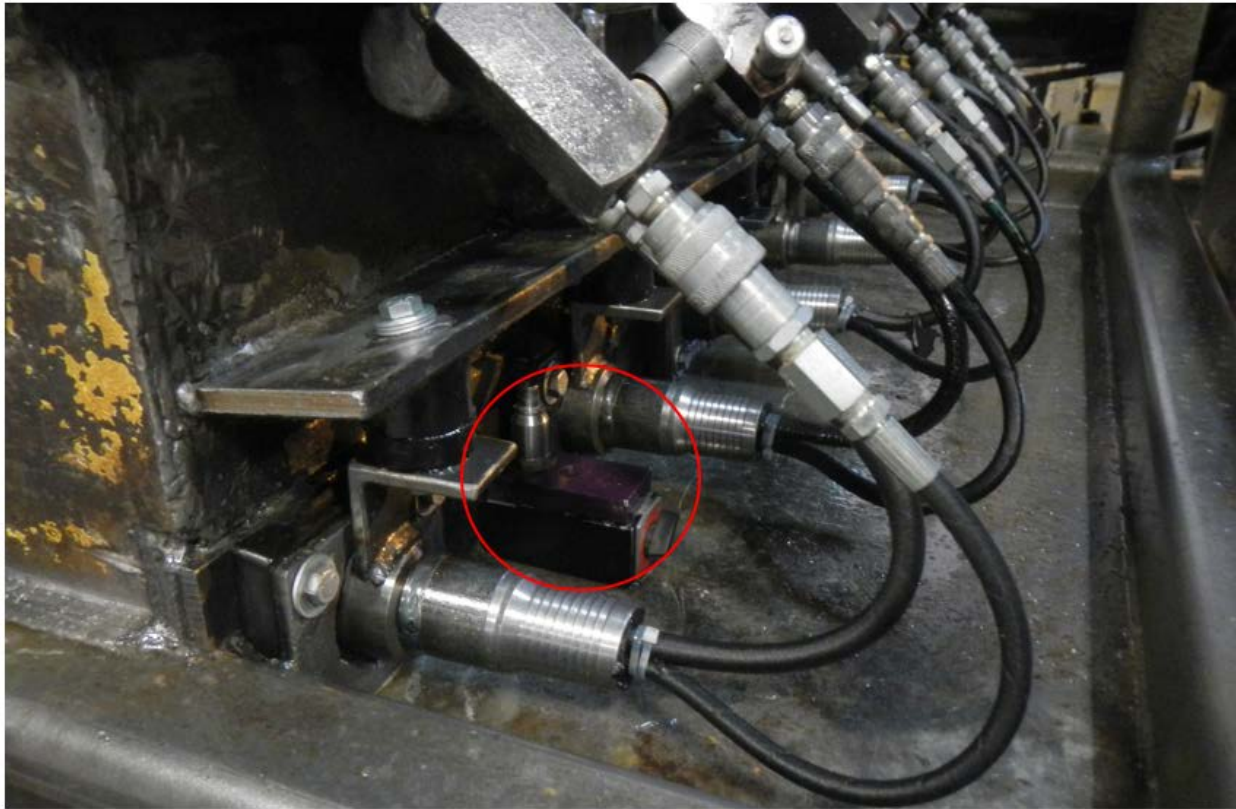


Figure 6.9. Accelerometer attached to the casting machine between two embedded vibrators

6.3 Plant B – Form Vibrator

The first sample was collected from the first concrete batch directly from the mixer. The second sample was taken from the fourth concrete batch at the casting machine level (before vibration). The third sample was also taken from the mixer, but it was sampled from the thirteenth concrete batch. The concrete fresh air content was measured each time the concrete was sampled. The concrete slump, unit weight, and temperature were measured on concrete sampled from the fourth batch and the thirteenth concrete batch from concrete collected from the casting machine.

In addition to these tests, hardened air void samples were collected six times per casting bed: two from the mixer (one from the first batch and one from the thirteenth batch), two from the casting machine before vibration (one from the fourth batch and one from the thirteenth batch), and two from the casting machine after vibration (one from the fourth batch and one from the thirteenth batch). Hardened air void samples were made from concrete collected from the casting machine and placed on top of the bed to vibrate for the entire period of casting for that bed in order to capture the effects of vibration on air content. Concrete samples at Plant B were collected between May 28, 2013, and June 21, 2013.

6.3.1 Fresh Concrete Properties

Concrete fresh air content, slump, temperature, and unit weight were measured at Plant B. Tests were performed on concrete sampled during discharge from the mixer into the conveyance bucket and from the concrete casting machine. Rheology measurements were performed on

concrete sampled from the mixer before delivery and after delivery to the casting machine at Plant B. Measurements with the ICAR rheometer included the stress growth test and the flow curve test.

6.3.2 *Vibration*

Form vibration was recorded using an accelerometer attached to the bed form, and concrete vibration was measured using a submersible accelerometer. The two accelerometers were set to record data at 20,000 Hz to ensure that sampling frequency was sufficiently higher than the concrete vibration frequency in order to obtain accurate measurements of concrete acceleration during the full range of a vibration cycle. The submerged accelerometer was installed on a setup that could be adjusted in order to measure various depths and widths. The depth of the submersible accelerometer was always measured from the bottom of the form upwards to the tip of the accelerometer. This setup included a magnet block attached to the top of the bed to ensure that the manufacturing process was not disturbed or affected by testing. Data were recorded at points along the bed at various depths in order to quantify vibration attenuation throughout the length of the crosstie. Figure 6.10 shows the two accelerometers in position to record vibration.



Figure 6.10. Two accelerometers in position for recording

Vibration recording lasted for approximately 10 seconds in most locations. Figure 6.11 shows the locations for recording vibration along the depths of the ties in their molds. Figure 6.12 and Figure 6.13 show the locations along the length, width and depth of the crosstie when measurements were taken.

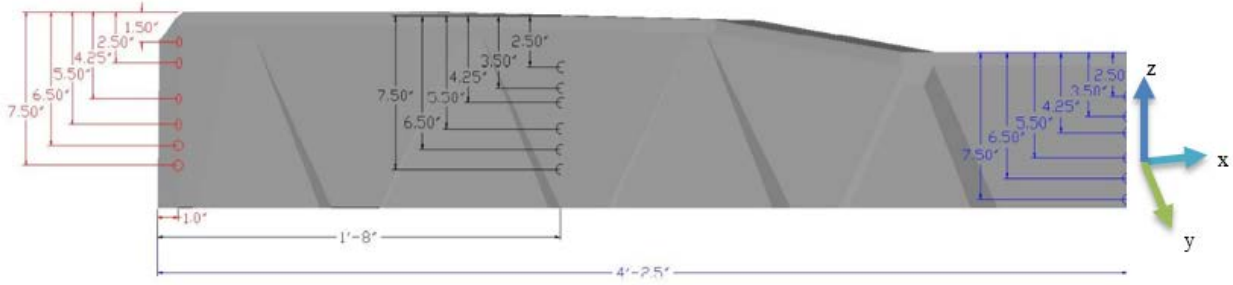


Figure 6.11. Vibration measurement depth location

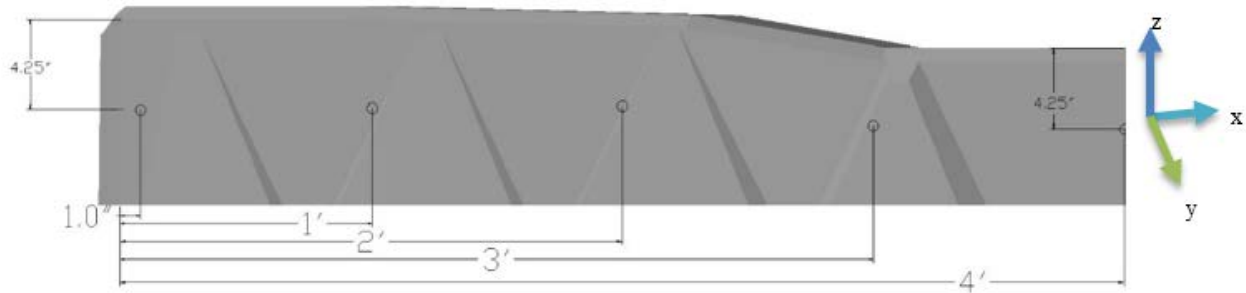


Figure 6.12. Half-tie representation for vibration measurement locations for 1-ft intervals (measurements were taken on the other end of the tie)

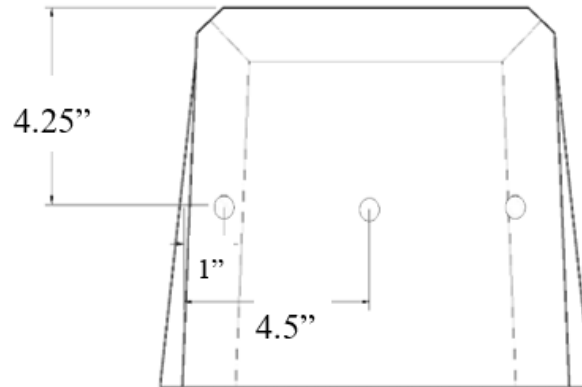


Figure 6.13. Vibration measurement locations for width of tie

Vibration measurements were taken along the length of the tie with two different intervals fixed at a depth of 4.25 in. Vibration measurements were recorded in the cross-tie width direction, as shown in Figure 6.13. In addition to these sets, vibration was recorded for the entire bed vibration period using the exterior accelerometer (form accelerometer) and for 15 minutes using the submersible accelerometer. The submersible accelerometer was removed after 15 minutes of immersion in the concrete because of low measured acceleration and because additional time in the concrete would cause difficulty in removing the sensors from the rapidly stiffening concrete or prevent reconsolidation of the concrete after sensor removal. Both accelerometers were installed at the beginning of the bed at 1 in. from the beginning of the tie in Cavity 1.

6.4 Plant C – Handheld Immersion Vibrator

Concrete was sampled three times for each batch. The first sample was collected directly from the mixer. The second sample was taken from the forms (before vibration). The third sample was also taken from the form, but was sampled after concrete vibration. The concrete fresh air content was measured from the first and second samples collected. The concrete unit weight, and temperature were measured on concrete sampled from the mixer. Plant C used concrete with properties near those of self-consolidating concrete.

In addition to these tests, hardened air void samples were collected for every batch: one from the mixer, one from the form before vibration, and one from the form after vibration. Concrete samples made for hardened air void analysis were not rodded or consolidated in any way in the sample containers after sampling. Concrete samples at Plant C were collected between August 4, 2014, and August 7, 2014.

6.4.1 Fresh Concrete Properties

Concrete fresh air content, temperature, and unit weight were measured at Plant C. Tests were performed on concrete sampled from the mixer and from the concrete forms. Rheology measurements were performed on concrete sampled from the mixer. Measurements with the ICAR rheometer included the stress growth test and the flow curve test.

6.4.2 Vibration

Plant C used handheld immersion vibrators to consolidate the concrete. Because the vibration induced by the handheld vibrator varies from one operator to another depending on the duration of vibration, the depth at which the vibrating rod was inserted, the angle of the vibrator and the location along the length of the tie, only the maximum acceleration and frequency were examined. Similar to the setup at Plant B the setup at Plant C included two accelerometers, one attached to the forms and another immersed in the concrete at variable depths.

6.5 Hardened Air Analysis

Hardened air void samples were made by placing the concrete in boxes with dimension of 3.5 x 4.5 x 6 in. and allowing them to harden undisturbed in-place. Samples were saw-cut and polished before scanning on a flatbed scanner. The saw-cut samples had a trapezoidal shape with parallel side dimensions between 4.5 and 5.5 in. The sample cut cross-section height was typically 6 in. Thickness of the saw-cut samples averaged 1 inch. Samples were polished for hardened air void analysis following the procedure outlined in Section 5.3.

After polishing, the samples were scanned in three steps using a modified procedure developed by Peterson (2001). Figure 6.14 presents an example of the three different scans taken of a sample. The original polished, untreated sample was scanned using a high-resolution desktop scanner, as shown in Figure 6.14a. After scanning the polished samples, the samples were treated with a phenolphthalein solution (1 percent w/v phenolphthalein indicator in 95 percent v/v alcohol) in order to stain the cement matrix pink or purple, as shown in Figure 6.14b. Phenolphthalein turns color in a pH above 10, and uncarbonated cement pastes typically have a pH above 13. The stain helped distinguish the cement matrix from the aggregates during image processing. After scanning the phenolphthalein-treated sample, the sample was covered with fluorescent orange chalk powder, and a rubber stopper was used to force the powder into the air

voids. Finally, the orange powdered polished sample was wiped in order to remove any powder residue not in an air void on the sample before scanning. Due to the high cost and lengthy process of scanning and analyzing an entire concrete sample, utilization of a three-dimension sample to scan a slice or a section of a concrete sample and to use as a base in order to generalize the entire sample is more efficient and can achieve a good level of generalization of air properties. Tested samples had a minimum area of 12 in², which met the ASTM C457 requirement for two-dimension image analysis results to approach three-dimension results. Testing performed by Peterson in 2001 showed that the resolution of scanned images affected the results in term of spacing factor and size distribution of air voids, but it had only a limited effect on air content (Peterson, K., 2001). Scans were taken using a resolution of 4800 dpi, resulting in a pixel length of 5.5 micrometers.

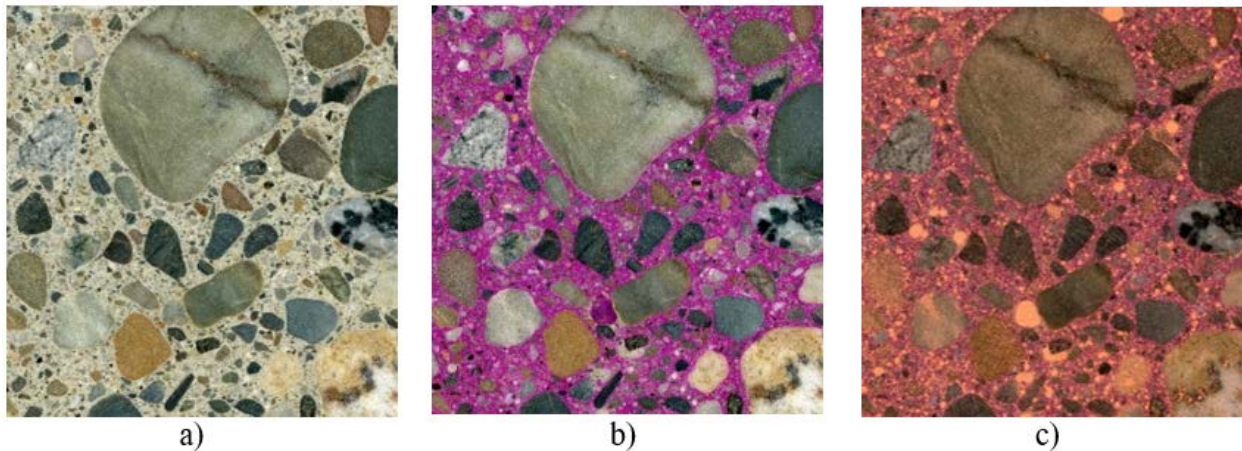


Figure 6.14. Scans of a) polished sample untreated, b) polished sample treated (with phenolphthalein), and c) polished sample powdered with orange chalk

Image processing software was used to separate the three main elements of the image: the paste, aggregate, and air voids. An example of this image classification is shown in Figure 6.15 for sample scans in Figure 6.14. Figure 6.15a shows the sample after detection of the aggregate, and Figure 6.15b shows air voids after detection. The paste is the area not defined as an aggregate or air void. Separated images were assigned unique colors and laid on top of each other in order to form the three-color simplified image shown in Figure 6.16.

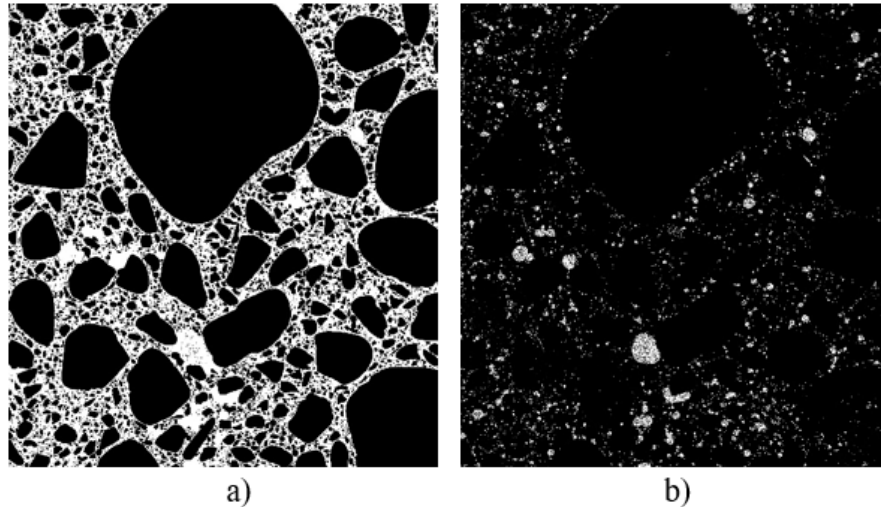


Figure 6.15. a) Aggregate image, and b) Air void image

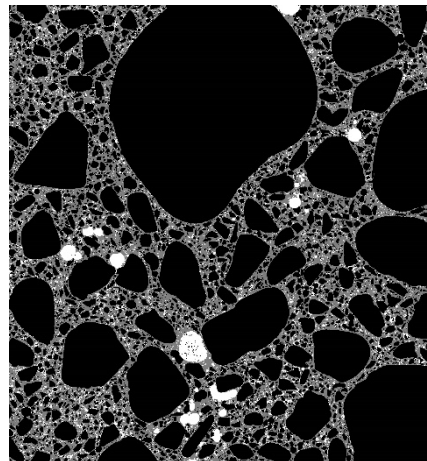


Figure 6.16. Three-color simplified image (black: aggregate; gray: paste; white: air)

A software used principles from the linear traverse method and calculations described in ASTM C457 in order to calculate the air void spacing factor in every sample. Every pixel across the height of the specimen was examined in order to measure various cord lengths of the paste, aggregate, and air. White pixels that represented air voids were counted and divided by the entire number of pixels in the image in order to calculate the total air content (A). Paste content (p) was also calculated by dividing the number of gray pixels by the entire number of pixels in the image. Equation 6.1 represents the linear traverse method for calculating the spacing factor according to ASTM C457 (ASTM Standard C 457, 2012).

$$\begin{aligned}
 & \text{Spacing Factor } (\bar{L}) \\
 & = \begin{cases} \frac{T_p}{4N} & \text{for } p/A < 4.342 \\ \frac{3T_a}{4N} \left[1.4 \left(1 + \frac{p}{A} \right)^{\frac{1}{3}} - 1 \right] & \text{for } p/A > 4.342 \end{cases} \quad \text{Equation 6.1}
 \end{aligned}$$

where T_p is the traverse length through paste (*pixels*), T_a is the traverse length through air (*pixels*), and N is the total number of air voids intersected.

6.6 Results and Discussion

Concrete fresh air content, slump, unit weight, temperature, and rheological parameters were measured. Table 6.1 summarizes the average fresh concrete parameters at the three Plants. Plant B had, on average, higher fresh concrete air content than Plant A, but also higher air loss during handling. The stiff concrete of Plant A lost an average of 0.6 percent air during handling compared to 3.0 percent air lost from the concrete from Plant B. The increased air content loss corresponded to the low concrete yield stress of concrete used in Plant B as measured by the static yield stress and slump test. The high viscosity measured for concrete from Plant B confirmed visual observations of the stickiness of concrete from Plant B. The average concrete static yield stress and plastic viscosity increase at Plant B between the mixing and the casting machine was most likely from the aggregate-absorbing mixing water. Table 6.2 summarizes the hardened air average and standard deviations for samples collected at both plants and the average fresh air content associated with these specimens.

Table 6.1. Experimental Results at Plant A, Plant B and Plant C

Plant		A		B		C		
Calculation		Average	Std. Dev	Average	Std. Dev	Average	Std. Dev	
Temperature, °C (°F)		21.1 (70)	2.1 (3.74)	31.94 (89.5)	1.8 (3.24)	28.2 (82.7)	0.53 (0.96)	
Unit Weight, kg/m ³ (lb/ft ³)		2292 (143.1)	21.5 (1.34)	2258.6 (141)	21.3 (1.33)	2285.8 (142.7)	49.8 (3.11)	
Theoretical Air content (%) (ASTM C138)		5.1	0.18	8.1	0.64	-	-	
Air Content (%)	At Mixer	7.1	0.65	9.7	1.18	4.87	1.97	
	At QC	6.5	0.64	6.8	0.94	3.09	0.37	
	Loss	0.6	0.40	3.0	1.49	1.5	0.75	
Slump, mm (in)	At Mixer	101.6 (4)	14.99 (0.59)	-	-	-	-	
	At QC	48.26 (1.9)	12.19 (0.48)	226.06 (8.9)	11.43 (0.45)	-	-	
	Loss	50.8 (2)	14.22 (0.56)	-	-	-	-	
Static Yield Stress, Pa (lb/ft ²)	At Mixer	1499 (29.24)	640 (13.37)	752 (15.71)	303 (6.33)	163.58 (3.42)	69.67 (1.46)	
	At QC	-	-	715 (14.93)	467 (9.75)	-	-	
Bingham Parameters	Dynamic Yield Stress, Pa (lb/ft ²)	At Mixer	825 (17.23)	604 (12.61)	208 (4.34)	144 (3.01)	16.21 (0.34)	12.22 (0.26)
		At QC	-	-	143 (2.99)	148 (3.09)	-	-
	Plastic Viscosity, Pa·s (lb·s/ft ²)	At Mixer	145 (3.03)	48 (1.003)	192 (4.01)	37 (0.77)	60.92 (1.27)	21.33 (0.45)
		At QC	-	-	345 (7.21)	102 (2.13)	-	-

Table 6.2. Measured Air Void Systems for Plant A, Plant B and Plant C

Plant		A		B		C	
Calculation		Average	Std. Dev	Average	Std. Dev	Average	Std. Dev
After Vibration (AV)	Air Content (%)	5.5	1.8	6.2	2.1	5.9	1.8
	Spacing Factor (in)	0.0065	0.0041	0.0086	0.0026	0.0075	0.0032
Before Vibration (BV)	Air Content (%)	7.6	2.3	8.4	1.5	5.6	1.7
	Spacing Factor (in)	0.0047	0.0029	0.0058	0.0012	0.0078	0.0033
Mixer (M)	Air Content (%)	9.5	2.4	9.6	1.5	8.0	2.6
	Spacing Factor (in)	0.0043	0.0021	0.0048	0.0009	0.0087	0.0062
Mixer Fresh Air (%)		7.5	0.6	10.3	1	4.9	2.0
Placing Machine Fresh Air (%)		6.7	0.7	7.2	1.2	3.1	0.4
Gravimetric Air content (%) (ASTM C138)		5.1	0.18	8.1	0.64	-	-

The concrete-hardened air content for Plant A was 2 percent higher when sampled from the mixer compared to the fresh concrete air content. The concrete in the stiff concrete mixture used in Plant A possibly contained higher amounts of entrapped air that were easily removed during rodding in order to consolidate the concrete in the pressure-based fresh air content test ASTM C231. However, samples made to measure the hardened air content were not consolidated. Concrete sampled at Plant C showed similar trends.

The hardened air void system for concrete sampled after vibration from Plant C had a slightly higher air content than concrete sampled before vibration. It is likely that this occurred because the concrete sampled before and after vibration was scooped out of the top of the forms because prestressing wires blocked access to concrete below the top level of reinforcing steel. It is likely that vibration caused entrained air from under the top row of reinforcing steel to migrate to the top of the concrete, concentrating at the top before exiting the concrete. These results showed that sampling concrete from the top couple of in. of the concrete to make freeze-thaw specimens results in biased samples that may not be representative of the majority of the concrete tie volume.

Fresh concrete air content measurements were taken at two separate times in the manufacturing process: one sample from the mixer and one sample from the placing machine. At Plant A, the concrete air content measured from concrete sampled from the mixer varied from 5.8 to 8.8 percent with an average of 7.1 percent and a standard deviation of 0.65 percent. The air content at the placing machine ranged from 5.3 to 7.3 percent with an average of 6.5 percent and a standard deviation of 0.64 percent. The reduction in air content between the mixer level and the Quality Control laboratory (QC lab) was very low, typically less than 1 percent. The calculated gravimetric air content varied between 4.14 percent and 8.5 percent with an average of 6.96

percent and a standard deviation of 1.04 percent. Figure 6.17 shows air content by the gravimetric method (ASTM C 138) as compared to air content measured using the pressure method (ASTM C 143).

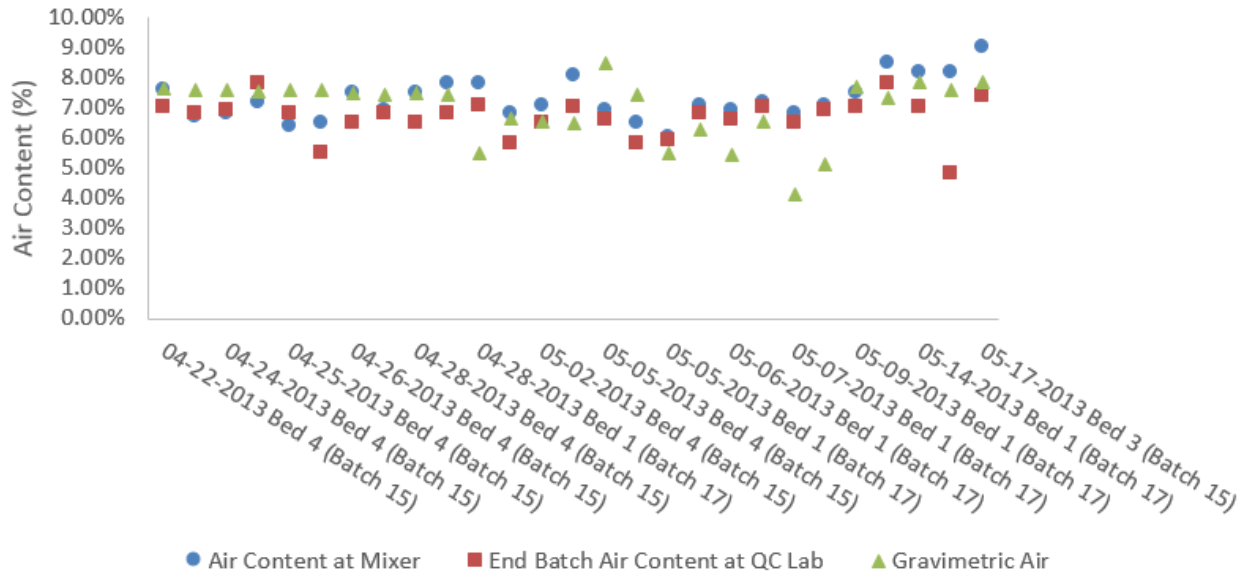


Figure 6.17. Air content of fresh concrete at Plant A

Figure 6.18 shows air content measured for Plant B from May 28, 2013, to June 21, 2013. The air content at the mixer level varied from 7.8 to 11.8 percent with an average of 9.7 percent and a standard deviation of 1.18 percent. The air content at the placing machine ranged from 5.3 to 8.3 percent with an average of 6.8 percent and a standard deviation of 0.94 percent. This higher reduction was likely due to the lower yield stress that created less resistance to bubbles rising and exiting the concrete during handling. The calculated gravimetric air content varied between 6.5 percent and 8.4 percent with an average of 8.1 percent and a standard deviation of 0.64 percent.

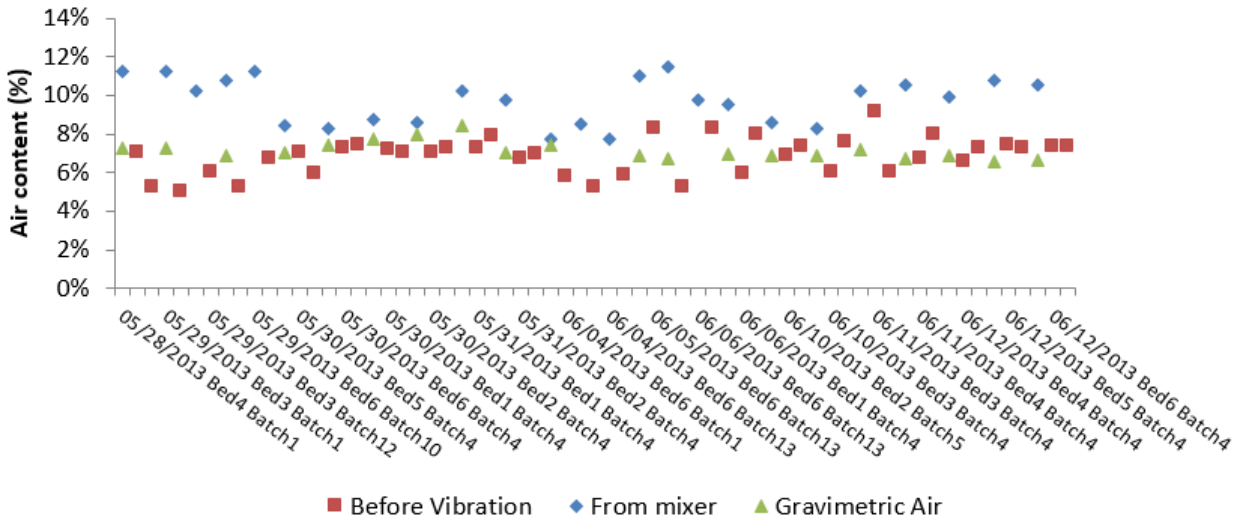


Figure 6.18. Air content of fresh concrete at Plant B

Figure 6.19 shows air content measured for Plant C from August 4, 2014, to August 7, 2014. The air content at the mixer level varied from 3.8 to 5.9 percent with an average of 4.9 percent and

a standard deviation of 2 percent. The air content at the placing machine ranged from 2.6 to 3.6 percent with an average of 3.1 percent and a standard deviation of 0.4 percent. This higher reduction was likely due to the lower yield stress that creates less resistance to bubbles rising and exiting the concrete during handling. The decreased air content could be also attributed to the use of concrete with properties near that of self-consolidating concrete.

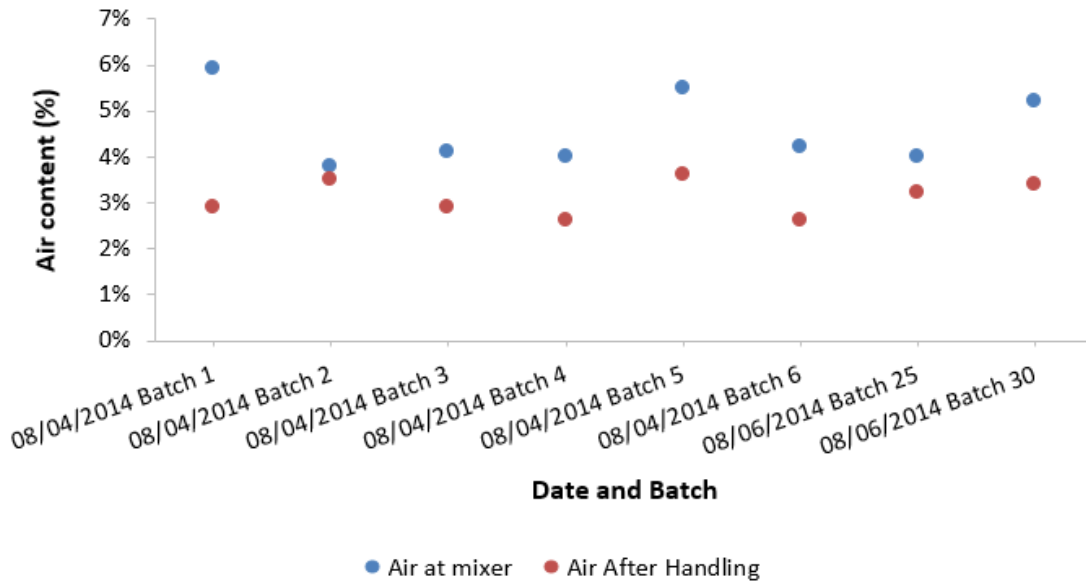


Figure 6.19. Air content of fresh concrete at Plant C

The concrete air content decreased significantly during the handling and consolidation operations. The hardened air content decreased from 9.5 percent to 5.5 percent for Plant A and from 9.6 percent to 6.2 percent for Plant B during the placement and consolidation operations. Figure 6.20 shows a comparison of concrete-hardened air content versus fresh air content for companion samples taken at various stages in the manufacturing process at Plant A. Spacing factors of companion concrete-hardened air void samples are shown in Figure 6.21. On average, spacing factors increased with additional handling and processing, however, the material standard deviation increased. The average spacing factor for the concrete remained below the commonly cited threshold of 0.008 in. required for good freeze-thaw performance (Meininger, R., and Tanesi, J., 2006). For each group, the average of all samples based on the location in the manufacturing process was calculated.

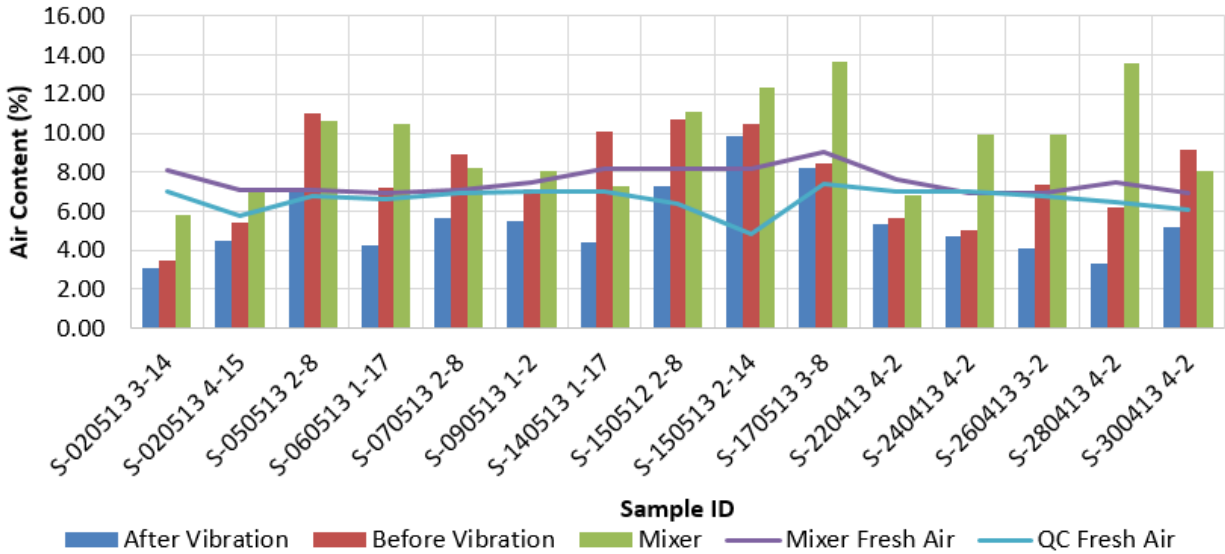


Figure 6.20. Concrete-hardened air content versus fresh air content at various stages of manufacturing process at Plant A

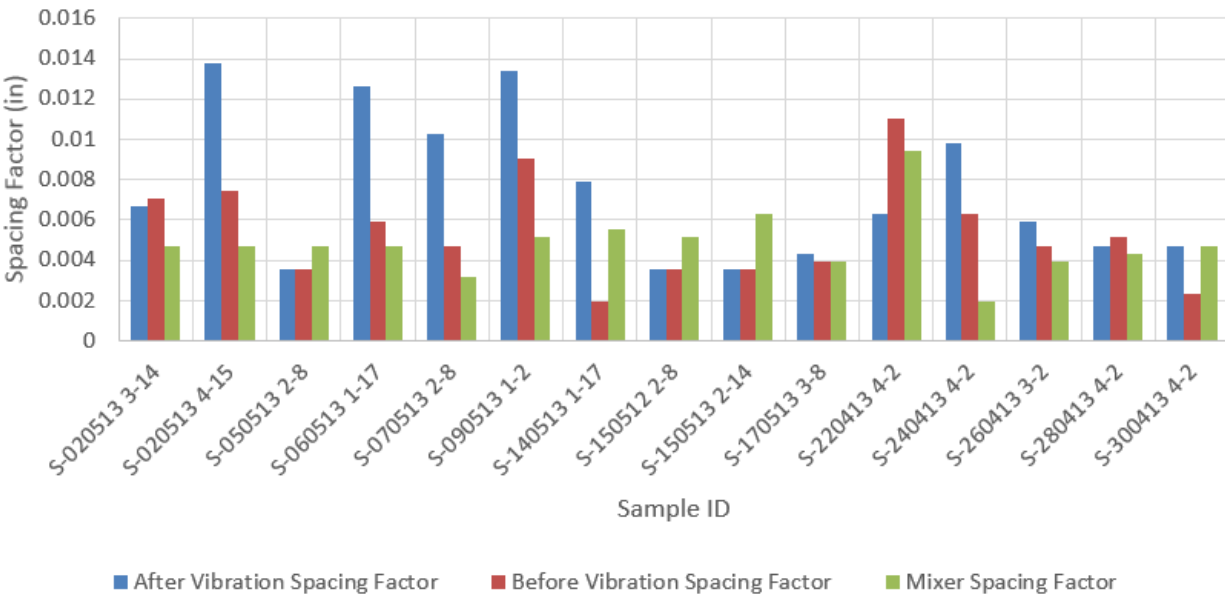


Figure 6.21. Air spacing factor at various stages of manufacturing process at Plant A

Figure 6.22 shows concrete-hardened air content versus fresh air content for companion specimens at various manufacturing stages at Plant B. Spacing factors increased more from vibration in Plant B than Plant A, as shown in Figure 6.23, potentially due to the low concrete yield stress and the use of form vibrators instead of immersion vibrators. Form vibrators imparted vibration to the concrete over a longer period of time and at a higher frequency of vibration than immersion vibrators used in Plant A. Figure 6.24 shows the difference in air void distribution between Plant A and Plant B. Plant A produced concrete with 50 percent of the air

voids smaller than 0.009 in. (0.23 mm) compared to concrete from Plant B that contained only 36 percent of the voids smaller than 0.009 in. (0.23 mm).

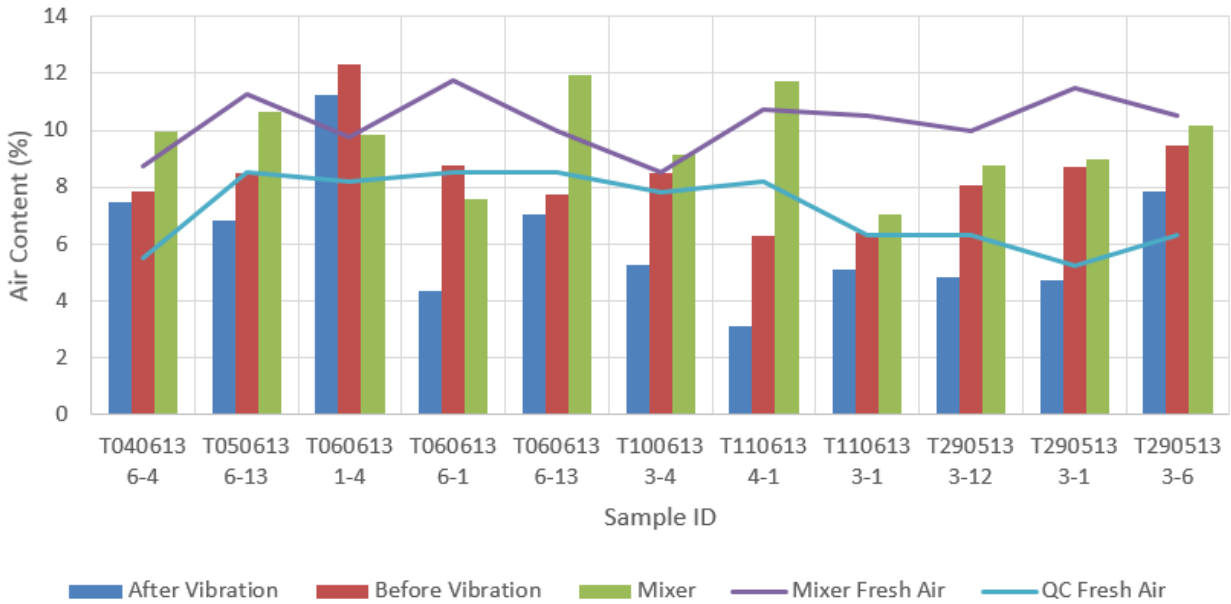


Figure 6.22. Concrete-hardened air content versus fresh air content at various stages of the manufacturing process at Plant B

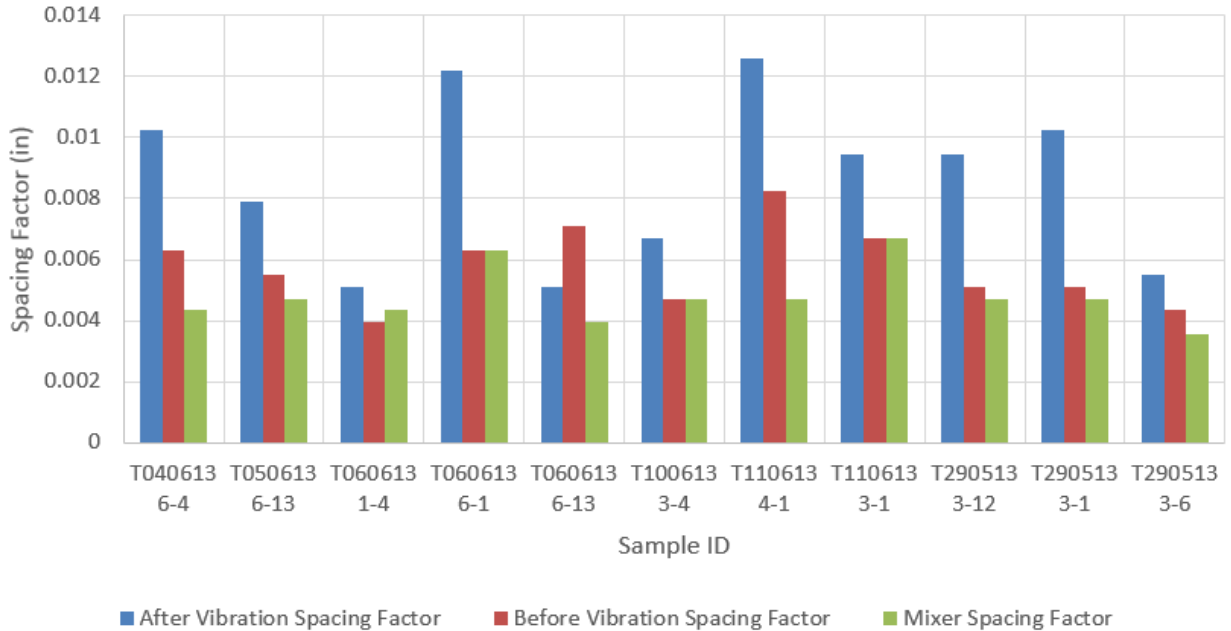


Figure 6.23. Air spacing factor at various stages of the manufacturing process at Plant B

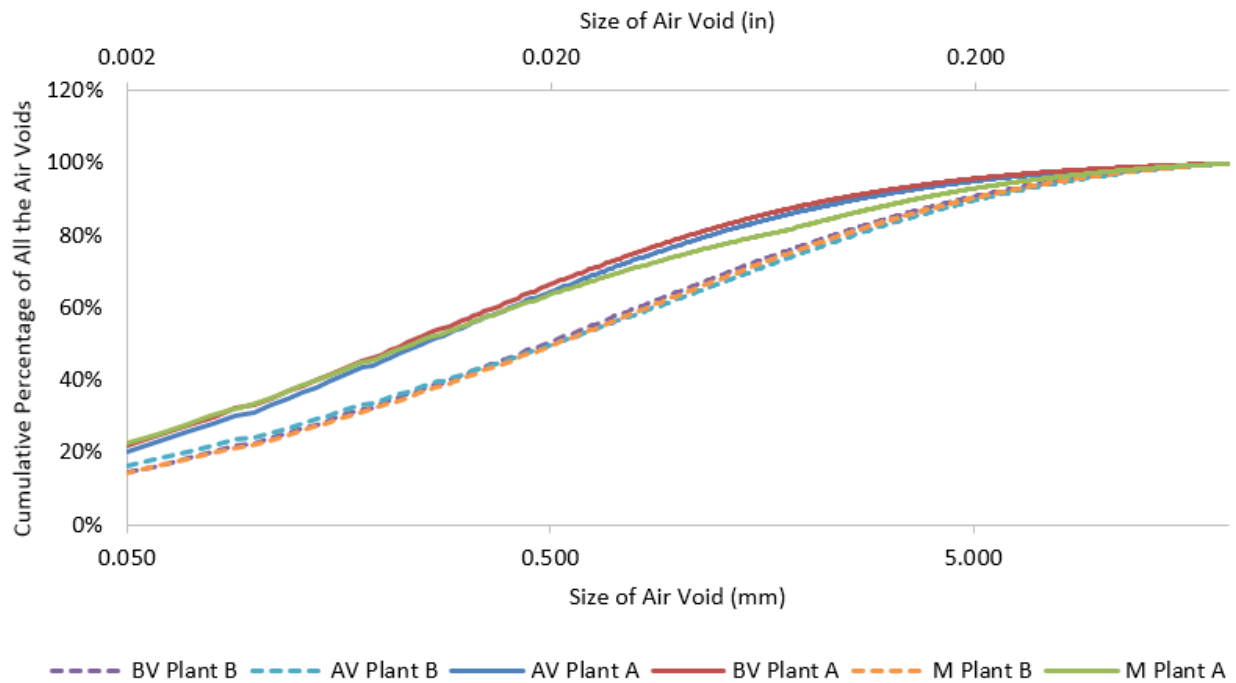


Figure 6.24. Average air void size distribution after vibration (AV), before vibration (BV), and mixer (M) samples for Plants A and B

Figure 6.25 shows concrete-hardened air content at various manufacturing stages at Plant C. Spacing factors for this plant do not appear to have a consistent pattern, as shown in Figure 6.26, potentially due to the use of a handheld immersion vibrator and sampling concrete from the top of the forms after vibration. The handheld immersion vibrator could vibrate the concrete in a less predictable pattern than form-mounted vibrators or fixed immersion vibrators. In addition, the use of handheld vibrators imparted vibration to the concrete at a higher frequency of vibration than seen from immersion and form vibrators used in Plant A and B.

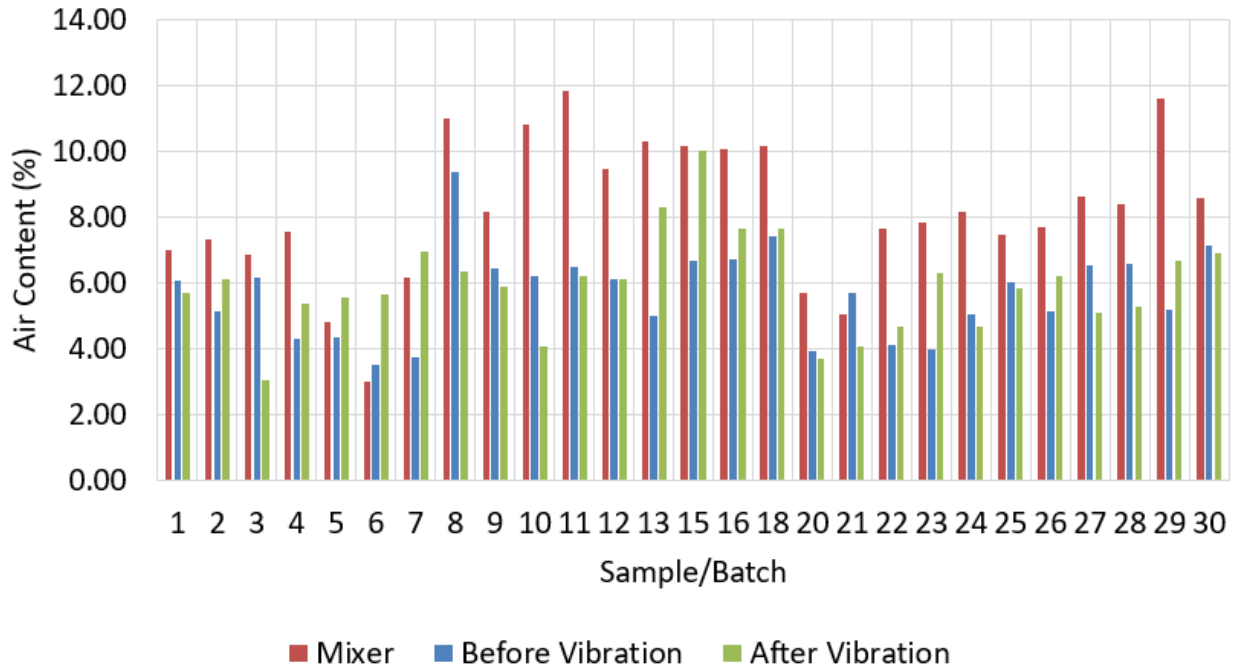


Figure 6.25. Concrete-hardened air content at various stages of the manufacturing process at Plant C

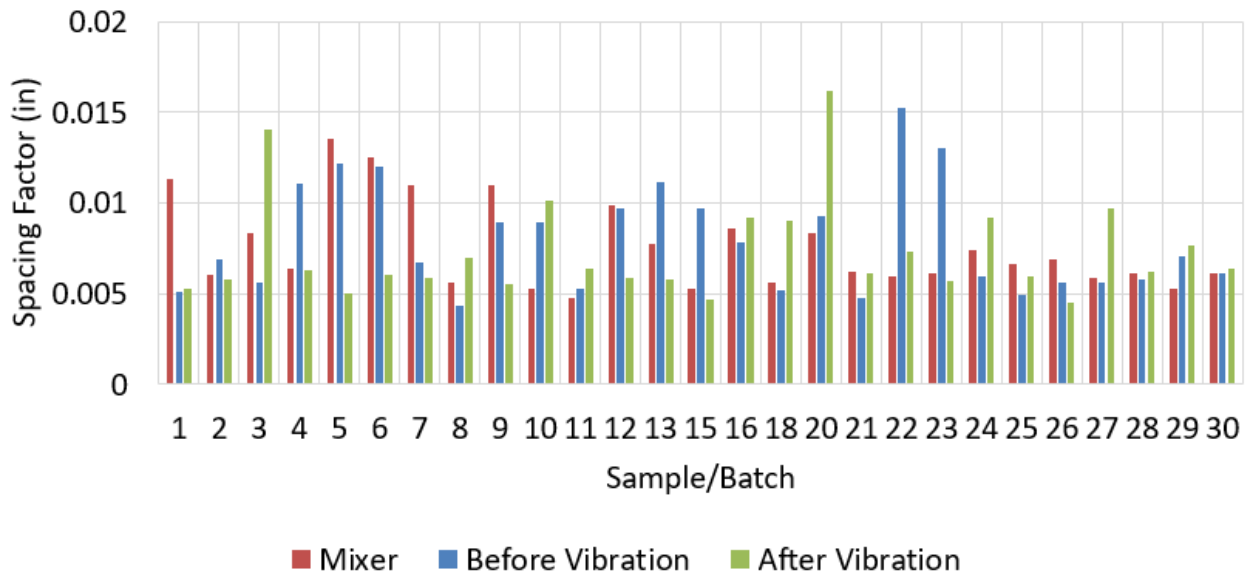


Figure 6.26. Air spacing factor at various stages of the manufacturing process at Plant C

Figure 6.27 shows variation in the fresh concrete unit weight measured at Plant A. The range of measured unit weights during the testing period was 140 to 145.3 lb/ft³ (2242 to 2327 kg/m³). Variation in the fresh concrete temperature is shown in Figure 6.28 with values ranging from 65 to 80 °F (18.3 °C to 26.7 °C). Figure 6.29 shows measured slump values. The reduction ranged from 3 in. to 0.5 in. with an average reduction of 2 in. (50.8 mm) and a standard deviation of 0.56 in. (14.2 mm).

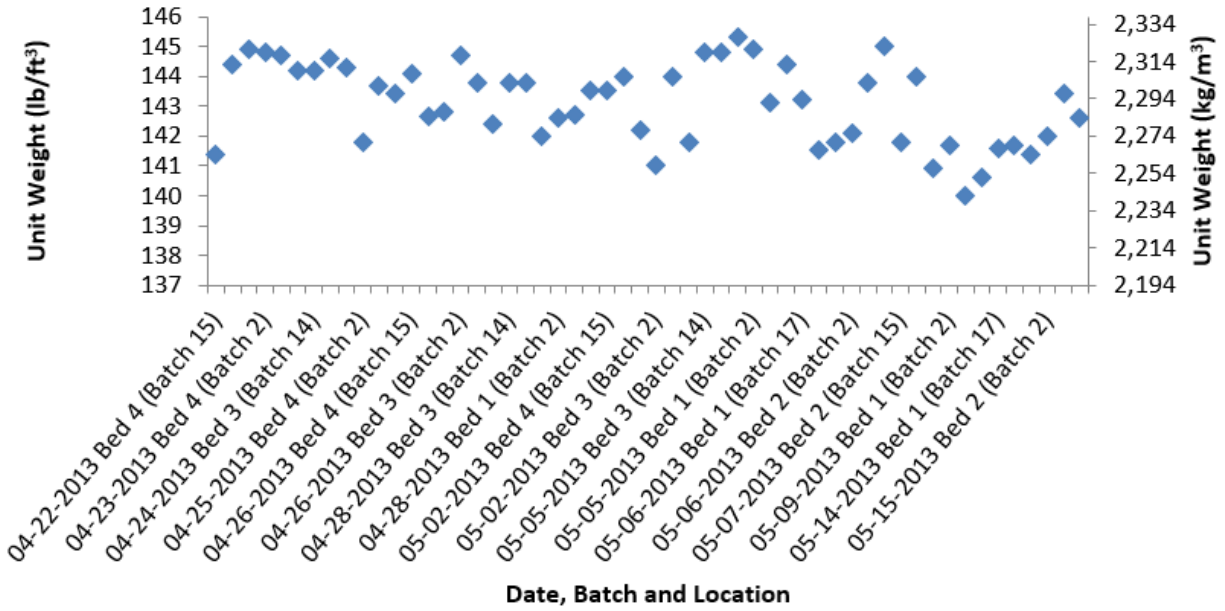


Figure 6.27. Concrete unit weight at Plant A

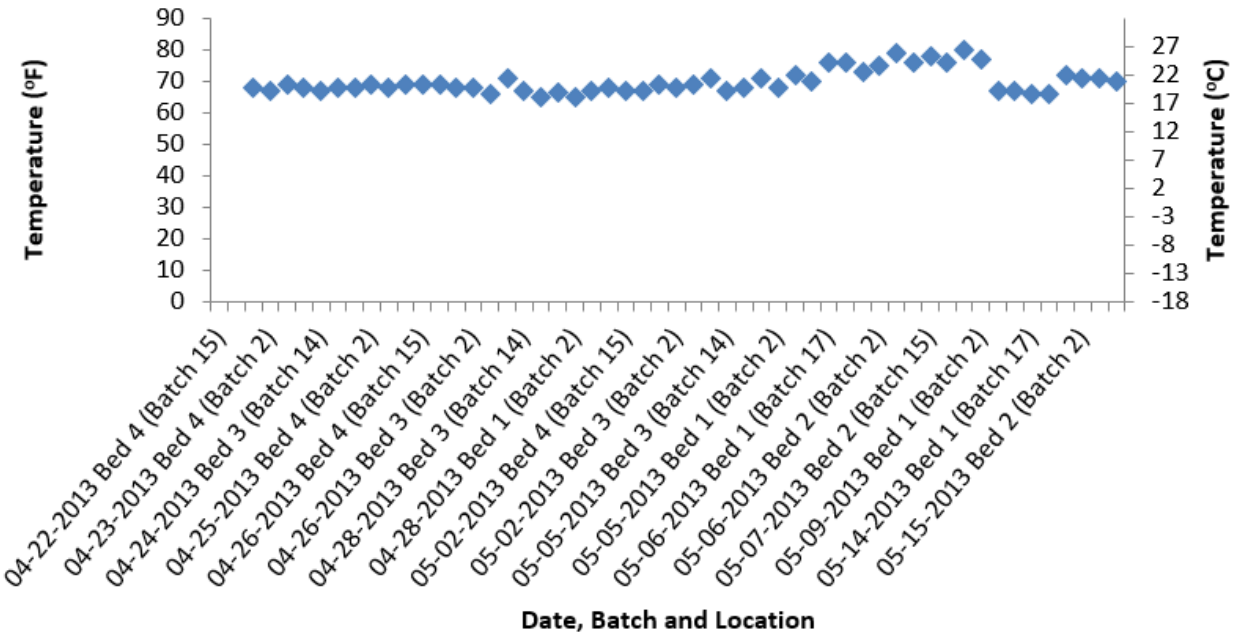


Figure 6.28. Temperature of fresh concrete at Plant A

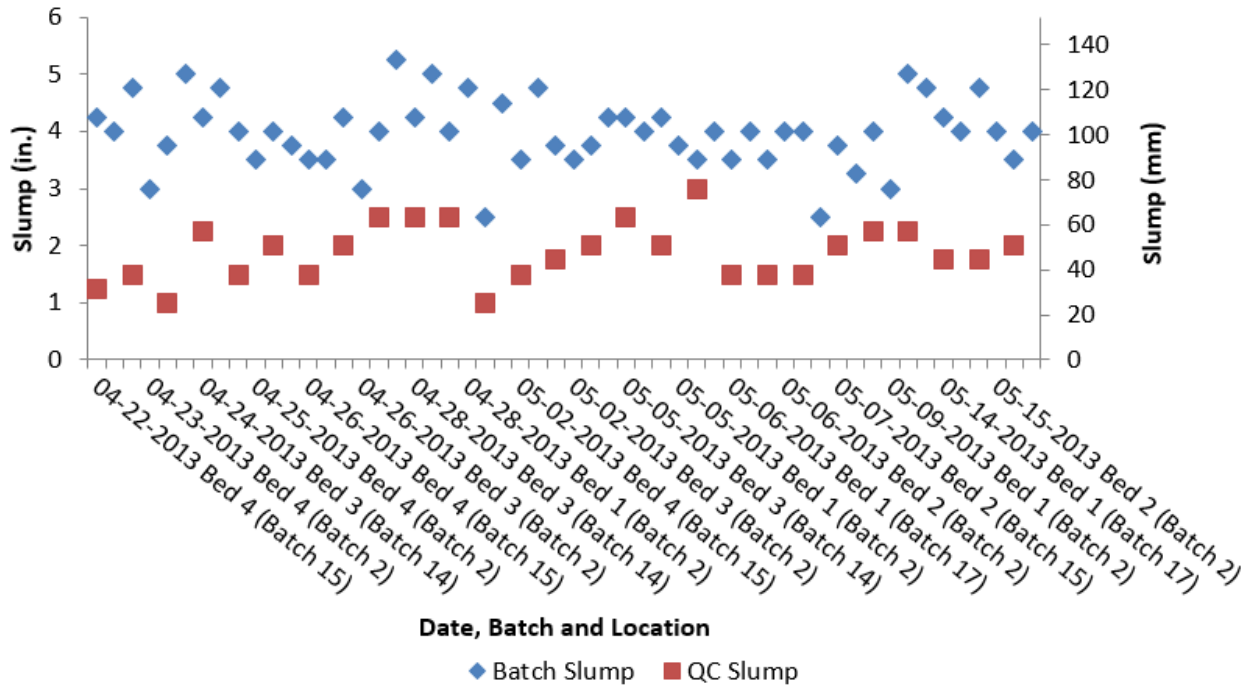


Figure 6.29. Slump of fresh concrete at Plant A

Figure 6.30 shows variation in the fresh concrete unit weight measured at Plant B. The measured unit weight range during the testing period was 136.8 to 144.8 lb/ft³ (21.5 to 22.8 kN/m³). The range in the fresh concrete temperature ranged from 80 to 95.8 °F (26.7 to 35.4 °C), as shown in Figure 6.31. Figure 6.32 shows measured slump values. The reduction was most likely due to water absorption by aggregates and cement particle flocculation/aggregation that trap water. Meanwhile, slump at the mixer level was not performed due to high fluidity of the concrete. Very fluid concrete mixtures spread enough during the slump test to leave a concrete patty, with the patty maximum height determined by maximum aggregate size, rendering the concrete slump test unable to differentiate the yield stress of very fluid mixtures.

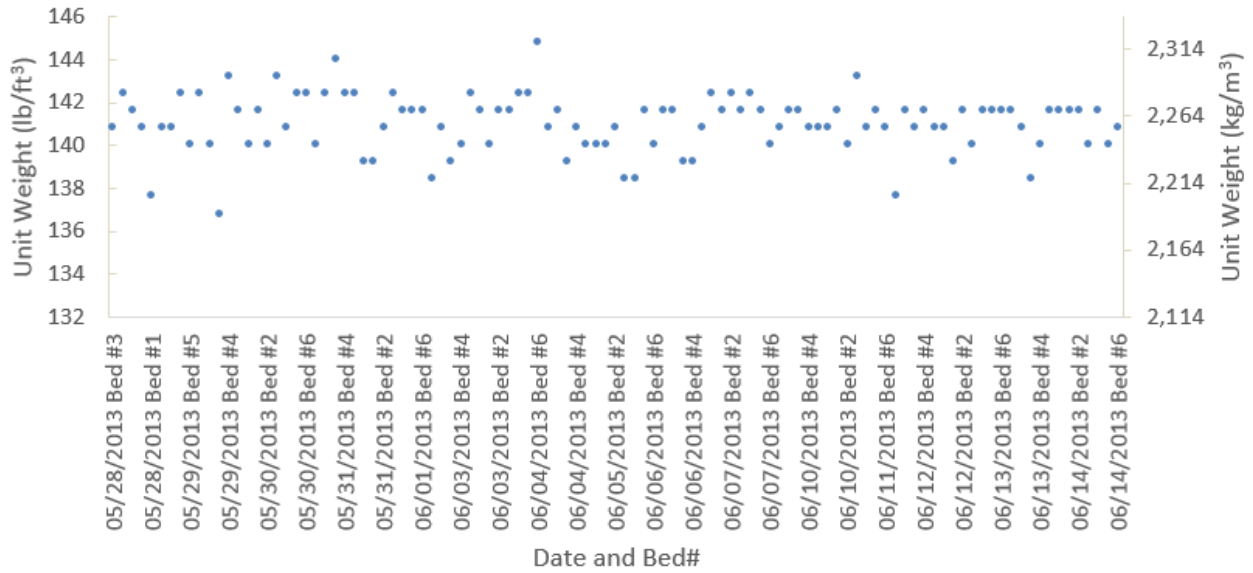


Figure. 6.30 Concrete unit weight at Plant B

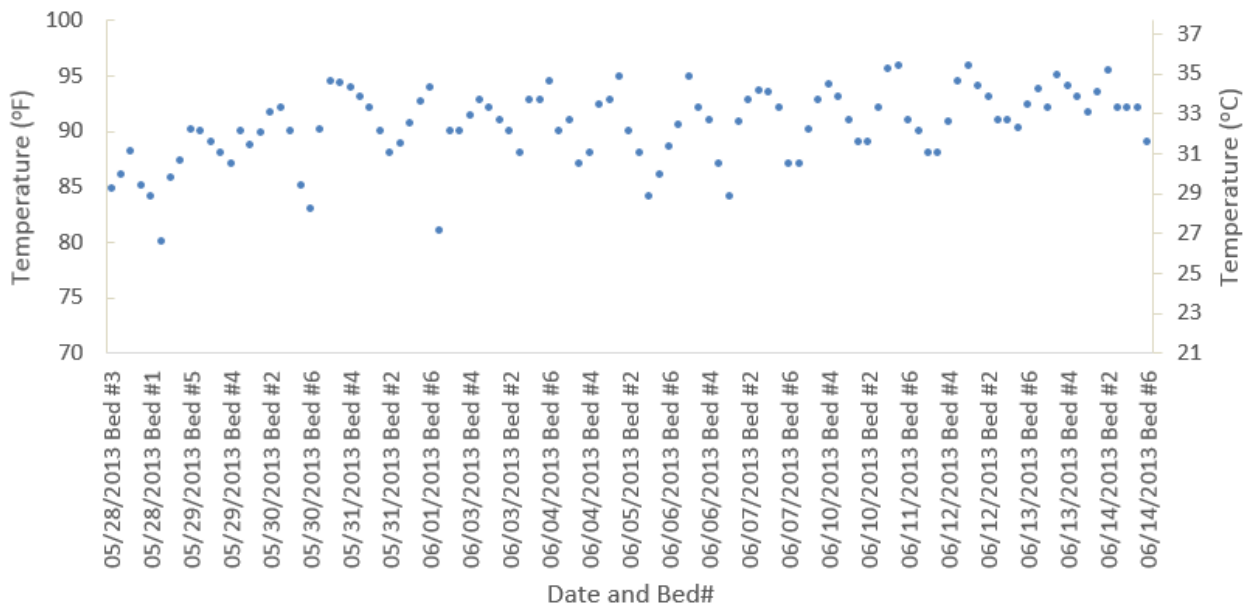


Figure 6.31. Temperature of fresh concrete at Plant B

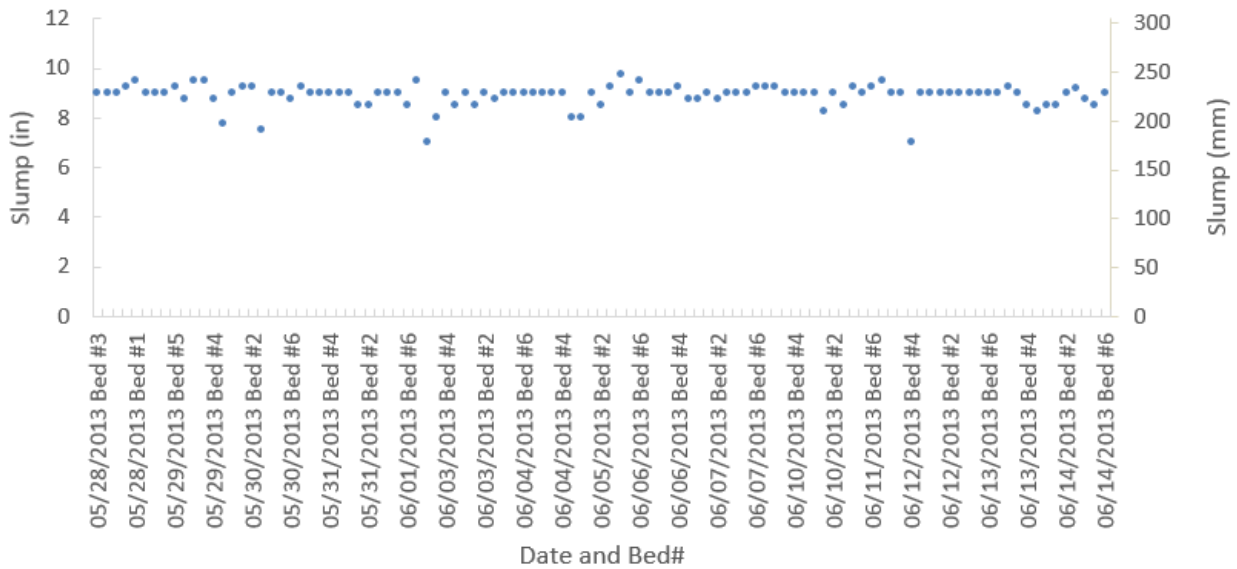


Figure 6.32. Slump of fresh concrete at Plant B

Various concrete rheological parameters could affect the rate of entrained air void loss during handling and vibration. Rheological parameters are also needed in order to understand the attenuation of shear waves in fresh concrete caused by vibration. Figure 6.33 shows the variation in measurements of static yield stress and dynamic yield stress (i.e., Bingham yield stress) measured at Plant A. As expected, measured dynamic yield stress was always lower than static yield stress because the material is easier to shear while it is flowing rather than shearing from a static position. Figure 6.34 shows variation in plastic viscosity of concrete throughout the period of study at Plant A. Figure 6.33 and Figure 6.34 show a large standard deviation of yield stress and plastic viscosity values. The static yield stress varied between 303.5 and 3027.4 Pa with an average of 1499.2 Pa and a standard deviation of 640 Pa, while plastic viscosity varied between 45.4 and 217.9 Pa.s with an average of 145.1 Pa.s and a standard deviation of 47.8 Pa.s. This shows that rheological properties can vary daily in concrete batch plants, based on factors such as temperature, slight variations in aggregate moisture content, and slightly different air. This fluctuation in rheology may also be due to the fact that the batch operator was given some tolerance in regards to modifying batch proportions during mixing in order to meet certain objectives. These small modifications could significantly affect rheological properties of the concrete mixture.

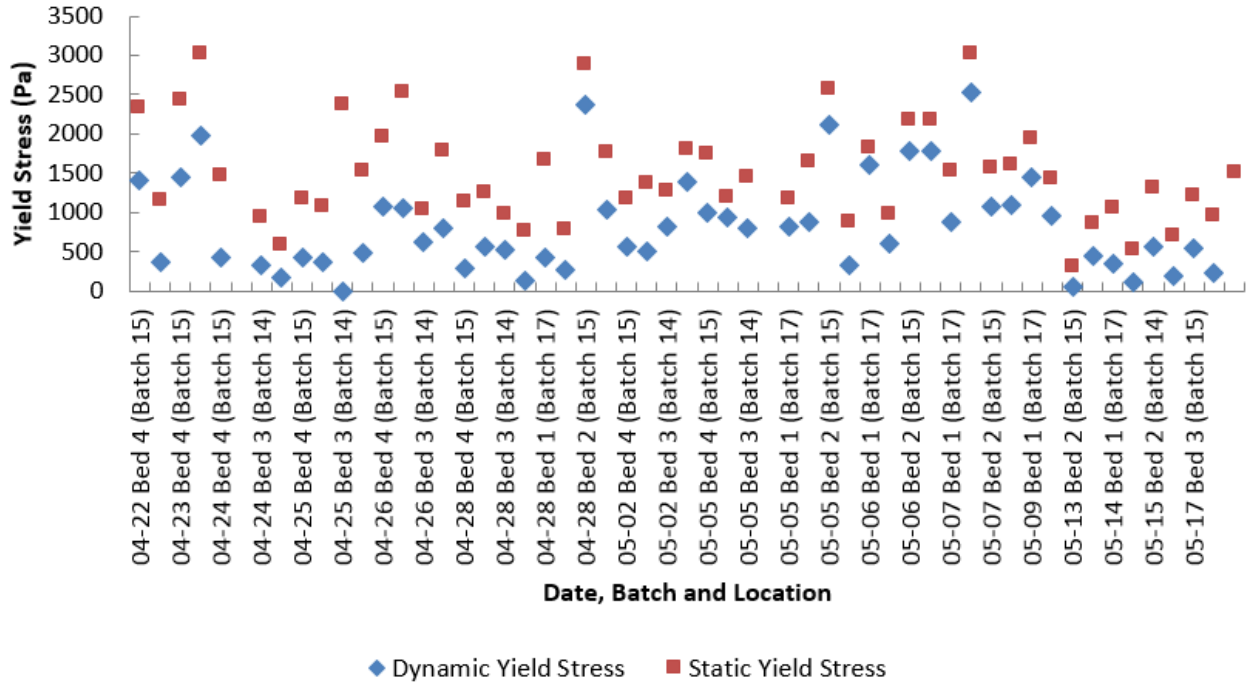


Figure 6.33. Yield stress of fresh concrete at the mixer level in Plant A

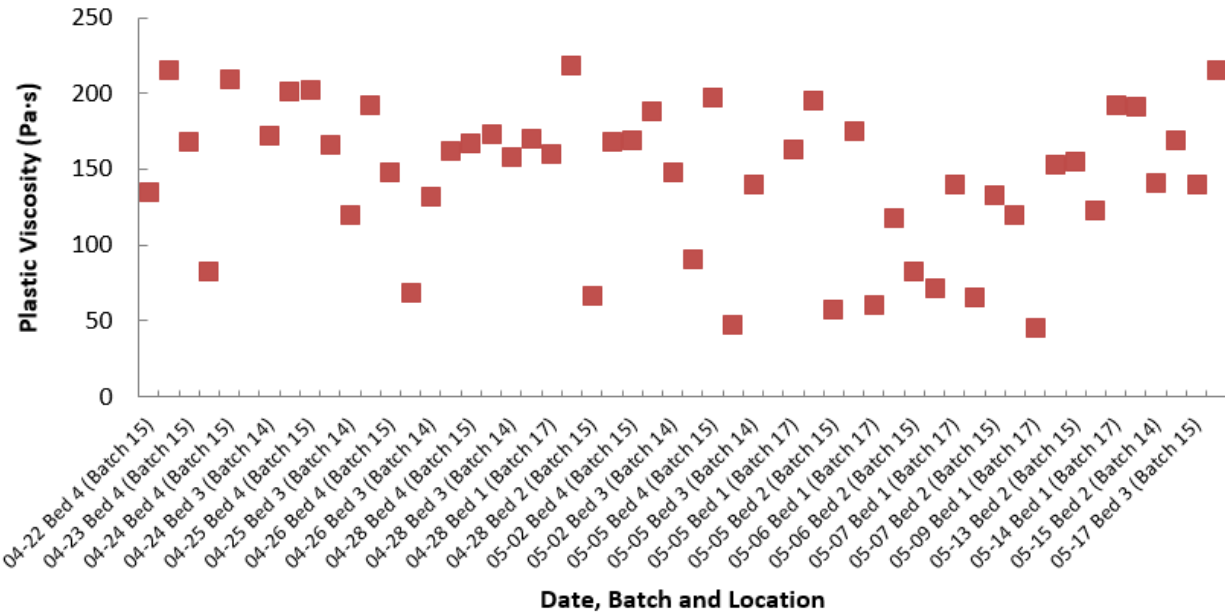


Figure 6.34. Plastic viscosity of fresh concrete at the mixer level in Plant A

Figure 6.35 presents variation in the measurements of static yield stress and dynamic yield stress throughout the study period at Plant B. Similar to Plant A observations, Figure 6.35 shows that dynamic yield stress was always lower than static yield stress at mixer and QC levels. Figure 6.36 shows variation in plastic viscosity of concrete throughout the period of study at Plant B. The static yield stress varied between 160.4 and 1148.7 Pa with an average of 751.8 Pa and a

standard deviation of 303.4 Pa, while plastic viscosity varied between 128.8 and 263.3 Pa.s with an average of 192 Pa.s and a standard deviation of 37.1 Pa.s. The overall trend shown in Figure 6.36 indicates higher plastic viscosity in concrete sampled from the casting machine. Figure 6.37 shows the change of rheological parameters with time for a single batch of concrete at Plant B. All rheological parameters increased with time possibly as a result of water absorption by aggregate and cement particle aggregation/ flocculation.

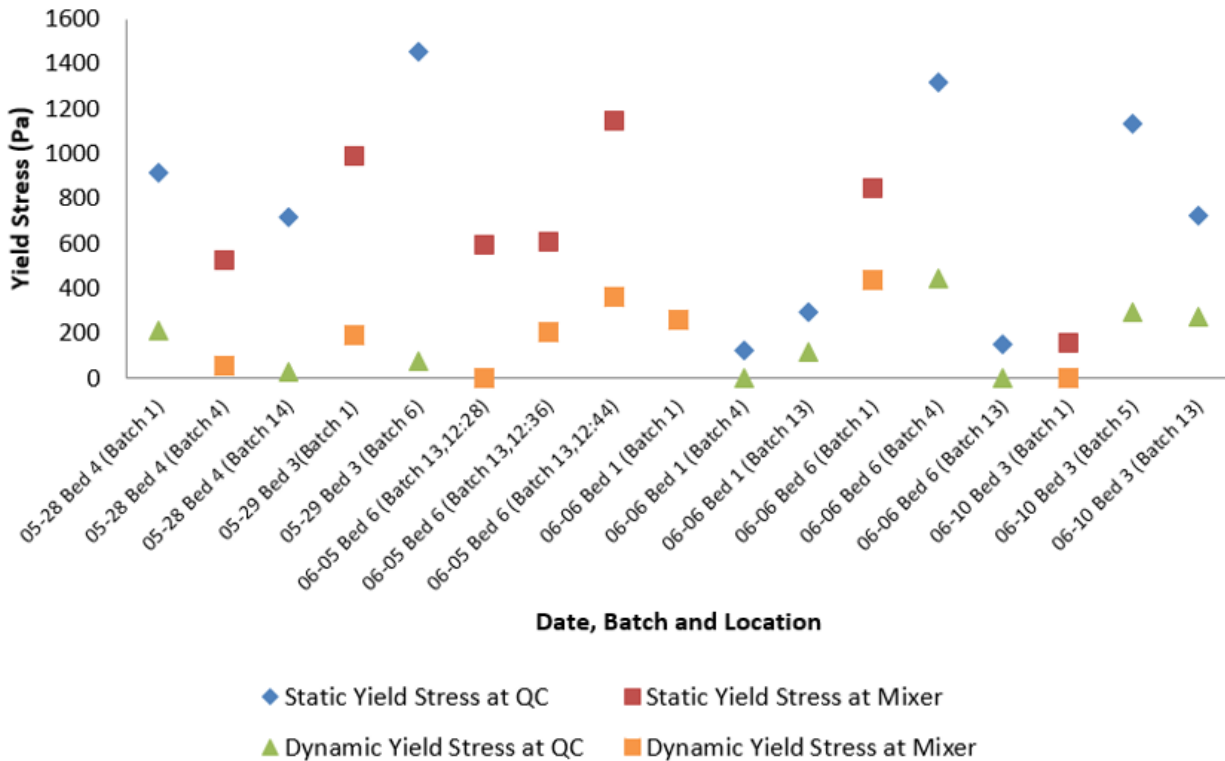


Figure 6.35. Yield stress of fresh concrete at Plant B

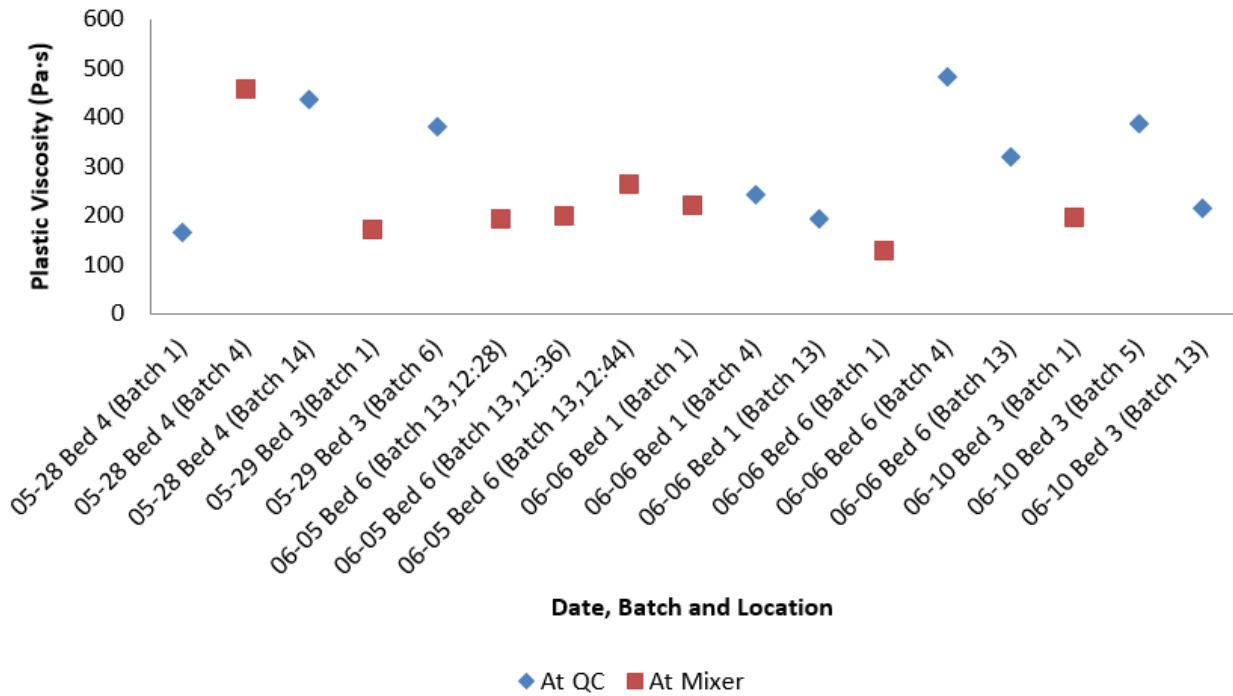


Figure 6.36. Plastic viscosity of fresh concrete at Plant B

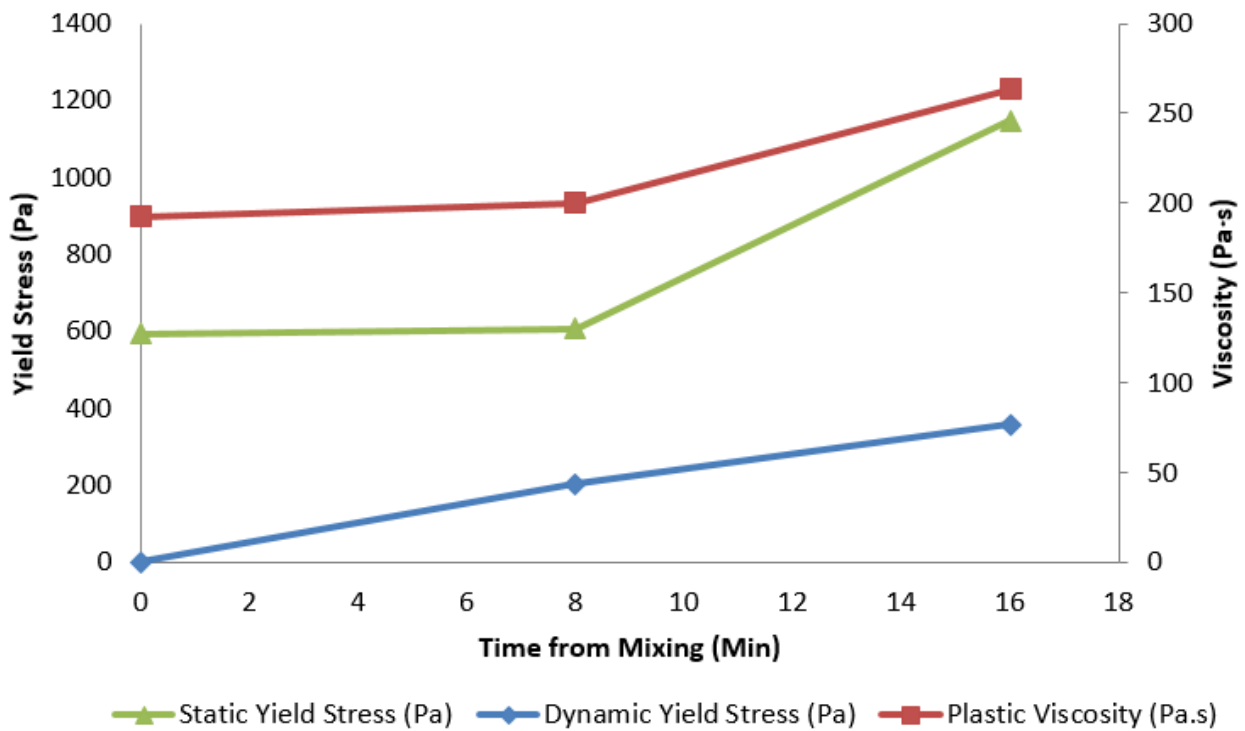


Figure 6.37. Rheological parameters versus time for a single batch at Plant B

Figure 6.38 shows variation in vibration frequency with time during the vibration of Bed 4 at Plant A. Immersion vibrator frequency was 110 Hz. Short-term frequency increases shown in Figure 6.38 were likely caused by the surrounding environment, such as workers and other machinery that impacted the casting bed or machine. Figure 6.39 presents an enlarged portion of the frequency curve obtained from the end of Bed 2 at Plant A.

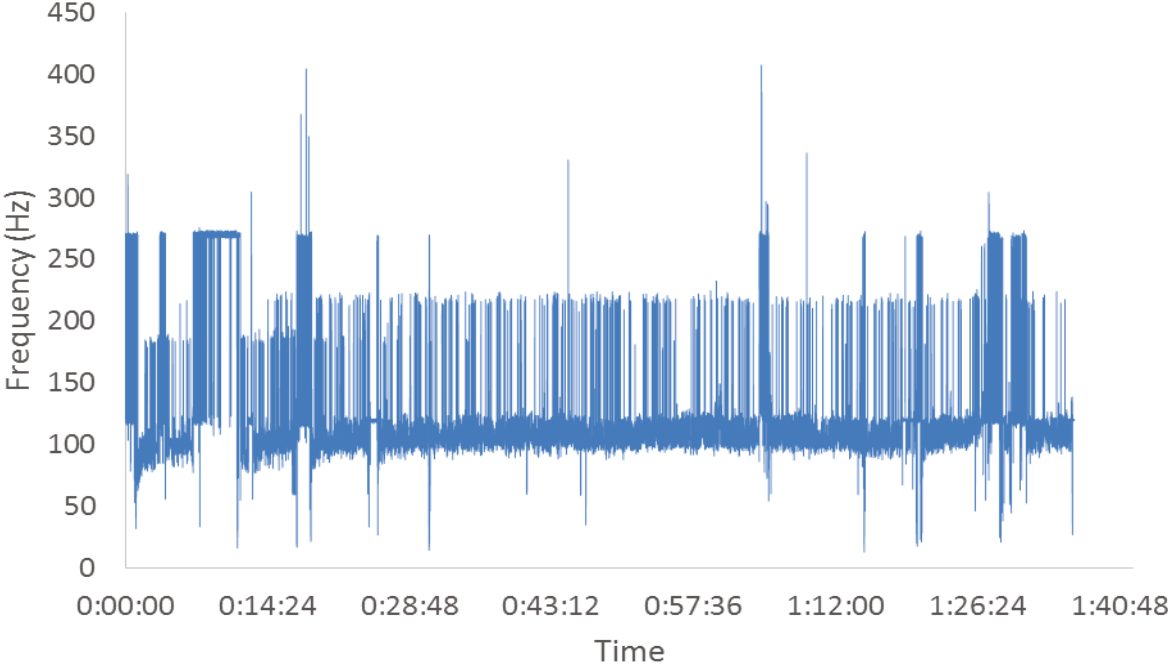


Figure 6.38. Frequency variation of vibration of Bed 4 at Plant A for 1 hour and 40 minutes

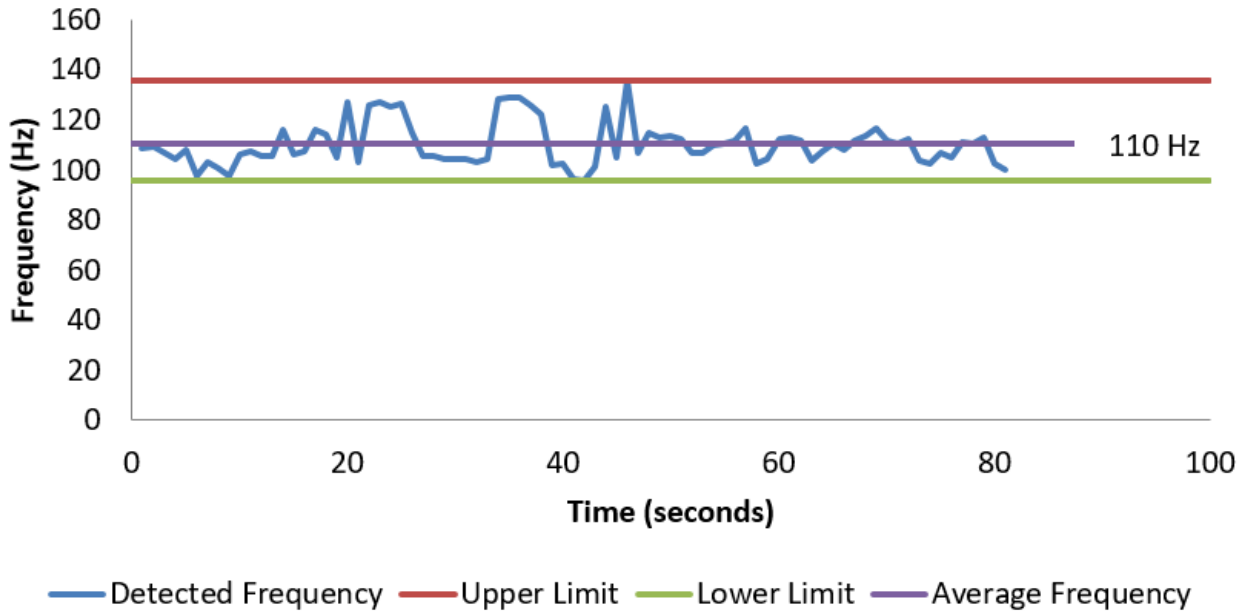


Figure 6.39. Average frequency in an 80-second interval at the end of Bed 2 of Plant A

Acceleration envelopes were found for maximum acceleration in the positive and negative direction, as shown in Figure 6.40. The average recorded maximum acceleration in Plant A was 2.5 g at the casting machine. The accelerometer measured an average acceleration of 0.5 g when attached to the forms at a distance of 1 ft. from the casting machine, as shown in Figure 6.41.

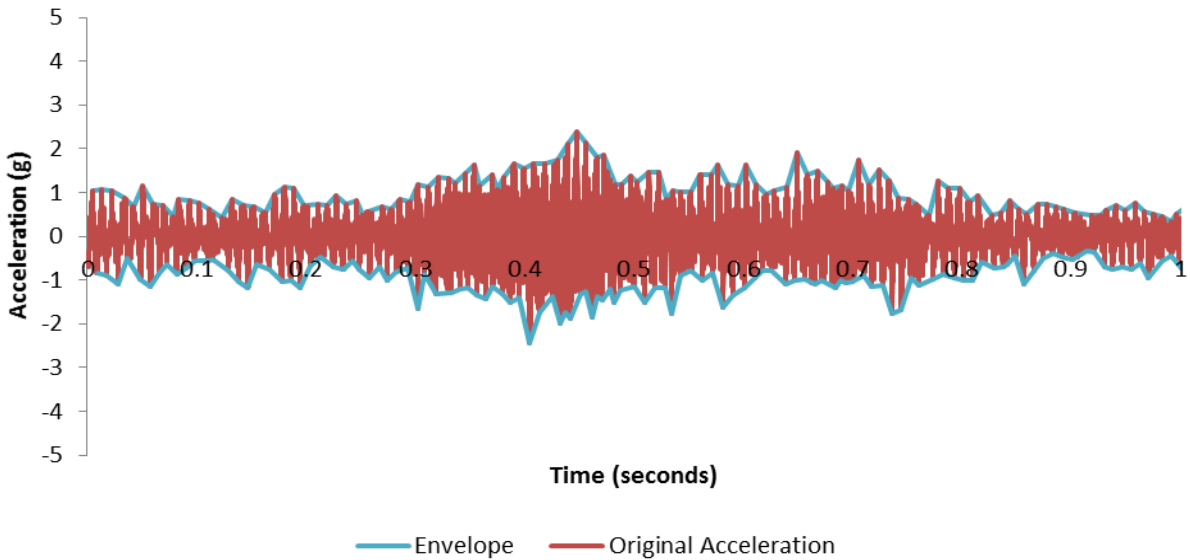


Figure 6.40. Acceleration with maximum acceleration envelope recorded over 1 second at the end of Bed 2 with an accelerometer attached to the casting machine of Plant A

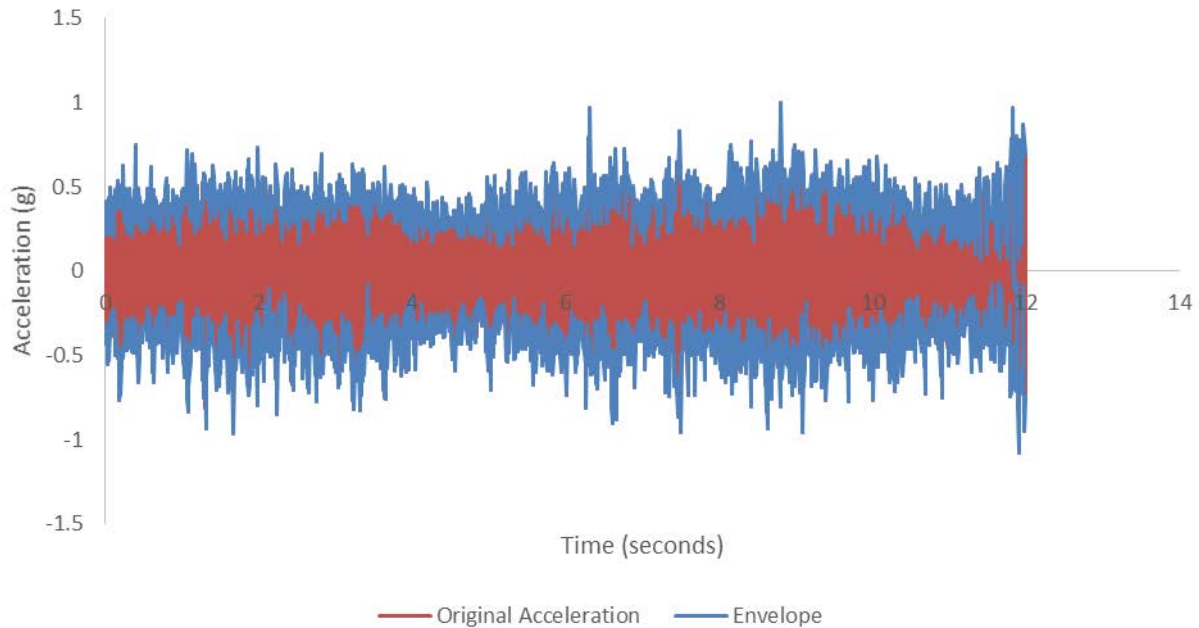


Figure 6.41. Acceleration with the envelope recorded over 12 seconds at the end of Bed 2 with the accelerometer attached to the forms of Plant A

Unlike Plant A, Plant B used a form-based vibration system in which the interior of the concrete was easily accessible. Vibration provided by the bed vibrator in this plant had an average frequency of 75 Hz. Short-term frequency increases shown in Figure 6.42 were likely caused by the surrounding environment for the form accelerometer readings. Short-term increases in concrete vibration measured by the submersible accelerometer could have been caused by the environment or the accelerometer contacting a wire during vibration. The average recorded acceleration in Plant B was 5 g.

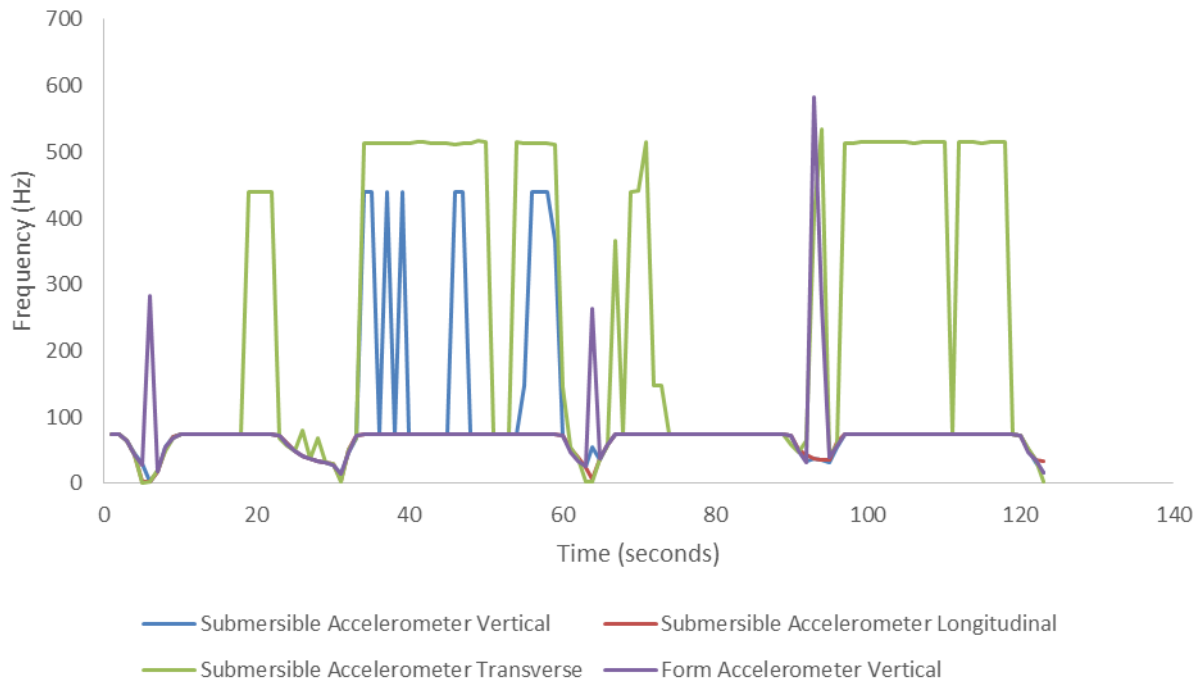


Figure 6.42. Average frequency in a 123-second interval at the end of Bed 2 in Cavity 1 of Plant B with the immersed accelerometer at a depth of 3.5 inches

Acceleration measurements inside the concrete were taken during vibration of the beds. Interior and exterior cavities were examined to identify differences in vibration acceleration induced into concrete at different cavities. Measurements of concrete acceleration were taken across the depth, along the length, and across the width of the cavity. Figure 6.43 shows the vertical acceleration envelope (i.e., peak accelerations for each cycle in the vertical direction versus time) along the length of Cavity 1 at 4.25 in. deep at 2-ft intervals. As shown, variations occurred in the peak accelerations at various locations along the cross-tie cavity. At some durations, peak acceleration experienced a sudden drop or rise due to switching on/off the vibrator and reversing rotation direction of the vibrator. The measured acceleration can be better understood by averaging the peak acceleration at each location without including the off periods, and plotting them versus location, as shown in Figure 6.44. Acceleration was higher near the vibrator in the midspan of the cavity compared to the edges. Acceleration in all directions ranged between 1.3g and 7.6g. Such vibration, however, results in the reflection of waves from boundaries of the cavities, leading to complicated constructive and destructive interferences.

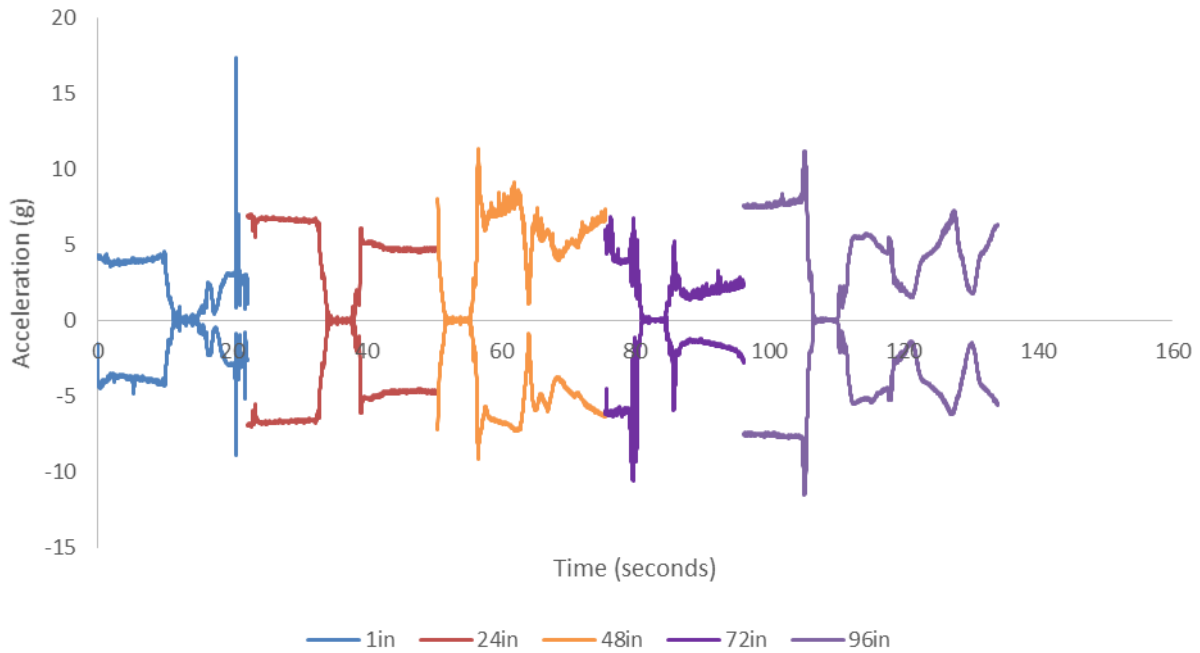


Figure 6.43. Vertical acceleration envelope along the length of Cavity 1 at a depth of 4.25 in. with 2-ft intervals for Plant B

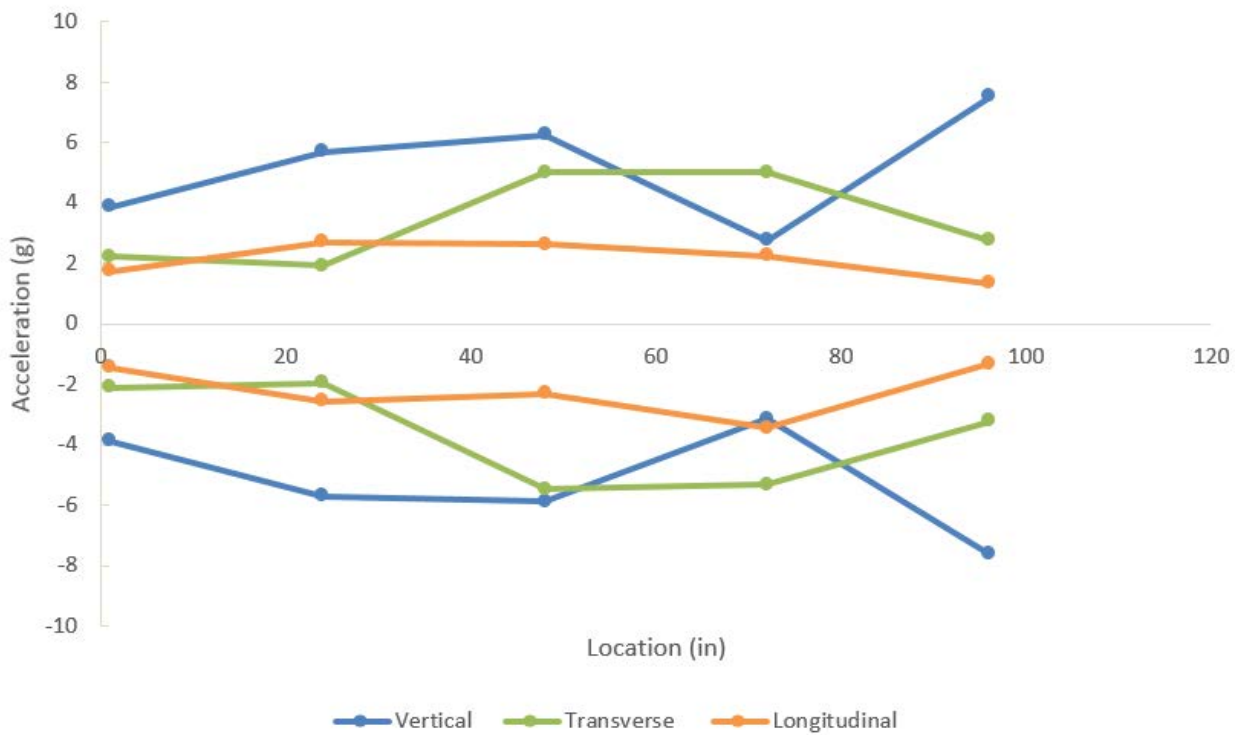


Figure 6.44. Average peak acceleration versus location along the length of Cavity 1 at a depth of 4.25 in. with 2-ft intervals without off periods for Plant B

Figure 6.45 shows average peak acceleration along the length of Cavity 2 at a distance of 4.25 in. from the concrete top surface and at 1-ft intervals. For this cavity, the behavior was non-uniform as compared to the previous case, although both cavities had the same vibrator. This could be due to vibration wave interference in the formwork or local vibration. The three vibrators used may have had small variation in acceleration and frequency that caused increased turbulence in the measurements. Nevertheless, the range of acceleration in this case was much larger, with 0.6 g as the lower bound and 9.7 g as the upper bound. This increase in the upper bound could be because Cavity 2 was closer to the vibrator than Cavity 1, resulting in higher vibration energy transmitted to the concrete in Cavity 2.

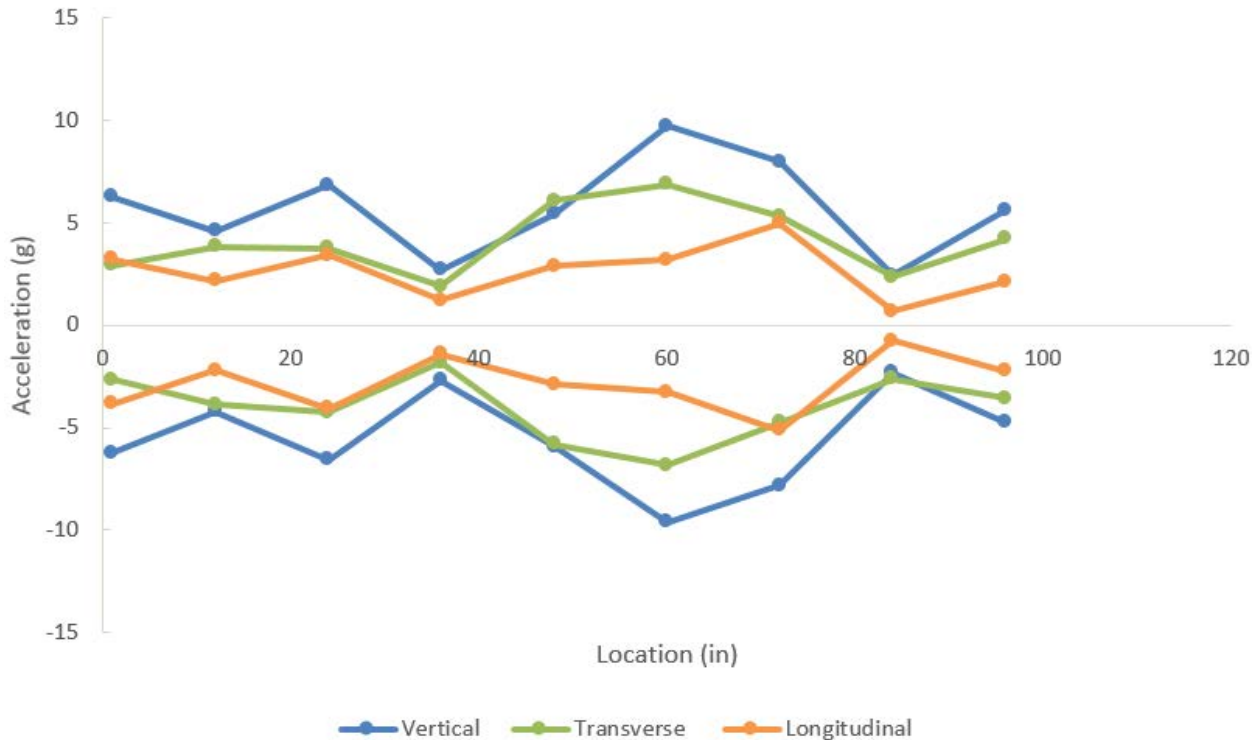


Figure 6.45. Average peak acceleration versus location along the length of Cavity 2 at a depth of 4.25 in. with 1-ft intervals for Plant B

Acceleration measurements shown in Figure 6.46 through Figure 6.48 indicate that maximum acceleration occurred in the middle of the cavity slightly away from the surface of the vibrating form as seen in Figure 6.11. The edges of the cavity also experienced increased acceleration compared to under the rail seats. Overall, the behavior showed non-uniformity, with the middle and edges of the cavity experiencing more acceleration closer to the vibrator compared to under the rail seat.

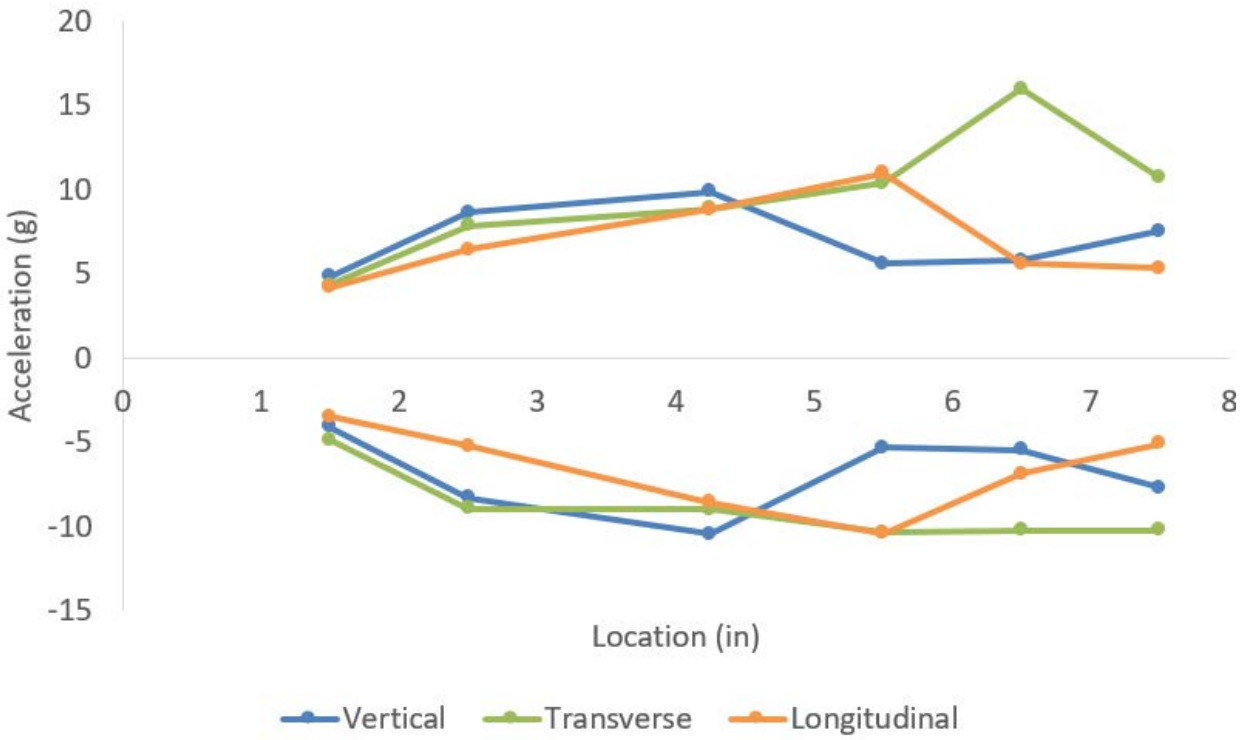


Figure 6.46. Average peak acceleration versus location across the depth of Cavity 2 at the middle of the cross-tie cavity for Plant B

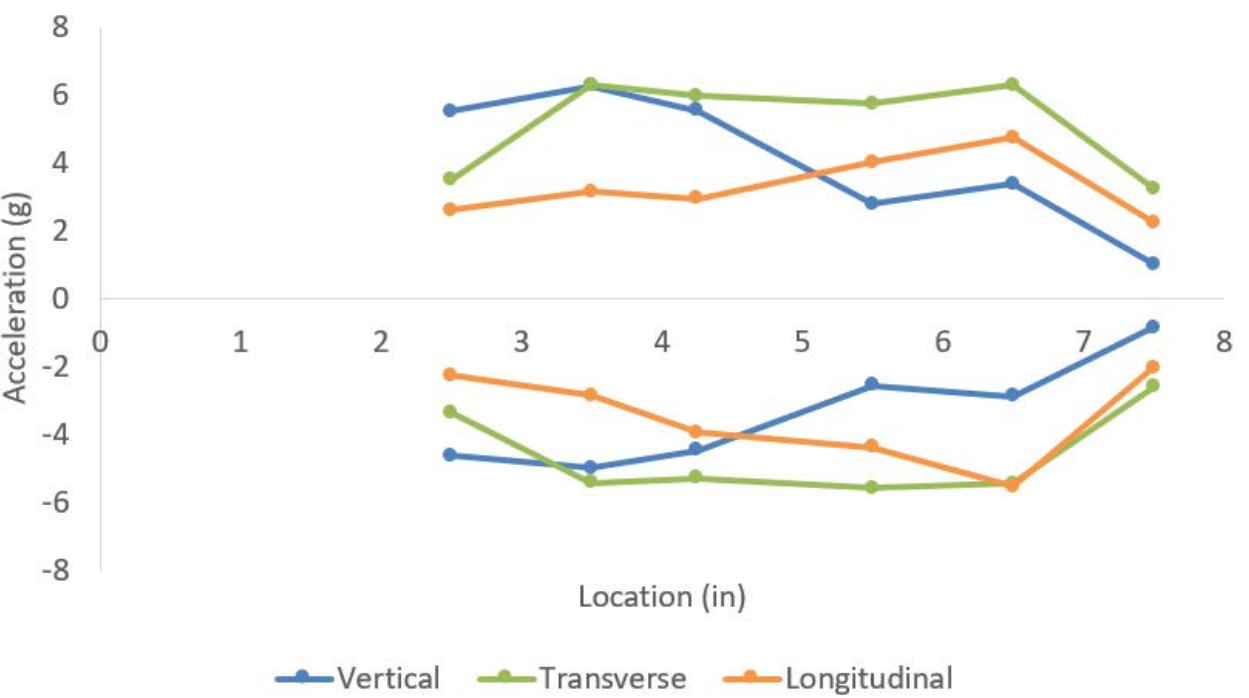


Figure 6.47. Average peak acceleration versus location across the depth of Cavity 2 1 in. from the edge of the cross-tie cavity for Plant B

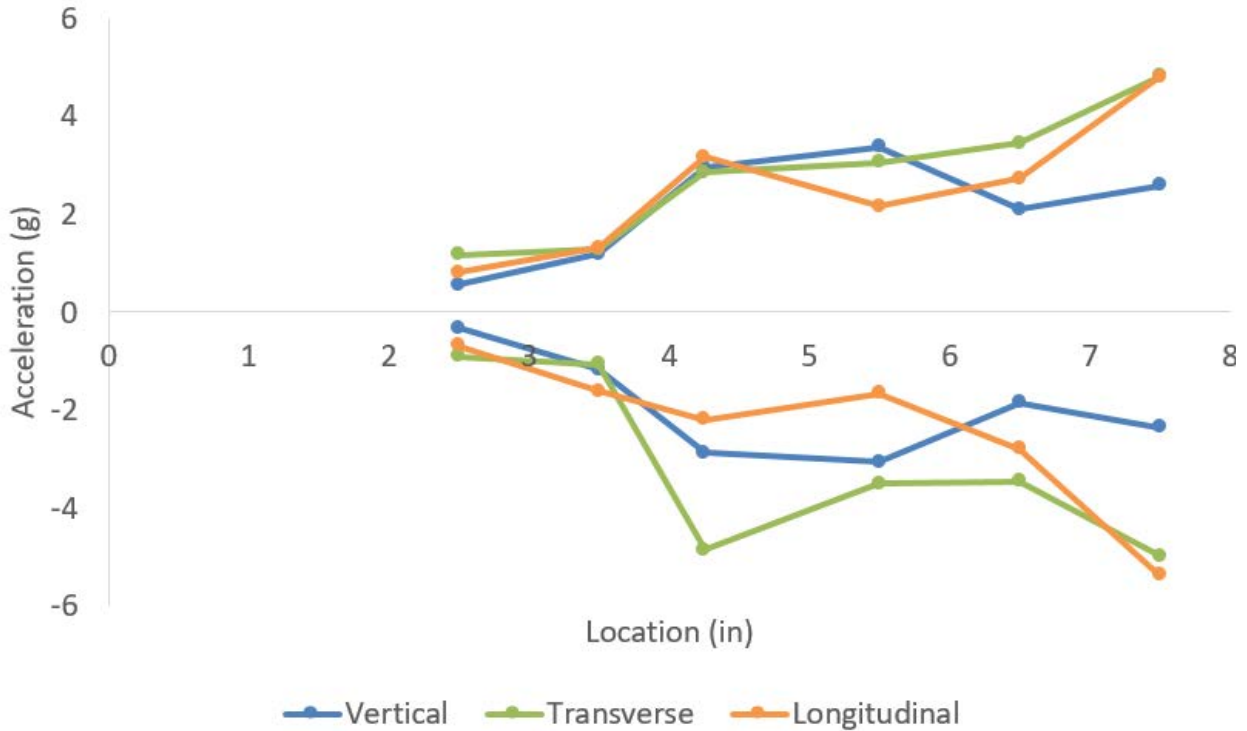


Figure 6.48. Average peak acceleration versus location across the depth of Cavity 2 under the rail seat for Plant B

Figure 6.49 shows average peak acceleration across the width of Cavity 2 measured 1 inch from the edges and the middle of the cavity. The two figures show that maximum acceleration occurred in the middle across the width of the cavity, whereas the edge closest to the vibrator experienced more acceleration compared to the edge farthest from the vibrator. A boundary condition effect occurred with the vibration. During vibration, the concrete moved separately from the formwork and air bubbles traveled to the concrete surface, possibly because the middle section received vibration peak waves from the three directions. Additionally, slip between the concrete and steel form could cause the form to vibrate differently than the concrete inside the form.

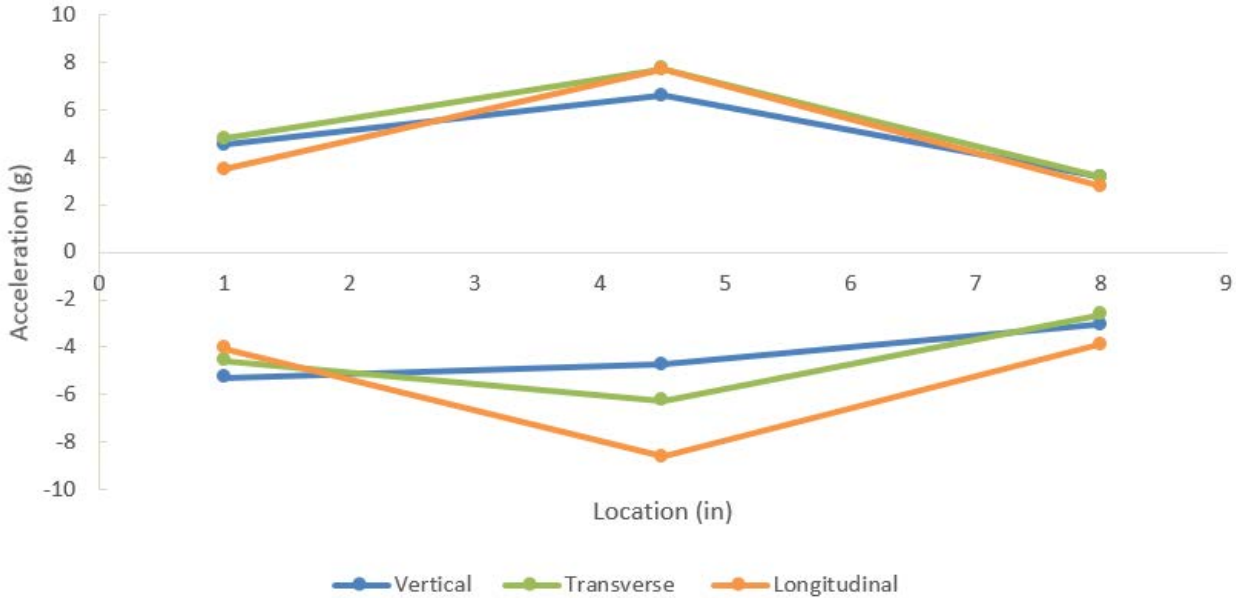


Figure 6.49. Average peak acceleration versus location across the width of Cavity 2 1 in. from the edge of the cavity for Plant B

Concrete crossties in a cavity were cast as a continuous concrete element with other crossties that were saw-cut after strand detensioning in order to separate individual ties. Because the concrete cavities were continuous, the concrete in a previously cast location experienced vibration from a form vibrator a considerable distance away. Vibration acceleration was recorded using the submersible accelerometer to measure vibration energy as a function of distance from the active vibrators, as shown in Figure 6.50. This was achieved by recording vibration as it moved away from the accelerometer and measuring the distance every time the vibration moved further away. The submersible accelerometer recorded vibration for approximately 15 minutes until the vibration had moved 30 ft away from the accelerometer. The accelerometer mounted on the form recorded form vibration for the entire period of casting, as shown in Figure 6.51.

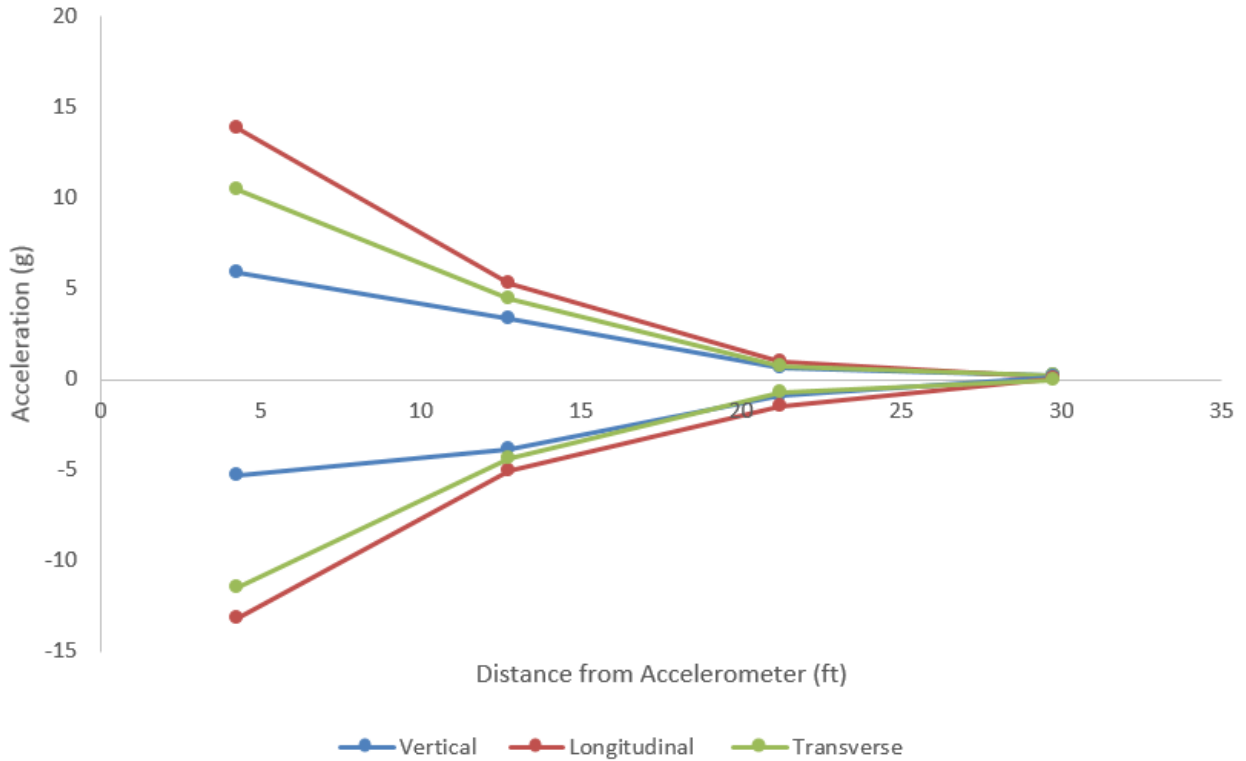


Figure 6.50. Average peak concrete acceleration versus location across 30 ft. of length of the bed in Cavity 1 1 in. from the start of the bed for Plant B

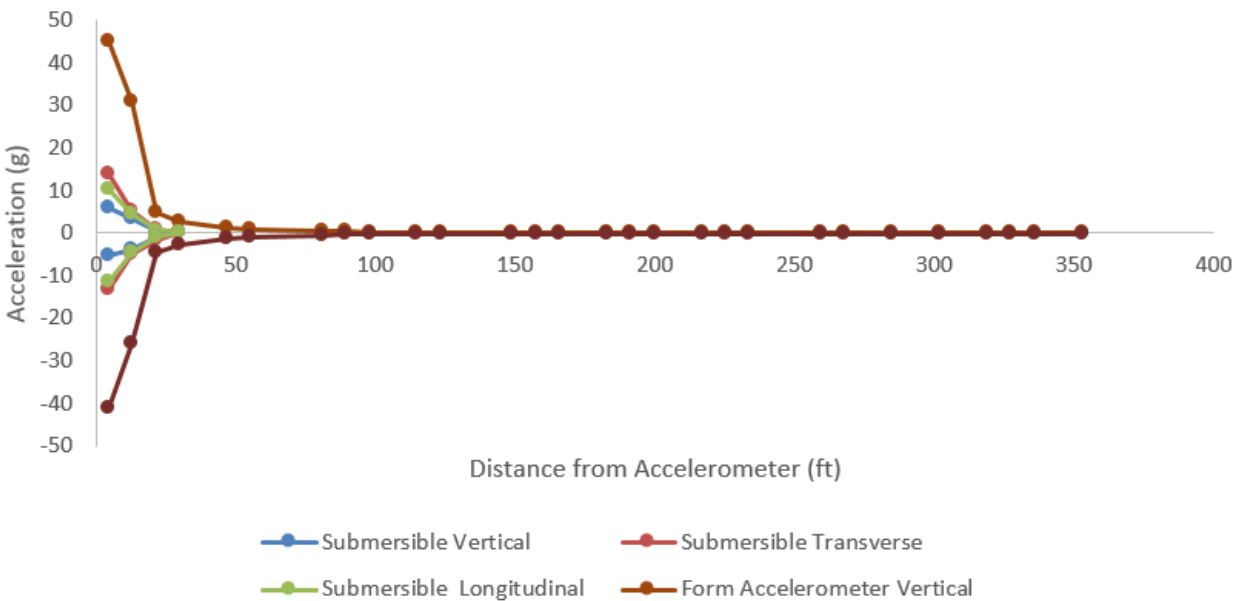


Figure 6.51. Average peak concrete and form acceleration versus location across the length of the entire bed in Cavity 1 1 in. from the start of the bed for Plant B

Vibration in the concrete was substantially less than vibration in the form, thus confirming visual observations that the form tended to move quite rapidly. However, some sloshing of the

concrete could have dampened some of the concrete acceleration. In addition, concrete acceleration remained high for some time after the form vibrator immediately underneath had been turned off. Vibration was another important factor. Form vibrators (Plant B) affected concrete for great distances after casting, as shown in Figure 6.50 and Figure 6.51, while immersion vibrators had smaller regions of influence. Immersion vibrators typically applied vibration for shorter but more effective intervals.

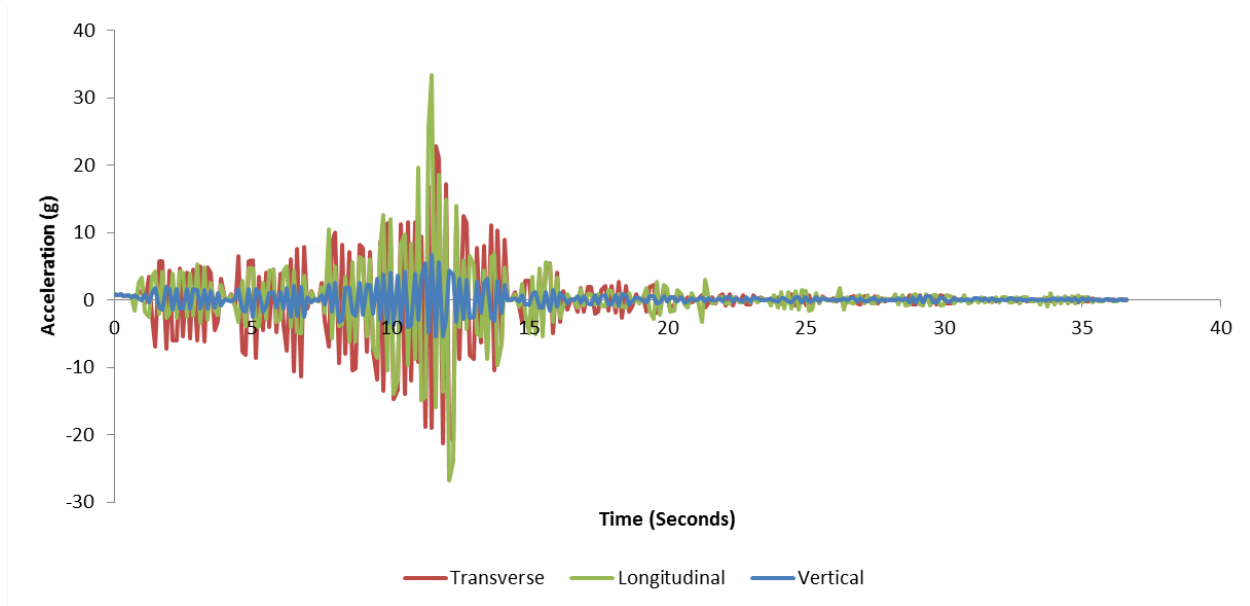


Figure 6.52. Acceleration recorded over 37 seconds at the start of bed with the accelerometer at 4.5 in depth for Plant C

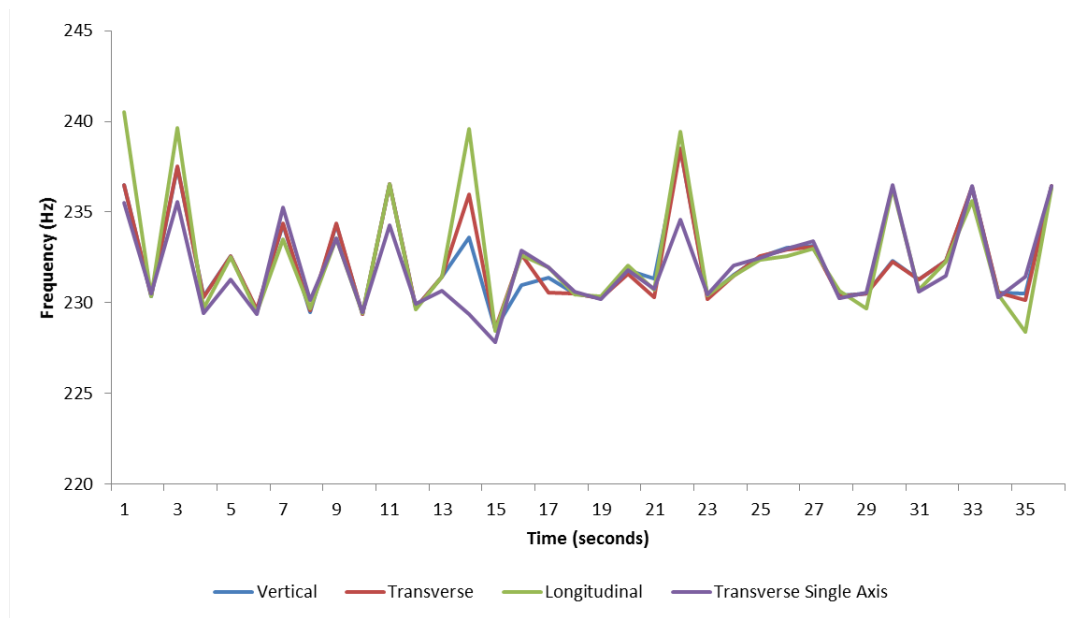


Figure 6.53. Frequency recorded over 37 seconds at the start of bed with the accelerometer at 4.5 in depth for Plant C

Vibration in the concrete varied substantially more than the other types of vibration from Plants A and B. This variation was the result of the variation in technique utilized by the various vibrator operators. In addition, some of the concrete were subjected to long variable intensities of vibrations due to the propagated of the acceleration waves as seen in Figure 6.52.

Acceleration also reached high values of 35 g in Plant C. Frequency was another important factor. Handheld vibrators (Plant C) affected concrete more severely than the other two types of vibration, this was the result of the high acceleration experienced and high fluidity.

6.7 Conclusions

The following conclusions can be made based on the experimental results conducted at three different precast concrete railroad tie manufacturing plants:

- The total air content at each plant was found to vary significantly batch-to-batch. The coefficient of variation for spacing factor after vibration varied between 30 and 63 percent. The coefficient of variation of the fresh total air content out of the mixer varied from 9 to 40 percent.
- Concrete air content decreased significantly during the handling and vibration stages of fabrication. Air loss between mixing and handling was found to be higher at the concrete tie manufacturing plants that used more fluid concrete mixtures. This led plants to add additional air during mixing to compensate for the loss, causing more variability. Concrete made with a lower viscosity was also found to lose more air during each stage of fabrication.
- Vibration methods vary widely from plant to plant. Each plant visited used a different method of vibration application. Vibration was found to be applied internally and through external form vibrators. Any vibration specifications to promote concrete freeze-thaw durability should be performance-based in order to accommodate different plant vibration methods.
- Vibration is not applied uniformly to the concrete. Vibration acceleration varied with depth and distance away from the form vibrator. Concrete ties placed first in a bed experience longer periods of vibration than the ties placed last in the bed. Formwork and wires were found to transmit vibration. This contributes to high rates of variability in hardened air content. Immersion probes vibrated the concrete for a shorter, more concentrated, and more effective period of time with less unwanted ongoing vibration from neighboring ties.

Chapter 7 – Temperature and Relative Humidity Profiles in Concrete Crossties

7.1 Deterioration of Railroad Concrete Crossties

Concrete crossties have been replacing timber ties over the last several decades because of their ability to sustain higher freight loads and higher train speeds (Zeman, 2010). Concrete crossties are typically manufactured in precast plants and are additionally pre-stressed for enhanced mechanical performance. As a result, concrete crossties manufactured in the United States in the 1970s with steam curing sometimes suffered deterioration mechanisms like delayed ettringite formation (Eriksson, B. -E., and Tepponen, P., 1967) (Ferdous, W., and Manalo, A., 2014). However, present-day concrete crossties are manufactured without steam curing and incorporate new chemical admixtures not previously available to manufacturers. These chemical (and mineral) admixtures have led to the development of high performance concrete that is highly flowable. However, field experience has suggested that concrete crossties remain vulnerable to deterioration mechanisms.

Deterioration mechanisms of concrete crossties are generally structural (e.g., abrasion, crushing) and material (e.g., cavitation erosion, hydraulic pressure) (Ferdous, W., and Manalo, A., 2014). It is also possible for freeze-thaw damage to occur within the concrete crosstie since the material is exposed to outdoor environments. Freeze-thaw damage can be problematic at the rail seat area where the confined geometry of the concrete crosstie, pad, clips, shoulder, and rail line converge. The highly confined rail seat area is thought to lead to persistent wet conditions from precipitation (rain or melting snow) which can lead to absorption of water, scaling, and freeze-thaw damage at low temperatures (Bakharev, T., and Struble, L. J., 1997). Recent research has demonstrated that freeze-thaw damage is exacerbated above critical levels of saturation higher than 86-88 percent (Castro, J., Li, W., Pour-Ghaz, M., and Weiss, J., 2012). As such, it is necessary to gain a better understanding of moisture levels and freezing temperatures inside concrete crossties to better assess their freezing-thawing damage potential.

7.1.1 One-Dimensional Modeling of Internal Relative Humidity Distribution

Concrete pavement research has included simulation of moisture and temperature gradients. Moisture and thermal curling of slabs leads to cracking and durability issues. As such, infinite halfspace solutions exist for pavements. In this study, two halfspace solutions to predict relative humidity and temperature distributions are applied to concrete crossties. The concrete crossties are assumed to be infinite halfspaces sitting atop a gravel ballast as shown in Figure 7.1.

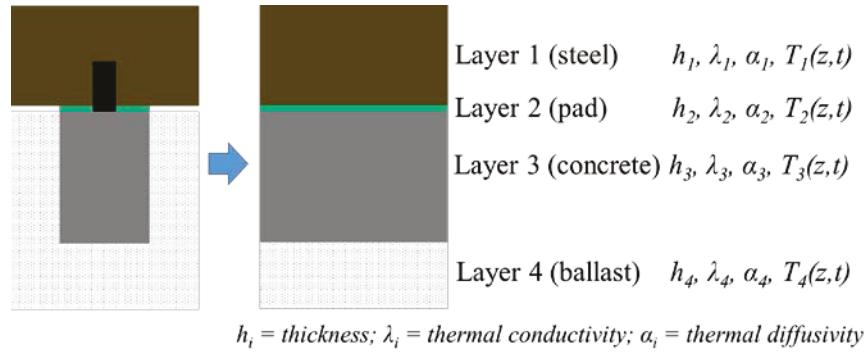


Figure 7.1. Depiction of a concrete cross-tie at the rail seat area (left) where the steel rail line, polyurethane pad, concrete cross-tie, and aggregate ballast are depicted as layered, infinite halfspaces (right)

Relative humidity can be modeled by the one-dimensional moisture transport equation (Kim, J. -K., and Lee, C. -S., 1999):

$$\frac{\partial RH(t,z)}{\partial t} = \text{div}(D \cdot \text{grad}(RH(t,z))) - \frac{\partial RH_s(t,z)}{\partial t} \quad \text{Equation 7.1}$$

where RH is a function of time (sec), t , and depth (m), z ; $\frac{\partial RH_s(t,z)}{\partial t}$ is the change in relative humidity due to hydration for early-age concrete (assumed as $\frac{\partial RH_s(t,z)}{\partial t} = 0$ for hardened concrete). D is the moisture diffusivity, which is a function of both internal relative humidity and concrete porosity. The moisture diffusivity factor is non-linear, where at low RH, vapor- and gas-pressure gradients govern transport properties while at high RH, capillary suction governs transport properties. The moisture diffusivity can be expressed by an effective diffusivity (Bazant, Z., and Najjar, L., 1972):

$$D = D_o \left(\alpha_o \frac{1 - \alpha_o}{1 + (1 - RH / 1 - RH_c)^n} \right) \quad \text{Equation 7.2}$$

Where D_o (m^2/s) is the moisture diffusivity at complete saturation. n is a regression coefficient ranging from 6 to 16 for concrete (Dux, P., Leech, C., and Lockington, D., 2003). $\alpha_o = D_l/D_o$, where D_l is the diffusivity at 0 percent RH; and RH_c is the bifurcate point above which capillary suction governs (typically 75 to 80 percent) (Hiller, J. E., and Qin, Y., 2014). The moisture diffusivity at complete saturation can be related to the water-to-cementitious ratio as shown in Table 7.1.

Table 7.1. Moisture Diffusivity at Saturation Estimated from w/c Ratio (from ¹ (Kang, S. -T., Kim, J. -K., Kim, J. -S., Lee, Y., and Park, Y. -D., 2012), and ² (Hiller, J. E., and Qin, Y., 2014))

w/c	D_o ($10^{-6} \text{ m}^2/\text{hour}$) ¹	D_o ($10^{-6} \text{ m}^2/\text{hour}$) ²
0.28	2.02	0.68
0.40	2.10	1.59
0.50	2.26	-
0.68	2.87	2.57

The boundary conditions are defined at the top and underside of the crosstie by two hygrometers installed within the ballast. The boundary condition at the top of the crosstie is modified in order to better represent wetting events due to precipitation (rain or melting snow). Table 7.2 shows weather conditions which increase the measured relative humidity value to 100 percent RH over a given time frame.

Table 7.2. Modified Boundary Condition at the Top of Concrete Crossties and Beams as Subject to Reported Weather Conditions (Adapted from (Hiller, J. E., and Qin, Y., 2014))

Reported Weather Condition	Modified Wetting Duration
Drizzle	
Fog	RH _{upper} =100 % for 1 hour
Mist	
Light Rain	
Light Thunderstorms and Rain	RH _{upper} =100 % for 4 hours
Thunderstorms and Rain	
Rain	RH _{upper} =100 % for 8 hours
Heavy Thunderstorms and Rain	
Heavy Rain	RH _{upper} =100 % for 10 hours
Light Snow	
Snow	RH _{upper} =100 % for 15 hours
Heavy Snow	RH _{upper} =100 % for 20 hours

Equation 7.1 is iteratively solved in MatLab until the $RH(t)$ converges to within 1 percent RH.

7.1.2 One-Dimensional Modeling of Internal Temperature Distribution

Several models exist to predict the temperature distribution inside concrete pavements (Barber, 1957) (Dempsey, B. J., and Thompson, M. R., 1970) (Kennedy, T. W., and Solaimanian, M., 1993). Dempsey and Thompson's model is well regarded for long-term pavement temperature predictions for long time periods. However, modeling a concrete crosstie presents two challenges. Ties have a finite-width and are multi-layered. Adopting a multi-layered, closed-form solution, assumes an incorrect representation of the crosstie. However, a first-principles understanding can be made where the suitability of a one-dimensional model can be evaluated for use in predicted concrete crosstie internal temperature distributions.

Wang and Roesler (Roesler, J. R., and Wang, D., 2014) proposed a separation of variables method to predict the internal temperature profile, $T_i(z,t)$, inside a multi-layered rigid pavement system. A one-dimensional heat transfer problem is modeled using:

$$\frac{\partial T_i}{\partial t}(z, t) = \alpha_i \frac{\partial^2 T_i}{\partial z^2}(z, t) \quad \text{Equation 7.3}$$

Where α_i is the thermal diffusivity coefficient (m^2/h); $H_{i-1} < z < H_i$ is the cumulative depth through the multi-layered system (m). $H_i = \sum_{k=1}^i h_k$ is the individual thickness of each layer (m). $i=1, 2, \dots, n-1$ are individual layers where $H_0=0$ and $H_n=\infty$, and $n \geq 4$ is the number of layers required in this analysis.

Two boundary conditions constrain the final solution to be continuous along the intermediary interfaces between any consecutive layers:

$$T_i(H_i, t) = T_{i+1}(H_i, t) \quad \text{Equation 7.4}$$

$$\lambda_i \frac{\partial T_i}{\partial t}(H_i, t) = \lambda_{i+1} \frac{\partial T_{i+1}}{\partial z}(H_i, t) \quad \text{Equation 7.5}$$

Where λ_i is the thermal conductivity coefficient ($\text{kcal}/\text{m h } ^\circ\text{C}$). The third boundary condition is an energy balance between the surface of the concrete and environmental conditions:

$$-\lambda_i \frac{\partial T_i}{\partial t}(0, t) = a_s Q(t) - F(t) + B[T_a(t) - T_1(0, t)] \quad \text{Equation 7.6}$$

Where a_s is the surface material absorptivity relative to the solar radiation (unitless). $Q(t)$ is the solar radiation flux ($\text{kcal}/\text{m}^2 \text{ h}$) at time t (hour), $F(t)$ is the irradiation flux emitted by the pavement surface ($\text{kcal}/\text{m}^2 \text{ h } ^\circ\text{C}$), B is the surface material convection coefficient ($\text{kcal}/\text{m}^2 \text{ h } ^\circ\text{C}$), and $T_a(t)$ is the ambient air temperature ($^\circ\text{C}$) at time t (hour). Continuous functions of $Q(t)$ and $T_a(t)$ are desired in order to produce a closed-form final solution, so an interpolatory trigonometric set of polynomials using the least squares approximation can be used (Roesler, J. R., and Wang, D., 2014) (Burden, R. L., and Faires, J. D., 2001). By incorporating these trigonometric polynomials and simplifying the irradiation energy by a factor of 1/3, then Equation 7.6 can be written in the compact form (Barber, 1957):

$$-\lambda_i \frac{\partial T_i}{\partial t}(0, t) = B[\sum_{i=1}^{2m} A_i \sin(\omega_i t + \phi_i) - T_1(0, t)] \quad \text{Equation 7.7}$$

Where $2m$ is the number of sub-intervals used to create the interpolatory trigonometric set of polynomials. A_i , ω_i , and ϕ_i are mathematical representations of amplitude, frequency, and phase angle, respectively, and are defined elsewhere (Roesler, J. R., and Wang, D., 2014).

Wang and Roesler observe that the sinusoidal term $\sin(\omega_i t + \phi_i)$ can be related to the complex number $e^{j(\omega t + \phi)}$ via the Euler formula where $j^2 = -1$. As such, the complex-valued function can be solved where the imaginary final solution corresponds to the real solution for the 1D temperature profile $T_i(z, t)$. Because the principle of superposition is applied j times in order to solve the complex-valued function, the individual solutions of $T_{ij}(z, t)$ must be summed across the j -th index in order to yield the final solution for the n -th layered temperature profile distribution. The solution from one iteration of solving the imaginary part of the complex-valued function are:

$$\begin{aligned} T_{ij}(z, t) &= \Delta_{11} e^{-v_1 z} \sin(\omega t - v_1 z + \delta_{11} + \phi) \\ &\quad + \Delta_{12} e^{v_1 z} \sin(\omega t + v_1 z + \delta_{12} + \phi) \end{aligned}$$

$$\text{Equation 7.8}$$

For $0 \leq z \leq H_i$;

$$\begin{aligned} T_{ij}(z, t) &= \Delta_{i1} e^{H_{i-1} v_{i-1} + v_i (H_{i-1} - z)} \sin(\omega t - v_i z + \delta_{i1} + \phi) \\ &\quad + \Delta_{i2} e^{H_{i-1} v_{i-1} - v_i (H_{i-1} - z)} \sin(\omega t + v_i z + \delta_{i2} + \phi) \end{aligned} \quad \text{Equation 7.9}$$

For $H_{i-1} \leq z \leq H_i$, and $i = 2, 3, \dots, n-1$; and

$$T_{nj}(z, t) = \Delta_n e^{H_{n-1}v_{n-1} + v_n(H_{n-1} - z)} \sin(\omega t - v_n z + \delta_{n1} + \phi) \quad \text{Equation 7.10}$$

For $z \geq H_{n-1}$. The variables Δ_{i1}, δ_{i1} for $i=1, 2, \dots, n$ and Δ_{i2}, δ_{i2} for $i=1, 2, \dots, n-1$ in Equations 7.8 through 7.10 can be found elsewhere (Roesler, J. R., and Wang, D., 2014).

7.1.3 Estimating Solar Radiation as an Input for the One-Dimensional Temperature Model

The temperature model requires two input parameters in order to predict the internal temperature profile distribution inside concrete: ambient air temperature and solar radiation. Although ambient air temperature is available in many locations from meteorological data, solar radiation is not as readily available and is prone to incomplete data sets (Al Riza, D. F., Aris, M. S., and ul Haq, S. I., 2011). Solar radiation estimation is employed within agricultural disciplines in order to understand soil temperature and soil moisture conditions. As such, a number of different estimations exist throughout the literature for solar radiation with varying degrees of simplicity (Monteith, 1965) (Bristow, K. L., and Campbell, C. S., 1984) (Hargreaves, G. H., and Samani, Z. A., 1985) (Liu D. L., 1996) (Jupp, D. L., and McVicar, T. R., 1999).

Spokas and Forcella estimate incoming solar radiation as affected by changing weather conditions and changing geo-temporal attributes at a given location (Forcella, F., and Spokas, K., 2006). Their model is advantageous because it is sensitive to changing hourly conditions as opposed to other models which only account for mean daily fluctuations and site-calibration. In their model, they assume that total incoming solar radiation, Q_T , is divided into two components:

$$Q_T = Q_B + Q_D \quad \text{Equation 7.11}$$

Where Q_B is direct beam radiation and Q_D is indirect, diffuse radiation. Direct beam radiation is transmitted parallel to the sun's rays (zenith angle) and is dependent upon the location on Earth, the time of day, the time of year, and the extent of transmittance through the atmosphere. Direct beam radiation is assumed to be (Jordan, R. C., and Liu, B. Y., 1960):

$$Q_B = Q_{B0} \tau^m \quad \text{Equation 7.12}$$

Where Q_{B0} is the solar constant ($1,360 \text{ W/m}^2$), τ is the atmospheric transmittance, and m is the optical air mass number. The optical air mass number is a function of atmospheric pressure, zenith angle, and elevation of the site (Campbell, G. S., and Norman, J. M., 1998). Indirect, diffuse radiation is reflected or absorbed in the atmosphere, clouds, or dust and a fraction of this radiation is scattered toward the surface of Earth. It is assumed to be (Jordan, R. C., and Liu, B. Y., 1960):

$$Q_D = 0.30(1 - \tau^m) Q_{B0} \cos \Psi \quad \text{Equation 7.13}$$

Where Ψ is the zenith angle in radians. The zenith angle is dependent upon the latitude of the site, standard time, time at solar noon, and calendar day (Campbell, G. S., and Norman, J. M., 1998). Figure 7.2 depicts the direct beam and diffuse solar radiation emanating from the sun, transmitting and reflecting through clouds and the atmosphere, and cumulatively hitting the top surface of the (simplified) multi-layered concrete cross-tie system.

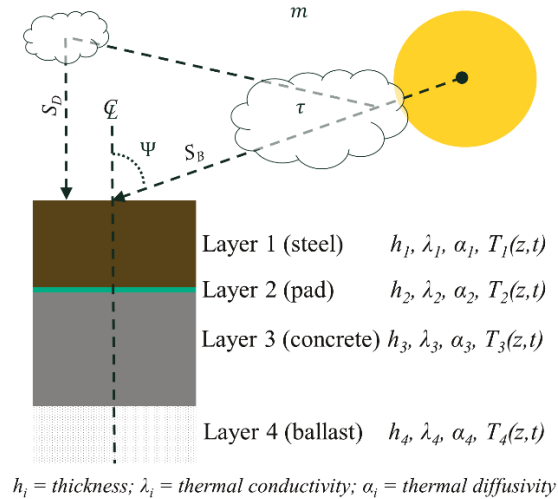


Figure 7.2. Depiction of a concrete cross-tie at the rail seat area where the steel rail line, polyurethane pad, concrete cross-tie, and aggregate ballast are depicted as layered, infinite halfspaces

7.2 Significance of Research

The distribution of internal liquid moisture within concrete cross-ties is not well understood. In particular, the state of liquid moisture at the rail seat area is complicated due to the configuration of the rail line, pad, clips, and shoulders. This study aims to enhance the concrete cross-tie industry's understanding of freeze-thaw susceptibility by measuring the internal relative humidity and temperature of instrumented cross-ties installed in track. Additionally, the results of this study can be compared against current standard tests in order to achieve improved environmental design criteria for concrete cross-tie freeze-thaw damage.

7.3 Sensor Type and Preparation of Installation Method

Hygrochron sensors known as iButtons (DS1923-F5) were selected because of their ability to record internal relative humidity and temperature using battery-power. These benefits eliminated the need to devise an external data-acquisition support system. For relative humidity measurements, the sensors make use of two electrodes joined by a capacitive film. When water vapor accumulates onto the film, then the dielectric constant, κ , measured between the two electrodes changes in a linear relationship. As such, a linear relationship can be established by experimentally measuring the dielectric constant with respect to changing relative humidity in controlled environments.

The sensors execute software correction algorithms for both relative humidity and temperature measurements based on the conversion of 8-bit or 16-bit data formats to decimal formats (Maxim, 2013). Additionally, whenever a capacitive film is exposed to high relative humidity environments (e.g., greater than 70 percent RH), for extended periods of time, then the reading may become affected in a phenomenon known as *saturation drift*. It is possible to account for this saturation drift by correcting the measured relative humidity value, RH_N , at the N^{th} hour the device has been continuously exposed to 70 percent RH and higher (or 20 percent RH and lower) with the following expression:

$$RH_{\text{saturation drift corrected}} = RH_N - \sum_{k=1}^N \frac{(0.0156)(\overline{RH}_k)(2.54^{-0.3502k})}{1 + (T_k - 25)/100} \quad \text{Equation 7.14}$$

where RH_N is the relative humidity at the end of the N^{th} hour when the device is exposed to high or low relative humidity, \overline{RH}_k is the average relative humidity through the k^{th} hour that that device has been exposed to high or low relative humidity, and \overline{T}_k is the average temperature (in Celsius) through the k^{th} hour the device has been continuously exposed to high or low relative humidity. The numbers in the equation are empirical and are derived from curve-fitted data sets (Maxim, 2013).

The sensors were fitted into iButton retainers (DS9098P) that provided soldering points for wiring. Multi-conductor shielded cabling was soldered onto the retainer in order to enable remote communication with each individual sensor. The sensor and retainer were fitted inside of a plastic dip coated eye bolt which was additionally affixed onto a steel angle bracket with unthreaded holes spaced 1 in. apart (see Figure 7.3). Eleven individual brackets with 2-in. nominal spacing (see Figure 7.4) were constructed. A single layer of GORE-TEX fabric (a fabric that allows water vapor to pass through, but not liquid water) was wrapped around each sensor in order to protect the wiring connections.



Figure 7.3. Construction of iButton sensors (left), fitted with rubber bands (center), and covered in gore-tex fabric (right)

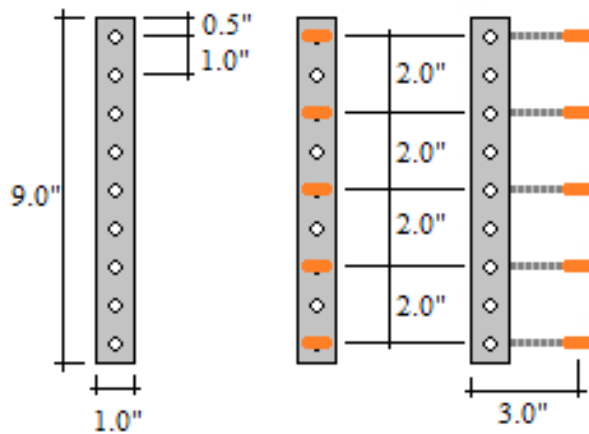


Figure 7.4. Depiction of nine in. tall brackets (left) with half-in. clearance at top and bottom. Sensors (orange) were affixed in regular two-in. increments (right)

7.3.1 Instrumentation of Concrete Crossties at Manufacturing Facility

Eleven brackets were installed into seven concrete crosstie molds at the LB Foster CXT Concrete Crossties production facility located in Tucson, AZ. The seven crossties are uniquely identified as A-444, A-445, A-446, A-447, A-448, A-449, and A-450. Crossties A-444 through A-447 were cast with brackets at both rail seat areas while crossties A-448 through A-450 were cast with brackets at one end only. The location of the sensor at either end of the crosstie was denoted by IDS or USA depending on the location of the identifying stamp number at either end of the crosstie. Each bracket was directly fastened onto the pre-stressed tendons utilizing zip ties. The bracket was positioned such that the center of the hygrothermal sensors corresponded to the geometric center of the rail seat area. The multi-conductor shielded cabling was routed to the nearest crosstie end where the cables were encased within a threaded PVC access plug. The access plug was firmly affixed onto the bottom surface of the mold such that the cable ends could be easily accessed after de-molding. After de-molding, a cap was added onto the PVC access plug to further protect the cabling ends during monitoring (see Figure 7.5).



Figure 7.5. De-molded concrete cross-ties with square cap added to PVC access plug where multi-conductor shielded cables are encased

The concrete cross-ties were manufactured no differently from the rest of the plant operations. The approximate concrete mixture design is shown in Table 7.3.

Table 7.3. Approximate Concrete Mix Design of Railroad Cross-ties

Material Type	Pounds Per Cubic Yard	Kilograms Per Cubic Meter
Type III Portland Cement	650	270
#57 Aggregate	1150	682
#8 Aggregate	750	445
Sand	829	492
Class F Fly Ash	195	116
Water	247	146
Air Entrainer	1.5 fl. oz. per 100 lb. cementitious	
High Range Water Reducer	8 fl. oz. per 100 lb. cementitious	

7.3.2 Installation of Cross-ties in Model Ballast and Track

Three of the seven cross-ties (A-444, A-448, and A-449) were transported to Rantoul, IL, where they were installed in ballast. The ballast was a 1–1.5 in. top-size yard ballast that conforms to Union Pacific Railroad (UP) Class-2 Ballast Specifications. The model ballast and concrete cross-ties were installed into a three-compartment box measuring 12-ft by 16-ft and 16 in. in

height (see Figure 7.6). Along the 16-ft length, the box was partitioned into approximately 5-ft sections for ease of construction and filling. A level surface of ballast was initially filled into each of the three compartments. The box sits atop an angled asphalt lot, which lead to one end of each of the compartments being filled with 5 to 6 in. of ballast while the other end was filled with 3 to 4 in. of ballast (see Figure 7.7). This angled surface at the underside of the model ballast also facilitated rainfall runoff and prevented stagnant water from building within the ballast. Each crosstie was lifted and positioned into the center of each compartment and seated atop the level ballast. Once the crosstie was positioned, additional ballast was then added in order to reach the top surface of the crosstie. Pads, clips, and sections of rail line were installed onto the crossties in order to better simulate track conditions.

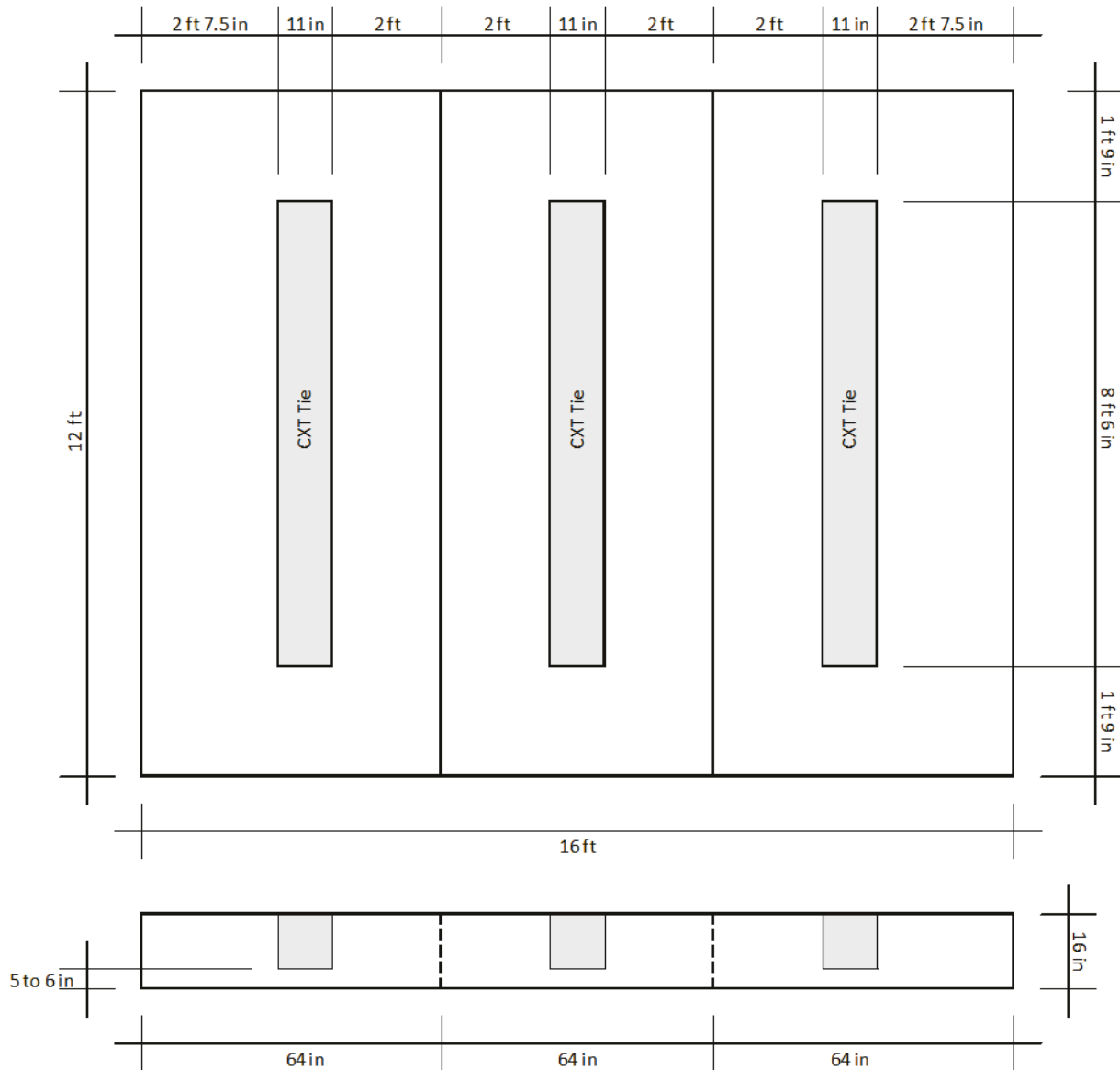


Figure 7.6. Three-compartment model ballast box housing three of the crossties atop yard ballast



Figure 7.7. Construction of ballast box (left) and final configuration (right)

Publicly available weather information at Rantoul, IL, reveals that there is an average annual snowfall of 37.1 in. and average annual rainfall of 18.2 inches. The average daily high and nightly low temperatures regularly fluctuate between freezing and non-freezing resulting in a relatively high number of approximately 80 to 100 annual freeze-thaw cycles (Hershfield, D. M., 1973).

The remaining four crossties (A-445, A-446, A-447, and A-450) were transported to a location approximately 10 kilometers south of Lytton, BC, to be installed in track. The selected track is owned by Canadian National Railway (CN) and runs between Hope and Lytton, BC, along the Trans-Canada Highway and Fraser River. The four crossties were installed near the Cisco Bridges along track mile markers 103.8 and 104.2 (see Figure 7.8). Additionally, hygrothermal sensors were installed in an electrical conduit box in order to record ambient air temperatures and relative humidity immediately adjacent to the installation site.



Figure 7.8. Google satellite image showing approximate location of four ties installed in track near Cisco Bridges, Lytton, BC (annotated and re-printed in accordance to Google Maps license of printed report and presentation media)

Publicly available weather information at Lytton, BC, reveals that there is extensive snowfall along this area of the Fraser River valley. Lytton, BC, records an average annual snowfall of 46.22 in. and average annual rainfall of 13.33 inches. The warm season lasts from June 17 to September 9, while the cold season lasts from November 15 to February 19. More importantly, the average daily high and nightly low temperatures regularly fluctuate between freezing and non-freezing from March to May and from September to November. This fluctuating temperature results in approximately 60 to 80 freeze-thaw cycles of (Fraser, J. K., 1959). After installation in October 2013, research partners at the University of British Columbia, Okanagan, retrieved recorded data every 3 months through March 2015.

7.3.3 Complementary Installations of Modulus of Rupture Beams and Model Concrete Crosstie in Model Ballast

Three instrumented modulus of rupture (MOR) beams measuring 6-in. by 6-in. by 21-in. and two model crossties measuring 9-in. by 9-in. by 16-inches. were installed into the model ballast such that their top surface was level with the crossties. The nominal concrete mixture design for these complementary members is shown in Table 7.4. The concrete mix design was intended to be comparable to the concrete crossties installed in track and in model ballast. Each MOR beam was instrumented with four hygrothermal sensors positioned 11.5 in. from either end of the beam

and at depths of 0.5, 1.5, 4.5, and 5.5 in., as shown in Figure 7.9. The benefit of these beams is that they are more easily removed from ballast than the crosssties in order to re-condition them in an environmentally controlled room whenever necessary. Each model crossstie was instrumented with four hygrothermal sensors positioned 8 in. from either end of the length and at depths of 0.5, 2.5, 5.5, and 8.5 in., as shown in Figure 7.10. Additionally, one model tie was constructed with anchors such that a polyurethane pad and section of rail could be fastened at a later point in time in order to better simulate track environments.

Table 7.4. Nominal Concrete Mix Design of Modulus of Rupture Beams and Model Crosssties

Material Type	Pounds Per Cubic Yard	Kilograms Per Cubic Meter
Type I Portland Cement	718	426
#7 Aggregate	2085	1236
Sand	1257	746
Water	216	128
High Range Water Reducer	12 fl. oz per 100 lb. cementitious	

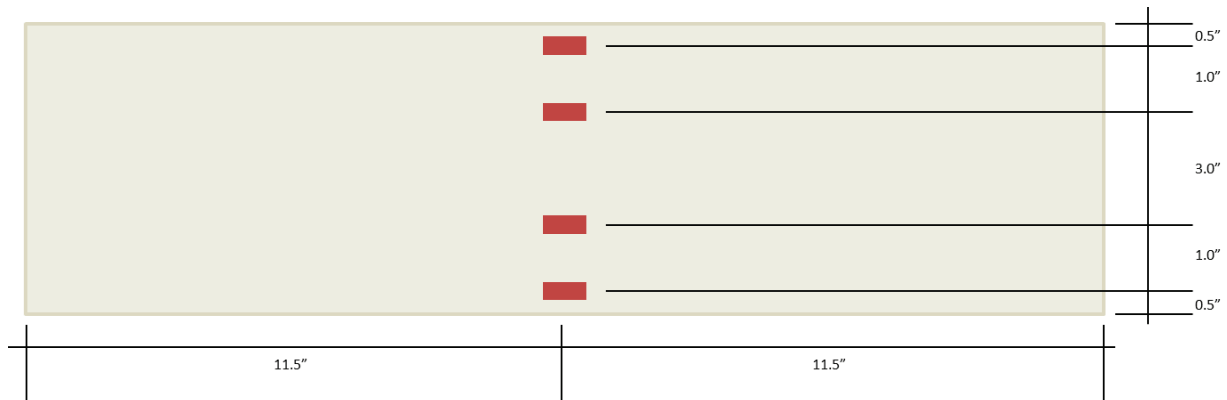


Figure 7.9. Diagram of instrumented modulus of rupture beam complementarily installed in model ballast in Rantoul, IL

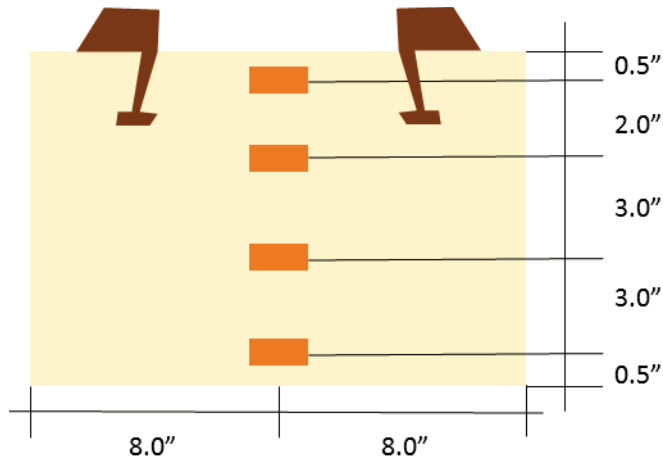


Figure 7.10. Diagram of instrument model cross-tie complementarily installed in model ballast in Rantoul, IL

7.4 Experimental Results

The instrumented concrete cross-ties, model cross-ties, and modulus of rupture beams yielded similar behaviors. Namely, hygrothermal sensors functioned appropriately at early ages and failed at later ages. However, the large data set observed over the 1 year period allows for meaningful observations and conclusions to be drawn. The following sections address internal temperature and relative humidity gradients as well as ambient temperature, precipitation, relative humidity, and solar radiation.

7.4.1 Relative Humidity Results over Observation Period

Although ambient relative humidity conditions fluctuate daily, the internal relative humidity of concrete members fluctuate in a more seasonal manner except for the near surface of the concrete surface. Figure 7.11 shows a model concrete cross-tie moved from a dry, indoor environment to model ballast in Rantoul, IL, where sensors closer to the exterior surface (0.5 and 8.5 in.) rise in relative humidity value. Internal relative humidity at depths of 2.5 and 5.5 in. remain significantly high and do not respond to the change in environment in a drastic manner. A similar trend is observed in a modulus of rupture beam installed in ballast (see Figure 7.12).

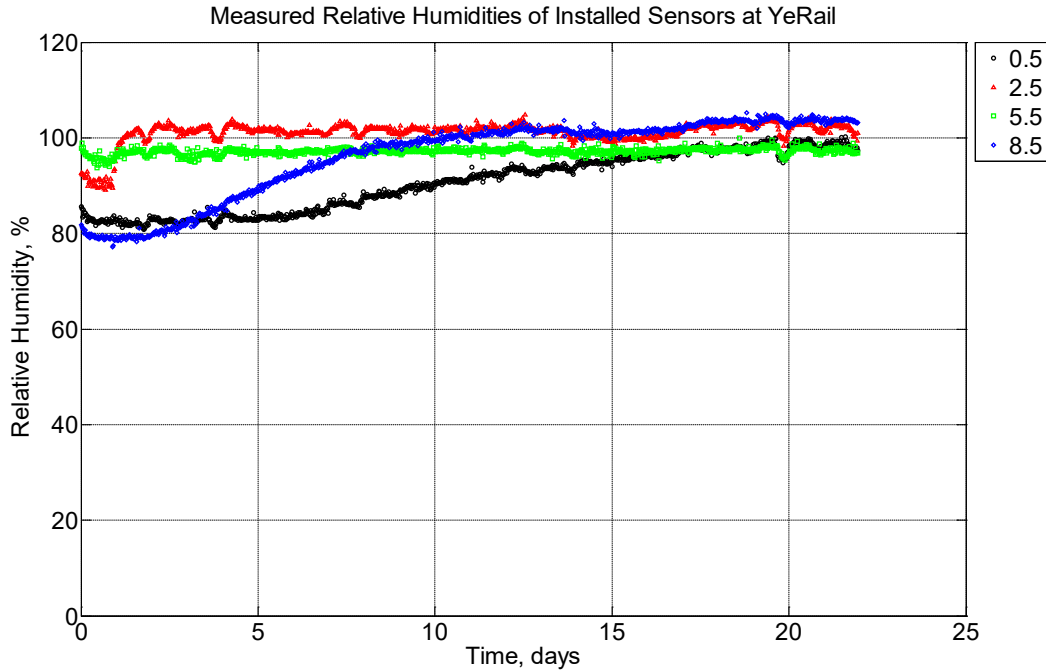


Figure 7.11. Measured relative humidity at depths of 0.5 in. (12.7 mm), 2.5 in.s (63.5 mm), 5.5 in. (139.7 mm), and 8.5 in. (215.9 mm) from the surface of a model concrete crosstie (labeled YeRail) installed in ballast in Rantoul, IL, between November 29, 2014, through December 21, 2014. An 8 mm thick polyurethane pad and 12 in. (30.48 cm) length 136 lb/yd (67.5 kg/m) section of steel rail are additionally installed atop the model concrete crosstie

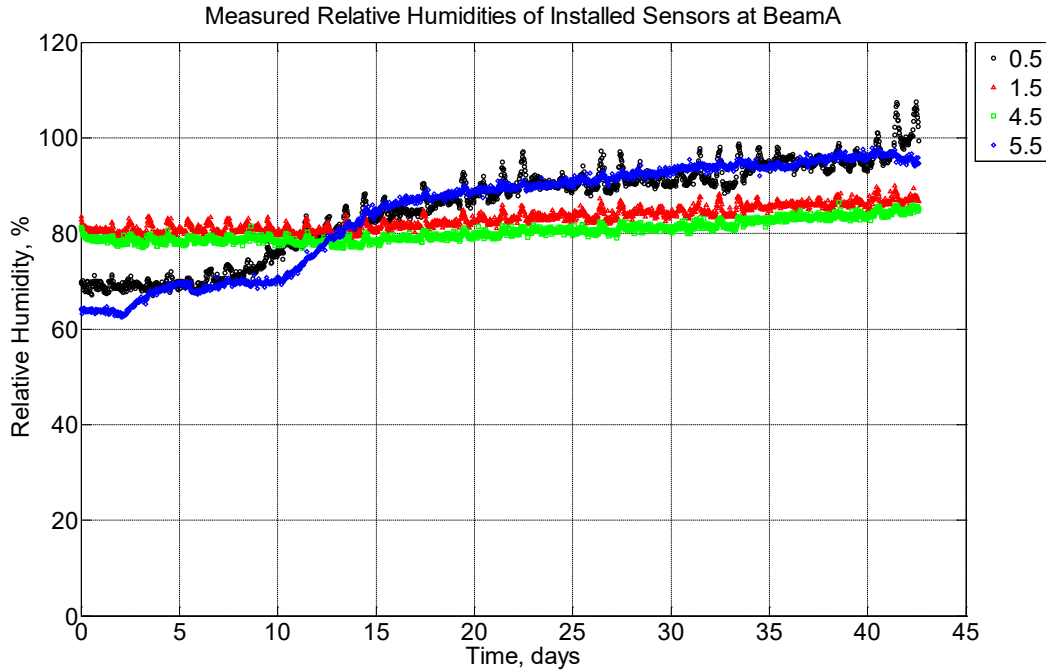


Figure 7.12. Measured relative humidity at depths of 0.5 in. (12.7 mm), 1.5 in. (38.1 mm), 4.5 in. (114.3 mm), and 5.5 in. (139.7 mm) from the surface of a modulus of rupture beam (labeled A) installed in ballast in Rantoul, IL, between October 19, 2014, through November 30, 2014

Whenever these concrete members were installed in ballast, measureable relative humidity values inside the concrete steadily increased and did not appreciably decrease. In order to confirm that the proposed one-dimensional relative humidity model is appropriate for the finite-width concrete member in a drying case, the modulus of rupture beams were removed from ballast, periodically, and moved into an environmentally controlled room where the ambient relative humidity was maintained at 50 percent relative humidity. The response of the sensors was as expected where internal humidity near the exterior of the concrete surface fell more quickly than what was measured at the interior of the concrete member (see Figure 7.13).

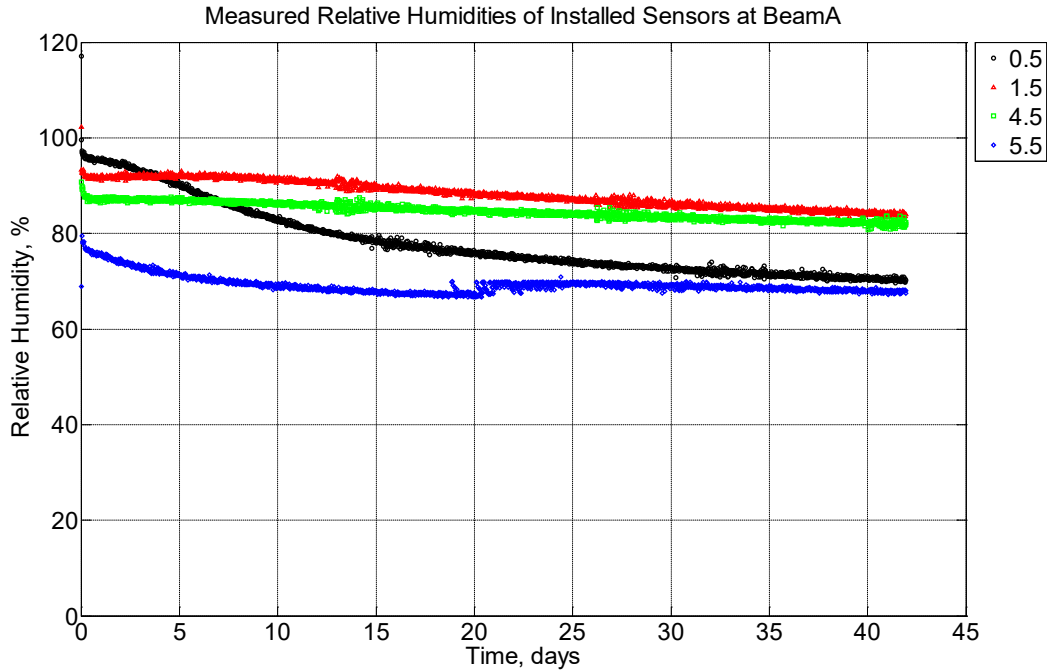


Figure 7.13. Measured relative humidity at depths of 0.5 in. (12.7 mm), 1.5 in. (38.1 mm), 4.5 in. (114.3 mm), and 5.5 in. (139.7 mm) from the surface of a modulus of rupture beam (labeled A) located inside an environmentally controlled room (50% RH, 23 °C) between July 29, 2014, through September 9, 2014

7.4.2 Temperature Results over Observation Period

Figure 7.14 shows a concrete crosstie installed in track near Lytton, BC, in the winter season. Each of its embedded hygrothermal sensors reported wide ranging temperature fluctuations reflecting the daily ambient temperature changes. Moreover, it was observed that fluctuations at the top and bottom of the crosstie experienced freezing in a cyclic manner. Figure 7.15 similarly depicts a concrete crosstie installed in model ballast in Rantoul, IL, in the summer months. Because of the shorter observation period shown in Figure 7.15, the daily and nightly fluctuations are more prominently evident. Near the surface of the concrete crosstie, the temperatures increased to values much higher than the interior of the member. During nighttime temperatures, the concrete crosstie appeared to reach comparable values.

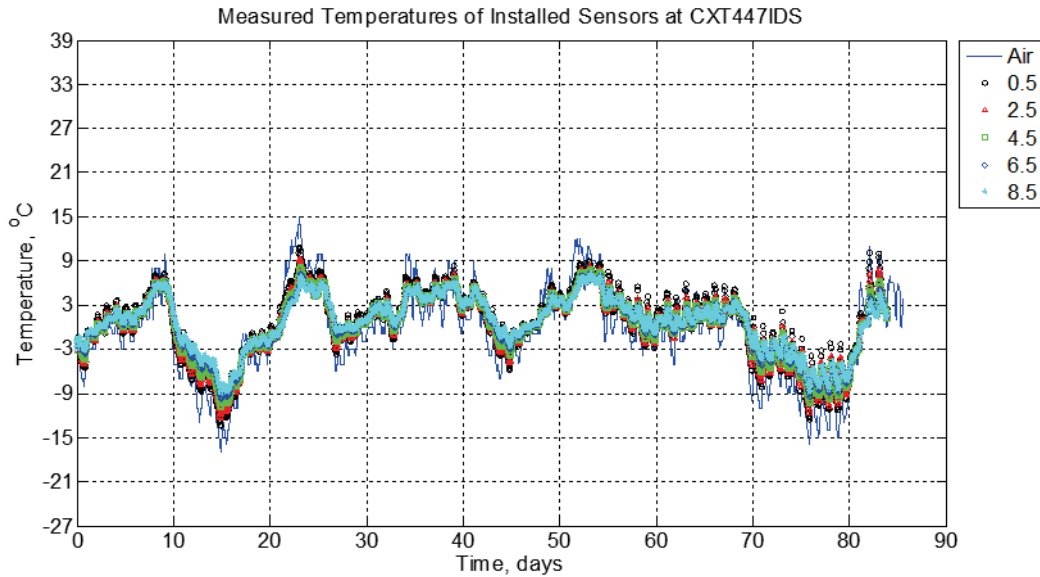


Figure 7.14. Measured air temperature and measured temperature values at depths of 0.5 in. (12.7 mm), 2.5 in. (63.5 mm), 4.5 in. (114.3 mm), 6.5 in. (139.7 mm), and 8.5 in. (215.9 mm) from the surface of a concrete crosstie (labeled CXT447IDS) installed in track near Lytton, BC, between November 22, 2013, through February 14, 2014. An 8 mm thick polyurethane pad and steel rail are additionally installed atop the concrete crosstie

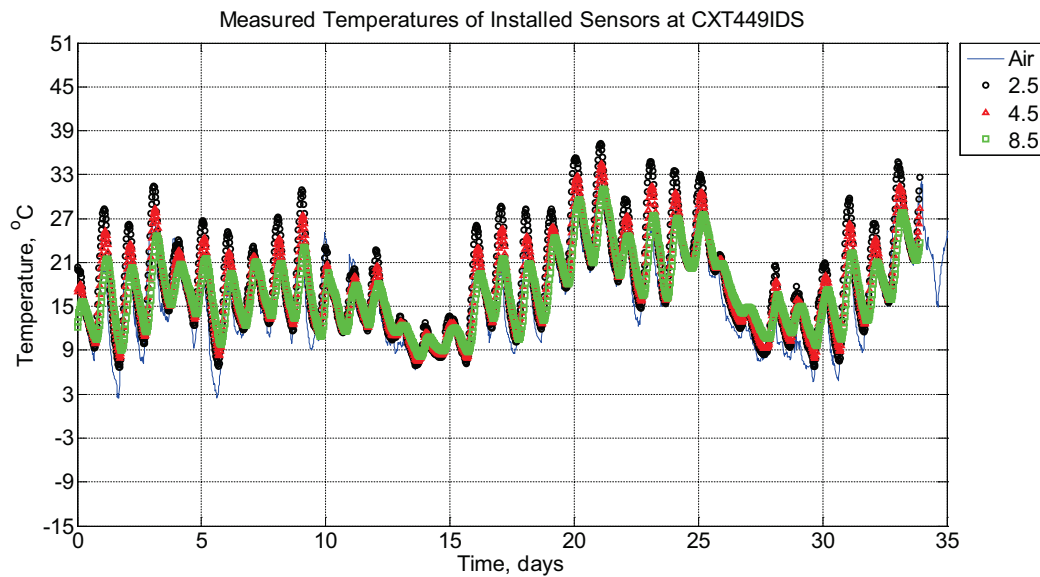


Figure 7.15. Measured air temperature and measured temperature values at depths of 2.5 in. (63.5 mm), 4.5 in. (114.3 mm), and 8.5 in. (215.9 mm) from the surface of a concrete crosstie (labeled CXT449IDS) without a polyurethane pad nor rail installed in ballast in Rantoul, IL, between April 17, 2014, through May 21, 2014

7.5 Internal Relative Humidity Distribution

The one-dimensional moisture transport equation shown in Equation 7.1 was executed in a Matlab script to predict the relative humidity distribution across the depth of 6 in. (153 mm) or 9 in. (230 mm) depending on whether the concrete sample being analyzed is a modulus of rupture beam or a (model) crosstie. Other parameters were held nearly constant throughout the analysis because of the similarity of the concrete mixture design. The moisture diffusivity at complete saturation is $0.86 \times 10^{-6} \text{ m}^2/\text{hr}$, the regression coefficient is selected as 15, α is 0.05, and the bifurcation relative humidity point is 75 percent RH (Kang, S. -T., Kim, J. -K., Kim, J. -S., Lee, Y., and Park, Y. -D., 2012).

In Figure 7.16, the depth across a model concrete crosstie is depicted with an initial condition where the interior of the concrete sample is saturated while the exterior of the concrete sample is in equilibrium with the surrounding environment (approximately 80 percent RH). The surrounding environment is defined as the boundary conditions where externally positioned hygrothermal sensors monitor the ballast conditions. The hygrothermal sensor located at the top surface of the ballast is additionally modified according to Table 7.2. Over the span of 20 days, the model concrete crosstie is subjected to high relative humidity values which leads to its relative humidity values to increase over time. This increase with respect to time is encapsulated by the model (continuous line) moving rightward, not exceeding 100 percent RH.

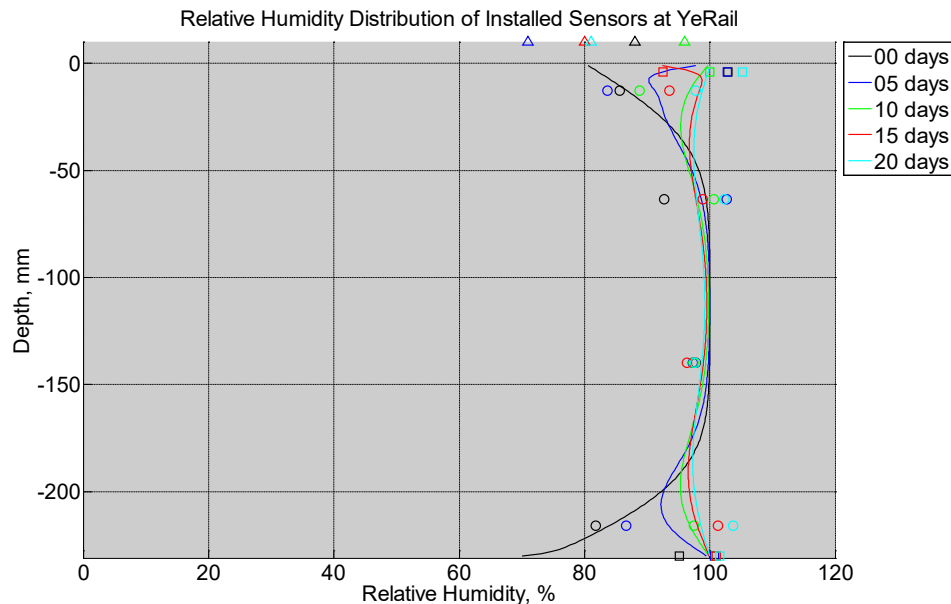


Figure 7.16. Measured (markers) and modeled (continuous line) relative humidity profile distribution as a function of depth inside a model concrete crosstie (labeled YeRail) installed in ballast in Rantoul, IL, between November 29, 2014, through December 21, 2014. An 8 mm thick polyurethane pad and 12 in. (30.48 cm) length 136 lb/yd (67.5 kg/m) section of steel rail are additionally installed atop the model concrete crosstie. The model does not incorporate a polyurethane pad nor steel rail line. Triangular markers denote relative humidity value from KTIP weather station, square markers denote measured relative humidity values from ballast, and circular markers denote measured relative humidity values inside concrete

The predicted values throughout the depth of the model concrete crosstie can be compared against the experimentally determined relative humidity values as measured by the hygrothermal sensors. This comparison produces Figure 7.17 where each point represents a singular moment in time and whose coordinates represent predicted and measured relative humidity values. A perfect prediction of relative humidity values would produce a scatter of data that suitably overlies the line of equality. Figure 7.17 shows a relatively good agreement between predicted and measured relative humidity values at each of the four depths inside the model concrete crosstie.

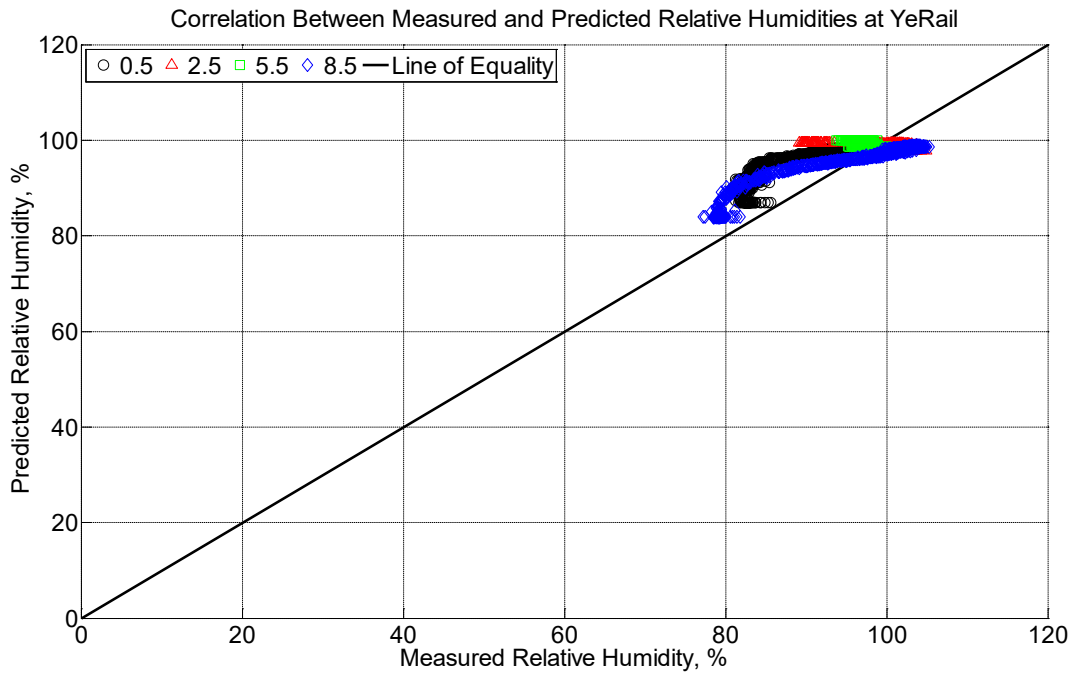


Figure 7.17. Correlation between measured and predicted relative humidity values 0.5 in. (12.7 mm), 2.5 in. (63.5 mm), 5.5 in. (139.7 mm), and 8.5 in. (215.9 mm) from the surface of a model concrete crosstie (labeled YeRail) installed in ballast in Rantoul, IL, between November 29, 2014, through December 21, 2014. An 8 mm thick polyurethane pad and 12 in. (30.48 cm) length 136 lb/yd (67.5 kg/m) section of steel rail are additionally installed atop the model concrete crosstie. The model does not incorporate a polyurethane pad nor steel rail line

The inclusion of modified boundary conditions to reflect moisture becoming entrapped by the polyurethane pad and rail line is not wholly isolated due to the finite-width nature of the model concrete crosstie. Figure 7.18 shows the same predictive model applied to a modulus of rupture beam similarly installed in the model ballast in Rantoul, IL. However, no confining polyurethane pad nor rail line were installed. In this scenario, the modulus of rupture beam is not wholly saturated at the interior at the start of the simulation. However, a similar trend is observed that the modeled line is moving rightward indicating an increase in predicted internal relative humidity. Figure 7.19 compares the predicted and measured relative humidity values to again find a comparably good agreement.

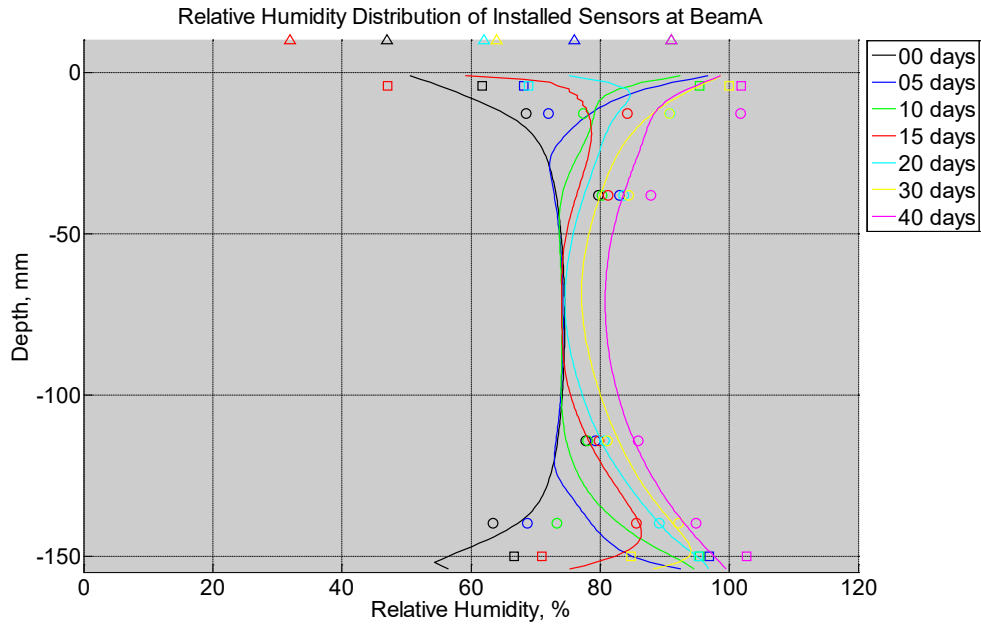


Figure 7.18. Measured (markers) and modeled (continuous line) relative humidity profile distribution as a function of depth inside modulus of rupture beam (labeled A) installed in ballast in Rantoul, IL, between October 19, 2014, through November 30, 2014. Triangular markers denote relative humidity value from KTIP weather station, square markers denote measured relative humidity values from ballast, and circular markers denote measured relative humidity values inside concrete

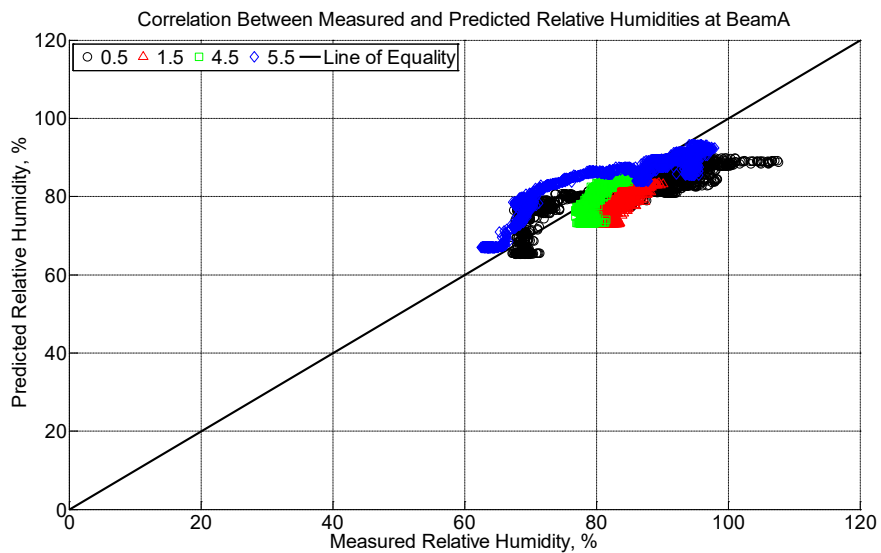


Figure 7.19. Correlation between measured and predicted relative humidity values 0.5 in. (12.7 mm), 1.5 in. (38.1 mm), 4.5 in. (114.3 mm), and 5.5 in.s (139.7 mm) from the surface of a modulus of rupture beam (labeled A) installed in ballast in Rantoul, IL, between October 19, 2014, through November 30, 2014

In instances of wetting as depicted in Figure 7.11 and Figure 7.12, the predictive moisture transport model is suitable for characterizing the increasing internal relative humidity. In the event of drying, the boundary conditions can be altered to remain constant at both the topside and underside of a modulus of rupture beam when it is moved to an environmentally controlled room. Figure 7.20 shows the predicted change in relative humidity when a nominally saturated concrete modulus of rupture beam is moved into a 50 percent RH controlled environment. It is evident that the predicted values (continuous line) shifts leftward indicating drying. When these predicted values are again compared to measured values (see Figure 7.21), the good agreement between predicted and measured relative humidity values becomes apparent again.

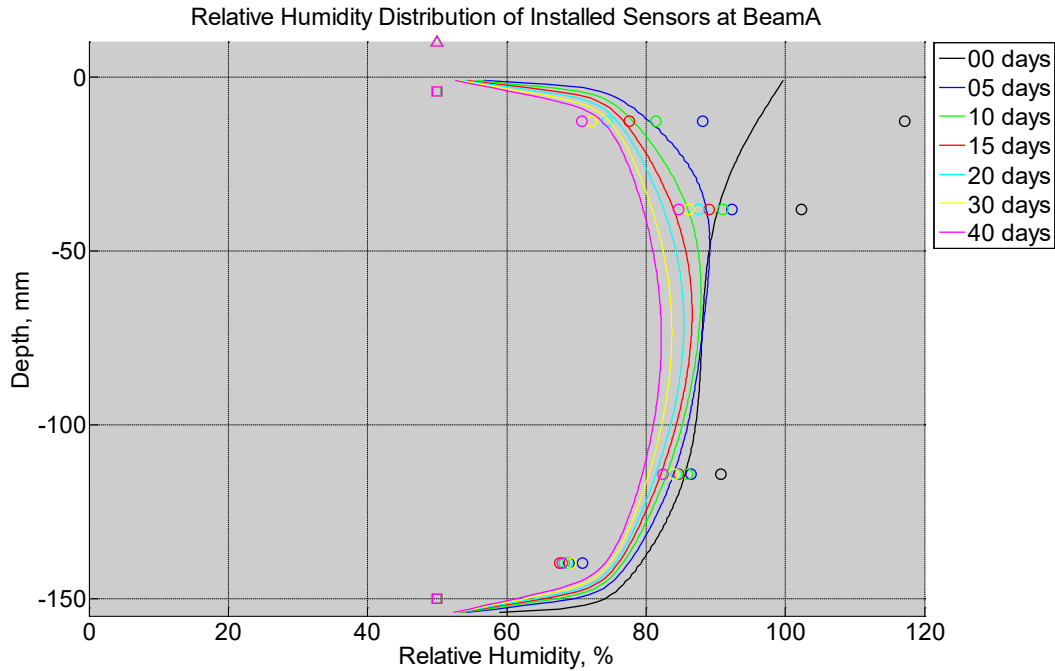


Figure 7.20. Measured (markers) and modeled (continuous line) relative humidity profile distribution as a function of depth inside modulus of rupture beam (labeled A) located inside an environmentally controlled room (50% RH, 23 °C) between July 29, 2014, through September 9, 2014. Triangular markers denote relative humidity value from control panel, square markers denote measured relative humidity values from ambient sensors, and circular markers denote measured relative humidity values inside concrete

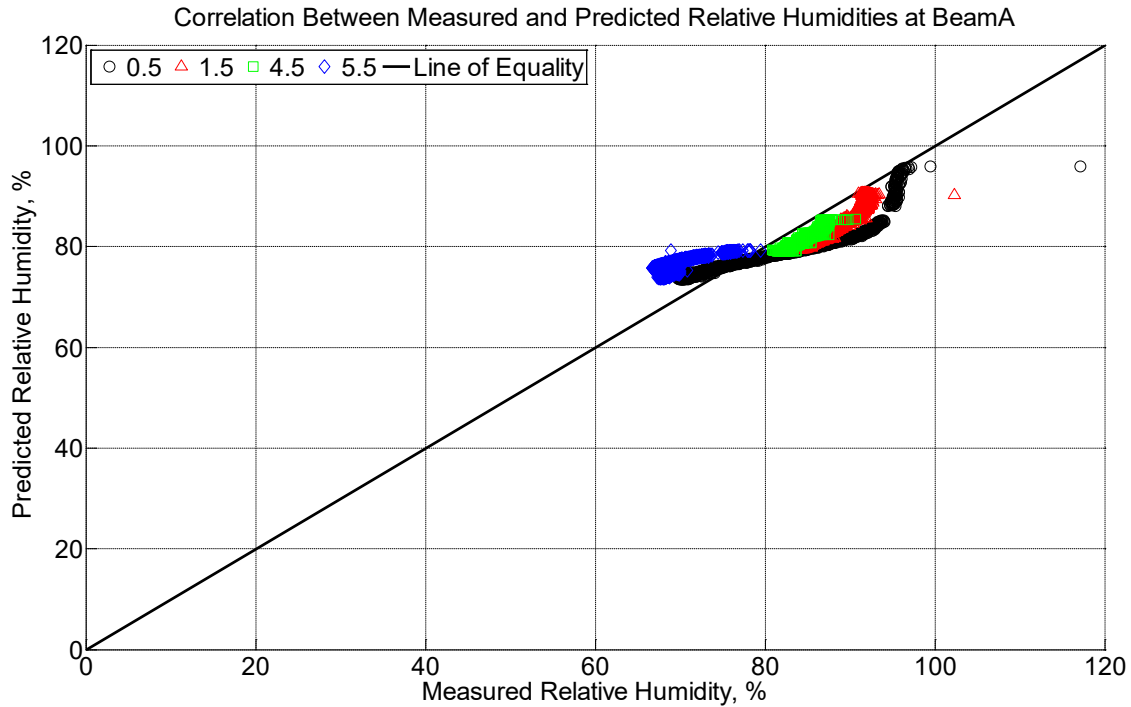


Figure 7.21. Correlation between measured and predicted relative humidity values 0.5 in. (12.7 mm), 1.5 in. (38.1 mm), 4.5 in. (114.3 mm), and 5.5 in. (139.7 mm) from the surface of a modulus of rupture beam (labeled A) located inside an environmentally controlled room (50% RH, 23 °C) between July 29, 2014, through September 9, 2014

7.5.1 Solar Radiation Estimation

The solar radiation at a given geo-temporal location must be estimated in order for the one-dimensional, multi-layered temperature model to work suitably. As such, Equation 7.11 is solved in order to estimate the total incoming solar radiation in Rantoul, IL, and Lytton, BC, throughout the same time period that the predictive temperature modeling is conducted. Figure 7.22 shows the observed temperature and relative humidity in Rantoul, IL, during cool, winter months. In this figure, the estimated solar radiation is relatively low in value. This is sensible due to the shorter length of daytime and increased amount of cloud cover in the winter months. Figure 7.23 shows a similar estimation of the solar radiation in Lytton, BC, during the summer months. Again, the increased estimated solar radiation during this time period is sensible due to lengthier daylight hours and decreased instances of extensive cloud cover.

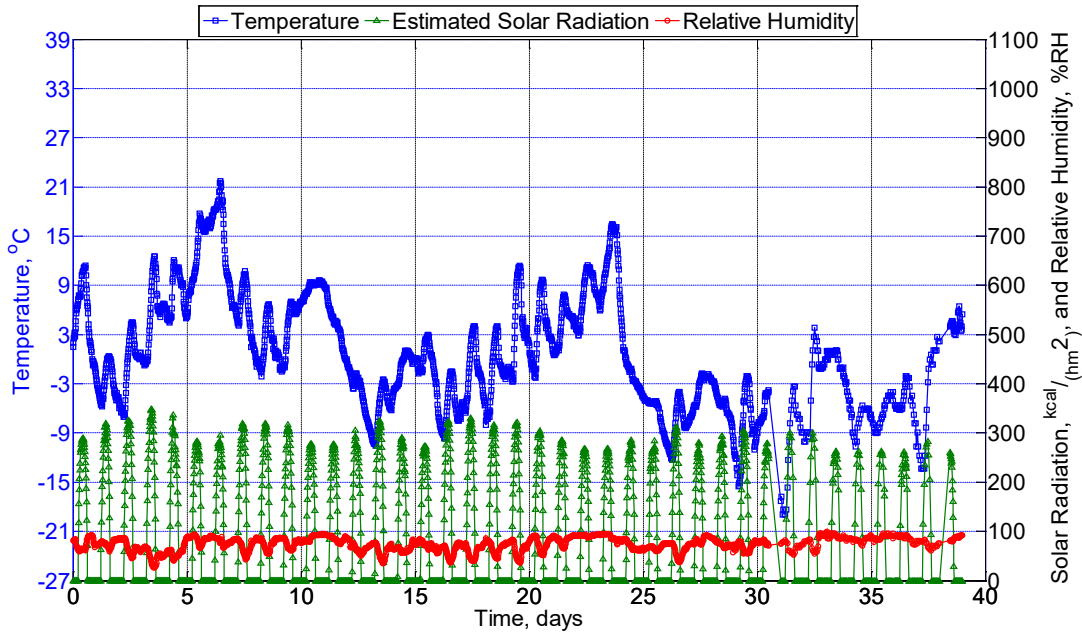


Figure 7.22. Temperature and relative humidity collected from weather station KTIP in Rantoul, IL, from November 12, 2013, through December 18, 2013. Solar radiation is estimated over this same timeframe

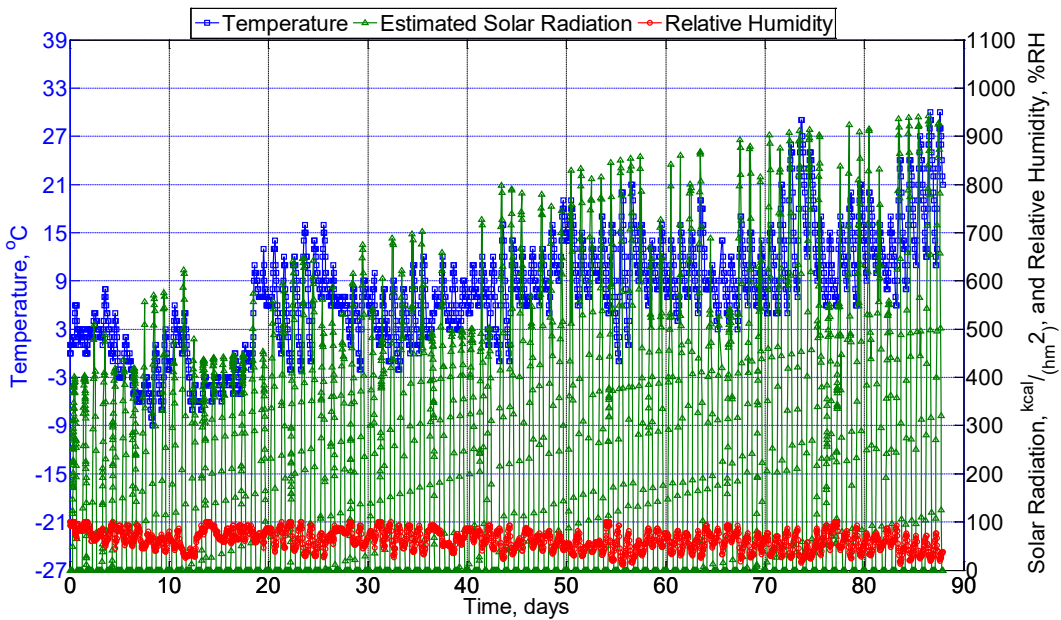


Figure 7.23. Temperature and relative humidity collected from weather station CWLY in Lytton, BC, from February 18, 2014, through May 14, 2014. Solar radiation is estimated over this same timeframe

7.5.2 Internal Temperature Distribution

The one-dimensional temperature equation shown in Equation 7.9 is executed in a Matlab script in order to predict temperature distribution across the depth of a 6 in. (153 mm) or 9 in. (230 mm) depending on whether the concrete sample being analyzed is a modulus of rupture beam or a (model) crosstie. The parameters involved in order to predictively solve the temperature distribution are held constant throughout the analysis. The pavement surface convection coefficient is 16.29 kcal/m²C°, the effective absorptivity is 0.55 throughout the entire time period, and the thermal conductivities and thermal diffusivities of each material type are defined in Table 7.5.

Table 7.5. Thermal Conductivity and Thermal Diffusivity of Material Types used in the Temperature Predictive Modeling. Values are Adapted from Either Reference Values, ¹ (Hiller, J. E., and Qin, Y., 2014) or ² (Pielichowski, J., Prociak, A., and Sterzynski, T., 2000).

Material Type	Thermal Conductivity, λ (kcal/hmC°)	Thermal Diffusivity, α (m ² /h)
1025 Carbon Steel	31.2480	0.0531
Polyurethane	0.0172	0.0022 ²
Portland Cement Concrete	1.85 ¹	0.0025 ¹
Aggregate	2.58 ¹	0.0030 ¹

In Figure 7.24, the model output is shown at seven points in time spanning 90 days of analysis of a concrete crosstie installed in track near Lytton, BC. The only inputs into this model are the ambient air temperature at the topside of the concrete crosstie as measured from a nearby weather station and the estimated solar radiation. The multi-layered temperature model was used in two configurations: with a polyurethane pad and steel rail, or without a polyurethane pad and steel rail. The results from these two configurations is documented in Appendices B4, B6, B8, and B10. It is readily observed that the incorporation of a polyurethane pad and steel rail line does not greatly enhance the predictive fit of the model. This is shown in Figure 7.26 where the predicted temperature values are compared against the measured temperature values and excellent fit is observed. This is accomplished despite not incorporating a polyurethane pad or steel rail line. In an effort to more properly depict the physical thicknesses of the overlying materials, an analysis is performed where the polyurethane pad is constructed with a thickness of 8 mm while the steel rail line is constructed with a thickness of 10 mm. The result of this fit is shown in Figure B10-24 in Appendix B where the increased insulation from the polyurethane pad blunts the effect of the ambient air temperature and the incoming solar radiation.

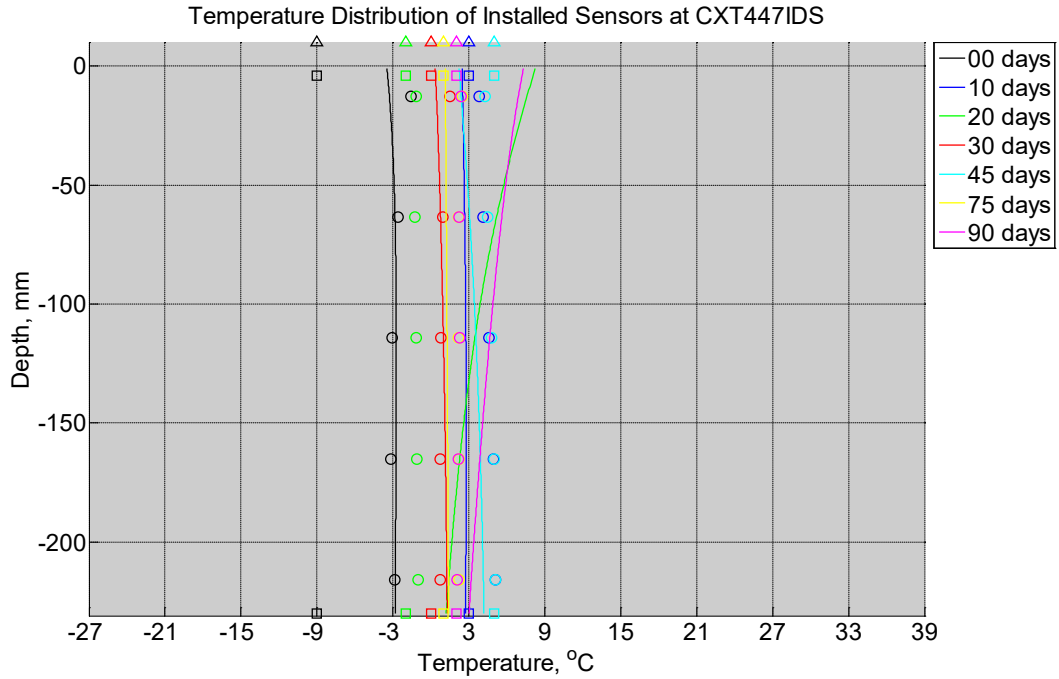


Figure 7.24. Measured (markers) and modeled (continuous line) temperature profile distribution as a function of depth inside a concrete crosstie (labeled CXT447IDS) installed in track near Lytton, BC, between November 22, 2013, through February 14, 2014. An 8-mm thick polyurethane pad and steel rail are additionally installed atop the concrete crosstie. The model does not incorporate a polyurethane pad nor steel rail line. Triangular markers denote temperature value from CWLY weather station, square markers denote assumed temperature values in ballast, and circular markers denote measured temperature values inside concrete

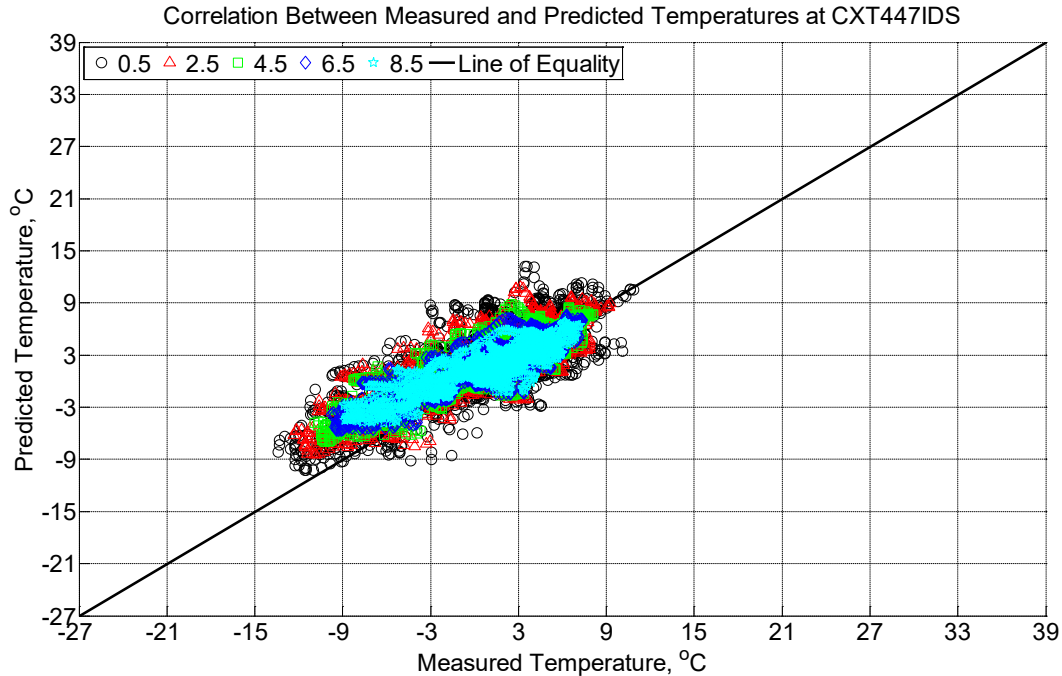


Figure 7.25. Correlation between measured and predicted temperature values 0.5 in. (12.7 mm), 2.5 in. (63.5 mm), 4.5 in. (114.3 mm), 6.5 in. (139.7 mm), and 8.5 in. (215.9 mm) from the surface of a concrete cross-tie (labeled CXT447IDS) installed in track near Lytton, BC, between November 22, 2013, through February 14, 2014. An 8 mm thick polyurethane pad and steel rail are additionally installed atop the concrete cross-tie. The model does not incorporate a polyurethane pad nor steel rail line

Figure 7.26 and Figure 7.27 are also predictions of internal temperature, although these depict summer months. Unlike the prediction during winter months in Figure 7.24 and Figure 7.25, it is evident that temperature is over-predicted in summer months. Several issues may explain the over-prediction. First, the temperature model is reliant upon an estimation of incoming solar radiation. Although the estimation adapted from Spokas and Forcella is demonstrably good, it is anticipated that there are inherent irregularities with regards to recorded weather when applied to specific instances in time (Forcella, F., and Spokas, K., 2006). Passing cloud cover, hazy conditions, and shade from nearby structures potentially obstruct the true incoming solar radiation. Secondly, and of greater importance, is the notion of applying a one-dimensional pavement model to a three-dimensional concrete cross-tie in ballast. Heat radiation is not occurring linearly through the multiple layers. Instead, heat is transmitting through the layers and is also transmitting through the ballast which is in contact with the side of the cross-ties. As such, it is likely that an improved model incorporate this additional transference of heat through the aggregate ballast.

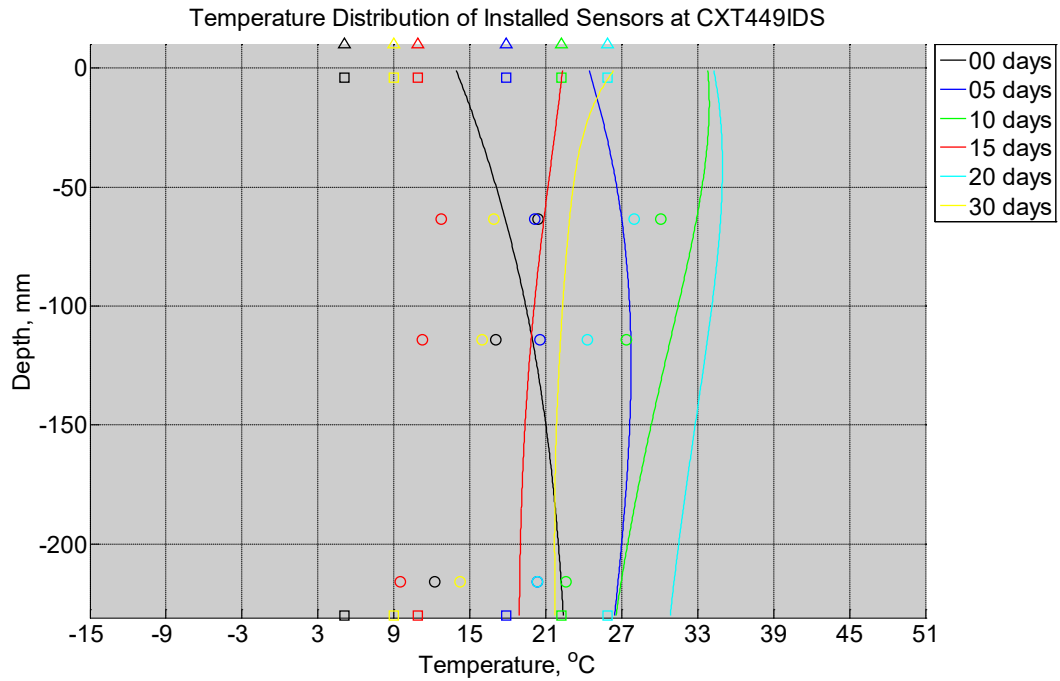


Figure 7.26. Measured (markers) and modeled (continuous line) temperature profile distribution as a function of depth inside a concrete cross-tie (labeled CXT449IDS) without a polyurethane pad nor rail installed in ballast in Rantoul, IL, between April 17, 2014, through May 21, 2014. Triangular markers denote temperature value from KTIP weather station, square markers denote measured temperature values from ballast, and circular markers denote measured temperature values inside concrete

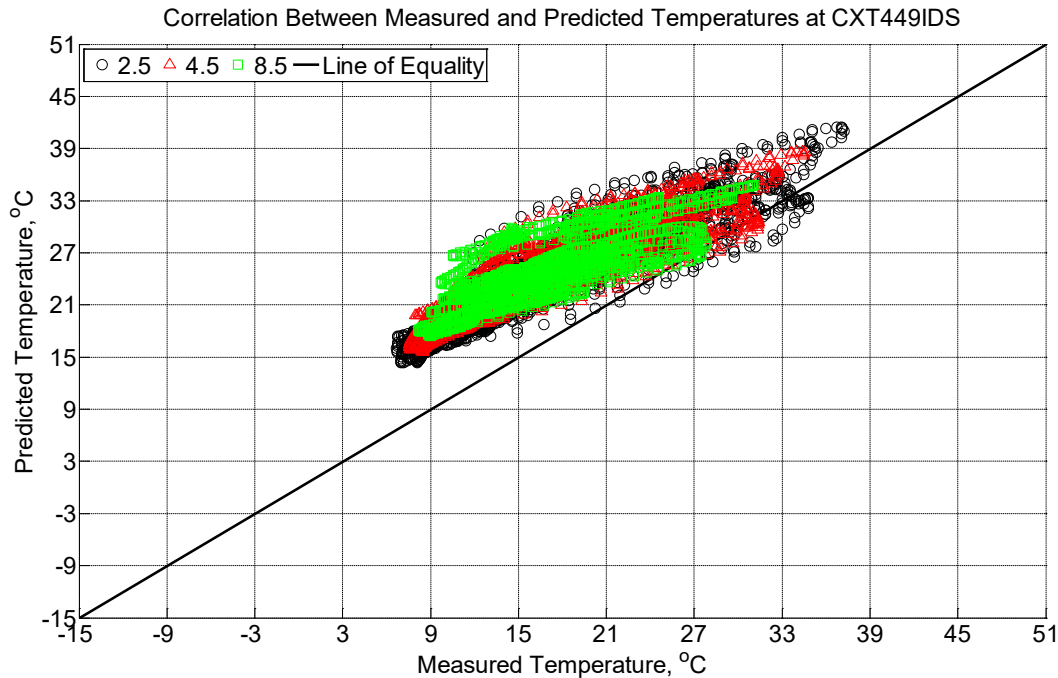


Figure 7.27. Correlation between measured and predicted temperature values 2.5 in. (63.5 mm), 4.5 in. (114.3 mm), and 8.5 in. (215.9 mm) from the surface of a concrete crosstie (labeled CXT449IDS) without a polyurethane pad nor rail installed in ballast in Rantoul, IL, between April 17, 2014, through May 21, 2014

7.5.3 Effect of Ballast Conditions

The effect of the ballast acts in two manners upon the concrete crosstie: firstly, it serves as a fast-track avenue for liquid moisture to travel through and (in a well-drained ballast) flow away from the crosstie, secondly, it acts as an additional source of heat transmittance. Both of these factors have an effect on the internal relative humidity and temperature of a concrete crosstie installed in ballast.

Hygrothermal sensors installed in ballast at the topside and underside of a concrete crosstie measured both relative humidity and temperature, depicted in Figure 7.28 and Figure 7.29, respectively. In Figure 7.28, it is evident that the sensor installed at the topside of a crosstie in the ballast reported large fluctuations that are comparable to the fluctuations seen in ambient relative humidity measurements. This indicates that aggregates in ballast react rapidly to changing moisture conditions and can act as a desiccating force for the concrete crosstie. However, at the underside of the concrete crosstie, it is evident that relative humidity can persist at high levels near 100 percent RH. This high relative humidity does not necessarily indicate a poorly draining ballast. It instead suggests that moisture is trapped within the highly absorptive aggregate and creates a locally humid environment. As a result, this drained, humid ballast acts to slow any drying of the concrete crosstie itself. In large part, this supports the results seen in Figure 7.11 through Figure 7.13 where the internal relative humidity of any concrete member is steadily rising whenever the member is installed within ballast.

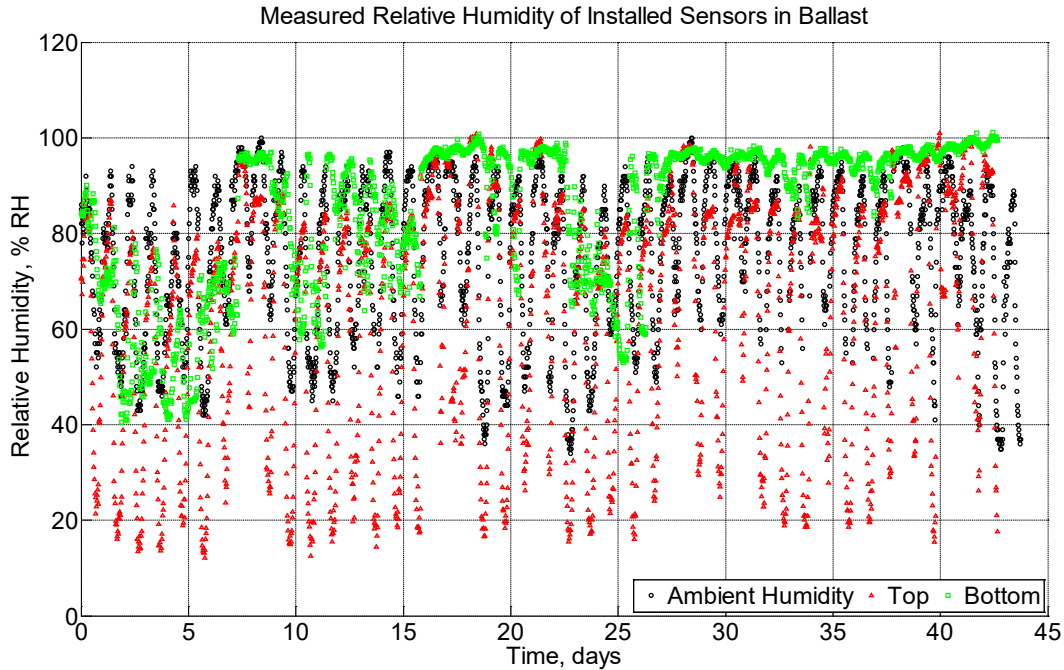


Figure 7.28. Measured relative humidity of model ballast at top and bottom of concrete cross-tie in Rantoul, IL, between August 1, 2015, through September 13, 2015. Ambient relative humidity measured from a nearby weather station KTIP is also shown

Similarly, temperature changes within the ballast are observed in Figure 7.29. At the topside of the ballast, measured temperatures fluctuate to values much higher than ambient air temperatures suggesting that incoming solar radiation is heating the ballast. In turn, this increased temperature immediately adjacent to the concrete cross-tie can supplement the rise in internal temperature in the summer months as evidenced in Figure 7.27. At the underside of the concrete cross-tie, the hygrothermal sensor installed in ballast shows a muted response due to changing daily temperatures suggesting that the ballast at the underside of the cross-tie functions as a thermal insulation. While this temperature observation in the ballast may not entirely affect concrete cross-tie freeze-thaw performance, this observation may have an impact on the frost heaving potential of the ballast.

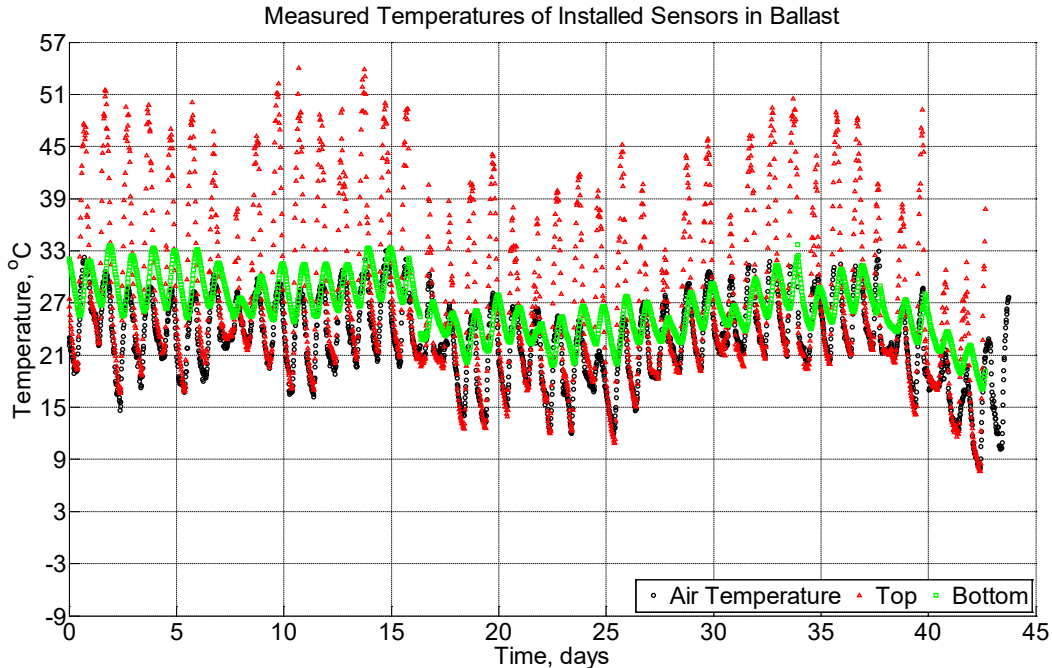


Figure 7.29. Measured temperature of model ballast at top and bottom of concrete crosstie in Rantoul, IL, between August 1, 2015, through September 13, 2015. Ambient air temperature measured from a nearby weather station KTIP is also shown

7.6 Conclusions

Concrete crossties were subjected to freezing-thawing climates across North America that can lead to freeze-thaw damage. Concrete crossties, modulus of rupture beams, and model crossties were instrumented with hygrothermal sensors to monitor their internal relative humidity and temperature in two locations: Rantoul, IL, and Lytton, BC. Two one-dimensional models are applied in the analysis to predict the three-dimensional response of the concrete crossties in track. It was found that:

- Hygrothermal sensors performed well at early-ages yet failed at later ages. At the time of failure, measured relative humidity values were in excess of 95 percent suggesting that a combination of persistently high relative humidity, alkalinity from the hydrated cement paste, and possibly high liquid moisture contributed to the material failure of the capacitance film of the hygrothermal sensor. This shows that the ties are very good at retaining moisture. The ballast acts to trap moisture, reducing the tie drying rate significantly. Because the ties are kept in a moist state much of the year, protection against freezing is needed.
- A predictive one-dimensional moisture transport model is adequate to predict the change of internal relative humidity of a concrete member installed in aggregate ballast. The suitability of the model is limited to the geometric center of the rail seat area where the hygrothermal sensors were installed. It is highly likely that the relative humidity closer to the sides of the crossties directly exposed to the aggregate ballast are subject to higher relative humidity values. An improved two-dimensional (or three-dimensional) model

may better predict the state of internal relative humidity inside a concrete crosstie installed in ballast.

- A predictive one-dimensional heat transfer model is adequate to predict the change of internal temperature of a concrete member installed in aggregate ballast particularly during wintry months. During this colder time of the year, it is likely that the effect of heat transferring from the immediately adjacent aggregate ballast is minimal. During the summer months, it is found that the model overly predicts the internal temperature. The effect of the polyurethane pad and steel rail is very limited on the predictive temperature model suggesting that a two- or three-dimensional model would better serve to predict summer months. In the case of identifying the instances of freezing events, a one-dimensional pavement model is adequate to predict the three-dimensional response of a concrete crosstie installed in aggregate ballast. Moreover, the temperature distribution between measured values and predicted values agree well with each where the upper portions of the concrete are more responsive to ambient temperature fluctuations than are interior portions of the concrete. This conclusion, however, is limited to the geometric center of the crosstie at the rail seat area where the study was conducted.

Chapter 8 – Relationship Between Relative Humidity and Concrete Degree of Saturation

8.1 Critical Degree of Saturation for Freeze-Thaw Damage

Freeze-thaw damage of concrete requires water inside the concrete microstructure. Upon freezing, water expands by 9 percent of its original volume which exerts pressure onto the microstructure and results in cracking damage. Air entrainment introduces microscopically-sized air bubbles that can alleviate stresses caused by freezing water in one of several manners: hydraulic pressure theory proposed by Powers in 1945, the diffusion and growth of capillary ice by Powers and Helmuth in 1953, the dual mechanism theory by Litvan in 1972, the osmotic pressure theory, the energy solidification theory, the ice nucleation theory, the freezing point depression, and unidirectional solidification (interface stability and stability criterion) (Carlos, 2005). Without the presence of water in any of these cases, however, freeze-thaw damage would not occur.

The degree of saturation, S , in concrete is defined as the volumetric amount of liquid (V_L) and solid (V_S) water filling the open pore volume (V_P):

$$S = \frac{V_L + V_S}{V_P} \quad \text{Equation 8.1}$$

Alternatively, the degree of saturation can be defined as the total volumetric amount of evaporable water (V_W) at 105 °C with respect to the open pore volume (Fagerlund, 1977). This extended definition, thus, more closely adheres to the study of psychrometry where the degree of saturation is additionally defined by the volume of water vapor filling the open pore volume.

Recent research indicates that there exists a critical degree of saturation (S_{CR}) necessary for significant freeze-thaw damage to occur. Li et al investigated the rate of fluid ingress of different concretes with increasing amounts of entrained air content (Castro, J., Li, W., Pour-Ghaz, M., and Weiss, J., 2012). They found that a degree of saturation above 86-88 percent leads to freeze-thaw damage regardless of the amount of entrained air. The same level of damage due to freeze-thaw damage was found to occur in both poorly and properly air-entrained slabs. Several other researchers have found that there may be a lower limit of saturation below which no freeze-thaw damage occurs (Bentz, D. P., Ehlen, M. A., Ferraris, C. F., and Garboczi, E. J., 2001) (Litvan, 1988) (Litvan, G. G., and Sereda, P. J., 1980) (Litvan, G. G., Sakai, K., and Shimada, H., 1991) (Beaudoin, J. J., and Cameron, M., 1972). Freeze-thaw damage is often alleviated by larger measured values of entrained air which results in smaller average distances between individual entrained air voids. Thus, a freezing event in concrete with a well-dispersed spacing of air bubbles does not result in high stresses in the concrete. Li et al, however, concluded that those specimens with poorly air-entrained voids achieved degree of saturation greater than 88 percent much more quickly (on the order of several days) whereas those specimens with good air-entrained voids surpassed a degree of saturation greater than 88 percent at a much later time (on the order of 3 to 6 years).

8.1.1 Extent of Liquid Moisture in High Performance Concrete

High performance concrete is characterized by several features, one of which is incomplete hydration of the Portland cement particles by design. This incomplete hydration is accomplished by designing a low water-to-cement mass ratio and increasing the dosage of water-reducing

admixtures in order to produce a workable mix that can be appropriately placed and consolidated. These low water-to-cement ratios range from 0.36 to 0.42. (Darwin, D., Mindess, S., and Young, J. F., 2003). As a consequence, the ingress of additional water into an incompletely hydrated concrete matrix may contribute to additional hydration, which results in solid-phased hydration products (and the depletion of free liquid moisture). This phenomenon is strongly desired as the additional hydration products fill the voids in the concrete microstructure leading to a more dense and impermeable concrete matrix. Other research has utilized saturated, porous aggregates to accomplish this purposely delayed, internal curing of the concrete microstructure (Bentz, 2009) (Bentz, D., Caston, J., Henkensiefken, R., Nantung, T., and Weiss, J., 2009). High performance concrete, has been postulated by some in the concrete industry to be sufficiently impermeable and resistant to the accumulation of free liquid moisture to warrant relaxed requirements on minimum air entrainment values. This is because low permeability concrete increases the time it takes for water to ingress into the concrete and saturate it. If the time it takes to saturate the concrete is known, it should be possible to predict the freeze-thaw service life (Castro, J., Li, W., Pour-Ghaz, M., and Weiss, J., 2012). In the specific case of railroad concrete crossties, hydrostatic pressure due to wheel impact loading accelerate saturation rates (Barkan, C. P. L., Edwards, J. R., Lange, D. A., and Zeman, J. C., 2010).

8.1.2 Relationship Between Degree of Saturation, Absolute Humidity, and Relative Humidity

Water inside the concrete microstructure can exist as solid ice, liquid water, and gaseous vapor. Absolute humidity is a measurement of water content present as a gaseous vapor irrespective of the amount of water content as solid ice or liquid water. A change in the temperature or pressure affects the maximum concentration of water content in the gaseous vapor. Table 8.1 shows the vapor pressure of water, or saturation pressure, with respect to increasing temperatures. At temperatures below 0 °C, the vapor pressure above solid ice is dominated by sublimation. In the presence of ions in solution, the water vapor pressure is driven downward in accordance to Raoult's Law of partial pressures, where the vapor pressure is proportional to the molar fraction of water in solution.

Absolute humidity is variable to several factors and is not often useful in assessing the degree of saturation of concrete. Instead, the absolute humidity at a given temperature can be normalized with respect to the absolute saturated humidity at that same temperature. This normalized value is called the relative humidity and is typically reported as a percent ranging from 0 to 100 percent when the value is measured over a flat surface of water. In order to understand the degree of saturation in concrete, it is necessary to understand its relationship to relative humidity.

Table 8.1. Change in Saturation Vapor Pressure with Respect to Temperature (Rotronic, 2005)

Temperature (°C)	Water Vapor Pressure Above Liquid (kPa)	Water Vapor Pressure Above Ice (kPa)	Ratio Ice/Liquid
-30	0.049	0.037	0.75
-25	0.081	0.064	0.78
-20	0.126	0.103	0.82
-15	0.191	0.165	0.86
-10	0.287	0.260	0.91
-5	0.422	0.402	0.95
0	0.611	0.611	1.0
10	1.23	-	-
20	2.34	-	-
30	4.24	-	-
40	7.37	-	-
50	12.33	-	-
60	19.92	-	-
70	31.18	-	-
80	47.34	-	-
90	70.11	-	-
100	101.33	-	-

8.1.3 Kelvin-LaPlace Equation, Modeling of Pores, and Hysteresis of Adsorption Isotherms

The Kelvin-LaPlace equation predicts the vapor pressure of a gas over the curved surface of a liquid. Its relationship is defined as:

$$\frac{RT}{V_L} \ln\left(\frac{p}{p_s}\right) = 2\gamma\kappa \quad \text{Equation 8.2}$$

Where R is the universal gas constant ($J/molK$), T is the temperature (Kelvin), V_L is the molar volume of the liquid, p is the absolute vapor pressure and p_s is the absolute saturated vapor pressure, γ is the surface tension of the pore fluid, and κ is the curvature of the liquid surface. For a sphere with radius r_{sphere} suspended in another medium, the curvature is equal to $2/r_{sphere}$. In concrete, liquid moisture does not suspend itself as a collection of spheres. Instead, it adheres onto surfaces in the complex concrete microstructure. Two simple models to describe this complicated pore structure are cylinders (see Figure 8.1a) and ink-bottles (see Figure 8.1b) (Espinosa, R. M., and Franke, L., 2006).

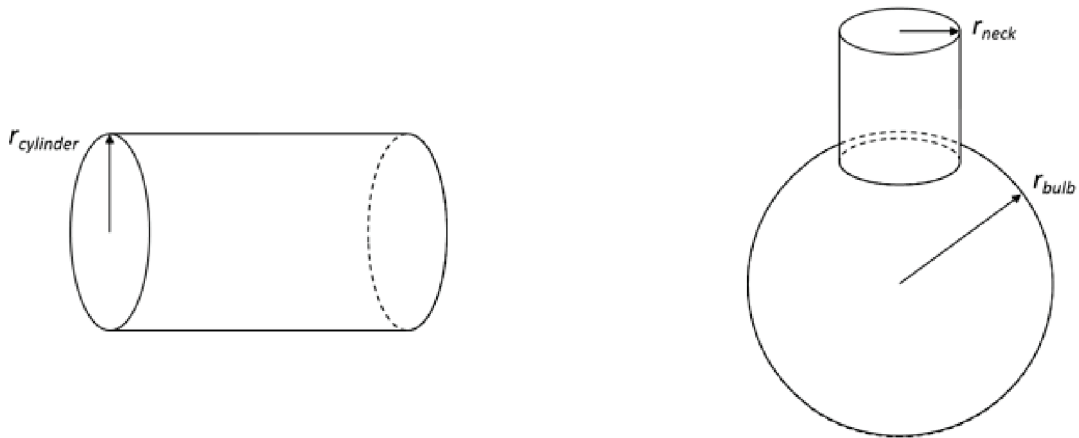


Figure 8.1. Simplification of concrete microstructure with a) cylinders (left) and b) ink-bottles (right)

For condensation of liquid onto the interior surface of a cylinder with radius $r_{cylinder}$, the curvature is equal to $-1/r_{cylinder}$. The thickness of the adsorbate, δ , can be accounted for by subtracting it from the radius as shown in Figure 8.2a. This correction leads to a revised curvature of $-1/(r_{cylinder} - \delta)$. After the cylindrical pore is fully saturated, the drying of the same cylindrical pore must be accomplished at the ends of the pore where a meniscus with radius $r_{meniscus}$ is the drying surface. The curvature of a meniscus adhered onto the interior of a cylindrical pore is $-2\cos\theta/r_{meniscus}$, where θ is the contact angle between the meniscus and the cylindrical wall. For small angles, this curvature can be approximated as $-2/r_{meniscus}$. Again, the thickness of the adsorbate can be accounted for leading to a curvature approximated as $-2/(r_{meniscus} - \delta)$ as shown in Figure 8.2b.

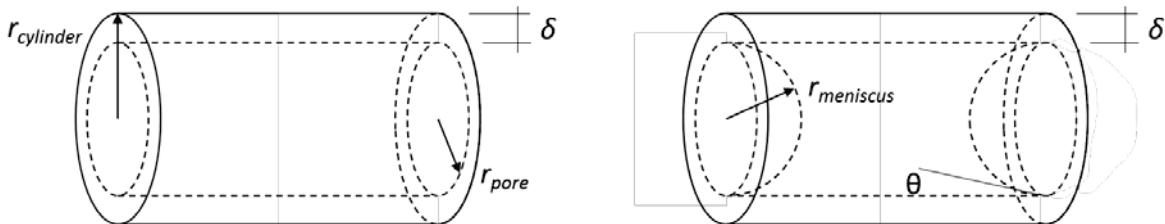


Figure 8.2. a) Wetting of the interior of a cylindrical pore with an adsorbate layer (left) and b) drying of the interior of a cylindrical pore with an adsorbate layer (right)

Details of this behavior deserve elaboration here for the benefit of future researchers seeking to measure moisture change and gradients in concrete. A similar effect is seen in an ink-bottle geometry where an adsorbate layer will grow on the inside surface of both the neck and bulb sphere of the ink-bottle until the neck becomes fully saturated. If the radius of the neck is smaller than the radius of the bulb sphere, then the neck is fully saturated while the sphere continues to grow an adsorbate layer. If the radius of the neck is larger than the radius of the bulb sphere, then the bulb sphere is fully saturated while the neck will transition to filling with a meniscus. Upon drying of the ink-bottle system, if the bulb sphere had been fully filled, then the

neck will dry with a meniscus until it reaches the sphere at which a complicated drying of the sphere occurs (transitioning from a meniscus to desorption of the adsorbate layer on the bulb sphere surface). If the bulb had not been fully filled, then the sphere undergoes desorption until a meniscus forms in the neck. While a cylindrical model of pores is easier to compute, it is found that an ink-bottle model better captures the hysteretic nature of concrete adsorption curves (Espinosa, R. M., and Franke, L., 2006).

A significant implication of the formation of menisci during the wetting and drying of pores is the resulting hysteric nature of an ideal adsorption isotherm. The wetting of a cylindrical pore has a curvature that is approximately half of the curvature of a drying meniscus. Equation 8.2 is applied to produce Figure 8.3 which is an idealized adsorption isotherm of an arbitrary distribution of pore sizes. It is evident that drying of pores results in a curve that is shifted higher than the wetting curve. This illustrates, additionally, that for a given relative humidity value, the saturation of pores can vary over a range of values as it is dependent upon the history of saturation.

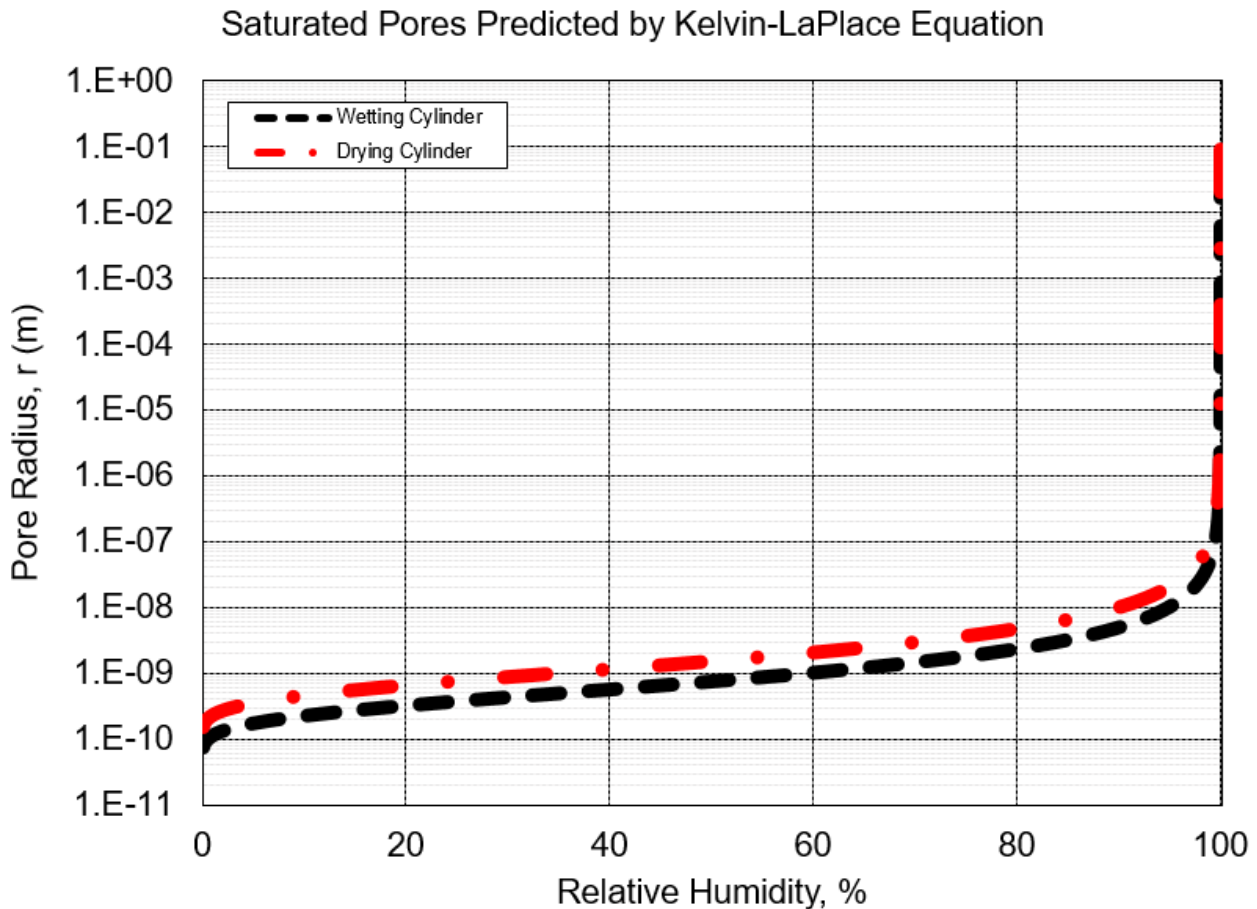


Figure 8.3. Idealized adsorption isotherm of cylindrical pores undergoing wetting and drying

Lastly, Figure 8.3 also implies that small-radius pores become fully saturated at relative humidity values of less than 100 percent RH. As such, localized saturation may occur while the bulk material is not yet fully saturated. Additionally, in order for large pores (on the order of 1 μm and larger) to become filled, it is necessary for there to be a constant relative humidity of 100

percent RH. At high relative humidity, equilibrium drives gaseous vapor to precipitate into liquid. As such, it is necessary to have both high relative humidity and a supply of adsorbate in order to continually fill very large-sized pores. Water in the larger concrete pores freeze at higher temperatures than the smaller pores, meaning that the more saturated the concrete, the higher probability of a freezing event causing significant damage.

8.1.4 Typical Adsorption Isotherms for Concrete and Mortar

Isotherms can be modeled in number of different ways (e.g., Freundlich, Langmuir, BET), yet concrete is often modeled with an empirical-fit because of the number of material challenges. Adsorption isotherms for concrete are complicated by several material factors such as age, type of cement, temperature, air entrainment, water-to-cement ratio, incorporation of pozzolanic mineral admixtures, and other material properties (Bazant, Z. P., Jennings, H. M., and Xi, Y., 1994) (Yang, Q., 1999) (Charles, S., and Poyet, S., 2009). The effect of pores has a tremendous effect on observed relative humidity measurements. At the nano-scale within calcium-silicate-hydrate (CSH) pores, for example, the nano-pores can become fully saturated at relative humidity values of 20 percent RH (Bonnaud, P. A., Coasne, B., Ji, Q., Pellenq, R. J. -M., and van Vliet, K. J., 2012). The adsorption of water within CSH swells the interlayer spacing which inherently affects the pore size distribution making this a non-linear problem. Moreover, at a larger scale of arbitrarily-sized nano-pores, the deposition of water molecules onto the pore surface can assume complicated hemispherical, conical, cylindrical, semi-elliptical, and paraboloidal menisci shapes (Dobruskin, V. K., 2008). Additionally, concrete is a heterogeneous material wherein the pore size distribution and extent of cracking within fine aggregate, coarse aggregate, low-density hydrated cement paste (in the interfacial transition zone), and high-density hydrated cement paste are not equal.

These complications result in simplified concrete sorption curves (see Figure 8.4) where the change in mass of a concrete is shown with respect to changing relative humidity at equilibrium. The shape of the curve (additionally evident in Figure 8.3) is characterized by three phenomena: a non-linear rise near 0–10 percent RH (dominated by condensation in nano- and micro-pores, linear rise between 10–80 percent RH (dominated by single- and multi-layer adsorption onto meso- and macro-pores), and non-linear rise at 80–100 percent RH (dominated by capillary condensation in macro-pores).

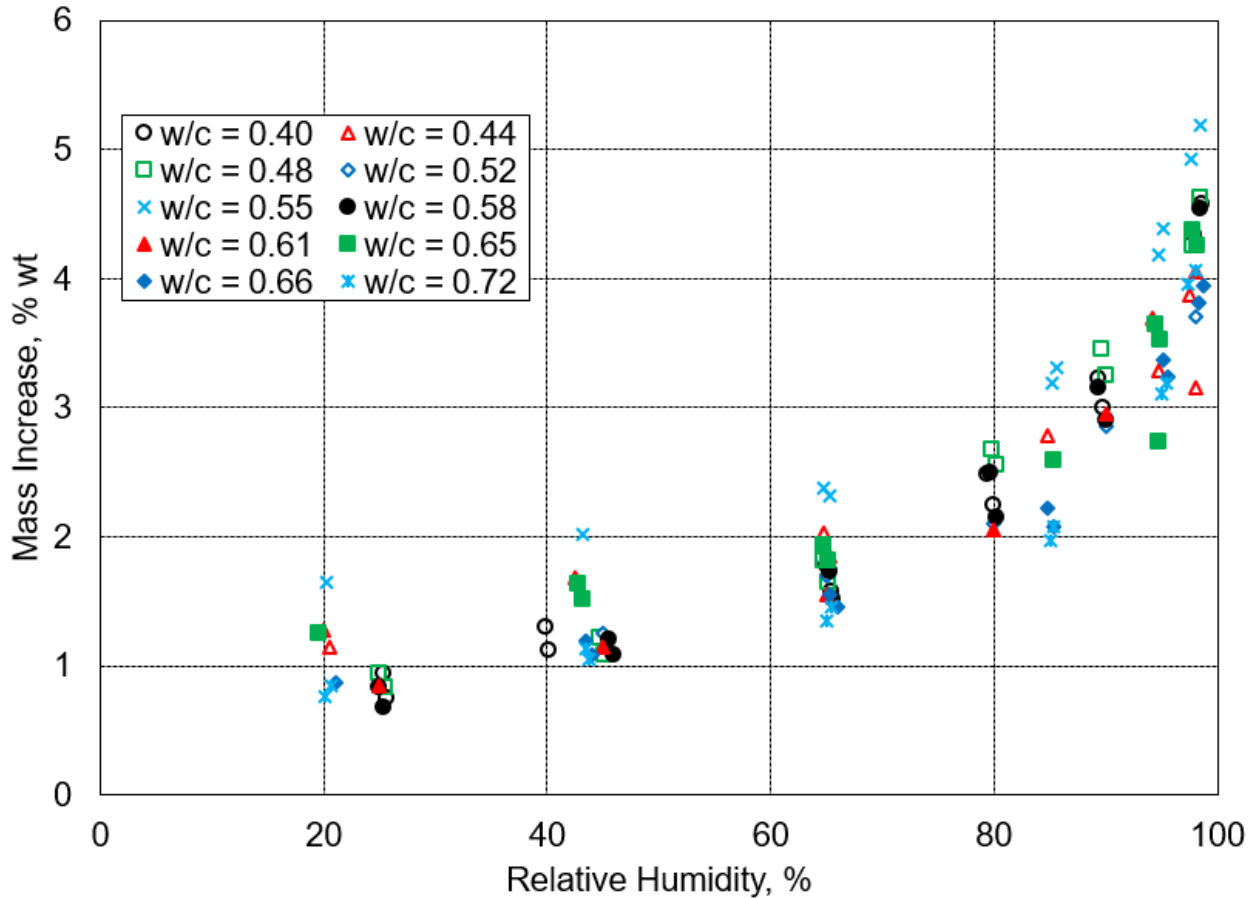


Figure 8.4. Adsorption isotherms for concrete with different water-to-cement ratios (Hansen, 1986)

A simple adsorption isotherm proposed by Pruckner disregards the changing material factors and assumes constant material properties as shown in Equation 8.3:

$$S = \frac{1 - \ln \left| \frac{RT \ln \left(\frac{p}{p_s} \right)}{\Delta \mu_{mono}} \right|}{1 - \ln \left| \frac{RT \ln(0.999)}{\Delta \mu_{mono}} \right|} \quad \text{Equation 8.3}$$

Where $\Delta \mu_{mono}$ is the change of chemical potential at monolayer coverage (Pruckner, 2013). Monolayer coverage of a cement-based material is primarily appropriate at low relative humidity because multi-layer coverage governs in capillary condensation. Because of this simplification, Pruckner empirically found $\Delta \mu_{mono} = -17.0$ kJ/mol while other researchers have estimated chemical potential values of 30.7 to 42.4 kJ/mol in hardened cement paste (Adolphs, J., and Setzer, M. J., 1996).

8.2 Significance of Research

Liquid moisture inside conventional concrete is often measured indirectly utilizing relative humidity sensors. However, relative humidity sensors alone cannot fully characterize the extent of liquid moisture within the microstructure since the relative humidity is a direct measure of vapor. Instead, it is necessary to develop a correlation between relative humidity and degree of

saturation, or directly measure the amount of liquid moisture. Electrical resistance blocks (or gypsum blocks) can be utilized to directly measure the degree of saturation inside concrete and be compared against relative humidity sensors. This correlation can be investigated in high performance concrete where there is incomplete hydration of the Portland cement particles. As such, a better understanding of the freeze-thaw damage potential of high performance concrete railroad crossties can be established.

8.3 Sensor Types

Two sensor types were used in order to measure both the relative humidity and the moisture level: hygrometers called iButtons (DS1923-F5) and moisture sensors called Delmhorst GB-1 Gypsum Sensor Blocks.

The hygrometers feature an internally powered data acquisition system whereby two electrodes joined by a capacitive film varies in its reported dielectric constant based on changing water vapor conditions. A linear relationship between dielectric constant and relative humidity is established and modified for instances of *saturation drift* using the following expression:

$$RH_{\text{saturation drift corrected}} = RH_N - \sum_{k=1}^N \frac{(0.0156)(\overline{RH}_k)(2.54^{-0.3502k})}{1 + (\overline{T}_k - 25)/100} \quad \text{Equation 8.4}$$

Where RH_N is the relative humidity at the end of the N^{th} hour when the device is exposed to high (< 70% RH) or low (< 20% RH) relative humidity, \overline{RH}_k is the average relative humidity through the k^{th} hour that that device has been exposed to high or low relative humidity, and \overline{T}_k is the average temperature (in Celsius) through the k^{th} hour the device has been continuously exposed to high or low relative humidity. The numbers in the equation are empirical and are derived from curve-fitted data sets (Maxim, 2013).

The hygrometers were fitted into iButton retainers (DS9098P) which have soldering points for multi-conductor shielded cabling in order to enable remote communication with each individual sensor. The sensor and retainer were fitted inside of a plastic dip coated eye bolt. A single layer of GORE-TEX fabric (a fabric that allows water vapor to pass through but not liquid water) was wrapped around each sensor in order to protect the wiring connections.

The moisture sensors are made of gypsum cast around two stainless steel electrodes and powered by an external source to induce an alternating current between the two electrodes. The advantage of an alternating current is that it prevents electrochemical effects from preferentially moving alkalis and other ions within the concrete microstructure, thusly affecting the measured results. The extent of liquid moisture soaked within the gypsum changes the observed impedance of the system—a high impedance denotes a dry sensor while a low impedance denotes a wet sensor. The sensors are manufactured under controlled conditions such that there is uniformity between each sensor as read by a KS-D1 Soil Moisture Meter. For this study, the moisture meter was not selected because of its inability to record and store data. Instead, an Arduino Uno R3 board was configured with an SD card microshield.

Pins 6 and 7 on the Arduino Uno R3 board connect to diodes (1N4148), which have a negligibly low resistance when current travels in one direction and a very high resistance in the other direction. As a consequence, an alternating current can be established by alternatively powering pins 6 and 7 off and on. After the current passes the diode connected to Pins 6 or 7, the current passes through the moisture sensor and a 1500 Ω resistor before continuing to Ground. The

voltage drop is recorded with respect to Ground. A simple illustration of the moisture sensor block connection to the Arduino Uno R3 is shown in Figure 8.5, while a breakout the current travel path for Pins 6 and 7 is shown in Figure 8.6.

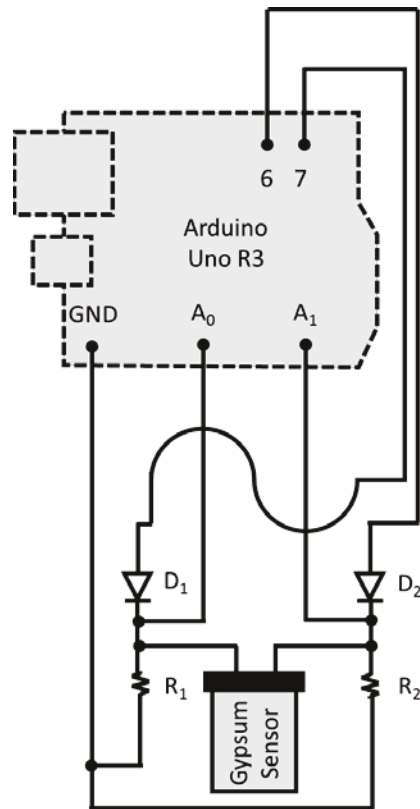


Figure 8.5. Simple illustration of one moisture sensor connected to two 1500 Ω resistors, two diodes (1N4148), and an Arduino Uno R3 microcontroller at Pins 6, 7, A0, A1, and GND

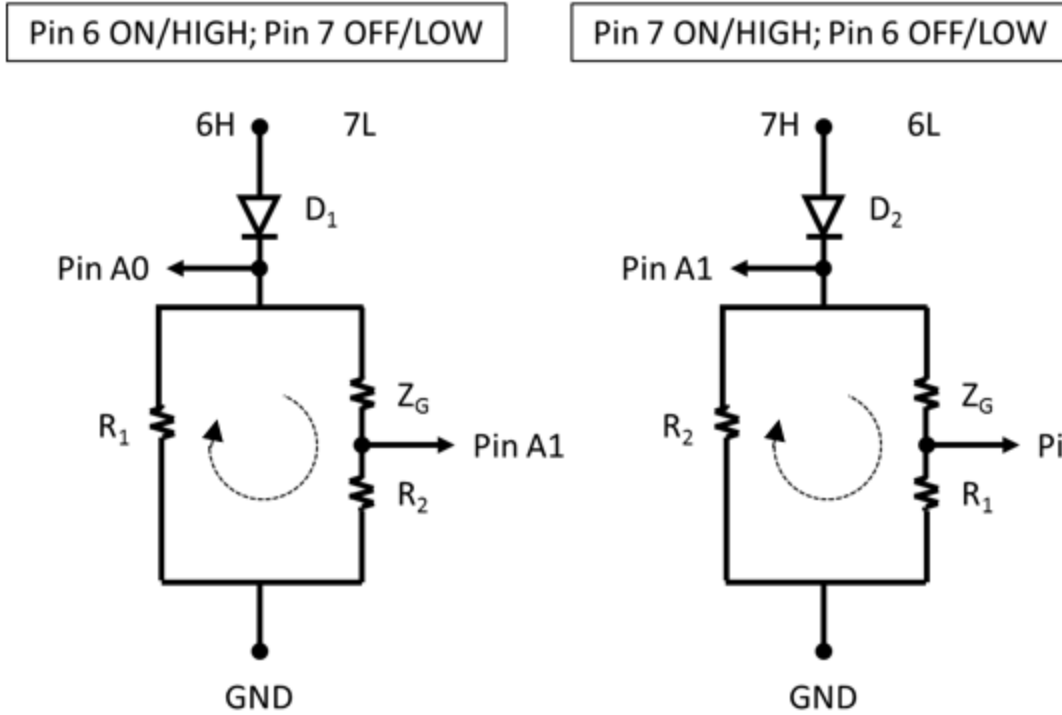


Figure 8.6. Simplified depiction of circuitry when a) Pin 6 voltage is HIGH (left) and b) when Pin 7 voltage is HIGH (right)

In the instance when Pin 6 is set to a HIGH voltage and Pin 7 is set to a LOW voltage (see Figure 8.6a), analog Pin A1 measures the voltage drop with respect to GND across R_2 on the right-hand-side of the circuit branch. The current across the right-hand-side, I_{RHS} , of the circuit can be expressed as:

$$I_{RHS} = \Delta V_{R2} / R_2 \quad \text{Equation 8.5}$$

Where ΔV_{R2} is the measured voltage drop with respect to GND across R_2 . Analog Pin A0 measures the voltage drop with respect to GND across the two branches of the circuit (left-hand-side and right-hand-side). Seemingly, Pin A0 measures a set of known and unknown resistors in parallel and series. However, Kirchoff's second law states that closed loops within a circuit must have its voltage drops and gains equate to zero. As such:

$$\sum \Delta V_{\psi} = \Delta V_{ZG} + \Delta V_{R2} - \Delta V_{R1} = 0 \quad \text{Equation 8.6}$$

Where ΔV_{R1} is the measured voltage drop with respect to GND across R_1 and where ΔV_{ZG} is the measured voltage drop with respect to GND across Z_G . As such:

$$\Delta V_{ZG} + \Delta V_{R2} = I_{RHS}(Z_g + R_2) = \Delta V_{R1} = I_{LHS}R_1 \quad \text{Equation 8.7}$$

Although the current along the left-hand-side and right-hand-side of the branches do not equal, by Kirchoff's first law, the current along the right-hand-side across both resistors must equal. As such, Equation 8.5 and 8.7 can be equated:

$$I_{RHS} = \Delta V_{R2} / R_2 = (\Delta V_{ZG} + \Delta V_{R2}) / (Z_g + R_2) \quad \text{Equation 8.8}$$

Following several simplifying mathematical steps, the unknown impedance of the moisture sensor, Z_G , can be solved as:

$$Z_g = R_2 / \Delta V_{R2} [(\Delta V_{ZG} + \Delta V_{R2}) - \Delta V_{R2}], \text{ or}$$
$$Z_g = R_2 / A1 [A0 - A1] \quad \text{Equation 8.9}$$

Where $A0$ and $A1$ are the voltage values measured by analog Pins A0 and A1, respectively. An analogous derivation can be made in the instance when Pin 7 is set to HIGH and Pin 6 is set to LOW (see Figure Figure 8.6). A single Arduino Uno R3 microcontroller board has six analog input pins meaning that three moisture sensor blocks can be configured if dual readings are made (setting Pins 6 and 7 HIGH on a single sensor). In order to increase the number of moisture sensors that can be monitored at a single installation site, a single reading can be taken (e.g., when Pin 7 is set to HIGH) while still exciting both pins in order to achieve an alternating current. In doing so, electrochemical processes can be prevented while a gain in the number of moisture sensors is achieved. Figure 8.7 shows the complete circuitry deployed where Pin 7 is set to HIGH during data recording.

The hardware is powered by a 10000 mAh external battery power pack and is housed inside a metal junction box in order to protect the circuitry from the natural elements (see Figure 8.8).

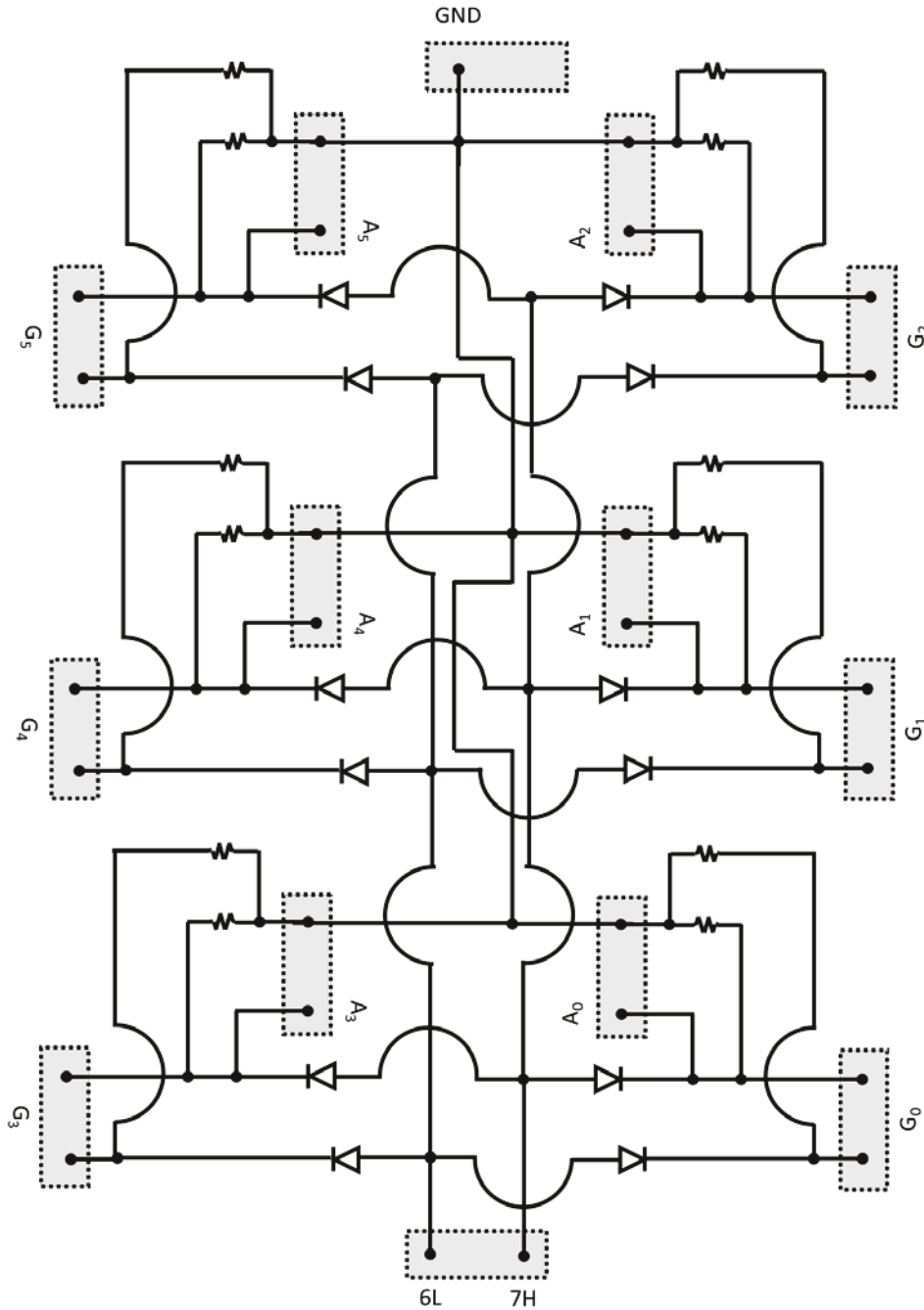


Figure 8.7. Complete circuitry scheme where six moisture sensor blocks (G0-G5) are measured for their change in impedance when Pin 7 on an Arduino Uno R3 microcontroller board is set to HIGH. In order to prevent electrochemical deterioration processes, Pin 6 is also set to HIGH in an alternative manner in order to mimic an alternating current

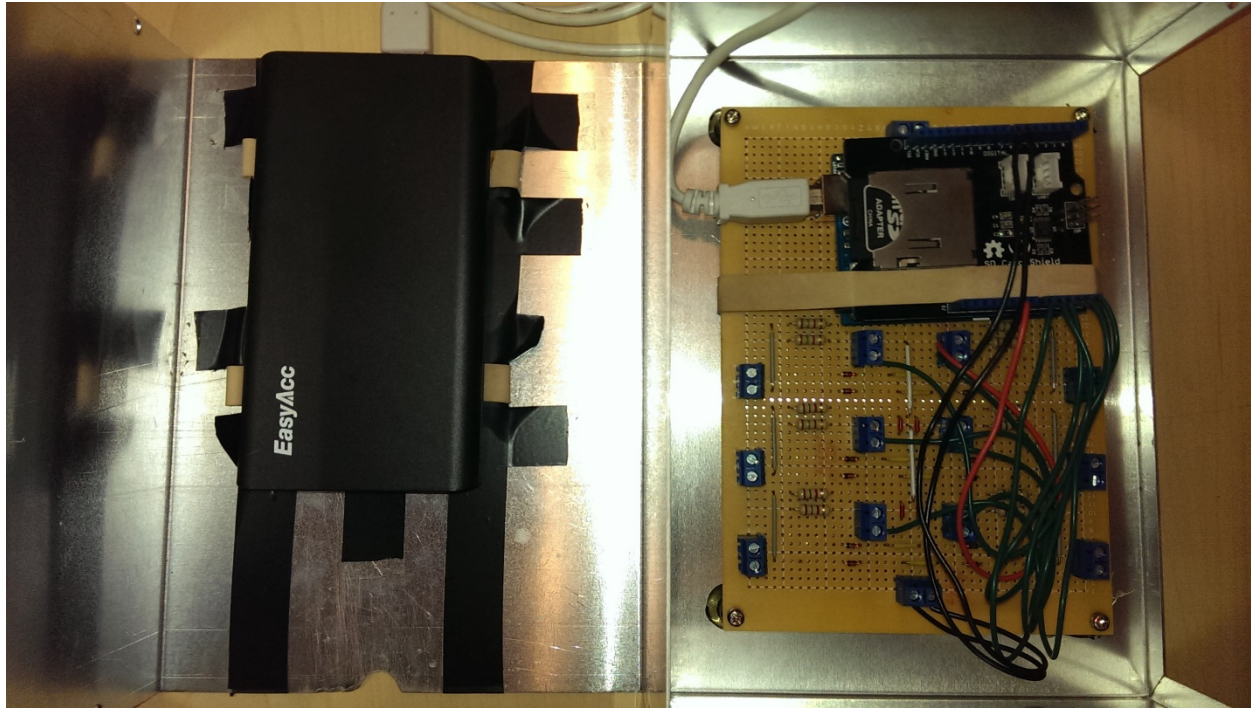


Figure 8.8. Image of hardware where an SD shield is connected above an Arduino Uno R3 microcontroller board. The Arduino and shield are securely fastened with a rubber band onto a circuit board that is wired in accordance in Figure Figure 8.7. A 10000 mAh external battery back provides an approximate 7-day charge for the hardware to operate independently. The entire setup is encased in a metal junction box

8.3.1 Calibration of Moisture Sensor

The moisture sensor block directly measures the impedance of the sensor. In order to calibrate the sensor reading to a degree of saturation, the mass of the sensor was measured with respect to the impedance. This calibration was accomplished by suspending the sensor at one end of an instrumented cantilever beam of known stiffness. The change in the bending moment before and after immersing the sensor in water is collected across several days. Repeated instances of wetting and drying of the moisture sensor block was performed in order to enhance confidence in the calibration.

8.3.2 Preparation of Installation Method

Both the hygrochron sensors and the moisture sensors were installed onto a steel angle bracket with unthreaded holes spaced one in. apart (see Figure 8.9). The hygrochron sensors were installed at depths of 0.5, 2.5, 5.5, and 8.5 in. from the top surface of the model concrete crosstie. The moisture sensors were installed at depths of 0.5, 2.5, and 8.5 in. from the same top surface (see Figure 8.10).

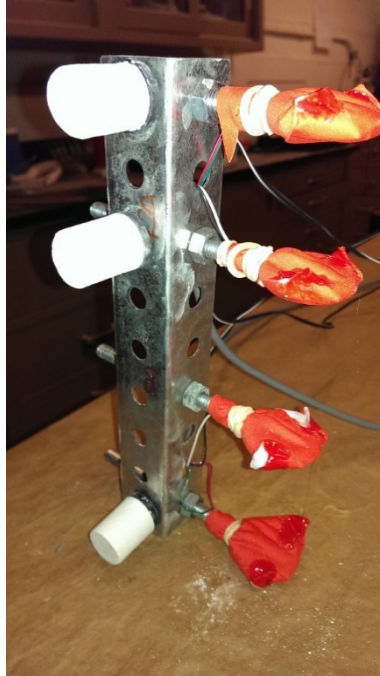


Figure 8.9. Construction of hydrochron sensors seated inside an iButton retainer installed in a plastic dip coated eye bolt and sealed with a single layer of GORE-TEX fabric. A rubber band securely holds the fabric in place. Moisture sensor blocks are additionally installed along the orthogonal face of the angled steel bracket

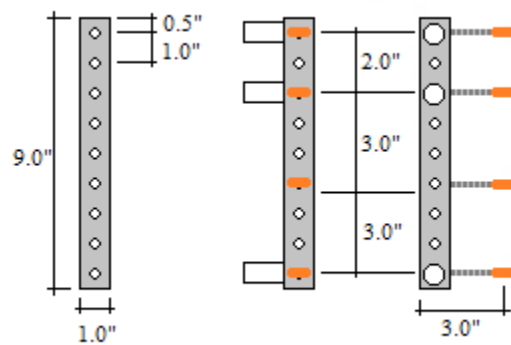


Figure 8.10. Depiction of 9 in. tall bracket (left) with 0.5-in. clearance at top and bottom. Hydrochron sensors (orange) and moisture sensors (white) are affixed at depths as depicted (right)

8.3.3 Instrumentation of Model Concrete Crossties and Installation in Model Ballast

The steel angle brackets were installed into two molds measuring 9-in. by 9-in. by 16-in. These dimensions were comparable to the cross-section dimensions of a typical concrete crosstie. One of the molds was fashioned with steel fastening anchors such that a polyurethane pad and rail section could be affixed at a later time (see Figure 8.11a). The instrumented bracket was

positioned such that the hygrochron sensor and moisture sensor were geometrically centered about the rail seat area and additionally symmetric to each other across the horizontal centerline of the mold (see Figure 8.11b). The concrete mixture design is shown in Table 8.2, and was intended to be comparable to typical high performance concrete crossties with a water-to-cement mass ratio of 0.30.

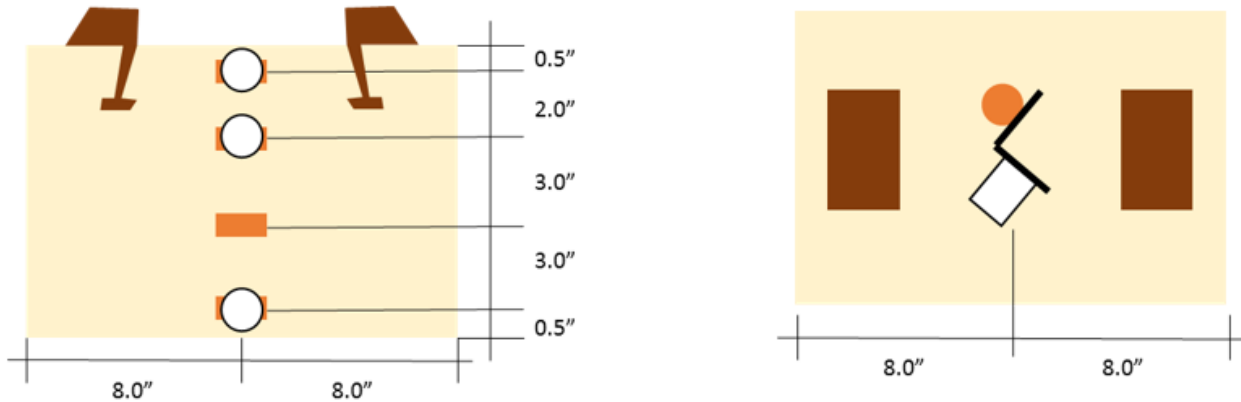


Figure 8.11. Diagram of instrumented model crosstie with both hygrothermal sensors and moisture sensors installed at various depths (left)

Table 8.2. Nominal Concrete Mix Design of Model Crossties

Material Type	Pounds Per Cubic Yard	Kilograms Per Cubic Meter
Type I Portland Cement	718	426
#7 Aggregate	2085	1236
Sand	1257	746
Water	216	128
High Range Water Reducer	12 fl. oz. per 100 lb. cementitious	

The model crossties were demolded (see Figure 8.12) and cured in an environmentally controlled room at 23 °C and 50 percent RH. Thereafter, the model crossties were installed in model ballast in Rantoul, IL. The model ballast was a 1-1.5 in. top-size yard ballast that conformed to UP Class-2 Ballast Specifications. The model ballast sat atop an angled asphalt lot, which facilitated rainfall runoff and prevented stagnant water from building within the ballast. The model crossties were installed at one end of the ballast where the distance separating the underside of the model crossties and the surface of the asphalt lot was 5 to 6 in. The model crosstie was positioned such that its surface was flush with the model ballast. Additionally, a polyurethane pad and steel rail section was added to the model crosstie with embedded anchors (see Figure 8.13a).



Figure 8.12. De-molded model concrete cross-ties with PVC access plug where multi-conductor shielded cables are encased



Figure 8.13. Model cross-ties installed in model ballast in Rantoul, IL

8.4 Experimental Results, Discussion, and Empirical Modeling

8.4.1 Relative Humidity Results

Although the relative humidity of ambient conditions fluctuates daily, the internal relative humidity of concrete members fluctuates in a more seasonal manner. Figure 8.14 shows a model concrete cross-tie installed in an aggregate ballast located in Rantoul. Relative humidity sensors near the surface of the model concrete cross-tie showed a gradual increase in relative humidity, while relative humidity sensors inside the bulk material (at 2.5 and 5.5 in. from the top surface) were unaffected by the installation.

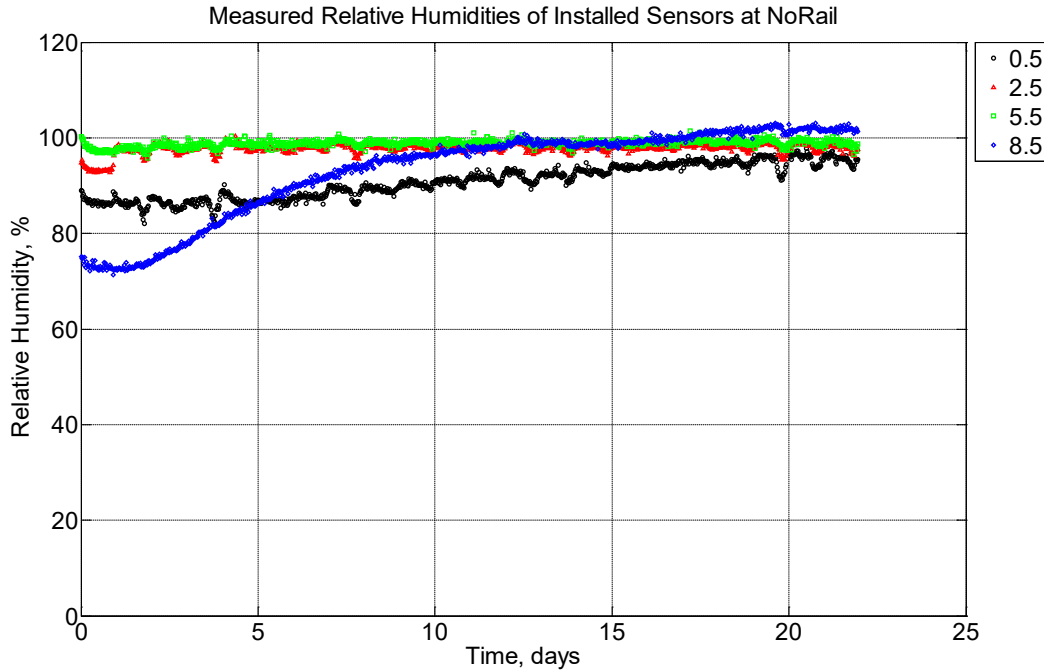


Figure 8.14. Measured relative humidity at depths of 0.5 in. (12.7 mm), 2.5 in. (63.5 mm), 5.5 in. (139.7 mm), and 8.5 in. (215.9 mm) from the surface of a model concrete crosstie (labeled NoRail) without a polyurethane pad nor rail installed in ballast in Rantoul, IL, between November 29, 2014, through December 21, 2014

8.4.2 Predicting Degree of Saturation Based on Measured Impedance

The moisture sensor blocks and Arduino algorithm (see Equation 8.9) directly report the impedance, Z_g , of each sensor. However, the impedance measurement can be calibrated against varying degrees of moisture. Figure 8.16 shows the graphical result of two uniformly manufactured moisture sensors undergoing drying and soaking cycles. A power-law function is fitted to a representative section of the data to with a high fit of R^2 of 0.98. As such, the independently measured impedance value, Z_g , and estimated degree of saturation, S , can be confidently related by the following power-law expression:

$$Z_g = 817.14S^{-1.284} \quad \text{Equation 8.10}$$

Equation 8.10 can be solved for in terms of S to yield:

$$S = \left(Z_g / 817.14 \right)^{(1/-1.284)} \quad \text{Equation 8.11}$$

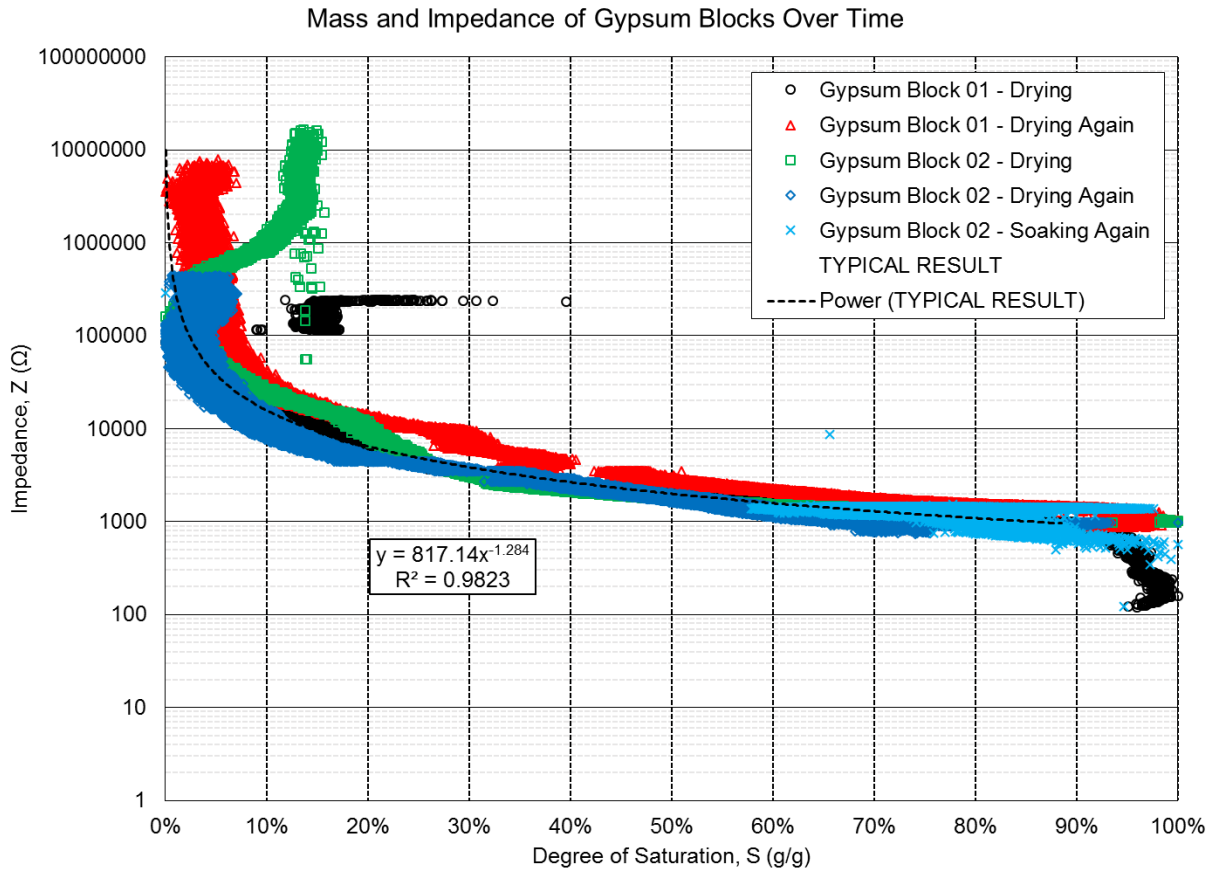


Figure 8.15. Change of mass and impedance of two moisture sensors undergoing drying and soaking

8.4.3 Degree of Saturation Results Over Observation Period

The degree of saturation inside the model concrete cross-ties was estimated based on Equation 8.11 and the measured impedance value of the moisture sensor block. The response of three moisture sensors soon after installation in aggregate ballast is shown in Figure 8.16. It is evident that the two sensors near the surface (0.5 and 8.5 in.) were at nearly at 0 percent degree of saturation, while the interior sensor (2.5 in.) maintained a high degree of saturation at 100 percent. However, soon after installation into the aggregate ballast, the moisture sensors indicated an increase in liquid moisture. In particular, the saturation in the sensor at the top surface (0.5 in.) gradually increased to a high degree of saturation by day 12. The sensor at 8.5 in. from the top surface showed an upward trend before stabilizing to a relatively low degree of saturation.

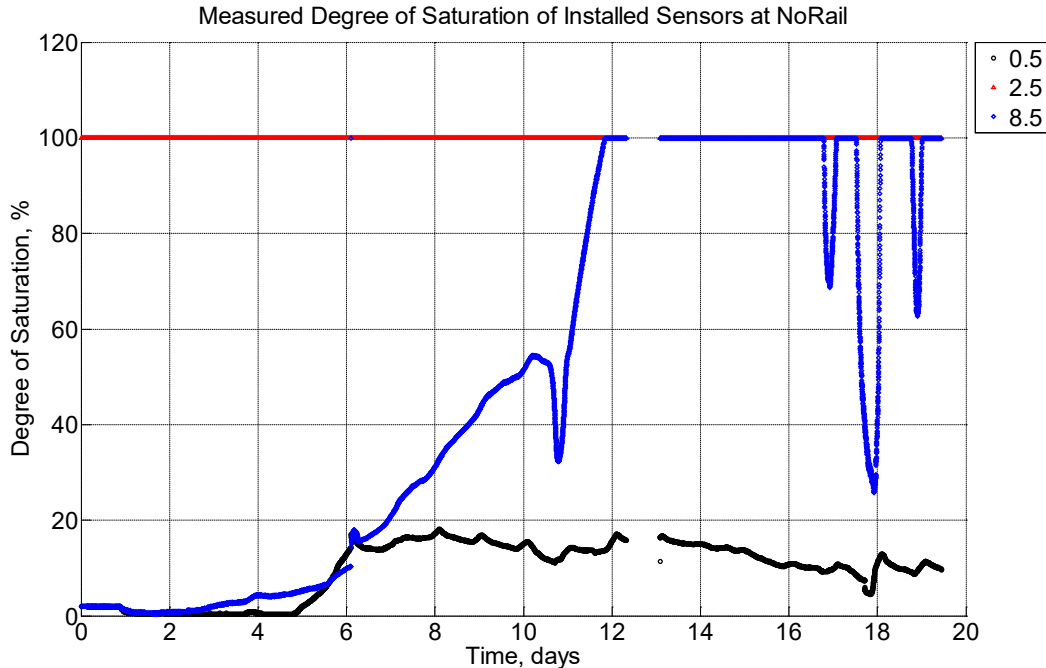


Figure 8.16. Measured degree of saturation at depths of 0.5 in. (12.7 mm), 2.5 in. (63.5 mm), and 8.5 in. (215.9 mm) from the surface of a model concrete crosstie (labeled NoRail) without a polyurethane pad nor rail installed in model ballast in Rantoul, IL, between December 1, 2014, through December 21, 2014

Two sensors (at 0.5 and 8.5 in. from the top surface) exhibited unusual and coincidental sudden troughs on days 10, 17, 18, and 19. On these days, the ambient temperatures fell to below 0 °C (see Figure B10-5 in Appendix B). It is likely that portions of the water inside the concrete crosstie and within the moisture sensor block transformed from liquid water to solid ice. As such, the impedance between the two electrodes was likely altered because of the difference in conductivity of liquid water and ice.

The degree of saturation in both NoRail and YeRail were persistently high. After several months, a breathable water-resistant tarp was installed over the two model crossties whilst they remained in ballast to allow the concrete to dry some. Figure 8.17 shows the measured degree of saturation of NoRail, which had an appreciable response to the tarp only after several days. The sensor located at a depth of 2.5 in. initially responded and began to dry after approximately 20 days. However, sensors located at 0.5 and 8.5 in. from the top surface did not appreciably show drying until 70 days after the tarp had been installed (see Figure 8.18). The model crosstie YeRail did not show any of the three sensors drying out. It was decided to conclude the experiment because companion relative humidity sensors had become unreliable or unresponsive rendering a correlation between relative humidity and degree of saturation in YeRail impossible.

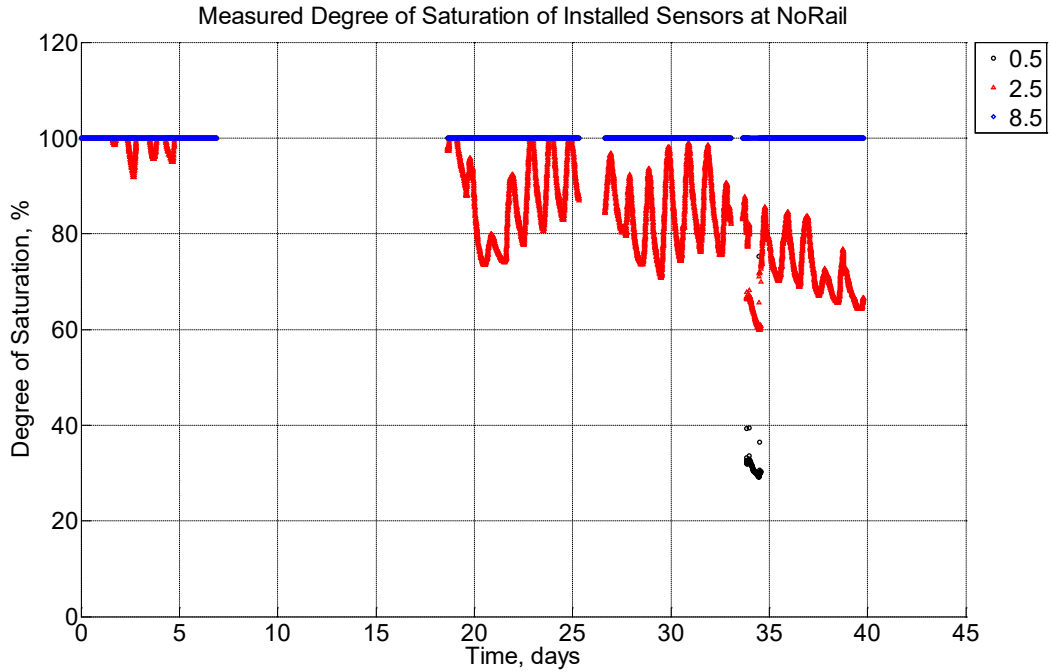


Figure 8.17. Measured degree of saturation at depths of 0.5 in. (12.7 mm), 2.5 in. (63.5 mm), and 8.5 in. (215.9 mm) from the surface of a model concrete cross-tie (labeled NoRail) without a polyurethane pad nor rail installed in model ballast in Rantoul, IL, between May 14, 2015, through June 20, 2015

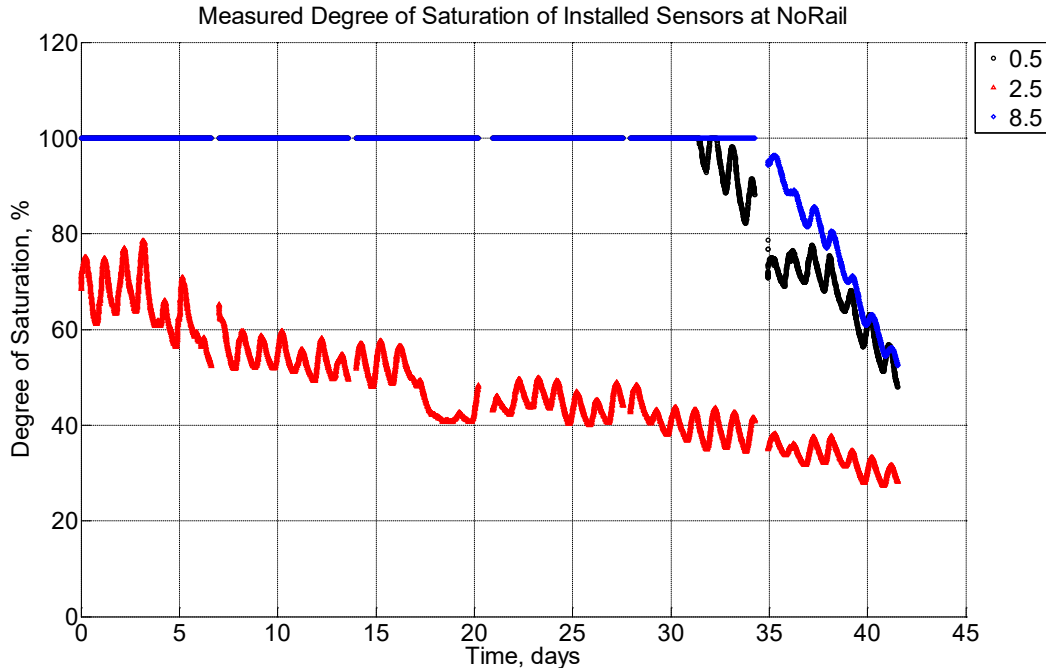


Figure 8.18. Measured degree of saturation at depths of 0.5 in. (12.7 mm), 2.5 in. (63.5 mm), and 8.5 in. (215.9 mm) from the surface of a model concrete cross-tie (labeled NoRail) without a polyurethane pad nor rail installed in model ballast in Rantoul, IL, between June 20, 2015, through August 1, 2015

8.4.4 Comparing Degree of Saturation with Relative Humidity Measurements

Measured relative humidity (such as in Figure 8.14) can be compared against measured degree of saturation (such as in Figure 8.16) to produce a correlation of data (see Figure 8.19). This depiction of the data is in keeping with how sorption isotherms are displayed. However, several key differences are noted:

- The temperature represented within Figure 8.19 was not constant, therefore no isothermal constraint on the result was used.
- Equilibrium of relative humidity and equilibrium of degree of saturation were not reliably attained due to extreme fluctuations due to ambient conditions.
- The distribution of pore sizes was assumed to be constant. This assumption was irrespective of the nature of high performance concrete which has unreacted Portland cement particles leading to densification of pore structure when exposed to additional liquid water.

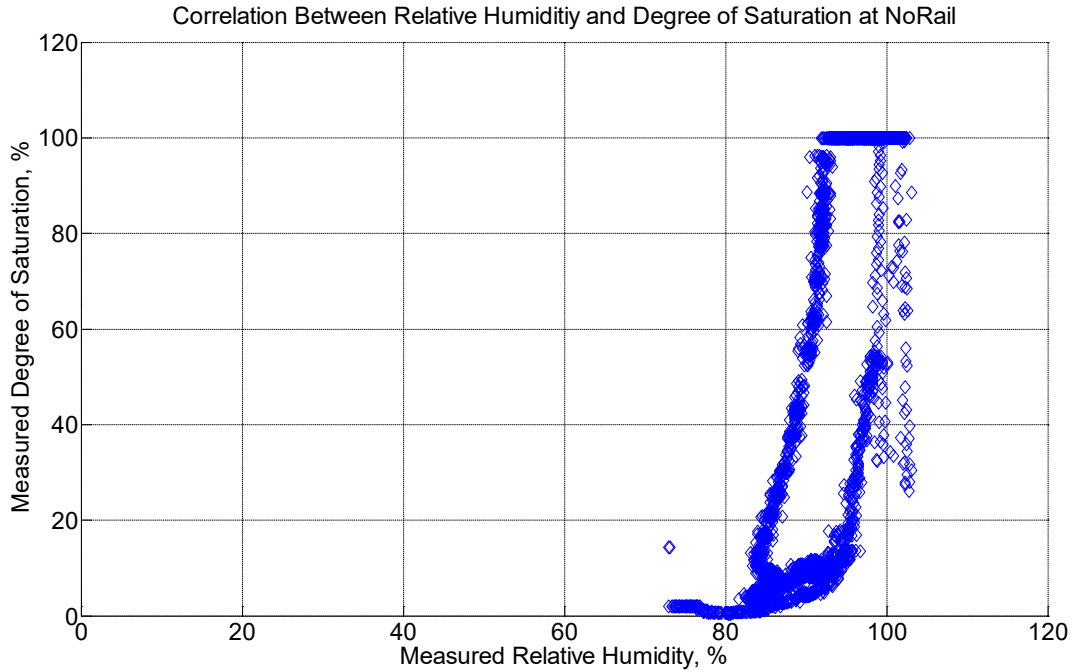


Figure 8.19. Correlation between measured relative humidity and degree of saturation at depth of 8.5 in. (215.9 mm) from the top surface of a model concrete cross-tie (labeled NoRail) without a polyurethane pad nor rail installed in model ballast in Rantoul, IL. The data represents two periods from December 1, 2014, through December 21, 2014, and June 20, 2015, through September 11, 2015

8.4.5 Comparing Degree of Saturation with Predictive Adsorption Isotherm

Any number of adsorption isotherms can be compared against the result in Figure 8.19. Figure 8.20 shows one such adsorption isotherm by Pruckner (Pruckner, 2013). It is readily apparent that the predictive adsorption isotherm does not represent the observed data set nor would many other isotherms. This is principally because the experimentally measured degree of saturation approaches 0 percent at instances when the relative humidity is greater than 80 percent. Such a behavior is mostly likely attributable to a low water-to-cement ratio leading to ongoing hydration of unreacted cement particles.

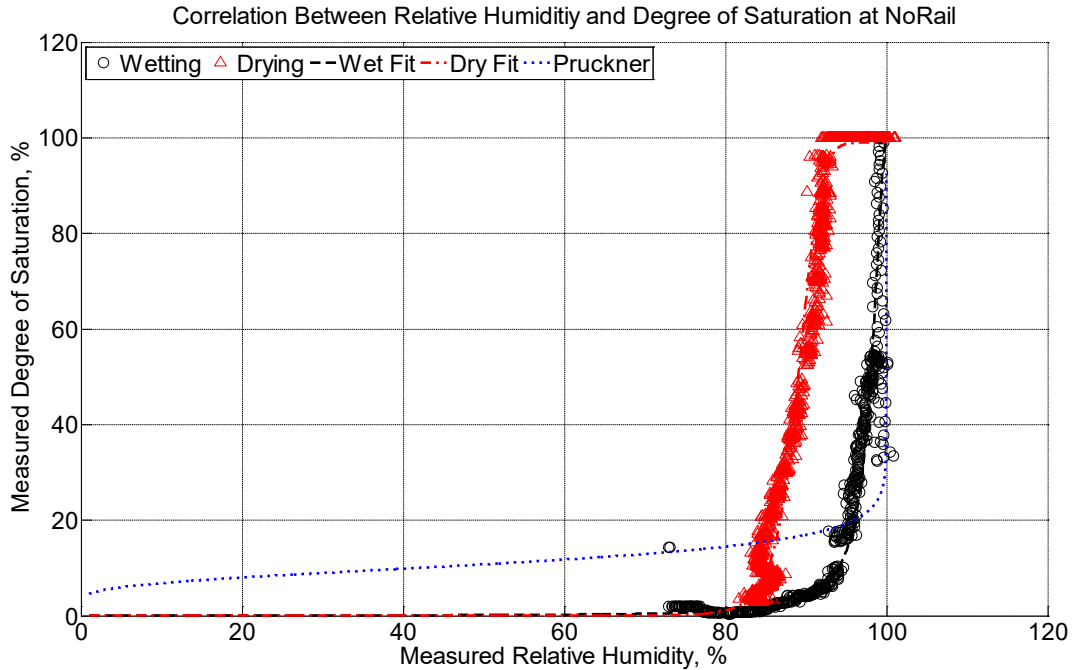


Figure 8.20. Correlation between measured relative humidity and degree of saturation at depth of 8.5 in. (215.9 mm) from the top surface of a model concrete crosstie (labeled NoRail) without a polyurethane pad nor rail installed in model ballast in Rantoul, IL

The correlation between degree of saturation and relative humidity in Figure 8.20 is also separated into two distinct phases: wetting and drying. When done so, it is apparent that there is hysteresis between the two curves. As such, the notion of a complex pore structure (e.g., cylindrical, ink-bottle) is evident. Moreover, it is important to note that the wetting curve was accomplished in less than 1 week, whereas the drying curve was accomplished in approximately 3 months. The drying curve was achieved by placing a breathable water-resistant canvas tarp over the model concrete crosstie. This was indicative of typically faster adsorption rates of concrete versus slower desorption rates. This implies that concrete ties can remain critically saturated and experience freeze-thaw damage for months after a precipitation event. Additionally, the hysteretic nature of the correlation between degree of saturation and relative humidity indicates that a single measurement of relative humidity (e.g., 93 percent RH) can be interpreted in two vastly different manners: a degree of saturation as low as 15 percent and as high as 100 percent. As such, a single measurement of relative humidity must be understood in a contextual manner as it cannot be understood as a singular event.

In the case where incomplete hydration of the Portland cement particles is evident (leading to a result where degree of saturation values fall to 0 percent while relative humidity remains high at values of 80 percent RH), it is possible to empirically fit an expression to predictively estimate the degree of saturation based on a measured relative humidity value. It is observed that a 3-parameter S-shaped curve can adequately represent the wetting and drying curves. As such, the degree of saturation, S , can be estimated as:

$$S = S_o \left(\alpha_o \frac{1 - \alpha_o}{1 + \left(\frac{1 - RH}{1 - RH_b} \right)^n} \right) \quad \text{Equation 8.12}$$

Where S_o is 100 percent RH, α_o is a fit parameter affecting the y-axis range, RH_b is a fit parameter affecting the x-axis range, and n is a fit parameter affecting the curvature of the graph. The values used for both the wetting and drying curves are shown in Table 8.3. These wetting and fitting curves represent envelopes of degree of saturation based on measured relative humidity values. In the event that relative humidity does not follow this envelope, then an intermediary expression predictively governs the relationship between degree of saturation and relative humidity.

Table 8.3. Fit Parameters used for 3-Parameter S-Shaped Curves for Wetting and Drying Curves

Parameter	Wetting Curve	Drying Curve
α_o	0.01	0.01
RH_b	98% RH	89% RH
n	2	7.5

8.5 Conclusions

Concrete crossties are subjected to freezing-thawing climates across North America that makes them vulnerable to freezing-thawing damage. Model concrete crossties were instrumented with hygrothermal sensors and moisture sensors in order to monitor their internal relative humidity and degree of saturation in rail ballast in Rantoul, IL. A simple adsorption isotherm is applied in order to predict the correlation between degree of saturation and relative humidity. It is found that:

- There is hysteresis between concrete adsorption and desorption curves. This means that it takes longer for concrete crossties to dry than saturate. This also means that concrete can remain critically saturated for long periods of time after precipitation events.
- Concrete field relative humidity measurements indicate that concrete crossties can have high moisture levels in track, even on well-drained ballast.
- The functions that govern wetting and drying of concrete crossties are complex due to a number of factors including lack of constant temperature, inability of achieve equilibrium due to fast-changing external environments, and non-constant pore size distribution.
- An empirical model for wetting and drying in concrete crossties has been developed and shown to produce satisfactory predictions for internal relative humidity and degree of saturation when calibrated for concrete mixture design and history of hydration. These models can be used to assess potential for freeze-thaw distress in concrete crossties in the field.

Chapter 9 – Freeze-thaw Damage Potential Based on Climatic Data

9.1 Introduction and Background

Concrete installed in outdoor environments is susceptible to the natural elements including instances of freezing and thawing ambient temperatures and the absorption of water due to moisture precipitation. Recent research suggests that a minimal degree of saturation must be present (approximately 86–88 percent) in order for significant freeze-thaw damage to manifest itself (Castro, J., Li, W., Pour-Ghaz, M., and Weiss, J., 2012). For damage to occur, the concrete must undergo a freeze-thaw cycle *while* critically saturated.

In 1974, Hershfield constructed a map across the United States detailing the number of freeze-thaw instances from weather station data (Hershfield, D. M., 1973). In 1959, Fraser similarly measured the frequency of freezing-thawing cycles occurring in Canada. Hershfield reports instances of approximately 200 freeze-thaw cycles in the central American Rocky Mountain range while Fraser reports approximately 80 freeze-thaw cycles in the southern Canadian Rocky Mountain range (Fraser, J. K., 1959). Severity of exposure is dependent on more than the yearly low temperature. Concrete that freezes and stays frozen experiences less damage than concrete that cycles between hot and freezing temperatures. The number of freeze-thaw cycles concrete is said to experience should take both moisture level and temperature into account.

9.1.1 Modeling Internal Temperatures and Degree of Saturation

The internal temperature and moisture gradients inside concrete can be modeled in a number of different ways including one-dimensional solutions. It has been previously shown that a separation of variables method to predict internal temperature values, $T_i(z, t)$, using estimated solar radiation, ambient air temperatures, and thermal properties in cold weather is sufficient. This expression, in a multi-layered system of materials, is expressed as:

$$T_{ij}(z, t) = \Delta_{11}e^{-v_1z} \sin(\omega t - v_1z + \delta_{11} + \phi) + \Delta_{12}e^{v_1z} \sin(\omega t + v_1z + \delta_{12} + \phi) \quad \text{Equation 9.1}$$

For $0 \leq z \leq H_1$;

$$T_{ij}(z, t) = \Delta_{i1}e^{H_{i-1}v_{i-1}+v_i(H_{i-1}-z)} \sin(\omega t - v_iz + \delta_{i1} + \phi) + \Delta_{i2}e^{H_{i-1}v_{i-1}-v_i(H_{i-1}-z)} \sin(\omega t + v_iz + \delta_{i2} + \phi) \quad \text{Equation 9.2}$$

For $H_{i-1} \leq z \leq H_i$, and $i = 2, 3, \dots, n - 1$; and

$$T_{nj}(z, t) = \Delta_n e^{H_{n-1}v_{n-1}+v_n(H_{n-1}-z)} \sin(\omega t - v_nz + \delta_{n1} + \phi) \quad \text{Equation 9.3}$$

For $z \geq H_{n-1}$. The variables Δ_{i1} , δ_{i1} , v_i for $i = 1, 2, \dots, n$ and Δ_{i2} , δ_{i2} for $i = 1, 2, \dots, n - 1$, ω , z , H_i , and ϕ in Equations 4-1 through 4-3 are found elsewhere (see Chapter 2) (Roesler, J. R., and Wang, D., 2014).

The moisture levels inside concrete can be predicted using a moisture transport model and a correlation between relative humidity and degree of saturation. A one-dimensional transport model to predict internal relative humidity using diffusivity and ambient relative humidity is sufficient and can be expressed as:

$$\frac{\partial RH(t, z)}{\partial t} = \text{div}(D \cdot \text{grad}(RH(t, z))) - \frac{\partial RH_s(t, z)}{\partial t} \quad \text{Equation 9.4}$$

Where RH is a function of time (sec), t , and depth (m), z ; $\frac{\partial RH_s(t,z)}{\partial t}$ is the change in relative humidity due to hydration for early-age concrete (assumed as $\frac{\partial RH_s(t,z)}{\partial t} = 0$ for hardened concrete; and D is the moisture diffusivity, which is a function of both internal relative humidity and concrete porosity. The moisture diffusivity factor is non-linear and can be expressed by an effective diffusivity (Bazant, Z., and Najjar, L., 1972):

$$D = D_o \left(\alpha_o \frac{1-\alpha_o}{1+(1-RH/1-RH_c)^n} \right) \quad \text{Equation 9.5}$$

Where D_o (m^2/s) is the moisture diffusivity at complete saturation; n is a regression coefficient ranging from 6 to 16 for concrete (Dux, P., Leech, C., and Lockington, D., 2003); $\alpha_o = D_l/D_o$, where D_l is the diffusivity at 0 percent RH; and RH_c is the bifurcate point above which capillary suction governs (typically 75 to 80 percent) (Hiller, J. E., and Qin, Y., 2014). The moisture diffusivity at complete saturation can be related to the water-to-cementitious ratio as shown in Table 9.1.

Table 9.1. Moisture Diffusivity at Saturation Estimated from w/c ratio (from ¹ (Kang, S. - T., Kim, J. -K., Kim, J. -S., Lee, Y., and Park, Y. -D., 2012) and ² (Hiller, J. E., and Qin, Y., 2014))

w/c	D_o (10^{-6} m ² /hour) ¹	D_o (10^{-6} m ² /hour) ²
0.28	2.02	0.68
0.40	2.10	1.59
0.50	2.26	-
0.68	2.87	2.57

The boundary condition at the top of the concrete is modified in order to better represent wetting events due to precipitation. Ballast is assumed to be well draining, however, experimental data from this study found that a high humidity persists in ballast even if liquid water can drain. As such, the boundary condition in the model at the underside of the concrete tie is assumed to be 10-times the value at the topside. Table 9.2 shows weather conditions which increase the measured relative humidity value to 100 percent RH over a given time frame.

Table 9.2. Modified Boundary Condition at the Top of Concrete as Subject to Reported Weather Conditions (Adapted from (Hiller, J. E., and Qin, Y., 2014))

Reported Weather Condition	Modified Wetting Duration
Drizzle	
Fog	RH _{upper} =100 % for 1 hour
Mist	
Light Rain	
Light Thunderstorms and Rain	RH _{upper} =100 % for 4 hours
Thunderstorms and Rain	
Rain	RH _{upper} =100 % for 8 hours
Heavy Thunderstorms and Rain	
Heavy Rain	RH _{upper} =100 % for 10 hours
Light Snow	
Snow	RH _{upper} =100 % for 15 hours
Heavy Snow	RH _{upper} =100 % for 20 hours

Equation 9.4 predicts the internal relative humidity distribution inside of concrete. A further correlation must be made between relative humidity and the degree of saturation in order to understand freeze-thaw cyclic damage. A number of adsorption isotherms (e.g., Freundlich, Langmuir, BE) can make these correlations, yet empirical fits are often selected because of the number of material challenges often posed by concrete. In the case of high performance concrete where unhydrated cement particles chemically react with the presence of water, it is found that a 3-parameter S-shaped curve adequately predicts the correlation between relative humidity and degree of saturation (see Equation 8.12).

The fitted-values used for both the wetting and drying curves are shown in Table 9.3. These wetting and fitting curves represent envelopes of degree of saturation based on measured relative humidity values. In the event that relative humidity does not follow this envelope, then an intermediary expression must govern the relationship between degree of saturation and relative humidity.

Table 9.3. Fit Parameters Used for 3-Parameter S-Shaped Curves in Equation 4-6 for Wetting and Drying Curves

Parameter	Wetting Curve	Drying Curve
α_o	0.01	0.01
RH _b	98% RH	89% RH
n	2	7.5

9.1.2 Rate and Duration of Temperature Freezing

Freeze-thaw damage susceptibility of concrete is often assessed with representative concrete prisms pursuant to ASTM C666 *Standard Test Method for Resistance of Concrete to Rapid Freezing and Thawing*. In this testing technique, concrete samples are soaked in lime water and then subjected to temperature variations from thawed (4 ± 2 °C) to freezing (-18 ± 2 °C) and back to thawed within a 2 to 5-hour period. These temperature fluctuations represent a ± 8.8 °C/hr to ± 22 °C/hr freezing or thawing rate assuming the total time period is simply halved and no considerations are taken for asymmetric thawing times (where ASTM C666 allows for no less than 25 percent of total time for Procedure A to be committed to thawing and no less than 20 percent of total time for Procedure B to be committed to thawing). These high freezing and thawing rates accelerate the instances of freezing-thawing cycles from several years to several weeks. As a consequence of this accelerated testing, the duration of freezing and thawing is also shortened compared to field conditions. In accelerated testing pursuant to ASTM C666, the period of transition between freezing and thawing cycle is not permitted to exceed 10 minutes meaning that ice crystal growth and associated stresses are not minimal in this test.

The thrust of this modeling study is to understand the effect of freeze-thaw cycles that occur in concrete when it is not fully saturated. As such, it is possible to predict the number of instances in which:

- A freeze-thaw cycle occurs due to ambient air temperature fluctuations (assuming that the microstructure is completely saturated)
- A freeze-thaw cycle occurs due to internally predicted temperature fluctuations (assuming that the microstructure is completely saturated)
- A freeze-thaw cycle occurs due to ambient air temperature fluctuations (assuming a variable internal degree of saturation)
- A freeze-thaw cycle occurs due to internally predicted temperature fluctuations (assuming a variable internal degree of saturation)

9.2 Modeling Framework

Publicly available temperature and relative humidity data from a weather station (KTIP) in Rantoul from September 3, 2013, through September 8, 2015, was used. Similar data was also retrieved from a weather station (CWLY) near Lytton, BC, from October 8, 2013, through March 17, 2015. In conjunction with latitudinal and longitudinal information known at both locations (and daily solar noon times across the observed time period), the internal temperature profile distribution within a 230-mm thick modeled concrete section overlaid atop a well-drained aggregate ballast layer is solved using Equation 9.2. The reported relative humidity values are used, along with reported weather conditions, to solve the internal relative humidity profile distribution within a 230-mm thick modeled concrete section using Equation 9.4.

9.2.1 Adaptive Correlation Between Relative Humidity and Degree of Saturation

The predicted internal relative humidity values must be correlated to the degree of saturation. However, the microstructure of cement-based materials leads to hysteric adsorption isotherms where capillary condensation governs the shape of drying and wetting curves at high relative humidity values. Figure 9.1 shows experimental data of an instrumented concrete prism

(measuring 9-in. by 9-in. by 16-in.) installed in well-drained aggregate ballast during two events: a short wetting event and a long drying event. The hysteric nature of the sorption is evident despite effects arising from non-constant temperatures, changing alkalinity of the pore fluid due to change in total moisture content in the microstructure, and changing pore size distribution due to ongoing hydration. Two 3-parameter S-shaped curves are utilized to mimic the shape of the experimental data and take the form described by Equation 9.6 with fit parameters described by Table 9.3.

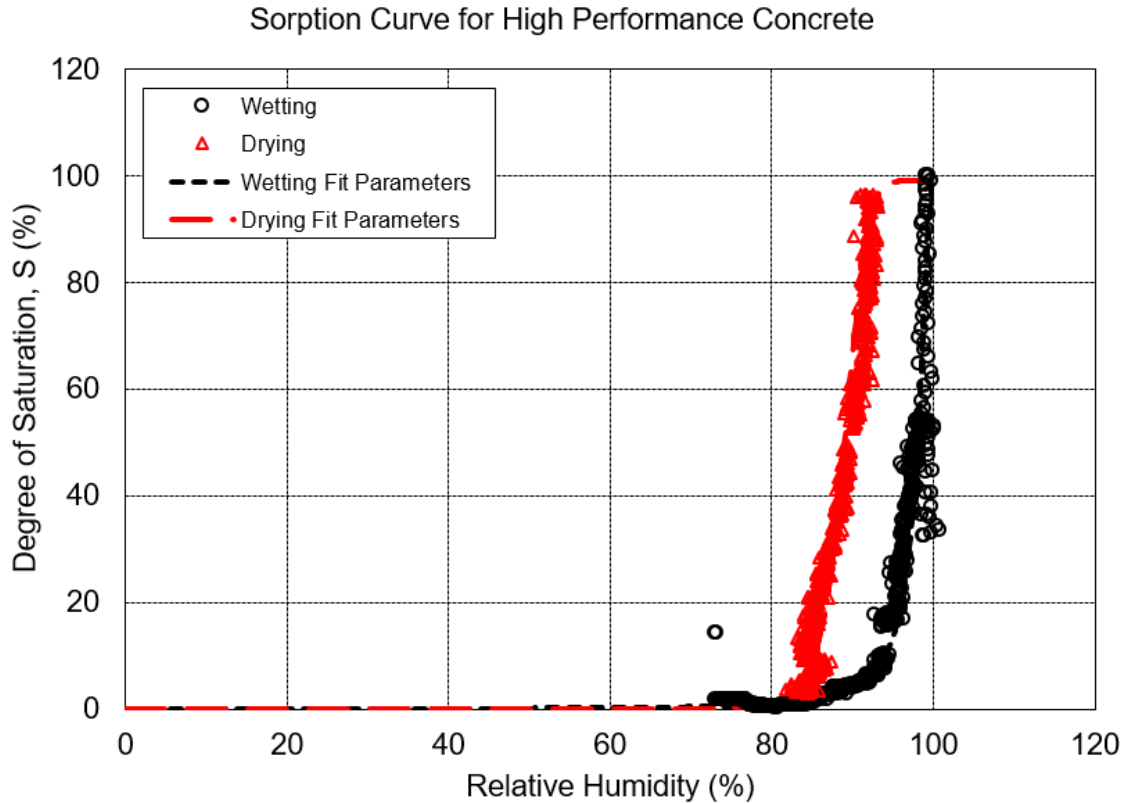


Figure 9.1. Correlation between measured relative humidity and measured degree of saturation of instrumented high performance concrete prism

In the event that a cement-based material is partially wetted and then fully dried, the resulting drying curve must take a new, revised form not fully described by Figure 9.2 where the drying path is an intermediary travel path between the two limiting (upper and lower) envelopes. In such a case, the drying path, S_{drying} , must begin at the last wetted point, S_{wetted} , as described in the following expression:

$$S_{drying} = S_{wetted} \left(\alpha_o \frac{1 - \alpha_o}{1 + (1 - RH / 1 - RH_b)^n} \right) \quad \text{Equation 9.6}$$

Where the fitting parameters are values described in Table 9.3 for a drying curve. Equation 9.6 can be plotted for instances when the initial degree of saturation is brought to 100, 95, 95, 90, 85, 80, 60, 40, or 20 percent before it is fully dried (see Figure 9.2). It is evident that each drying curve maintains a characteristic plateau where the degree of saturation is maintained momentarily while relative humidity decreases in value. After an initial drying plateau, the drying curves collapse onto the drying envelope as described by Equation 9.6.

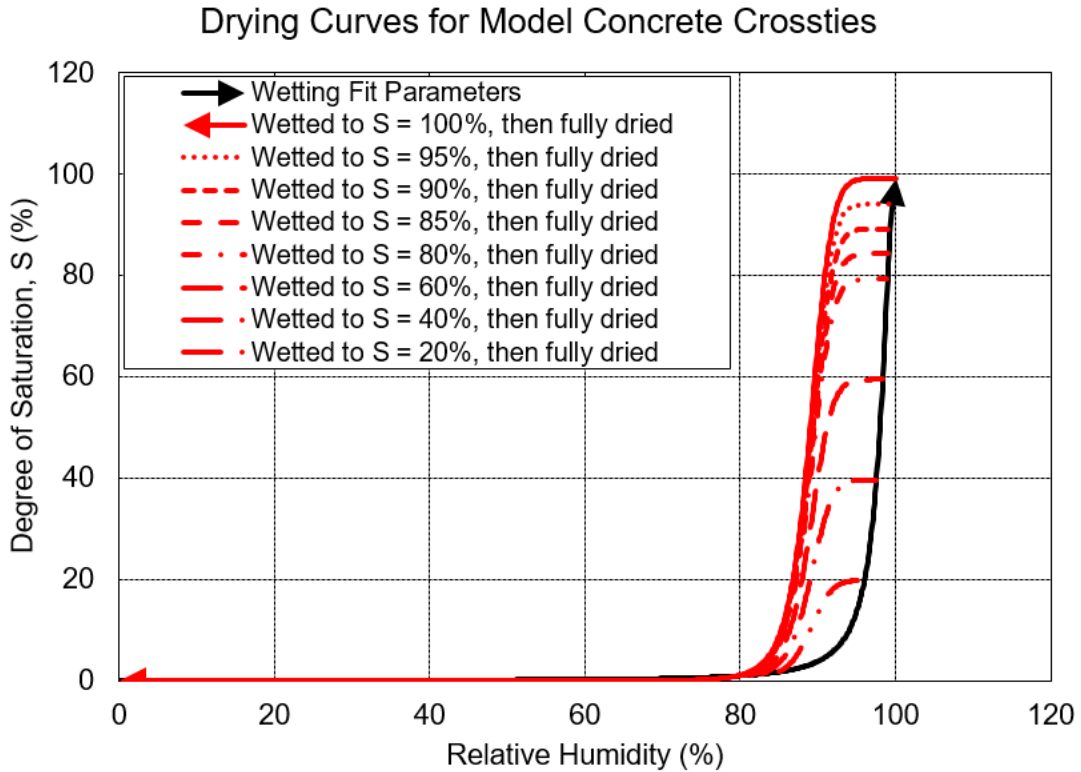


Figure 9.2. Modeled instances of drying when the concrete is initially wetted to $S=100, 95, 90, 85, 80, 60, 40,$ or 20% of its degree of saturation

Similarly, a wetting event when a cement-based material is partially dried results in a revised set of curves. The wetting path, $S_{wetting}$, begins at the last dried point, S_{dried} , as described in Equation 9.7:

$$S_{wetting} = (S_o - S_{dried}) \left(\alpha_o \frac{1 - \alpha_o}{1 + (1 - RH / 1 - RH_b)^n} \right) + S_{dried} \quad \text{Equation 9.7}$$

Where the fitting parameters are those values described in Table 9.3 for a wetting curve. Similarly, Equation 9.7 can be plotted for instances of where the degree of saturation is initially brought to 100 percent before it is dried to values of 0, 20, 40, 60, 80, 85, 90, or 95 percent and subsequently re-wetted to 100 percent (see Figure 9.3).

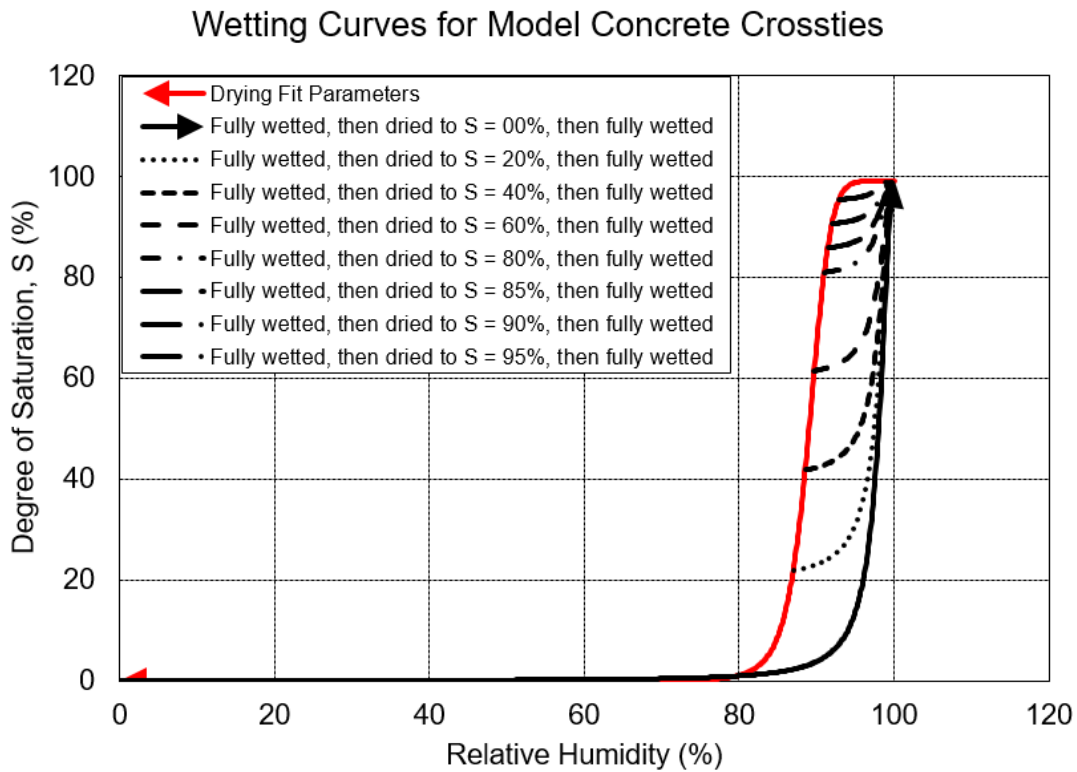


Figure 9.3. Modeled instances of wetting when the concrete is initially wetted to $S=100\%$, then dried to $S = 0, 20, 40, 60, 80, 85, 90,$ and 95% of its degree of saturation before being re-wetted to $S=100\%$

Equations 9.6 and 9.7 empirically correlate a predicted relative humidity value (from Equation 9.4) to a degree of saturation under wetting or drying conditions. It is possible to determine drying or wetting conditions by observing the difference in experimentally measured relative humidity values. In the case when the difference between two successively measured relative humidity values is negative, then it is assumed that the high performance is undergoing drying. Alternatively, if the difference between successively measured relative humidity values is positive, then the high-performance concrete is assumed to be undergoing wetting.

A simplified scenario is also assumed when applying Equation 9.6 and 9.7 in this study. In the case when the modeled concrete switches from drying to wetting (or vice-versa), then a switch occurs from Equation 9.6 and 9.7 (or vice-versa). However, the last predicted saturation value may be an intermediary point that does not lie on either governing (upper or lower) envelope. In such a case, it is necessary to interpolate S_{dried} and S_{wetted} as the switch between Equation 9.6 to 9.7 is made. If not, a non-continuous solution of S is found which can vary by approximately 2-5 percent. However, the number of instances between rapid drying and wetting cycles inside concrete is observed to be minimal, so this consideration is not of great consequence. As such, the decision between either Equation 9.6 or 9.7 is binary and an interpolated S value is not determined.

9.2.2 Criteria for Freeze-Thaw Event

Four scenarios are evaluated to depict the effect of differing assumptions to produce a singular freeze-thaw cycle event. The first scenario is the observation of ambient air temperatures

dropping below 0 °C before rising to a thawed temperature. This sequence of temperatures constitutes a single reported freeze-thaw event. The second scenario is the observation of modeled temperatures values inside the concrete (at depths of 5, 15, 25, 50, 100, 150, and 200 mm from the top surface) when temperatures drop to below 0 °C before rising. This sequence of temperatures constitutes a single reported freeze-thaw event. A third scenario reflects temperature changes when the degree of saturation is greater than a critical degree of saturation (ranging from 5, 10, 25, 50, and 85 percent). A fourth scenario applies the previously mentioned constraints with regards to temperature fluctuation while additionally adding a freeze-thaw rate dependency (of a minimum freezing rate of -8, -10, -12, -15, -18, and -22 °C/hr).

9.3 Modeling Results

The following depicts the predicted results of how concrete behaves under specific temperatures and saturation in Rantoul, IL, and Lytton, BC, Canada.

9.3.1 *Predicted Temperature and Saturation of Model Concrete in Rantoul, IL, United States*

The recorded air temperature of Rantoul, IL, from weather station KTIP is shown in Figure 9.4. Additionally, the predicted internal temperature of concrete at several depths is also shown. Predicted internal temperature values are computed using a 2-layered system whose upper concrete layer is defined by a thermal conductivity, λ , value of 1.85 kcal/hmCo and a thermal diffusivity, α , value of 0.0025 m²/h. The underlying aggregate ballast layer is defined by a thermal conductivity, λ , value of 2.58 kcal/hmCo and a thermal diffusivity, α , value of 0.0030 m²/h. It is evident that there are daily fluctuations, but there is a general seasonal trend of high temperatures in the summer months and low temperatures in the winter months. Moreover, the vertical range of the data (daily fluctuation) is constrained to a more narrow range as the observation is into the model concrete at deeper depths. This is indicative of thermally insulating behavior.

Measured Air Temperature and Predicted Temperatures Inside Concrete

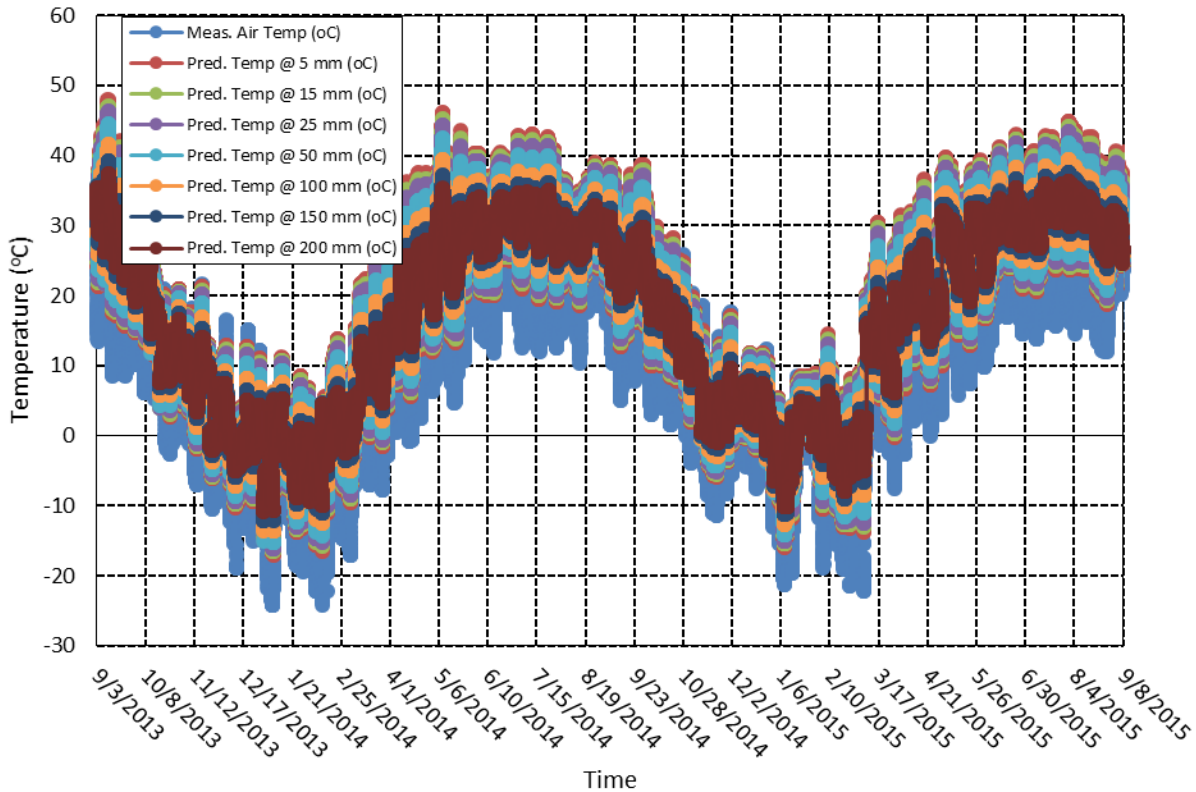


Figure 9.4. Measured air temperature and predicted temperature inside model concrete in Rantoul, IL, from September 3, 2013, through September 8, 2015

The predicted degree of saturation of model concrete located in Rantoul is shown in Figure 9.5. The concrete is defined by a diffusivity (at S=100%) value of $0.86 \times 10^{-6} \text{ m}^2/\text{hr}$, a regression coefficient, n , of 15, α value of 0.05, and an empirical correlation between relative humidity and degree of saturation. The simulation is initialized with an even distribution of 85 percent RH throughout the depth of the concrete. One observation of this data set is the effect of the boundary condition at the topside (5 mm) and underside (200 mm) of the model concrete. The boundary condition at the underside exacerbates wetting conditions as described by Table 9.2 by a factor of 10. As a result, the extent of high moisture saturation increases over a longer period of time at the underside than at the topside which experiences large increases in saturation followed by significant drying. Similar to temperature, seasonal fluctuations are observed. In the precipitously wet winter months, there is a general spike in the amount of predicted saturation. In the summer months, there is generally a lower amount of precipitation so there is also a lower amount of saturation. At the interior of the concrete (150 mm), it is observed that saturation steadily increases with respect to time. This is most likely due to the increase of relative humidity with slow drying occurring.

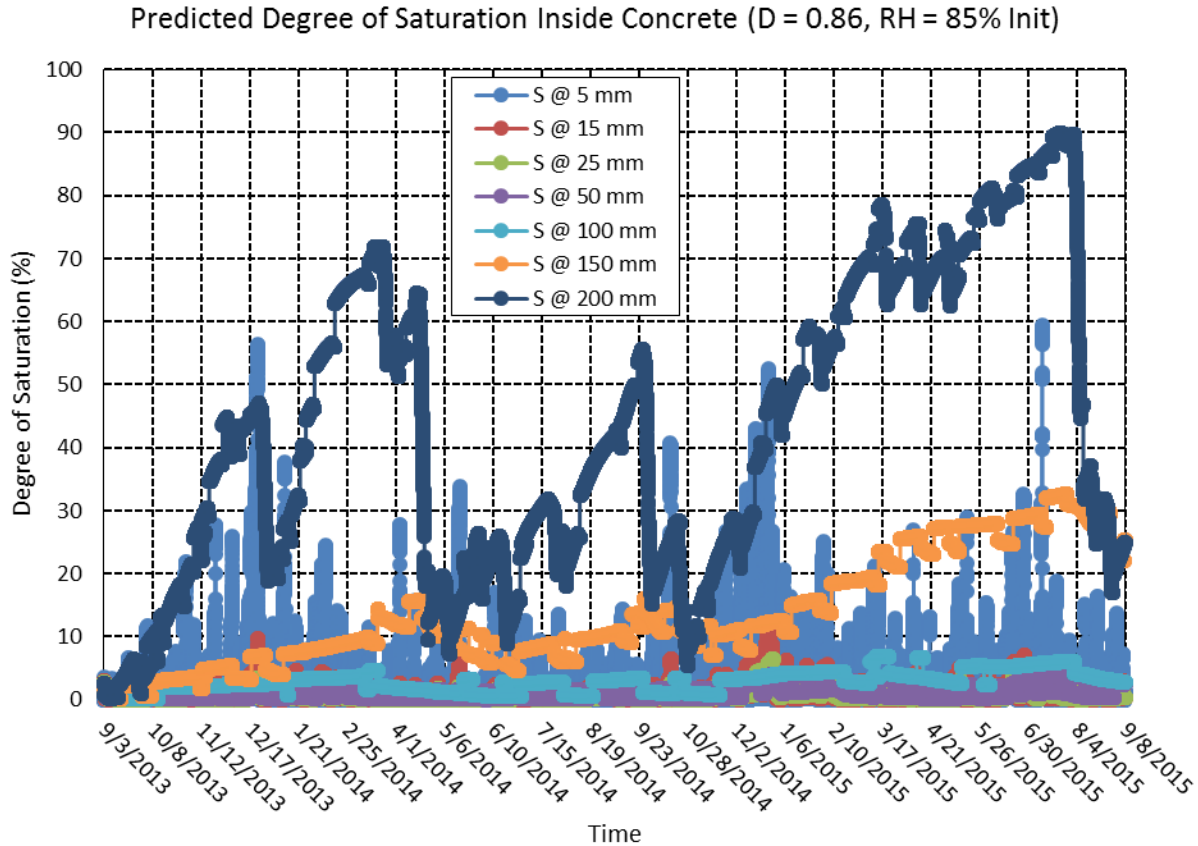


Figure 9.5. Predicted degree of saturation inside a one-layered concrete system in Rantoul, IL, from September 3, 2013, through September 8, 2015

9.3.2 Predicted Temperature and Saturation of Model Concrete in Lytton, BC, Canada

The recorded air temperature of Lytton, BC, from weather station CWLY is shown in Figure 9.6. Predicted internal temperature values are computed using a two-layered system whose upper concrete layer is defined by a thermal conductivity, λ , value of 1.85 kcal/hmCo and a thermal diffusivity, α , value of 0.0025 m²/h. The underlying aggregate ballast layer is defined by a thermal conductivity, λ , value of 2.58 kcal/hmCo and a thermal diffusivity, α , value of 0.0030 m²/h. Much like the temperature values shown in Figure 9.4, there are seasonal fluctuations. Figure 9.7 shows the predicted degree of saturation of model concrete in Lytton, BC, initialized with an even distribution of 85 percent RH. The concrete is defined by a diffusivity (at S=100%) value of 0.86×10^{-6} m²/hr, a regression coefficient, n , of 15, α value of 0.05, and an empirical correlation between relative humidity and degree of saturation. Again, there is an observation of seasonal variation of the degree of saturation between wet, wintry months and dry, summer months. At the underside of the model concrete (200 mm), it is evident that there is a slight offset rightward suggesting that the well-drained ballast is able to retain moisture past significant moisture events that occur earlier in the simulation. Also, contrasted against Figure 9.5, it is observed that for the same material conditions (diffusion coefficient and initialization of

moisture conditions), there is a starkly higher number of instances of degree of saturation. This is indicative of the differences in weather conditions leading to this result.

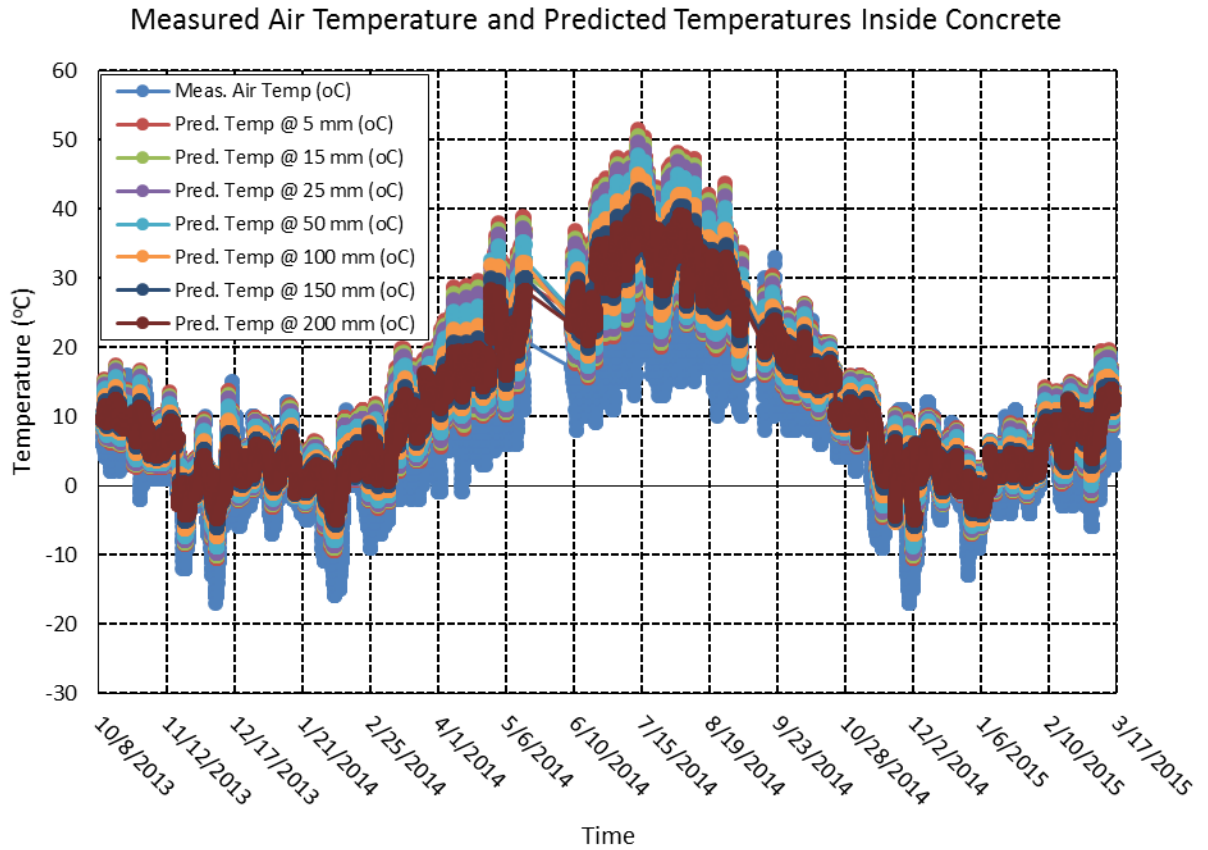


Figure 9.6. Measured air temperatures and predicted temperature inside model concrete in Lytton, BC, from October 8, 2013, through March 17, 2015

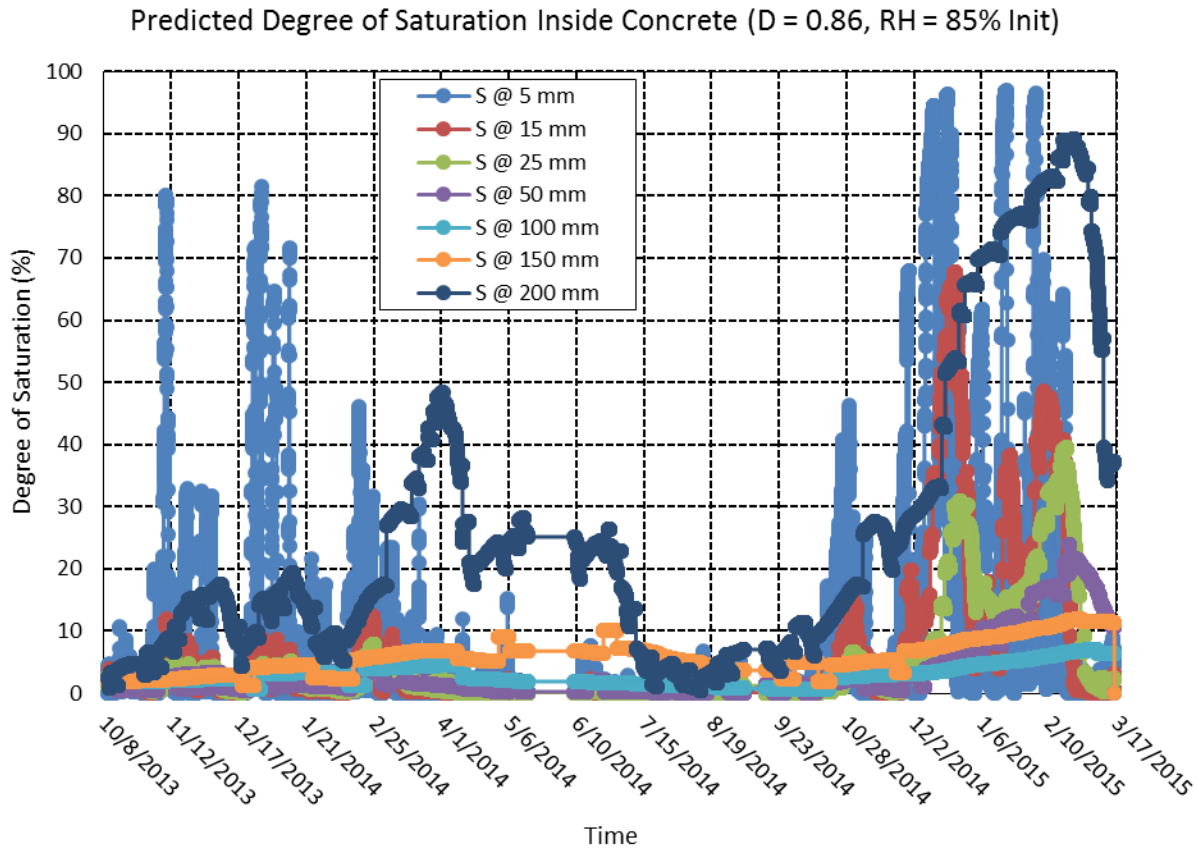


Figure 9.7. Predicted degree of saturation inside a one-layered concrete system in Lytton, BC, from October 8, 2013, through March 17, 2015

9.4 Discussion of Modeling Results and Framework

A brief overview of modeling results and discussion is presented in the following section. For a complete overview of all considered test cases, refer to Appendix C, which is separate from the report.

9.4.1 Difference Between Observed air Temperatures and Internal Concrete Temperatures

Figure 9.8 shows the cumulative number of freezing-thawing cycles that occur in Rantoul, over the observed time period. At the end of the first winter season, the number of freeze-thaw cycles by recorded air temperatures is approximately 90. After a second winter season, the cumulative number of freeze-thaw cycles increases to approximately 180. This observed number is in agreement with Hershfield's estimated number of freeze-thaw cycles in this region of 90-100 freezing thawing cycles per year. Although only two winter seasons are considered in the scope of this study, it is important to note that there are inherent discrepancies between seasons (due to long time-scale weather phenomenon). As such, it would be more representative to average the yearly number of freeze-thaw cycles over several years.

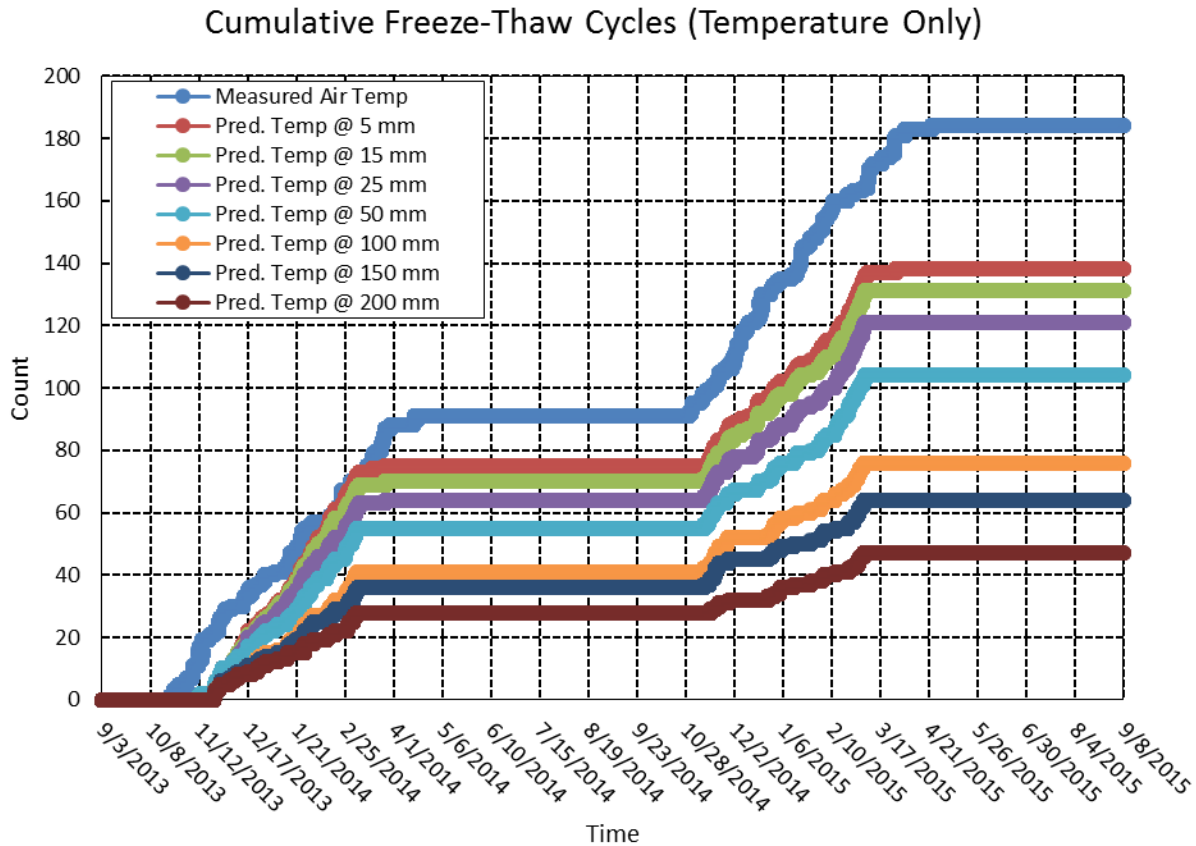


Figure 9.8. Cumulative number of freeze-thaw cycles in Rantoul, IL, from September 3, 2013, through September 8, 2015

In the case when the concrete (conventional or otherwise) is fully saturated, then the cumulative number of freeze-thaw cycles becomes depth-dependent as observed in the model concrete in Figure 9.8. Near the surface (5 mm), the number of freeze-thaw cycles is significantly diminished when compared to the number of freeze-thaw cycles observed due to air temperature alone. At shallow depths, the number of cycles is higher than at deeper depths. Moreover, the number of freeze-thaw cycles as measured by air does not equal the number of freeze-thaw cycles at shallow depths. This is due to the heat-capacity of concrete where it can retain heat from solar radiation. As nighttime air temperatures fall in early or late winter to near or below freezing, the concrete can sufficiently retain heat such that it does not fall below freezing.

9.4.2 Validation of Predictive Model Against Experimentally Measured Values

The observation of the reduction of cumulative freeze-thaw cycles from predicted internal temperatures in concrete (Figure 9.8) is similarly seen in another location: Lytton, BC. Figure 9.9 shows the number of cumulative freeze-thaw cycles as predicted with the one-dimensional model using another set of weather conditions. Moreover, a finite-width instrumented concrete crosstie installed in ballast is also shown to undergo an unequal number of freeze-thaw cycles based on the depth of the sensor. Near the surface (5 mm), the number of cumulative freeze-thaw cycles is significantly reduced from what occurs in the ambient air temperatures. Additionally, at successively deeper depths, the number of cycles is diminished. At comparable

deep depths of 200 mm (7.9 in), the number of freeze-thaw cycles in the predictive model reaches 20 which compares favorably to the measured value of 20.

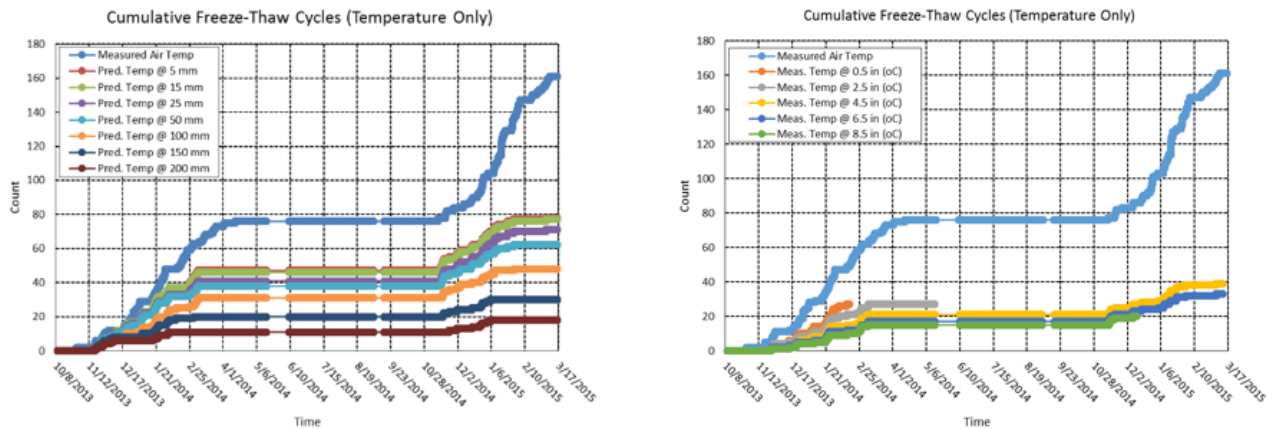


Figure 9.9. Predicted (left) and measured (right) cumulative number of freeze-thaw cycles in Lytton, BC, from October 8, 2013, through March 17, 2015

It is observed that the predicted degree of saturation in Figure 9.5 suddenly spikes upward when relative humidity is near 100 percent RH. However, the desiccation of moisture as predicted by Equation 9.6 does not appreciably capture the time-delay in which drying occurs in a concrete member with an installed polyurethane pad and steel rail line. This is seen by the persistently high moisture content in Figure 8.16. This discrepancy suggests that the drying curve for a concrete crosstie is not well supported by Equation 9.5 in field conditions as field experience suggests that crossties are persistently wet. As such, it is likely that near-surface conditions are not well predicted using this model and that a conservative approach is to consider the surface of the crosstie to be fully saturated at all times at the rail seat area. In such a case, the number of freeze-thaw cycles is dependent upon temperature alone which is more confidently predicted. Additionally, the quantitative number of freeze-thaw cycles in such a scenario conforms to observations of freeze-thaw damage of concrete crossties installed in ballast.

9.4.3 Effect of Predicted Degree of Saturation on Number of Freeze-Thaw Cycles

A freeze-thaw cycle can also occur when the concrete microstructure is not fully saturated. In such a case, it is possible to add a constraint which discounts a freeze-thaw occurrence if a minimum degree of saturation is not present in the microstructure. Figure 9.10 shows the cumulative number of freeze-thaw cycles in Lytton, BC, as a minimum degree of saturation constraint is added to freezing air temperatures. When any degree of saturation is valid ($S > 0\%$), then the number of freeze-thaw cycles equals the ambient air cycles. In Lytton, BC, it is observed that in the first winter season, approximately 80 freezing-thawing cycles occur. At the end of the second winter, approximately 160 cumulative freezing thawing cycles have occurred. This number compares well with Fraser's reported estimate of 80 freeze-thaw cycles per year in this region of Canada.

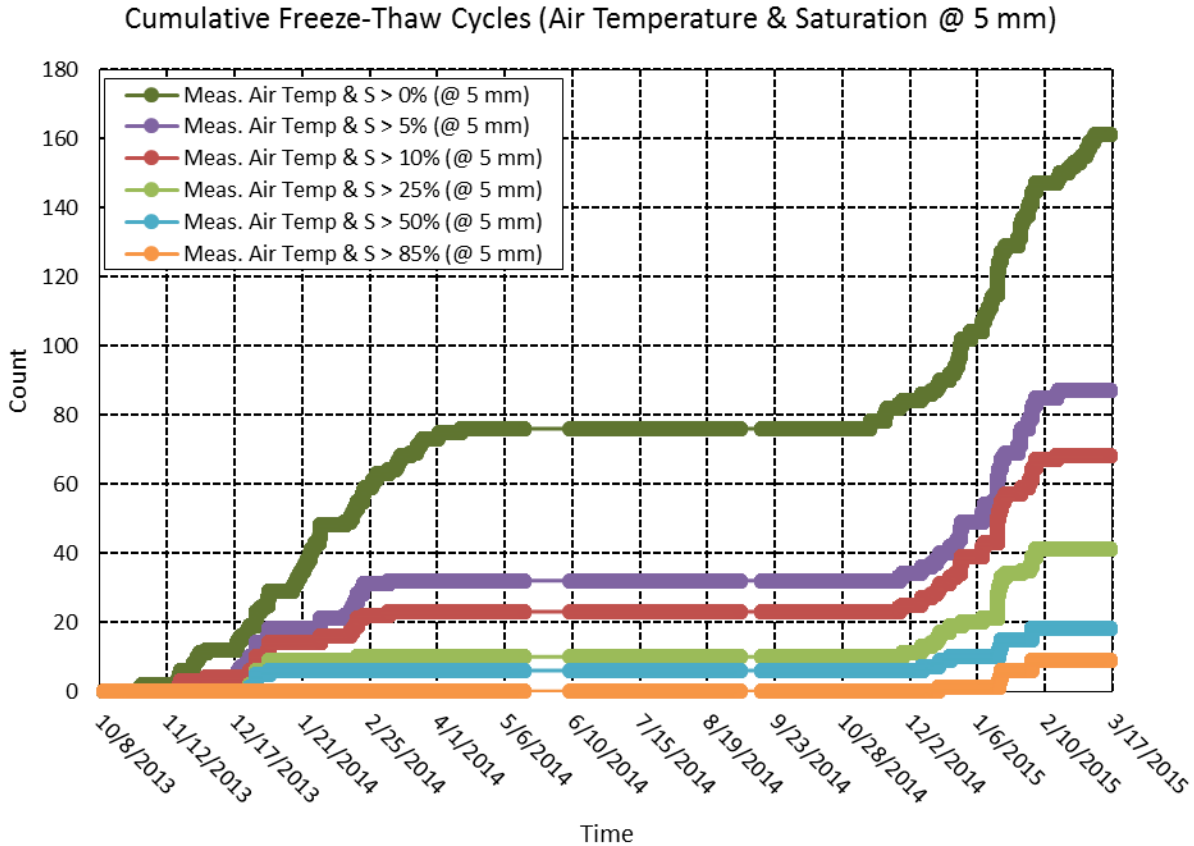


Figure 9.10. Cumulative number of freeze-thaw cycles in Lytton, BC, from October 8, 2013, through March 17, 2015, at a depth of 5 mm when both freezing air temperatures and minimum degree of saturation is achieved at time of freezing. Predicted degree of saturation is defined by a diffusivity (at S=100%) value of $0.86 \times 10^{-6} \text{ m}^2/\text{hr}$, a regression coefficient, n , of 15, α value of 0.05, and an empirical correlation between relative humidity and degree of saturation. The simulation is initialized with an even distribution of 85 percent RH throughout the depth of the concrete

When a minimum degree of saturation of 5 percent is added as a constraint, then the number of freeze-thaw cycles is appreciably diminished. As the minimum degree of saturation is increased upward to 85 percent (a value comparable to Li et al’s reported critical degree of saturation), then the number of freezing-thawing cycles is greatly diminished. This observation is also seen in Figure 9.11 which shows the same minimum degree of saturation criteria applied to predicted internal temperatures at a shallow depth of 5 mm. Figure 9.11 shows that the number of freeze-thaw cycles that coincide with the concrete degree of saturation higher than a given value drops as the given degree of saturation value increases. This means that as the critical degree of saturation or the level of saturation required to cause damage during a freezing and thawing event increases, the number of annual weather events that would cause damage decreases. However, this observation does not definitively claim that the concrete is less likely to undergo freezing-thawing damage. Instead, the observation is that the correlation between the 300 freezing-thawing cycles of ASTM C666 may not represent partially saturated high performance concrete.

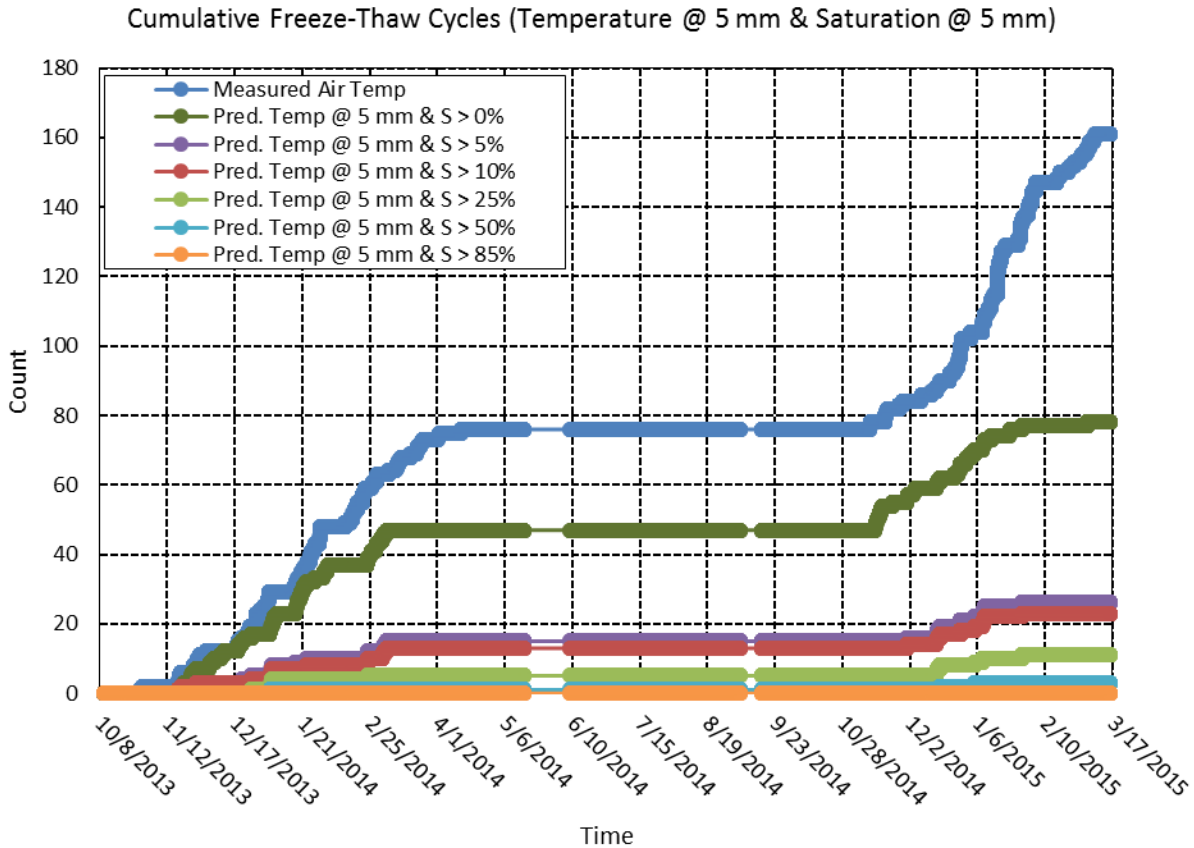


Figure 9.11. Cumulative number of freeze-thaw cycles in Lytton, BC, from October 8, 2013, through March 17, 2015, at a depth of 5 mm when both freezing temperatures and minimum degree of saturation is achieved at time of freezing

The modeling result of Figure 9.10 and Figure 9.11 suggests that there is a significant decrease in the number of freeze-thaw cycles when degree of saturation is additionally added as a constraint.

9.4.4 Reduction of Freeze-Thaw Cycles Due to Rate of Freezing Criterion

A point of consideration is that ASTM C666 is an accelerated testing regimen with high freezing rates of fully saturated concrete prisms. Figure 9.12 and Figure 9.13 shows the cumulative number of freezing-thawing cycles of model concrete when air temperature and predicted internal temperature at a shallow depth of 5 mm are additionally constrained with increasing temperature freezing rates. This constraint demonstrates that fast freezing rates do not often occur in typical weather environments and do reduce the number of freeze-thaw cycles.

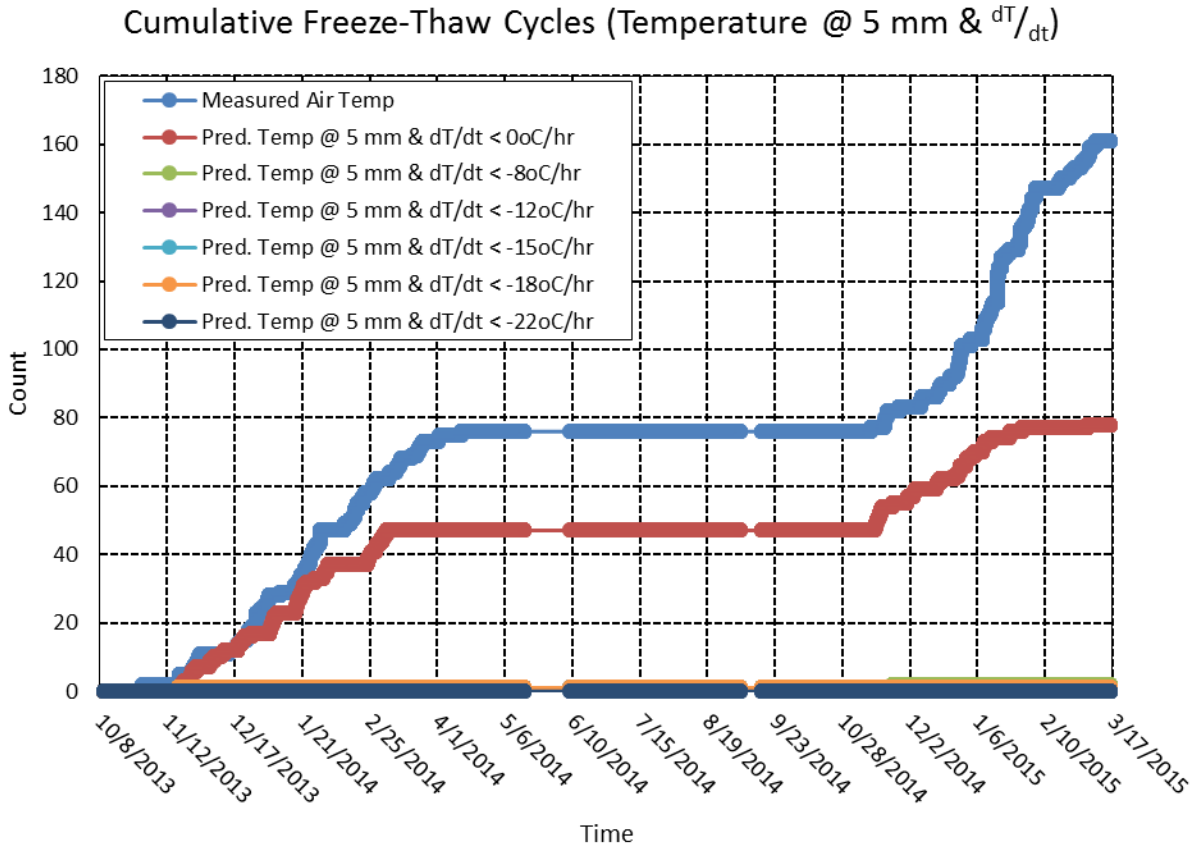


Figure 9.13. Cumulative number of freeze-thaw cycles in Rantoul, IL, from September 3, 2013, through September 8, 2015, when both freezing temperatures at a depth of 5 mm and minimum rate of freezing is achieved at time of freezing

The occurrence of freeze-thaw cycles can be summarized with the mean, median, and mode. Table 9.4 shows statistically relevant values of the freezing rate when time intervals between successively measured temperature values is greater than 15 minutes. Table 9.5 similarly shows the relevant values of the freezing rate when time intervals between successively measured temperature values is greater than 60 minutes. When a successive time interval is 1 minute or less, then a change of temperature of 1 °C can result in a maximum freezing rate of 60 °C/hr. Alternatively, limiting the observed freezing rates to time intervals of 60 minutes (see Table 9.5) results in a maximum freezing rate of 3 °C/hr. While the maximum freezing rate can yield unfavorable freeze-thaw damage in hardened concrete, the mean freeze rate is 1.36 °C/hr as shown in Table 9.4 and 0.94 °C/hr as shown in Table 9.5. The mean freeze rate can increase upwards to 5.07 °C/hr when a 1-minute time interval between measured temperature values is considered. In any of these cases, the average freezing rate is significantly less than the freezing rate of 8.8 °C/hr to 22 °C/hr as stipulated in ASTM C666. Moreover, the realistic maximum freezing rate of 2-3 °C/hr observed in a 60-minute time interval is comparable to that seen in concrete pavement studies.

Table 9.4. Mean, Median, and Mode of Freezing Rates in Lytton, BC, from October 8, 2013, Through March 17, 2015. Instances of Freeze Rate are as Large as 8 °C/hr Because of Observed 2 °C Change in the Span of a 15-Minute Time Interval

Mean Freeze (-) Rate (°C/hr)	Std. Dev. Freeze (-) Rate (°C/hr)	Mode Freeze (-) Rate (°C/hr)	Median Freeze (-) Rate (°C/hr)	Min Freeze (-) Rate (°C/hr)	Max Freeze (-) Rate (°C/hr)
1.36	0.76	1.00	1.00	0.01	8.00

Table 9.5. Mean, Median, and Mode of Freezing Rates in Lytton, BC, from October 8, 2013, Through March 17, 2015. Instances of Freeze Rate are as Large as 3 °C/hr Because of Observed 3 °C Change in the Span of a 60-Minute Time Interval

Mean Freeze (-) Rate (°C/hr)	Std. Dev. Freeze (-) Rate (°C/hr)	Mode Freeze (-) Rate (°C/hr)	Median Freeze (-) Rate (°C/hr)	Min Freeze (-) Rate (°C/hr)	Max Freeze (-) Rate (°C/hr)
0.94	0.56	0.50	1.00	0.01	3.00

9.4.5 Effect of Water-to-Cement Ratio on Number of Freeze-Thaw Cycles in Concrete

A diffusion coefficient of $D_o=0.86 \times 10^{-6}$ m²/hr is representative of a low water-to-cement ratio of approximately 0.30 by mass. When concrete is subjected to micro- and macro-scale cracking, then external water can more easily permeate into the interior of the structure. As such, the diffusivity can increase steadily over time. Alternatively, the initial concrete mixture design can be made with a conventional water-to-cement ratio of approximately 0.35 to 0.45 by mass. In order to observe the effect of changing water-to-cement ratio and extent of cracking, the diffusion coefficient can be changed in the model. Figure 9.14 shows the saturation history of model concrete in Lytton, BC, when the diffusion coefficient is increased by 50 percent from its original value to 1.29×10^{-6} m²/hr. When compared against Figure 9.7, it is observed that saturation peaks are slightly increased in magnitude. This results in a minimal change in the number of cumulative freezing-thawing cycles as shown in Figure 9.15. It is expected that as the diffusion coefficient increases in value, the number of freeze-thaw cycles increases until it reaches the maximum boundary limit that is equal to the number of freeze-thaw cycles due to air temperature fluctuations alone.

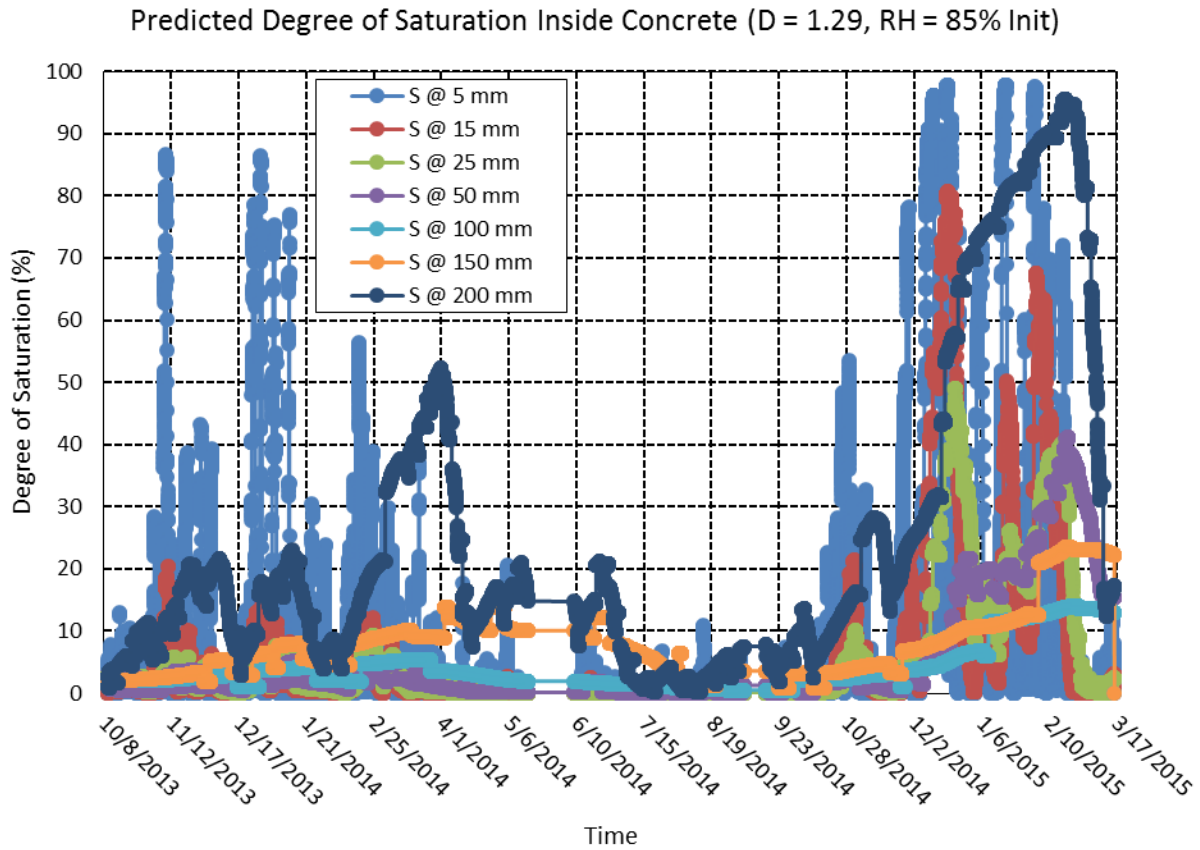


Figure 9.14. Predicted degree of saturation inside a one-layered concrete system in Lytton, BC, from October 8, 2013, through March 17, 2015. The concrete is defined by a diffusivity (at S=100%) value of $1.29 \times 10^{-6} \text{ m}^2/\text{hr}$, a regression coefficient, n , of 15, α value of 0.05, and an empirical correlation between relative humidity and degree of saturation

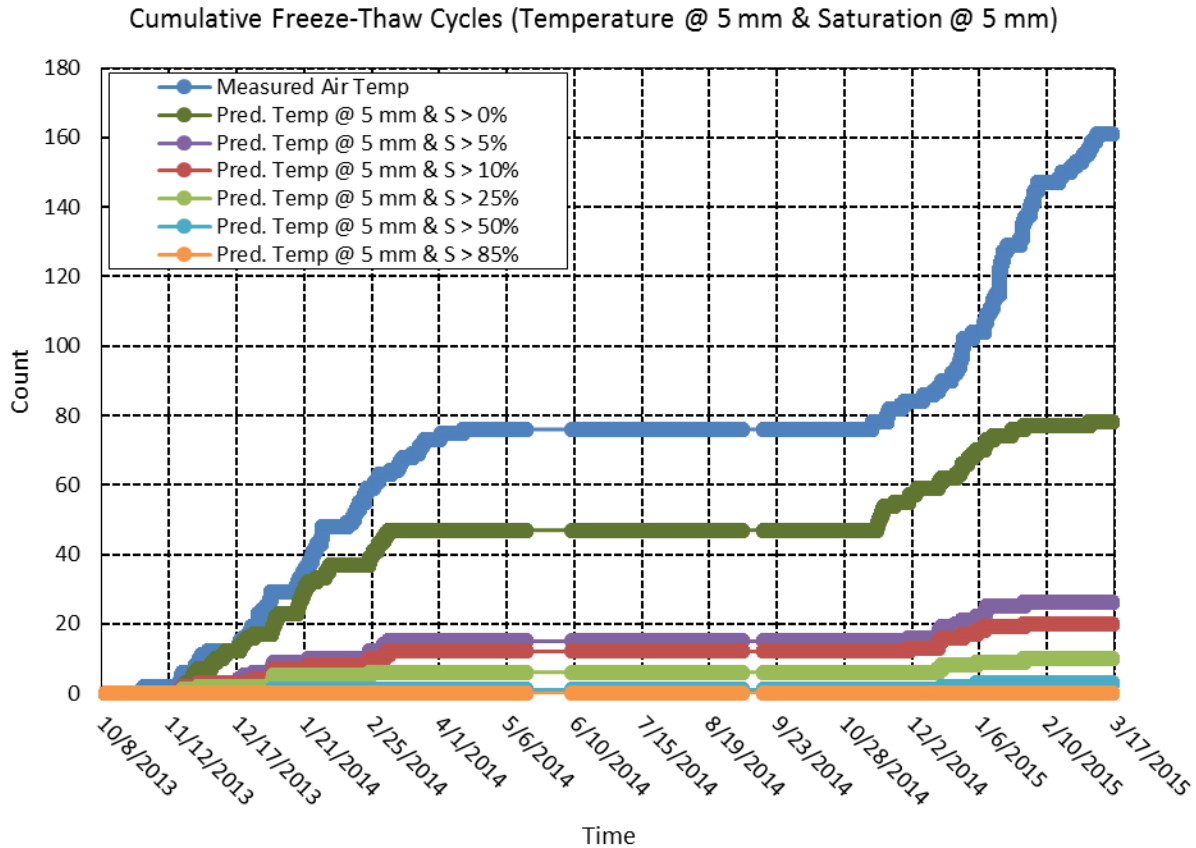


Figure 9.15. Cumulative number of freeze-thaw cycles in Lytton, BC, from October 8, 2013, through March 17, 2015, at a depth of 5 mm when both freezing temperatures and minimum degree of saturation is achieved at time of freezing. Predicted degree of saturation is defined by a diffusivity (at S=100%) value of $1.29 \times 10^{-6} \text{ m}^2/\text{hr}$

9.5 Conclusions

High performance concrete is subject to freeze-thaw climates where recorded air temperatures fluctuate from above freezing to below freezing particularly during winter months. Freeze-thaw damage is most likely when freezing temperatures occur when there is a high degree of saturation in the concrete material. The record of cumulative freeze-thaw cycles for Rantoul and Lytton, BC shows that:

- The ambient air experiences a greater number of freeze-thaw cycles than the concrete material. It was observed that an air temperature cycle above and below the freezing point would translate to a concrete tie temperature cycle above and below the freezing point only about 80 percent of the time.
- The number of freeze-thaw cycles experienced by a concrete tie while the concrete had a degree of saturation exceeding 85 percent is much lower than the total number of freeze-thaw cycles. This means that the number of cycles that may cause concrete damage is much lower than the number of freeze-thaw cycles in the ambient air.

- At shallow depths in the concrete, the number of cycles is higher than at deeper depths. Moreover, the number of freeze-thaw cycles as measured by air does not equal the number of freeze-thaw cycles at shallow depths. This is due to the heat-capacity of concrete where it can retain heat from solar radiation.

Chapter 10 – Effects of Prestressing and Saw-Cutting on Freeze-Thaw Durability

10.1 Introduction

There is a concern that concrete tie exposure to cold, damp environmental conditions in track could lead to freeze-thaw damage. Questions have arisen about the best way to measure the freeze-thaw durability of concrete railroad ties. The prestressing typically used in concrete railroad ties leads to compression forces in the longitudinal direction and tensile forces in the transverse direction. There is a concern that the stress state caused by the prestressing makes it difficult to extract representative concrete samples from ties to test in freezing and thawing cycles without damaging them during the extraction process.

Samples currently used for freeze-thaw quality control tests are typically tested per ASTM C666 Procedure A. Some manufacturers test concrete samples saw cut from concrete ties and others using prisms made from concrete sampled from the plant but not vibrated in the same way as the concrete railroad ties. ASTM C666 allows for two Procedures to be used: Procedure A and Procedure B. Procedure A involves rapid freezing and thawing in water, while Procedure B entails rapid freezing in air and thawing in water. Concrete specimens tested according to ASTM C666 should be between 3 x 3 x 11 in. (75 x 75 x 279 mm) and 5 x 5 x 16 in. (125 x 125 x 405 mm). These specimens are saturated in a lime water bath for at least two days, and then conditioned at 40 °F (4 °C). The concrete is then frozen to 0 °F (-18 °C) and thawed to 40 °F (4 °C), usually for 300 freeze-thaw cycles. The freezing in this test is quite rapid, with up to 12 cycles performed per day. A freeze-thaw cycle can be completed in 2 to 5 hours, with the thawing period requiring 25 percent of the cycle time for Procedure A and 20 percent for Procedure B, resulting in a cooling rate of 10.8 °F/h (6 °C/h) to 27 °F/h (15 °C/h) (Pigeon, M., and Pleau, R., 1995). During testing, samples are immersed in water or frozen in air and thawed by flooding the chamber that contained the concrete samples with water (ASTM Standard C666, 2008). Damage is monitored by measuring the dynamic modulus of elasticity, length change, and mass loss after at least every 36 cycles.

Concrete micro-cracking from freeze-thaw deterioration can be quantified by length change, mass change, or a change in wave propagation properties through concrete. As concrete cracks, the volume occupied by the crack causes the overall volume of the concrete prism tested in freeze-thaw to increase. This can be measured during freeze-thaw tests by a change in concrete specimen length. Water will fill the microcracks, resulting in initially a mass increase for damaged concrete prisms. As deterioration progresses, however, concrete may spall off the specimens and reduce the specimen mass. Relative dynamic modulus of elasticity measurements has been used to measure concrete internal damage. Concrete micro-cracking will decrease wave propagation speed through concrete and change the concrete resonant frequency.

Two methods are commonly used to determine resonant frequency of a concrete specimen: the forced resonance method and the impact resonance method (ASTM C 215-14, 2014). The forced resonance method uses an electromechanical driving unit to vibrate a supported specimen while measuring vibration of the surface of the specimen. The specimen is vibrated at various frequencies, and the frequency that corresponds to the maximum amplitude is the resonance frequency (RF) (ASTM C 215-14, 2014). In the impact resonance method, a rounded impactor (rounded hammer) strikes the specimen, and an accelerometer records the impact wave. The

recorded wave is analyzed using Fast Fourier transform (FFT) in order to obtain RF. RDME obtained by the resonant frequency method depends on specimen size and shape (Yang, Z., 2004). Wave induced by impact on the surface of the concrete causes the concrete to vibrate at its own natural frequencies (Carino, N. J., and Malhotra, V., 2003), but amplitudes of these natural frequencies can be affected by cracking or air pockets. A drop in amplitude is known as damping capacity. This damping capacity increases significantly as a result of increased porosity, voids, a cracked location, or a weakness in the paste (Popovics, 1998). The damping effect tends to be more prominent in smaller sections because of their higher initial frequencies compared to low frequencies of large sections.

Ultrasonic Pulse Velocity (UPV) can be used to evaluate the condition of concrete specimens with various shapes and sizes. In UPV, a transmitting transducer (electro-acoustical transducer) is used to generate mechanical wave bursts from voltage pulses (International Atomic Energy Agency, 2002). A receiving transducer is placed at a known distance from the transmitting transducer in order to measure the time interval between the transmission and reception of the pulse. These two transducers should be coupled to the concrete surface using a proper medium (grease or cellulose paste) (International Atomic Energy Agency, 2002). The generated pulse can travel through the concrete but not through air, causing the pulse to travel around cracks, thereby increasing travel time and lowering velocity. These transducers are typically arranged in one of three configurations: direct transmission, semi-direct transmission or diagonal transmission, and indirect or surface transmission. Direct transmission results in maximum sensitivity because the two transducers face each other and they do not require any wave reflection. As concrete deterioration develops, changes are reflected as a decrease in pulse velocity (International Atomic Energy Agency, 2002).

Impact Echo (IE) has been used to detect structure thickness, internal delamination, honeycombing, and cracking parallel to the surface (Bedon, R., Lieberle, C., Olson, L. D., and Tinkey, Y., 2003). During an IE test, a solenoid impactor is used to induce a displacement wave (P-Wave) in the concrete that is picked by an accelerometer (Bedon, R., Lieberle, C., Olson, L. D., and Tinkey, Y., 2003). Wave energy is reflected when the medium for wave travel changes, usually from concrete to air or water as a result of cracking, delamination, or the end of the section or depth. In order to identify resonant echoes, the frequency domain is utilized instead of the time domain. FFT analysis is then performed on the collected data in order to obtain the resonant echo peak and concrete depth (Bedon, R., Lieberle, C., Olson, L. D., and Tinkey, Y., 2003).

10.2 Test Methods

Although saw-cutting of concrete for freeze-thaw testing remains an acceptable method according to ASTM C666, its effects on prestressed concrete are unknown. Limited research has been conducted on the effects of saw-cutting and stress release caused by saw-cutting prestressed concrete members. To investigate these effects, concrete railroad ties were saw-cut in different sizes and subjected to freeze-thaw testing.

10.2.1 Large-Scale Samples

Six prestressed concrete railroad ties were saw-cut in half and soaked in a lime water bath at 73.4 ± 3 °F (23 ± 1.7 °C) for 7 days, as shown in Figure 10.1. The saw-cut ends of the ties were epoxied in order to reduce water absorption. One of the ties was made with non-air-entrained

concrete to investigate if concrete freeze-thaw durability could be imparted by using a low water-cement ratio (w/c) concrete instead of air entrainment. The tested half ties were 8.5 ft (2.6 m) long with a trapezoidal cross section (10 in. (254 mm) top, 11 in. (280 mm) bottom, and 10.5 in. (267 mm) height). Initial testing was performed after the samples were soaked for 2 days and 7 days and after the samples were cooled to 40 °F following the 7-day soaking. After the soaking period, the half ties were removed from the lime water bath and wrapped with a wet burlap sheet. The wet burlap was placed around the ties to ensure that free water was present all around the half ties for the duration of the test. In addition, the samples were wrapped with plastic wrap to avoid evaporation during freezing stage. UPV measurements were conducted over the top surface of the half ties, as shown in Figure 10.2. Sensors of the UPV were placed 38 in. (0.97 m) apart.



Figure 10.1. Soaked half ties covered with burlap

UPV readings were performed using an Olson Instruments NDE 360. Half ties were weighed using a 1,000-lb (454 kg) crane scale with a resolution of 0.1 lb (0.05 kg). The crane scale was attached to a 2-ton gantry crane with a 14.5-ft (4.4 m) span. During the testing period, the half ties were kept wet.

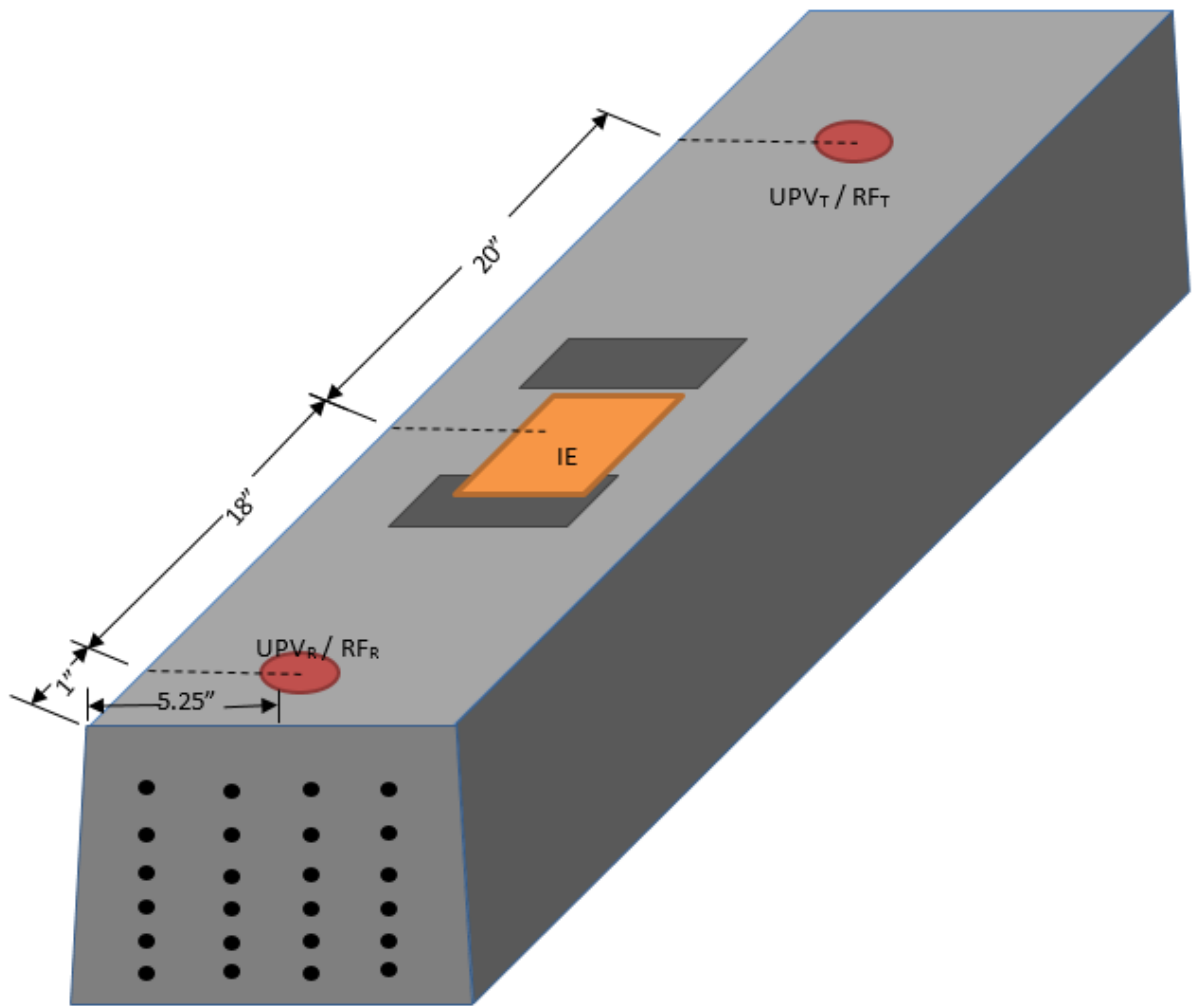


Figure 10.2. Measurement locations on half ties (R represents the receiver and T represents the transmitter)

After initial testing, the sample was subjected to 300 freeze-thaw cycles in a large freeze-thaw chamber. The chamber was designed to hold three whole ties and perform freeze-thaw cycles from 0 ± 3 °F (-18 ± 1.7 °C) to 40 ± 3 °F (4 ± 1.7 °C). The temperatures were maintained at a distance of 4.5 in. (114.3 mm) from the top surface of the ties, thereby allowing 3.13 cycles each day with cycle lengths of 460 minutes. Figure 10.3 shows typical temperatures measured by thermocouples from the center of the half tie during freeze-thaw cycles. Half ties were tested every 36 cycles or less. Testing included the same tests performed during initial testing.

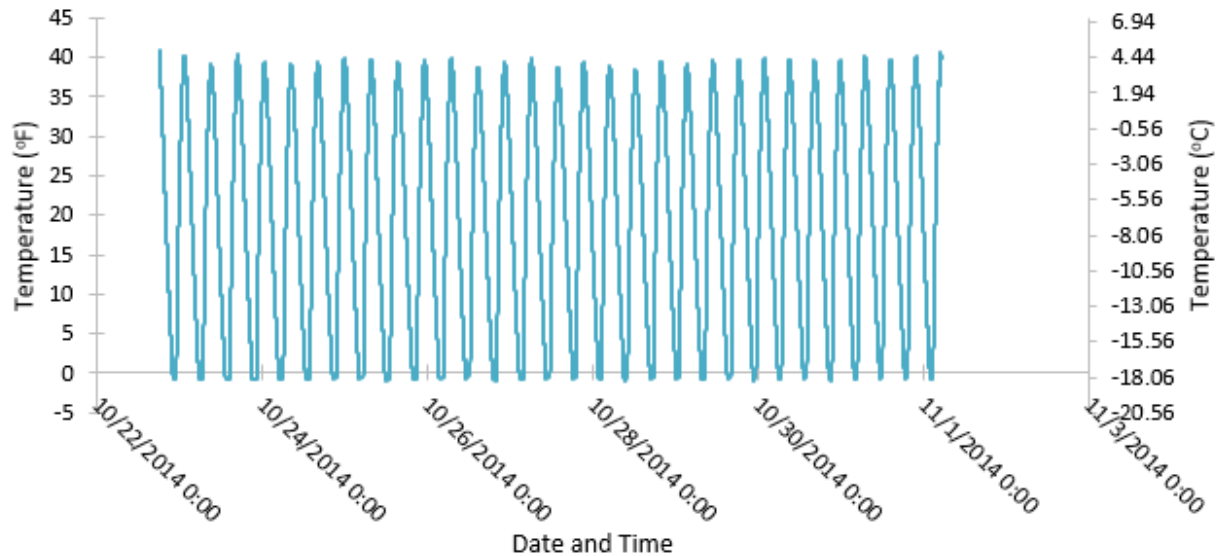


Figure 10.3. Typical freeze-thaw cycle temperatures measured 4.5 in. (114 mm) from the concrete tie surface

10.2.2 Saw-Cut Samples

In order to understand the effects of saw-cutting and reinforcement, concrete ties were cast with prestressing wires, un-prestressed wires, and without steel reinforcement. Each type of reinforcement consisted of two ties, one air-entrained and one non-air-entrained, resulting in a total of six ties. In addition to these ties, four additional air-entrained prestressed concrete ties were obtained from prestressed concrete ties sampled from track before going into service. Three samples were excised from each tie and tested in freeze-thaw conditions. The other halves of the prestressed ties were used in the freeze-thaw testing described in the Section 10.2.1. Three samples were excised from one end of each tie, as shown in Figure 10.4. The samples had dimensions of 3 x 4 x 11 in. (76.2 x 101.6 x 279.4 mm), as shown in Figure 10.5. End pins were then installed on the saw-cut samples in order to measure change in length resulting from freeze-thaw testing. Finally, the samples were soaked in lime water for 2 days at 40 ± 3 °F (4 ± 1.7 °C) before beginning freeze-thaw testing.



Figure 10.4. Saw-cutting samples from the tie end

Initial testing was performed on the samples after they reached 40 ± 3 °F (4 ± 1.7 °C). Initial testing included change in weight, change in length, and transverse RF. In order to satisfy requirements of ASTM C666 Procedure A, the samples were tested at least every 36 freeze-thaw cycles. The samples were tested according to ASTM C666 with at least five cycles per day. A typical saw-cut sample is presented in Figure 10.6. For the excised samples, results of the three samples were averaged for each tie.

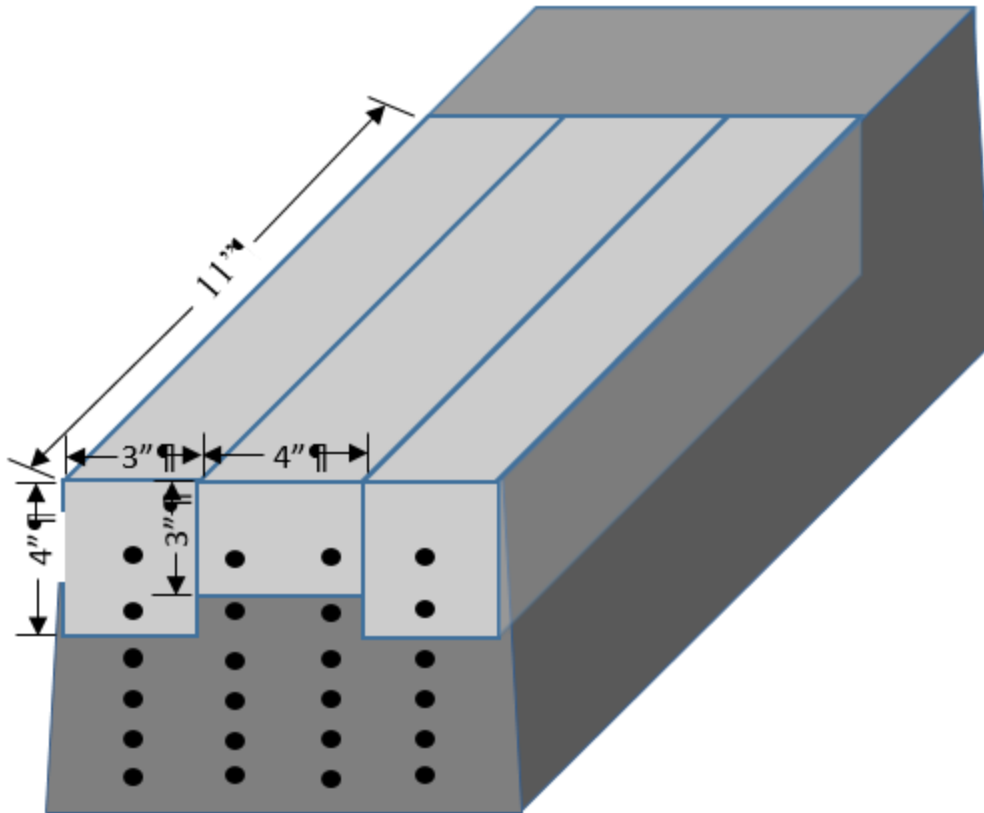


Figure 10.5. Three saw-cut samples from the tie end



Figure 10.6. Typical 4 x 3 x 11 in. saw-cut freeze-thaw sample

10.2.3 Cast Samples

In addition to the half ties and saw-cut samples, four cast prisms were made from the same concrete. Two of the samples were made with air-entrained concrete and two without air entrainment. The samples had embedded pins in order to measure change in length. The cast samples were larger than the saw-cut samples, with dimensions of 3 x 4 x 16 in. (76.2 x 101.6 x 406.4 mm). Initial preparation and testing of these samples was done after the samples cured for 14 days.

Table 10.1 represents all samples used in this part of the study and testing done on each sample. The half ties were given the designation HT#, followed by the tie number, and the excised set of samples were given the designation SHT#, where HT# corresponded to the other half of the same tie used in the half tie testing. The sample ID used for the excised set of samples corresponds to replicate samples extracted from the same half-tie. Some samples were assigned the letter W instead of a number in order to represent samples with embedded vibrating wire gauge sensors. Samples without half ties tested in freeze-thaw conditions were given other designation that represented material and structural properties of the tie.

Table 10.1. Freeze-Thaw and Non-Destructive Testing Performed on Large Concrete Tie Samples

Set	Sample ID	Air Entrained	Type					Tests Performed			
			Half Tie	Prestressed	Not Prestressed	No Wire	Cast	Weight	Length Change	Fundamental Frequency	Ultrasonic Pulse Velocity
	HT1	•	•					•			•
	HT2	•	•					•			•
	HT3	•	•					•			•
	HT4	•	•					•			•
	HT5	•	•					•			•
	HT6		•					•			•
SHT1	A	•		•				•	•	•	
	B	•		•				•	•	•	
	C	•		•				•	•	•	
SHT2	A	•		•				•	•	•	
	B	•		•				•	•	•	
	C	•		•				•	•	•	
SHT3	A	•		•				•	•	•	
	B	•		•				•	•	•	
	C	•		•				•	•	•	
SHT4	A	•		•				•	•	•	
	B	•		•				•	•	•	
	C	•		•				•	•	•	
SHT5	A	•		•				•	•	•	
	B	•		•				•	•	•	
	C	•		•				•	•	•	

Set	Sample ID	Air Entrained	Type					Tests Performed			
			Half Tie	Prestressed	Not Prestressed	No Wire	Cast	Weight	Length Change	Fundamental Frequency	Ultrasonic Pulse Velocity
SHT6	PNA-1			•				•	•	•	
	PNA-2			•				•	•	•	
	PNA-W			•				•	•	•	
NPA	NPA-1	•			•			•	•	•	
	NPA-2	•			•			•	•	•	
	NPA-W	•			•			•	•	•	
NPNA	NPNA-1				•			•	•	•	
	NPNA-2				•			•	•	•	
	NPNA-W				•			•	•	•	
NWA	NWA-1	•					•	•	•	•	
	NWA-2	•					•	•	•	•	
	NWA-W	•					•	•	•	•	
NUNA	NUNA-1						•	•	•	•	
	NUNA-2						•	•	•	•	
	NUNA-W						•	•	•	•	
Cast Prism	C1-A	•					•	•	•	•	
	C4-A	•					•	•	•	•	
Cast Prism/No Air	C1-NA						•	•	•	•	
	C4-NA						•	•	•	•	

10.3 Results

Initial fresh air content, when available, and hardened air void analysis for the concrete ties tested is shown in Table 10.2.

Table 10.2. Fresh and Hardened Air Content of all Tested Samples

Sample or Set of Samples	Fresh Air Content (%)	Hardened Air Content (%)	Spacing Factor (in)
HT1, SHT	-	3.6	0.0117
HT2, SHT2	-	2.5	0.0131
HT3, SHT3	8.5	4	0.0098
HT4, SHT4	-	4	0.0133
HT5, SHT5, C1-A, C4-A	7	6.1	0.0049
HT6, SHT6, C1-NA, C4-NA	0.9	2.3	0.0083
NPA	7	4.9	0.0030
NPNA	0.9	3.5	0.0090
NWA	7	3.5	0.0088
NWNA	0.9	3.2	0.0033

Out of the six excised sample sets, three sets failed after 70 cycles or less, one set failed after 121 cycles, and 2 sets did not fail per RDME measurements, as shown in Figure 10.7. Failure in the excised samples began as cracking between the prestressing wires parallel to wires on the surfaces of the samples, as shown in Figure 10.8. This cracking could have developed as a result of three main parameters: thermal diffusivity differences between the concrete and steel, prestress release due to saw-cutting, and higher absorption rates caused by damage from saw-cutting near the reinforcement. Because thermal diffusivity is the rate at which a material conducts thermal energy relative to storing that energy, the difference between concrete and steel thermal diffusivity rates can lead to deterioration. The difference in thermal diffusivity between the steel (11.72 mm²/s) and concrete (0.76 to 1.97 mm²/s) typically causes the steel to drop in temperature at much faster rates than the concrete, causing the concrete surrounding the steel to be subjected to more severe freeze-thaw cycles, thereby cooling at faster rates and resulting in cracking and deterioration (Chan, 2013).

Because of deterioration and cracking, some samples lost some mass surrounding the prestressing wires, as indicated in Figure 10.9 and Figure 10.10. This mass loss was accompanied by concrete expansion as result of cracking and water freezing in the cracks. Figure 10.11 shows the sample expansion in the excised samples from the six ties. For samples from SHT2 and SHT3, the RDME tests conducted on these excised samples gave a false sense of durability, an indication that the samples from set SHT2 and SHT3 did not suffer failure. However, visual inspection revealed cracks, as shown in Figure 10.8.

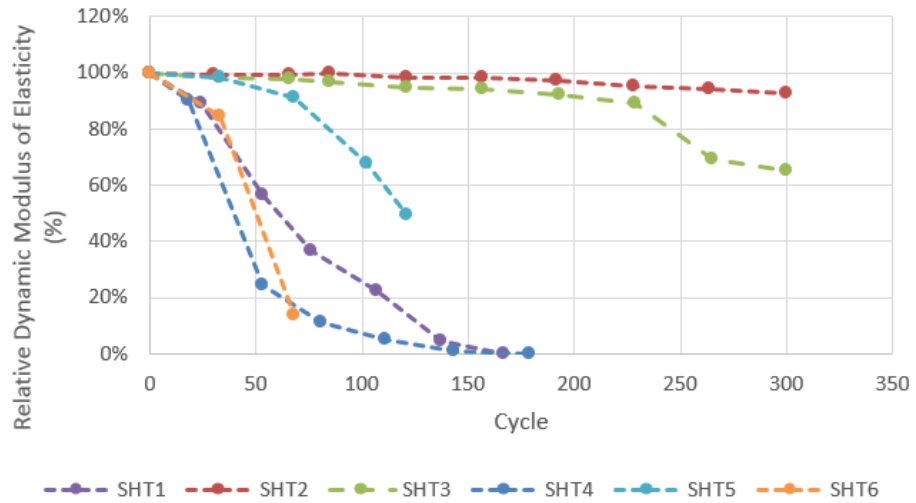


Figure 10.7. Average RDME results of the six sets of excised samples



Figure 10.8. Cracking pattern in saw-cut samples in freeze-thaw testing (SHT3)

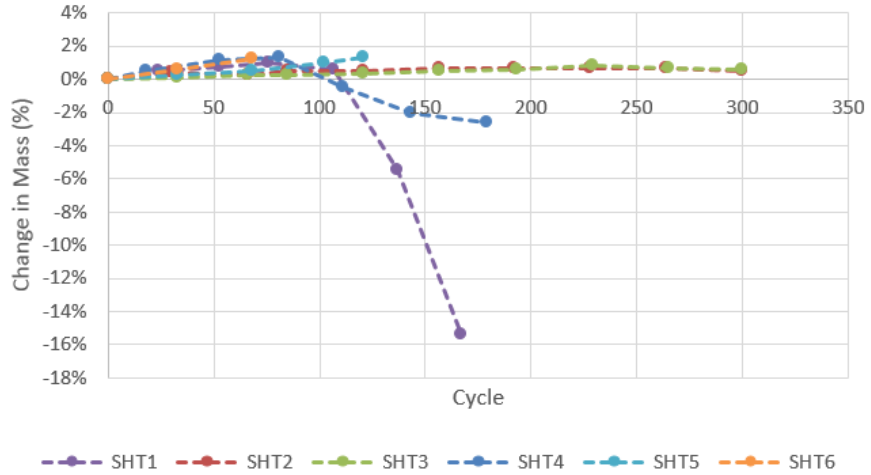


Figure 10.9. Change in mass for the six sets of excised samples



Figure 10.10. Mass loss for saw-cut samples in freeze-thaw testing (SHT4)

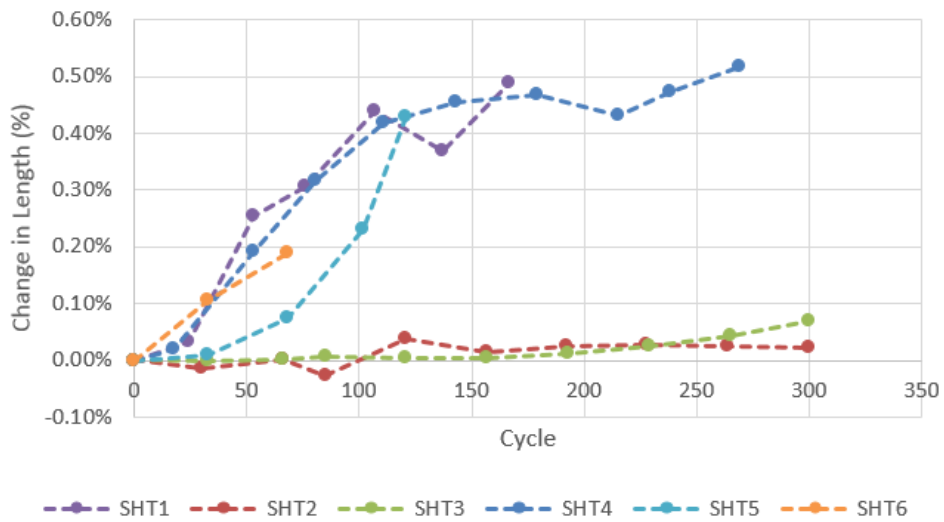


Figure 10.11. Change in length for the six sets of excised samples

In order to examine the effects of thermal diffusivity and saw-cutting through the wire on freeze-thaw durability, the set of samples excised from ties with non-prestressed wires and without wires were compared. Figure 10.12 shows the average change in mass for the sets of samples excised from the reinforced ties but not prestressed, and the unreinforced ties, as compared to the companion cast small freeze-thaw prisms. The difference in freeze-thaw performance can be attributed to damage caused by sawcutting through wires. This is significant when comparing air-entrained plain samples (NWA) to air-entrained non-prestressed samples (NPA) in terms of length change and RDME, as shown in Figure 10.13 and Figure 10.14, respectively.

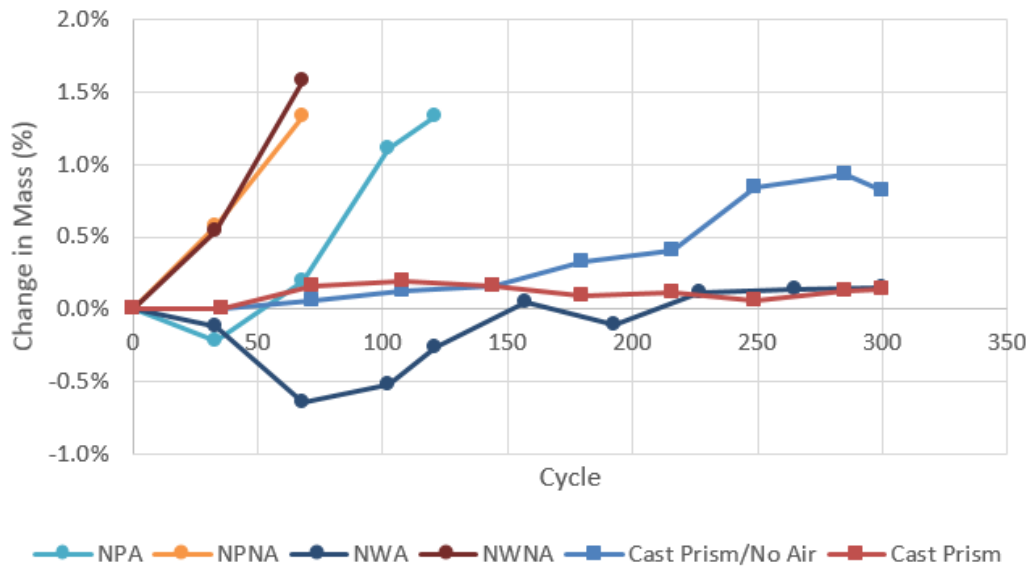


Figure 10.12. Change in mass for the saw-cut non-prestressed, saw-cut plain, and cast prisms samples with and without air entrainment

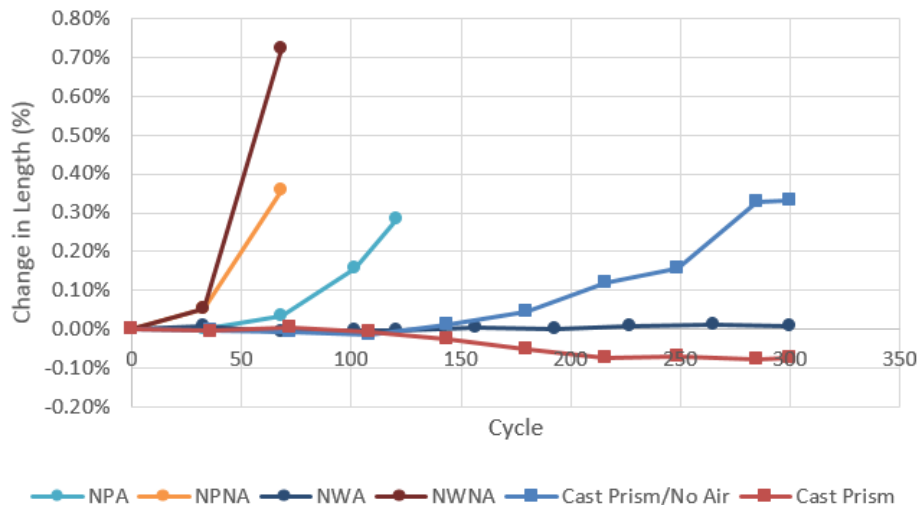


Figure 10.13. Change in length for the saw-cut non-prestressed, saw-cut plain, and cast prisms samples with and without air entrainment

Saw-cut plain samples (NWA) did not show deterioration over the 300 cycles of the freeze-thaw testing. The performance difference seen can be attributed to micro-cracking in the concrete caused by sawcutting through wires. This form of deterioration is an artifact of the sample preparation process. Sawcut samples that fail freeze-thaw testing are not representative of the concrete tie material durability.

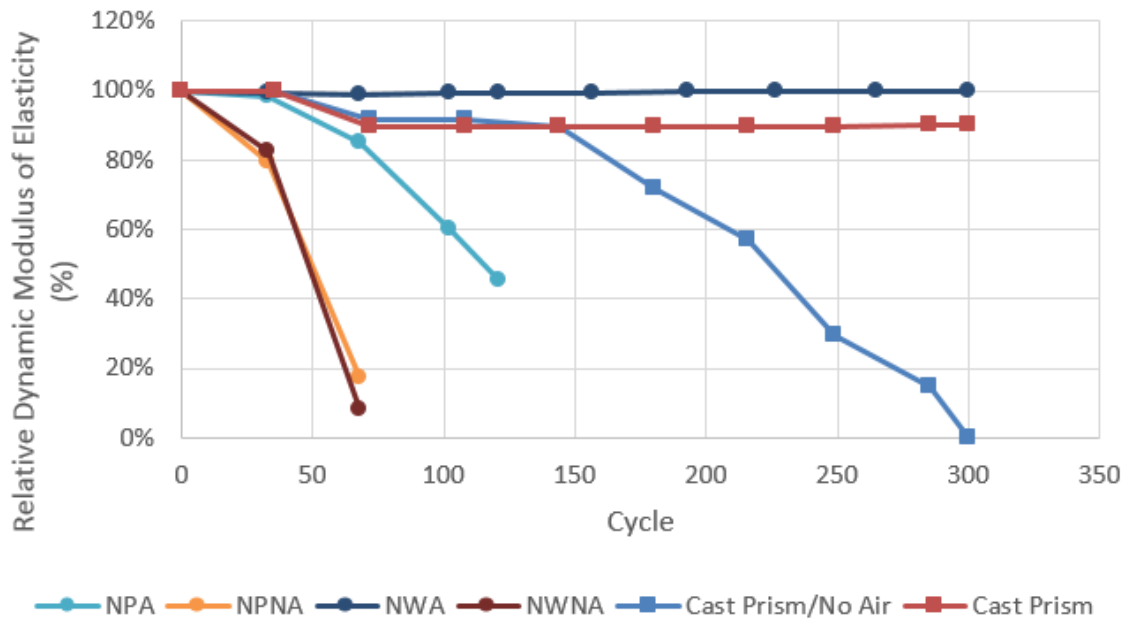


Figure 10.14. Average RDME results for the saw-cut non-prestressed, saw-cut plain, and cast prisms samples with and without air entrainment

Only one half tie (HT5) passed the freeze-thaw testing without significant deterioration. In addition, deterioration for half ties HT2, HT3, and HT4 was determined to be caused by cracking resulting from the saw-cutting process since propagation of the crack started from the saw-cut (epoxied) end. This is likely because saw-cutting the ties in the center where the cross section is reduced results in very high bursting strains, causing splitting cracks to initiate. This deterioration due to saw-cutting is shown in Figure 10.15. Figure 10.16 shows that excised samples for freeze-thaw testing failed at a much faster rate compared to the ties from which they were excised. Meanwhile, two half ties showed excessive deterioration: the tie without air entrainment (HT6), which failed at 215 cycles, and HT1, which failed at 143 cycles. This excessive deterioration is shown in Figure 10.17. Deterioration for sample HT1 began at the tie end, not the middle of the tie saw-cut, after delivery to KSU. Deterioration of this tie was the result of a poor air void system, high degree of saturation, and damage from wires during saw-cutting during manufacturing. A summary of all initial and final results after freeze-thaw testing are presented in Table 10.3.

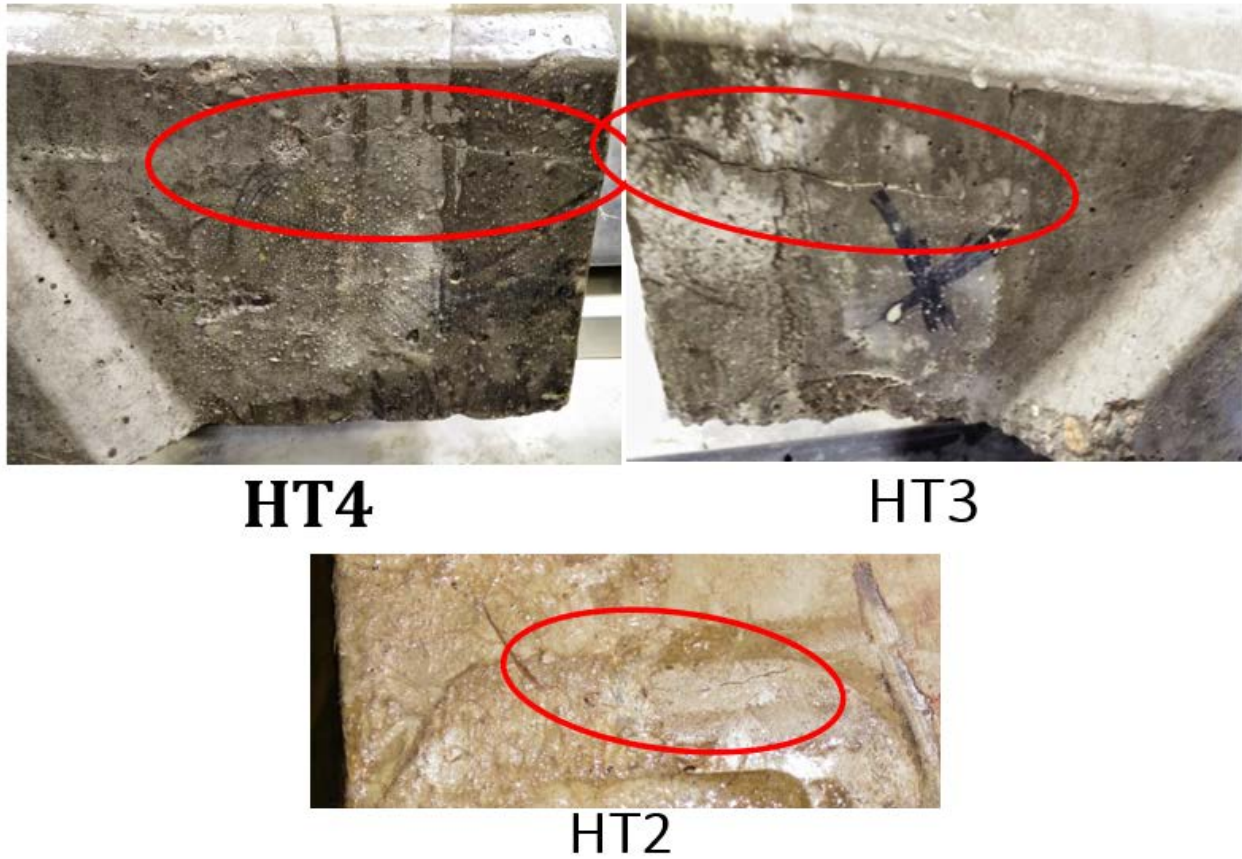


Figure 10.15. Half ties that developed cracking from the saw-cut (epoxied) end

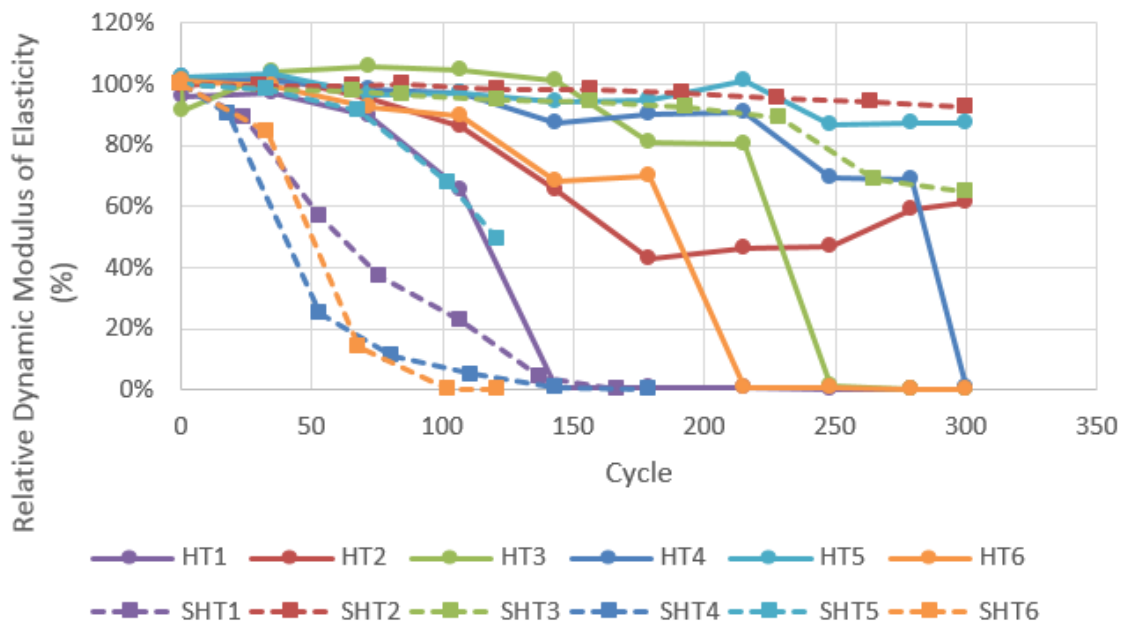


Figure 10.16. Average RDME results for half ties as compared to excised samples from the same ties



HT1



HT6

Figure 10.17. Half ties with excessive deterioration (HT6 made with 0.9% fresh air content and no air-entraining agent)

Table 10.3. Summary of all Sample Results at Failure Compared to Initial Values

Sample	Failing Cycle	Initial Values			Results at Failure or at 300 Cycles					
		Weight (lb)	Fundamental Frequency (Hz)	UPV (ft/s)	Weight (lb)	Length Change (%)	Fundamental Frequency (Hz)	UPV (ft/s)	RDME (%)	Pass or Fail?
HT1	143	350.1	-	9974.4	350.2	-	-	817.4	0.7	Fail
HT2	179	351.9	-	9760.2	352	-	-	7510.3	59.2	Fail
HT3	248	339.2	-	7765	339.9	-	-	817.4	1.1	Fail
HT4	300	349.2	-	9213	351.7	-	-	817.4	0.8	Fail
HT5	-	481.3	-	9413.4	481.6	-	-	8788.9	87.2	Pass
HT6	215	500.4	-	9532.4	504.4	-	-	739.5	0.6	Fail

Sample	Failing Cycle	Initial Values			Results at Failure or at 300 Cycles					
		Weight (lb)	Fundamental Frequency (Hz)	UPV (ft/s)	Weight (lb)	Length Change (%)	Fundamental Frequency (Hz)	UPV (ft/s)	RDME (%)	Pass or Fail?
SHT1 A	76	5	4072	-	5.1	1	2806	-	47.5	Fail
SHT1 B	76	4.5	3638	-	4.5	0.2	1797	-	24.4	Fail
SHT1 C	53	5.6	3765	-	5.7	0.2	2398	-	40.6	Fail
SHT2 A	-	5.1	3530	-	5.1	0	3520	-	99.4	Pass
SHT2 B	-	5.2	3477	-	5.2	0	3145	-	81.8	Pass
SHT2 C	-	5.1	3574	-	5.1	0	3550	-	98.7	Pass
SHT3 A	-	3.7	2925	-	3.8	0	2878	-	96.8	Pass
SHT3 B	-	4.1	3008	-	4.2	0	2980	-	98.1	Pass
SHT3 C	265	4.8	3467	-	4.9	0.1	1208	-	12.1	Fail
SHT4 A	53	3.3	2837	-	3.3	0.1	1953	-	47.4	Fail
SHT4 B	53	3.8	3066	-	3.8	0.1	1675	-	29.8	Fail
SHT4 C	53	5.3	3633	-	5.4	0.3	1338	-	13.6	Fail
SHT5 A	121	4.3	3335	-	4.4	0.2	2529	-	57.5	Fail
SHT5 B	102	4.6	3438	-	4.7	0.5	2563	-	53.5	Fail
SHT5 C	102	5.6	3403	-	5.7	0.6	2642	-	60	Pass
SHT6 A	68	4.6	3398	-	4.6	0.1	1787	-	27.7	Fail
SHT6 B	68	5.3	3652	-	5.4	0.2	1367	-	14	Fail
SHT6 C	68	5.3	3560	-	5.4	0.5	44	-	0	Fail
NPA-1	102	4.7	3467	-	4.8	0.2	2578	-	55.3	Fail
NPA-2	121	4.7	3335	-	4.8	0.3	2248	-	45.4	Fail
NPA-W	102	5.4	3599	-	5.4	0.1	2754	-	58.6	Fail
NPNA-1	68	5	3315	-	5.1	0.2	1016	-	9.4	Fail
NPNA-2	68	4.8	3301	-	4.9	0.5	1401	-	18	Fail
NPNA-W	68	5.7	3560	-	5.7	0.5	1777	-	24.9	Fail
NWA-1	-	4.5	3408	-	4.5	0	3394	-	99.2	Pass
NWA-2	-	4.5	3325	-	4.5	0	3311	-	99.2	Pass
NWA-W	-	5.4	3560	-	5.4	0	3569	-	100	Pass
NWNA-1	68	5.3	3540	-	5.4	0.7	1182	-	11.1	Fail
NWNA-2	68	4.6	3311	-	4.7	1	44	-	0	Fail
NWNA-W	68	5.2	3330	-	5.3	0.5	1201	-	13	Fail
C1-A	-	7.6	2008	-	7.6	-0.1	1885	-	89.1	Pass
C4-A	-	7.7	2008	-	7.7	-0.1	1904	-	91.6	Pass
C1-NA	249	7.6	1860	-	7.6	0.1	1162	-	39.1	Fail

Sample	Failing Cycle	Initial Values			Results at Failure or at 300 Cycles					
		Weight (lb)	Fundamental Frequency (Hz)	UPV (ft/s)	Weight (lb)	Length Change (%)	Fundamental Frequency (Hz)	UPV (ft/s)	RDME (%)	Pass or Fail?
C4-NA	180	7.6	2008	-	7.6	0.1	1387	-	47.7	Fail

Sample notation:

HT: Half tie sample

SHT: Sample excised from half tie

Number/ letter at the end: tie sample number

PA: Prestressed and Air-entrained

PNA: Prestressed and Non-air-entrained

NPA: Not-Prestressed and Air-entrained

NPNA: Not-Prestressed and Non-air-entrained

NWA: No reinforcement and Air-entrained

NWNA: No reinforcement and Non-air-entrained

C1-A and C4-A: Cast prisms and Air-entrained

C1-NA and C4-NA: Cast prisms and Non-air-entrained

For all samples: (-W: is the sample that have the Vibrating Wire Gage, -1 or -2 are the other two samples)

10.3.1 Laboratory Cast Samples

In order to verify the results from field samples, an additional set of samples were made in the lab. All the additional samples were made from a single mixture. This mixture was made with an admixture combination that had performed well in other freeze-thaw prism experiments and with relatively high initial air content of 5.1 percent. This was done to ensure that any measured failures would not occur because of a poor air void system. Also, the mixture was chosen to be very fluid in order to ensure proper consolidation since it was not subjected to vibration. The plain and reinforced prisms were prepared using 3 x 4 x 16 in. molds while reinforced saw-cut prisms were saw-cut from a 3 x 4 in. beam that is 85 in.-long. The saw-cut samples presented here were only saw-cut from the ends. Figure 10.18 shows the relative dynamic modulus of elasticity versus the number of cycles of freezing and thawing for all the samples. It can be observed that all of them showed little decrease in RDME with no issues except for one sample. This sample lost a large chunk of concrete caused by a big crack after the 70th cycle but that did not show much loss in the relative dynamic modulus of elasticity. Figure 10.19 through Figure 10.23 show some pictures of the cracked sample. The cause of this crack is believed to be due to the stresses from the steel strands since the crack happened at the interface between concrete and steel as shown in Figure 10.21 and Figure 10.23. These stresses are believed to be due to saw-cutting.

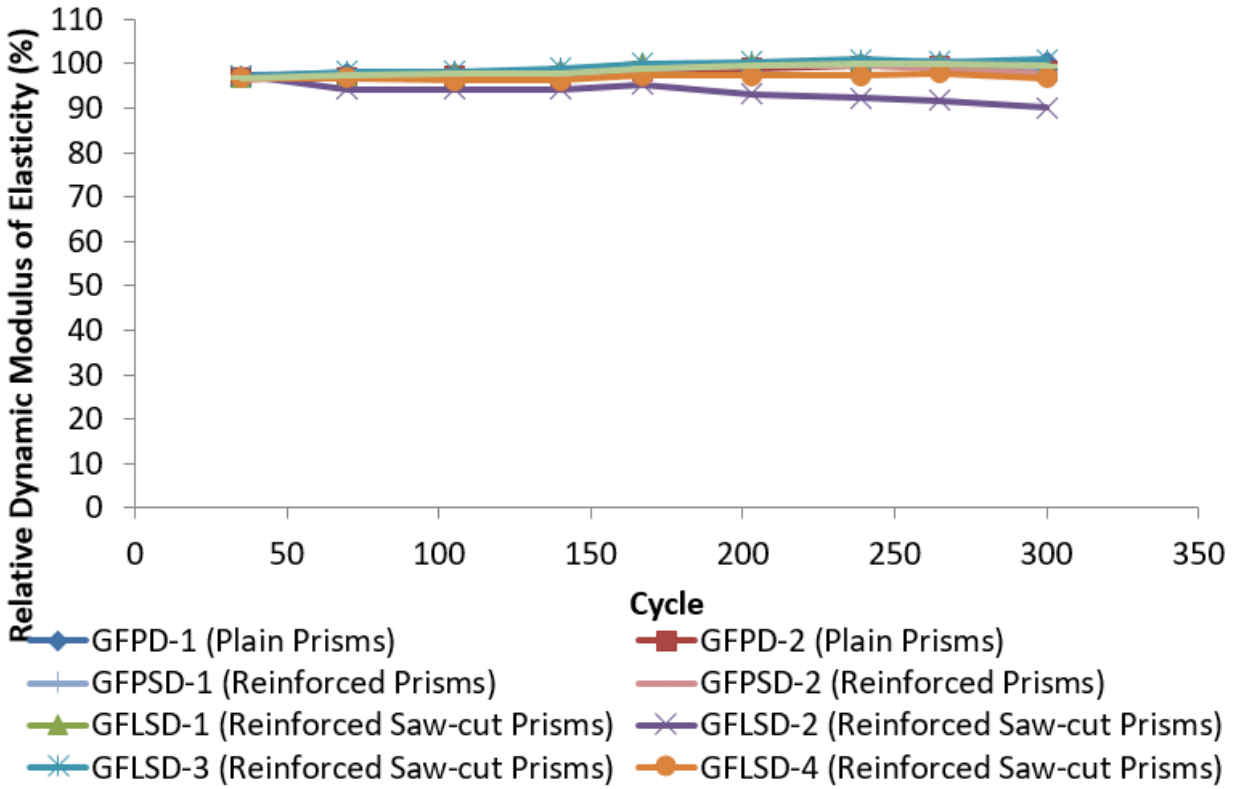


Figure 10.18. Freeze-thaw performance of Plain vs Reinforced vs Reinforced Saw-Cut concrete



Figure 10.19 Cracked saw-cut sample (angle 1)



Figure 10.20. Cracked saw-cut sample (angle 2)



Figure 10.21. Cracked saw-cut sample (angle 3)



Figure 10.22. Cracked saw-cut sample (angle 4)



Figure 10.23. Cracked saw-cut sample (angle 5)

10.4 Bursting Strains During Sawcutting

Vibrating wire gauges were installed in six concrete railroad ties in a triaxial configuration as shown in Figure 10.24. These gauges were installed to determine if the high stresses that caused micro-cracking and freeze-thaw damage during sawcutting small ASTM C666 prisms also occurred during sample fabrication. A set of triaxial-configured gauges (Geokon 4202x) were placed at 6.5 in. (165.1 mm) from each end of the instrumented ties. The gauges were not attached to any prestressing wires but were suspended in the concrete between the wires as shown in Figure 10.25. The installation process was performed at a prestressed concrete manufacturing facility. Ties were made upside down in a long-line bed. Separators with holes allowing the wires in a bed to pass were used on each tie end. Once the prestressing wires were in place, the concrete was placed into the forms. Two of the ties were unreinforced. Figure 10.26 shows the unreinforced tie under cover for curing. Another two were made with twenty-four 0.209 in. (5.32 mm) diameter wires but not prestressed. The remaining two ties were made with the same twenty-four 0.209 in. (5.32 mm) diameter wires and were prestressed to 7000 lbs per wire. The prestressed and non-prestressed ties were made with two stirrups at each end for each tie. These wire stirrups fully encircled the prestressing wires, as shown in Figure 10.25. The manufactured ties were 8.5 ft (2.6 m) long, with a trapezoidal cross section 10 in. (254 mm) wide on top, 10.5 in. (267 mm) on the bottom and 10.5 in. (267 mm) in height.



Figure 10.24. Vibration wire gauges inside the ties

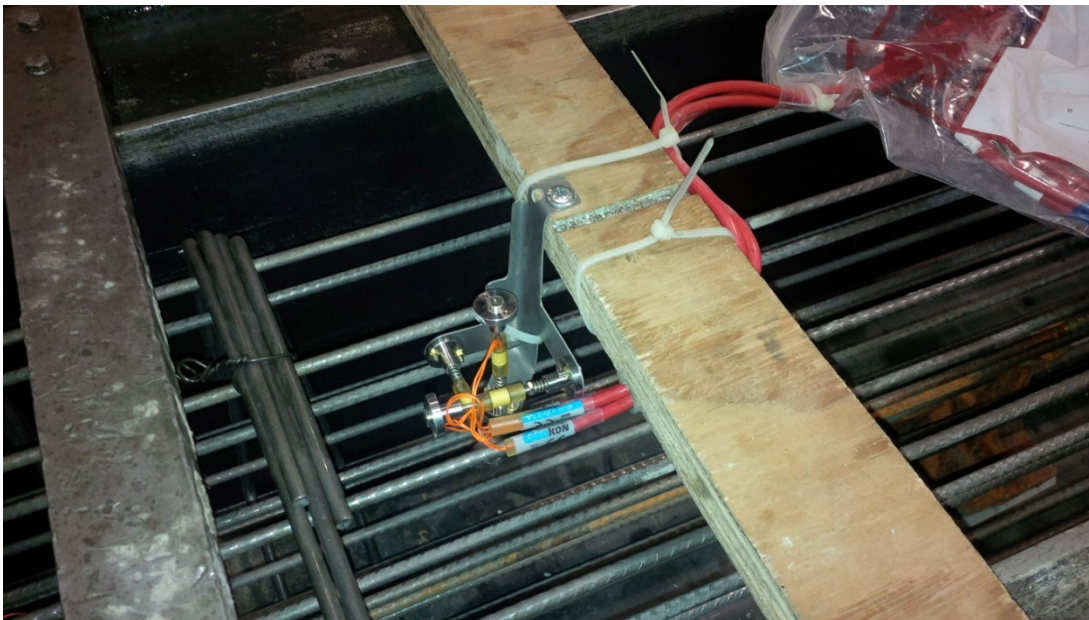


Figure 10.25. Vibrating wire gages in the tie next to the two stirrups



Figure 10.26. Unreinforced tie covered in plastic

A handheld vibrating wire gage reader (GK-404) was used to take strain and temperature readings; after hardening, after detensioning, after demolding and wires saw-cutting, after delivery to Kansas State University, after saw-cutting the ties in half and after excising the ASTM C666 samples. Unfortunately, some of the delicate vertical and transverse gauges stopped working either after the concrete hardened or after detensioning. The locations of the cuts made and the gauge are shown in Figure 10.27.

Readings recorded from the handheld GK-404 device were from apparent strains (ϵ_{ap}) and had to be corrected in order to obtain actual strains (ϵ_{actual}). Equation 10.1 was used to correct for the temperature and to obtain actual strains.

$$\begin{aligned} \epsilon_{actual} = & \left((\epsilon_{ap})_{current} - (\epsilon_{ap})_{initial} \right) B \\ & + (T_{current} - T_{initial})(C_s - C_c) \end{aligned} \quad \text{Equation 10.1}$$

Where B is the batch calibration factor, $T_{current}$ is the current temperature, $T_{initial}$ is the initial temperature, C_s is the steel coefficient of expansion, and C_c is the concrete coefficient of expansion. A list of all gauges used, the ties were installed in, and the types of ties they were installed in are presented in Table 10.4. Two types of concrete were utilized to make these ties: one with air entrainment agent and one without an air entrainment agent. Properties of these two concrete mixtures are presented in Table 10.5.

Table 10.4. Summary of Ties Made and Vibrating Wire Gauges Used

Vibrating Wire Gage #	Type				Tie/End
	Air Entrained	Prestressed	Not Prestressed	No Wire	
L 1 A			•		1 / Dead End
T 2 A			•		
V 3 A			•		
L 4 A			•		1 / Live End
T 5 A			•		
V 6 A			•		
L 7 A	•		•		2 / Dead End
T 8 A	•		•		
V 9 A	•		•		
L 10 A	•			•	3
T 11 A	•			•	
V 12 A	•			•	
L 13 A	•		•		2 / Live End
T 14 A	•		•		
V 15 A	•		•		
L 1 B				•	4
T 2 B				•	
V 3 B				•	
L 4 B		•			5 / Dead End
T 5 B		•			
V 6 B		•			
L 7 B		•			5 / Live End
T 8 B		•			
V 9 B		•			
L 10 B	•	•			6 / Dead End
T 11 B	•	•			
V 12 B	•	•			
L 13 B	•	•			

Vibrating Wire Gage #	Type				Tie/End
	Air Entrained	Prestressed	Not Prestressed	No Wire	
T 14 B	•	•			6 / Live End
V 15 B	•	•			

Table 10.5. Properties of Concrete Used

	Non-Air Entrained	Air Entrained
Temperature (°F)	82.2	83.6
Unit Weight (lb/ft ³)	148.4	138
Fresh Air Content (%)	0.9	7
Compressive Strength at Release (psi)	6850	6630
Splitting Tensile Strength at Release (psi)	410	560
Compressive Strength at 28 days (psi)	13570	12380
Splitting Tensile Strength at 28 days (psi)	740	760

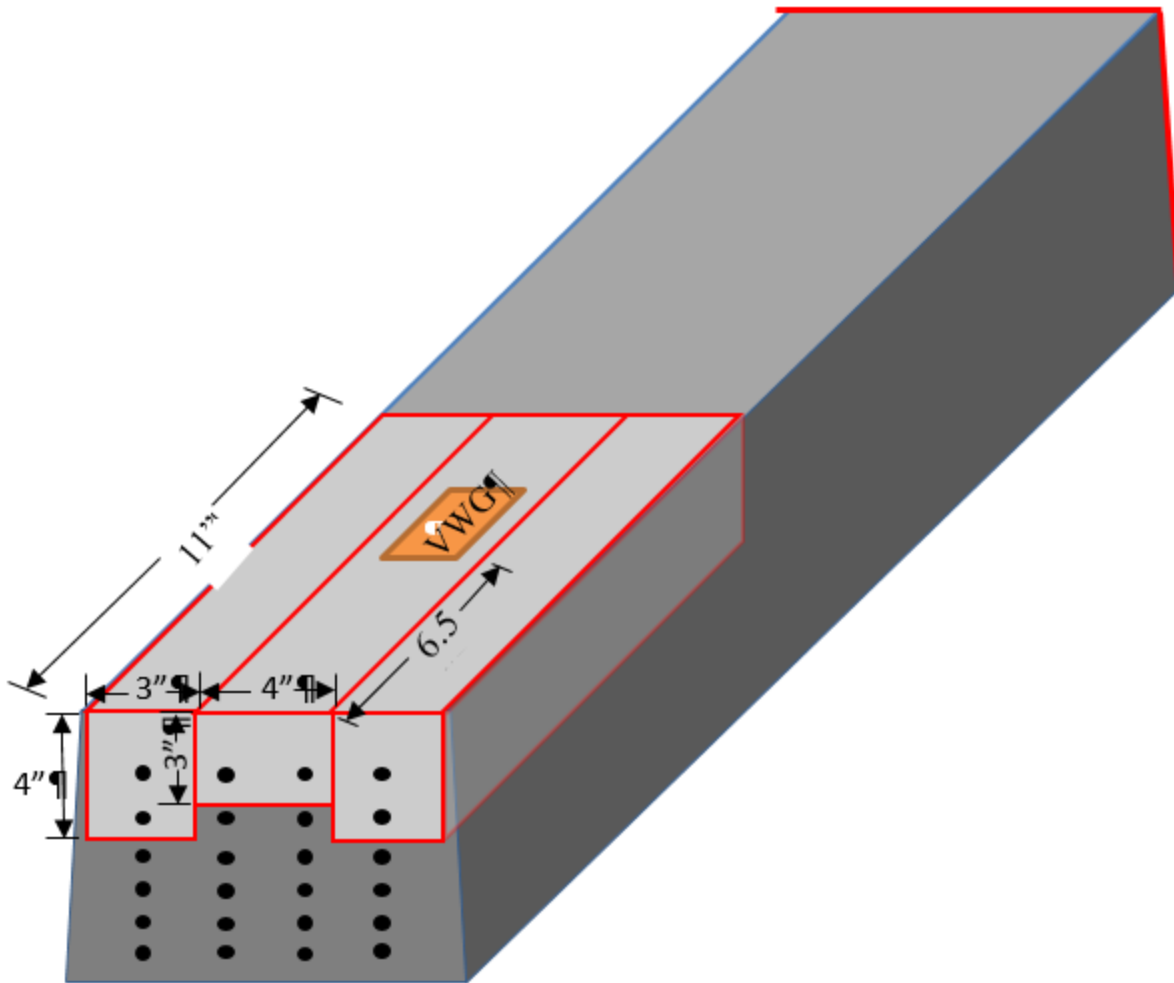


Figure 10.27. Saw-cutting locations on ties (red) and saw-cutting locations on the gauge (VWG) (green)

Table 10.6 includes a list of all the gauges that remained functional after concrete hardening. The large number of non-functional gauges can be the result of either the strains going beyond limits of the gauge ($4000 \mu\epsilon$) or the gauges were damaged during the placement or the hardening process. The results obtained shows that the ties in the longitudinal direction underwent compression as a result of the prestressing as shown in Figure 10.28. Furthermore, no apparent effects on the strains in the longitudinal direction were seen as a result of air entrainment, as expected. While one of the gauges in the non-air entrained samples failed after saw-cutting the tie in half, it is most likely that the strains jumped to values beyond the limits of the gauges.

Table 10.6. Vibrating Wire Gauges that Remained Operational After Concrete Hardening

Vibrating Wire Gage #	Functional	Vibrating Wire Gage #	Functional
L 1 A		L 1 B	
T 2 A		T 2 B	
V 3 A		V 3 B	
L 4 A	•	L 4 B	•
T 5 A		T 5 B	
V 6 A		V 6 B	
L 7 A	•	L 7 B	•
T 8 A		T 8 B	
V 9 A		V 9 B	
L 10 A	•	L 10 B	•
T 11 A	•	T 11 B	•
V 12 A	•	V 12 B	
L 13 A	•	L 13 B	
T 14 A	•	T 14 B	
V 15 A	•	V 15 B	•

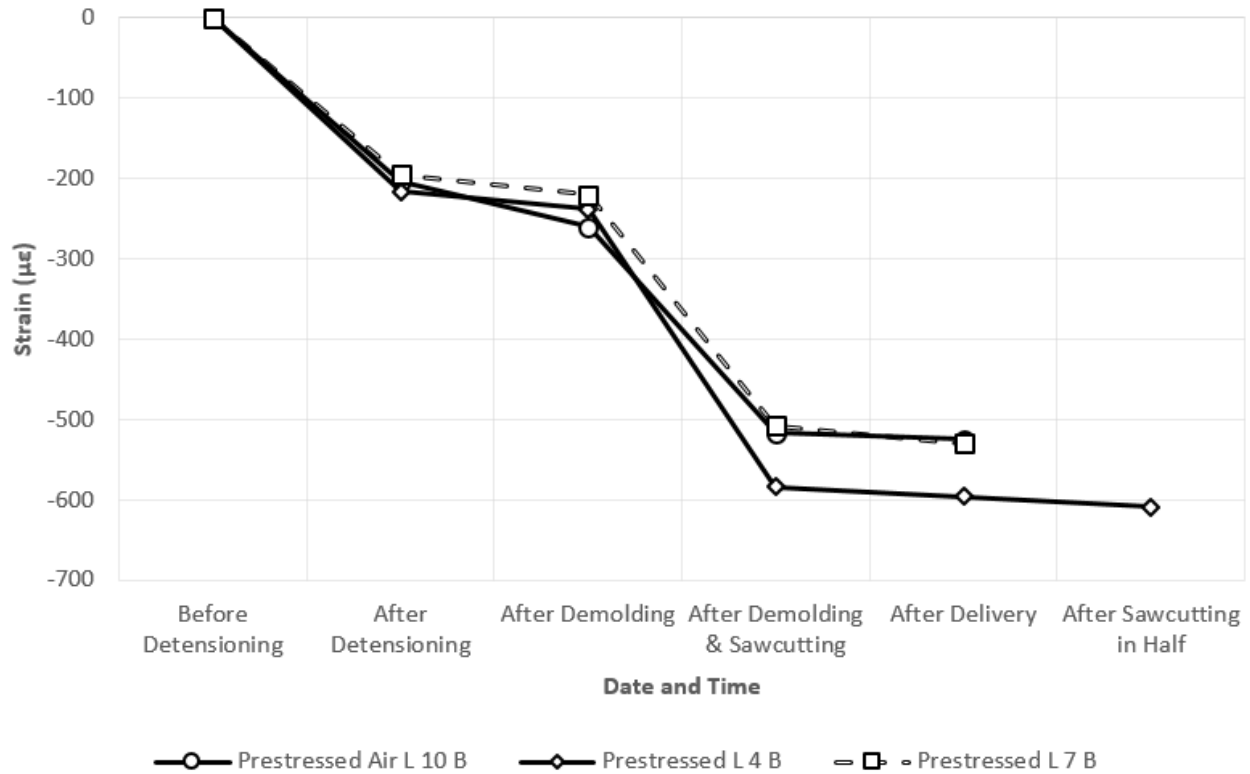


Figure 10.28. Longitudinal strain development in non-air-entrained concrete samples versus air-entrained concrete

When comparing the prestressed strains to the non-prestressed strains of non-air entrained concrete in the longitudinal direction in Figure 10.29, it can be seen that there are compression strains even in the non-prestressed tie likely from autogenous or thermal shrinkage. The longitudinal strains in the prestressed tie were three times that of the non-prestressed tie. The transverse strains recorded for the air entrained samples are presented in Figure 10.30. The transverse strains show that the samples were under tension in the transverse direction resulting either from the prestressing force in the case of the prestressed sample or the shrinkage in the non prestressed samples.

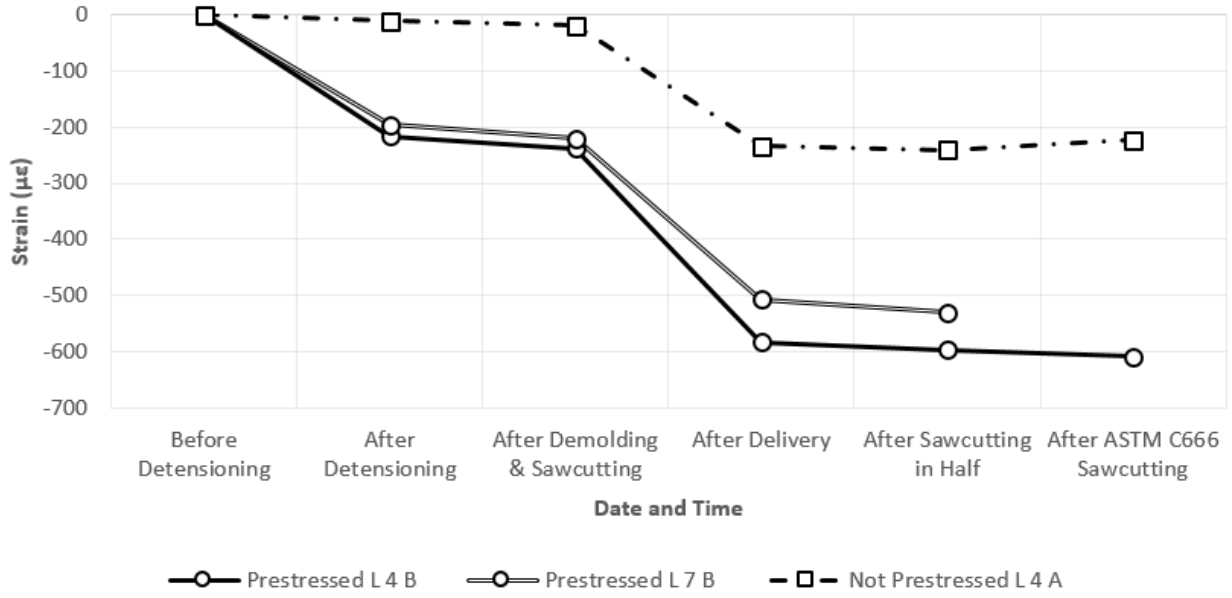


Figure 10.29. Longitudinal strain development in non-air-entrained concrete samples

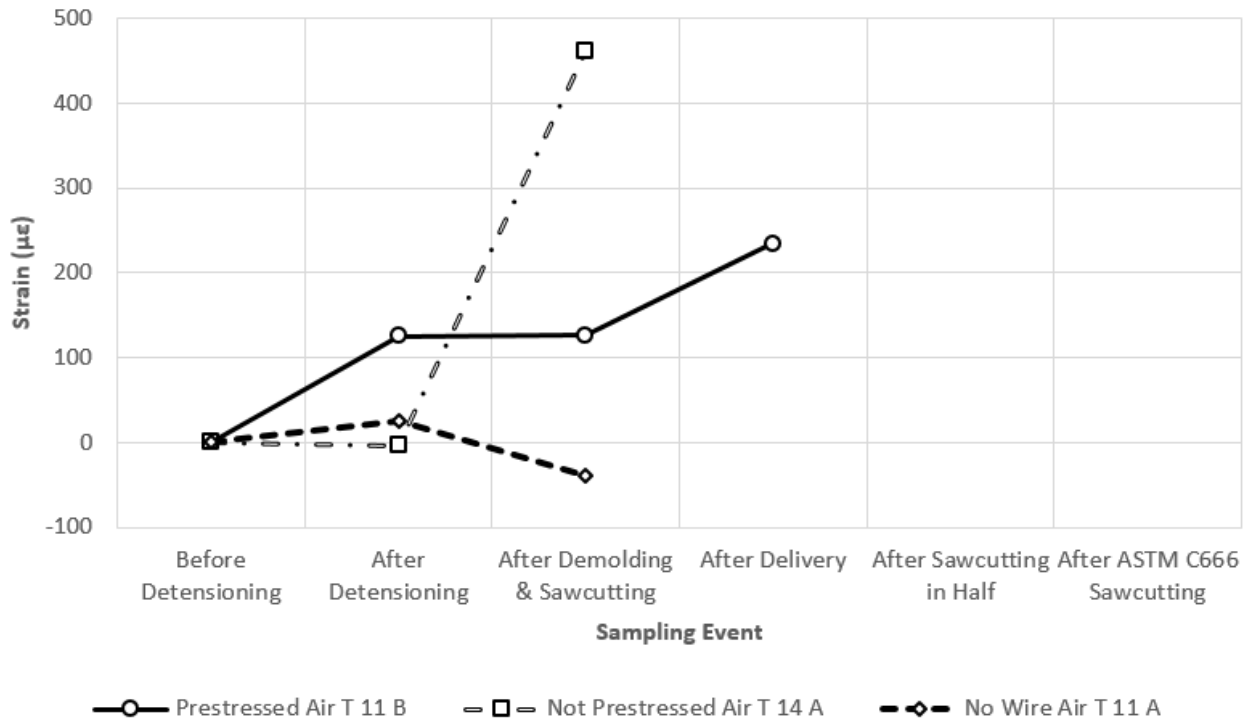


Figure 10.30. Transverse strain development in non-air-entrained concrete samples

As for the air entrained concrete ties, the longitudinal strains in the non-prestressed and plain ties varied between +290 $\mu\epsilon$ and -50 $\mu\epsilon$. These variations in compression and tension can be the result of variation in the thermal and shrinkage stresses inside the ties. These longitudinal strains, in the non-prestressed and plain ties, remain smaller than that of the prestressed tie since the prestressed tie had the prestressing force on top of the thermal and shrinkage stresses. Figure

10.31 represent the variation in the longitudinal strains of the air entrained non-prestressed and plain concrete ties in comparison to the prestressed air-entrained tie. Similar to the non-air entrained concrete, the longitudinal strain in the prestressed tie tends to increase from one stage to the next. This increase was more prominent in the case of vibrating wire gauge L 10 B which can be the result of gauge failure.

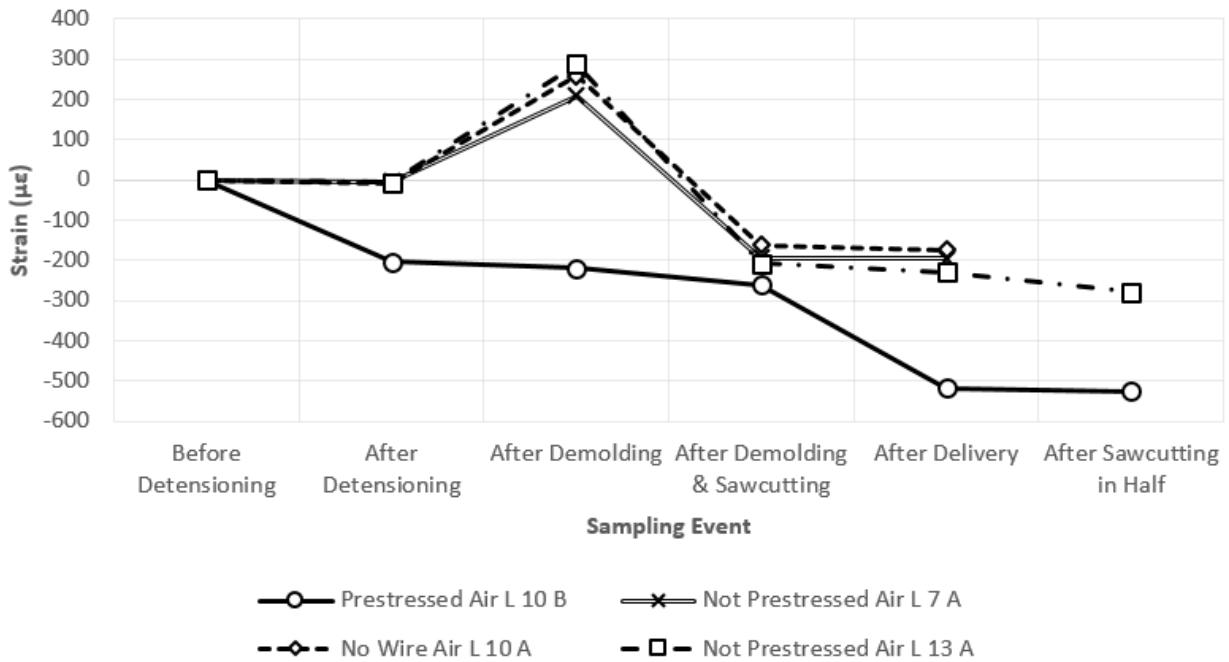


Figure 10.31. Longitudinal strain development in air-entrained concrete samples

While no transverse gauges remained working in the case of the air entrained concrete ties, the vertical gauges remained operational to a certain stage as shown in Figure 10.32. The recorded vertical strains in the case of the air entrained non-prestressed tie were higher than that of the air entrained prestressed the plain tie. This can be the result of: shrinkage, creep, temperature variation between the concrete and the gauges.

The bursting strain required to exceed the concrete tensile strength can be estimated using the concrete unit weight, compressive strength at release, splitting tensile strength, and ACI equation for elastic modulus as seen in Equation 10.2.

$$\epsilon_{cracking} = \frac{f_t}{w_c^{1.5} 33 \sqrt{f_c}} \quad \text{Equation 10.2}$$

Where $\epsilon_{cracking}$ is the bursting strain required to cause cracking ($\mu\epsilon$), f_t is the concrete tensile strength (psi), w_c is the concrete unit weight (lb/ft^3), and f_c is the concrete compressive strength (psi), resulting in 83 and 128 $\mu\epsilon$ for non-air-entrained and air-entrained concrete mixtures, respectively. These strain values were easily exceeded in the vertical direction between saw-cutting and delivery. The ties instrumented included stirrups to prevent the ties from cracking during fabrication, which may explain why cracking was not seen in the ties until after saw-cutting small ASTM C666 samples.

All these increases in the strains in the various directions, but especially in the longitudinal direction, can be described as bursting strains. The effects of these bursting strains, increase in

strains, can be very apparent when the saw-cut samples crack on their own without any freeze-thaw testing, as can be seen in Figure 10.33. It was noticed that many of the samples saw-cut to the small ASTM C666 compliant sample sizes tended to crack in a direction parallel to the prestressing wires. Even when increasing the concrete cover, which could only be increased to 0.75 in (19 mm) in the case of the tested ties, the concrete still cracked in some of the saw-cut samples. In addition, some of the wires in some of the samples slipped inside the concrete for 0.04 in (1 mm) indicating a new sample transfer length was created when the sample was saw-cut, creating stresses and cracking. This cracking and reinforcing wire shrinkage could be exaggerated when the samples containing any of these outcomes of bursting strains are subjected to freeze-thaw cycles.

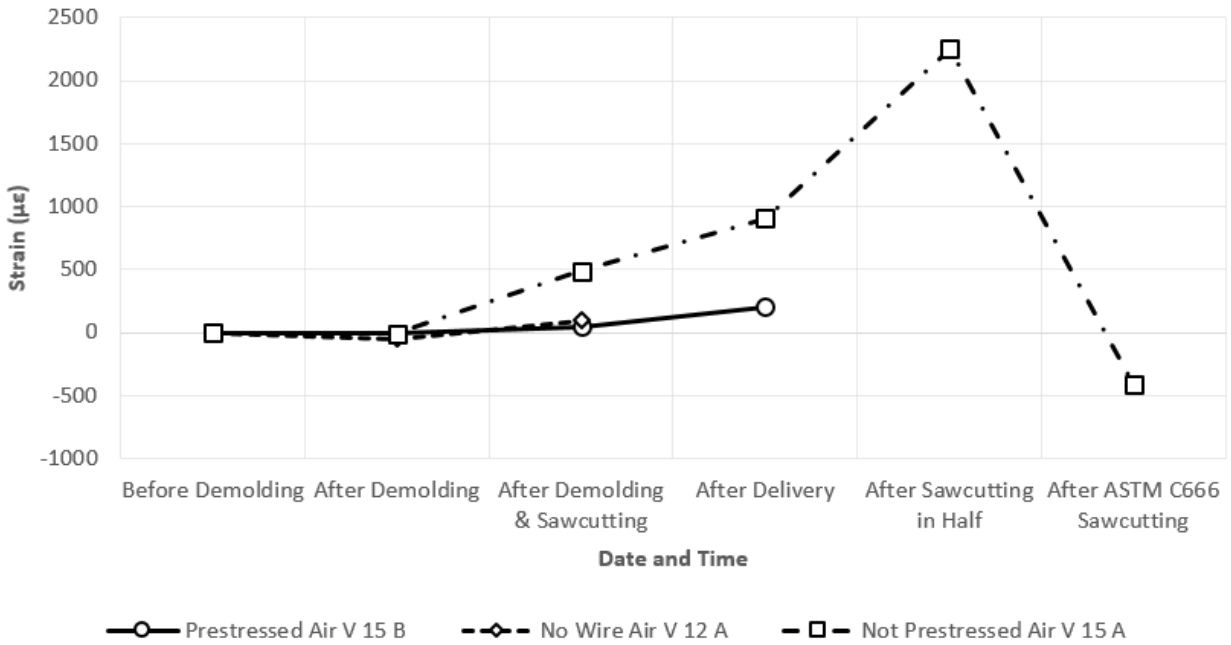


Figure 10.32. Vertical strain development in air-entrained concrete samples



Figure 10.33. Cracking due to stress release from saw-cutting

10.5 Conclusions

The effects of excising samples from prestressed concrete by saw-cutting on freeze-thaw durability were studied. Based on the experimental results obtained, the following conclusions can be made:

- Damage during freeze-thaw cycles was found to be accelerated in small ASTM C666 specimens compared to half-tie specimens. This was because of the faster freezing rate and greater influence of local damage on the overall specimen performance.
- Saw-cutting through reinforcement to make concrete prisms for ASTM C666 freeze-thaw testing caused microcracking and damage to the specimens. This damage caused freeze-thaw durable concrete to fail the ASTM C666 freeze-thaw test.
- Saw-cut reinforced concrete prisms should not be used for ASTM C666 freeze-thaw quality control testing.

References

- Abu-Lebdeh, T., Hamoush, S., Mohamed, A., and Picornell-Darder, M. (2011). Freezing and Thawing Durability of Very High Strength Concrete. *American Journal of Engineering and Applied Sciences*, 4(1), 42-51. doi:10.3844/ajeassp.2011.42.51
- ACI Committee 621. (1961). Selection and Use of Aggregates for Concrete. *Journal of the American Concrete Institute*, 58(11), 513-542.
- Adolphs, J., and Setzer, M. J. (1996). Energetic Classification of Adsorption Isotherms. *Journal of Colloid and Interface Science*, 184(2), 443-448. Retrieved from <https://doi.org/10.1006/jcis.1996.0639>
- Al Riza, D. F., Aris, M. S., and ul Haq, S. I. (2011). Hourly Solar Radiation Estimation Using Ambient Temperature and Relative Humidity Data. *International Journal of Environmental Science and Development*, 2, 188-193. Retrieved from <http://www.ijesd.org/papers/122-S017.pdf>
- Albahtiti, M., Beck, B. T., Bodapati, N., D., Castaneda, Ghadban, A., Koch, J., Lange, D. A., Peterman, R., Riding, K. A., Yu Song, A., Zou, R. (2018). *Material and Manufacturing Requirements for Freeze-Thaw Durable Concrete Railroad Ties: Volume I*. Washington, DC: Federal Railroad Administration.
- American Concrete Institute. (2008). *Report on Behavior of Fresh Concrete During Vibration*. Farmington Hills, MI: ACI Committee.
- Amziane, S., Boulkebatche, B., Chemrouk, M., and Hamrat, M. (2010). Flowability of fibre-reinforced concrete and its effect on the mechanical properties of the material. *Construction and Building Materials*, 24(9), 1664-1671.
- Amziane, S., Ferraris, C. F., and Koehler, E. P. (2005). Measurement of Workability of Fresh Concrete Using a Mixing Truck. *Journal of Research of the National Institute of Standards and Technology*, 110(1), 55-66.
- Amzjane, S., Ferraris, C. F., Fowler, D. W., and Koehler, E. P. (2006). A New, Portable Rheometer for Fresh Self-Consolidating Concrete. *ACI Special Publication*, 233(7), 97-116.
- Assaad, J., and Khayat, K. H. (2002). Air-Void Stability of Self-Consolidating Concrete. *ACI Materials Journal*, 99(4), 408-416.
- ASTM C 215-14. (2014). *Standard Test Method for Fundamental Transverse, Longitudinal, and Torsional Resonant Frequencies of Concrete Specimens*. West Conshohocken, PA: ASTM International.
- ASTM Standard C 1064/C 1064M-12. (2012). *Standard Test Method for Temperature of Freshly Mixed Hydraulic-Cement Concrete*. West Conshohocken, PA: ASTM International. doi:10.1520/C1064_C1064M-12
- ASTM Standard C 138. (2013). *Standard Test Method for Density (Unit Weight), Yield, and Air Content (Gravimetric) of Concrete*. West Conshohocken, PA: ASTM International. doi:10.1520/C0138_C0138M

- ASTM Standard C 143/C 143M-12. (2012). *Standard Test Method for Slump of Hydraulic-Cement Concrete*. West Conshohocken, PA: ASTM International. doi:10.1520/C0143_C0143M-12
- ASTM Standard C 173. (2014). *Standard Test Method for Air Content of Freshly Mixed Concrete by the Volumetric Method*. West Conshohocken, PA: ASTM International. doi:10.1520/C0173_C0173M
- ASTM Standard C 231. (2010). *Standard Test Method for Air Content of Freshly Mixed Concrete by the Pressure Method*. West Conshohocken, PA: ASTM International. doi:10.1520/C0231_C0231M-10
- ASTM Standard C 457. (2012). *Standard Test Method for Microscopical Determination of Parameters of the Air-Void System in Hardened Concrete*. West Conshohocken, PA: ASTM International. doi:10.1520/C0457_C0457M-12
- ASTM Standard C666. (2008). *Standard Test Method for Resistance of Concrete to Rapid Freezing and Thawing*. West Conshohocken, PA: ASTM International. doi:10.1520/C0666_C0666M-03R08
- Auberg, R., Heine, P., Kasparek, S., Palecki, S., and Setzer, M. J. (2001). CIF-Test-Capillary suction, Internal damage and Freeze thaw test. *Materials and Structures*, 34(9), 515-525. Retrieved from <https://www.rilem.net/images/publis/1123.pdf>
- Backstrom, J. E., Flack, H. L., Mielenz, R. C., and Wolkodoff, V. E. (1958). Origin, Evolution, and Effects of the Air Void System in Concrete: Part 1. *ACI Journal Proceedings*, 55(7), 95-121.
- Baker, P. H. (1988). The effect of vibration on the rheological properties of fresh concrete. *Magazine of concrete research*, 40(143), 79-89.
- Bakharev, T., and Struble, L. J. (1997). Microstructural Features of Railseat Deterioration in Concrete Ties. *Journal of Civil Engineering Materials*, 9, 146-153.
- Banfill, P. F., and Tattersall, G. H. (1983). *The rheology of fresh concrete*. Pitman Advanced Pub. Program.
- Banfill, P. F., Craik, R. J., and Teixeira, M. A. (2011). Rheology and vibration of fresh concrete: Predicting the radius of action of poker vibrators from wave propagation. *Cement and Concrete Research* 41.9, 932-941.
- Barber, E. S. (1957). Calculation of Maximum Pavement Temperatures from Weather Reports. *Highway Research Board Bulletin*, 168, 1-8. Retrieved from <http://onlinepubs.trb.org/Onlinepubs/hrbulletin/168/168-001.pdf>
- Barkan, C. P. L., Edwards, J. R., Lange, D. A., and Zeman, J. C. (2010). Evaluating the Potential for Damaging Hydraulic Pressure in the Concrete Tie Rail Seat. *Proceedings of the 2010 Joint Rail Conference*. Urbana, IL.
- Barrat, A., D'anna, G., Loreto, V., Mayor, P., and Nori, F. (2003). Observing Brownian motion in vibration-fluidized granular matter. *Nature* (424)6951, 909-912.
- Bazant, Z. P., Jennings, H. M., and Xi, Y. (1994). Moisture diffusion in cementitious materials. *Advanced Cement Based Materials*, 1, 248-257.

- Bazant, Z., and Najjar, L. (1972). Nonlinear water diffusion in nonsaturated concrete. *Materials and Structures*, 5, 3-20.
- Beaudoin, J. J., and Cameron, M. (1972). Dimensional changes of hydrated Portland cement paste during slow cooling and warming. *Cement and Concrete Research*, 2, 225-240.
- Bedon, R., Lieberle, C., Olson, L. D., and Tinkey, Y. (2003). Impact Echo Scanning Technology for Internal Grout Condition Evaluation in Post-Tensioned Bridge Ducts. *International Symposium Non-Destructive Testing in Civil Engineering 2003*.
- Behringer, R. P., Jaeger, H. M., and Nagel, S. R. (1996). Granular solids, liquids, and gases. *Reviews of Modern Physics*, 68(4), 1259-1271. Retrieved from <http://tid.uio.no/~dansh/pdf/author/jaeger-RMP.pdf>
- Bentz, D. P. (2009). Influence of internal curing using lightweight aggregates on interfacial transition zone percolation and chloride ingress in mortars. *Cement and Concrete Composites*, 31, 181-193.
- Bentz, D. P., Ehlen, M. A., Ferraris, C. F., and Garboczi, E. J. (2001). Sorptivity-Based Service Life Predictions for Concrete Pavements. *7th International Conference on Concrete Pavements*. Orlando, FL.
- Bentz, D., Caston, J., Henkensiefken, R., Nantung, T., and Weiss, J. (2009). Water absorption in internally cured mortar made with water-filled lightweight aggregate. *Cement and Concrete Research*, 39, 883-892.
- Beris, A. N., and Tsamopoulos, J. A. (1985). Creeping motion of a sphere through a Bingham plastic. *Journal of Fluid Mechanics* 158, 219-244.
- Bond, W. N. (1927). LXXXII. Bubble and drops and Stokes' law. *The London, Edinburgh, and Dublin Philosophical Magazine and Journal of Science* , 4(24), 889-898.
- Bonnaud, P. A., Coasne, B., Ji, Q., Pellenq, R. J. -M., and van Vliet, K. J. (2012). Thermodynamics of water confined in porous calcium-silicate-hydrates. *Langmuir*, 28, 11422-11432.
- Bristow, K. L., and Campbell, C. S. (1984). On the relationship between incoming solar radiation and daily maximum temperature and minimum temperature. *Agricultural and Forest Meteorology*, 31, 159-166.
- Burden, R. L., and Faires, J. D. (2001). *Numerical Analysis 7th Ed*. Pacific Grove, CA: Brooks/Cole.
- Campbell, G. S., and Norman, J. M. (1998). *Introduction to Environmental Biophysics 2nd Ed*. New York: Springer-Verlag.
- Cao, J. (2014). *A study of effects of a new agricultural-based deicer on the properties of pavement concrete*. Ames, IA: Iowa State University.
- Carino, N. J., and Malhotra, V. (2003). *Handbook on Nondestructive Testing of Concrete, Second Edition*. West Conshohocken, PA: CRC Press.
- Carlos, C. (2005). *Microscopic observations of internal frost damage and salt scaling*. Berkeley: University of California, Berkeley.

- Castaneda, D. I., Lange, D. A., Riding, K. A., Song, Y., and Zou, R. (2017). Advances in Measuring Air-Void Parameters in Hardened Concrete Using Flatbed Scanner. *ASTM Journal of Testing and Evaluation*.
- Castro, J., Li, W., Pour-Ghaz, M., and Weiss, J. (2012). Water Absorption and Critical Degree of Saturation Relating to Freeze-Thaw Damage in Concrete Pavement Joints. *Journal of Materials in Civil Engineering*, 24, 299-307.
- Chan, J. (2013). *Thermal properties of concrete with different Swedish aggregate materials*. Lund, Sweden: Lund University. Retrieved from <http://lup.lub.lu.se/luur/download?func=downloadFile&recordId=4358448&fileId=4358449>
- Chancey, R., Folliard, K. J., Juenger, M. C., and Ley, M. T. (2009). The physical and chemical characteristics of the shell of air-entrained bubbles in cement paste. *Cement and Concrete Research*, 39(5), 409-416.
- Charles, S., and Poyet, S. (2009). Temperature dependence of the sorption isotherms of cement-based materials: heat of sorption and Clausius-Clapeyron formula. *Cement and Concrete Research*, 39, 1060-1067.
- Chateau, X., Ducicou, L., Goyon, J., Kogan, M., and Pitois, O. (2013). Mixtures of foam and paste: suspensions of bubbles in yield stress fluids. *Rheologica Acta* (52)3, 237-253.
- Chateau, X., Mahaut, F., Mokeddem, S., Ovarlez, G., and Roussel, N. (2008). Effect of coarse particle volume fraction on the yield stress and thixotropy of cementitious materials. *Cement and Concrete Research*, 38, 1276-1285. Retrieved from <https://hal.archives-ouvertes.fr/hal-00498881/document>
- Chen, F., McLean, D. I., and Qiao, P. (2012). *Concrete Performance Using Low-Degradation Aggregates*. Pullman, WA: Washington State Department of Transportation.
- Choo, J., Kang, D. H., Kim, K. Y., Shin, H. S., and Yun, T. S. (2012). Determination of air-void parameters of hardened cement-based materials using X-ray computed tomography. *Construction and Building Materials*, 37, 93-101.
- Darwin, D., Mindess, S., and Young, J. F. (2003). *Concrete 2nd Ed*. Upper Saddle River, NJ: Prentice Hall.
- Dempsey, B. J., and Thompson, M. R. (1970). A heat transfer model for evaluating frost action and temperature related effects in multilayered pavement systems. *Highway Research Record*, 342, 39-56.
- Dobruskin, V. K. (2008). Effect of Meniscus Geometry on Equilibrium Pressures of the Lennard-Jones Liquids. *Langmuir*, 24, 9375-9380.
- Dolch, W. L. (1996). Air-Entraining Admixtures. In *Concrete Admixtures Handbook: Properties, Science and Technology* (pp. 518-537). Ottawa, Canada: National Research Council Canada.
- Du, L., and Folliard, K. J. (2005). Mechanisms of air entrainment in concrete. *Cement and Concrete Research*, 35(8), 1463-1471.

- Dux, P., Leech, C., and Lockington, D. (2003). Unsaturated diffusivity functions for concrete derived from NMR images. *Materials and Structures*, 36, 413-418. Retrieved from <http://demo.webdefy.com/rilem-new/wp-content/uploads/2016/09/1260.pdf>
- Einstein, A. (1905). Viscosity of a dilute suspension. *Ann Physik*, 17, 549.
- Eriksson, B. -E., and Tepponen, P. (1967). Damages in concrete railway sleepers in Finland. *Nordic Concrete Research*, 6, 199-209.
- Espinosa, R. M., and Franke, L. (2006). Influence of the age and drying process on pore structure and sorption isotherms of hardened cement paste. *Cement and Concrete Research*, 36, 1969-1984.
- Fagerlund, G. (1977). The critical degree of saturation method of assessing freeze/thaw resistance of concrete. *Réunion Internationale des Laboratoires et Experts des Matériaux Committee*, 4.
- Ferdous, W., and Manalo, A. (2014). Failures of mainline railway sleepers and suggested remedies -- review of current practice. *Engineering Failure Analysis*, 44, 17-35.
- Forcella, F., and Spokas, K. (2006). Estimating hourly incoming solar radiation from limited meteorological data. *Weed Science*, 54, 182-189.
- Foy, C., Pigeon, M., and Plante, P. (1989). The influence of water-reducers on the production and stability of the air void system in concrete. *Cement and Concrete Research*, 19(4), 621-633.
- Fraser, J. K. (1959). Freeze-Thaw Frequencies and Mechanical Weathering in Canada. *ARCTIC North American*, 12(1). Retrieved from <http://citeseerx.ist.psu.edu/viewdoc/download?doi=10.1.1.579.1476&rep=rep1&type=pdf>
- Hanotin, C., Michot, L. J., and de Richter, S. K. (2015). Viscoelasticity of vibrated granular suspensions. *Journal of Rheology*, 253-273.
- Hansen, K. K. (1986). *Sorption Isotherms - A Catalogue*. Technical University of Denmark, Department of Civil Engineering, Building Materials Laboratory.
- Hanson, T. D. (2012). *Evaluation of the RapidAir 457 Air Void Analyzer*. Ames, IA: Iowa Department of Transportation.
- Hargreaves, G. H., and Samani, Z. A. (1985). Reference Crop Evapotranspiration from Temperature. *Applied Engineering in Agriculture*, 1, 96-99.
- Helmuth, R. A. (1961). Dimensional Changes of Hard-ened Portland Cement Pastes Caused by Temperature Changes. *Proceedings of the Fortieth Annual Meeting of the Highway Research Board*, 40, pp. 315-336. Washington, DC.
- Hershfield, D. M. (1973). The Frequency of Freeze-Thaw Cycles. *Journal of Applied Meteorology*, 13, 348-354.
- Higginson, E. C. (1952). Some Effects of Vibration and Handling on Concrete Containing Entrained Air. *ACI Journal Proceedings*, 49(9), 1-12.
- Hiller, J. E., and Qin, Y. (2014). Simulating moisture distribution within concrete pavement slabs: model development and sensitivity study. *Materials and Structures*, 47, 351-365.

- Hooton, R. D., and Ramezaniapour, A. M. (2010). Evaluation of Two Automated Methods for Air-Void Analysis of Hardened Concrete. *Journal of ASTM International*, 7(2).
- Hover, K. (2003). Air in concrete: expect variability in gaining, losing, and measuring: part 2 of a two part series. *Concrete Construction*, 48(1), 55-59.
- Hover, K. C. (2001). Vibration Tune-Up. *Concrete International*, 23(9), 31-35.
- Hover, K. C. (2006). Air Content and Density of Hardened Concrete. In J. F. Lamond, & J. H. Pielert (Eds.), *ASTM STP 169D: Significance of Tests and Properties of Concrete and Concrete-Making Materials* (pp. 288-308). Bridgeport, NJ: The American Society for Testing and Materials.
- Hover, K., Natesaiyer, K., and Snyder, K. (2001). *The Stereological and Statistical Properties of Entrained Air Voids in Concrete: A Mathematical Basis for Air Void System Characterization*. Westerville, OH: S. Mindess and J. Skalny, Eds., American Ceramic Society.
- International Atomic Energy Agency. (2002). *Guidebook on non-destructive testing of concrete structures*. Vienna, Austria: Industrial Applications and Chemistry Section. Retrieved from https://www-pub.iaea.org/mtcd/publications/pdf/tcs-17_web.pdf
- Jiang, Q., and Struble, L. J. (2004). Effects of Air Entrainment on Rheology. *ACI Materials Journal*, 101(6), 448-456.
- Jolicoeur, C., and Mikanovic, N. (2008). Influence of superplasticizers on the rheology and stability of limestone and cement pastes. *Cement and Concrete Research*, 38, 907-919.
- Jordan, R. C., and Liu, B. Y. (1960). The interrelationship and characteristic distribution of direct, diffuse, and total solar radiation. *Solar Energy*, 4, 1-19.
- Jupp, D. L., and McVicar, T. R. (1999). Estimating one-time-of-day meteorological data as inputs to thermal remote sensing based on energy balance models. *Agricultural and Forest Meteorology*, 96, 219-238.
- Kamal, H., Khayat, K. H., and Assaad, J. (2002). Air-Void Stability in Self-Consolidating Concrete. *ACI Materials Journal*, 99(4), 408-416. Retrieved from <http://imcyc.com/biblioteca/ArchivosPDF/Concreto%20Autocompactado/Air-Void%20Stability%20in%20Self-Consolidating%20Concrete.pdf>
- Kang, S. -T., Kim, J. -K., Kim, J. -S., Lee, Y., and Park, Y. -D. (2012). Moisture diffusivity of early age concrete considering temperature and porosity. *KSCE Journal of Civil Engineering*, 16, 179-188.
- Kennedy, T. W., and Solaimanian, M. (1993). Predicting Maximum Pavement Surface Temperature Using Maximum Air Temperature and Hourly Solar Radiation. *Transportation Research Record*, 1417, 1-11. Retrieved from <http://onlinepubs.trb.org/Onlinepubs/trr/1993/1417/1417-001.pdf>
- Kerkhoff, B., Kosmatka, S. H., and Panarese, W. C. (2002). *Design and Control of Concrete Mixtures* (14th ed.). Skokie, IL: Portland Cement Association.
- Khayat, K. H., and Nasser, K. W. (1991). Comparison of Air Contents in Fresh and Hardened Concretes Using Different Airmeters. *Cement, Concrete, and Aggregates*, 13(1), 18-24.

- Kim, J. -K., and Lee, C. -S. (1999). Moisture diffusion of concrete considering self-dessication at early ages. *Cement and Concrete Research*, 29, 1921-1927.
- Klieger, P., and Perenchio, W. F. (1976). *Further Laboratory Studies of Portland-Pozzolan Cements*. Skokie, IL: Portland Cement Association.
- Kuhne, H. C., Meng, B., Roussel, N., and Vasilic, K. (2011). Flow of fresh concrete through steel bars: A porous medium analogy. *Cement and Concrete Research* 41.5, 496-503.
- Landgren, R., and Verbeck, G. (1960). Influence of Physical Characteristics of Aggregates on the Frost Resistance of Concrete. *Proceedings of the American Society for Testing Materials*, 60, 1063-1079.
- Lane, D., Stutzman, P. E., and Walker, H. N. (2006). *Petrographic Methods of Examining Hardened Concrete: A Petrographic Manual*. McLean, VA: Federal Highway Administration.
- Łazniewska-Piekarczyk, B. (2012). The influence of selected new generation admixtures on the workability, air-voids parameters and frost-resistance of self compacting concrete. *Construction and Building Materials*, 31, 310–319.
- Łazniewska-Piekarczyk, B. (2013). The type of air-entraining and viscosity modifying admixtures and porosity and frost durability of high performance self-compacting concrete. *Construction and Building Materials*, 40, 659-671.
- Litvan, G. G. (1988). The mechanism of frost action in concrete - theory and practical implications. *Proceedings of Workshop on Low Temperature Effects on Concrete*. Montreal, Canada.
- Litvan, G. G., and Sereda, P. J. (1980). Freeze-Thaw Durability of Porous Building Materials. *Durability of Building Materials and Components ASTM STP 691*, 455-463.
- Litvan, G. G., Sakai, K., and Shimada, H. (1991). Acoustic emissions of mortar subjected to freezing and thawing. *Durability of Concrete: Second International Conference*. Detroit, MI.
- Litwinowicz, F. J., and Scripture, E. W. J. (1949). Effects of Mixing Time, Size of Batch and Brand of Cement on Air Entrainment. *Journal of the American Concrete Institute*, 45(5), 653-662.
- Liu, D. L. (1996). Incorporation diurnal light variation and canopy light attenuation into analytical equations for calculating daily gross photosynthesis. *Ecological Modelling*, 93, 175-189.
- Maxim. (2013). *DS1923 Revision 5*. Maxim Integrated.
- Mehta, P. K. (1990). Durability of High-Strength Concrete. *ACI Special Publication*, 122, 19-27.
- Meininger, R., and Tanesi, J. (2006). *Freeze-Thaw Resistance of Concrete With Marginal Air Content*. McLean, VA: FHWA Office of Infrastructure Research and Development, FHWA-HRT-06-117.
- Monteith, J. L. (1965). Evaporation and the Environment. In the state and movement of water in living organisms. *Proceedings of the 19th Symposium Society for Experimental Biology*. Cambridge.

- Nagi, M. (2007). *Evaluating Air-Entraining Admixtures for Highway Concrete*. Washington, DC: Transportation Research Board.
- Nmai, C. K. (2006). Freezing and Thawing. In *ASTM STP 169D: Significance of Tests and Properties of Concrete and Concrete-Making Materials* (pp. 154-163). Bridgeport, NJ: American Society for Testing and Materials.
- Olek, J., Peterson, K., Radlinski, M., and Zhang, Q. (2010). Evaluation of the Critical Air-Void System Parameters for Freeze-Thaw Resistant Ternary Concrete Using the Manual Point-Count and the Flatbed Scanner Methods. *Journal of ASTM International*, 7(4).
- Ozyildirim, C. (1991). Comparison of the Air Contents of Freshly Mixed and Hardened Concretes. *Cement, Concrete, and Aggregates*, 13(1), 11-17.
- Page, C. L., and Page, M. M. (Eds). (2007). *Durability of Concrete and Cement Composites*. Cambridge, England: Woodhead Publishing.
- Papo, A., and Piani, L. (2004). Effect of various superplasticizers on the rheological properties of Portland cement pastes. *Cement and Concrete Research*, 34, 2097-2101.
- Peterson, K. (2001). *Air void analysis of hardened concrete via flatbed scanner*. Houghton, MI: Unpublished Master's Thesis, Michigan Technological University.
- Peterson, K. W., Sutter, L. L., and Van Dam, T. J. (2002). An Experiment with a High Resolution Flatbed Scanner to Examine Variability in ASTM C 457 Test Results from a Single Concrete Specimen. *ASTM Cement Concrete Aggregates Symposium*.
- Peterson, K., Sutter, L., and Van Dam, T. (2002). Air void analysis of hardened concrete with a high-resolution flatbed scanner. *Proceedings of the 24th International Conference on Cement Microscopy*. San Diego, CA. Retrieved from <http://citeseerx.ist.psu.edu/viewdoc/download?doi=10.1.1.566.9775&rep=rep1&type=pdf>
- Pielichowski, J., Prociak, A., and Sterzynski, T. (2000). Thermal diffusivity of rigid polyurethane foams blown with different hydrocarbons. *Polymer Testing*, 19, 705-712.
- Pigeon, M., and Pleau, R. (1995). *Modern Concrete Technology 4: Durability of Concrete in Cold Climates*. New York: CRC Press.
- Pomeroy, D. (1987). Concrete Durability: From Basic Research to Practical Reality. *ACI Special Publication*, 100, 111-130.
- Popovics, S. (1998). *Strength and Related Properties of Concrete: A Quantitative Approach*. Hoboken, NJ: John Wiley & Sons.
- Powers, T. C. (1945). A Working Hypothesis for Further Studies of Frost Resistance of Concrete. *Journal of the American Concrete Institute*, 16(4), 245-271.
- Powers, T. C., and Willis, T. F. (1949). The Air Requirement of Frost Resistant Concrete. *29th Annual Highway Research Board*, 29, pp. 184-211. Washington, DC.
- Powers, T.C. (1968). *The Properties of Fresh Concrete*. New York: John Wiley & Sons.
- Pruckner, F. (2013). RH Measurements for Assessing Moisture Conditions in Concrete Structures. *Beton-und Stahlbetonbau*, 108, 865-874.

- Roesler, J. R., and Wang, D. (2014). One-dimensional temperature profile prediction in multi-layered rigid pavement systems using a separation of variables method. *International Journal of Pavement Engineering*, 15, 373-382.
- Roscoe, R. (1952). The viscosity of suspensions of rigid spheres. *British Journal of Applied Physics*, 3(8), 267.
- Rotronic. (2005). *The Rotronic Humidity Handbook*. Rotronic Instrument Corp.
- SawanI, J. S. (1987). Cracking Due to Frost Action in Portland Cement Concrete Pavements--A Literature Survey. *ACI Special Publication*, 100, 781-804.
- Scherer, G. W., and Sun, Z. (2008). Kinetics of Ice Growth in Cement and Concrete. *International RILEM Symposium on Concrete Modeling - ConMod '08*, (pp. 183-190).
- Schlroholtz, S. (1998). *Image Analysis for Evaluating Air Void Parameters of Concrete*. Ames, IA: Iowa Department of Transportation.
- Stark, D., and Whiting, D. (1983). *Control of Air Content in Concrete*. Washington, D.C.: Transportation Research Board. Retrieved from <https://trid.trb.org/view/194803>
- Struble, L. J., and Sun, G. -K. (1993). Cement Viscosity as a Function of Concentration. *Proceedings of the Materials Research Society Symposium*, 289, 173-176.
- Vazques, E. (2004). Admixtures for Concrete-Improvement of Properties. *Proceedings of the International RILEM Symposium*. CRC Press.
- W.W Grainger, Inc. (n.d.). *Roll-a-Meter, Aluminum*. Retrieved March 18, 2014, from <http://www.grainger.com/product/RollAMeter-Air-Indicator-5ZPX1?Pid=search>
- Winter, A. G. (2011). *Biologically Inspired Mechanisms for Burrowing in Undersea Substrates*. Diss. Massachusetts Institute of Technology.
- Yang, Q. (1999). Inner relative humidity and degree of saturation in high-performance concrete stored in water or salt solution for 2 years. *Cement and Concrete Research*, 29, 35-43.
- Yang, Z. (2004). *Assessing cumulative damage in concrete and quantifying its influence on life cycle performance modeling*. West Lafayette, IN: Purdue University.
- Zeman, J. C. (2010). *Hydraulic Mechanisms of Concrete-Tie Rail Seat Deterioration*. Urbana, IL: University of Illinois at Urbana-Champaign.

Abbreviations and Acronyms

AV	After Vibration
AEA	Air Entraining Agents
<i>A</i>	Air Content
BV	Before Vibration
BH	Bottom-Half
CN	Canadian National Railway
S_{CR}	Critical Degree of Saturation
P-Wave	Displacement Wave
DF	Durability Factor
V_w	Evaporable Water
FFT	Fast Fourier Transform
HRWR	High Range Water Reducers
IDOT	Illinois Department of Transportation
IE	Impact Echo
ITZ	Interfacial Transition Zone
ICAR	International Center for Aggregate Research
LRWR	Low-Range Water Reducer
M	Mixer
MOR	Modulus of Rupture
<i>p</i>	Paste Content
V_P	Open Pore Volume
QC	Quality Control Laboratory
RH	Relative Humidity
SCC	Self-Consolidating Concrete
TH	Top-Half
UPV	Ultrasonic Pulse Velocity
UP	Union Pacific Railroad
V_L	Volumetric Amount of Liquid
V_S	Volumetric Amount of Solid
W/CM	Water-Cementitious Material Ratio
W/C	Water-Cement Ratio

AV

After Vibration

WR

Water Reducers